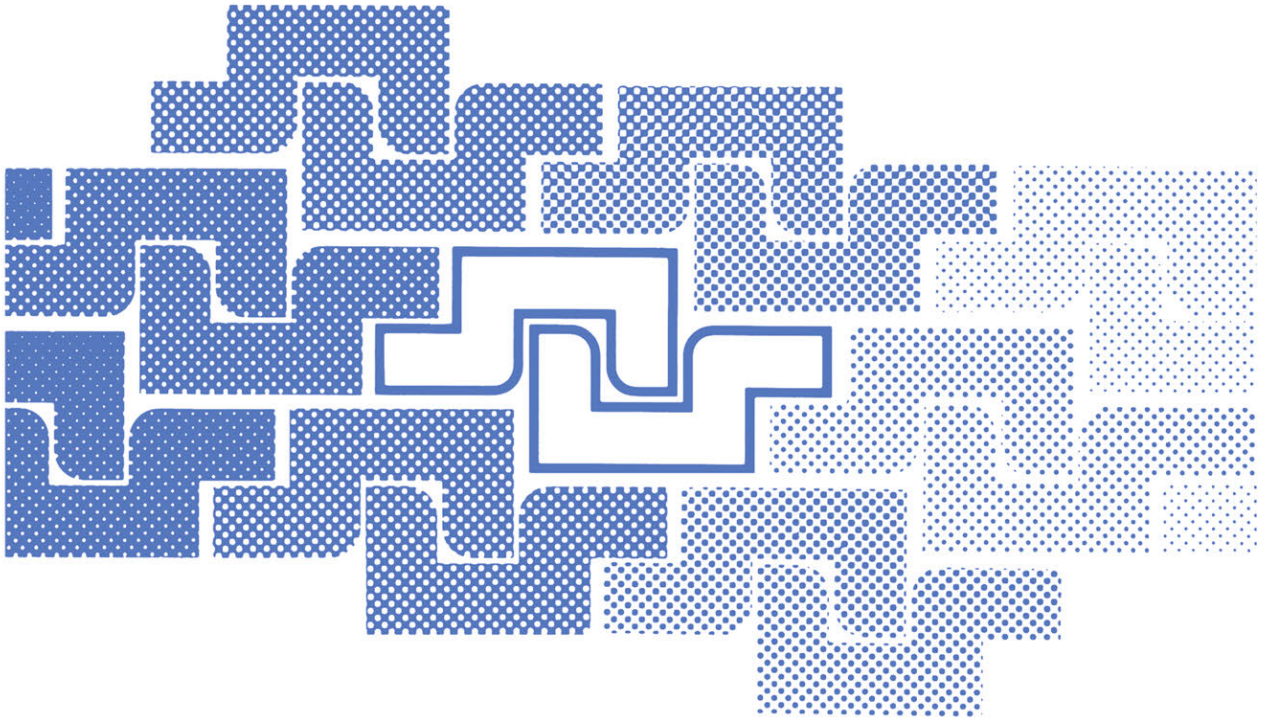

Photonic Band Gaps and Localization

Edited by

C. M. Soukoulis

NATO ASI Series

Series B: Physics Vol. 308

Photonic Band Gaps and Localization

NATO ASI Series

Advanced Science Institutes Series

A series presenting the results of activities sponsored by the NATO Science Committee, which aims at the dissemination of advanced scientific and technological knowledge, with a view to strengthening links between scientific communities.

The series is published by an international board of publishers in conjunction with the NATO Scientific Affairs Division

A Life Sciences **B Physics**	Plenum Publishing Corporation New York and London
C Mathematical and Physical Sciences **D Behavioral and Social Sciences** **E Applied Sciences**	Kluwer Academic Publishers Dordrecht, Boston, and London
F Computer and Systems Sciences **G Ecological Sciences** **H Cell Biology** **I Global Environmental Change**	Springer-Verlag Berlin, Heidelberg, New York, London, Paris, Tokyo, Hong Kong, and Barcelona

Recent Volumes in this Series

Volume 306 — Ionization of Solids by Heavy Particles
edited by Raúl A. Baragiola

Volume 307 — Negative Differential Resistance and Instabilities in 2-D Semiconductors
edited by N. Balkan, B. K. Ridley, and A. J. Vickers

Volume 308 — Photonic Band Gaps and Localization
edited by C. M. Soukoulis

Volume 309 — Magnetism and Structure in Systems of Reduced Dimension
edited by Robin F. C. Farrow, Bernard Dieny, Markus Donath, Albert Fert, and B. D. Hermsmeier

Volume 310 — Integrable Quantum Field Theories
edited by L. Bonora, G. Mussardo, A. Schwimmer, L. Girardello, and M. Martellini

Volume 311 — Quantitative Particle Physics: *Cargèse 1992*
edited by Maurice Lévy, Jean-Louis Basdevant, Maurice Jacob, Jean Iliopoulos, Raymond Gastmans, and Jean-Marc Gérard

Volume 312 — Future Directions of Nonlinear Dynamics in Physical and Biological Systems
edited by P. L. Christiansen, J. C. Eilbeck, and R. D. Parmentier

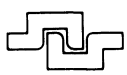

Series B: Physics

Photonic Band Gaps and Localization

Edited by

C. M. Soukoulis

Ames Laboratory and Department of Physics
Iowa State University
Ames, Iowa

Springer Science+Business Media, LLC

Proceedings of a NATO Advanced Research Workshop on
Localization and Propagation of Classical Waves in Random and Periodic Structures,
held May 26–30, 1992,
in Aghia Pelaghia, Heraklion, Crete

NATO-PCO-DATA BASE

The electronic index to the NATO ASI Series provides full bibliographical references (with keywords and/or abstracts) to more than 30,000 contributions from international scientists published in all sections of the NATO ASI Series. Access to the NATO-PCO-DATA BASE is possible in two ways:

—via online FILE 128 (NATO-PCO-DATA BASE) hosted by ESRIN, Via Galileo Galilei, I-00044 Frascati, Italy

—via CD-ROM "NATO-PCO-DATA BASE" with user-friendly retrieval software in English, French, and German (©WTV GmbH and DATAWARE Technologies, Inc. 1989)

The CD-ROM can be ordered through any member of the Board of Publishers or through NATO-PCO, Overijse, Belgium.

Library of Congress Cataloging in Publication Data

Photonic band gaps and localization / edited by C. M. Soukoulis.
p. cm.—(NATO ASI series. Series B, Physics; vol. 308)
"Published in cooperation with NATO Scientific Affairs Division."
"Proceedings of a NATO Advanced Research Workshop on Localization and Propagation of Classical Waves in Random and Periodic Structures, held May 26–30, 1992, in Aghia Pelaghia, Heraklion, Crete"—T. p. verso.
Includes bibliographical references and index.

1. Anderson model—Congresses. 2. Wave-motion, Theory of—Congresses. 3. Electromagnetic waves—Transmission—Congresses. 4. Photon transport theory—Congresses. I. Soukoulis, C. M. II. North Atlantic Treaty Organization. Scientific Affairs Division. III. NATO Advanced Research Workshop on Localization and Propagation of Classical Waves in Random and Periodic Structures (1992: Aghia Pelaghia, Greece). IV. Series: NATO ASI series. Series B, Physics; v. 308.
QC176.8.E4P53 1993 93-8664
530.4'1—dc20 CIP

ISBN 978-1-4899-1608-2 ISBN 978-1-4899-1606-8 (eBook)
DOI 10.1007/978-1-4899-1606-8

Originally published by Plenum Press, New York in 1993.
Softcover reprint of the hardcover 1st edition 1993

PREFACE

This volume contains the papers presented at the NATO Advanced Research Workshop on *Localization and Propagation of Classical Waves in Random and Periodic Media* held in Aghia Pelaghia, Heraklion, Crete, May 26-30, 1992.

The workshop's goal was to bring together theorists and experimentalists from two related areas, localization and photonic band gaps, to highlight their common interests. The objectives of the workshop were (i) to assess the state-of-the-art in experimental and theoretical studies of structures exhibiting classical wave band gaps and/or localization, (ii) to discuss how such structures can be fabricated to improve technologies in different areas of physics and engineering, and (iii) to identify problems and set goals for further research.

Studies of the propagation of electromagnetic (EM) waves in periodic and/or disordered dielectric structures (photonic band gap structures) have been and continue to be a dynamic area of research. Anderson localization of EM waves in disordered dielectric structures is of fundamental interest where the strong el-el interaction effects entering the electron-localization are absent. Also, in analogy to the case of electron waves propagating in a crystal, classical EM waves traveling in periodic dielectric structures will be described in terms of photonic bands with the possibility of the existence of frequency gaps where the propagation of EM waves is forbidden. The potential applications of such photonic band gaps are very interesting. It has been suggested that the inhibition of spontaneous emission in such gaps can be utilized to substantially enhance the performance of semiconductor lasers and other quantum electronic

devices. Photonic band gap materials can also find applications in frequency-selective mirrors, band-pass filters, and resonators. In addition, it has been proposed that Anderson localization of light near a photonic band gap might be achieved by weak disordering of a periodic arrangement of spheres.

This book contains papers summarizing the "state-of-the-art" of the photonic band gap and classical localization areas of research. The collection of the papers is roughly balanced between theory and experiment. It contains chapters that present latest research results appropriate of an advanced research workshop, as well as ones that review a particular field, with the goal of providing the reader with a sufficient overview and extensive references for a more detailed study. The book is divided into three parts representing the various topics discussed at the workshop. Part I covers those topics that are primarily related to the localization of waves in disordered media. Part II provides an up-to-date experimental and theoretical review of the photonic band gap field. It also discusses the potential applications of the photonic band gaps. Finally, Part III covers the more mathematical aspects of the wave propagation in disordered media and in addition some specific topics are also given.

The workshop was made possible through the generous support of the NATO Scientific Affairs Division, Brussels, Belgium and the Ames Laboratory, operated by the U.S. Department of Energy by Iowa State University under Contract No. W-7405-Eng-82. I would like to thank the organizing committee, E. N. Economou, S. John, and A. Lagendijk for their valuable help on the organization of the program and the workshop. I would like to express my appreciation to Rebecca Shivvers, who prepared the conference materials and edited the manuscripts for this book. Finally, I wish to express my deepest appreciation to all the participants for making this a lively and enjoyable workshop.

C. M. Soukoulis
Physics Department
Ames Laboratory
Iowa State University
Ames, Iowa 50011 U.S.A.

CONTENTS

LOCALIZATION, DIFFUSION, AND CORRELATION

PHOTONIC BAND GAPS

WAVE PROPAGATION IN RANDOM MEDIA

THE LOCALIZATION OF LIGHT

Sajeev John

Department of Physics
University of Toronto
Toronto, Ontario, Canada M5S 1A7

ABSTRACT

I present a theoretical overview of photon localization in disordered and periodic structures. Some possible new directions are suggested.

1. INTRODUCTION

Wave propagation in strongly scattering media is a subject with a long and diverse history. The quantum mechanical wave nature of ordinary matter on the microscopic scale is based on an analogy with the scattering and interference of classical waves. Yet it is only recently that the analogy has been reversed and the possibility that phenomena normally associated with quantum mechanical de-Broglie waves might be observed with classical waves has been fully explored. Electromagnetism is the mediator of fundamental interactions in condensed matter physics and quantum optics. The localization of photons in analogy with the localization of electrons[1] is a fundamental alteration of these interactions. It opens the door to a number of new physical phenomena which are only beginning to be explored theoretically and experimentally. In this article, I review the underlying physics of photon localization in disordered and periodically ordered dielectric materials. In addition, I discuss areas of current activity within the field and suggest some possible new avenues for basic research.

Light localization[2] is an effect which arises entirely from coherent multiple scattering and interference. It may be understood purely from the point of view of classical electromagnetism. In traditional studies of electromagnetic wave propagation in dielectrics, scattering takes place on scales much longer than the wavelength of light. Localization of light, much the same as electrons, occurs when the scale of coherent multiple scattering is reduced to the wavelength itself. This is an entirely new and unexplored regime of optical transport with both fundamental and practical significance. Unlike its electronic counterpart, a photon in lossless dielectric media provides an ideal realization of a single excitation in a static random medium at room temperature. It is not hampered by the inevitable presence of electron-electron interactions and electron-phonon interactions which occur in the study of electron

Photonic Band Gaps and Localization, Edited by
C.M. Soukoulis, Plenum Press, New York, 1993

localization. High resolution optical techniques offer the unique possibility studying the angular, spatial and temporal dependence of wave field intensities near a localization transition. From a fundamental point of view, photon localization offers the most direct experimental test of our understanding of transport in strongly scattered media. On the practical side, multiple scattering spectroscopy is already proving to be a valuable tool in studying the hydrodynamics of colloids, suspensions and other dense complex fluids. In the field of medicine, multiply scattered electromagnetic waves already provide a valuable noninvasive probe of biological tissue.

Light localization which occurs at a purely classical level, also has fundamental consequences at the quantum level. This is most easily seen in the extreme limit of a dielectric exhibiting a complete photonic band gap in frequency in analogy with the electronic energy band gap of a semiconductor. Such a microstructure consists of a periodic array of high dielectric spheres of diameter (and lattice constant) comparable to the wavelength of light. Strictly speaking, in such a structure there are no allowed electromagnetic modes in the forbidden frequency range. However, as in a semiconductor an impurity placed within the material will introduce localized modes into the gap. In this photonic analog of a semiconductor, an impurity atom with a transition frequency in the localization regime will not exhibit spontaneous emission of light, but instead, the emitted photon will form a bound state to the atom! Both the classical electrodynamics which leads to localization and the concomitant alteration of quantum electrodynamics suggest new frontiers of basic research spanning the disciplines of condensed matter physics and quantum optics.

2. ANALOGY BETWEEN PHOTONS AND ELECTRONS

In the case of electron localization, nature provides a variety of readily available materials. Localization is more often the rule than the exception. This is easily seen from the Schrödinger equation for an electron with effective mass m^*:

$$\left[\frac{-\hbar^2}{2m^*}\nabla^2 + V(x)\right]\psi(x) = E\psi(x) \ . \tag{1}$$

A random potential $V(x)$ can trap electrons in deep local potential fluctuations when the energy E is sufficiently negative. As the energy increases, the probability of finding another nearby potential fluctuation into which the trapped electron can tunnel increases. To quantify these ideas, consider $V(x)$ to have a root mean square amplitude $V_{\rm rms}$ and a length scale a on which random fluctuations take place. The correlation length to the disorder a defines an energy scale $\epsilon_a \equiv \hbar^2/(2m^*a^2)$. For example, in an amorphous semiconductor a is the interatomic spacing, ϵ_a plays a role analogous to the conduction band width of the semiconductor, and the zero of energy corresponds to the conduction band edge of the corresponding crystal. In the weak disorder limit $V_{\rm rms} \ll \epsilon_a$, a transition takes place as the electron energy is increased to about $-V_{\rm rms}^2/\epsilon_a$ in which successive tunnelling events allow the electron to traverse the entire solid by a slow diffusive process and thereby conduct electricity. This transition energy has been termed a mobility edge by N.F. Mott.[3] At higher and higher energies the scale on which multiple scattering takes place grows larger and larger than the electron's de Broglie wavelength and the electron traverses the solid with relative ease. If the disorder is made strong $V_{rms} \gg \epsilon_a$, the mobility edge moves into the conduction band continuum ($E > 0$) and eventually the entire band may be engulfed by states exhibiting Anderson localization. Since disorder is a nearly universal

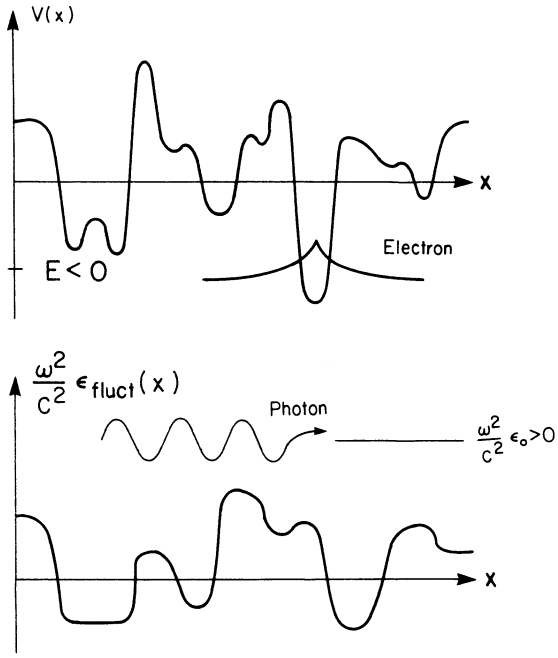

Fig. 1 In the case of photon localization, $\frac{\omega^2}{c^2}\epsilon_{\text{fluct}}(x)$ plays the role of the scattering potential. Unlike the picture for electrons, the eigenvalue $\frac{\omega^2}{c^2}\epsilon_0$ is always higher than the highest of the potential barriers in the case of a real, positive dielectric constant.

feature of real materials, electron localization is likewise an ubiquitous ingredient in determining electrical, optical and other properties of condensed matter.

In the case of monochromatic electromagnetic waves of frequency ω propagating in an inhomogeneous but nondissipative dielectric medium, the classical wave equation for the electric field amplitude $\vec{E}$ may be written in a form resembling the Schrödinger equation:

$$-\nabla^2\vec{E} + \vec{\nabla}(\vec{\nabla}\cdot\vec{E}) - \frac{\omega^2}{c^2}\epsilon_{\text{fluct}}(x)\vec{E} = \epsilon_0\frac{\omega^2}{c^2}\vec{E} \ . \tag{2}$$

Here, I have separated the total dielectric constant $\epsilon(x) = \epsilon_0 + \epsilon_{\text{fluct}}(x)$ into its average value ϵ_0 and a spatially fluctuating part $\epsilon_{\text{fluct}}(x)$. The latter plays a role analogous to the random potential $V(x)$ in the Schrödinger equation, and scatters the electromagnetic wave. For the case of a lossless material in which the dielectric constant $\epsilon(x)$ is everywhere real and positive, several important observations concerning the Schrödinger equation-Maxwell equation analogy are in order. First of all, the quantity $\epsilon_0\omega^2/c^2$ which plays a role analogous to an energy eigenvalue is always positive, thereby precluding the possibility of elementary bound states of light in deep negative potential wells. It is also noteworthy that the laser frequency ω multiplies the scattering potential $\epsilon_{\text{fluct}}(x)$. Unlike an electronic system, where localization was enhanced by lowering the electron energy, lowering the photon energy instead leads to a complete disappearance of the scattering mechanism itself. In the opposite, high

frequency limit, geometric ray optics becomes valid and interference corrections to optical transport become less and less effective. In both limits the normal modes of the electromagnetic field are extended, not localized. Finally, the condition that $\epsilon_0 + \epsilon_{\text{fluct}} > 0$ everywhere, translates into the requirement that the energy eigenvalue is always greater than the effective potential $|\frac{\omega^2}{c^2}\epsilon_{\text{fluct}}(x)|$. Unlike the familiar picture of electronic localization (Figure 1), what we are really seeking in the case of light is an intermediate frequency window of localization within the positive energy continuum and which lies at an energy higher than the highest of the potential barriers! It is for this simple reason that ordinary dielectrics appearing in nature do not easily exhibit photon localization.

It should be pointed out here, that in the above analogy I have emphasized similarities more than actual differences. The vector nature of the electromagnetic wave equation (2) makes it even *more* difficult to localize light than the above analogy would suggest. The polarization density term $\vec{\nabla} \cdot \vec{E}$ has no analog in the electronic case. Even in the absence of scattering, this term leads to a difference between the *microscopic* dielectric constant ϵ_0 and the average *macroscopic* dielectric constant which is measured on scales comparable to the electromagnetic wavelength λ. This latter subtlety, however, does not alter the subsequent discussion of scattering and localization provided that $\vec{E}$ in equation (2) is interpreted as the coarse-grained electric field which is the spatial average of the true microscopic electric field in which polarization effects on scales smaller than λ have been incorporated.

Independent Scatterers

The underlying physics of the high and low frequency limits in the case of photons can be made more precise by considering scattering from a single dielectric sphere. Consider a plane wave of wavelength λ impinging on a small dielectric sphere of radius $a \ll \lambda$ of dielectric constant ϵ_a embedded in a uniform background dielectric ϵ_b in $d = 3$ spatial dimensions. The scattered intensity I_{scatt} at a distance R from the sphere can be a function of only the incident intensity I_0, the dielectric constants ϵ_a and ϵ_b and the lengths R, λ and a. In particular I_{scatt} must be proportional to the square of the induced dipole moment of the sphere which scales as the square of its volume $\sim (a^d)^2$ and by conservation of energy must fall off as $1/R^{d-1}$ with distance from the scattering center:

$$I_{\text{scatt}} = f_1(\lambda, \epsilon_a, \epsilon_b)\frac{a^{2d}}{R^{d-1}} I_0 \ . \tag{3}$$

Since the ratio I_{scatt}/I_0 is dimensionless, it follows that $f_1(\lambda, \epsilon_a, \epsilon_b) = f_2(\epsilon_a, \epsilon_b)\ /\lambda^{d+1}$ where f_2 is another dimensionless function of the dielectric constants. The vanishing of the scattering cross section for long wavelengths as $\lambda^{-(d+1)}$ is the familiar result for why the sky is blue. This weak scattering is the primary reason that electromagnetic modes are extended in most naturally occurring three-dimensional systems. For a dense random collection of scatterers, this behavior remains evident in the elastic mean free path ℓ which is proportional to λ^{d+1} for long wavelengths. This generalization of Rayleigh scattering to d spatial dimensions is also applicable to anisotropic dielectric scattering systems. For example, a layered random medium in which scattering is confined to directions perpendicular to the layers would be described by setting $d = 1$. Alternatively, a collection of randomly spaced uniaxial rods[4] in which scattering is confined to the plane perpendicular to the axis of the rods would be described by setting $d = 2$. A consequence of the scaling theory of localization, which

applies to electrons in disordered solids as well as electromagnetic waves in disordered dielectrics, is that in one and two dimensions, all states are localized but with localization lengths ξ_{loc}, which diverge due to Rayleigh scattering in the low frequency limit, behaving as $\xi_{loc} \sim \ell$ in one dimension and $\xi_{loc} \sim \ell \exp(\frac{\omega}{c}\ell)$ in two dimensions.

It is likewise instructive to consider the opposite limit in which the wavelength of light is small compared to the scale of the scattering structures. For scattering from a single sphere it is well known that for $\lambda \ll a$ the cross section saturates at a value $2\pi a^2$. The factor of two includes the rays which are weakly diffracted out of the forward direction near the surface of the sphere. This is the result of geometric optics. For a dense random collection of scatterers, it is useful to introduce the notion of a correlation length a. On scales shorter than a, the dielectric constant does not vary appreciably except for the occasional interface where the physics of refraction and diffraction apply. The essential point is the elastic mean free path never becomes smaller than the correlation length. This classical elastic mean free path ℓ plays a central role in the physics of localization. Wave interference effects lead to large spatial fluctuations in the light intensity within the disordered medium. However, if $\ell \gg \lambda$, these fluctuations tend to average out to give a physical picture of essentially noninterfering, multiple scattering paths for electromagnetic transport. When $\ell \to \lambda/2\pi$ interference of multiple scattering paths drastically modifies the average transport properties and a transition from extended to localized normal modes takes place. If one adopts the most naïve version of the Ioffe Regel[5] condition $2\pi\ell/\lambda \simeq 1$ for localization, with λ being the vacuum wavelength or even an effective medium wavelength of light, it follows that extended states are expected at both high and low frequencies. However, as depicted in Figure 2, for strong scattering, there arises the distinct possibility of localization within a narrow frequency window when the quantity $\lambda/2\pi \simeq a$. It is this intermediate frequency regime which we wish to analyze in greater detail.

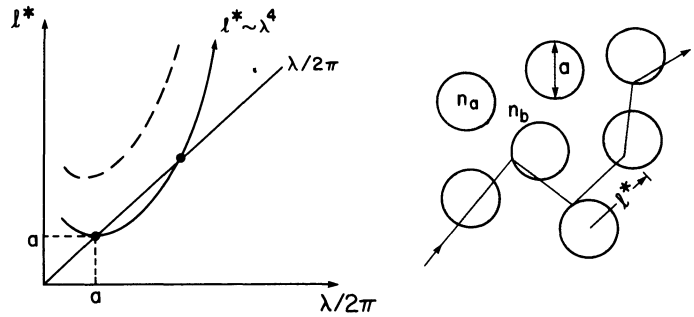

Fig. 2 The classical transport mean free path ℓ^* plays the role of the step length in the photon's random walk through the scattering medium. If the scattering microstructures have a single characteristic length scale a, then $\lambda \gg a$ and $\lambda \ll a$ are weak scattering regimes of Rayleigh scattering and classical geometric optics, respectively. For low refractive index contrast n_a/n_b, all states are extended (upper curve). For $n_a/n_b \gtrsim 2$, $\ell^* \sim \lambda/2\pi$, when $\lambda/2\pi \simeq a$ suggesting an intermediate frequency window of localization (lower curve).

I will refer to the aforementioned criterion for localization as the free-photon Ioffe-Regel condition. This particular result is based on perturbation theory about free photon states which undergo multiple scattering from point-like objects and a disorder average is performed over all possible positions of the scatterers. In effect, statistical weight is evenly distributed over all possible configurations of the scatterers and the medium has an essentially flat structure factor on average.

The first correction to this picture is to associate some nontrivial structure to the individual scatterers. The theory of Mie resonances for scattering from dielectric spheres immediately tells us this can have profound consequences on the elastic mean free path. For instance, for spheres of radius a, of dielectric constant ϵ_a embedded in a background dielectric ϵ_b, and for a ratio $\epsilon_a/\epsilon_b \simeq 4$, the first Mie resonance which occurs at a frequency given by $\omega/c(2a) \simeq 1$, yields a scattering cross section $\sigma \simeq 6\pi a^2$. For a relatively dilute collection of spheres of number density n, the classical elastic mean free path becomes $\ell \sim \frac{1}{n\sigma} = \frac{2a}{9f}$. Here I have introduced the volume filling fraction f of the spheres. Extrapolating this dilute scattering result to higher density, it is apparent that for a filling fraction $f \simeq 1/9$, the free-photon Ioffe Regel condition is satisfied on resonance. It is tempting to increase the density of scatterers to further decrease the mean free path. However, the fact that the cross section on resonance is 6 times the geometrical cross section indicates that a given sphere disturbs the wavefield over distances considerably larger than the actual sphere radius. The existence of the resonance requires the "spheres of influence" of the scatterers do not overlap. Indeed, for higher densities the spheres become optically connected in this sense and the mean free path increases rather than decreases. From the single scattering or microscopic resonance point-of-view, the free photon criterion for localization is a very delicate one to achieve. This conclusion has been borne out in the initial experiments by A.Z. Genack and M. Drake[6] on light scattering from randomly arranged dielectric spheres.

The Localization Criterion

The resolution of this dilemma is obtained by a careful reconsideration of the criterion for localization, introduced by Thouless for electrons. This criterion reduces to the Ioffe-Regel criterion provided that the phase space available for propagation is that of free photons. However, when the scattering microstructures cause a change in the overall photon density of states, significant modifications of the free-photon Ioffe-Regel criterion follow.

In the scaling theory of localization, the localization critical point is defined by a condition of the form

$$\rho(\omega)D(\omega)\ell^* \simeq 1 \qquad (d=3)$$

Here $\rho(\omega)$ is the photon density of states at frequency ω, $D(\omega)$ is the classical diffusion coefficient for light in a multiple scattering medium and ℓ^* is the classical transport mean free path. If the scattering microstructures do not significantly alter the photon density of states from its form in vacuum $\rho_{\text{vac}}(\omega) = \frac{1}{c}\left(\frac{\omega}{c}\right)^2$, then the localization criterion becomes $\left(\frac{\omega}{c}\ell^*\right)^2 \simeq 1$ as suggested by Ioffe and Regel. Here, we have used the fact that $D(\omega) \sim c\ell^*$. More generally, we may interpret the factor $4\pi\left(\frac{\omega}{c}\right)^2$ as representing the total phase space available for propagation of a photon of frequency ω. The general criterion for localization is then given by

$$(\text{phase space}) \times (\ell^*)^2 = 4\pi$$

In the event the phase space is reduced by some form of resonant scattering, it is apparent that localization may occur even if ℓ^* is considerably longer than the vacuum wavelength λ. This point is most graphically illustrated in the case of the photonic bandgap.

Coherent Scatterers and the Photonic Bandgap

The approach based on independent, uncorrelated scatterers overlooks one of the most important avenues for phase space reduction. In a sense it is the fundamental theorem of solid state physics: certain geometrical arrangements of identical scatterers can give rise to large scale or macroscopic resonances. The most familiar example is the Bragg scattering of an electron in a perfectly periodic crystal. Such an effect is not given the required statistical weight by a disorder average which improperly averages over all positions of the scatterers.

Consider, for instance, a fluctuating dielectric constant $\epsilon(x) - \epsilon_0 \equiv \epsilon_{\text{fluct}}(x) = \epsilon_1(x) + V(x)$ where $\epsilon_1(x) = \epsilon_1 \sum_{\vec{G}} e^{i\vec{G}\cdot\vec{x}}$ is a perfectly periodic Bravais superlattice and $V(x)$ is a small perturbation arising from disorder. Here $\vec{G}$ runs over the appropriate reciprocal lattice and its value for the dominant Fourier component $U_{\vec{G}}$ is chosen so the Bragg condition $\vec{k} \cdot \hat{G} = (1/2)G$ may be satisfied for a photon of wavevector $\vec{k}$. Such a structure is attainable, albeit in a low dielectric contrast regime, with charged polystyrene balls in aqueous suspension. These exhibit charge induced *fcc* and *bcc* superlattice arrangements as well as a number of disordered phases. Setting $V(x) = 0$ for the time being, the effect of the periodic modulation of the photon spectrum may be estimated within a nearly-free-photon approximation. Unlike scalar electrons, there is a degeneracy between two possible optical polarization states. If the electric field vector is perpendicular to the plane defined by the vectors $\vec{k}$ and $\vec{k}$-$\vec{G}$ (optical *s*-wave), the resulting photon dispersion is the same as for scalar wave scattering. If on the other hand the polarization vector lies in the plane of Bragg scattering, the scattering amplitude is diminished by a factor of $\cos\theta$, where θ is the angle between $\vec{k}$ and $\vec{k}$-$\vec{G}$ (optical *p*-wave). The associated photon dispersion relations are depicted in Figure 3, with the gap for the optical *p*-wave being diminished by precisely $|\cos\theta|$.

The existence or near existence of a gap in the photon density of states is of paramount importance in determining transport properties and especially localization.[2] Such a possibility was completely overlooked in the derivation of the free-photon Ioffe-Regel condition which assumed an essentially free-photon density of states. In the vicinity of a band edge, the character of propagating states is modified. To a good approximation the electric field amplitude of the propagating wave is a linear superposition of the free photon with wavevector $\vec{k}$ and its Bragg reflected partner at $\vec{k}$-$\vec{G}$. As ω moves into the allowed band, this standing wave is modulated by an envelope function whose wavelength is given by $2\pi/q$, where q is the magnitude of the deviation of $\vec{k}$ from the Bragg plane. Under these circumstances the wavelength which must enter the localization criterion is that of the envelope. In the presence of even very weak disorder, the criterion $2\pi\ell/\lambda_{\text{envelope}} \sim 1$ is automatically satisfied as the photon frequency approaches the band edge frequency. In fact near a bandedge ω_c, $\lambda_{\text{envelope}} \sim |\omega - \omega_c|^{-\frac{1}{2}}$.

In the presence of a complete photonic band gap, the phase space available for photon propagation is restricted to a set of narrow symmetry related cones in $\vec{k}$-space analogous to the pockets of electrons near a conduction band edge well known in semiconductor physics. The perturbative introduction of randomness in the position of the dielectric scatterers leads to a mixing of all nearly degenerate photon branches. In complete analogy with semiconductors, the band gap is replaced by a pseudogap

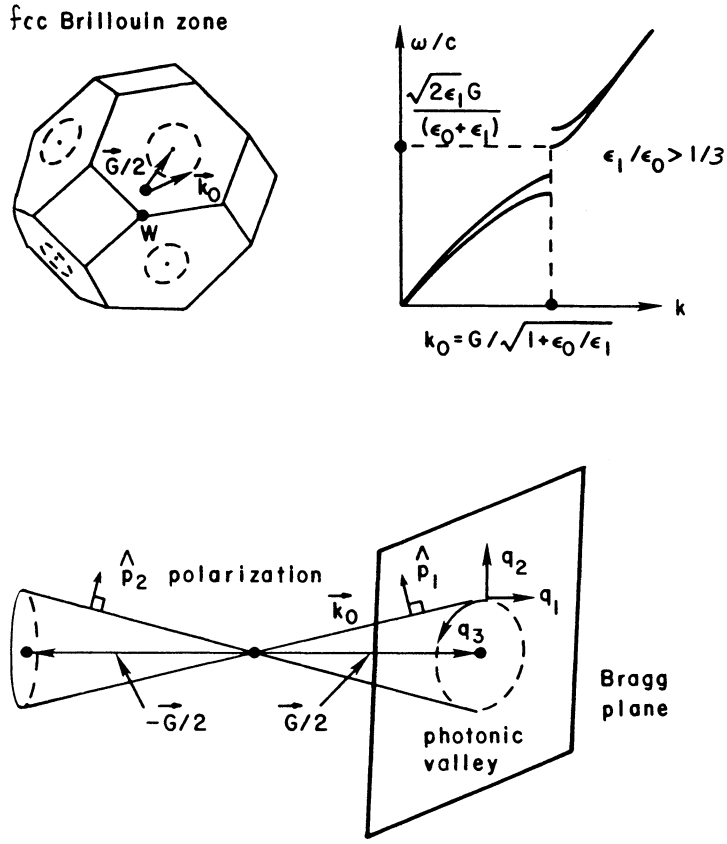

Fig. 3 In the case of coherent scattering from a periodic array of dielectric spheres, the phase space available for optical propagation is drastically modified from the vacuum. The dispersion relation exhibits a gap in any given direction of the wavevector $\vec{k}$. The inner and outer dispersion branches describe p- and s-polarized Bragg scattering, respectively. For a large refractive index contrast, this gap persists over the entire surface of the fcc Brillouin zone, giving rise to a gap in the total photon density of states. The phase space for optical propagation near this gap is restricted to a narrow set of symmetry related cones in the nearly free photon approximation.

consisting of localized states (Figure 4). Localization is favored here by the severe restriction of the phase space available for propagation. Photon localization arises here not as the by-product of a high degree of uncontrolled disorder, but rather as a result of a subtle interplay between order and disorder. The true criterion for localization, in fact, depends strongly on the underlying static structure factor of the medium. What I have discussed in detail are the two extreme limits of a structureless random medium for which the criterion $2\pi\ell/\lambda \simeq 1$ applies and of a medium with nearly sharp Bragg peaks and a band gap for which $2\pi\ell/\lambda_{\text{envelope}} \simeq 1$ yields localization. It is invariably the case that a continuous crossover occurs between these conditions as the structure factor of a high dielectric material evolves from one limit to the other.

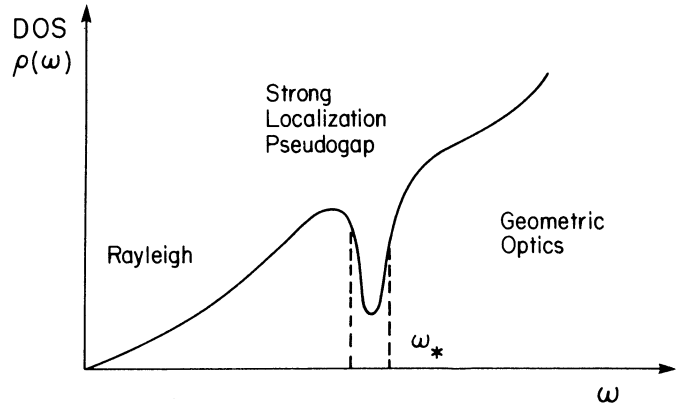

Fig. 4 For a disordered lattice of coherent dielectric scatterers the photon density of states exhibits low frequency Rayleigh scattering and high frequency classical ray optics regimes. The photonic band gap however is replaced by a pseudogap of strongly localized states in analogy with pseudogaps in amorphous semiconductors. The existence of a localization window is highly sensitive to the static structure factor of the dielectric material.

In the strong scattering regime required to produce a significant depression of the photon density of states, important corrections to the nearly free photon picture of band structure emerge. This was evident in initial experimental studies by Yablonovitch[7] who observed a photonic pseudogap in the microwave regime. For a dielectric material with refractive index 3.5 containing an fcc lattice of spherical air cavities, a nearly complete photonic band gap is observed when the solid volume fraction $f \simeq .15$. For a frequency range spanning about 6% of the gap center frequency, propagating electromagnetic modes are absent in all but a few directions. When the solid volume fraction is either increased or decreased from .15, the magnitude of the gap drops sharply. The existence of such an optimum in the sphere density illustrates a very fundamental principle concerning the origin of photonic band structures as opposed to electronic band structure. In an ordinary semiconductor, a band of allowed electronic states arises from a coalescence of individual atomic orbitals. In the propagation of light through a periodic dielectric, there is no precise analog of such atomic orbitals. Photons cannot be bound to a single dielectric sphere. Instead of bound states, one observes Mie scattering resonances when the diameter of the sphere is an integral multiple of the wavelength of light. A large photonic band gap arises when the density of dielectric spheres is chosen such that the Mie scattering resonance occurs at the same wavelength as the macroscopic Bragg resonance of the array. This principle may be illustrated by a simple example of one-dimensional wave propagation through a periodic array of square wells of width a and spaced by a distance L. Suppose the refractive index is n inside each well and is unity outside. Then the Bragg scattering condition is given by $\lambda = 2L$, where λ is the vacuum wavelength of light. The analog of a Mie resonance in one dimension is a maximum in the reflection coefficient from a single well and this occurs when a quarter wavelength fits into the well: $\lambda/(4n) = a$. Combining these two conditions yields the optimum volume filling fraction $f \equiv a/L = 1/(2n)$. In analogy to the formation of an electronic band, the

photonic band gap is the direct result of the coalescence of Mie scattering resonances of individual spheres.

Since the initial work on periodic dielectrics in three dimensions, considerable progress has been made in identifying and fabricating microstructures with a *complete* photonic bandgap. In addition to the synergy between microscopic and macroscopic resonances, *connectivity* of *both* the dielectric and void regions of the material appears to be an important contributing factor to the creation of a complete gap. The first theoretical demonstration of a complete gap for electromagnetic waves was given by Ho, Chan and Soukoulis.[8] This was demonstrated in a diamond lattice of air spheres in a solid background. Subsequently, Yablonovitch and co-workers successfully demonstrated a complete gap for air cylinders drilled in a solid host with a gap to center frequency ratio of 20 percent.

3. COHERENT BACKSCATTERING AND THE PHOTON MOBILITY EDGE

The analogy between electrons and photons suggests the fabrication of a new class of dielectrics which are the photonic analogs of semiconductors. For the case of a periodic array of dielectric spheres, a photonic band gap arises. Positional disorder of these spheres alters this picture. As in a semiconductor, the band gap is replaced by a pseudogap of localized states. In this section, I review the process by which a propagating photon becomes localized and discuss experimental manifestations of this phenomenon from the standpoint of classical electrodynamics.

In a disordered dielectric, a photon propagates by means of a random walk process in which the length of each random step is given by the classical transport mean free path ℓ^*. On length scales long compared to ℓ^*, it is convenient to regard this as the diffusion of light in which the diffusion coefficient is given by $D = \frac{1}{3}c\ell^*$. Here c is some effective speed of light in the dielectric medium. Unlike a classical random walker, light is a wave and this diffusion process must be described by an amplitude rather than a probability. That is to say, the interference of all possible classical diffusion paths must be considered in evaluating the transport of electromagnetic energy. In the case of optical waves propagating through a disordered dielectric medium, this interference effect has been vividly demonstrated by a beautiful series of experiments initiated by Kuga and Ishimaru, van Albada and Lagendijk, and Wolf and Maret.[9] This is the phenomenon of coherent backscattering. In these experiments, incident laser light of frequency ω enters a disordered dielectric half space or slab and the angular dependence of the backscattered intensity is measured. For circularly polarized incident light, the intensity of the backscattering peak for the helicity preserving channel is a factor of two larger than the incoherent background intensity. Coherent backscattering into the reversed helicity channel, however, yields a considerably reduced backscattering intensity. The angular width of the peak in either case is roughly $\delta\theta \sim \lambda/(2\pi\ell)$.

As shown in Figure 5, one possible process is that in which incident light with wavevector $\vec{k}_i = \vec{k}_0$ is scattered at points $\vec{x}_1, \vec{x}_2, \ldots, \vec{x}_N$ into intermediate (virtual) states with wavevectors $\vec{k}_1, \vec{k}_2, \ldots, \vec{k}_{N-1}$ and finally into the state $\vec{k}_N = \vec{k}_f$ which is detected. For scalar waves undergoing an identical set of wavevector transfers, the scattering amplitudes at the points $\vec{x}, \ldots, \vec{x}_N$ are the same for the path γ and time reversed path $-\gamma$ (dashed line). To understand the interference of these two paths in greater detail, we utilize an argument originally given by Bergmann in the context of

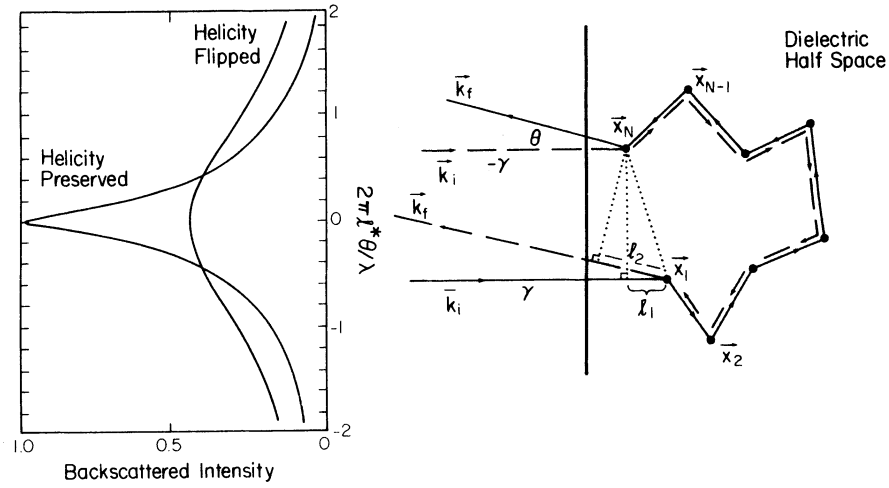

Fig. 5 Coherent backscattering is the precursor to localization. For light incident on a disordered dielectric, the scattering path (γ) and the time reversed path ($-\gamma$) interfere coherently for small angles θ. The result is a pair of peaks in the backscattered intensity I over and above the diffuse background intensity of reflected light labelled as $I = 0$. The larger peak describes backscattering in which the incident photon helicity is preserved, whereas the smaller peak describes photons whose final helicity has been flipped during the multiple scattering trajectory.

electron localization. Consider the path shown in Figure 6 with wave-vector transfers $\mathbf{g}_j = \mathbf{k}_j - \mathbf{k}_{j-1} (j = 1, 2, \ldots, N)$. By time-reversing the sequence of transfers, it is apparent the corresponding intermediate states $\mathbf{k}'_1, \mathbf{k}'_2, \ldots, \mathbf{k}'_{N-1}$ no longer lie on the energy shell for nonzero $\mathbf{q}$. This is allowed since these are virtual states with a lifetime $\tau = l/c$ and the energy shell is accordingly smeared by an amount $\hbar/\tau$. For small $\mathbf{q}$, the corresponding intermediate states differ in energy by an amount $E_{N-j} - E'_j \simeq c\hbar\mathbf{q} \cdot \hat{k}_{N-j} (J = 1, \ldots, N-1)$ where k_{N-j} are unit vectors in the direction of propagation of the intermediate plane wave states. The resulting phase difference $\Delta\phi = \hat{k}_{N-j} \cdot \mathbf{q}l$. Since the direction of intermediate states is random, it follows that after an N step random walk the accumulated root mean square phase difference $\Delta\phi_{\text{rms}} \simeq \sqrt{N/3}(ql)$. Therefore, only steps with $N \lesssim 3/(lq)^2$ contribute to the backscattering peak at the angle defined by $\mathbf{q}$. This accounts for the rapid decrease of coherent intensity for large $\mathbf{q}$.

At larger angles few paths contribute and the backscattered intensity decreases rapidly. A detailed derivation of the backscattered lineshape has been given by Akkermans, Wolf and Maynard[10] for scalar waves. This has been extended to electromagnetic waves by Stephen and Cwilich.[10]

As shown by Mackintosh and John,[10] these results are most transparent in the helicity representation. In addition to time reversal invariance, there is parity of the right and left hand circular polarization states. These symmetries may be broken by the Faraday effect and by natural optical activity respectively. Detailed lineshapes have been calculated and are shown in Figure 5. Depicted is the excess relative intensity with respect to the incoherent background. For instance, an intensity level of 1.0 corresponds to a precise doubling of the light intensity in a particular direction

relative to the diffuse background level which is labeled with excess intensity 0.0. The angle Θ (measured in radians) is the angle which the wavevector of the backscattered light makes with respect to the vector $-\vec{k}_i$, where $\vec{k}_i$ is the incident direction.

The arguments presented thus far for coherent backscattering enhancement have relied heavily on the existence of the free photon phase space or spherical energy shell. The occurrence of a photonic pseudogap or any other modification of the photon density of states from free photons will accordingly manifest itself in the backscattering lineshape. This is most easily seen in the case of weak disordering of a photonic bandgap crystal. Suppose that a backscattering experiment is performed on such a sample with radiation of wavelength short compared to the underlying lattice constant of the crystal. Bloch's theorem ensures that $\omega_{\vec{k}} \simeq \omega_{\vec{k}+\vec{G}}$ in the case of weak disorder whenever $\vec{G}$ is a reciprocal lattice vector of the original crystal. It follows

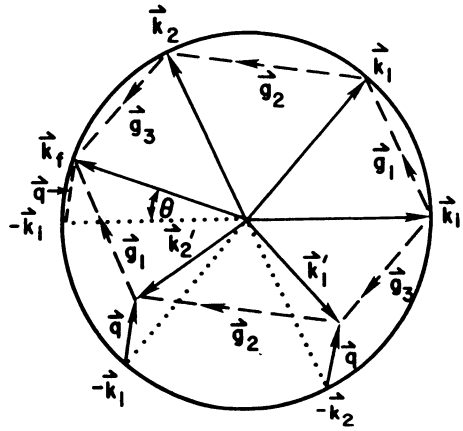

Fig. 6 A typical path drawn in momentum space. Equality of scattering amplitudes requires that the wavevector transfers $\mathbf{q}_j$ be the same but in the reversed order for the time-reversed path. Corresponding states differ in energy by an amount $E_{N-j} - E'_j \simeq c\hbar\mathbf{q} \cdot \hat{k}_j$, which leads to a phase difference $(\Delta\phi)_{\rm rms} \simeq \sqrt{N/3}ql$.

that the previous argument for loss of coherence for backscattering into the direction $-\vec{k}_i + \vec{q}$ (here $\vec{k}_i$ is the incident wave vector) is no longer applicable. In particular, whenever $\vec{q}$ lies in the vicinity of a reciprocal lattice vector, coherent enhancement persists, resulting in a satellite peak. The result, after ensemble averaging over the weak disorder, should be a ring of coherent intensity at an angle $\theta \simeq G/k$ over and above the diffuse intensity that arises from the ensemble average of the random speckle pattern. The occurrence of satellite structure in the backscattering profile has been pointed out by E. Gorodnichev et al.[11]

The incorporation of coherent backscattering into the theory of diffusion of wave energy leads to a simple renormalization group picture of transport (see Figure 7). In a situation where wave interference plays an important role in determining transport, the spread of wave energy is not diffusive at all in the sense that a photon performs a

classical random walk. This presents a very complicated situation. Fortunately, there is a way of applying the concept of classical diffusion here provided we make one major concession in our classical way of thinking: the diffusion coefficient is no longer a local quantity determined by a classical mean free path and a speed of propagation, but depends on the macroscopic coherence properties of the entire illuminated sample. In a random medium it is reasonable to expect that scatterers which are very far apart do not, *on average*, cause large interference corrections to the classical diffusion picture. (The word average here is very important. Changes in distant scatterers *can* give rise to significant fluctuations about the average.) It follows there exists a coherence length $\xi_{\rm coh} \gtrsim \ell$ which represents a scale on which we must very carefully incorporate interference effects in order to determine the effective diffusion coefficient at any point within the coherence volume. To put it in other words, the possible amplitudes for a photon to diffuse from point A to point B within a coherence volume $\xi_{\rm coh}^d$ interfere significantly with each other. Depending on the distance between the point A at which the photon is injected into the medium and the point B at which it is detected, the effective diffusion coefficient of the photon is strongly renormalized by wave interference. Another example is that of a finite size sample of linear size L. By changing the scale of the sample, the number of diffusion paths which can interfere changes giving rise to an effective diffusion coefficient $D(L)$ at any point within the sample which depends on the macroscopic scale L of the sample. In the vicinity of a mobility edge, on length scales L in the range $\ell < L < \xi_{\rm coh}$ the spread of energy is subdiffusive in nature as a result of coherent backscattering which gives a significant wave interference correction to classical diffusion. In this range, the spread of wave energy may be interpreted in terms of a scale dependent diffusion coefficient which behaves roughly as $D(L) \simeq \frac{c\ell}{3}(\frac{\ell}{L})$. On length scales long compared to $\xi_{\rm coh}$, the photon resumes its diffusive motion except with a lower or renormalized value $\frac{c\ell}{3}(\frac{1}{\xi_{\rm coh}})$ of the diffusion coefficient.

This physical picture is summarized by the scaling theory of localization which was obtained by Abrahams, Anderson, Licciardello and Ramakrishnan[12] based on the ideas of Thouless. In three dimensions, this theory predicts that when the laser frequency ω is close to a mobility edge ω^*, the scale dependent diffusion coefficient may be written as

$$D(L) \simeq \frac{c\ell}{3}\left(\frac{\ell}{\xi_{\rm coh}} + \frac{\ell}{L}\right) \tag{4}$$

and that $\xi_{\rm coh} \sim |\omega - \omega^*|^{-1}$ diverges as ω approaches ω^*.

The relevance of this result to an optical transmission experiment in the absence of dissipation or absorption is depicted in Figure 7. Consider first the case in which the coherence length is short compared to the slab thickness. The time required for an incident photon to traverse the thickness L is given by $\tau(L) = L^2/D(L)$. For $\ell \lesssim \xi_{\rm coh} \ll L$, the average displacement R of the photon as a function of time is that of classical diffusion $R \sim t^{\frac{1}{2}}$. In the case of incipient localization $\ell \ll L \ll \xi_{\rm coh}$, the diffusion coefficient has the value $D(L) = \frac{c\ell}{3}(\frac{\ell}{L})$. The transit time from one face of the slab to the other now scales as $\tau(L) \sim L^3$. In other words, the mobility edge regime is characterized by a critical slowing down of the photon which now traverses a distance $R \sim t^{\frac{1}{3}}$ rather than that of a classical random walker.

Anomalies associated with incipient localization may appear in the total transmitted intensity through a disordered dielectric slab illuminated by a steady monochromatic plane wave source. For the case of classical diffusion, the transmission coefficient T defined as the ratio of the total transmitted intensity to the total incident intensity is given by the relation $T = \ell/L$, where ℓ is the classical elastic mean free path.

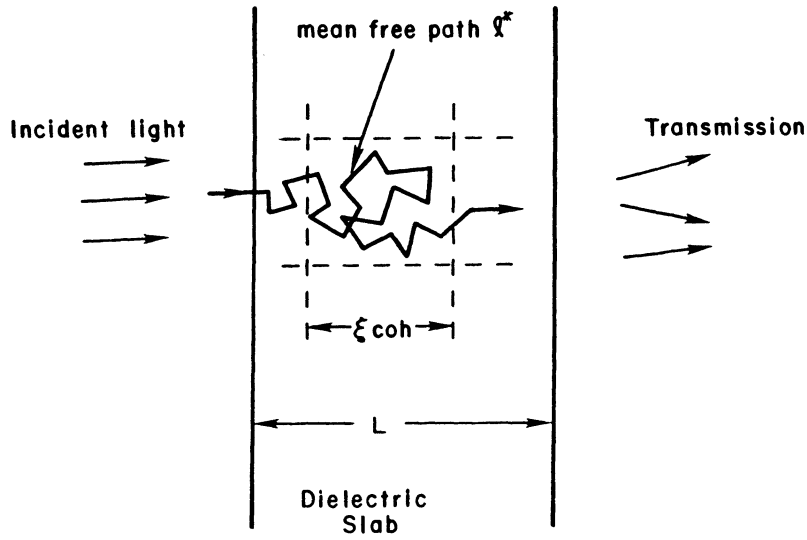

Fig. 7 A simple physical picture describes optical transport near a photon mobility edge. On scales short compared to the coherence length $\xi_{\rm coh}$, the spread of electromagnetic energy is subdiffusive in nature due to coherent backscattering. On scales longer than $\xi_{\rm coh}$, the photon resumes its diffusive behavior on average except with a renormalized diffusion coefficient $D \simeq c\ell^*/3$ $(\ell^*/\xi_{\rm coh})$.

This may also be written as $T = \frac{3D}{cL}$. This then leads to a transmission coefficient $T \sim \ell^2/(\xi_{\rm coh}L)$ for $\ell \lesssim \xi_{\rm coh} \ll L$ and to a new scale dependence $T \sim \ell^2/L^2$ in the incipient localization regime $\ell \ll L \ll \xi_{\rm coh}$. Scale dependent diffusion of precisely this nature has been observed by Genack and Garcia[13] in microwave scattering from a disordered collection of teflon and aluminum spheres.

In the case of electrons, there is a conservation law which prevents their total number from changing. Photons, on the other hand, can be absorbed. Therefore, the discussion of photon localization is incomplete without the analysis of wave propagation in a weakly dissipative disordered medium. By weak dissipation, I mean that the inelastic mean free path or typical distance between absorption events is large compared to ℓ but nevertheless smaller than the sample size L. This may be introduced by means of a small imaginary part ϵ_2 to the dielectric constant $\epsilon(x) = \epsilon_0 + \epsilon_{\rm fluct}(x) + i\epsilon_2$. The optical absorption coefficient α is defined as the decay constant for the intensity from a source of intensity I_0 : $I = I_0 e^{-\alpha x}$. This absorption coefficient describes the average absorption on scales long compared to the transport mean free path l. It should not be confused with the scattering length of the incident beam which may, in fact, be much shorter than l. For radiation at frequency ω, classical electromagnetic theory yields $\alpha = \sqrt{\omega\epsilon_2/D}$. The effects of coherent wave interference may be incorporated into this picture by means of the scaling theory of localization. For an infinite medium ($L = \infty$), the diffusion coefficient vanishes as the coherence length diverges. If $\ell_{\rm inel} > \xi_{\rm coh}$, it follows that the absorption coefficient increases in the same manner that the diffusion coefficient $D(\omega) \sim \omega - \omega_*$ decreases as the mobility edge frequency ω_* is approached from the extended state side: $\alpha(\omega) \sim \sqrt{\epsilon_2/|\omega - \omega_*|}$. On the other hand, if the coherence length exceeds the inelastic length, then $\ell_{\rm inel}$ acts as

a long distance cuttoff for coherent wave interference. In this case, there is a residual diffusivity given by $D(\omega_*) \simeq \frac{c\ell}{3}(\frac{\ell}{\ell_{\rm inel}})$. Since $\ell_{\rm inel} = \sqrt{D\tau_{\rm inel}}$ and $\tau_{\rm inel} \sim 1/(\epsilon_2\omega)$, it follows that the residual diffusivity $D(\omega_*) \sim \epsilon_2^{\frac{1}{3}}$. Substituting the value of the residual diffusivity into the expression for α reveals that the absorption coefficient exhibits an anomalous scaling behavior with ϵ_2: $\alpha(\omega_*) \sim \epsilon_2^{\frac{1}{3}}$. The physical origin of the critical exponent $\frac{1}{3}$ is the critical slowing down of the photon as it approaches localization. This leads to a greater probability of absorption.

The above argument relies heavily on the idea that an absorbing medium causes phase incoherence in the fraction of light that continues to propagate without being absorbed. The degradation of phase information is associated with the linewidth of the actual absorption centers in the medium. An absorber may be regarded as an oscillator which is excited by photons but which, in turn, is coupled to vibrational or other low energy thermal excitations of the medium. The optical energy may either be degraded into heat by the oscillator or scattered back as light with a random phase determined by the heat bath to which it is coupled. In a more detailed microscopic picture of the absorption process such as this, the question of how precisely the phase coherence length is related to the absorption length arises. In the previous argument leading to the anomalous scaling behavior of $\alpha(\omega_*)$, we assumed that both of these lengths were the same and described the parameter $\ell_{\rm inel}$. This, however, need not be true in general. In fact, the observation of mobility edge behavior would be greatly facilitated in real materials for which the phase coherence length over which renormalization of D takes place is larger than the absorption length. Nevertheless, we require that *some* finite phase coherence length exists in an absorbing medium so the absorption coefficient α remains finite as the frequency ω approaches the mobility edge ω_*.

The anomalies in absorption associated with localization are a general indication of enhanced coupling of the electromagnetic field to matter. This leads to some profound new phenomena in atomic physics which I now describe using the framework of quantum electrodynamics.

4. QUANTUM ELECTRODYNAMICS OF LOCALIZED LIGHT

When an atom or molecule is placed within a dielectric material exhibiting photon localization, the usual laws governing absorption and emission of light from the atom must be reexamined. This is most easily seen in the strong localization limit obtained for a dielectric exhibiting a complete photonic band gap. For a single excited atom with a transition energy $\hbar\omega_0$ to the ground state, which lies within the band gap, there is no true spontaneous emission of light. A photon which is emitted by the atom finds itself within the classically forbidden energy gap of the dielectric. If the nearest bandedge occurs at frequency ω_c, this photon will tunnel a distance $\xi_{\rm loc} \simeq c/|\omega_0 - \omega_c|$ before being Bragg reflected back to the emitting atom. The result is a coupled eigenstate of the electronic degrees of freedom of the atom and the electromagnetic modes of the dielectric. This photon-atom bound state[14] is the optical analog of an electron-impurity level bound state in the gap of a semiconductor. The atomic polarizability, which is normally limited by the vacuum natural linewidth of the transition, can grow sufficiently large near resonance, in the absence of spontaneous emission, to produce a localized electromagnetic mode from the nearby propagating band states of the dielectric. The fundamental weakness of the vacuum photon-atom interaction, as expressed by the fine structure constant $\alpha \equiv \frac{1}{137}$, is completely offset by this nearly

unrestricted resonance. The alteration of the quantum electrodynamic vacuum by the dielectric host also appears in the spectroscopy of atomic levels. The ordinary Lamb shift of atomic levels is dominated by the emission and reabsorption of high energy virtual photons. Within a photonic band gap, this self-dressing is instead dominated by the real, bound photon. In general, this will lead to some anomalous Lamb shift. If this level lies near a photonic band edge, a more striking effect is predicted to occur. In this case, the atom is resonantly coupled to photons of vanishing group velocity. The resultant self-dressing of the atom is sufficiently strong to split the atomic level into a doublet. The atomic level is essentially repelled by its electromagnetic coupling to the photonic band edge. One member of the doublet is pulled into the gap and retains a photon bound state, whereas the other member is pushed into the continuum and exhibits resonance fluorescence. In the nearly free photon approximation to electromagnetic band structure, the splitting of a hydrogenic $2p\frac{1}{2}$ level is predicted to be as large as $10^{-6}\hbar\omega_0$. This is analogous to the observed (Mollow) atomic level splittings which occur when an atom is subjected to an intense external laser field. For a dielectric exhibiting photon localization, the same effect may be achieved without any external field.

Additional new phenomena are expected when a collection of impurity atoms is placed into the dielectric. A single excited atom can transfer its bound photon to a neighboring atom by a resonance dipole-dipole interaction. For a band gap to center frequency ratio $\Delta\omega/\omega_0 = .05$, the photon tunnelling distance ξ_{loc} is on the scale of $10a$ and the lattice constant a of the dielectric is on the scale of the photon wavelength. For impurity atoms spaced by a distance $R = 10\text{Å}-1000\text{Å}$, the suppression of dipole-dipole interaction suggested by Kurizki and Genack[14] can be neglected. The matrix element M describing the hopping of a bound photon from one atom to another is given roughly by $M \sim \mu^2/R^3$, where the atomic dipole $\mu \simeq ea_0$ is given by the product of the electronic charge and the atomic Bohr radius a_0. This can be approximately related to the transition energy $\hbar\omega_0 \sim e^2/a_0$ by writing M as $(e^2/a_0)(a_0/R)^3$. For the case of a finite density of impurity atoms separated by $R \gtrsim 10\text{Å}$, it follows that photonic hopping conduction will occur through a narrow photonic impurity band of width $\sim (\hbar\omega_0)(a_0/R)^3$ within the larger band gap (Figure 8).

The occurrence of photonic impurity band suggests frontiers in the subject of nonlinear optics and laser physics. The strong coupling of light to matter suggests enhanced nonlinear effects which are highly sensitive to the impurity atom spacing. For example, when neighboring impurity atoms A and B are both excited, second harmonic generation may occur by the transfer of the bound state from atom A to atom B. Since atom B is already excited, the transferred photon creates a virtual state which may then be emitted as a single photon of energy $2\hbar\omega_0$ outside the photon band gap. The transfer can take place by dipole μ emission from atom A followed by a quadrupole Q virtual absorption by atom B. This process has an amplitude $\mu Q/R^4$. The resulting virtual excitation on atom B has odd parity and may then decay by a dipole emission process. The rate of spontaneous second harmonic generation is given by the square of the corresponding amplitude and depends sensitively $\sim (a_0/R)^8$ on the impurity atom spacing. Another significant question is that of laser activity within the impurity band when many photons are present. The impurity band defines a novel quantum many-body system in which the processes of spontaneous and stimulated emission of light are completely confined to and mediated by photonic hopping conduction between atoms. The intriguing possibility arises of a superfluid-like state of photons in which the hopping process causes macroscopic occupation of a single extended mode of the impurity band. This is the analog

of Bose-Einstein condensation of excitons. In the context of the photonic impurity band, the "superfluid" order parameter is actually the atomic polarization operator. This spontaneously acquires a nonzero expectation value in the superfluid state. If a single classical electromagnetic mode is now introduced into the photonic bandgap, superradiance into this mode may also occur. Depending on the precise phase of the photonic hopping conduction, the superfluid and superradiant states may compete with each other or act synergetically.

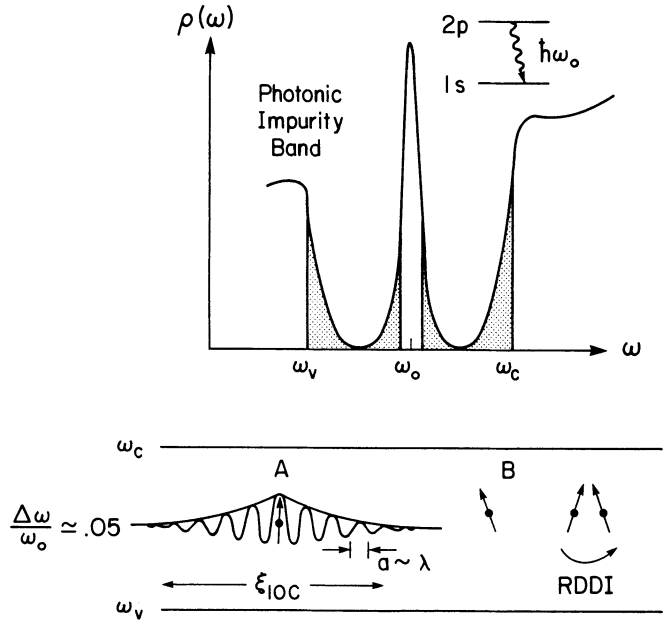

Fig. 8 Quantum electrodynamics predicts the occurrence of a photon-atom bound state when an impurity atom with a transition frequency ω_0 is placed within the localization gap $\Delta\omega$ of the dielectric. For $\Delta\omega/\omega_0 = .05$, the bound photon may tunnel a distance $\xi_{loc} \simeq 10a$, where a = the dielectric lattice spacing, before being Bragg reflected and reabsorbed by the atom. For a collection of atoms spaced by a distance $R \ll \xi_{loc}$, photons exhibit hopping conduction by means of the atomic resonance dipole-dipole interaction. This leads to the formation of a narrow photonic impurity band within the larger photonic band gap.

5. DISCUSSION

In closing, I discuss three areas of current and future activity in the field of photon localization. The first of these, which I have discussed already, is that of new physical phenomena. The second and perhaps most vital area at the present time is that of materials fabrication. Finally, I describe some potential applications and spin-offs from the first two areas of research.

(i) New Physical Phenomena

One of the new effects I have described is the inhibition of spontaneous emission of light from excited atoms and the concomitant formation of photon-atom bound states. Unlike its counterpart in small metal cavities with reflecting walls, the photon-atom state occurs in an infinite medium in which the bound photon may tunnel many optical wavelengths from the atom which it dresses. Unlike traditional cavity quantum electrodynamics in which there is a waveguide (or other) cutoff to low frequency electromagnetic propagation, the photonic bandgap allows the propagation of lower frequency radiation which may be used to nonlinearly excite or probe the photon-atom bound state. It is straightforward to show that in the absence of nonradiative decay, the lifetime of the bound photon is on the scale of 1 minute per kilometer of absorption length of the host dielectric. This follows from the fact that near midgap, the fraction of time which the photon spends orbiting the atom is about 10^{-7} compared to the time it spends in exciting the atom. The first goal in the study of quantum optical effects in the photonic band gap is the experimental realization of the photon-atom bound state. The crucial step here is the control lifetime broadening of this novel state by interaction with vibrational degrees of freedom of the solid host. For atoms in a dilute gas phase, this will involve Doppler cooling of the atoms in the void regions of the dielectric so as to minimize nonradiative relaxation associated with atom-solid collisions. The elimination of homogeneous line broadening from vibrational sidebands is more difficult for single impurity atoms embedded in the solid fraction of the dielectric microstructure. However, it may be possible to achieve long lifetime photon-molecule bound states within the solid fraction for certain aromatic hydrocarbon molecules. Such molecules are known to exhibit very high luminescence efficiencies in solids and may be candidates for the experimental observation of a single localized photon.

Theoretical and experimental work are needed to develop ways of probing the isolated photon-atom state. A possible mechanism to initially excite the state is by stimulated or inverse electronic Raman scattering. Here, a probe beam of photons with frequency above the gap would electronically excite the photon bound state and undergo a Raman Stokes shift to frequency below the gap. The process could be enhanced by a stimulating coherent monochromatic beam at the lower frequency. The presence of the photon-atom bound state could then be detected by the optical analogue of photo-emission. Here, a low frequency probe beam could eject the bound photon by undergoing an anti-Stokes shift from below to above the gap. Again, the process can be coherently enhanced by means of a stimulating beam above the gap.

In addition to localized modes arising from resonant impurity atoms and molecules, deviations from perfect periodicity of the host dielectric microstructures will induce exponentially decaying modes at frequencies within the gap region of the periodic system. Unlike the photon-atom bound states, these are classical or coherent states of the electromagnetic field. Such states can perform the function of a high quality Q optical cavity. The Q-factor may be estimated by taking the product of the optical frequency ω and the finite lifetime τ of a photon localized in such a mode. For an absorption length, $\ell_{\text{abs}} = 1$ km, $\tau \sim 10^{-5}$ sec. At optical frequencies, this translates into a quality factor of approximately 10^{10} per kilometer of absorption length. With fiber optic quality dielectric materials ($\ell_{\text{abs}} \sim 10^3$ km), this exceeds the Q factors which are readily attainable in metal cavities.

A quantitative description of electromagnetic transport and the photon density of states in disordered dielectric microstructures is necessary to establish material

properties for large scale samples in which deviations from perfect periodicity are inevitable. For strongly disordered systems, a quantitative evaluation of the phase, group and energy transport velocities near a photon mobility edge starting from the full Maxwell equations are necessary to interpret recent experiments on optical transmission, absorption and time resolved propagation near the Anderson localization transition. This involves the theoretical description of vector waves interacting with a dense random collection of resonant dielectric scatterers. In the case of short range ordered dielectric microstructures, it is expected that strong localization of photons is accompanied by a pseudogap in the electromagnetic density of states analogous to the pseudogap in semiconductors such as amorphous silicon. A clear theoretical description of the relationship between the extent of ordering (as determined by the static structure factor) and the resulting modification of the density of states and transport properties are needed. These will establish the robustness of the photonic bandgap against disordering effects.

In addition to disorder effects, new physical phenomena are expected if the host dielectric material has a Kerr nonlinearity. In this case, self localized states or moving gap solitons are possible at frequencies within the photonic band gap. These gap solitons have been carefully studied for one-dimensional periodic bandgaps. They can be described theoretically in terms of a multi-component envelope function which satisfies an effective nonlinear Dirac type equation.[16]

(ii) Materials Fabrication

Although recent advances in reactive ion etching have led to the creation of photonic band gap materials on the optical scale, these samples have a relatively small number of unit cells and the localization length of the most strongly localized states is comparable to the overall sample size. The creation of larger scale samples by this type of engineering is both time consuming and expensive. The samples once produced have few or no variable parameters. Although valuable for specific device applications, they are less useful for the study of fundamental physics because of this lack of variability.

A possible solution to this problem is a careful study of structures which *are* thermodynamically favored. The basic criteria such a structure must satisfy are periodicity, low absorption, and high refractive index contrast. A well-known system which satisfies the first two of these criteria but not the third is polystyrene balls in water. Here, the refractive index contrast is 1.5 to 1.3 and is too small for any photonic bandgap. On the other hand, TiO_2 has a refractive index of 2.8. Monodisperse spheres and ellipsoids of roughly the required size (5000 Å) are now commercially available. A self-assembling, thermodynamically favored periodic suspension could be produced if surface charges could be fixed onto these particles. This charging could be achieved by some polymer coating on the surface which naturally becomes charged in certain solutions or by ultraviolet flashing which creates electron-hole pairs across the TiO_2 semiconducting gap. The retention of this surface charge with time appears to be the single obstacle which remains to be overcome in this scheme. The advantage of charged semiconductor colloidal suspensions of this type is that the lattice structure and lattice constant can be varied in situ by changes in temperature and pH of the solvent. Disorder can be controllably introduced by means of mechanical agitation. Other candidates for "thermodynamically engineered" materials include porous silicon and low temperature molecular-beam-epitaxy-grown silicon, where periodic arrays of microvoid regions have recently been observed to occur.

(iii) Applications

The applications of research into photon localization can be divided into two general categories. The first arises from the new physical phenomena and the second is one of spectroscopy, the ability to describe and interpret the detailed propagation characteristics of light in the multiple scattering regime. I discuss first those applications associated with localized states. The applications of the second type are associated with multiply scattered extended states and are related to problems of current interest in other fields such as remote sensing and medical imaging.

Despite the current scientific focus on the development of *three-dimensional* photonic bandgap structures, many of the technological applications of localized, classical electromagnetic modes are also available in *two-dimensional* bandgap materials. These include filters, oscillators, and two-dimensional laser arrays. The advantage of these two-dimensional systems is they avail themselves to layered fabrication and thin films. Another quasi two-dimensional system which might be useful in the visible spectrum is a suspension of polydiacytelene rods. These are long hollow cylinders of diameter comparable to the wavelength of light in which nematic ordering can be induced. If these rods can be filled with a high refractive index material, the approximate conditions for a two-dimensional photonic band gap or pseudogap may be achieved.

A simple device application can be seen by the following argument. Whether in two- or three-dimensional systems, transmission of light through a slab of material containing a localization pseudogap may occur by the coupling of an external electromagnetic wave to one of the localized states in the gap. Due to the high degree of coherent multiple scattering through this disordered system, the travel time through the slab is exponentially long in the ratio of the slab thickness to the localization length. Accordingly, the frequency width of the peak in transmission will be exponentially narrow. The effect is that of an ultra high resolution macroscopic filter in the visible spectrum. The device will also exhibit exponentially high contrast since the total transmission coefficient approaches unity if light couples to a state localized near the center of the slab but exponentially decreases with the offset of the localized state from the slab center.

Further applications of localized electromagnetic modes arise if the system described above is modulated by an external field. The long photon path through the medium arising from coherent multiple scattering implies that the transmission coefficient depends sensitively on the state of the material. Changing the phase relationships electro-optically or with a second optical pulse (which induces nonlinear changes in the refractive index) will alter the transmission through the sample. Such a device can function as a high speed optical switch or an optical transistor.

In addition to localized states of the classical coherent electromagnetic field, single photon localization leads to important applications. From the viewpoint of applications, the photon-molecule bound state acts as a very long-lived excited molecular state. This has important applications in photochemistry and catalysis. One example is the excited state of TiO_2 which acts as a catalyst in the purification of water. The efficiency of this catalytic process can be greatly enhanced if the relevant photon is bound to the TiO_2 molecule.

Another possible application is in the formation of excimers. When a pair of impurity atoms or molecules is present in the bandgap material, a bound photon can hop from one molecule to the other by means of the resonant dipole-dipole interaction. This provides an attractive pairing force between the molecules in the excited state which is absent in the ground state. An additional attractive force of this nature may

facilitate the development of current excimer lasers as well as lead to the occurrence of entirely new excimer systems within a photonic bandgap material.

The final application of photon localization research is that of spectroscopy of disordered systems. One of the most compelling of these is in the field of medical imaging. The development and refinement of this field is directly related to both experimental techniques and formal mathematical methods which have been pioneered in the field of photon localization. In particular, we have derived a complete microscopic theory of electric field and light intensity autocorrelation functions in a multiple scattering medium including absorption and the crossover from ballistic to diffusive propagation. This is directly relevant to imaging tumors and other inhomogeneities in biological tissue.

Current medical imaging techniques utilize radiation at opposite ends of the electromagnetic spectrum. Short wavelength radiation is employed in x-ray based tomography while long wavelength radiation is used in magnetic resonance imaging. Light offers a window of intermediate wavelengths with certain advantages over short wavelengths. Light is nonionizing and at low intensities does not represent a biological hazard. In addition, the existence of intrinsic, spatially localized, metabolically active chromophores suggests that imaging with light should provide a valuable approach to the problem of metabolic imaging. The construction of spatial maps of optical absorption in the multiple scattering regime may be used for the visualization and functional localization of medically important metabolites. It is, therefore, likely that photon diffusion imaging, with the aid current research in photon localization, may be developed as a quick and inexpensive alternative to x-ray and magnetic resonance imaging as an early diagnostic tool.

REFERENCES

1. P.W. Anderson, *Phys. Rev.* **109**, 1492 (1958).
2. S.John, *Phys. Rev. Lett.* **53**, 2169 (1984);
   S. John, *Phys. Rev. Lett.* **58**, 2486 (1987);
   P.W. Anderson, *Phil. Mag.* **B52**, 505 (1985).
3. N.F. Mott, *Metal-Insulator Transitions;* Taylor and Francis, London (1974).
4. I. Freund, M. Rosenbluh, R. Berkovits and M. Kaveh, *Phys. Rev. Lett.* **61**, 1214 (1989).
5. A.F. Ioffe and A.R. Regel, *Prof. Semicond.* **4**, 237 (1960).
6. A.Z. Genack, *Phys. Rev. Lett.* **58**, 2043 (1987);
   M. Drake and A.Z. Genack, *Phys. Rev. Lett.* **63**, 259 (1989).
7. E. Yablonovitch, *Phys. Rev. Lett.* **58**, 2059 (1987);
   E. Yablonovitch and T.J. Gmitter, *Phys. Rev. Lett.* **63**, 1950 (1989).
8. K.M. Ho, C.T. Chan and C.M. Soukoulis, *Phys. Rev. Lett.* **65**, 3152 (1990);
   K.M. Leung and Y.F. Lui, *Phys. Rev. Lett.* **65**, 2646 (1990);
   Z. Zhang and S. Satpathy, *Phys. Rev. Lett.* **65**, 2650 (1990);
   E. Yablonovitch, T.J. Gmitter and K.M. Leung, *Phys. Rev. Lett.* **67**, 2295 (1991).
9. Y. Kuga and A. Ishimaru, *J. Opt. Soc. Am.* **A1**, 831 (1984); M. van Albada and A. Lagendijk, *Phys. Rev. Lett.* **55**, 2692 (1985);
   P.E. Wolf and G. Maret, *Phys. Rev. Lett.* **55**, 2696 (1985).
10. E. Akkermans, P.E. Wolf and R. Maynard, *Phys. Rev. Lett.* **56**, 1471 (1986);
    M.J. Stephen and G. Cwilich, *Phys. Rev.* **B39**, 7564;
    F.C. Mackintosh and S. John, *Phys. Rev.* **B37**, 1884 (1988).

11. E.E. Gorodnichev, S.L. Dudarev, D.B. Rogozkin, M.I. Rayzanov, *Sov. Phys.* JETP **69** (5), 1017 (1989).
12. E. Abrahams, P.W. Anderson, D.C. Licciardello, T.V. Ramakrishnan, *Phys. Rev. Lett.* **42**, 673 (1979).
13. A.Z. Genack and N. Garcia, *Phys. Rev. Lett.* **66**, 2064 (1991).
14. S. John and J. Wang, *Phys. Rev. Lett.* **64**, 2418 (1990);
G. Kurizki and A.Z. Genack, *Phys. Rev. Lett.* **61**, 2269 (1988).
15. J. Martorell and N.M. Lawandy, *Phys. Rev. Lett.* **65**, 1877 (1990).
16. S. John and N.Akozbek, submitted for publication.

PHOTON DIFFUSION, CORRELATION AND LOCALIZATION

A.Z. Genack, J.H. Li, N. Garcia and A.A. Lisyansky
Department of Physics, Queens College of CUNY, Flushing, NY 11367

The gladsome current of our youth,
Ere passion yet disorders,
Steals lingering like a river smooth
Along its grassy borders.
Thomas Campbell (1774-1844)

1. INTRODUCTION

Because the transport of sound, light, radio and microwave radiation through the turbulent atmosphere are essential for communication, the propagation of classical waves in random media has long been of interest. This interest has intensified in the last decade with the realization of the fruitfulness of the analogy between classical and quantum waves in disordered systems.[1] Particularly important have been the predictions and observations of coherent backscattering,[2,3] short[4-9] and long-range[10-20] intensity correlation, photon localization,[21-27] and the photonic bandgap.[28] These effects are most clearly exhibited in strongly scattering samples containing a high density of high index scatterers with size comparable to the wavelength λ. Here we consider the quantitative analysis of a wide variety of phenomena in these complex samples. Such studies of classical wave propagation promise to stimulate a deeper understanding of propagation and localization. On the one hand, the absence of interaction between quanta of classical fields, such as occur for electrons, simplifies the description of transport. On the other hand, the availability of tunable single frequency sources, short pulses and subwavelength spatial resolution as well as the ability to assemble collections of randomly positioned and movable scatterers make possible the statistical characterization of propagation in an *ensemble* of random samples.

In this chapter, we examine some of the key questions raised and follow up opportunities for exploration suggested by our previous studies which were reviewed in *The Scattering and Localization of Classical Waves* edited by Ping Sheng.[29] In section 2,

Photonic Band Gaps and Localization, Edited by
C.M. Soukoulis, Plenum Press, New York, 1993

we give a description of steady-state transport in which interfacial interactions are incorporated within the framework of the photon diffusion model. The self consistency of the model is demonstrated in a series of optical experiments in which the interfacial scattering parameters are overdetermined. These results allow us to determine the regime of validity of the diffusion model and to obtain accurate values for the interfacial scattering parameters as well as for the transport mean free path ℓ. We also confirm a general relationship between spatial distributions and angular field correlation functions and show that angular correlation functions in transmission are consistent with diffusion theory. In Sec. 3, we compare microwave measurements of intensity correlation in random dielectric samples with predictions of the Langevin approach and of the macroscopic random matrix method. Excellent quantitative agreement is obtained using the measured value of ℓ. We also illustrate the role of long-range intensity correlation in the intensity distribution. In Sec. 4, we consider the impact of microstructure resonances upon propagation. Microwave measurements of the frequency dependence of the diffusion coefficient D and of ℓ in collections of dielectric spheres provide the connection between steady state and dynamic measurements of transport. In Sec. 5, we discuss observations of an Anderson localization transition for microwave radiation in mixtures of aluminum and teflon spheres which is rounded by absorption.

2. INTERFACIAL SCATTERING AND DIFFUSION

Photon Diffusion

In previous work, in a wedge sample of rutile titania embedded in a polystyrene matrix, we found that measurements of the scale dependence of transmission $T(L)$,[5] the time of flight distribution of transmitted photons $T(t)$,[6] and the cumulant intensity correlation function of transmitted intensity as a function of frequency shift $C(\Delta\nu)$[5,6] were well described by functional forms given by the photon diffusion model.[29] Notwithstanding the qualitative success of diffusion theory, ℓ could not be accurately determined from these results. It could only be estimated from steady state measurements using assumptions regarding the coupling of the wave in and out of the sample or from time and frequency domain measurements using assumptions regarding the nature of wave interactions with the sample microstructure.[30-40]

In this section we use a set of optical measurements to provide a quantitative description of steady state propagation without making specific assumptions about the internal structure of the sample. We provide a description of transport in a finite system utilizing the diffusion formalism with three interfacial coupling parameters and then test the consistency of the model by performing a series of experiments in which these parameters are overdetermined. These parameters are the coherent penetration depth z_p which is the distance from the input surface at which the incident wave is effectively randomized, and the extrapolation lengths $z_b^{(in,out)}$ beyond the input and output

boundaries at which the intensity inside the sample extrapolates to zero. *Each* of these lengths is varied independently by changing either the incident angle of the beam or the index mismatch at the sample surface.[40]

The distance z_b beyond the physical surface of a sample with reflectivity R at which the intensity inside the medium appears to extrapolate to zero, in the absence of absorption, is given by,[34,37]

$$z_b^{(in,\ out)} = \tfrac{2}{3}\ell(1 + R^{(in,\ out)})/(1 - R^{(in,\ out)}) \tag{1}$$

The solution of the Milne equation, which gives the result of transport theory in the absence of internal reflection, gives a factor of 0.7104 instead of the factor of ⅔ in Eq. (1).[41] This correction will be used below in determining ℓ from results in the case where $R = 0$.

The transmission coefficient is given by the expression,[34,42]

$$T(L) = \left(z_b^{(in)} + z_p\right)\Big/\left(L + z_b^{(in)} + z_b^{(out)}\right) \tag{2}$$

Measurements of $T(L)$ were made on a weakly scattering, free standing, 0.0182 rad wedge of sintered alumina which starts at a thickness of 40 ± 1 μm using the arrangement shown schematically in Fig. 1a. The total energy of the incident, transmitted, and reflected light is measured using an integrating sphere as shown in Fig. 1b. A 3 mw He-Ne laser beam is focused to a 5 μm spot on the sample surface. The ratio of the transmitted light to the part of the incident beam which is not specularly reflected from the input surface gives the transmission coefficient. The absolute transmission could only be measured for the sample in air. The wedge was fabricated by polishing a slab of 99.7% purity polycrystalline alumina with 0.97 solid fraction

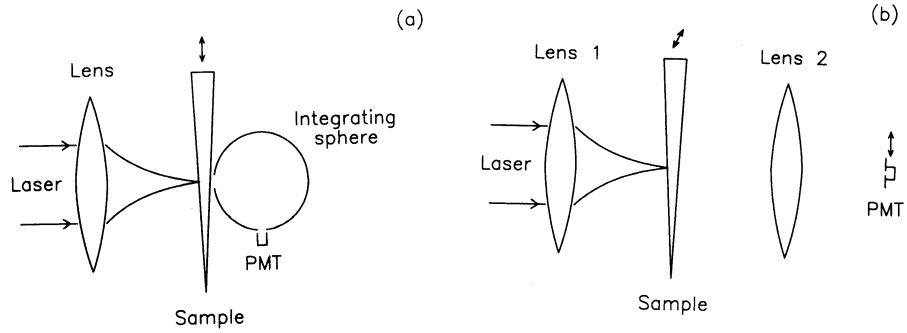

Figure 1. Schematic diagram of the experimental setup used to measure (a) the total transmission and (b) the intensity profile at the output of the sample.

provided by Valley Design Corporation. Electron micrographs of the material show random grains of average size 2 μm. The specular reflection coefficient near normal incidence is measured to be 7.2%. The internal reflection coefficient at either interface can be changed by modifying the index mismatch at the surface by bringing that interface into contact with various liquids or air. Specular reflection vanishes when the sample is immersed in a fluid with a refractive index of 1.70, which is close to the index of 1.76 of crystalline alumina. The transverse intensity profile at the output surface of the sample is measured using the setup shown schematically in Fig. 1b. The intensity profile is imaged near the normal to the surface with an $f/1.4$, 5.5 cm focal length Nikon lens. The image is magnified 30 times and is recorded by scanning a photomultiplier tube with an affixed 20 μm aperture in the image plane located 175 cm from the sample. Measurements of the intensity distribution in reflection are made by looking at the backwards scattered light using a beam splitter placed before the focussing lens. Large fluctuations are observed in the speckle pattern. The results reported for the transverse intensity distribution $I(\rho, L)$ are averages obtained by scanning the sample at fixed thickness as the data is collected. Related intensity correlation functions were computed from measurements of intensity spectra for a fixed sample as a function of detector angle with the imaging lens in Fig. 1b removed. The angular dependence of the intensity was also measured with the incident beam and the detector fixed while the sample is rotated.

Measurements of total transmission and reflection versus thickness for the sample in air are shown in Fig. 2a. Within the experimental error of 1% their sum is unity, indicating the low level of absorption in the sample. For $L > 100$ μm, the inverse of $T(L)$ is a straight line as shown in Fig. 2b, in agreement with the expression for $T(L)$ in Eq. (2). Fitting Eq. (2) to the linear portion of the curve for $T(L)^{-1}$ gives $z_p = 24.8$ μm and assuming that $z_b^{(in)} \approx z_b^{(out)}$, we get $z_b = 190.9$ μm with standard deviation of 0.1 μm and 0.3 μm respectively. To check whether $z_b^{(in)} \approx z_b^{(out)}$, we measured the relative transmission versus thickness in cases where either the input or output surface is index matched. The sum $z_b^{(in)} + z_b^{(out)}$ obtained from the slopes of $T(L)^{-1}$ for the two cases are the same within the experimental error of 2%. We will therefore assume their equivalence for the moment and denote their value by z_b. From measurements of the variation in intensity with the angle at which laser beam enters the integrating sphere, we estimate that the relative transmission is uncertain to 0.5%. In addition uncertainties of 1 μm in the thickness of the thinnest part of the sample results in uncertainties of 1 μm in z_p and 1.5 μm in z_b.

To find ℓ, we measure the transmission with the sample immersed in index matching fluid so that $R = 0$. Although the absolute transmission could not be measured directly in this case, from the x-intercept of the linear fit of $T(L)^{-1}$ to the data, we obtain $z_b = 22.3 \pm 1.5$ μm. Using Eq. (1) for the index matched case and including the Milne factor 0.701, gives $\ell = 31.4 \pm 1.5$ μm. Using this value for ℓ and the value of z_b in air in Eq. 1, gives $R = 0.81$ at the sample/air interface.

Scattering parameters may be obtained independently from measurements of the angular dependence of total transmission. Within the framework of the present simple

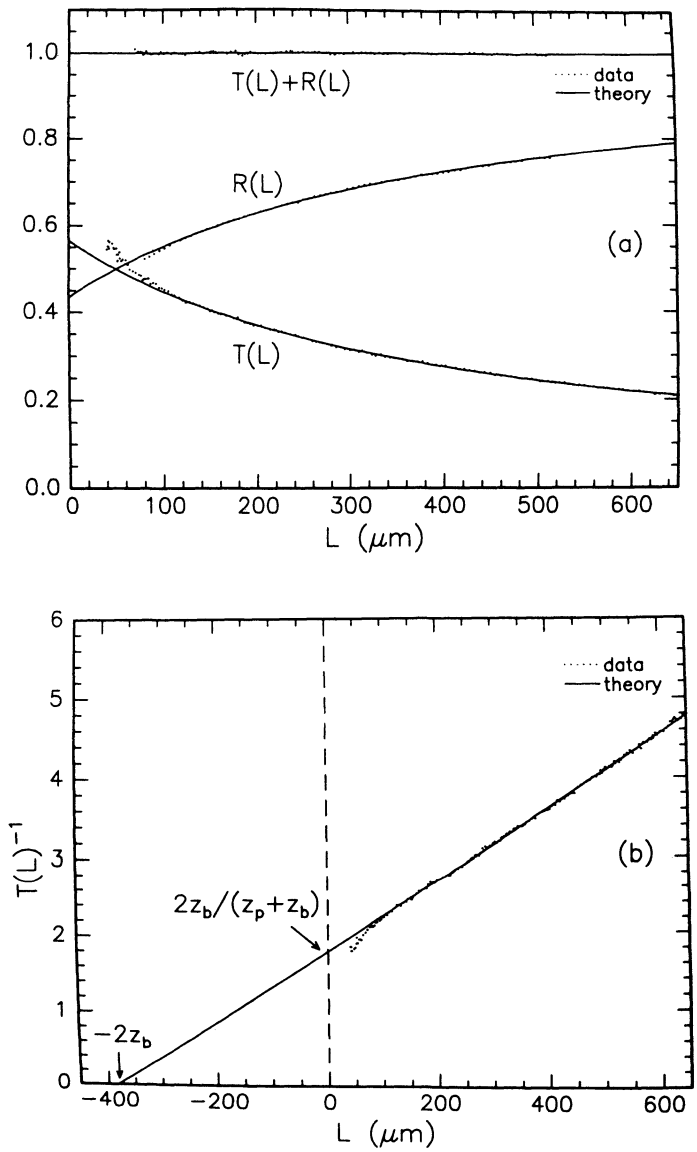

Figure 2. (a) Scale dependence of the total transmission, reflection and their sum for the alumina wedge in air. (b) The dots are the inverse of $T(L)$ given in Fig. 2a. The solid lines through the transmission data in both (a) and (b) represent the fit of Eq. (2) to the data. The reflection data is fitted by 1 - $T(L)$.

diffusion model, we expect that the longitudinal penetration depth varies with angle of incidence θ as $z_p\cos\theta_r$, where θ_r is the angle of refraction in the random medium, whereas the surface extrapolation length remains the same. We have then,

$$T(\theta) = (z_p\cos\theta_r + z_b)/(L + 2z_b). \quad (3)$$

A measurement of $T(\theta)$ for the index matched alumina sample of $L = 640\ \mu$m is shown in Fig. 3. In this case $\theta = \theta_r$. The solid line is a plot of Eq. (3) using the values of z_p and z_b found from measurements of $T(L)$ for the case $\theta = 0$.

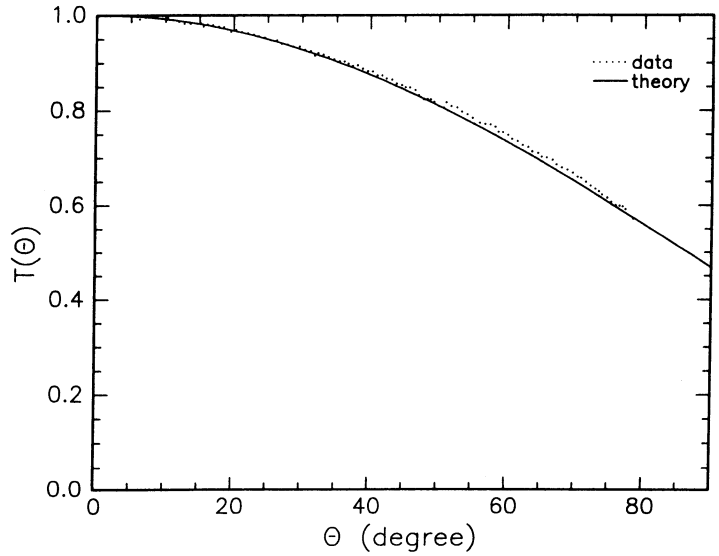

Figure 3. Transmission through an index-matched alumina sample of $L = 640\ \mu$m as a function of the angle between the incident beam and the normal to the plane of the sample. The solid line is calculated from Eq. (3).

Another independent test of diffusion theory is given by the comparison of the intensity profile at the output face obtained using diffusion theory and the values of the scattering parameters above with the measured intensity distribution.[3,42-44] The normalized intensity profile measured for $L = 640\ \mu$m and $L = 89\ \mu$m in air and the calculated distribution using the parameters found above are shown in Fig. 4. Intensity measurements are shown along a line going through the center of the distribution which is taken as the origin in the figure.

We find good agreement with diffusion theory for samples in air whenever $L \geq 150\ \mu$m. For thinner samples, diffusion fails to describe $I(\rho; L)$ even at thicknesses which

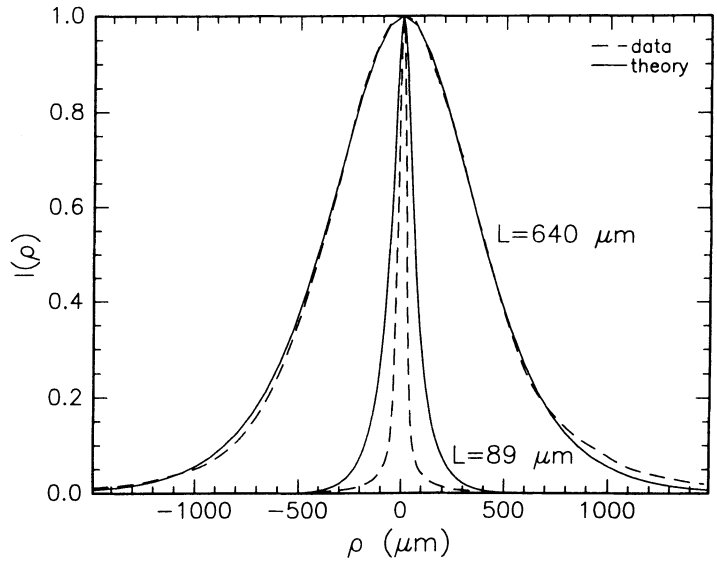

Figure 4. The dashed lines are the experimentally determined intensity profiles at the output surface for samples with $L = 640\ \mu m$ and $89\ \mu m$. The solid lines are the predictions of diffusion theory.

are considerably larger than ℓ. In contrast, $T(L)$ is seen in Fig. 2 to conform to the predictions of diffusion for $L \geq 100\mu m$. The reason for this difference is that $I(\rho, L)$ is measured using a lens to collect light in the forward direction. Light that has not been fully randomized is more sharply peaked in the forward direction. This portion of the light, which also has a narrower distribution in the transverse direction, has a larger Fresnel transmission coefficient at the output surface and therefore makes a proportionately greater contribution to the measured $I(\rho; L)$ than light that has been more completely randomized. On the other hand, the total transmission in samples in which L is several times larger than ℓ is relatively insensitive to the angular distribution of light at the output surface. Though the transmission coefficient depends strongly upon the orientation at which the light strikes the output surface, the probability is high that photons which have reached the output surface will eventually emerge from that surface, even if only after several reflections.

The intensity distributions in reflection for parallel and perpendicular polarizations as well as the prediction of diffusion theory using the parameters found above from measurements of total transmission are shown in Fig. 5. The difference in the intensity profile for different polarizations cannot be described within the framework of diffusion theory. Moreover, the distributions for either polarization are narrower than the prediction of diffusion theory. In transmission no appreciable difference was observed in the intensity profile for both polarizations at thickness for which the

diffusion model accurately described $I(\rho, L)$. We conclude, therefore, that diffusion theory does not accurately describe distributions in reflection. Considerable caution must therefore be used when interpreting measurements of coherent backscattering or angular, spectral or temporal correlation functions in reflection.

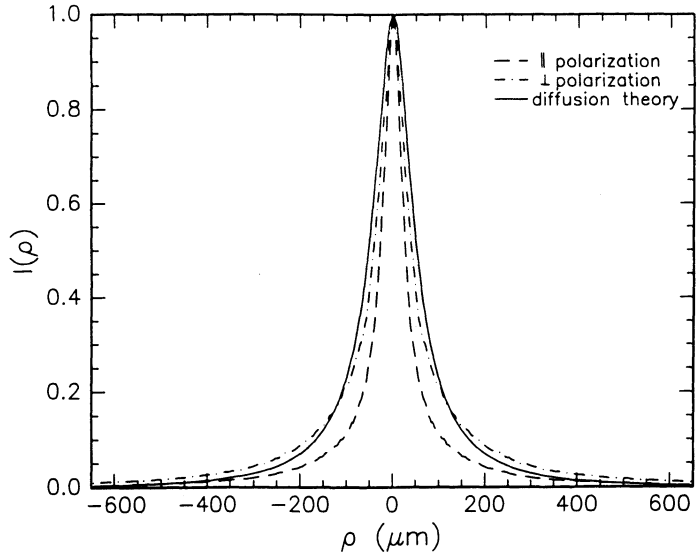

Figure 5. Intensity profiles in reflection for parallel and perpendicular polarizations for an alumina sample of $L = 640\ \mu m$. The solid lines represent the predictions of the diffusion model.

The validity of the photon diffusion model is also tested in measurements of intensity of microwave inside a sample contained in a copper tube.[39,42] We find that the integrated intensity at a given depth is accurately given by diffusion theory even within a mean free path of the output surface.

Wave Correlation

We have shown above that the surface intensity distribution in transmission is given by the photon diffusion model. The underlying wave nature of propagation in random media is seen in intensity fluctuations that result from the random phases and amplitudes of partial waves reaching a point. Here we examine various angular correlation functions of the far field which reflect the wave properties associated with corresponding surface intensity profiles. We show that these wave and particle aspects of propagation are Fourier transform pairs and demonstrate these results experimentally.

We consider the field-field correlation function, $I_{k_b, k_{b'}} \equiv \langle E(k_b) \cdot E^*(k_{b'}) \rangle$, of monochromatic light scattered in the direction k_b with light scattered in the direction $k_{b'}$. The field at points ρ_a and ρ_b of the input and output surfaces and in the far field of the transmitted speckle pattern can be expressed respectively as sums of partial waves as follows,

$$E(\rho_a) = \int A(k_a) \exp(i k_a \cdot \rho_a)\, dk_a , \tag{4a}$$

$$E(\rho_b) = \int E(\rho_a)\, p(\rho_a, \rho_b)\, d\rho_a , \tag{4b}$$

$$E(k_b) = \int E(\rho_b) \exp(-i k_b \cdot \rho_b)\, d\rho_b , \tag{4c}$$

where $A(k_a)$ is the Fourier amplitude of the incident wave, $p(\rho_a, \rho_b)$ is a propagation factor between points on the input and output surfaces of the sample, $f(\rho_b, k_b)$ is a coupling factor between the field at ρ_b and the detected field in a direction k_b. The phase difference associated with propagation to and from points ρ_a and ρ_b relative to the center of the distribution on the a and b surfaces are $k_a \cdot \rho_a$ and $k_b \cdot \rho_b$ respectively. We assume that fluctuations in propagation and coupling factors are uncorrelated. The short-range correlation in the propagation and coupling factors over which we integrate can be expressed as,

$$\langle p(\rho_a, \rho_b) p^*(\rho_{a'}, \rho_{b'}) f(\rho_b, k_b) f^*(\rho_b, k_{b'}) \rangle = P(\rho_a, \rho_b) g(k_b, k_b) \delta(\rho_a - \rho_{a'}) \delta(\rho_b - \rho_{b'}). \tag{5}$$

Here, $P(\rho_a, \rho_b) \equiv \langle |p(\rho_a, \rho_b)|^2 \rangle$ is the intensity propagator from ρ_a to ρ_b. Since it depends only on the difference $\rho = \rho_a - \rho_b$, it can be expressed as $I_0(\rho)$. $g(k_b, k_{b'}) \equiv \langle f(\rho_b, k_b) f^*(\rho_b, k_{b'}) \rangle$, gives the influence upon the correlation function of the angular intensity distribution and is independent of ρ_b. Using Eqs. (4) to express the field as,

$$E(k_b) = \int\int\int A(k_a) \exp(i k_a \cdot \rho_a)\, p(\rho_a, \rho_b) \exp(-i k_b \cdot \rho_b) f(\rho_b, k_b)\, dk_a\, d\rho_a\, d\rho_b ,$$

and using Eq. (5) to calculate the correlation function of this field with a field produced by shifting each of the incident Fourier components by Δk_a and detecting the field in a direction shifted by Δk_b from the initial direction of detection gives the result,

$$I_{k_b, k_{b'}} = g(k_b, k_a) \int\int I(\rho_a) \exp\left[i(\Delta k_b - \Delta k_a) \cdot \rho_a\right] P(\rho_a, \rho + \rho_a) \exp(i \Delta k_b \cdot \rho)\, d\rho_a\, d\rho , \tag{6}$$

where $I(\rho_a)$ is the intensity distribution on the input surface. Since $g(k_b, k_{b'})$ changes slowly over the experimental range, its variation will be neglected below. This neglect is further justified in the comparison with experiments below because the intensity spectra used in the calculation of correlation functions are normalized by the average of all spectra to simplify the interpretation of these results.

In the case, $\Delta k_a = 0$, we find when we sum over ρ_a in Eq. (6),

$$I_{k_b, k_{b'}} \propto \int I(\rho_b) \exp(i \Delta k_b \cdot \rho_b)\, d\rho_b, \qquad \Delta k_a = 0, \tag{7a}$$

where $I(\rho_b) = \int I(\rho_a) P(\rho_a, \rho_a + \rho) d k_a$, is the intensity distribution on the output face. Eq. (7a) shows that the field correlation function of the transverse component of the wavevector and the intensity distribution of the transverse displacement on the surface are a Fourier transform pair. This is essentially the van Cittert-Zernike theorem.[45]

In the case, $\Delta k_a = \Delta k_b \equiv \Delta k$, we find,

$$I_{k_b, k_{b'}} \propto \int P(\rho) \exp(i \Delta k \cdot \rho)\, d\rho, \qquad \Delta k_a = \Delta k_b, \tag{7b}$$

where $P(\rho) \equiv P(\rho_a, \rho_a + \rho)$ which is independent of ρ_a. The condition $\Delta k_a = \Delta k_b$ can be achieved by rotating a slab without changing the direction of the incident and detected beams. The correlation function in the case that $\Delta k_a = \Delta k_b$[9,14,31,33,46] has been called the "memory effect" because it allows one to determine the incident beam direction by measurements of the wave transmitted through a random medium. Eq. (7b) implies that measurements of the intensity correlation function in this case yield the intensity propagator.

These results are compared to experiment in Fig. 6.[47] The output intensity distribution for a wide and a focussed beam at the input of a 280 μm thick slab is shown in Fig 6a. The normalized cumulant intensity correlation function versus detector angle in the output plane for these two cases , $C(\Delta\theta) = <\delta I(\theta)\delta I(\theta + \Delta\theta)>$, is shown in Fig. 6b. The intensity spectra are normalized by the average of all spectra, which is the angular intensity distribution, so that the δI are fractional fluctuations form the average intensity. In the absence of long-range intensity correlation, $C(\Delta\theta)$ is given by factorizing the fields and is the amplitude square of the field correlation function. The narrower correlation function in Fig. 6b corresponds to the broader intensity distribution in Fig. 6a. The solid line in Fig. 6b is the complex square of the Fourier transform of $I(\rho_b)$ for each of the cases shown in Fig. 6a. This demonstrates that the connection between surface intensity distributions and the angular correlation functions in the transmitted wave is given by Eq. (7a). Since $I(\rho_b)$ for the case of tight focussing corresponds to the diffusion propagator, this confirms that angular correlation measurements are consistent with diffusion theory. The cumulant intensity correlation function versus rotation angle of the sample, $\Delta\theta$, for wide and focussed beams are shown in Fig. 6c. These results give the same correlation functions as that shown in Fig. 6b for the tight focussing case, demonstrating that the corresponding distribution is the diffusion propagator and confirms Eq (7b).

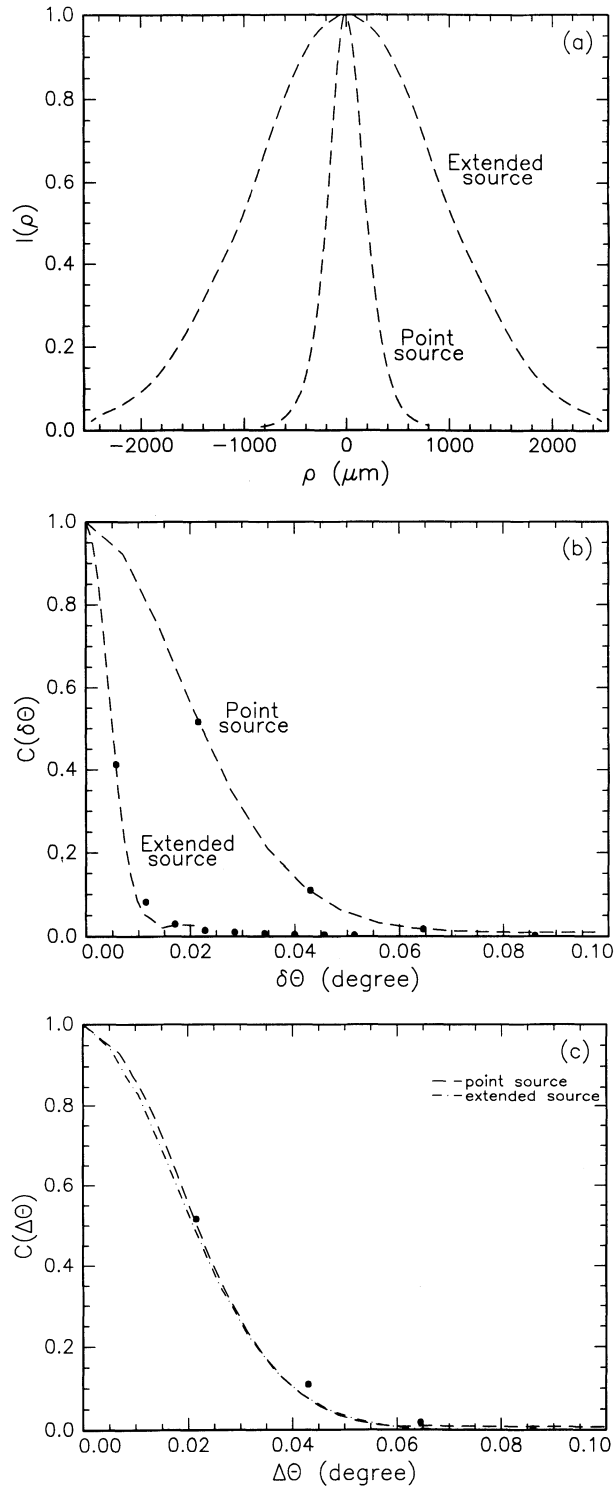

Figure 6. (a) Intensity profiles at the output surface of an alumina sample of $L = 280\ \mu m$ for wide and focused incident beams. (b) Correlation functions versus detector angle with a fixed sample for the two cases of Fig. 6a. (c) Intensity correlation function versus rotation angle of the sample for the two cases of Fig. 6a. The dots in (b) and (c) are the Fourier transforms of the two curves in (a).

Equivalent relationships to Eqs. 6 and 7 are found which relate intensity distributions in time and field correlation functions with frequency. The equivalent of Eq. (7b) was demonstrated experimentally by showing that the correlation function between monochromatic fields at ω and ω', corresponding to the case in which the incident and detected fields are shifted by the same amount $\Delta\omega$, is the Fourier transform of the transmitted picosecond pulse, corresponding to the temporal intensity propagator, $I_{\omega,\omega'} \propto \int T(t)\exp(i\Delta\omega t)dt$.[6]

3. LONG-RANGE INTENSITY CORRELATION

Intensity Correlation

In Refs. 17 and 18, we reported the observation of long-range intensity correlation of microwave radiation in randomly positioned polystyrene spheres contained in a copper tube, but calculations of spectral and spatial correlation in the presence of absorption had not been carried out. A detailed comparison with recent calculations of Pnini and Shapiro[15] and of Kogan and Kaveh[16] is now made.[48] Excellent agreement is found. We also demonstrate the connection between long-range intensity correlation and departures of intensity statistics from negative exponential behavior. Because the field is coherent throughout the sample, these results for the intensity correlation and distribution allow us to study the microscopic origin of the statistical description of conductance in mesoscopic systems.

The random sample within the copper tube, shown schematically in Fig. 7, is analogous to an electronic resistor. The corresponding dimensionless conductance is the product of the number of modes in the tube, $N \approx Ak^2$, where A is the cross-sectional area of the tube and k is the magnitude of the wavevector, and the transmission

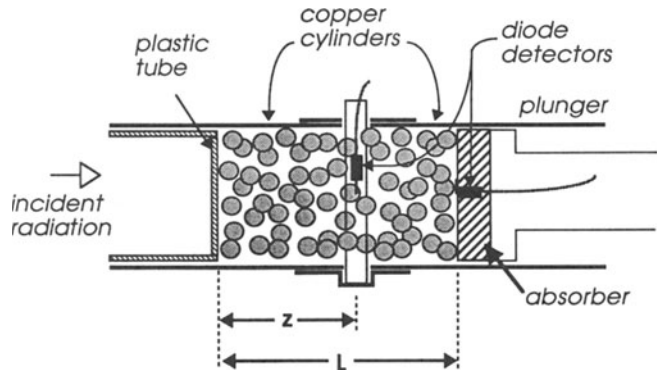

Figure 7. Schematic diagram of the experimental setup used to measure microwave intensity at the output and inside a sample of ½-in polystyrene spheres.

coefficient ℓ/L, $g \approx N\ell/L$. The results given below indicate that even in the presence of absorption, the degree of correlation between two typical points on the output surface is approximately $1/g$. Whereas the transverse extent of the wave in a slab is of order L, the confinement of the microwave radiation by the highly reflecting walls enhances the degree of long-range intensity correlation as compared to its value in a slab by a factor of L^2/A.[29] This makes it possible to study intensity correlation as a function of space and frequency even in the case of locally weak scattering. The waveguide geometry used here also has important computational advantages. Because modes are completely mixed in this geometry, it is possible to carry out a macroscopic matrix calculation for the amplitude of the correlation function in which the difference between short and long-range correlation is clearly manifested. In this geometry, the analysis of correlation measurements is simplified because the spatial and spectral variations of the correlation functions on the output surface factorizes.

We consider a waveguide which has N modes at a given frequency ω. These modes, or linear combinations of them, define N channels which form a basis for describing incoming and outgoing radiation from a random medium inside the waveguide. We denote by T_{ba} the transmission coefficient from channel a on the left of the disordered region to channel b on the right. In the present study, a mode is launched down a copper tube and the intensity is detected at points on the output face of the disordered region. Therefore, the incoming channel a corresponds to a waveguide mode, whereas the outgoing channel b corresponds, roughly, to regions of area $(A/N) \approx \lambda^2$ on the output face, where A is the cross sectional area of the tube.

Perfect mixing of channels by the scattering medium implies that the ensemble average of T_{ba}, $\langle T_{ba}\rangle$, does not depend on a or b. The correlation matrix, $C_{ab,a'b'} = \langle \delta T_{ba}\delta T_{b'a'}\rangle/\langle T_{ba}\rangle^2$, is then the sum of three distinct terms,[12,14]

$$C_{ab,a'b'} = C_1 + C_2 + C_3 = \tilde{A}_1\,\delta_{aa'}\,\delta_{bb'} + \tilde{A}_2\,(\delta_{aa'} + \delta_{bb'}) + \tilde{A}_3. \tag{8}$$

The leading contributions to the coefficients $\tilde{A}_1$, $\tilde{A}_2$ and $\tilde{A}_3$ were calculated in Ref. 12. Using the results of these references to calculate higher order corrections gives,[48]

$$\tilde{A}_1 = 1 - \frac{2}{3g_0} + \frac{13}{45g_0^2}, \tag{9a}$$

$$\tilde{A}_2 = \frac{2}{3g_0} - \frac{14}{45g_0^2}, \tag{9b}$$

$$\tilde{A}_3 = \frac{2}{15g_0^2}, \tag{9c}$$

where g_0 is the leading contribution to the average conductance. The results above are for a fixed frequency in the absence of absorption. However, it is of interest to study correlation between T_{ba} at frequency ω and $T_{b'a'}$ at frequency ω' in the presence of absorption. Since the frequency shift $\Delta\omega$ and absorption do not affect the perfect mixing of channels, the structure of Eq. (8) is not changed. The coefficients of the Krönecker deltas in Eq. (8), however, do depend upon the frequency shift $\Delta\omega$, and the inverse absorption rate $\Gamma = 1/\tau_a$ and become functions of $\tau\Delta\omega$ and $\tau\Gamma$, where $\tau = L^2/D$. These coefficients may be written as products of frequency independent functions A_i and frequency form factors F_i:

$$\tilde{A}_i(g_0,\tau\Gamma,\tau\Delta\omega) = A_i(g_0,\tau\Gamma)F_i(g_0,\tau\Gamma,\tau\Delta\omega), \tag{10}$$

where, $F_i(g_0,\tau\Gamma,0) = 1$ and $A_i(g_0, 0)$ are given by eq. (9).

In the limit of large g_0 and strong absorption ($g_0, \tau\Gamma \gg 1$), the form factors F_1 and F_2 on the output face of the sample are given by,[15-20]

$$F_1 = \frac{\sqrt{\tilde{\alpha}^4 + \tilde{\beta}^4}}{\cosh(2\gamma_+) - \cos(2\gamma_-)} \frac{\cosh(2\tilde{\alpha}) - 1}{\tilde{\alpha}^2}, \tag{11a}$$

$$F_2 = \frac{\sqrt{\tilde{\alpha}^4 + \tilde{\beta}^4}}{\cosh(2\gamma_+) - \cos(2\gamma_-)} \frac{\gamma_+ \sinh(2\gamma_+) - \gamma_-\sin(2\gamma_-) - \tilde{\alpha}\sinh(2\tilde{\alpha})}{\tilde{\beta}^4/4}, \tag{11b}$$

where $\tilde{\alpha}^2 \equiv \tau\Gamma$, $\tilde{\beta}^2 \equiv \tau\Delta\omega$, and $\gamma_\pm^2 \equiv \frac{1}{2}(\sqrt{\tilde{\alpha}^4 + \tilde{\beta}^4} \pm \tilde{\alpha}^2)$. F_1 is obtained within the field-factorization approximation, and decays as a result of the randomization of phase with frequency shift,[4-6,11] whereas F_2 results from the diffusion of short-range intensity fluctuations which arise in the field factorization approximation.[13-20] The role of internal reflection at the sample interfaces, which is small in this sample, is neglected here.[49]

Measurements of intensity correlation of microwave radiation are made in a random sample of ½-inch polystyrene spheres at a volume fraction of 0.56 in a 7.3 cm diameter copper tube. Small air bubbles occupy 4.5% of the volume of the spheres. The intensity is detected by two Schottky diodes with parallel antenna separated by 2.5 cm at the output surface of samples of variable length. Because the diode junction is microscopic compared to the microwave wavelength, local measurements of intensity can be made. This is confirmed by our observations of negative exponential intensity statistics in reflection from weakly scattering samples. The most likely intensity value can be near zero, as is observed in this case, only when the transverse dimensions of the area over which the flux is detected is negligible compared to the wavelength. The random configuration of spheres inside the tube may be changed by tumbling the tube.

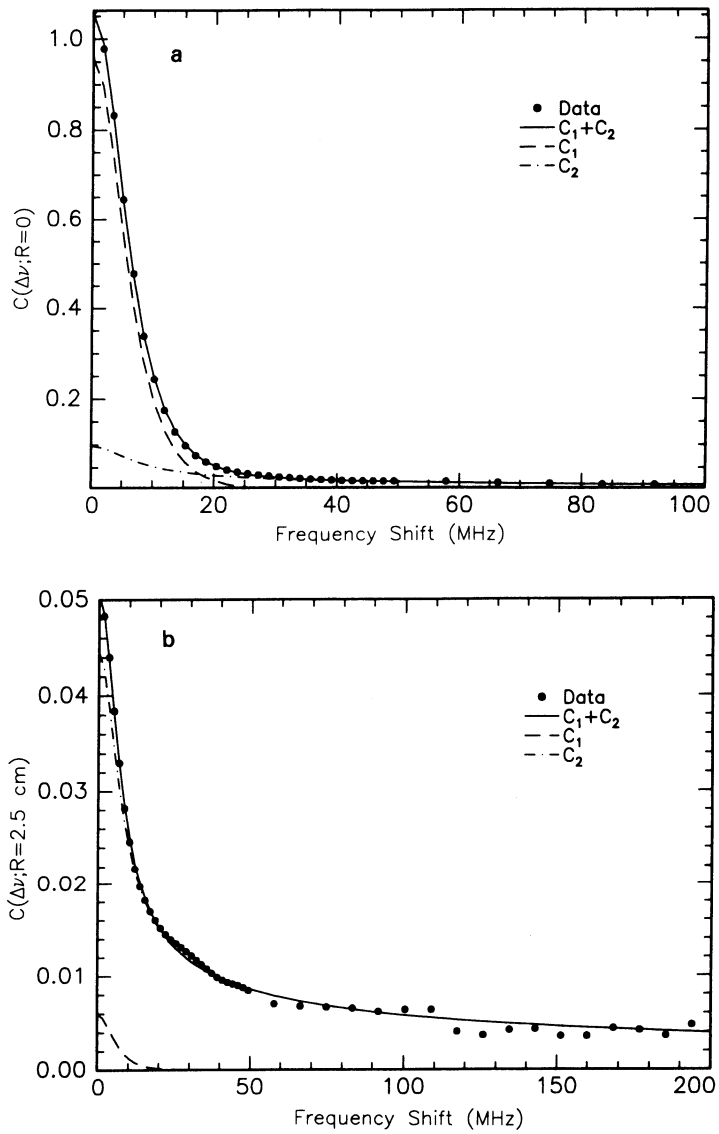

Figure 8. (a) Autocorrelation function for points at the output of a 150 cm sample of ½-in polystyrene spheres. (b) Crosscorrelation function for two points of the output of the same sample. The contribution of the first two terms in Eq. (8) to both correlation functions is shown.

Spectra are taken in successive static configurations as the frequency is swept between 20 and 21.7 GHz. Each spectrum is normalized by dividing the measured spectrum by the average of all spectra recorded by the detector for the medium. This eliminates instrumental frequency variations from the spectra. We computed the autocorrelation function with frequency of 6,400 spectra taken with each of the diodes as well as the crosscorrelation function with frequency of spectra in the two diodes for each of these configurations. These correlation functions for a sample of length $L = 150$ cm are given by the points in Fig. 8. These data are fit by the expression, $A_1F_1(\Delta\omega) + A_2F_2(\Delta\omega) +$ *Const.*, using A_1, A_2, D and *Const.* as fitting parameters and using the value of the absorption length $L_a \equiv (L/\alpha) = 34$ cm at 20.8 GHz, determined from measurements of the variation of intensity inside the sample with displacement along the tube axis.[39,42] The variation with frequency of L_a, D and ℓ in this sample is shown in the next section. The fit and the separate contributions of C_1 and C_2 to the auto and crosscorrelation functions are shown as the curves in Fig. 8. The frequency variation of C_3 is not included because it has not been calculated and in any case this term is small. We find, however, that including a constant in the fitting expression improved the fit. A frequency independent contribution to the correlation function might arise as a result of drift in the oscillator output or as a result of variations in the average opacity of different realizations of the sample. The fit to the autocorrelation function gives $D = 3.5 \times 10^{10}$ cm^2/s at 20.8 GHz.

A Langevin calculation of the magnitude of the leading order term in the contribution of C_2 to the crosscorrelation function, C^x, for $L > L_a$ gives,[15,16]

$$C^x = (3\pi/4)(1/Ak^2)(L/\ell). \tag{12}$$

We note that C^x is essentially the inverse of the dimensionless conductance and is independent of absorption for $L > L_a$. This suggests that the approach to the localization threshold for extended waves is independent of absorption. The value of ℓ in the present sample, determined from measurements of intensity inside the sample[39,42] at 20.8 GHz, is found to be $\ell = 5.9$ cm. Using this value in Eq. (12), gives $C^x = 0.043$, in good agreement with the results shown in Fig. 8. In the absence of absorption, C^x is 4/3 the value for absorbing samples given in Eq. (12).[16] Equating this with the first term in Eq. (9b) gives, $g_0 = (2/3\pi)Ak^2\ell/L$. Evaluating g_0 in the present absorbing sample gives, $g_0 = 12$.

The sharp drop in the magnitude of C_1 as the separation is changed from zero to 2.5 cm is consistent with the short-range of the field factorization contribution to the correlation function.[4,18] The contribution of C_1 to the auto and crosscorrelation functions at different sample lengths is shown in Fig. 9. The small length-independent contribution of C_1 to the crosscorrelation function is expected because C_1 depends only upon separation of the detectors. The contribution of C_1 to the autocorrelation function is very close to unity, but drops slightly as L increases in agreement with Eq. (9a).

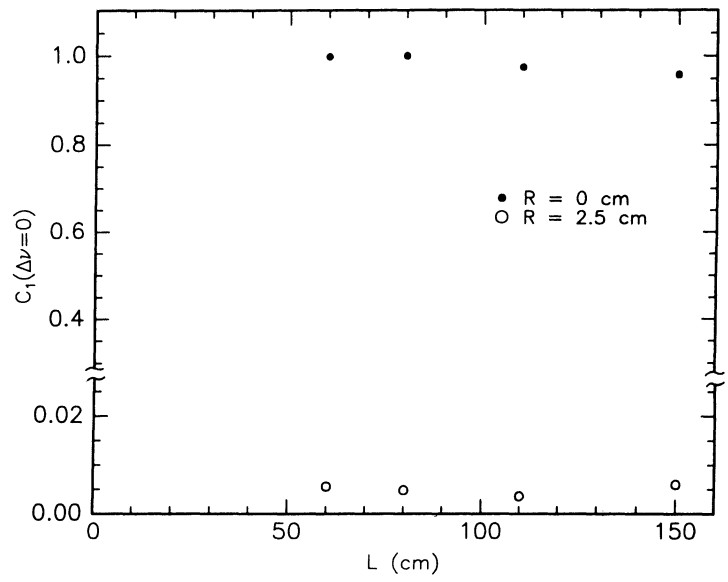

Figure 9. Scale dependence of the C_1 term of the auto and crosscorrelation functions for samples of ½-in polystyrene spheres.

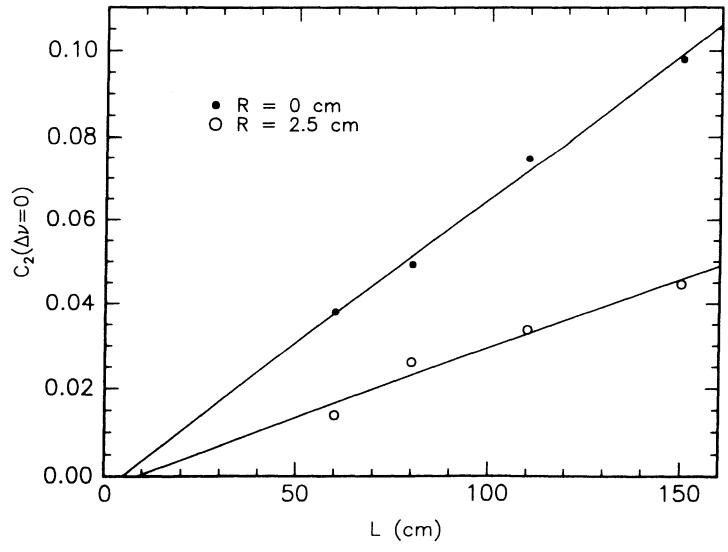

Figure 10. Scale dependence of the C_2 term of the auto and crosscorrelation functions for the samples of Fig. 9.

The scale dependence of the contribution of C_2 to the auto and crosscorrelation functions is shown in Fig. 10. The nearly linear dependence of C_2 in the crosscorrelation function is in accord with Eq. (11). Moreover, the contribution of C_2 to the autocorrelation function is twice as large as its contribution to the crosscorrelation function. This is a consequence of the structure of the C_2 term, which for the case $a = a'$ and $b = b'$, gives the factor $(\delta_{aa'} + \delta_{bb'}) = 2$.

The correlation in intensity between a point on the output surface and points the interior of the sample along the cylinder axis is observed to fall linearly with separation of the points.[18] This long-range behavior has been found in recent calculations by Kogan and Kaveh and by Pnini and Shapiro.[15,16]

Intensity Statistics

In the limit in which the degree of correlation in the phase and amplitude of partial waves reaching a point is negligible, the distribution of values of a given polarization component of a monochromatic field must be a Gaussian by the central limit theorem.[50] The corresponding distribution $P(\bar{I})$ of intensities normalized by the ensemble average value $\bar{I} = I/\langle I\rangle$ is then a negative exponential, $P(\bar{I}) = \exp(-\bar{I})$ with moments $\langle \bar{I}^n \rangle = n!$. Increasingly large departures from negative exponential statistics are found in the polystyrene sample studied above as the sample length increases.[17] Shnerb and Kaveh[51] have recently proposed an expression for the intensity distribution in nonabsorbing random media which includes the lowest order correction due to the interference of partial waves associated with paths which intersect once in the medium. To this order, the moments of the distribution are given by,

$$\langle \bar{I}^n \rangle = n! + n(n-1)n!\,S/2 \tag{13}$$

Using the Fourier-transform method, this yields the distribution,[51]

$$P(\bar{I}) = \exp(-\bar{I})[1 + \tfrac{1}{2}S(\bar{I}^2 - 4\bar{I} + 2)]. \tag{14}$$

The physical significance of S can be found by expressing the second moment of the intensity distribution in terms of the variance, $\langle \bar{I}^2 \rangle = \langle (\delta\bar{I})^2 \rangle + 1$. Comparing this with the expression for the second moment given by Eq. (13), $\langle \bar{I}^2 \rangle = 2 + 2S$, and identifying the variance, $\langle (\delta\bar{I})^2 \rangle$, with the value of the autocorrelation function at zero frequency shift C^a gives,[52]

$$S = \tfrac{1}{2}(C^a - 1). \tag{15}$$

From Eqs. (9a,9b), we find that, $C^a = 1 + C^x$, to order $1/g_0$. Thus,

$$S = \tfrac{1}{2}C^x. \tag{16}$$

We study the connection of correlation to the intensity distribution and the adequacy of Eq. (14) by considering the intensity distribution of microwave radiation for the 150 cm long polystyrene sample, compiled from the spectra used to compute the intensity correlation functions above. The measured intensity distribution is given by the points in Fig. 11. A fit of Eq. (14) to the distribution for $0.1 \leq \overline{I} \leq 8$ using S as a fitting parameter is shown as the solid line in the figure.[52] The departure from negative exponential statistics can be seen in the deviation of the data from the straight dashed line. The fit gives $S = 0.046 \pm 0.001$. This value may be compared to the values of S found from its connection to correlation, Eqs. (15,16). The magnitude of the

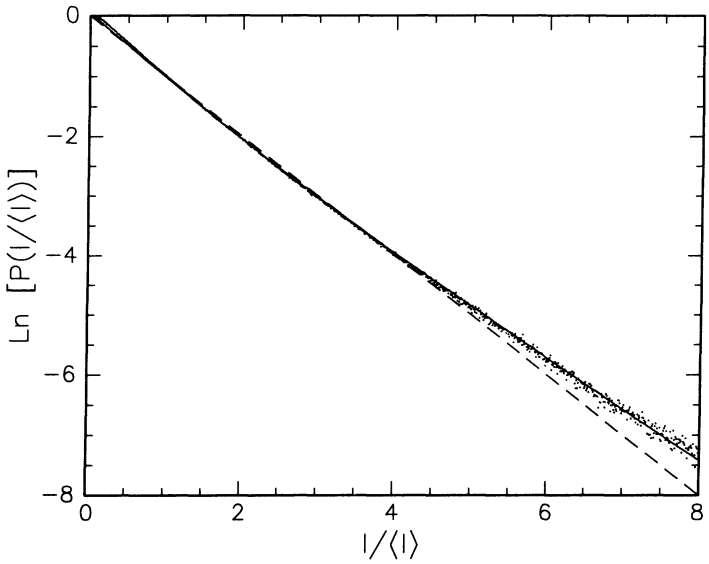

Figure 11. Natural logarithm of the measured distribution of polarized intensities for the sample of Fig. 8. The curve through the dots is a fit of Eq. (14) to the data. The dash line gives the prediction of negative exponential statistics.

autocorrelation function, as seen in Fig. 8a, is $C^a = 1.062 \pm 0.015$. Using eq. (15), this gives, $S = 0.031 \pm 0.010$. A large uncertainty exists in the value of S obtained from C^a because C^a is the difference between two terms of order unity. Greater accuracy can be obtained from measurements of the crosscorrelation function. The results in Fig. 8b give $C^x = 0.045 \pm 0.004$. Using Eq. (16), this gives $S = 0.023 \pm 0.002$, which is half the value obtained above from the fit of Eq. (14) to the intensity distribution.

The source of the discrepancy can be found by determining the values of S which need to be used in Eq. (14) to give the nth moment calculated using the data in Fig. 11. These values, S_n, are plotted in Fig. 12. As n decreases, values of S_n approach the value

obtained from measurements of the intensity correlation function. To leading order in the expansion parameter $1/g$, S_2 is given by $\frac{1}{2}C^x$. The increasing discrepancy for higher values of n are due to terms not included in the derivation of Eq. (14).[51] This indicates that the contribution of higher order corrections associated with multiple crossings in the sample is greater for higher moments. The close connection between the intensity distribution and the degree of correlation suggests that for $L > L_a$ $P(\overline{I})$is independent of absorption and depends only upon g as is the case for the degree of correlation. Thus the proximity of extended waves to the localization threshold appears to be independent of absorption.

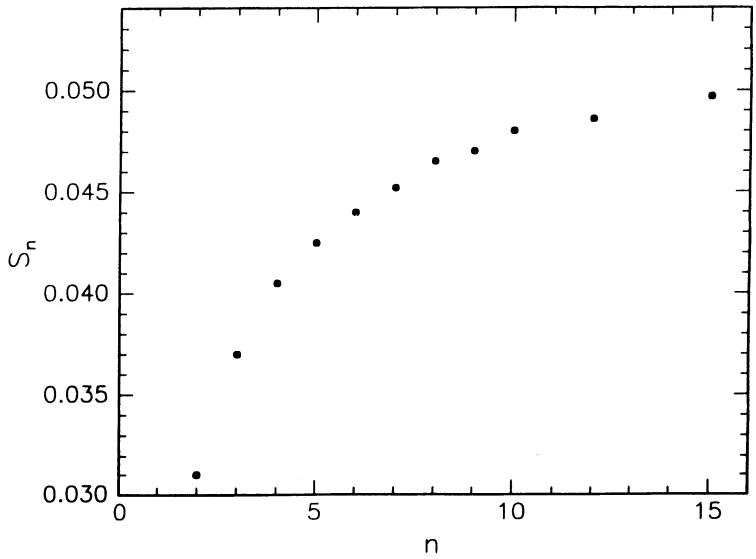

Figure 12. Calculated values of S using the experimentally determined nth moment and Eq. (14).

4. MICROSTRUCTURE RESONANCES

In the preceding sections we have seen that spatial and spectral, and hence temporal, transport measurements are well described by the diffusion formalism. We now consider the connection between these measurements in terms of the fundamental bulk transport parameters in space and time, ℓ and D. This may be succinctly expressed by introducing an additional phenomenological parameter, the transport velocity v, defined by the relation, $D = \frac{1}{3}v\ell$.[35] For point scatterers, v is the phase velocity v_p and varies slowly with frequency. For scatterers comparable in size to the wavelength, however, both v and v_p are frequency dependent as a result of resonances with the

scatterers.[35,36] It is presently an open question as to whether v and v_p differ in the low density limit.[35,53-55]

The transport and phase velocities may be readily distinguished, however, in the case illustrated schematically in Fig. 13. of a collection of metallic boxes containing random holes. The mean free path is essentially the box size since this is the distance travelled before the transport direction is randomized. Thus, the transmission through the sample is independent of the size of the holes except insofar as the holes influence the reflectivity at the sample's surface. The transit time, however, does depend upon the size of the holes because the mean dwell time of the wave in a box increases as the hole size is reduced. As a result, D and v depend upon the size of the holes and varies with frequency. In contrast, v_p is independent of the hole size and frequency.

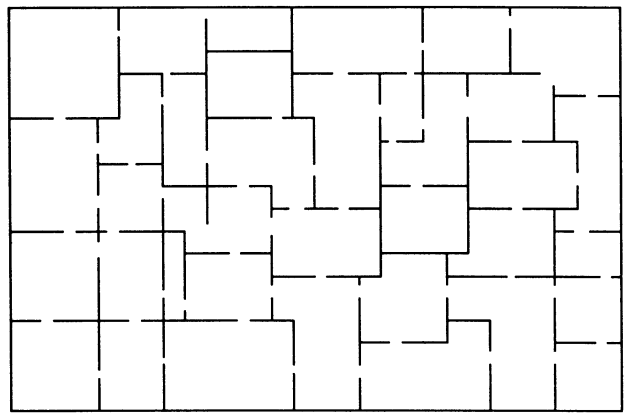

Figure 13. Juxtaposition of metallic boxes with holes.

Diffusive transport gives important clues to the nature of the localization transition. In the absence of microstructure resonances, spatial and spectral arguments lead to equivalent localization criteria. For localized waves, the reduced intensity at the borders of a block of a random sample corresponds to weak coupling between equivalent blocks of the disordered sample and to the exponential attenuation of the wave as the sample size is increased by juxtaposing boxes.[56] This leads to the criterion for spatial localization that the dimensionless conductance is less than unity.[56,57] In the absence of inelastic scattering, the localization transition for point scatterers is predicted to occur when the level width equals the separation between levels of the block.[56] At this point coupling between adjacent blocks is suppressed. This leads to the spectral criterion for localization that the Thouless number δ, which is the ratio of the level width to the level

spacing, is less than unity.[58] In the absence of microstructure resonances $g = \delta$. However, in the presence of such resonances, these quantities may differ. One can readily imagine a structure, such as that in Fig. 13, in which $\ell \gg \lambda$, but in which $\delta < 1$. The question then arises as to whether g or δ is the appropriate scaling parameter of the localization transition or indeed whether there is a single scaling parameter that describes all aspects of transport. It should be noted that the intensity distribution must be influenced by δ since it is the macroscopic resonant structure of the sample that leads to large transmission fluctuations that are characteristic of localized waves. Certainly the degree of correlation is a measure of the proximity to the localization threshold. Eq. (12) and the measurements of the previous section suggest that the calculated and measured amplitude of C^x is $1/g$. However, a hidden assumption in the calculation is that the mean distance in which the phase of the wave is randomized is ℓ, the distance in which the direction of the wave is randomized. This may not be the case if the scatterers are not point scatterers. The experimental verification that $C^x \approx 1/g$ can only be taken as definitive if it is carried out over a broad frequency range in which the values of g and δ differ significantly. Preparatory work for such a study is described here.

A full study of transport in the case in which the wave may be in resonance with the microstructure of the sample requires the evaluation of both v and v_p. To find v, it is necessary to determine both ℓ and D. ℓ can only be obtained once interfacial interactions are properly taken into account in phenomena that can be described by the photon diffusion model. It cannot be accurately determined, therefore, from a single measurement of transmission or from measurements of distributions or correlation in reflection. On the other hand, D can be reliably obtained from measurements of spectral correlation functions or from pulsed measurements in transmission. As long as $L \gg z_b$, spectral correlation functions and the time of fight distribution are not significantly influenced by internal reflectivity. To find v_p, it is necessary to determine the fraction of the time the wave spends in the high and low refractive index portions of the sample. This can be found from a determination of the absorption rate in the random sample and in the bulk material of the scatterers. The results below are not yet the complete set of experiments that are needed to resolve all the questions posed above, but they do show that these issues can be settled experimentally.

We have studied the frequency dependence of microwave propagation in two samples in which sphere resonances are clearly exhibited. The first is the sample of polystyrene spheres which we have discussed in the previous section. The region near the first Mie resonance of the spheres is investigated. The second type of sample is a mixture of nearly spherical, ⅜-inch diameter particles of 90% alumina supplied by Coors Ceramics Inc. and hollow polypropylene spheres of the same diameter. The index of refraction of the solid spheres is 3.0 and the frequency range near the second Mie resonance is explored. By varying the volume fraction f of alumina spheres, it is possible

to find the density range in which the independent scatterer model adequately describes propagation and to discover the filling fraction and frequency at which the strongest scattering occurs. This sample was also chosen to allow us to investigate the source of the small optical diffusion coefficient measured near the second Mie resonance of anatase titania spheres with index of 2.2.[59]

The results for polystyrene spheres is shown in Fig. 14. The absorption coefficient, $\alpha = 1/L_a = 1/(D\tau_a)^{1/2}$, which is shown in Fig. 14a, and the extrapolation length on the output surface z_b at each frequency are determined by fitting the expression for the intensity inside the sample versus distance, $L - z$, from the output face, $I(z) \propto \sinh[\alpha(L - z + z_b)]$, to measurements inside the sample of length 150 cm .[39,42] The values of ℓ and of the reflection coefficient R at 18.5 Ghz are determined from measurements of z_b at the output surface and of the relative transmission through the sample with and without additional copper plates with a variety of holes on the output face of the sample. These measurements give $\ell = 6.5 \pm 0.3$ cm and $R = 0.13$ at 18.5 GHz.[39,42] We expect that the value of R does not display strong resonant behavior over the K band for this high density sample. We will, therefore, use the value of the R at 18.5 GHz over this frequency range. The frequency dependence of the transport mean free path is then found by solving the relation,[39,52]

$$z_b = (1/2\alpha)\ln[(1 + 0.71\alpha\ell(1+R)/(1-R))/(1 - 0.71\alpha\ell(1+R)/(1-R))], \qquad (17)$$

using the measurements of the frequency variation of z_b and α. The results are given in Fig 15b.

The frequency dependence of D, shown in Fig. 14c, is found using the procedure outlined in the previous section for fitting the autocorrelation function using spectra with a narrow frequency range and the values of the absorption coefficient in Fig. 14a. From the ratios of the data in Figs. 14c and 14b, we obtain the transport velocity, $v = 3D/\ell$ shown in Fig. 14d. A broad dip in the value of v is observed with a minimum transport velocity of $v \approx 1.8 \times 10^{10}$ cm/s. This is comparable to the phase velocity in the high index medium and hence considerably less than the phase velocity in the collections of spheres in air. The absorption rate is obtained using the data in Figs. 14a and 14c using the relation, $1/\tau_a = D\alpha^2$.

In Fig. 15 we show the frequency and density dependence of the diffusion coefficient in the alumina sample.[36] Quite surprisingly, sharp sphere resonances in these samples are observed up to $f = 0.40$. At $f = 0.56$, D is nearly independent of frequency, indicating the breakdown of the independent scatterer model. Though the diffusion coefficient is quite small in this sample, propagation is well described by the photon diffusion model. The degree of correlation in the $f = 0.30$ sample at a length of 20 cm cm is never more than 0.03.

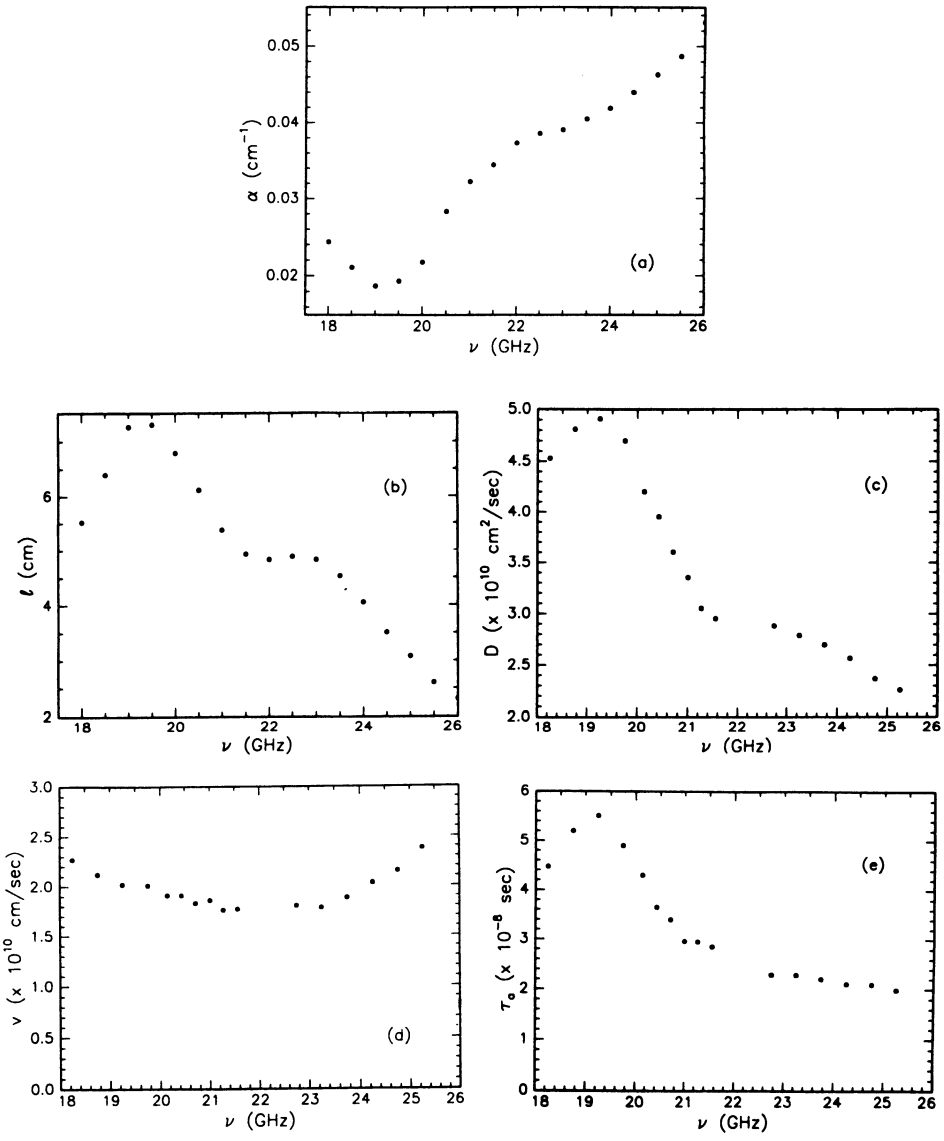

Figure 14. Frequency dependence of (a) the absorption coefficient, (b) mean free path, (c) diffusion coefficient, (d) transport velocity and (e) absorption time for a sample of ½-in polystyrene spheres.

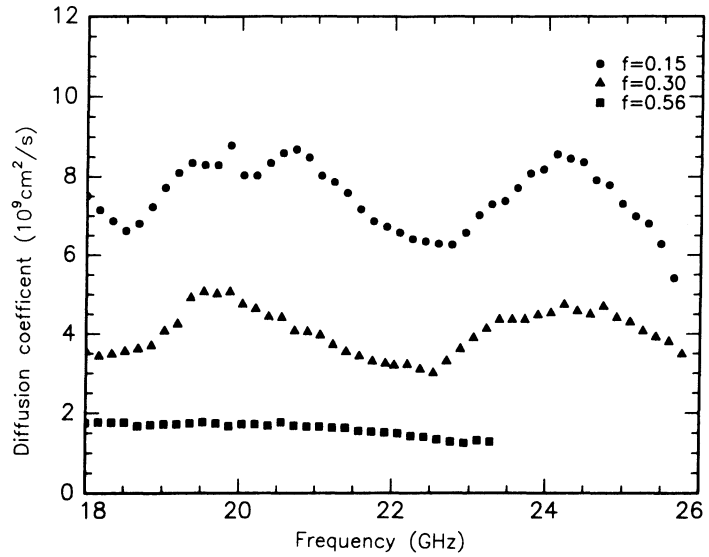

Figure 15. Frequency dependence of the diffusion coefficient for mixtures of 3/8-in solid alumina and hollow polypropylene spheres for various filling fractions f of alumina spheres.

Localization

In Ref. 29, we reported slight deviations from diffusive behavior in measurements of $T(L)$ in mixtures of ⅛-inch aluminum spheres and polystyrene spheres. These spheres were chosen to be near the first resonance at which Condat and Kirkpatrick[25] had predicted that localization might be observed. Since the largest suppression in transmission occurred at the high frequency end of our K band microwave oscillator, we attempted to bring the spheres into resonance by increasing the diameter of the scatterers to 3/16-inch. Spatial and spectral measurements were made for various volume filling fractions f of aluminum spheres from $f = 0.15$ to $f = 0.45$.

In strongly scattering samples in which $k\ell \approx 1$ and $g \approx 1$, the extent of coherent backscattering increases as the thickness of the sample increases because a larger fraction of paths leaving any point returns to the point. Transmission may then be described using an effective scale dependent diffusion coefficient $D(L)$.[21-23,57] For localized waves $D(L) \rightarrow 0$ as $L \rightarrow \infty$. For extended waves, the scaling theory of localization[57] gives, $D(L) = (v\ell/3)(\ell/\xi)$, where ξ is given by, $1/\xi = 1/\xi_0 + 1/L_\phi + 1/L$, where L_ϕ is the dephasing length, and $\xi_0 = \ell^2/(\ell\text{-}\ell_c)$ is the coherence length in an infinite sample in the absence of inelastic processes. At the mobility edge, $\ell = \ell_c$, ξ_0 diverges and the effective diffusion coefficient is, therefore, $D_c(L) = (v\ell_c^2/3)(1/L + 1/L_\phi)$. In the absence of dephasing or absorption, the transmission for $L < \xi_0$ is given by $T(L) \approx D(L)/vL \approx \ell_c^2/L^2$. This $1/L^2$ falloff of transmission is a signature of the critical regime.

For $\ell < \ell_c$, the wave is localized. Transmission then falls exponentially on length scales greater than the localization length. However, transmission also falls exponentially for extended waves for samples thicker than the absorption length L_a. Nonetheless, a rounded localization transition can be identified by the nature of the change in the character of transport and in the statistics of propagation when the interaction of the wave and medium goes through the Anderson localization transition as the density of scatterers is changed or as the frequency is varied.

Such a transition is observed in mixtures of aluminum and teflon spheres.[26,27]. The scale dependence of transmission at 19 GHz in the $f = 0.20, 0.30$ and 0.35 samples is shown in Fig. 16 and the frequency dependence of the attenuation coefficient in these sample is shown in Fig. 17. At $f = 0.20$, transmission falls as $1/L$ for $L < L_a$, indicating that propagation is diffusive at this concentration. The absorption and diffusion coefficients are independent of frequency in the K band for this sample. At $f = 0.30$, transmission falls initially as $1/L^2$, indicating that the wave is near the mobility edge. The attenuation coefficient becomes frequency dependent for $f > 0.25$. At $f = 0.35$, transmission drops exponentially for sample thicknesses greater than the wavelength. The diffusion coefficient is smaller than could be obtained by renormalization of the

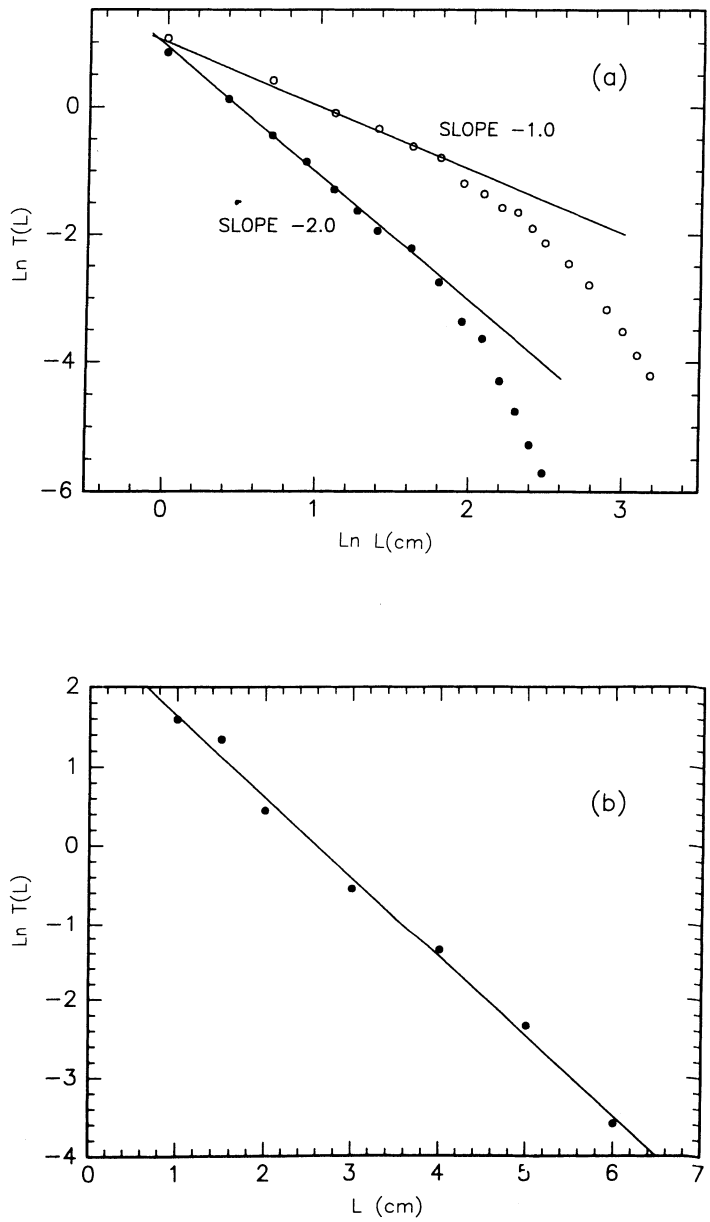

Figure 16. Scale dependence of the relative transmission for three different mixtures of 3/16-in aluminum and teflon spheres. (a) In samples with aluminum filling fraction $f = 0.20$ (open circles) $T(L) \sim 1/L$ for $L < L_a$, whereas for $f = 0.30, T(L) \sim 1/L^2$ for $L < L_a$. (b) For $f = 0.35$ transmission drops exponentially for sample thicknesses greater than the wavelength.

scale dependent diffusion coefficient in the critical regime over the length scales in which absorption is negligible. This behavior occurs over a narrow frequency range and the attenuation coefficient is also enhanced over the same narrow range. This corresponds to a narrow window of localization[21] which is hypothesized to lie between the long wavelength limit, in which effective medium theory is appropriate, and the short wavelength limit, in which propagation approaches the geometric optics limit. The peak scattering near 19 GHz presumably occurs because of the proximity to both the first sphere resonance and the waveguide cutoff frequency for typical spacing between spheres.

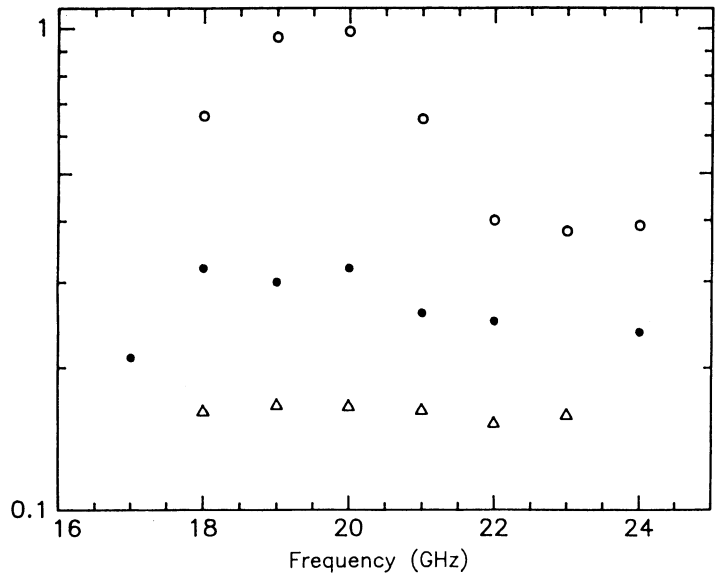

Figure 17. Frequency dependence of the absorption coefficient for three different mixtures of aluminum and teflon spheres: $f = 0.20\,(\Delta)$, $f = 0.25\,(\bullet)$ and $f = 0.35\,(\circ)$.

Another indication of the correlated nature of transport can be seen in the measurements of the fractional correlation of intensity between a point at the output surface and interior points shown in Fig. 18 for the $f = 0.20$ and $f = 0.30$ samples. Unlike the linear decrease in correlation with detector separation that is observed in the $f = 0.20$ sample, which is characteristic of diffusive transport,[18] the correlation function for the $f = 0.30$ sample drops abruptly over the same length scale on which $T(L)$ decreases by a factor of five. This indicates that this length corresponds to the correlation length ξ.

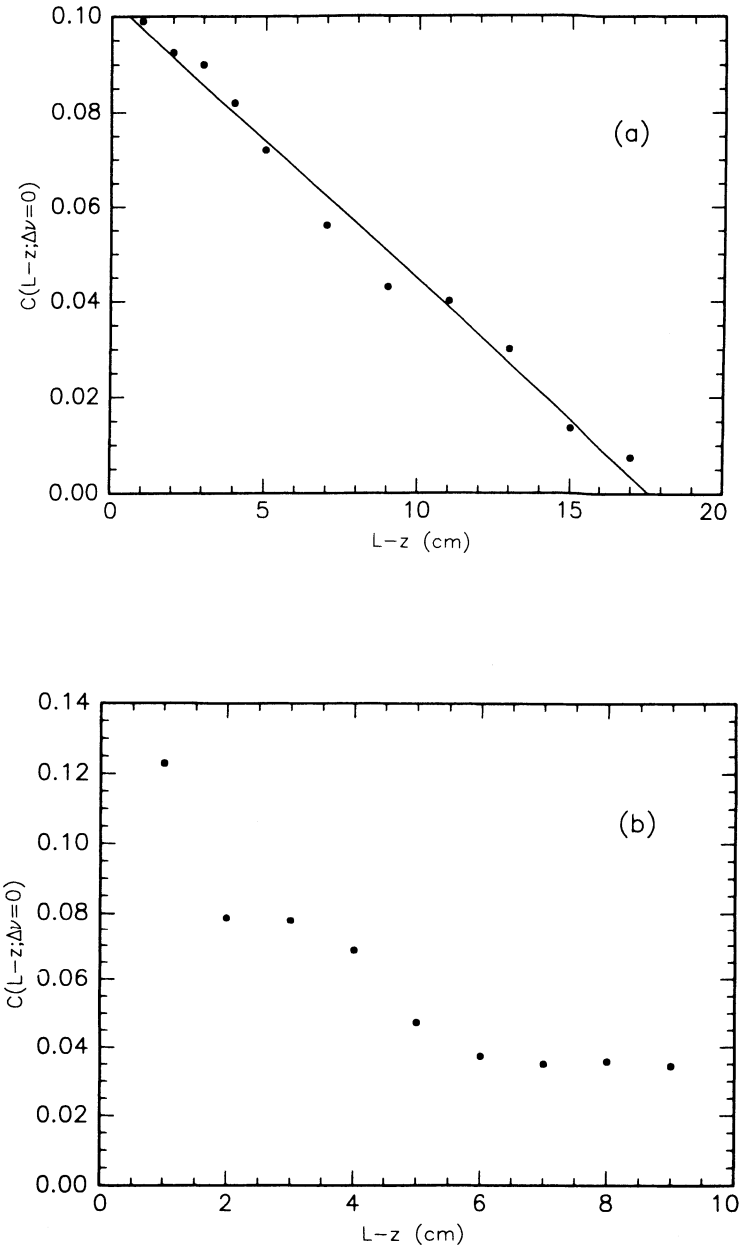

Figure 18. Scale dependence of the crosscorrelation function for two mixtures of aluminum and teflon spheres. (a) In the sample with $f = 0.20$ a nearly linear falloff is observed. (b) For $f = 0.30$ a sharp drop in $C(L - z)$ is observed between 1 and 2 cm. In this thickness range, transmission drops by a factor of five.

It was recognized in the early discussion of photon localization by John[21] that absorption becomes increasingly important as the localization threshold is approached. The renormalization of the diffusion coefficient as L increases leads to a shortening of the absorption length. It was assumed that $D(L)$ would not be renormalized on length scales greater than the absorption length since partial waves following paths with greater excursions are unlikely to return to a point at the input before being absorbed. The attenuation length at larger length scales would therefore reflect the diffusion coefficient at $L \approx L_a = (D(L_a)\tau_a)^{1/2}$. The peak in the attenuation coefficient as a function of frequency which we observed in random mixtures of aluminum spheres at $f > 0.25$ was attributed to an enhanced attenuation coefficient associated with a renormalized diffusion coefficient $D(L_a)$.[22]

Recently Weaver[60] and Yosefin[61] have proposed that absorption does not cut off the renormalization of $D(L)$. Indeed waves that return to a point along time reversed paths are in phase even though the probability of return is reduced by absorption. That the phase coherence within a strongly absorbing static random sample is not diminished by absorption is evidenced by the observation of nulls in the intensity distribution which can occur only if the intensity at such points does not fluctuate in time. We have also found that the degree of long-range intensity correlation and the intensity distribution in the polystyrene sample are insensitive to absorption. It therefore appears that the closeness to the mobility edge of extended waves is not influenced by absorption. It should be noted however that absorption plays a more significant role for localized waves than for extended waves. For example, large values of intensity occur when the incident frequency is resonant with a localized state near the center of the sample.[62] Because the transit time through the sample is exponentially long for such states, however, such large fluctuations are most strongly suppressed by absorption.

If we assume, nonetheless, that absorption does not cut off the renormalization flow, the anomalously large and frequency dependent exponential attenuation found in the aluminum-teflon mixtures would be due to renormalization of $D(L)$ even for $L > L_a$. The attenuation length would then essentially be the localization length, though it may be modified somewhat by absorption. Thus, the peak in the attenuation coefficient remains a signature of the localization transition. These results support the conclusion that photons in the system under study are localized regardless of whether renormalization is or is not cut off by absorption. Evidence of localization is also found in the small value of the diffusion coefficient as inferred from measurements of $C(\Delta\nu)$ and in values of the intensity variance which becomes as large as 2.4 at 19 GHz for $f = 0.35$. To study the role of absorption, it will be useful to investigate cooled samples in which absorption is weak and to examine the spatial variation of intensity in the medium at fixed times following pulsed excitations.

6. CONCLUSION

On balance, the progress made in the study of photon diffusion, correlation and

localization supports the hope that all fundamental questions regarding the character of wave propagation in random media can be addressed experimentally. That many major issues are not yet resolved will surely serve to stimulate research in the coming years. Among the important questions that will be addressed in future research are the connection between intensity correlation and localization, the influence of absorption on localization, the relationship between spatial and temporal aspects of transport in the diffusive and localized regimes, the time of flight distribution and intensity distribution for localized waves, the number of parameters needed to fully describe wave propagation, the value of the critical exponent, and the relationship between various localization criteria.

This work was supported by the NSF under grant DMR-9001335, by the Petroleum Research Fund of the ACS under grant 22800-AC,7, and by several PSC-CUNY awards. We are grateful to B. Shapiro and R. Pnini for stimulating interactions supported by the United States - Israel Binational Science Foundation. We thank T.D. Cheung, D. Livdan and W. Polkosnik for their contributions and thank E. Kuhner for expert technical assistance.

REFERENCES

1. "The Scattering and Localization of Classical Waves," P. Sheng, ed., World Scientific Press, Singapore (1990).
2. Y. Kuga and A. Ishimaru, J. Opt. Soc. Am. A 1:831 (1984); M.P. van Albada and A. Lagendijk, Phys. Rev. Lett. 55:2692 (1985); P.E. Wolf and G. Maret, Phys. Rev. Lett. 55:2696 (1985).
3. E. Akkermans and R. Maynard, J. Phys. France Lett. 46:L1045 (1985).
4. B. Shapiro, Phys. Rev. Lett. 57:2168 (1986).
5. A.Z. Genack, Phys. Rev. Lett. 58:2043 (1987).
6. A. Z. Genack and J.M. Drake, Europhys. Lett. 11:331 (1990).
7. G. Maret and P.E. Wolf, Z. Phys. B 65:409 (1987); M. Rosenbluh, M. Hosen, I. Freund and M. Kaveh, Phys. Rev. Lett. 58:2754 (1987); A.A. Golubentsev, Sov. Phys. JETP 59:26 (1984); M.J. Stephen, Phys. Rev. B 37:1 (1988); A.G. Yodh, P.D. Kaplan and D.J. Pine, Phys. Rev. B 42:4744 (1990).
8. F.A. Erbacher, R. Lenke and G. Maret, preprint.
9. I. Freund, M. Rosenbluh and S. Feng, Phys. Rev. Lett. 61:2328 (1988).
10. For references to electronic correlation see "Mesoscopic Phenomena in Solids," B.L. Altshuler, P.A. Lee and R.A. Webb, eds. North Holland, Amsterdam (1991).
11. M.J. Stephen and G. Cwilich, Phys. Rev.Lett. 59:285 (1987).
12. P.A. Mello, Phys. Rev. Lett. 60:1089 (1988); P.A Mello, E Akkermans and B. Shapiro, Phys. Rev. Lett. 61:459 (1988).
13. B.Z. Spivak and A.Yu Zyuzin, Solid State Comm. 65:311 (1988).

14. S. Feng, C. Kane, P.A. Lee and A.D. Stone, Phys. Rev. Lett. 61:834 (1988).
15. R. Pnini and B. Shapiro, Phys. Lett. A 157:265 (1991); Phys. Rev. B 39:6986 (1989).
16. E. Kogan and M. Kaveh, Phys. Rev. B 45:1049 (1992).
17. N. Garcia and A.Z. Genack, Phys. Rev. Lett. 63:1678 (1989).
18. A.Z. Genack, N. Garcia and W. Polkosnik, Phys. Rev. Lett. 65:2129 (1990).
19. M.P. van Albada, J.F. de Boer and A. Lagendijk, Phys. Rev. Lett. 64:2787 (1990).
20. J.F de Boer, M.P. van Albada and A. Lagendijk, Phys. Rev. B 45:658 (1992).
21. S. John, Phys. Rev. Lett. 53:2169 (1984).
22. J.B. Pendry and P.D. Kirkman, J. Phys. C 17:6711 (1984).
23. P.W. Anderson, Philos. Mag. 52:505 (1985).
24. P. Sheng and Z.Q. Zhang, Phys. Rev. Lett. 57:1879 (1986).
25. C.A. Condat and T.R. Kirkpatrick, Phys. Rev. Lett. 58:226 (1987).
26. N. Garcia and A.Z. Genack, Phys. Rev. Lett. 66:1850 (1991).
27. A.Z. Genack and N. Garcia, Phys. Rev. Lett. 66:2064 (1991).
28. E. Yablonovitch, Phys. Rev. Lett. 58:2059 (1987); S. John, Phys. Rev. Lett. 58:2486 (1987); E. Yablonovitch, T.J. Gmitter and K.M. Leung, Phys. Rev. Lett. 67:2295, (1991); S.L. McCall, P.M. Platzmann, R. Dalichaouch, D. Smith, and S. Schultz, Phys. Rev. Lett. 67:2017 (1991); J. Martorell and N.M. Lawandy, Phys. Rev. Lett. 65:1877 (1990).
29. A.Z. Genack, *in*: "The Scattering and Localization of Classical Waves," P. Sheng, ed., World Scientific Press, Singapore (1990), p. 207.
30. A. Lagendijk, R. Vreeker and P. de Vries, Phys. Lett. A 136:81 (1989).
31. I. Freund, M. Rosenbluh and R. Berkovits, Phys. Rev. B 39:12403 (1989).
32. F.C. MacKintosh, S. John, Phys. Rev. B 40:2383 (1989).
33. I. Freund and R. Berkovits, Phys. Rev. B 41:496 (1990).
34. N. Garcia, J.H. Li, W. Polkosnik, T.D. Cheung, P. Tsang, A.A. Lisyansky and A.Z. Genack, Physica B 175:9 (1991).
35. M.P. van Albada, B.A. Tiggelen, A. Lagendijk and A. Tip, Phys. Rev. Lett. 66:3132 (1991).
36. J.H. Li, N. Garcia and A.Z. Genack, Bull. Amer. Phys. Soc. 36:358 (1991).
37. J.X. Zhu, D.J. Pine, and D.A. Weitz, Phys. Rev. A 44:3948 (1991).
38. P.M. Saulnier and G.H. Watson, Opt. Lett 17:946 (1992).
39. N. Garcia, A.Z. Genack, and A.A. Lisyansky, Phys. Rev. B 46:14475 (1992).
40. J.H. Li, A.A. Lisyansky, T.D. Cheung, D. Livdan and A.Z. Genack, preprint.
41. P.M. Morse and H. Feshbach. "Methods of Theoretical Physics," McGraw-Hill, NY (1953).
42. A.A. Lisyansky, J.H. Li, D. Livdan, N. Garcia, T.D. Cheung and A.Z. Genack, this volume.
43. A. Ishimaru, Y. Kuga, R.L.T. Cheung and K. Shimizu, J. Opt. Soc. Am. 73:131 (1983).

44. M. Lax, V. Nayaramamurti, and R.C. Fulton, *in*: "Proceedings of the Symposium on Laser Optics and Condensed Matter," J.L. Birman, H.Z. Cummins and A.A. Kaplyanskii, eds.
45. See M. Born and E. Wolf. "Principles of Optics," 3rd edition, Pergamon, Oxford (1965).
46. R. Berkovits, M. Kaveh and S. Feng, Phys. Rev. B 40:737 (1989).
47. J.H. Li, T.D. Cheung and A.Z. Genack, preprint.
48. N. Garcia, A.Z. Genack, R. Pnini and B. Shapiro, preprint.
49. A.A. Lisyansky and D. Livdan, Phys. Lett. A 170:53 (1992).
50. J.W. Goodman. "Statistical Optics," J. Wiley, New York (1985).
51. N. Shnerb and M. Kaveh, Phys. Rev. B 43:1279 (1991).
52. A.Z. Genack and N. Garcia, preprint.
53. Yu.N. Barabanenkov and V.D. Ozrin, Phys. Rev. Lett. 69:1364 (1992).
54. G. Cwilich and Y. Fu, preprint.
55. J. Kroha, C.M. Soukoulis and P. Wölfle, preprint.
56. D.J. Thouless, Phys. Rev. Lett. 39:1167 (1977).
57. E. Abrahams, P.W. Anderson, D.C. Licciardello and T.V. Ramakrishnan, Phys. Rev. Lett. 42:673 (1979).
58. A.Z. Genack, Europhys. Lett. 11:733 (1990).
59. J.M. Drake and A.Z. Genack, Phys. Rev. Lett. 63:259 (1989).
60. R.L. Weaver, preprint.
61. M. Yosefin, preprint.
62. M.Ya. Azbel, Solid St. Comm. 45:527 (1983).

THE SPEED OF DIFFUSING LIGHT: RIGOROUS SOLUTIONS

Bart A. van Tiggelen[a] and Ad Lagendijk[a,b]

[a] FOM-Institute for Atomic and Molecular Physics
Kruislaan 407, 1098 SJ Amsterdam, The Netherlands
[b] Van der Waals-Zeeman Laboratory, University of Amsterdam
Valckenierstraat 65-67, 1018 XE Amsterdam, The Netherlands

1. INTRODUCTION

Quite recently we reported [1] on a very small transport velocity v_E entering the diffusion constant D of light according to,

$$D = \frac{1}{3} v_E \ell . \tag{1}$$

Here ℓ is the transport mean free path. In a particular case we measured a factor of about six lowering of the diffusion constant. The decrease turned out to be due to a small velocity rather than a small transport mean free path. The last feature is anticipated near the Anderson mobility edge, at which the correlation length ξ diverges and the transport mean free path vanishes according to $\ell \sim 1/\xi$.

The surprising conclusion that the velocity is responsible for the low diffusion constant emerged from careful steady-state transmission experiments giving a direct value for the transport mean free path. Recent measurements [2] of the frequency-frequency intensity correlation function confirmed the extremely small velocity that can be associated with the propagation of the *diffusive* component of light in a random dielectric medium.

From the theoretical side we have pointed out [1] [3] that the incorrect handling of conservation laws, so-called Ward identities, can be held responsible for the fact that this interesting phenomenon was not predicted earlier. These identities were originally developed for electron-impurity scattering and were then simply taken over for classical waves. For the first time we indicated that the notion of an "energy-dependent" potential in the classical wave equations generates extra terms in the equation of continuity. These terms are dynamic in origin and are not present in the steady-state limit.

Such terms are also present in the case of multiple elastic electron-impurity scattering. However, the above mentioned Ward identities demonstrate unambiguously that these extra terms cancel all together for an energy-independent potential. Translating this electron-impurity result straightforwardly to classical wave scattering would lead us to the erroneous conclusion that v_E would always be of the order of the phase velocity. In this paper we discuss briefly under what conditions the transport velocity equals

Photonic Band Gaps and Localization, Edited by
C.M. Soukoulis, Plenum Press, New York, 1993

the phase velocity, and when not. We present some *exact* solutions for scalar classical waves (waves obeying the scalar wave equation, thus ignoring polarization), among which are the "scalar" Mie sphere, the "scalar" reflector, and the point scatterer.

2. SOLUTIONS OF THE SCALAR WAVE EQUATION

The main theoretical results of Refs. [1] and [3] can be summarized by the following expression for the transport velocity, in units of c_0,

$$v_E(E) = \frac{1}{v_p} \frac{1}{1 + n\,\delta_1(E)} \tag{2}$$

The dynamic vertex correction is, in terms of the single-scatterer t-matrix $t_{\mathbf{pp}'}(E)$, with complex phase $\Phi(\Omega, E)$,

$$\delta_1(E) = -\frac{\partial \mathrm{Re}\, t_{\mathbf{pp}}(E)}{\partial(E^2)} + \int d\Omega \frac{d\sigma}{d\Omega} \frac{\partial \Phi(\Omega, E)}{\partial E} \tag{3}$$

The phase velocity is given by,

$$\frac{1}{v_p} = \sqrt{1 - n \frac{\mathrm{Re}\, t_{\mathbf{pp}}(E)}{E^2}} \tag{4}$$

and n is the number density of the scatterers. The second term in Eq. (3) is a *scattering* contribution; without this term v_E would be equal to the strongly anomalous group velocity [4]. It is understood that the t-matrices are evaluated on the energy shell: $p = p' = |E|$, but derivation is to be performed at constant momenta. In principal this requires knowledge of the *off-shell* t-matrix, which is usually not given by textbooks, because it is more difficult to calculate. One suitable approximation that circumvents this difficulty is the replacement of the partial derivatives by *total* derivatives, thereby including some derivatives with respect to momenta. This approximation for δ_1 will be referred to as the Wigner approximation and is denoted by δ^W. This quantity turns out to be (proportional to) the *Wigner delay time* [5] in three dimensions.

Let us make a comment on this approach. The Ward identity for electrons proves that $\delta_1(E) = 0$ in that case [6]. On the other hand, one knows that the Wigner delay time (proportional to δ^W) does not vanish. Thus, the Wigner approximation for $\delta_1(E)$ does *erroneously* suggests that dynamic vertex corrections are also present for electron-impurity scattering. We anticipate that such corrections would only come in if the scattering object is given internal degrees of freedom which can scatter the electrons elastically with considerable delay. The concept of an energy-dependent or "optical" potential also arises after having integrated out (resonant) internal degrees [7] and is very similar to the energy-dependent potential that is *inherently* present in the scalar wave equation.

We will next present an *exact* calculation of δ_1. In view of the Schrödinger equation, one can identify in the scalar wave equation an "energy" E^2 and a "potential" $V(\mathbf{r}, E) = [1 - \epsilon(\mathbf{r})]E^2 \equiv g(\mathbf{r})V_0(E)$. These concepts can be translated straightforwardly to monochromatic scattering properties among which the scattering amplitude. We apply the identity,

$$\left.\frac{\partial}{dE^2}\right)_{\mathbf{pp}'} = \left.\frac{\partial}{dE^2}\right)_{V_0, \mathbf{p}\,\mathbf{p}'} + \frac{dV_0}{dE^2} \times \frac{d}{dV_0} \tag{5}$$

to Eq. (3). The derivatives at "constant potential" in δ_1 must cancel by the Ward

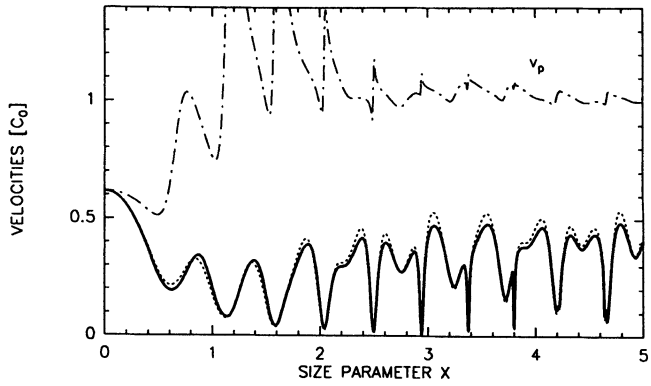

Figure 1: Transport velocity (bold) and phase velocity v_p (dashed dotted) for scalar Mie spheres with packing fraction 25 % and an index of refraction $m = 2.73$. The dotted line is the Wigner approximation.

identity for potential scattering. We conclude that δ_1 is essentially given by derivatives of the *on-shell* t-matrix with respect to potential, rather than energy. Hence,

$$\delta_1(E) = \left[-\frac{\partial \mathrm{Re}\, t_{\mathbf{pp}}(E)}{\partial V_0} + 2E \int d\Omega \, \frac{d\sigma}{d\Omega} \frac{\partial \Phi(\Omega, E)}{\partial V_0} \right] \times \frac{dV_0}{dE^2} \tag{6}$$

Using results from time-dependent scattering theory, we are able to prove the validity of the following equivalent representations [8]:

$$\delta_1(E) = -\frac{dV_0}{dE^2} \left\langle \psi_E^+ \right| g \left| \psi_E^+ \right\rangle = E \frac{dV_0}{dE^2} \lim_{\mathrm{Im} V_0 \to 0} \frac{\sigma_{\mathbf{abs}}}{\mathrm{Im} V_0} \tag{7}$$

We introduced $|\psi_E^+>$ as the normalized continuum eigenfunction at frequency E. Furthermore, $\sigma_{\mathbf{abs}}$ is the cross-section for absorption. The first equality relates the vertex correction δ_1 to the "potential energy" within the dielectric scatterer, energy not subject to propagation. It shows that the transport velocity relates to the *dwell time* [9] in the potential region rather than the delay time. The second equality is very convenient for numerical purposes. The equivalence of the energy inside the dielectric and absorption arguments, expressed in Eq. (7), was already noticed numerically by Bott [10]. In our paper Ref. [3] absorption and charging arguments were successfully introduced heuristically for vector scatterers. They are seen to become exact for scalar scattering.

There has been some confusion about the existence of a third term in Eq. (3). It has even been argued that this term will cancel the whole effect [11]. We confirm the existence of a third contribution indeed. It can be cast into the form,

$$\Delta\delta(E) = -\frac{4\pi}{E} \sum_{\mathbf{p}} \frac{\partial \mathrm{Re}\, G(E,p)}{\partial E^2} \mathrm{Im}\, \Sigma(E,p) \tag{8}$$

It can be demonstrated straightforwardly that we are in fact dealing with a effect that is *second-order* in density (and thus part of δ_2). To this end let $\ell_s = 1/n\sigma_{\mathbf{scat}}$ be the scattering mean free path. If we assume for simplicity that $-\mathrm{Im}\, \Sigma(E,p) = E/\ell_s(E)$ does not depend on p (which is exact for point scatterers [12]), the integral can be performed in all orders of the density. The result reads,

$$\Delta\delta(E) = \frac{1}{4} \frac{d}{dE^2} \left(\frac{1}{\ell_s^2} \right) + \mathcal{O}(n^3) = \frac{n^2}{4} \frac{d\sigma_{\mathbf{scat}}^2}{dE^2} \quad \text{q.e.d.} \tag{9}$$

This conclusion can be generalized for non-point scatterers using the identity (5).

For the "scalar" Mie sphere with on-shell t-matrix,

$$t_{\mathbf{pp}'}(E) = -\frac{4\pi i}{E}\sum_{n=0}^{\infty}(2n+1)\,P_n(\cos\theta)b_n^*(x) \tag{10}$$

Eq. (7) can be rearranged to,

$$\delta_1(E) = V_m \times \frac{3}{8}\frac{m^2-1}{mx}\frac{Q_{\mathbf{abs}}}{m_i} \tag{11}$$

Here $V_m = 4\pi a^3/3$ and $m + im_i$ is the index of refraction; b_n is the Van de Hulst coefficient for the TE mode of the vector Mie sphere [13], and $x = Ea$ the size parameter. Figure (1) shows the corresponding exact solution for the transport velocity, as well as the Wigner approximation for an index of refraction $m = 2.73$. The latter is given by [3],

$$\delta^W(E) = V_m \times \frac{3}{2x^2}\sum_{n=0}^{\infty}(2n+1)\left(\frac{d\beta_n}{dx} - \frac{\mathrm{Im}\,b_n}{x}\right) \tag{12}$$

In the resonant regime the Wigner approximation is very accurate. This justifies its use in calculations invoking the vector nature of light [1] [3]. At low frequencies, resonant behavior is absent and phase and transport velocity coincide. The choice $m = 1/2.73$ in figure (2) corresponds to a "repulsive dielectric".

We next demonstrate that the transport velocity is directly related to the phase velocity if resonant behavior is absent. To this end we consider two models for which an exact solution is at hand. The first model is the scalar point scatterer [12] which has t-matrix,

$$t_{\mathbf{pp}'}(E) = \frac{-4\pi E^2}{1/\alpha - iE^3} \tag{13}$$

where $\alpha > 0$ by causality [5]. Due to its pointlike nature it does not depend on the momenta so that the Wigner approximation is exact. Using Eq. (3) we obtain the convenient result that,

$$\frac{1}{v_E} = \frac{1}{v_p} = \sqrt{1 + \frac{4\pi n/\alpha}{1/\alpha^2 + E^6}} > 1 \tag{14}$$

This is a manifestation of the conjecture that transport and phase velocity coincide if no energy is being stored. If the t-matrix above is given a finite resonant frequency [14], phase and transport velocity no longer coincide, the latter being always less than unity. This is already known for 25 years [4] [15] . Nobody realized that this well-documented transport velocity also describes the propagation of diffusing classical waves. This makes it an observable quantity, rather than some artificial velocity obeying causality.

Another model is the ideal "scalar" reflector, obtained by letting $m = \infty$ in the t-matrix (10). Since there are no waves inside the barrier, we deduce $\delta_1 = 0$. Consequently $v_E = 1/v_p$. Figure (3) demonstrates the results. It is inferred that $v_E < 1$, but $v_p > 1$. We also displayed the results when the s-wave is incorporated (as opposed to light scattering starting with p-waves!). There is a cut-off frequency at which the phase velocity diverges and the transport velocity vanishes. Below this cut-off only evanescent waves are present and the density-of-states is small. We encounter a fascinating similarity to waveguides, where the group velocity vanishes at the cut-off frequency. Since scattering is absent there, transport and group velocity coincide.

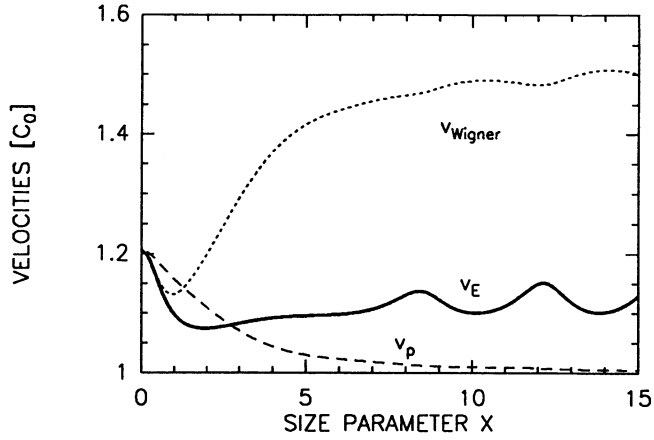

Figure 2: The same as in figure 1, but now with an index of refraction of 1/2.73 and a packing fraction of 36 %.

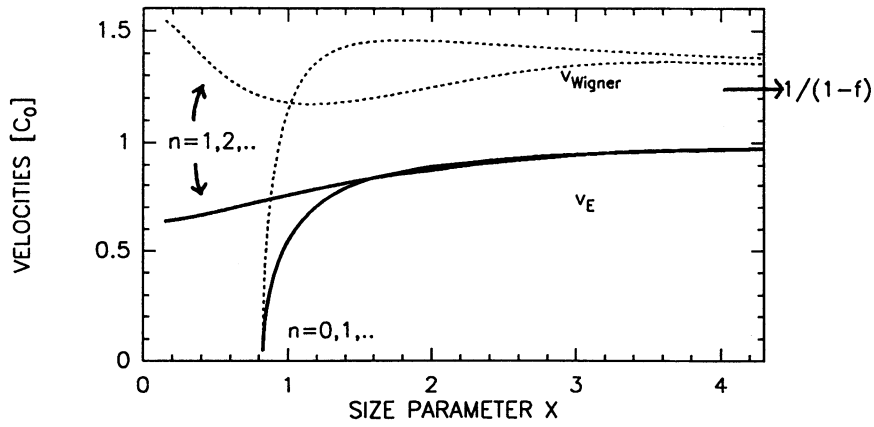

Figure 3: The transport velocity (bold) for perfectly reflecting spheres ($m = \infty$) with packing 20 %. The Wigner delay time (dotted) approaches the causality threshold [5] $1/(1-f) = 1.25$. At low frequency the s-wave dominates and has a frequency cut-off at which v_E vanishes and v_p diverges.

3. CONCLUSIONS

We have demonstrated a strong decrease of the transport velocity of light, by definition the speed at which the incoherent (diffusive) light propagates, near resonances of scattering. In this case a lot of energy is temporarily stored inside the (dielectric) scatterer. The only assumption in our theory is the restriction to lowest order of the density.

Alternatively (or equivalently), one can attribute the decrease to an enormous dwell time of the wave in the scatterer. Since the dwell time of the wave in the same region *without* scatterer is negligible to the one *with* scatterer if resonant scattering takes place, we expect beforehand that this delay must be very accurately given by the Wigner phase delay time. This is indeed seen to be the case numerically.

Our results completely agree with the semi-classical approaches by Brillouin and Loudon for an oscillator. If resonant behavior is absent, the transport velocity is located somewhere between the phase velocity v_p and c_0^2/v_p.

This work is part of the research program of the "Stichting voor Fundamenteel Onderzoek der Materie" (FOM) and was made possible by financial support from the Nederlandse Organisatie voor Wetenschappelijk Onderzoek (NWO).

References

[1] M.P. van Albada, B.A. van Tiggelen, A. Lagendijk, and A. Tip, *Phys. Rev. Lett.* **66**, 3132 (1991).

[2] J.F. de Boer, M.P. van Albada, and A. Lagendijk, *Physica B* **175**, 17 (1991).

[3] B.A. van Tiggelen, A. Lagendijk, M.P. van Albada and A. Tip, *Phys. Rev. B* **45**, 12233 (1992).

[4] R. Loudon. *J. Phys. A* **3**, 233 (1970).

[5] E.P. Wigner, *Phys. Rev. B* **98**, 145 (1955).

[6] D. Vollhardt and P. Wölfe, *Phys. Rev. B* **22**, 4666 (1980).

[7] C.J. Joachain, *Quantum Collision Theory* (North-Holland, New York, 1975).

[8] B.A. van Tiggelen, Ph.D. Thesis, University of Amsterdam (1992).

[9] M. Büttiker, *Phys. Rev. B* **27**, 6178 (1983).

[10] A. Bott and W. Zdunkowski, *J. Opt. Soc. Am. A* **4**, 1361 (1987).

[11] Yu.N. Barabanenkov and V.D. Ozrin, *Phys. Rev. Lett.* **69**, 1364 (1992).

[12] B.A. van Tiggelen, A. Lagendijk and A. Tip, *J. Phys. C: Cond. Matter* **2**, 7653 (1990).

[13] H.C. van de Hulst, *Light Scattering by Small Particles* (Dover, New York, 1981).

[14] Th.M. Nieuwenhuizen, A. Lagendijk and B.A. van Tiggelen, *Phys. Lett. A* **169**, 191 (1992).

[15] L. Brillouin, *Wave Propagation and Group Velocity* (Academic, New York, 1960) pages 98-124.

DIFFUSION OF CLASSICAL WAVES IN RANDOM MEDIA

J. Kroha,[1] C. M. Soukoulis,[2] and P. Wölfle[1]

[1] Institut für Theorie der Kondensierten Materie
Universität Karlsruhe
7500 Karlsruhe 1 Germany

[2] Ames Laboratory and
Department of Physics and Astronomy
Iowa State University
Ames, IA 50011, USA

INTRODUCTION

In recent years there has been growing interest in studies of the propagation of classical waves in random media.[1,2] The revival of interest in the longstanding problem of multiple scattering of classical waves was initiated by the discovery of the importance of quantum interference effects for the transport properties of electrons in disordered systems.[3] While some of the features associated with electron localization, such as enhanced coherent backscattering, have been detected in light scattering experiments[4] as well, the localization of electromagnetic waves or other classical waves in random systems has not been established beyond doubt. The question of localization of classical waves has attracted attention for two reasons. First, the properties of classical waves such as light waves, microwaves, and acoustic waves in random media are of fundamental interest for their own sake. Second, classical waves can serve as a model system for testing the theory of Anderson localization of electrons experimentally in a clean way, without the complication of strong inelastic scattering and other effects of electron-electron and electron-phonon interaction. On the other hand, it is harder to localize classical waves, mainly due to the fact that at low frequency the effect of disorder tends to average out in this case, whereas electrons at low energy

Photonic Band Gaps and Localization, Edited by
C.M. Soukoulis, Plenum Press, New York, 1993

are trapped more effectively, even by a weak random potential. Existing theories predict localization of classical waves under certain circumstances.[5-8] However, there is no conclusive experimental evidence yet, although the recent experiments by Genack and collaborators provide strong indications for the existence of localization of light.[9]

The outstanding problem in classical wave localization is to find the optimal conditions for its realization. It has been suggested that an intermediate frequency window of localized states separates the low-frequency extended states characterized by Rayleigh scattering from the high frequency extended states described by geometric optics. Theories based on the weak scattering limit and on the Coherent Potential Approximation (CPA) predict frequency intervals within which localization should be observed.[7,8] These predictions are based on extrapolation of results obtained in the weak disorder regime. In addition, it was recently recognized that considerable care must be exercised in transforming the results of the theory of localization of electrons to the case of classical waves.[10,11] In particular, the Amsterdam group[10] presented experimental results for the diffusion coefficient D and the transport mean free path ℓ. These results demonstrated that in a strongly scattering random dielectric medium, the low values of the diffusion coefficient $D=c(\omega)\ell/3$ were caused by extremely small values of the transport velocity $c(\omega)$ and not by the small[9] values of ℓ, which signify strong localization.[9] It is, therefore, possible that in a random media the transport velocity can be very much lower than the phase velocity. To explain this discrepancy, the Amsterdam group[10] presented a treatment of the transport velocity based on the low-density approximation of the Bethe-Salpeter equation. They argued that their approach confirmed the observed smallness of the transport velocity. However, Barabanenkov and Ozrin,[11] as well as Kroha et al.,[12] also developed a theory based on the low-density approximation of the Bethe-Salpeter equation, with a generalized Ward identity for scalar waves. Their conclusion was the correct expression for the transport velocity coincides with the phase velocity. Therefore, the experimental data, from the Amsterdam group which indicates a much smaller transport velocity, remains to be explained.

This somewhat difficult situation has led to suggestions of alternative pathways to localization. John[13] has proposed that classical localization may be more easily achieved for a weakly disordered system of periodically arranged dielectric structures in the frequency regime near a band gap. The question of photonic band structure in periodic dielectric

structures is a fascinating subject (which was also a major theme of our conference) with potential applications in the telecommunication, information processing, optical storage, and sensor technology.

In this paper we present a microscopic theory for the diffusion coefficient and the tranport velocity in the low-density approximation, as well as a self-consistent theory of localization of classical waves, similar to the one developed for electron localization.[14-16] There are important differences in the formulation of such a theory for classical waves as compared to the case of electrons. The most important is the equivalent of particle density is not conserved. Unfortunately, this fact has not been given sufficient attention in an earlier attempt[7] to derive a self-consistent theory, as pointed out recently.[10] The quantity conserved here is energy, not mass, leading to diffusion behavior of the energy density. Another difference is the scattering potential is energy dependent. As a consequence, a new phenomenon appears: The energy transport velocity entering the diffusion coefficient for a strongly disordered system may get appreciably renormalized,[10] and consequently, diffusion coefficients can be quite small even far from the localization transition. Also, in previous versions of a self-consistent theory of localization[7] the single-particle quantities and the coupling constants were calculated in the low density or the weak scattering approximation. It is known from the electron transport problem[15] how to improve upon this unnecessary simplification by calculating the noncritical quantities in CPA.

PROPAGATION OF CLASSICAL WAVES: TRANSPORT VELOCITY

We consider the propagation of classical waves in a random medium described by the wave equation for the scalar field $\Psi(r,t)$

$$[\varepsilon(r) \frac{\partial^2}{\partial t^2} - \nabla^2] \Psi(r,t) = 0. \qquad (1)$$

Here, $\varepsilon(r)$ characterizes the randomly varying phase velocity $c(r) = 1/\sqrt{\varepsilon(r)}$. In the approximation where the vector nature of the electromagnetic field is neglected, Eq. (1) describes the propagation of electromagnetic waves in a dielectric medium with spatially varying dielectric constant $\varepsilon(r)$. We will assume the fluctuations of $\varepsilon(r)$ to be spacially uncorrelated, such that $\langle\varepsilon(r)\rangle = \bar{\varepsilon}$ and $\langle\varepsilon_1(r)\varepsilon_1(r')\rangle = W\delta(r-r')$, where $\varepsilon_1(r) = \varepsilon(r) - \bar{\varepsilon}$.

The (unaveraged) Green's function of the wave equation (1), Fourier

transformed w.r.t. time, satisfies the Dyson equation

$$G(r,r';\omega) = G^{\circ}(r,r';\omega) + \int d^{d}r'' G^{\circ}(r-r'';\omega)U(r'';\omega)G(r'',r';\omega) \qquad (2)$$

with the "interaction potential" $U(r,\omega) = -\omega^2(\varepsilon(r) - 1)$ and the free propagator G° given by its Fourier transform $G_k^{\circ R,A}(\omega) = \left[(\omega \pm i0)^2 - k^2\right]^{-1}$.

The impurity averaged Green's function $G_k^{R,A}(\omega)$ is given in terms of the mass operator $\Sigma_k^{R,A}(\omega)$ by $G_k^{-1} = G_k^{\circ -1}(\omega) - \Sigma_k$. The one-particle properties are expected to be uncritical at the localization transition and hence, may be calculated in CPA, i.e., in single-site-approximation[4,17] when $\Sigma_k(\omega) = \Sigma_o(\omega)$ is independent of the wave vector.

The transport properties of the system can be extracted from the averaged two-particle Green's function $\Phi_{kk'}^{\omega}(q,\Omega) = -\left\langle G^{R}(k_+,k'_+;\omega_+)G^{A}(k'_-,k_-;\omega_-)\right\rangle$, where $\omega_{\pm} = \omega \pm \Omega/2$, $k_{\pm} = k \pm q/2$, $k'_{\pm} = k' \pm q/2$ and Ω, q are the center of mass frequency and wave vector, respectively. The long wavelength, low frequency behavior of the classical wave system is not governed by particle number conservation, in contrast to the electronic case, but by the conservation of energy, with $\varepsilon(\partial\Psi/\partial t)^2$ being the energy density of the wave field. The quantity $\Phi_{\varepsilon\varepsilon}^{\omega} = \left(\frac{\omega}{c_{ph}}\right)^2 \sum_{k,k'} \Phi_{k,k'}^{\omega}(q,\Omega)$ may be interpreted as an energy density correlation function, where the phase velocity c_{ph} is defined from the zero of the real part of the inverse of $G_k(\omega)$ as $c_{ph}^{-2}(\omega) = 1 - \mathrm{Re}\Sigma_o(\omega)/\omega^2$. $\Phi_{\varepsilon\varepsilon}^{\omega}$ can be shown to have the diffusion pole structure

$$\Phi_{\varepsilon\varepsilon}^{\omega}(q,\Omega) = c(\omega)\frac{i\left(\frac{\omega}{c_{ph}}\right)\mathrm{Im}G_o^{A}(\omega)}{\Omega + iD(\Omega)q^2} \qquad (3)$$

in the limit Ω, $q \to 0$ ($c(\omega)$ and $G_o^{A}(\omega)$ will be defined below). In the regime of localized waves, the diffusion coefficient $D(0)$ vanishes identically. In the following we will calculate $D(\Omega)$ as a function of disorder and show that a localization transition takes place in the model of point scatterers in the regime $\omega \simeq 2\pi/a$ for sufficiently strong coupling $\tilde{\varepsilon}$.

The starting point for a calculation of the averaged two-particle Green's function $\Phi_{kk'}^{\omega}(q,\Omega)$ is the Bethe-Salpeter equation

$$\Phi_{kk'}^{\omega}(q,\Omega) = G_{k+}^{R}(\omega_+)G_{k-}^{A}(\omega_-)\left[\delta_{k,k'} + \sum_{k''}\gamma_{kk''}^{\omega}(q,\Omega)\Phi_{k''k'}^{\omega}(q,\Omega)\right], \qquad (4)$$

where $\gamma^{\omega}_{kk'}(q,\Omega)$ is the sum of all irreducible diagrams of the four-point vertex function. We can write (4) as a kinetic equation with the help of the Ward identity

$$\Sigma^{R}_{k_+} - \Sigma^{A}_{k_-} = \sum_{k'} \gamma^{\omega}_{kk'}\left[G^{R}_{k'_+} - G^{A}_{k'_-}\right] + \frac{\omega\Omega}{\omega^2 + (\Omega/2)^2}\left[\Sigma^{R}_{k_+} + \Sigma^{A}_{k_-} + \sum_{k'} \gamma^{\omega}_{kk'}\left(G^{R}_{k'_+} + G^{A}_{k'_-}\right)\right] \qquad (5)$$

where $\Sigma^{R}_{k_+} = \Sigma^{R}_{k_+}(\omega_+)$, etc. Compared to the case of electrons, there is an additional (the last) term on the r.h.s. of (5), which has been missed in Ref. 7. This term arises because of the explicit frequency dependence of the perturbation $U(r,\omega) \propto \omega^2$ in (2).

Energy conservation is expressed by the equation

$$\Omega\Phi^{\omega}_{\varepsilon\varepsilon} - q\Phi^{\omega}_{j\varepsilon} = ic(\omega)\frac{\omega}{c_{ph}}ImG^{A}_{o}, \qquad (6)$$

where the energy current correlation function corresponding to $\Phi^{\omega}_{\varepsilon\varepsilon}$ has been defined as $\Phi^{\omega}_{j\varepsilon} = c(\omega)\frac{\omega}{c_{ph}}\Sigma_{k,k'}(k\cdot\hat{q})\Phi^{\omega}_{kk'}(q,\Omega)$. Here we have introduced a renormalized velocity $c(\omega)$ characterizing energy diffusion. In the limit of small q, Ω, $c(\omega)$ is given by

$$\left(\frac{c(\omega)}{c_o}\right)^{-1} = \left(\frac{c_{ph}}{c_o}\right)\left[1 - \frac{1}{\omega^2}\left(\gamma_o ReG^{A}_{o} + Re\Sigma^{A}_{o}\right)\right] \qquad (7)$$

where $G^{A}_{o}(\omega) = \Sigma_k G^{A}_{k}(\omega), \gamma_o = Im\Sigma^{A}_{o} / ImG^{A}_{o}$ is the irreducible vertex function calculated in CPA, and $c_o \equiv 1$ is the phase velocity in the homogeneous background medium. The renormalization of c is a consequence of the additional term in the Ward identity (5), which is of order Ω, while energy conservation is already guaranteed by the $\Omega \to 0$ limit of (5).

Equation (7) can be written in its more general form as

$$\frac{c_o}{c(\omega)} = \frac{c_{ph}}{c_o}\left[1 - \frac{1}{\omega^2}\left(\sum_{k'} \gamma_{k_o k'}(q,\Omega)ReG_{k'}(\omega) + Re\Sigma_{k_o}(\omega)\right)\right], \qquad (7a)$$

where $k_o = \omega/c_{ph}$ or by using the small q and Ω dependendence of the Ward identity (Eq.(5)), the equation of the transport velocity is given by

$$\frac{c_o}{c(\omega)} = \frac{c_{ph}}{c_o}\left[1 - \frac{1}{2\omega}\frac{\partial}{\partial\omega}Re\Sigma_{k_o}(\omega) - \frac{i}{\omega}\sum_{k'}\frac{\partial}{\partial\Omega}\gamma_{k_o k'}(0,\Omega)ImG_{k'}(\omega)\right.$$

$$+\frac{1}{2\omega}\sum_{k'}\gamma_{k_o k'}(0,0)\frac{\partial}{\partial\omega}\mathrm{Re}G_{k'}(\omega)\Big] \qquad (7b)$$

which agrees with the expression given by Barabanenkov and Ozrin (Ref. 11), but disagrees with Ref. 10, where the last term is missing.

van Tiggelen and Lagendijk[18] have argued that the third term on the r.h.s. of Eq. 7b is of second-order in density. In order to obtain this result they have assumed that the ImΣ which is proportional to $\gamma_{k_o k}$, is independent of the momentum k, and that the upper limit of the

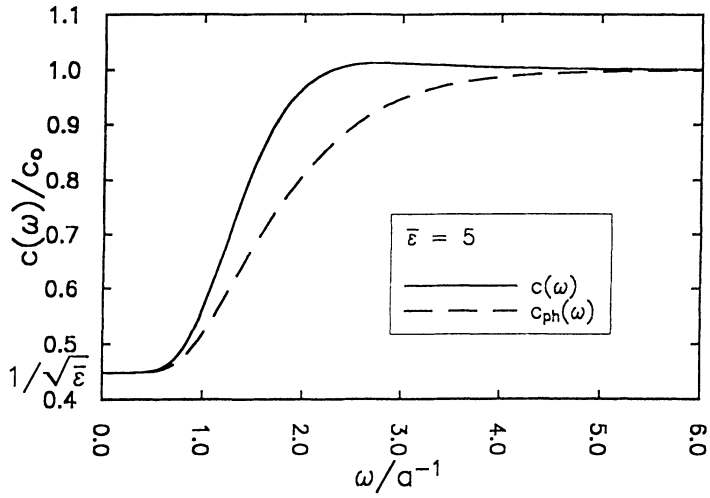

Figure 1: The transport velocity c(ω), normalized to c_0, the phase velocity in the homogeneous background medium, is shown for $\bar{\varepsilon}$=5. Also shown is the effective phase velocity $c_{ph}(\omega)$ in the disordered system. c(ω) and c_{ph} (ω) coincide for ω<<2π/α and for ω>>2π/α.

summation of the third term is infinite. However, ImΣ may be weakly momentum dependent over a wide range. It always decays to zero at momenta inversely proportional to the size of the scatters. Thus, ImΣ always introduces an upper cutoff to the k summation. The summation over k in this finite range depends, in general, on the upper limit and is different than zero and therefore the third term is also of first order in density.

We have calculated $G_o(\omega)$ and $\Sigma_o(\omega)$ in CPA and evaluated $c(\omega)$ in this approximation. The result is shown in Fig. 1. At low frequencies $c(\omega)$ is substantially smaller than one (for positive $\Delta\varepsilon$), as already noted in Ref. 10, the limiting value as $\omega \to 0$ being given by $c(\omega) \to \frac{1}{\sqrt{\bar{\varepsilon}}}$ whereas at high frequency $c(\omega) \to 1$. The velocity of energy transport $c(\omega)$ and the phase velocity $c_{ph}(\omega)$ are seen to agree well. In fact, whenever the imaginary part of the mass operator Σ is small (e.g., in the limit of low density of scatterers), c and c_{ph} coincide. This is seen immediately from (7) for the case of point scatterers, and was shown in Ref. (11) for general momentum dependent scattering within a low-density approximation. Therefore, one may conclude that the strong reduction of $c(\omega)$ w.r.t. c_{ph}, as measured experimentally by van Albada et al.,[10] is purely an effect of resonant scattering: In the vicinity of resonances $\mathrm{Im}\Sigma$ is always large even for small density and may cause the reduction of $c(\omega)$. However, the correct low density treatment[11,12] gives that the transport velocity and the phase velocity are renormalized in a similar way, even for finite scatterers. We believe that the main issue here is how to define an energy density and an energy current density for scalar waves that satisfy the continuity equation. In addition, the low density limit must give a diffusion coefficient and therefore a transport velocity which is much lower than the phase velocity, and also agrees with the semi-classical approaches[10,18] of Brillouin and Loudon. It has been correctly argued[10,18] that the transport velocity differs considerably from the phase velocity. In the presence of finite scatterers the formation of standing (resonance) waves inside the scatterers is responsible for the considerable delay of the scattering and therefore the low transport velocity. As of now, no theory, even within the Boltzman low-density limit, has demonstrated this behavior.

For classical waves the energy density U_E is given by

$$U_E = \frac{1}{2}\varepsilon\left(\frac{\partial\psi}{\partial t}\right)^2 + \frac{1}{2}\left(\frac{\partial\psi}{\partial x}\right)^2, \tag{8}$$

while the corresponding energy current J_E is

$$J_E = \frac{\partial\psi}{\partial t}\frac{\partial\psi}{\partial x}. \tag{9}$$

Of course, Eqs. (8) and (9) satisfy the continuity equation $\partial U_E/\partial t + \partial J_E/\partial t = 0$. However, in order to study the diffusive motion of the scalar waves, one needs the solution of a transport equation, which is derived from the

Bethe-Salpeter equation (see Eq. (4)). Equation (4) has been written down assuming that the energy density is given by $|\psi(x,t)|^2$ for classical waves too. This is the case for electrons but not for classical waves as one can clearly see from Eq. (8).

LOCALIZATION EFFECTS

Let us turn to localization effects now. Employing the techniques developed for the case of electron transport,[14,15] one may derive an equation of motion for $\Phi_{j\varepsilon}$ from the Bethe-Salpeter equation (4), which relates back to $\Phi_{\varepsilon\varepsilon}$, and hence, allows to derive the diffusion form (3) for $\Phi_{\varepsilon\varepsilon}$. In the approximation for the irreducible vertex $\gamma_{kk'}(q)$ employed in the case of electron transport,[14,15]

$$\gamma_{kk'}(q,\Omega)=\frac{1}{\omega^2}\left(\mathrm{Im}\Sigma_o^A\right)^2\left(\mathrm{Im}G_o^A\right)^{-3}\mathrm{Im}G_k^A(\omega)\Phi_{\varepsilon\varepsilon}^{\omega}\left(|k+k'|,\Omega\right),$$

the diffusion coefficient D(Ω) is found to satisfy the selfconsistency equation

$$D(\Omega)=\left[1-\frac{i\omega\Omega}{\mathrm{Im}\Sigma_o^A}\right]^{-1}\left[D_o+2c^2(\omega)\left(\frac{c_{ph}}{\omega}\right)^2\frac{\mathrm{Im}\Sigma_o^A}{\left(\mathrm{Im}G_o^A\right)^2 D_o}K\left\{\frac{-i\Omega}{D(\Omega)}\right\}\right], \qquad (10)$$

where

$$K\{z\}=\sum_{k,k'}(k\cdot\hat{q})\frac{\mathrm{Im}G_k^A\left(\mathrm{Im}G_{k'}^A\right)^2}{z+\left(k+k'\right)^2}(k'\cdot\hat{q}). \qquad (11)$$

In CPA the bare diffusion constant is given by

$$D_o=2c(\omega)\frac{c_{ph}}{\omega}\frac{1}{\mathrm{Im}G_o^A}\Sigma_k(k\cdot\hat{q})^2\left(\mathrm{Im}G_k^A\right)^2.$$

For simplicity, we will in the following consider an idealization of a real system, such as dense packed dielectric spheres of random size scattering classical waves. For example, light: A system of point scatterers distributed statistically throughout the system. Then, the only length scale characterizing the system is the mean spacing of neighboring scatterers a. In the two limits of wavelength λ of the incident wave small or large in comparison with a, one expects effective medium theory to work well, whereas for $\lambda = 2\pi/\omega \simeq$ a localization of waves should occur for sufficiently large scattering strength. In the model of point scatterers, ε(r) is given by $\varepsilon(r)-1=\left(\Delta\varepsilon V_s\right)\Sigma_{i=1}^{N_I}\delta\left(r-r_i\right)$, with N_I the number and $n_I = N_I/V$ =

$1/a^d$ the density of scatterers (d is the spatial dimension). The point scatterers may be thought of as an idealization of spheres of dielectric materials of volume V_s and dielectric constant $1 + \Delta\varepsilon$ embedded in a matrix with $\varepsilon = 1$. The two parameters characterizing the model may be chosen as the average dielectric constant $\bar{\varepsilon} = 1 + (V_s/a^d)\Delta\varepsilon$ and the average separation of scattering centers a.

We have solved (10) numerically for $D(\Omega)$, using the CPA results for G_0, Σ_0, $c(\omega)$ and D_0. It is easily shown that in CPA the parameter a can be absorbed into the rescaled frequency $a\omega$, so that the only relevant parameter in the model is the average dielectric constant $\bar{\varepsilon}$.

In Fig. 2, we present the mobility edge trajectory separating extended from localized states. Notice that the model correctly describes the underlying physics. In particular, there are only extended states for all frequencies ω when $\bar{\varepsilon}$ is less than 2.7. In addition, for low (Rayleigh scattering) and high (geometric optics) frequencies, as expected, there are only extended states for any value of $\bar{\varepsilon}$. In Fig. 3, the dc diffusion coefficient D(0) for spatial dimension d=3 is shown as a function of wave frequency ω for $\bar{\varepsilon}$ =5. For values $\bar{\varepsilon} \geq 2.7$ (corresponding to energy velocity $c(0) \lesssim 0.6$), D(0) is found to be zero within a frequency window centered at $a\omega \approx 2$. One may define the localization length ξ by $\xi^2 = \lim_{\Omega\to 0} \frac{D(\Omega)}{(-i\Omega)}$, which characterizes the spatial extension of wave packets localized in the system. $(\xi/a)^{-1}$ is also shown in Fig. 3 as a function of ω. D(0) is seen to vanish linearly as ω approaches the critical frequencies $\omega_{1,2}$, whereas $\xi \propto |\omega - \omega_{1,2}|^{-1}$. Note that from (10) $\omega_{1,2}$ is independent of the renormalization of the transport velocity $c(\omega)$. The critical exponents for D(0) and ξ found here, s=1 and ν=1, are the same as those for the electron case. In dimensions $d \leq 2$ classical waves are found to be localized for arbitrarily weak disorder.

In the region where the wavelength is large compared to the size of the scatterers, i.e., where the approximation by point scatterers is appropriate, the description of the localization transition as a function of $a\omega$ and $\bar{\varepsilon}$ presented here is expected to be semiquantitative, with the possible exception of a narrow critical regime, judging from the very good agreement of a similar theory for electron localization[14,15] with exact numerical results for finite systems. The predictions of the theory may be tested experimentally in systems with a sufficiently large relative difference of dielectric constants $\Delta\varepsilon$, such that the disorder parameter $\bar{\varepsilon}$ may be large even for small density.

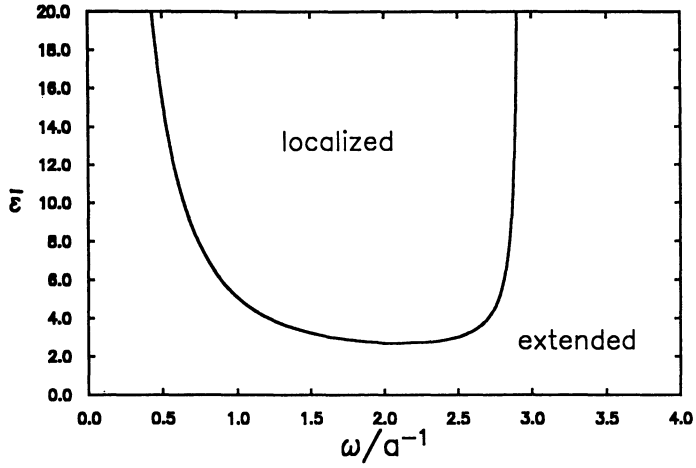

Figure 2: The mobility edge trajectory in the dielectric constant-frequency plane separating extended from localized states is shown.

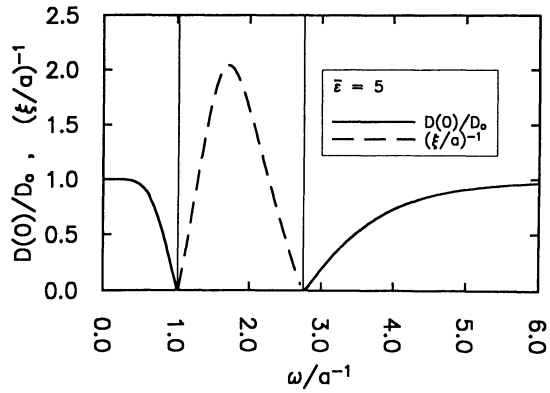

Figure 3: The diffusion coefficient D(0) and the inverse localization length ξ^{-1} are shown as a function of wave frequency ω for $\bar{\varepsilon}$=5.

CONCLUSIONS

We have developed a self-consistent theory for classical waves, which presents the correct Ward identity for classical waves valid for all frequencies. It points out that the long wavelength, low frequency behavior of the classical wave system is not governed by particle number conservaton as in the case of electrons, but by the conservation of energy. It provides the correct low density approximation of the energy velocity and of the Boltzman equation. It also reveals that the energy velocity and the phase velocity are renormalized in the same way. Finally, it provides a CPA solution of the classical wave localization problem with results which agree well with more exact numerical predictions for the scalar use.

ACKNOWLEDGMENTS

CMS is grateful for the hospitality of the Institüt Für Theorie der Kondensierten Materie, Universität Karlsruhe where this work was done. This work has been partially supported by the Deutsche Forschungsgemeinschaft (J.K.) and Heraeus Stiftung (C.M.S.) and USDOE under grant No. W-7405-ENG-82 (C.M.S.).

REFERENCES

1. S. John, *Phys. Rev. Lett.* **53**, 2169 (1983); *Phys. Rev.* **B32**, 304 (1985); *Comments Condensed Matter Physics* **14**,193 (1988).

2. P.W. Anderson, *Phil. Mag.* **B52**, 505 (1985).

3. For a review see: P.A. Lee and T.V. Ramakrishnan, *Rev. Mod. Phys.* **57**, 287 (1985).

4. For a review see: *Scattering and Localization of Classical Waves in Random Media*, Ping Sheng, ed. (World Scientific, Singapore, 1990).

5. Ping Sheng and Z.Q. Zhang, *Phys. Rev. Lett.* **57**, 1879 (1986).

6. K. Arya, Z.B. Su and J.L. Birman, *Phys. Rev. Lett.* **57**, 2725 (1986).

7. C.A. Condat and T.R. Kirkpatrick, *Phys. Rev. Lett.* **58**, 226 (1987); *Phys. Rev.* **B32**, 495 (1985).

8. C.M. Soukoulis, E.N. Economou, G.S. Grest, and M.H. Cohen, *Phys. Rev. Lett.* **62**, 575 (1989); E.N. Economou and C.M. Soukoulis, *Phys. Rev.* **B40**, 7977 (1989).

9. J. M. Drake and A.Z. Genack, *Phys. Rev. Lett.* **63**, 259 (1989); A. Z. Genack, N. Garcia, and W. Polkosnik, *Phys. Rev. Lett.* **65**, 2129 (1990).

10. M.P. Albada, B.A. van Tiggelen, A. Lagendijk, and A. Tip, *Phys. Rev. Lett.* **66**, 3132 (1991); *Phys. Rev. B*, **45**, 12233 (1992).

11. Yu. N. Barabanenkov and V.D. Ozrin, *Phys. Rev. Lett.* **69**, 1364 (1992); see also *Phys. Lett.* **A154**, 38 (1991).

12. J. Kroha, C. M. Soukoulis, and P. Wölfle, *Phys. Rev. B. (Rapid Commun.)* to be published.

13. S. John, *Phys. Rev. Lett.* **58**, 2486 (1987); S. John and R. Ranjavajan, *Phys. Rev.* **B38**, 10101 (1988).

14. D. Vollhardt and P. Wölfle, *Phys. Rev.* **B22**, 4666 (1980); P. Wolfle and D. Vollhardt, in *Anderson Localization*, Y. Nagaoka and H. Fukuyama, eds. (Springer, Berlin, 1982), p. 26.

15. J. Kroha, T. Kopp and P. Wölfle, *Phys. Rev.* **B41**, 888 (1990); J. Kroha, *Physica* **A167**, 231 (1990).

16. For a review see: D. Vollhardt and P. Wölfle, in *Electronic Phase Transitions*, W. Hanke and Y.V. Kopaev, eds. (North-Holland, Amsterdam, 1992).

17. C.M. Soukoulis, E.N. Economou, G.S. Grest and M.H. Cohen, *Phys. Rev. Lett.* **62**, 575 (1989).

18 . B. A. van Tiggelen and A. Lagendijk, these proceedings.

ACCURATE MEASUREMENT OF BACKSCATTERED LIGHT FROM RANDOM MEDIA

P.N. den Outer[1], M.P. van Albada[2], and Ad Lagendijk[1,2]

[1]Van de Waals-Zeeman Laboratorium, University of Amsterdam,
Valkenierstraat 65- 67, 1018 XE Amsterdam, The Netherlands
[2]FOM instituut voor Atoom- en Molecuulfysica
Kruislaan 407, 1098 SJ Amsterdam, The Netherlands

INTRODUCTION

Anderson localization is known as the phenomena of a dramatic change in the transport properties of electrons when they are subject to a spatially random potential.[1] Electron waves are multiple scattered and as a consequence of interference, the diffusion constants vanishes. The dimension of the system plays a crucial role for the occurrence of Anderson localization. In one and two dimensions any degree of disorder will lead to a finite localization length, whereas in three dimensions first a critical mean-free path should be reached to enter the localized regime:

$$l < \frac{\lambda}{2\pi}. \tag{1}$$

This is the Ioffe-Regel criterium, modified by Mott[2] (l is the mean-free path and λ is the wavelength).

It is quite clear that the concept of localization is much broader, in principle for any wave equation localized solutions can be obtained, when solved for a random medium. This has been recognized by several researchers; experiments have been suggested and ranges of experimental parameters have been put forward for which Anderson localization of classical waves like sound and light is expected.[3]-[5]

Photonic Band Gaps and Localization, Edited by
C.M. Soukoulis, Plenum Press, New York, 1993

A precursor of Anderson localization, enhanced backscattering as a result of interference, was first reported by Kuga and Ishimaru[6], by van Albada and Lagendijk[7], and by Wolf and Maret[8]. It is well understood as an interference effect between time-reversed paths. By a path we mean a sequence of scattering events starting and ending at the boundaries of the sample.

Experimentally, electron localization is studied through the electrical conductance of a sample, where an important aspect is the possibility to influence the interference by applying a magnetic field. In experiments with light one can not easily influence the interference, but in contrast to the electronic case, one can preform angular and time resolved transmission and reflection measurements. In this paper we will concentrate on the multiple scattered light reflected by a random medium.

LIGHT SCATTERING FROM RANDOM MEDIA

To study multiple light scattering the samples should consist of a random mixture of two nonabsorbing materials with a high contrast of refractive index. The particle size of the materials should be in the order of the wavelength to scatter most efficiently.

One might think that as a consequence of the multiple scattering, the angular resolved reflected diffuse intensity will be essentially angle independent, when averaged over the disorder. However at exactly backscattering the phase difference between time-reversed waves is always zero, and does not depend on the relative position of the scatterers involved. In this direction the interference contribution survives averaging over the disorder, and the backscattered intensity will be twice what it would have been without interference contributions. (In fact, this holds only for the copolarized component in the backscattered light). Moving away from the direction of exact backscattering, the phase difference between time-reversed paths increases and becomes a function of the positions of the first and last scatterers: the phase difference $\Delta\phi = \vec{q_t} \cdot (\vec{r_i} - \vec{r_f})$, with q_t being the transfer wave vector $\vec{k_i} + \vec{k_f}$. For angles larger than $\lambda / \mid \vec{r_i} - \vec{r_f} \mid$ the interference averages out. The angular-resolved average intensity thus shows a narrow cone around the backscatter direction with its top at twice the background intensity. The width will be inversely proportional to the mean-free path of the sample.

There are however classes of light paths that behave differently: single scattering, and multiple scattering sequences that begin and end on the same scatterer, loops. The former class has no interference term, and the interference contribution of the latter is angle independent. These classes will contribute to the background only, and therefore lower the enhancement factor, which is defined as the top of the cone relative to the background.

The contribution of loops will play a significant part only in very dense random media: for loops to contribute, the cross-section of the first scatterer and the distance between the first and the nth scatterer must still define a significant solid angle. The contribution of loops is thus negligible for large mean-free paths. For small mean-free paths an observation of loop diagrams can in principle be made by an observed reduction of the enhancement factor.

The purpose of this paper is to get more insight in the magnitude of the angle-independent interference contributions to the backscattered light for samples with large mean-free paths. Or put it differently, to find out which parameters of the

sample and of the incident light are important in the description of the scattering that occurs in the interface layer between a random sample and the surrounding medium.

A theoretical treatment of the influence of the refractive index mismatch on enhanced backscattering was given by Lagendijk *et al.*[9]. These authors looked at the effect of finite internal reflectivity at the interface on the propagation of waves inside a strongly scattering medium. In this treatment only an overall reflectivity was taken into account, and was shown to result in a narrowing of the cone of enhanced backscattering.

It is likely that surface roughness and particle size are also important parameters for the magnitude of the angle-independent contribution. In addition to the diffuse reflection, at a smooth interface a specularly reflected beam will also occur. At a certain angle of incidence we even observe a minimum for the p-polarized reflected

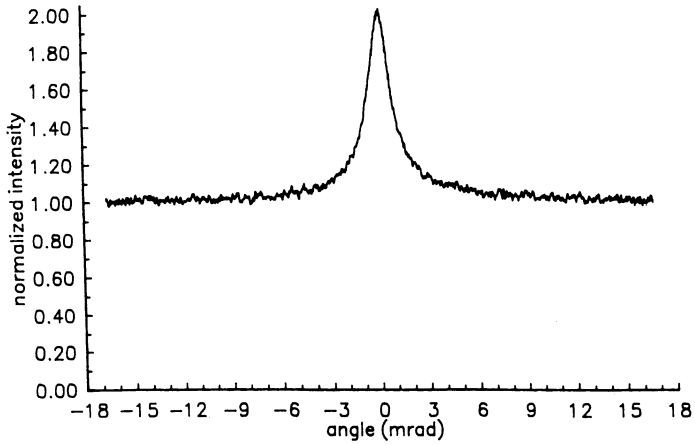

Figure 1: Difference backscatter cone. $L1 = 400\mu m$ $L2 = 50\mu m$, $\lambda_{mf} = 30\mu m$.

light, corresponding to a Brewster minimum. The Brewster angle is the angle of incidence for which the Fresnel reflection for p-polarized light is zero.

Since surface reflectivity is related with lower-order scattering it should some how affect the enhancement factor.

MEASUREMENTS

The experimental setup to measure backscattered light is standard. The sample is illuminated through a beamsplitter, which then reflects the scattered light onto a detector. All scattering form components, other than the sample will affect the enhancement factor and should be carefully avoided. A good test for the performance of the setup is the measured enhancement factor for difference cones. Difference

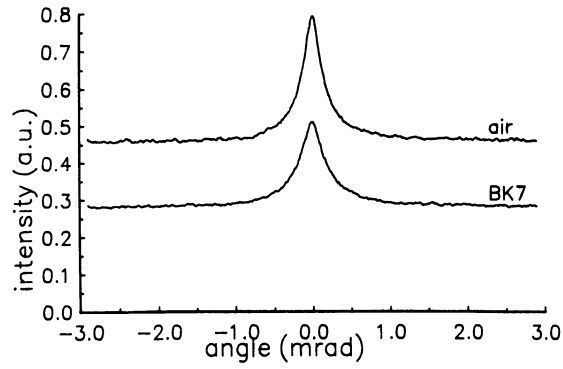

Figure 2: Backscatter cones for different refractive index contrast at the interface of the sample.

cones are obtained from liquid samples where the thickness can be varied.[10] After subtracting the intensity patterns of slabs with thicknesses L_1 and $L_2(< L_1)$, only the contributions of light that has been in the deeper part of the slab, L2 to L1, remains. In the "deep" part of the slab single scattering and loops are unimportant. Results from this difference technique indeed reveal an enhancement factor of 2.00 ± 0.02, see fig.1.

To vary the scattering properties of the interface, we change the refractive index contrast by putting the sample behind (wet) glass. We compare surfaces of different roughness, and monitor the enhancement factor as a function of incident angle. (According to the Rayleigh criterium[11] the surface roughness is essentially a function of the incident angle.)

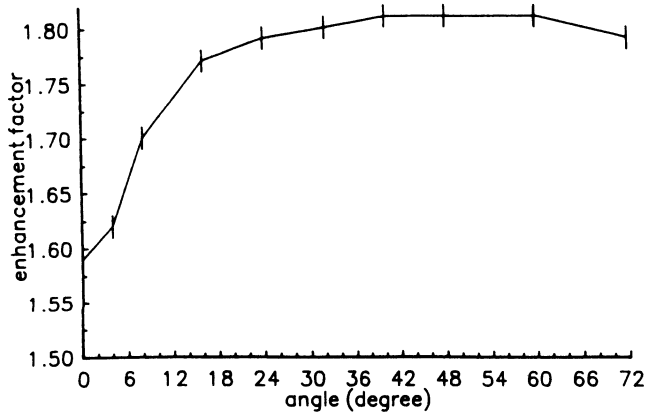

Figure 3: Enhancement factor of the backscatter cone from a teflon sample as a function of the angle of incidence.

In fig.2 backscatter cones are shown for an air/teflon interface and for a glass/teflon interface. We use a BK7-window with an index of refraction of 1.54, and Benzyl-Alcohol (n=1.54) as a matching fluid. The width of the glass/teflon cones is 1.23 times the width of the air/teflon cone. This can be explained by taking internal reflectivity into account. The refractive index contrast between sample and window is lower than that between sample and air. Using 1.4 as the refractive index for teflon the calculation in ref.[9] agrees with the measured broadening. Interestingly the enhancement factor has also increased from 1.63(1) to 1.79(1). The higher detected intensity in the unmatched (sample-air) experiment is due to the fact that light which reaches the interface under large angles is (internal) reflected and then rescattered into all directions (including that of the detector). In the matched experiment it just leaves the sample and is trapped in the glass-window.

In fig.3 we plot the measured enhancement factors as a function of the angle of incidence on a teflon sample. We use s-polarized light and measure the copolarized light by moving the detector parallel to the polarization of the incident light. Starting at normal incidence, the enhancement factor increases from 1.6 to 1.8, and than saturates. We conclude that this effect is most probably due to a blurred specular reflection. The observation of an angle independent enhancement factor of 1.8 in index-matched experiments supports this conclusion.

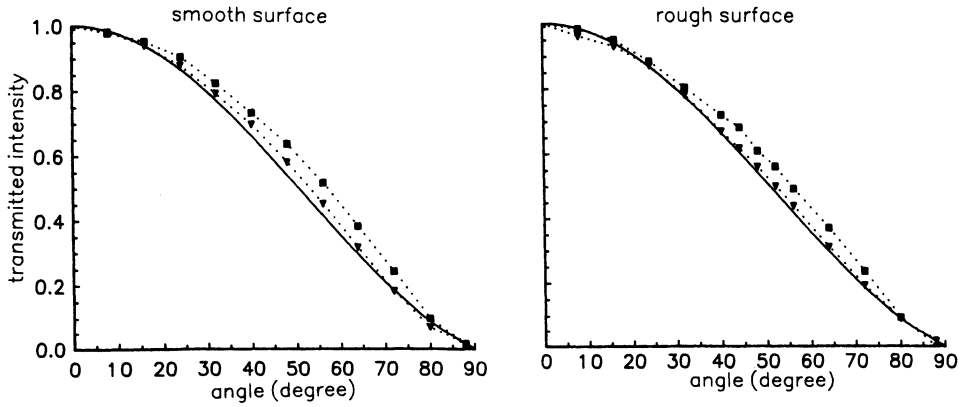

Figure 4: Transmission through a slab of 60 mean-free paths for different polarizations of the detected light. Left plot: smooth surface, Right plot: rough surface. Solid lines: diffusion theory, squares: p-polarized light, triangles: s-polarized light.

Finally we present in fig.4 measurements of angular resolved transmission of incoherent light through multiple scattering media. The thickness of these samples is in the order of 60 mean free paths, one had a rough surface (no specular reflection) and the other a smooth surface. We clearly see a difference for the p-polarized and s-polarized component of the transmitted light. The curve for s-polarized light for the rough surface is well reproduced by (scalar) diffusion theory, in all other cases we see deviation. The influence of the roughness of the interface is not that clear that we can draw strong conclusions from these two measurements.

It is clear that our new results call for a detailed theory describing the interface between a scattering and a non-scattering medium, including the effects of polarization and angle-dependent reflection coefficients. We are presently working on this problem.

SUMMARY

We have studied in detail the enhancement factor of enhanced back-scattered light form random scattering media. We have varied the scattering properties of the interface between scattering and non-scattering media. Also we performed angular resolved transmission measurements. The experiments clearly show that the interface between the sample and surrounding medium has a great influence on the backscattered light. The refractive index mismatch between sample and surrounding medium affects both the shape and the enhancement factor, also the roughness of the interface is of importance. Transmission experiments show that the escaping probability depends on polarization, even for rough interfaces. This also should have its influence on the backscatter cone, but good experimental evidence has not yet been found. It is clear that more experimental and theoretical attention should be paid to investigate and describe the rough interface between a scattering and non-scattering medium. Further experiments on this subject are in preparation.

ACKNOWLEDGEMENT

This work is part of the research program of the "Stichting voor Fundamenteel Onderzoek der Materie (FOM), which is financially supported by the "Nederlandse Organisatie voor Wetenschappelijk Onderzoek (NWO).

REFERENCES

[1] P.W. Anderson, Phys. Rev. **109** (1958) 1492.

[2] N.F. Mott, Adv. Phys. **16** (1967) 49; see also:
N. Gee and G.R. Freeman, Can. J. Chem. **64** (1986) 1810.

[3] S. John and M.J. Stephen, Phys. Rev. B **28**, (1983) 6358.

[4] M.Ya. Azbel, Phys. Rev. B, (1983) 4106.

[5] T.R. Kirkpatrick, Phys. Rev. B **31**, (1985) 5746.

[6] Y. Kuga and A. Ishimaru, J. Opt. Soc. Am. A1 (1984) 831.

[7] M.P. van Albada and A. Lagendijk, Phys. Rev. Lett. **55** (1985) 2692.

[8] P.E. Wolf and G. Maret, Phys. Rev. Lett. **55** (1985) 2696.

[9] A. Lagendijk, R. Vreeker, and P. de Vries, Phys. Lett. A **136** (1989) 81.

[10] M.P. van Albada, M.B. van der Mark, and A. Lagendijk, Phys. Rev. Lett. **58** (1987) 361.

[11] *see for instance* A. Ishimaru, *Wave Propagation and Scattering in Random Media* (Academic, New York, 1978) Vol. II

OPTICAL SPECKLE PATTERNS AND COHERENT BACKSCATTERING IN STRONG MAGNETIC FIELDS

Frank Erbacher, Ralf Lenke and Georg Maret

Grenoble High Magnetic Field Laboratory
Max Planck Institut für Festkörperforschung and Centre National de la Recherche Scientifique. B.P.166, F-38042 Grenoble Cedex 9, France

ABSTRACT

We report the first observation of Faraday rotation of light in multiple scattering media. We find that speckle patterns, generated by diffusive transport of laser light through turbid samples made of magneto-optically active glass micro-particles, are strongly modified by magnetic fields as high as 23 tesla. The intensity correlation function of the speckles, measured at various sample thicknesses and Verdet constants, decays in agreement with a simple model discussed. We also find that the coherent backscattering cone is substantially reduced by strong magnetic fields, again in qualitative agreement with the model. The latter effect provides a unique way to destroy interferences between time reversed optical scattering paths and may be expected to affect light localization.

INTRODUCTION

Since the discovery of optical coherent backscattering from colloidal suspensions of microscopic latex spheres [1], multiple scattering of various types of classical waves in inhomogeneous media has been increasingly studied [2]. In particular, as enhanced backscattering of light results from constructive interference between time-reversed multiple scattering sequences, the possibility of using photons to study phenomena relevant in electron transport - such as weak localization - has been widely explored in recent years. Situations of *strong* optical multiple scattering have been investigated [3, 4] with the goal to achieve *optical* Anderson localization [5]. Very small diffusion constants of light were reported and interpreted first as evidence for the approach of light localization [3] and later as caused by a small propagation velocity due to resonant Mie scattering [4]. The outstanding properties of laser beams (coherence, monochromacity, low divergence, high power density) and of optical detection techniques (photon counting, high angular and spectral resolution) have revealed very powerful and sometimes

Photonic Band Gaps and Localization, Edited by
C.M. Soukoulis, Plenum Press, New York, 1993

crucial in these studies, and have allowed, in addition, to investigate novel correlations [6] in spectral [7], angular [8] and temporal [9, 10] intensity fluctuations. These experiments clearly illustrated many specific advantages of using photons as compared to electrons; but the fact that significant phase shifts between scattering paths of electrons can be easily generated by magnetic fields was considered a unique feature and powerful experimental tool in electronic systems.

Golubentsev [11] and later MacKintosh and John [12] pointed out theoretically that coherent optical backscattering can be destroyed by Faraday rotation of the polarization, since the Faraday effect is known to break the time reversal symmetry of light propagation [13]. In addition, the Faraday effect is expected to affect the interferences between *different* scattering paths which give rise to optical speckle patterns.

We report here the first experimental observation of Faraday rotation in the regime of optical multiple scattering. We observe (1) an almost complete change of the polarized speckle patterns in transmission through a diffusive slab and (2) a partial destruction of the coherent backscattering cone, induced by a strong magnetic field (up to 23 tesla). The field dependences of the intensity correlation function of the transmission speckle and of the angular cone shape agree with the prediction of a simple model we outline below. These experiments illustrate that interferences of multiply scattered light waves, in particular those between time reversed paths, can be significantly manipulated by laboratory strength magnetic fields. This opens, we think, various new experimental possibilities in optical multiple scattering.

FARADAY EFFECT IN MULTIPLE LIGHT SCATTERING - A SIMPLE MODEL

In the Faraday effect, the magnetic field induces a difference of the refractive index between the right and left circularly polarized light components. The corresponding phase difference results in a rotation of the plane of linear polarization of light. For propagation through a *homogeneous* Faraday active material of thickness s, the rotation angle is $\alpha = VsB\cos\varphi$, V being the so-called Verdet - or Faraday - constant and φ the angle between the field $\vec{B}$ and the direction $\vec{s}$ of light propagation.

To describe the Faraday effect in *multiple* scattering, we consider diffusive transport of an incident plane wave of monochromatic light of wavelength λ in a solid slab of thickness L containing Mie-scatterers. We restrict ourselves to the diffusive regime, that is $L \gg l^*$, l^* being the photon transport mean free path [14, 15]. In this sense scattering is a *strong* process, as most photons are scattered many times before leaving the sample. We assume uncorrelated scattering paths, which is also known as "factorization approximation". This requires $l^* \gg \lambda$, that is any localization effects [5] are small perturbations and correlations [6] are essentially short range. In this sense scattering is *weak*. The incident polarization is completely lost in the process of high order multiple scattering [16-19]. Therefore, as light propagation is coherent throughout the entire sample, individual speckle spots have arbitrary, but well defined, polarization states. The polarization change occurs gradually on a length scale of order of l^* depending on the incident polarization state, on the particle size, and on the particle shape [17, 19, 20]. As in high order multiple scattering all polarization states are scanned, we may introduce an effective average polarization decay length l_p^* relevant for essentially all of the sample, except for a small surface layer (of thickness l^*). In order to further simplify our model, let us make the rather unphysical assumption that the polarization state remains unchanged over a distance l_p^*, and then undergoes a sudden

change which depends on the local configuration of the scattering path. Because of the random nature of the scattering paths, the polarization change is arbitrary. Let us further assume that the Faraday rotation of the polarization state on length scale l^* is small, since this turns out to be the case in all our experiments. Then, the configurations of individual multiple scattering paths will not be significantly changed by the Faraday effect. For very small distances $s < l$, l being the scattering mean free path [14, 15], α is given as above, since light propagation is straight. For longer paths $(s > l), s \leq l_p^*$, the average increment $d\alpha_i$ due to the i^{th} scattering event can be written as $d\alpha_i = lVB\cos\varphi\langle\cos\Theta_i\rangle$; Θ_i is the angle between the first and the i^{th} scattering step and $\langle\rangle$ denotes the average over path configurations with fixed φ, φ being the angle between $\vec{B}$ and the first step $\vec{l}_1$. In this picture the average Faraday rotation accumulated along an ensemble of isotropic random paths with identical starting directions is finite and given by $\alpha = VBl^*\cos\varphi$, since $l^* \equiv l\sum_{i=1}^{N}\langle\cos\Theta_i\rangle$ for $N = s/l \gg l^*/l \gg 1$. As polarization memory is lost within a sphere of radius l_p^* (which is of order l^*), the correlation length of the Faraday effect should be equal to l^* in this model. For $s \gg l^*$, φ arbitrarily changes for the consecutive steps of length l^*, and hence the total Faraday rotation α_t is expected to be a widely distributed function with zero mean $\langle\alpha_t\rangle = 0$ and variance $\langle\alpha_t^2\rangle = s/l^* \cdot V^2B^2l^{*2}/3 = s/l^* \cdot \alpha_{l^*}^2$. Therefore, the phases of a given circular polarization component along the high order scattering paths should be randomly changed by a field B. This has the following consequences on speckle patterns and coherent backscattering cones: (1) Polarization states - and hence intensities for a given polarization - of individual speckle spots are changed randomly and, in contrast to optically thin (transparent) materials, there is no field induced average rotation of the polarization of the speckle. (2) Because along each elementary step l^*, the field induced phase shifts on a given circular polarization state have opposite signs for the two time reversed waves, the constructive interference between the latter is destroyed and hence the coherent backscattering peak should decrease.

Magnetic Field Correlation Function of Speckle Patterns

Using the above simple arguments, we can calculate the cross correlation function $G_1(B) = \langle E(0)E^*(B)\rangle/\langle E^2\rangle$ of the total scattered field E, which is a measure of the degree of similarity of $E(0)$ and $E(B)$. We first consider $G_1(B,s)$, the correlation function for a given polarization averaged over all scattering paths of equal length s. Since Faraday rotation is correlated over a length l^*, $G_1(B,s)$ is the product of s/l^* equal terms, describing the magnetic field induced decorrelation of E per step l^*:

$$G_1(B,s) = \langle\cos(\alpha_{l^*})\rangle^{\frac{s}{l^*}} \approx \exp\left(-\frac{V^2B^2l^{*2}}{6}\right)^{\frac{s}{l^*}}. \tag{1}$$

In order to obtain the total correlation function $G_1(B)$, we simply have to sum over all $G_1(B,s)$, as paths are independent.

$$G_1(B) \approx \int_{l^*}^{\infty} P(s)\,G_1(B,s)\exp\left(-\frac{sl^*}{3L_a^2}\right)\quad ds. \tag{2}$$

The exponential factor of the righthand side describes absorption with an absorption length $3L_a^2/l^*$ along the path contour. The intensity weight $P(s)$ of paths of length s depends on the sample geometry and may be obtained from solving the diffusion equation. For transmission through an infinite slab of thickness L, one obtains with the help of the method of multiple images [21]

$$P(s) = \frac{2}{L}\sum_{n=1}^{\infty} \exp(-\frac{n^2\pi^2 s l^*}{3L^2}) \sin\frac{n\pi\gamma l^*}{L} \sin\frac{n\pi(L-\gamma l^*)}{L}. \tag{3}$$

We thus obtain for $L_a \gg l^*$

$$G_1(B) = \frac{\sinh[\gamma l^* \sqrt{\frac{(VB)^2}{2} + (\frac{1}{L_a})^2}] \sinh[\frac{L}{L_a}]}{\sinh[L\sqrt{\frac{(VB)^2}{2} + (\frac{1}{L_a})^2}] \sinh[\gamma\frac{l^*}{L_a}]}, \tag{4}$$

γ being of a coefficient of order 1. For thick slabs, $G_1(B)$ is rather insensitive to the actual value of γ. For negligible absorption ($L_a \to \infty$), this expression becomes $G_1(B) \approx \exp(-V^2B^2L^2/15)$ in the weak field limit ($V^2B^2L^2 \ll 1$) and $G_1(B) \approx VBL\exp(-VBL/\sqrt{2})$ at large VBL. Under the above approximations, the distribution of the scattered light fields in the transmission speckle is Gaussian [22] and, hence, $G_1(B)$ is related to the normalized intensity-intensity cross correlation function $G_2(B) = \langle I(0)I(B)\rangle/\langle I\rangle^2$ by the Siegert relation $G_1^2(B) = G_2(B) - 1$.

Angular Shape of Coherent Backscattering Cones

Within the framework of the simple model discussed above, it is easy to derive expressions for the angular dependence of the coherent backscattering cone in the presence of Faraday effect. It has been shown [23, 16] that for scalar waves the angular dependence of the coherent enhancement $\alpha(q)$, i.e., the excess intensity above the incoherent, diffuse, wide angle background can be written - very similar to the above expressions - as

$$\alpha(q) = \frac{1}{\alpha(0)}\int_{l^*}^{\infty} P(s)\exp(-\frac{sl^*}{3L_a^2})\exp(-\frac{s}{l^*}\cdot\frac{q^2l^{*2}}{3})ds, \tag{5}$$

where the incoherent background $\alpha(0)$ is given by

$$\alpha(0) = \int_{l^*}^{\infty} P(s)\exp(-\frac{sl^*}{3L_a^2})ds. \tag{6}$$

q denotes the external scattering vector, $q = 2\pi\theta/\lambda$ and θ the external scattering angle, both measured off backscattering. $q^2l^{*2}/3$ can be considered as the average contribution of an elemental step of length l^* to the mean square phase shift between time reversed scattering paths under variation of θ. The phase shift induced by the Faraday effect between two time reversed waves travelling a straight segment of length l^* is $2Vl^*B\cos\varphi$, since both paths contribute equal amounts of rotation, but with opposite sign. The φ-averaged decrease of $\alpha(q)$ per single scattering step will thus be $\langle\cos(2VBl^*\cos\varphi)\rangle_\varphi \approx \exp(-2V^2B^2l^{*2}/3)$. As successive steps are uncorrelated, the total average decrease along paths of length s is $\approx \exp(-s/l^* \cdot 2V^2B^2l^{*2}/3)$. Since the phase shifts due to Faraday rotation are independent of the phase shifts due to variations of the external scattering angle, we may write for $\alpha(q, B)$ in the presence of a magnetic field

$$\alpha(q,B) = \frac{1}{\alpha(0)}\int_{l^*}^{\infty} P(s)\exp(-\frac{sl^*}{3L_a^2})\exp(-\frac{s}{3l^*}\cdot(q^2l^{*2} + 2V^2B^2l^{*2}))ds. \tag{7}$$

Various expressions for $\alpha(q)$ have been given in the literature (see e.g., ref. [14, 24]). They depend somewhat on the details of the description of light propagation near the sample surface and, hence, differ at larger scattering angles ($q \approx \lambda/l^*$). However, as $P(s) \propto s^{-3/2}$ in the diffusion approximation, the backscattering cone has a triangular shape around $q = 0$, whatever the form of P(s) at small s. As seen from Eq.(7) this singularity is rounded off both by finite absorption and by Faraday rotation in a finite magnetic field; this is because long scattering paths are more strongly absorbed, and also acquire larger Faraday rotation, than short ones. Note that, because the incoherent wide angle scattered intensity (to which Eq.(7) is normalized) decreases in the presence of *absorption* just like the coherent part, the coherent enhancement remains 1 under absorption; the enhancement factor with respect to the incoherent wide angle background will be 2. On the other hand, the enhancement factor lowers as a function of the *magnetic field*, as B does not act on the incoherent scattered intensity, but does so on the phase between time reversed paths.

EXPERIMENTAL

Samples

In our experiments we used a commercial, rare-earth doped paramagnetic Faraday rotator glass (FR5 from Hoya Optics,Inc., Japan). Bulk glass samples which were a gift of the Societé Maris del Four, Instruments Optiques, Paris, were milled to a powder. The grain diameter had a broad distribution between 0 and 60 μm with its maximum at 2.6 μm and an average diameter of about 22 μm. For the transmission experiments, the powder was suspended in glycerol at volume fractions ϱ between 0.25 and 0.4 and sandwiched between two windows. The sample diameter was 6 mm, the thickness L was varied between 0.7 mm and 1.3 mm. For the backscattering experiments, the powder was mixed with paraffin and a macroscopically homogeneous sample made by briefly melting the paraffin. Samples were free-standing cylindrical pellets of about 10 mm diameter and about 2 mm thickness without windows. Samples were cooled down to temperatures T between 30 K and 90 K using an optical cryostat in order to obtain a larger Faraday rotation. Note that in these samples the *scatterers* are the carriers of the Faraday effect. This contrasts to our model where Faraday rotation occurs in the medium surrounding the scatterers.

Setup

The experimental setups for measurements of transmission speckle patterns and backscattering cones are shown in Figure 1. Samples were illuminated using a monomode Ar^+ laser operated at wavelengths λ of 457.9 nm or 514.5 nm. A beam diameter of $\approx$ 1.5 mm and $\approx$ 2.5 mm was used in transmission and reflection, respectively. The polarization state of the incident beam was linear or circular. The sample was supported by a metallic cooling finger and emerged in a 1 bar helium heat exchange gas atmosphere. The cooling power of the cryostat was about 6 W, the laser power impinging on the sample varied between 30 mW and 100 mW. One of the two independent (linear or circular polarized) transmission speckle patterns was selected by a corresponding analyzer and speckle patterns of about 600 independent speckle spots were recorded using a PC based 512 $\times$ 512 pixel video imaging system of 8 bit reso-

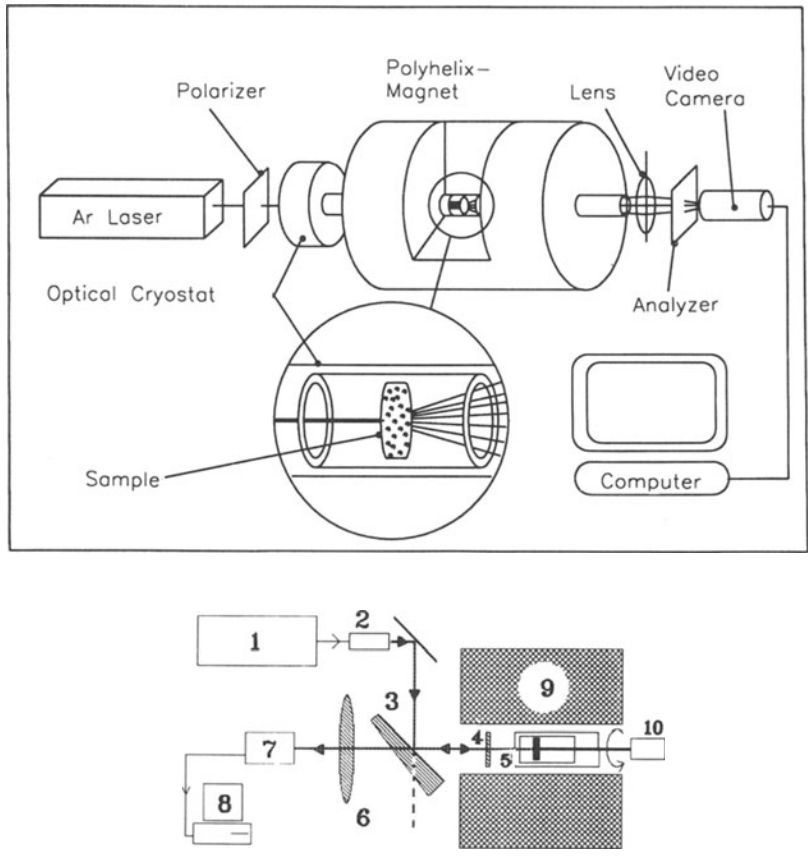

Figure 1. Experimental setup to measure transmission speckle patterns (top) and coherent backscattering (bottom) in magnetic fields up to 23 Tesla. 1) Laser, 2) Beam expander, 3) Beam splitter, 4) Polarizer, 5) Optical cryostat and sample, 6) Lens, 7) Video camera, 8) PC, 9) Solenoid producing a horizontal magnetic field parallel to the incident laser beam, 10) Motor.

lution. Backscattering cones were monitored using a semi-transparent wedge-shaped beamsplitter and focusing the scattered light with a 330 mm focal distance lense onto the video system. The backscattering speckles were averaged out by motor-driven rotation of the sample about an axis normal to its surface. A resistive polyhelix magnet was used to generate magnetic fields of up to 23.5 T. The Faraday rotation of unmilled glass samples was measured at both wavelengths as a function of T and B, giving, for example, a Verdet constant V_{bulk} of 26.2 ^{o} T^{-1} mm^{-1} at $\lambda = 514.5$ nm, $T = 77$ K and $B < 8$ T. The Faraday rotation tends to saturate in higher fields, particularly at lower temperatures, and we corrected the measured multiple scattering data for this experimentally determined field dependence.

Exhaustive tests were performed to check the mechanical and thermal stability of the setup and sample, which turned out very critical for the transmission speckle measurements. We require a reproducible speckle pattern after a complete field sweep and measurement cycle, which takes typically about 20 min. The sample displacement perpendicular to the laser beam during a field cycle, as caused by magnetic forces on the cryostat and temperature variations of the magnet bore, was always less than 50 μm. The resulting small translation of the pattern could easily be corrected by the video system. Magnetostriction was measured to be less than $\lambda/1000$ for sample lengths of about 1 mm, corresponding to rms phase changes smaller than $2\pi/1000$ for a typical scattering path. Displacement of scatterers due to paramagnetic forces was found negligible as tested by measurements of $G_1(B)$ in high field gradients in the off-center region of the solenoid. The Voigt constant of the bulk material was found to be less than 0.5 ^{o} mm^{-1} in 10 T.

RESULTS

Transmission speckle intensity correlation function

Figure 2 shows the same section of a speckle pattern monitored at $B = 0T$ and $B = 23.5T$. An almost complete change of the pattern is observed, which is fully reversible on return to $B = 0T$. We calculated $G_2(B)$ by multiplying pixel by pixel the speckle pattern at $0T$ with the one at field B, averaging over all ($2.56 * 10^5$) pixels and dividing by the square of the average intensity. In Figure 3 we plot this function for three different cases out of about 40 measured. These data are compared to a sample of similar optical thickness (white paper) but with no Faraday effect. The small decay in the latter case is due to the independently measured Faraday rotation of the windows. All data were corrected for this effect. The correlation decay of the samples is found quadratic in B for small fields changing into a negative exponential [25] for higher fields. It increases for higher volume fractions, thicker samples (Figure 4) and higher Verdet constant which was varied by changing temperature (Figure 5) and wavelength (Figure 6). The correlation function is independent of the incident and detected polarization as shown by comparison with measurements using circular polarizers (Figure 7). All these observations qualitatively agree with our model.

In order to make the comparison of our data with Eq.(4) more quantitative, we need values for l^* and L_a. We determined l^* and L_a by absolute transmission measurements as follows. The diffuse transmitted intensity $I(L)$ was measured for samples at thicknesses L between 0.6 mm and 1.9 mm, as shown in Figure 8. In the presence of absorption, the solution of the diffusion equation for an infinite slab yields for $L_a \gg l^*$:

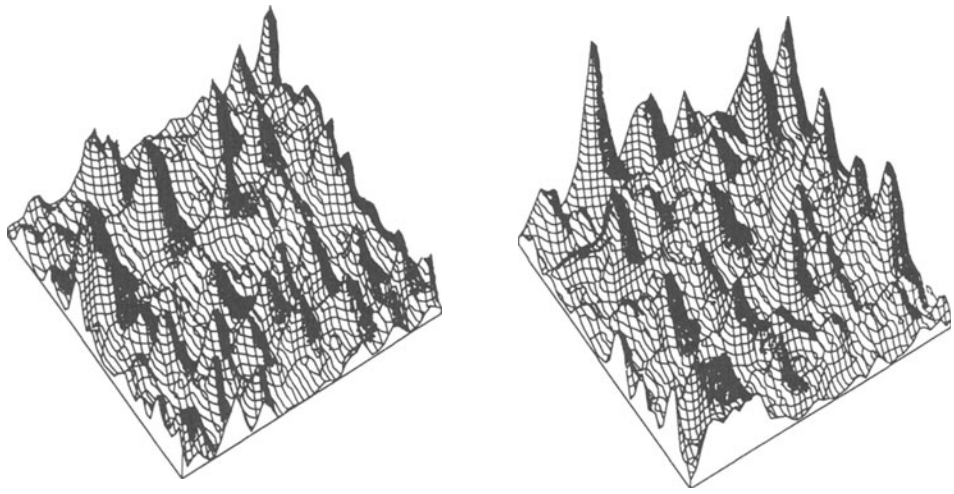

Figure 2. Intensity plots of transmission speckle patterns of a magneto-optical active multiple scattering sample in $B = 0\ T$ (left) and $B = 23\ T$ (right). The section shown corresponds to a solid angle of $\approx 0.1\ ^o$ by $0.1\ ^o$.

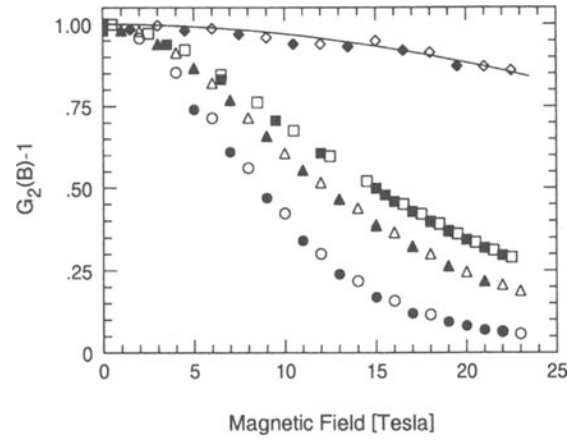

Figure 3. Magnetic field dependence of the speckle intensity correlation function for three samples , (o) $L = 1.22\ mm, \varrho = 0.25$, ($\triangle$) $L = 0.76\ mm, \varrho = 0.30$, ($\square$) $L = 0.76\ mm, \varrho = 0.25$ in comparison to a ($\diamond$) paper screen ($V \approx 0$). Incident and detected polarization were linear. Open or closed symbols correspond to a field sweep up or down, respectively. $\lambda = 514.5\ nm, T = 77\ K$. The small decay of the paper sample is due to Faraday rotation of the windows (continuous line: from measured Faraday effect of the windows without diffusor).

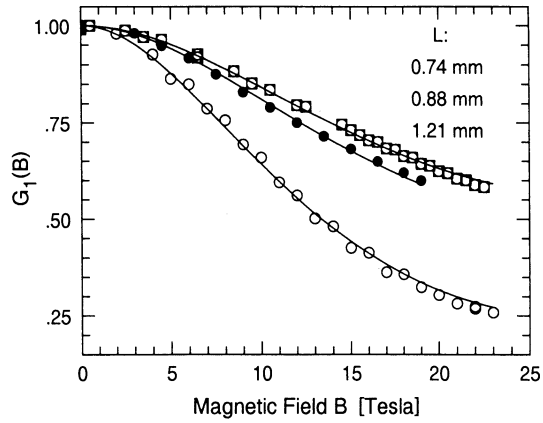

Figure 4. Field-field correlation function $G_1(B)$ for different sample thicknesses L, $\lambda = 514\ nm$, $\varrho = 0.25$, $T = 77\ K$. The continuous lines correspond to a fit of Eq.(4) with E_V as the free parameter, taking into account the experimentally determined field dependence of the Verdet constant. We find (□) $E_V = 2.26$, (•) $E_V = 2.13$, (○) $E_V = 2.53$. The different data fall on a single curve when plotted vs. B^2L^2, as suggested by Eq.(4).

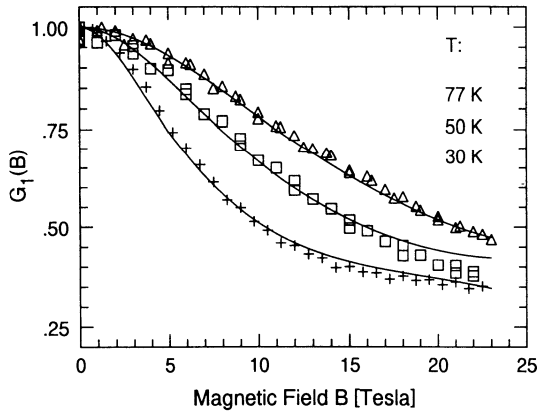

Figure 5. $G_1(B)$ at different temperatures, for $\lambda = 514.5\ nm$, $\varrho = 0.3$ and $L = 0.76\ mm$. (△) $E_V = 2.25$, (□) $E_V = 2.20$, (+) $E_V = 2.20$. The data fall on a single curve when plotted vs. B^2V^2 as suggested by Eq.(4). The saturation of the Faraday rotation at high fields is most clearly visible in the data at 30 K.

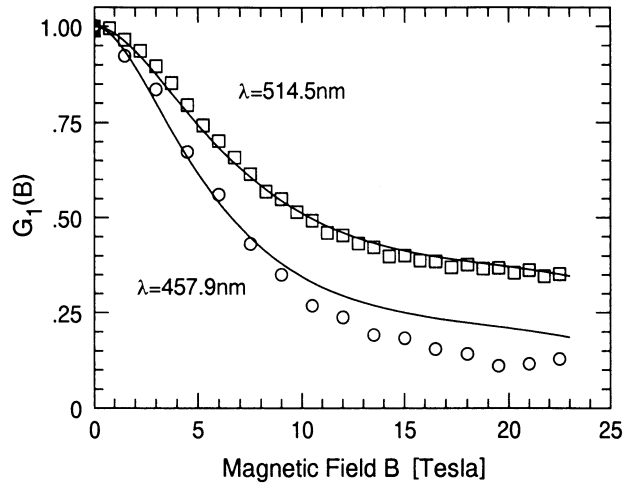

Figure 6. $G_1(B)$ at two different wavelengths, $\varrho = 0.3$, $L = 0.76\ mm$, $T = 30K$. The data reflect the larger V-values at $\lambda = 457\ nm$. (□) $E_V = 2.20$, (○) $E_V = 2.27$.

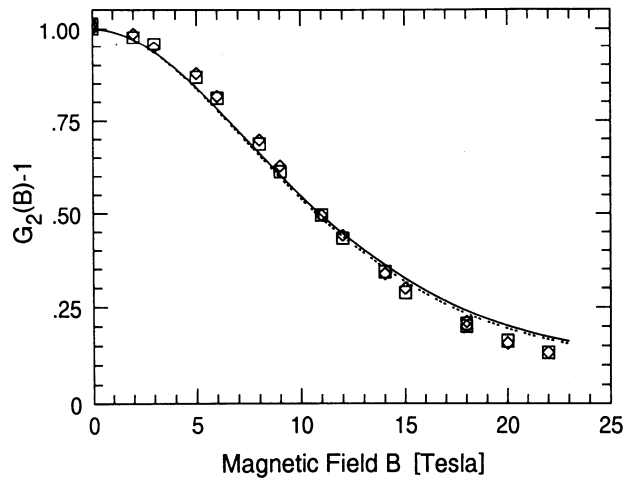

Figure 7. Correlation function $G_2(B)$ measured for (◇) circular and (□) linear incident polarization. $\lambda = 514.5\ nm$, $T = 77\ K$, $\varrho = 0.4$, $L = 0.76$. (◇) $E_V = 2.14$ and (□) $E_V = 2.15$.

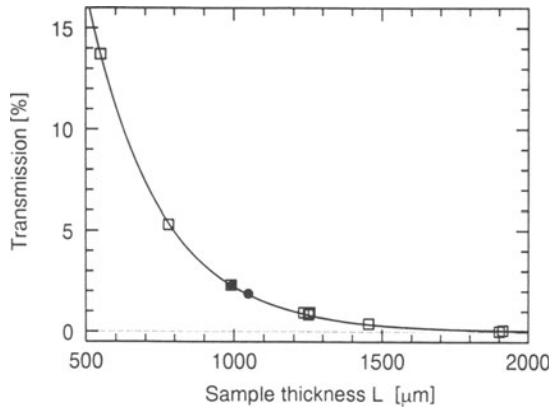

Figure 8. Angular-integrated transmission of slabs of various thicknesses. $\varrho = 0.3$, $\lambda = 514\ nm$. The uncalibrated transmission data (□) were calibrated by scaling them such that the point at $L = 1000\ \mu m$ superimposes on the absolute measurement (•). Continuous line: Fit of Eq.(8).

$$I(L) = I_0 \quad \frac{\sinh[\frac{\gamma l^*}{L_a}]}{\sinh[\frac{L}{L_a}]}. \tag{8}$$

I_0 was determined using a nonabsorbing suspension of polystyrene spheres with known $l^*(= 26.1 \pm 2\ \mu m)$ and $L = 1\ mm$, with transmission $I(L)/I_0 = 5l^*/3L$ [15]. By fitting the data shown in Figure 8 to Eq.(8), we obtain for our Faraday samples $l^* = (72 \pm 10)\ \mu m$ and $L_a = (270 \pm 30)\ \mu m$ [26].

In our experiment, the Faraday effect occurs inside the scatterers; thus it would seem natural to simply use $V = \varrho V_{bulk}$ as the effective Verdet constant V_e in Eq.(4). This corresponds to a single passage of light through a scatterer. However, the recent observation of very low effective propagation speed of light due to Mie resonances or internal reflections inside the scatterers [4] may suggest longer average internal light paths; this effect also would give rise to larger V_e-values. Unfortunately, in contrast to the case of spherical scatterers, this effect cannot be calculated for our randomly shaped particles. We determined therefore the effective light speed v_E in some of our samples by a photon time-of-flight experiment. We used a frequency-doubled Nd:YAG laser with a pulse width of about 4 ps at $\lambda = 532\ nm$. The light was focused onto the sample and the delayed and broadened transmitted pulse was recorded using a Hamamatsu Syncroscan streak camera. We measured the pulse shape for 4 samples with $\varrho = 0.3$ and L varying between 0.9 mm and 1.9 mm. One example is shown in Figure 9. We determined the diffusion constant $D = v_E l^*/3$ by fitting the data to the time dependent solution of the diffusion equation:

$$T(t,L) = \frac{\exp[-\frac{t}{\tau_a}]}{(4\pi Dt)^{\frac{1}{2}}} \sum_{m=-\infty}^{\infty} \Big(\exp[-\frac{((2m-1)L - 2\gamma l^*)^2}{4Dt}] - \exp[-\frac{((2m-1)L)^2}{4Dt}]\Big) \tag{9}$$

$\tau_a = 3L_a^2/(l^* v_E)$ is the absorption time which dominates the exponential decay of $T(t,L)$

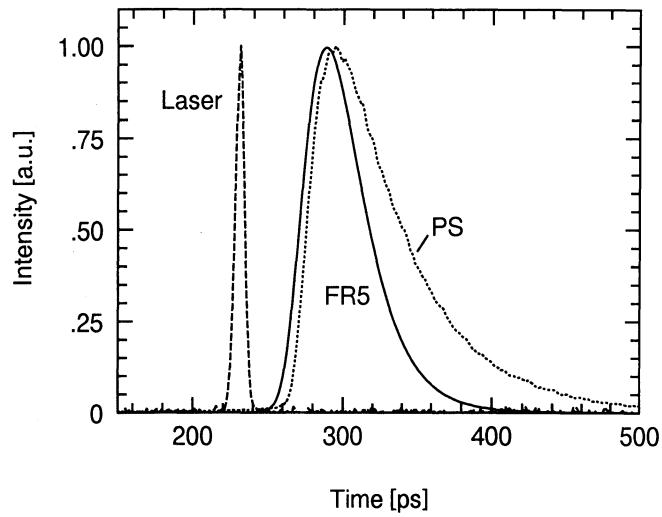

Figure 9. Photon time-of-flight measurement. Dashed-dotted line: incident laser pulse. Continuous line: delayed and broadened light pulse after passage through a sample with thickness $L = 1455\ \mu m.$, $\varrho = 0.3$. Dotted line: Reference measurement on a colloidal suspension of polystyrene spheres, $L = 2\ mm$, $l^* = 108\ \mu m$.

at long times. Using l^* and L_a as given above we deduce $v_E = c_0/(2.5 \pm 0.5)$, c_0 being the vacuum light speed. In order to check experimental reliability, we performed similar experiments on suspensions of $0.8\ \mu m$ polystyrene spheres at $\varrho = 0.023$ with no absorption ($L_a > 20cm$), and with $L_a = 308\ \mu m$ adjusted by adding appropriate amounts of an absorbing dye (Rhodamine 6G) to the suspension. These measurements revealed a 11% reduction of the effective speed in both cases, which is consistent with Mie scattering theory.

In addition, we have observed the light transmitted through individual FR5-particles using polarization microscopy. The light was found strongly depolarized, the depolarization being essentially independent of the orientation of the particles. This qualitative observation also argues for the importance of internal reflections in our samples.

Taking into account the refractive indices of glycerol ($n_g = 1.47$) and FR5 ($n_f = 1.70$) and the volume fraction ϱ of FR5, the above speed reduction translates into an effective Verdet constant V_e exceeding ρV_{bulk} by a factor:

$$E_V = V_e/\varrho V_{bulk} = \frac{\left(\frac{c_0}{v_E}\right) - n_g(1-\varrho)}{n_f \cdot \varrho} = 2.9 \pm 0.9.$$

On the other hand, fitting of 40 data sets at $\lambda = 514.5\ nm$ to Eq.(4) with E_V as the only free parameter consistently yields an average value of $E_V = 2.20 \pm 0.21$. Examples are shown as continuous lines in Figs.4, 5, 6, 7. The agreement between fits and data is remarkably good over the entire range of parameters explored - perhaps with the exception of the lower curve in Figure 6 (which actually represents the largest disagreement we observed). The fact that E_V is independent of the varied parameters means that $G_1(B)$ essentially scales with $B^2V(B)^2L^2$, since absorption in our samples only weakly affects the functional form of $G_1(B, V, L)$. It appears, thus, the measured correlation function $G_2(B)$ agrees quite well with our model and the Faraday rotation in this

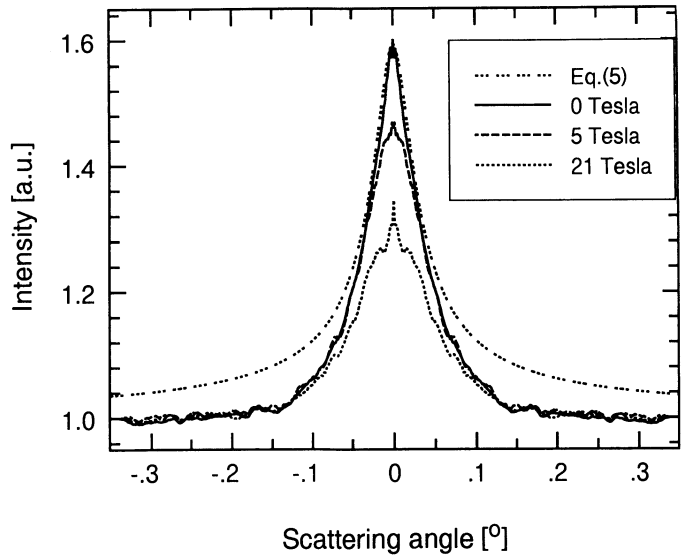

Figure 10. Angular dependence of the scattered light intensity in the vicinity of backscattering, normalized to the flat background at 0.33°, for one of our samples at $T = 30\ K$, $\lambda = 514.5\ nm$, $\varrho = 0.4$ in different magnetic fields. Dashed line according to Eq.(5), see text.

type of samples is more than doubled because of internal reflections inside the scatterers.

Coherent backscattering cones

The coherent backscattering data reported below were measured with the incident and detected light having the *same* circular polarization. Video images of the intensity scattered into a solid angle of about 0.6° by 0.6° around backscattering were obtained by averaging 255 individual pictures. The angular dependence of the scattered intensity was obtained by searching for the pixel position of the maximum intensity and consecutive azimuthally averaging by summing over pixels at constant distance from this position. Intensities were normalized to the intensity at the largest angle scanned by this procedure. The latter intensity is very close to the incoherent background, because the detected angular range is much larger than the cone width at half height. Because of (unavoidable) diffuse stray light, which essentially adds to the incoherent background, experimental enhancement factors at $B = 0T$ were smaller than 1, ranging from 0.4 to 0.8. In Figure 10 cones obtained at three magnetic field values are shown. A field induced decrease of the cone height at backscattering ($\theta = 0$) is clearly visible. The observed field effect becomes weaker at larger scattering angles. These observations qualitatively agree with the simple model outlined above, and with the predictions of Golubentsev [11] and MacKintosh and John [12].

In order to make the comparison more quantitative, we have determined l^* from measurements of the radial intensity profile around a small laser spot on the sample [27], and L_a from a thickness-dependent transmission experiment as above. We find $l^* = 117\ \mu m$ and $L_a = 310\ \mu m$. The dashed-dotted line in Figure 10 represents the expression (Eq.4) of Akkermans et.al. [23], which is a solution of Eq.(5), using $\gamma = 5/3$, the above values for l^* and L_a, and adjusting the amplitude at backscattering. The agreement with the experiment is good at *small* angles, indicating that this expression gives a fair estimate of the cone shape in the angular range where the diffusion approximation

is valid. A similar conclusion was drawn earlier from measurements on monodisperse spherical polystyrene latex samples [14, 28]. At *larger* scattering angles, the data fall well below the scalar wave theory [23]. This could be due to the use of identical circular polarization of the incident and detected beam: one may expect that the light scattered at wider angles (which is dominated by contributions from low order scattering paths) has more intensity of opposite helicity than estimated by a scalar wave theory, as backscattering flips the helicity.

Figure 11a shows the field dependent decrease of the enhancement at backscattering in comparison with a measurement (Figure 11b) on a reference sample with negligible Faraday rotation, but having a similar cone width. As Eq.(5) and Eq.(7) have the same functional form, we can use the solution for the angular dependence of $\alpha(q, B = 0)$ [23] to calculate the field dependence of $\alpha(q = 0, B)$. Figure 11a shows a fit of this solution to the data, using the above values for l^*, L_a, γ, E_V, ϱ and the experimental field dependent Faraday rotation. The only fit parameter is the coefficient a in the term $\exp(-\frac{s}{3l^*} \cdot (aVBl^*)^2)$. We find $a = 0.9$ as compared to $\sqrt{2}$ predicted by Eq.(7). In view of the simplicity of our model, the scattering of our data points, and having neglected corrections due to internal reflections [29], the agreement between data and model appears good.

CONCLUSIONS

Our observations of the magnetic field induced decay of the intensity correlation function of transmission speckle patterns and of the destruction of the coherent backscattering cone illustrate that the Faraday effect in the optical multiple scattering regime can be understood in terms of a random walk of the field induced polarization changes on top of the light diffusion through the disordered medium. The quantitative agreement with the simple model discussed suggests the possibility to measure the Faraday effect of powders and ceramics, even in the presence of absorption.

In addition, our observations illustrate that it is possible to affect coherent backscattering and hence weak localization of light by laboratory strength magnetic fields, provided a properly choosen magneto-optically active material is used. This novel effect seems the only experimental way so far - to our knowledge - to generate significant phase shifts between time reversed *optical* scattering paths. In this sense it resembles the magnetic field induced phase shift on the electronic wave function in the Aharonov-Bohm and related effects, despite of the different – and much weaker – coupling mechanism of the field to the light wave. We think that Faraday rotation may become of importance in various optical multiple scattering studies, perhaps even in the search for light localization. A challenge in this kind of new experiments is to evaluate how much the interferences between time reversed waves contribute to the diffusion constant - as compared to the classical "Drude-type" value - in the generally highly concentrated samples of strongly correlated scatterers. The results reported here suggest that the contributions of these interferences could be determined, at least in principle, by using the Faraday effect.

Acknowledgments

Many fruitful discussions with E.Akkermans, D.Bicout, A.Martinez, R.Maynard and P.E.Wolf are kindly acknowledged. We thank W.Rühle and A.Heberle for the opportunity to use their ps-laser set-up and for their help during the pulse experiments at the MPI für Festkörperforschung, Stuttgart.

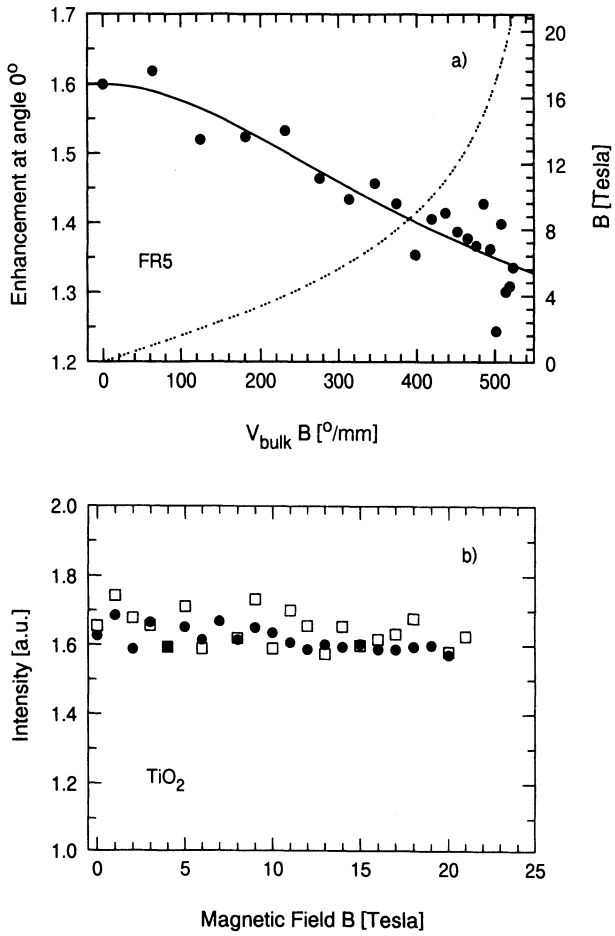

Figure 11. Backscattered intensity (at $q = 0$) normalized to the incoherent wide angle background (a) as a function of $V_{bulk}(B) \cdot B$ for the sample as specified in Figure 10. Dots are data, the continuous line is a fit to Eq.(7), see text, the dotted line indicates the measured field dependence of V_{bulk}. (b) as a function of B, for a reference sample with negligible Faraday rotation: 0.28 μm diameter TiO_2 particles embedded in paraffin at a concentration adjusted as to provide a cone width comparable to our samples (Figure 10). $T = 50K$. Other parameters like in (a).

References

[1] Y. Kuga and A. Ishimaru, *J. Opt. Soc. Am.* **A 8**, 831 (1984). M.P. van Albada and A. Lagendijk, *Phys. Rev. Lett.* **16**, 2692 (1985). P.E. Wolf and G. Maret, *Phys. Rev. Lett.* **55**, 2696 (1985).

[2] See e.g. *Scattering and Localization of Classical Waves in Random Media*, P.Sheng, ed., World Scientific Publishing, London, (1990).

[3] J.M. Drake and A.Z. Genack, *Phys. Rev. Lett.* **63**, 259 (1991).

[4] M.P. van Albada, B.A. van Tiggelen, A.Lagendijk and A.Tip, *Phys. Rev. Lett.* **66**, 3132 (1991).

[5] P.W.Anderson, *Phil. Mag.* **52**, 505 (1985).

[6] S.Feng, C.Kane, P.A.Lee and A.D.Stone, *Phys. Rev. Lett.* **61**, 834 (1988).

[7] M.P. van Albada, J.F. de Boer and A.Lagendijk, *Phys. Rev. Lett.* **64**, 2787 (1990).

[8] I. Freund, M.Rosenbluh and S.Feng, *Phys. Rev. Lett.* **61**, 2328 (1988).

[9] G.Maret and P.E.Wolf, *Z.Phys.* **B 65**, 409 (1987).

[10] D.Pine, D.A.Weitz, P.M.Chaikin and E.Herbolzheimer, *Phys. Rev. Lett.* **60**, 1134 (1988).

[11] A.A.Golubentsev, *Sov. Phys. JETP* **59**, 26 (1984).

[12] F.C.MacKintosh and S.John, *Phys.Rev. B* **37**, 1884 (1988).

[13] Lord Rayleigh, *Phil. Trans.* **176**, 343 (1885), Scientific Papers **2**, 360 (1900) and **3**, 163 (1902), Cambridge.

[14] P.E.Wolf, G.Maret, E.Akkermans and R.Maynard, *J. Phys. (Paris)* **49**, 63 (1988).

[15] A.Ishimaru, *Wave Propagation and Scattering in Random Media*, Academic, New York, (1978), Vol 1.

[16] E.Akkermans, P.E.Wolf, R.Maynard and G.Maret, *J. Phys. (Paris)* **49**, 77 (1988).

[17] F. MacKintosh, J.X. Zhu, D.J. Pine and D.A.Weitz, *Phys. Rev. B* **40**, 9342 (1989).

[18] S.M. Cohen, D. Eliyahu, I. Freund and M. Kaveh, *Phys. Rev. A* **43**, 5748 (1991).

[19] A.Martinez and R.Maynard, this volume.

[20] F.Erbacher, Doctoral Thesis, University of Konstanz (1992).

[21] See e.g., P.M.Morse and H.Feshbach, *Methods of Theoretical Physics*, McGraw-Hill, New York (1953).

[22] The intensity distribution function of our speckle patterns have been checked to obey $P(I) = 1/\langle I\rangle \exp(-I/\langle I\rangle)$ above $0.2 \cdot \langle I\rangle$, corresponding to experimental $G_1(0)$-values of typically 0.9.

[23] E.Akkermans, P.E.Wolf and R.Maynard, Phys. Rev. Lett. **56**, 1471 (1986).

[24] E.E.Gorodnichev, S.C.Dudarev and D.B.Rogozkin, *Phys. Lett.* **A 144**, 48 (1990).

[25] Note that in non-diffusing media $G_2(B)$ is an oscillating function of B.

[26] Time integration of the transmitted light pulses discussed below gave consistent values $L_a = (263 \pm 30)\ \mu m$.

[27] R.Lenke, unpublished.

[28] S.Fraden and G.Maret, *Phys. Rev. Lett.* **65**, 512 (1990).

[29] A.Lagendijk, R.Vreeker and P. de Vries, *Phys. Lett.* **A 136**, 81 (1989). I.Freund, R.Berkovits and S.Feng, *Phys. Rev.* **B 41**, 496 (1990).

POLARIZATION STATISTICS IN MULTIPLE SCATTERING OF LIGHT: A MONTE CARLO APPROACH

A.S. Martinez and R. Maynard

Expérimentation Numérique
Centre de Recherche sur les Très Basses Températures
Maison des Magistères CNRS
BP 166
38042 Grenoble Cedex 9 France

ABSTRACT

The statistics of the depolarization of light by multiple scattering is a complex problem in the regime of Mie scattering. Nevertheless, the correlation functions (Stokes intensities) can be entirely determined by studying the loss of memory of both initial linear and circular polarizations as a function of the thickness of a slab (L) in units of the transport mean free path (l^*).

These multiple scatterings of light have been simulated by a Monte Carlo algorithm in the approximation of independent paths and large spheres. We find that, contrary to what is observed for Rayleigh scatterers, the depolarization rate is about twice as large for the linear incident polarization as for the circular one. Also, the mechanism of depolarization is more complex than envisaged previously, since the most probable intermediate states are elliptical rather than linear or circular.

The randomization of the wave vector and helicity of light can be readily seen by the geometrical picture furnished by the Poincaré representation. The polarization states are projected on a sphere, with the linear states located on the equator, the circular ones on the poles and the elliptical ones on the hemispheres. The depolarization process is seen as the spreading-out of the polarization state cloud around the incident state.

These studies lead to new concepts of specific characteristic lengths, which are associated with the vectorial nature of the fields, enriching the standard concept of transport mean free path introduced in the context of scalar multiple scattering.

I. INTRODUCTION

The multiple scattering of waves in random media is well-known so far within four major approximations: *i)* scalar waves, *ii)* point-like scatterers, *iii)* independent Feyman paths, and *iv)* weak concentration of disorder. If the scattering is elastic, the wave interferences are not destroyed by the sample averaging. If the system presents time-reversal invariance, the weak localization effect is then observed through the coherent

Photonic Band Gaps and Localization, Edited by
C.M. Soukoulis, Plenum Press, New York, 1993

back-scattered cone.[1] The consequences of this residual interference phenomenon can be observed in various physical systems, among them, electrons diffusing in impure metals (mesoscopic scale) or light diffusing in turbid suspensions.

For the case of light, the polarization must be taken into account because of the vectorial nature of the field. This is a difficult problem for the following reason: during the successive multiple scatterings, the transverse electrical field is transformed by the Mie scattering amplitudes and in each step the electric field must be projected onto the scattering plane. This transformation can be simply described by the product of the complex 2x2 (Jones) matrices in the local scattering frame.[2] The difficulty occurs when this transformation is projected in the laboratory frame, to take into account the geometrical boundary condition.

For point-like scatterers (Rayleigh scattering) a great simplification occurs, since for incident linear polarization, the scattered light remains linearly polarized and it is only parametrized by the emerging wave vector. This is expressed by a real 3x3 matrix in the lab. frame.[3-5] The multiple Rayleigh scattering of n-th order can be treated[5] analytically by a system of recurrent equations. Its solution yields the depolarization degree as well as the various correlation functions for polarization.

The simplest experimental configuration for measuring the polarization correlation is the slab geometry confining the scatterers. The incident and emerging wave vectors of the plane waves are perpendicular to the slab planes or equivalently parallel to z for transmission or anti-parallel for reflection. For this geometry, the incident and emergent electric fields are in the x-y plane and several symmetries are present: rotation around the z axis and reflection by a plane containing this axis. Remarkably, for this simple geometry, only three parameters are necessary to characterize entirely the random medium. Following the notation of reference 6, these parameters are called a_1, a_2 and a_4. They are the elements of the diagonal Mueller matrix acting on the incident Stokes vector.[6] They have a simple physical meaning: a_1 describes the total transmitted or reflected intensity, $|a_2|$ and $|a_4|$ (divided by a_1) are the polarization degree for incident linear and circular polarization, respectively. Therefore, when the absolute value of the multiply scattered intensity is not relevant, only two measurements are necessary for characterizing the medium, leading to $a'_2 = a_2/a_1$ and $a'_4 = a_4/a_1$.

The scattering by Mie particles, with $a \gtrsim \lambda$, where a is the sphere radius and λ the wave length, is different from Rayleigh scattering. In this case, the characteristic lengths of the multiple-scattering medium must be scaled by the transport mean free path, as was observed in the coherent backscattering experiments.[7] By measuring the time-correlation of the intensity in a reflection experiment, it was observed[8,9] that the rate of decorrelation is reversed in the regime of large spheres. For point-like scatterers, the circular polarization decreases faster than the linear one. It is just the opposite for large spheres, the circular polarization is more persistent than the linear one. Moreover, the characteristic length for the randomization of the helicity of circular polarized light is greater than the transport mean free path l^*.

Several problems remain in the context of the multiple scattering of electromagnetic field and call for a deepening of the analysis. For a very large number of scalar wave scatterings, corresponding to thick slabs for instance, the general frame of the theory is the diffusion equation. This leads to a well-known distribution function for the length of the Feyman paths $P(s)$. This "pure" diffusion regime corresponds to complete depolarization of the light. But the approach to the diffusion regime, or still, the cross-over between the single scattering and the "pure" diffusion regime, that we call intermediate regime, raises important problems. What are the polarization decays for the two basic incident polarized light - linear and circular - and how do they depend on the particle size and shape? More precisely, is the approach to complete depolarization state for large spheres given as an

effective Rayleigh regime, in the space scale ℓ^* instead of the mean free path ℓ? What are the effects of the boundary conditions on the correlation functions?

To progress in the understanding of this complex problem, we have written a complete computer program based on the Mie scattering and a Monte Carlo algorithm for generating the independent sequences of scatterings. The correlations for polarization can be obtained in transmission or reflection, through a slab of variable thickness, for different incident polarization states. Contrary to what is observed for Rayleigh scatterers, the circular polarization is more persistent than the linear one. The depolarization rate is about twice as large for the linear incident polarization than for the circular one. Also, the mechanism of depolarization is more complex than envisaged previously by the helicity flip model.[8] The partial polarization of light is elliptical rather than linear or circular. It is better represented on the Poincaré sphere, the space of the Stokes parameters, rather than in the $\boldsymbol{k}$, space where the trajectories are described. Our results fit well the experimental data.[10]

The paper is divided as follows. In section II, a brief review is presented of Mie scattering, Stokes intensities and Poincaré sphere. In section III, the multiple Mie scattering is introduced using the Jones formalism. The consequences of the approximation of independent paths are briefly discussed in the context of polarization statistics and the distribution of the polarization states is obtained analytically on the Poincaré sphere. The description of the Monte Carlo simulation program is given in section IV. Results and discussions of the multiple scattering correlations are reported in section V.

II. SINGLE MIE SCATTERING, STOKES INTENSITIES AND POINCARE REPRESENTATION

The scattering of polarized light by a sphere of arbitrary size can be calculated exactly and it is known as Mie scattering. A plane electromagnetic wave with electric field, $\boldsymbol{E_0}$, propagates toward the positive z with wave vector $\boldsymbol{k}$, in an isotropic, homogeneous and non-absorbing medium with refractive index n_m. It is then scattered by a sphere of radius a and refractive index n_S , located at the origin of a coordinate system. If n_S is real, the scattering is elastic and the scattered wave propagates in the direction $\boldsymbol{k'}$, with $|\boldsymbol{k}| = |\boldsymbol{k'}|$. The plane containing the directions $\boldsymbol{k}$ and $\boldsymbol{k'}$ is called the scattering plane. In spherical coordinates, at the position r, so that $\rho >> ka$ ($\rho = kr$), the scattered electric field $\boldsymbol{E_S}$ is nearly transverse (far-field approximation). The electric field components parallel and perpendicular to the scattering plane, direction θ and ϕ ,respectively, where ϕ is the azimuthal angle and θ the angle between $\boldsymbol{k}$ and $\boldsymbol{k'}$, are given by:

$$\mathbf{E_S} = \frac{je^{j\rho}}{\rho} \boldsymbol{J}(\theta,\phi)\mathbf{E_O} \ , \tag{2.1.1}$$

where $j = \sqrt{-1}$ and $\boldsymbol{J}$ is the Jones matrix given by the product:

$$\boldsymbol{J} = \begin{bmatrix} S_{//}(\theta) & 0 \\ 0 & S_{\perp}(\theta) \end{bmatrix} \cdot \begin{bmatrix} cos\phi & sin\phi \\ -sin\phi & cos\phi \end{bmatrix} . \tag{2.1.2}$$

The second matrix, ϕ dependent, projects $\boldsymbol{E_0}$ on the parallel and perpendicular directions of the scattering plane. The first one, θ dependent, is diagonal, reflecting the spherical symmetry of the scatterer and its elements are the parallel and perpendicular scattering

amplitude $S_{//}(\theta)$ and $S_{\perp}(\theta)$, respectively, found in references 6 and 11. We notice that from the Mie theory, the equality $S_{//}(0) = S_{\perp}(0)$ means that forward scattering does not change the incident polarization state and that $S_{//}(\pi) = -S_{\perp}(\pi)$ means that the backward scattering reverses the helicity of the incident polarization state. The intensity and polarization are given by the Stokes intensities $i = |E_x|^2 + |E_y|^2$, $q = |E_x|^2 - |E_y|^2$, $u = 2Re(E_xE_y^*)$ and $v = 2Im(E_xE_y^*)$, and obey the Stokes sum rule $i^2 = q^2 + u^2 + v^2$. A geometrical representation for the polarization states is provided by the Poincaré representation.[11] In this representation $q = icos(2\chi)cos(2\psi)$, $u = icos(2\chi)sin(2\psi)$ and $v = isin(2\chi)$, where ψ is the inclination angle of the ellipse (of the electric field) with respect to given axes and $tan\chi$ is the ratio between the semimajor and semiminor axes of the ellipse. The positive and negative values $tan\chi$ stand for left- and right-handed polarizations. On the Poincaré sphere the north and south poles represent left- and right-handed circular polarization, respectively. The northern and southern hemispheres represent left- and right-handed elliptic polarizations and the equator represents linear polarizations.

The differential scattering cross section can be written as:

$$\sigma_d(\theta,\phi,\mathbf{E_o}) = \tfrac{1}{2}[|S_{//}(\theta)|^2 + |S_{\perp}(\theta)|^2 + [|S_{//}(\theta)|^2 - |S_{\perp}(\theta)|^2]\, f(\mathbf{E_o},\phi) \ , \qquad (2.2)$$

where $f(\mathbf{E_o},\phi) = (q_o cos2\phi + u_o sin2\phi)/i_o$. The differential scattering cross section is dependent on θ and ϕ; moreover it is parametrized by the incident Stokes intensities. For a circular polarized incident wave ($q_o = u_o = 0$), the differential cross section and the Stokes intensities are independent of the azimuthal angle ϕ. From $\sigma_d(\theta,\phi,\mathbf{E_o})$, one gets the scattering cross section σ_S by integrating over the solid angle $d\theta cos\theta d\phi/(4\pi)$.

We emphasize that the Mie scattering is anisotropic and changes the polarization of the incident wave which, in general, becomes elliptically polarized. This scattering is governed by two parameters, the size parameter ka and the relative refractive index $m = n_s/n_m$. Fixing m, three regimes are identified, *i)* Rayleigh for $ka << 1$, *ii)* intermediate for $ka \sim 1$ and *iii)* large spheres for $ka >> 1$. This is apparent from the variation of the function (in percent):

$$F(ka) = 100\,\frac{Max[||S_{//}(\theta)|^2 - |S_{\perp}(\theta)|^2|]}{Max[|S_{//}(\theta)|^2 + |S_{\perp}(\theta)|^2]} \ , \qquad (2.3)$$

where *Max* takes the maximum of its argument when θ varies from *0* to π (Fig. 1). This function points out the difference between the parallel and perpendicular scattering amplitudes. For the Rayleigh regime, the scattering amplitudes are well-known and *F(ka)* has a maximum value of *50%*, while, for large spheres, a good approximation is to consider $|S_{//}(\theta)|^2 \sim |S_{\perp}(\theta)|^2$. This illustrates quantitatively which regime must be considered in a particular situation. For $ka = 6.5$, *F(ka)* is less than *0.5%*, which justifies the approximation of a large sphere, where the dependence on ϕ and $\mathbf{E_o}$ is neglected on Eq. (2.2). This approximation will be used in the numerical simulation. Anisotropy is characterized by : $\langle cos\theta \rangle = \frac{1}{4\pi\sigma_S} \int_0^{\pi} d\theta\, sin\theta \int_0^{2\pi} d\phi\, \sigma_d(\theta,\phi)\, cos\theta$ and $\ell^*/\ell = n^* = 1/(1 - \langle cos\theta \rangle)$.

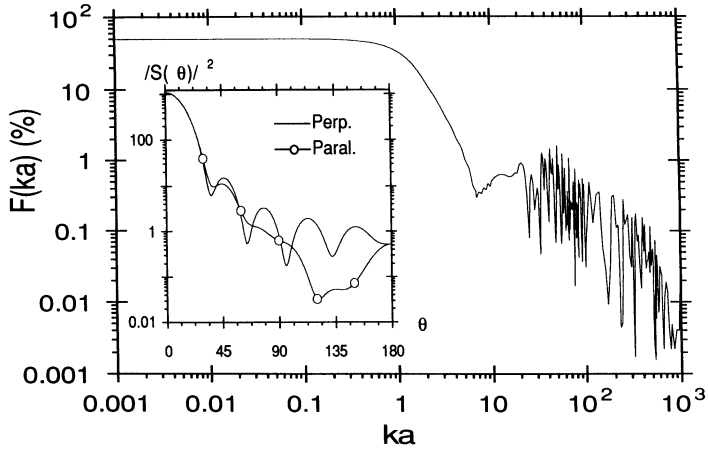

Figure 1. Variation of F (Eq. 2.3) as a function of ka for relative refraction index $m = 1.19$. Rayleigh regime is observed for $ka << 1$, the intermediate one for $ka \sim 1$ and the large sphere regime for $ka >> 1$. Inset: The square of the parallel and perpendicular Mie amplitudes for $ka = 6.5$, $m = 1.19$ and $n^* = 12.6$.

III. MULTIPLE MIE SCATTERINGS

To study the multiple scattering of light by a disordered sample, let us consider a fixed laboratory coordinate system (x,y,z) and random distributed spheres of radius a in a slab parallel to the x-y plane placed between $z = 0$ and $z = L$. Moreover, the far-field approximation is assured by $kl >> 1$, where l is the mean free path. The light source and the receivers are far away from this region and detection is performed in the direction of the incident light either in transmission or in reflection. A partial field trajectory is obtained by considering a plane electromagnetic wave, with electric field $\boldsymbol{E}_o$, propagating along the positive z axis and then scattered by a sphere. A new coordinate system is considered (x_1,y_1,z_1) with origin at the center of this sphere and directions $x_1 = x$, $y_1 = y$ and $z_1 = z$. In the frame (x_1,y_1,z_1), the scattering angles are θ_1, ϕ_1 and at r_1 for the scattered wave vector $\boldsymbol{k}_1$ and in the far field approximation the scattered electric field is given by Eq. (2.1.1). Let us consider a second sphere at this position. Again, at the center of this sphere we consider a new coordinate system (x_2,y_2,z_2) with $x_2 = \theta_1$, $y_2 = \phi_1$ and $z_2 = \boldsymbol{k}_1$. The partial field is scattered along $\boldsymbol{k}_2$ and this procedure is repeated until the partial field meets the n-th and last sphere of this sequence. For the last scattering, we impose the angles θ_n and ϕ_n are such that $\theta_n = x$, $\phi_n = \pm\ y$ and $\boldsymbol{k}_n = \pm z$. In the laboratory frame the multiply scattered partial field by the ν-th sequence is given by:

$$\boldsymbol{E}_\nu = \frac{jexp(j\rho_n)}{\rho_n}\boldsymbol{J}(\theta_n,\phi_n)\ldots\frac{jexp(j\rho_2)}{\rho_2}\boldsymbol{J}(\theta_2,\phi_2)\frac{jexp(j\rho_1)}{\rho_1}\boldsymbol{J}(\theta_1,\phi_1)\boldsymbol{E}_o \ . \qquad (3.1)$$

By the choice of the angles of the last scattering, we impose that the photon emerges from the medium along the z direction, with a wave vector either parallel or anti-parallel (transmission or reflection) to the incident one.

The transmitted and reflected electric field of the sample μ is given by the summation $E^{(\mu)} = \Sigma_{\nu=1}^{M} E_\nu/\sqrt{M}$. For a large number of independent sequences ν, by virtue of the central limit theorem, the real and imaginary parts of the superposed photon field $E^{(\mu)}_x = |E^{(\mu)}_x| exp(j\phi^{(\mu)}_x)$ and $E^{(\mu)}_y = |E^{(\mu)}_y| exp(j\phi^{(\mu)}_y)$ are Gaussian variables.[12] Thus, in polar representation, the modules $|E^{(\mu)}_x|$ and $|E^{(\mu)}_y|$ are distributed following the Rayleigh probability density[12] and the phases $\phi^{(\mu)}_x$ and $\phi^{(\mu)}_y$ are uniformly distributed in the interval $[0,2\pi]$.[12] The phase difference $\phi^{(\mu)} = \phi^{(\mu)}_x - \phi^{(\mu)}_y$ is also uniformly distributed in the physical interval $[-\pi,\pi]$.

Consider now an ensemble of samples μ,. The ensemble averaged Stokes intensities are related to $\langle |E^{(\mu)}_x|^2 \rangle_e$, $\langle |E^{(\mu)}_y|^2 \rangle_e$ and $\langle E^{(\mu)}_x E^{(\mu)}_y{}^* \rangle_e$ where $\langle ... \rangle_e = \Sigma_{\mu=1}^{N} .../N$, with $N >> 1$. A standard approximation is to consider that the phases are random in the product $E^{(\mu)}_l E^{(\mu)}_m{}^*$, (with $l,m = x,y$), since they come from independent paths. The mean intensity is the summation of the intensities of the M sequences of the sample μ and summation over N samples divided by NM. This is equivalent to consider the intensities of one sequence per sample, but NM samples. This equivalence simplifies the calculation because each scattered partial field can be considered as a photon field. This is possible for the calculation of the first moment of the physical quantities, but not for the higher moments which must obey Gaussian statistics. This point will be detailed in section V.

The ensemble average makes the system invariant by the symmetries of the sample. For a slab and perpendicular incidence and detection, these symmetries are: *i)* rotation around the incident wave vector and *ii)* reflection by a plane containing this vector. The averaged Stokes intensities are: $I = \langle i \rangle_e = a_1 i_o$, $Q = \langle q \rangle_e = a_2 q_o$, $U = \langle u \rangle_e = a_3 u_o$ and $V = \langle v \rangle_e = a_4 v_o$, where $a_3 = \pm a_2$, the sign plus for transmission and minus for reflection.[6]

The degree of polarization is defined as:

$$P = \sqrt{\frac{Q^2 + U^2 + V^2}{I^2}} = \sqrt{(\frac{a_2}{a_1})^2 + \frac{a_4^2 - a_2^2}{a_1^2}(\frac{v_o}{i_o})^2} \quad , \tag{3.2}$$

where we have used the Stokes sum rule for the incident polarized light. For incident linear ($v_o = 0$) and circular ($v_o = \pm i_o$) polarized light, P is given, respectively, by $|a_2|/a_1$ and $|a_4|/a_1$, hence only two parameters are necessary to characterize completely the scattering medium.

A Hermitian matrix can be constructed from the Stokes intensities. This is called the coherence matrix:[12]

$$\boldsymbol{C} = \frac{1}{2}\begin{bmatrix} I + Q & U + jV \\ U - jV & I - Q \end{bmatrix} , \tag{3.3}$$

The eigenvectors are orthogonal and the eigenvalues are real. In the eigenvector basis, the eigenvalues are independent intensities, and the phase difference of the electric fields is also independent and uniformly distributed, by virtue of the central limit theorem. The basis which diagonalizes $\boldsymbol{C}$ is the basis that preserves the symmetry of the wave polarization and slab. For linearly polarized light, this basis is the lab. frame (x,y,z), since $U = V = 0$, following the central limit theorem. The amplitudes $|E_x|$ and $|E_y|$ are obtained from the Rayleigh distribution:[12]

$$P_R(|E_x|) = 2\frac{|E_x|}{I_x} exp(\frac{-i_x}{I_x}) \quad , \tag{3.4}$$

where $I_x = (I + Q)/2$ and $i_x = |E_x|^2$. The joined probability density is the product of the distributions of the independent variables:

$$P_J(|E_x|,|E_y|,\phi) = \frac{P_R(|E_x|)P_R(|E_y|)}{2\pi} \quad . \tag{3.5}$$

For linearly polarized incident light, we notice that $U = V = 0$ and the polarization degree is merely $P = |Q|/I$. The distribution for i and q as variables is:

$$P_J(i,q,\phi) = \frac{1}{\pi I^2(1 - P^2)} exp[\frac{-2(i - qP)}{(I(1 - P^2))}] \quad . \tag{3.6}$$

This distribution is parametrized by the mean total intensity and by the polarization degree, and it is completely equivalent to the distribution obtained recently in reference 13. In terms of the variables $u = cos\phi\sqrt{i^2 - q^2}$ and $v = sin\phi\sqrt{i^2 - q^2}$, one has a new distribution, which leads to the expected mean values $\langle i\rangle_e = I$, $\langle q\rangle_e = IP$, $\langle u\rangle_e = \langle v\rangle_e = 0$, and to the variances $\sigma_i^2 = \sigma_q^2 = I^2(1 + P^2)/2$ and $\sigma_u^2 = \sigma_v^2 = I^2(1 - P^2)/2$, where $\sigma_x^2 = \langle x\rangle_e^2 - \langle x^2\rangle_e$. The variances of the Stokes intensities are not all independent and for any incident polarization, they must satisfy the relation:

$$\sigma_q^2 + \sigma_u^2 + \sigma_v^2 = \sigma_i^2 + I^2(1 - P^2) \quad , \tag{3.7}$$

which comes from the Stokes sum rule.

Still considering linearly polarized incident light, the distribution can be transformed to the Poincaré variables i, 2χ *and* 2ψ and it reads:

$$P_J(i,2\chi,2\psi) = \frac{icos(2\chi)exp[-2i[1 - Pcos(2\chi)cos(2\psi)]/(I(1 - P^2))]}{\pi I^2(1 - P^2)} \quad . \tag{3.8}$$

Using the reduced intensities q/i, u/i and v/i, the polarization states are projected onto a spherical surface of the Poincaré representation, and one obtains the distribution of the Poincaré angles by integrating over the intensity i. The probability to have a polarization state in the interval $[2\chi, 2\chi + d(2\chi)]$ and $[2\psi, 2\psi + d(2\psi)]$ is given by:

$$P_L(2\chi,2\psi)d(2\chi)d(2\psi) = \frac{1 - P^2}{4\pi[1 - Pcos(2\chi)cos(2\psi)]^2} cos(2\chi)d(2\chi)d(2\psi) \quad , \tag{3.9}$$

where $cos(2\chi)d(2\chi)d(2\psi)$ is the surface element of the Poincaré sphere. For totally depolarized emerging light from the slab $(P = 0)$ the polarization states are uniformly distributed on the sphere. Within this representation, one can geometrically see that a quasi-circular state (located around the pole) is less probable to occur than a quasi-linear one (located around the equator). This distribution leads to the first moments and to the second moments:

$$\langle\frac{q}{i}\rangle_e = \frac{1}{P}[1 - \frac{1 - P^2}{2P} ln(\frac{1 + P}{1 - P})] \quad \text{and} \quad \langle\frac{u}{i}\rangle_e = \langle\frac{v}{i}\rangle_e = 0 \quad , \tag{3.10}$$

$$\langle(\frac{q}{i})^2\rangle_e = \frac{2}{P^2}[1 - \frac{1-P^2}{2P} ln(\frac{1+P}{1-P})] - 1 \text{ and } \langle(\frac{u}{i})^2\rangle_e = \langle(\frac{v}{i})^2\rangle_e = \frac{1-P^2}{P^2}[\frac{1}{2P} ln(\frac{1+P}{1-P}) - 1]. \tag{3.11}$$

Let us consider circular incident polarization. The basis which diagonalizes the coherence matrix is $(x + jy)/\sqrt{2}$, $(x - jy)/\sqrt{2}$. Spanning the Stokes intensities in this basis, one sees that v plays exactly the same role as q for incident linear polarization in the lab. frame. The distribution of the Stokes intensities is then given by replacing q by v in Eq. (3.3). The distribution of the Poincaré angles is then given by:

$$P_C(2\chi,2\psi)d(2\chi)d(2\psi) = \frac{1 - P^2}{4\pi[1 - P\sin(2\chi)]^2}\cos(2\chi)d(2\chi)d(2\psi) \ , \qquad (3.12)$$

while the angle 2ψ is uniformly distributed (rotation symmetry around the v/i-axis).

For $P = 0$, Eq. (3.7) yields the same function as the distribution for linearly polarized incident light, but the approach to this regime is drastically different. The distribution of polarization states on the Poincaré sphere preserves the symmetry of the incident polarization state. For linearly polarized light the intensity is invariant by a reflection on a plane containing the electric field and by reflection on a plane parallel to it. Circular incident polarization is invariant by a rotation around the propagation direction. The first and second moments are obtained by interchanging the intensities q and v in Eqs. (3.10) and (3.11), respectively .

The statistics of the depolarization of light is completely determined by the knowledge of $P_L(2\chi,2\psi)$ and $P_C(2\chi,2\psi)$, but these distributions are parametrized by the polarization degree P which is known only for Rayleigh scatterers but not in general. Moreover, the polarization degree depends on the thickness of the slab.

For non-Rayleigh scatterers, the polarization degree was studied numerically by the radiative transfer theory.[14] Although this approach takes into account the phase difference between the electric field components, it does not furnish the absolute phase for a given scattering sequence. Moreover, the intermediate regime $L \sim l^*$ is poorly described by this theory. The numerical simulation based on the Monte Carlo algorithm is more flexible.

IV. MONTE CARLO SIMULATION

To simulate sequences of Mie scatterings in a slab of length L, we have used a Monte Carlo method. The spherical Bessel functions, needed to calculate the Mie coefficients, have been obtained using the Lentz algorithm,[15] and the coefficients were obtained as described in reference 16. The Newmann functions and the Legendre polynomials are obtained from adapted algorithms found in reference 17.

The distance that a photon travels without suffering a collision is given by the distribution $\exp(-r/l)/l$. The distance $l = 1/(\phi_c\sigma_s)$ is the mean free path, where ϕ_c is the concentration of spheres and σ_s is the scattering cross section. We are interested on the dependence of physical quantities as a function of the reduced slab length L/l^*. In practice, this is generally performed by fixing L and varying ϕ_c. In our simulation, we consider l fixed, such that $kl = 1000$, corresponding to weak concentration, justifying the far field approximation, and we vary L. Therefore, the electric fields of each Mie scattering are calculated within the far-field approximation.

In the slab, the photon history starts at the origin of the laboratory frame (x,y,z). It propagates along the z axis until $z' > 0$. This distance is generated following the exponential distribution. If $z' > L$, the photon leaves the slab without suffering a collision and the electric field is calculated on the plane $z = L$. On the other hand, if $0 < z' < L$, a sphere of radius a is present and the electric field is calculated at this position. A new coordinate system (x_1,y_1,z_1) is considered, just as described in section II. The scattering

angles θ_1 and ϕ_1 are generated by the Mie distribution and a new distance r_1 by the Poisson distribution. This new position (θ_1,ϕ_1,r_1) is then calculated in the lab. frame. If its z-component is greater than L the photon is transmitted, if it is negative, the photon is reflected. In both cases the field is calculated on the boundary of the slab. We notice that after every scattering the field is normalized. If the photon does not escape the slab, new angles are chosen following the Mie distribution and a new distance is generated. This process is repeated successively till the moment a sphere lies outside the slab. The last scattering is not random, the photon is forced to escape perpendicularly to the plane of the slab. A weight is then assigned to each sequence. This weight is the probability for a photon to be scattered in the direction θ' and ϕ' that are the calculated angles for the photon to leave the slab perpendicularly. In transmission, the multiply scattered electric field is calculated in the lab. frame (x,y,z) but in reflection, it is calculated in the frame $(x,y,z)_r$. This frame is obtained by an improper rotation of the lab. frame ($x \rightarrow x$, $y \rightarrow -y$, $z \rightarrow -z$).

An important step of the method resides in the choice of the scattering angles θ and ϕ. We emphasize that the complete Mie distribution is not separable (Eq. (2.2)). Even worse, it is parametrized by the incident field. Generating this distribution numerically, by the rejection method, is very time consuming. For large spheres, the distribution takes a simpler form. It is independent of both ϕ and of the incident field. Therefore, the angle ϕ can be chosen following a uniform distribution and the angle θ is given by the approximate large sphere Mie distribution $[|S_{//}(\theta)|^2 + |S_{\perp}(\theta)|^2]/(2\sigma_s)$. This simplification has already been used in previous simulations.[18-20] In this case, the angle θ can be generated by the cumulative function (the integral of the large sphere Mie distribution). This method is very efficient, since a single random number is needed for each θ. The values of the cumulative function can be tabulated as well as the values of the scattering amplitudes. The tables are divided in intervals of $1°$ in θ and data are obtained from these tables by linear interpolation.

We emphasize here that the numerical study of the distribution of polarization states on the Poincaré sphere is done by considering the summation over the partial fields and then the intensity is calculated for each sample. On the other hand, the polarization degree is obtained considering one sequence per sample since only the mean values of the Stokes intensities are necessary. The polarization degree for incident linearly polarized light is scaled by L/ℓ^* as shown in reference 20.

V. POLARIZATION MEMORY: RESULTS AND DISCUSSION

1. Transmission

The polarization degrees for incident linear and circular polarization were obtained by our numerical simulation for the following values $ka = 6.5$, $m = 1.19$ and $k\ell = 1000$ leading to $l/\ell^* = 12.6$ and $\sigma_s/\pi a^2 = 2.41$. The experimental counterpart[10] corresponds to $\lambda_{vac} = 514.5\ nm$ propagating in water $(n_m = 1.33)$ and polystyrene $(n_s = 1.58)$ spheres of mean radius $400\ nm$ in a slab of $L = 1\ mm$ leading to $ka = 6.5$, $m = 1.19$ and the concentration in volume is varied to alter the ratio L/ℓ^*. The results of the simulation and experiment are plotted in Fig. 2.

For very thin slabs $(L/\ell^* << 1)$, $P(L/\ell^*)$ is close to one. This means that the photons cross the slab with trajectories which are very close to a straight line, since each single scattering is strongly peaked forwards (Fig. 1 inset). This does not alter significantly the

incident polarization state. For $L \sim 2\ell^*$, the transmission coefficient is close to *50%*. This value happens because a photon needs, in average, a distance ℓ^* to turn its direction of $\pi/2$, (ℓ^* is a gyration radius) and then they can either be transmitted or reflected with equal probability. $L \cong 3\ell^*$ is a limiting value for the dominant effects of the boundaries. This value can be understood in the following way: by subtracting ℓ^* from each boundary, the trajectories still have at least one gyration radius for an "isotropization" of $\boldsymbol{k}$. When $L > 3\ell^*$ the degree of polarization decreases exponentially with L/ℓ^*. A characteristic depolarization length can then be assigned to the incident circular and linear state from the fitted curves (ae^{bL/ℓ^*}):

$$P_L(L/\ell^*) \sim e^{-0.716L/\ell^*} \quad \text{and} \quad P_C(L/\ell^*) \sim e^{-0.358L/\ell^*} . \tag{5.1}$$

These characteristic lengths are:

$$\ell^{**}_{linear} = 1.39\ell^* \quad \text{and} \quad \ell^{**}_{circular} = 2.79\ell^* , \tag{5.2}$$

so that $\ell^{**}_{circular}/\ell^{**}_{linear} = 2.00$.

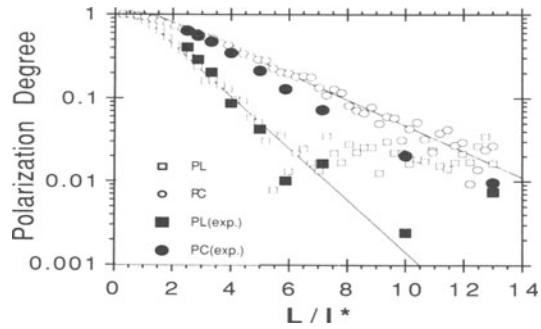

Figure 2. Degree of polarization in transmission for linearly and circularly incident polarized light polarization as a function of L/ℓ^*, for at least *10000* outcoming photons, with the parameters $ka = 6.50$ $kl = 1000$ and $m = 1.19$. The simulation data are fitted, for $L/\ell^* > 2.5$ by $P(L/\ell^*) = ae^{bL/\ell^*}$ with $a = 1.84$ and $b = -0.716$ for incident linear polarization and $a = 1.68$, and $b = -0.358$ for incident circular polarization. The experimental data are found in reference 10.

To emphasize the strong difference between the Rayleigh and the Mie regime, we have plotted the variable $\delta = P_L - P_C$ as a function of L/ℓ^*. The Rayleigh expression of δ is obtained from the simple expression of the basic parameters a'_2 and a'_4 as a function of the number of scatterings n for large n,[5,21] convoluted with the standard distribution $P(s/L)$ of the diffusion theory:

$$P_L(L/\ell) \sim e^{-1.07L/\ell} \quad \text{and} \quad P_C(L/\ell) \sim e^{-2.08L/\ell} . \tag{5.3}$$

The most striking difference is the change of sign for δ showing the non universal behavior of the multiple scattering regime (Fig. 3). These results are reported in Table 1 where the characteristic lengths for the different regimes are collected.

The change of the sense of the inequality between P_L and P_C can be understood in a simple way:[8] in the Rayleigh regime, isotropy of the scattering weights equivalently the forward- and backscattering. For incident linear polarization both scattering modes preserve the linear polarization and maintain the polarization degree at a high value. The situation is reversed for circular polarization since the backscatterings flip the helicity of the incident polarization, hence $P_L > P_C$. For Mie or large spheres, the scattering is strongly peaked forwards and the randomization of the azimuthal angle ϕ affects considerably the linear polarization while the circular one is almost preserved, hence $P_L < P_C$.

Table 1. Differences of the characteristic lengths for scalar and vectorial fields and for Rayleigh and Mie regimes.

Characteristic Length	Scalar Fields	Vectorial Fields	
		Linear	Circular
Rayleigh	l	$0.935l$	$0.481l$
Mie	l^*	$1.39l^*$	$2.79l^*$

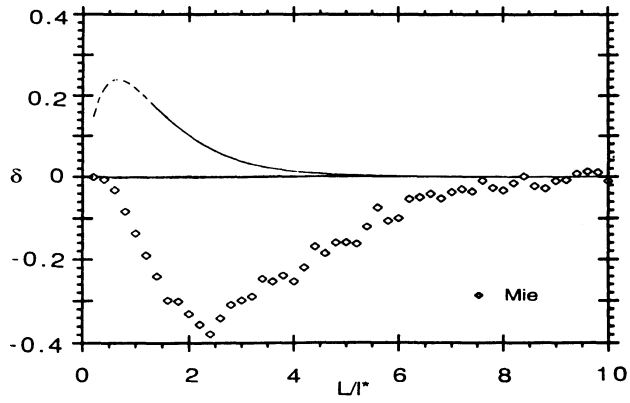

Figure 3. $\delta = P_L - P_C$ as a function of L/l^* for the Rayleigh and Mie regimes. Contrary to the point-like scatterers δ is negative for large spheres.

2. Reflection

For the same values of the parameters *ka*, *kl* and *m*, the polarization degree is obtained in the reflection geometry and represented in Fig. 4. The main result is the non-vanishing asymptotic value of P_C for large L/l^* (up to *50*), exhibiting a strong persistent degree of polarization for very thick slabs. This result was previously reported[8] for indirect measurements of the depolarization by dynamical correlation function or by numerical solution[14] of the radiative transfer equation. Indeed, it originates from the dominant weight of the short loops for the reflection geometry (in the diffusion theory $P(s) \sim s^{-3/2}$, see, for example, reference 22). We stress that, like in references 8 and 14, we have not taken into account the contribution of the reversed sequences, which gives rise to the back-scattering cone.

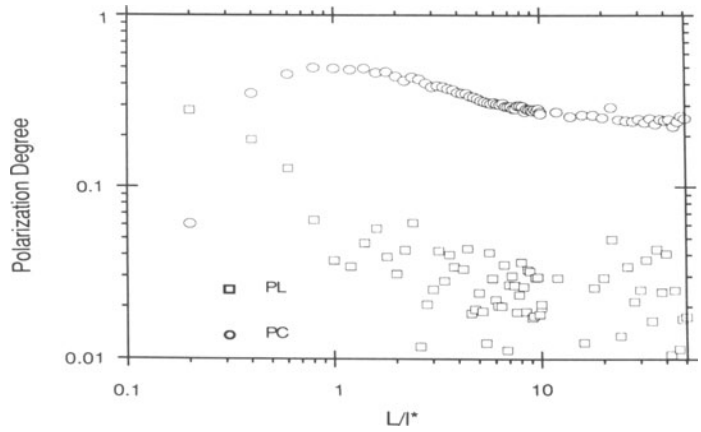

Figure 4. Polarization degree as a function of L/l^* in reflection. The parameters are the same as in Fig. 2. For incident circular polarization, the degree of polarization converges asymptotically to a value around *0.25*. The polarization memory of circular polarized light is then observed in the Mie regime.

For thinner slabs $L \sim l^*$, P_C has a maximum. This situation corresponds to slabs where the first loops of gyration l^* can be put within the thickness. The degree of circular polarization remains high, since the helicity is almost preserved along these loops. When $L < l^*$, these loops are inhibited and only the very rare (but efficient) backscattering collisions subsist. Concerning the linear polarization, the degree is always very weak by efficient ϕ-randomization, previously mentioned.

It may be concluded that the diffusion theory is not the appropriate context for the analysis of these results: both the boundary effect and the anisotropy of the scattering ($l^* = 12.6l$) provide features which must be handled by other considerations.

3. Poincaré Sphere

A description of depolarization processes is given by the complete distribution of the polarization states. A useful geometrical picture of the two depolarization modes, one associated with the randomization of the direction of the electric field and the other associated with the randomization of the helicity of the wave, is given by the Poincaré representation. The polarization state of each outcoming recomposed field is projected onto the Poincaré sphere of unit radius with axes q/i, u/i and v/i. The Poincaré clouds are shown in the plane-sphere representation of Fig. 5 for several slab lengths in transmission.

For very thin slabs, the polarization states on the Poincaré sphere are concentrated close to the incident state, respectively, on the equator for linear polarization and on one of the poles for circular state. As the slab thickens, the polarization states for the linear incident mode migrate towards east and west and to the north and south indicating that the depolarization is caused by the randomization of direction of the electric field and helicity. This can be seen more quantitatively by the variation of the first and second moments of the reduced Stokes intensities as a function of P (Eqs. 3.10 and 3.11). For $L/\ell^* \sim 3$, this distribution converges to the diffusion law, where the states are uniformly distributed on the sphere. For the incident circular polarization state, the distribution is independent of the angle 2ψ. This rotation symmetry around the axis v/i reflects the fact that each Mie scattering is independent of the azimuthal angle ϕ. This distribution migrates towards the equator as L increases. For $L/\ell^* \sim 3$, one hemisphere is almost filled. This distribution starts populating the opposite hemisphere for larger values of L. For $L/\ell^* > 6$, the distribution is practically uniform on the sphere.

An advantage of the Poincaré representation is the possibility to exhibit clearly the important difference between the processes of depolarization through Rayleigh and Mie regimes. Now we consider the intensities of each scattering sequence (not the recomposed field). For Rayleigh scatterings, the linear polarization is completely destroyed in a few scatterings by transitions on the equatorial circle. Also, the incident circular polarization is flipped to the opposite helicity in few scatterings. A good approximation is to consider the equator line (ϕ- or 2ψ-depolarization) and the v/i-axis (helicity or 2χ-depolarization), both as one manifold on the Poincaré sphere. Hence, the mechanism proposed recently[8] describes correctly the Rayleigh regime. Quite different is the polarization process for the Mie or large sphere scatterings. Here, it is seen as the spreading-out of the polarization state cloud around the incident state. The implied phase space is actually of two-dimensional nature on the Poincaré sphere and the elliptical polarization is largely dominant. A theorical approach founded on renormalization methods is in progress.

The enhanced factor *2* for the incident circular polarization can be explained tentatively by exploring the rotation symmetry around the v/i axis on the Poincaré sphere for circular incident polarization. Linear polarization can be written as a sum of right- and left-handed circular polarization with equal amplitudes. The right and left-handed circular polarizations are represented on the Poincaré sphere as the south and north pole, respectively. As the slab becomes thicker, the two circular distributions migrate towards the equator, so the diffusion distribution will be reached about twice as fast as for a single circular state. The reasoning that two linear states dephased of $\pi/2$ form a circular state cannot be applied, because the rotation of the sphere around q/i or u/i is not symmetric and a composition rule is not easily found. For Rayleigh particles, this argurment cannot be applied since there is no continous filling of the elliptical states.

Linear

Circular

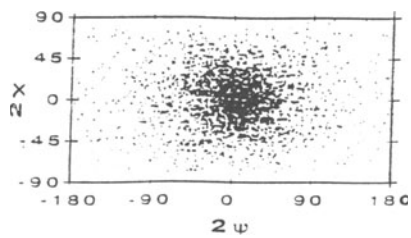

a) $P = 0.753$

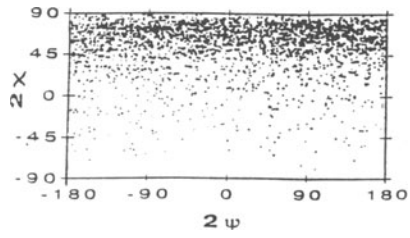

d) $P = 0.881$

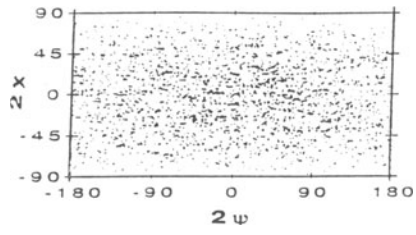

b) $P = 0.113$

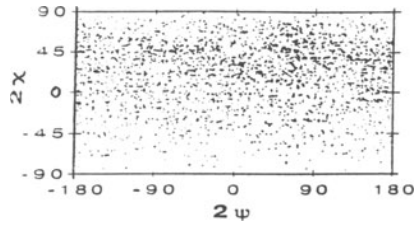

e) $P = 0.418$

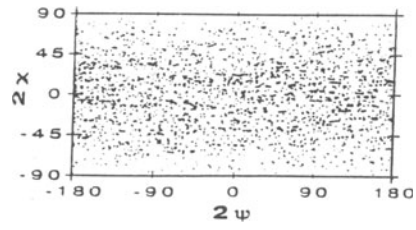

c) $P = 0.0480$

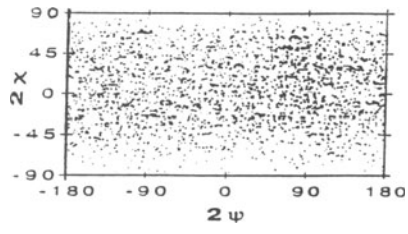

f) $P = 0.110$

Figure 5. Plane-sphere of the Poincaré representation for different thickness of slabs. These figures have been generated by the recomposition of about *625* partial fields and at least *625* transmitted polarization states have been plotted. The parameters are the same as in Fig. *2*. Linear and circular incident polarization states correspond to the left and right columns. Slab thicknesses of $L = 1,3$ and 6^* correspond to the first, second, and third rows, respectively.

VII. CONCLUSION

The numerical approach of the complex problem of the polarization correlation is based on the exact Mie scattering amplitudes and on a Monte Carlo algorithm for generating independent sequences of multiple scattering. In the intermediate regime of non-zero polarization degree, the Mie, or large spheres, multiple scattering is quite different from the point-like or Rayleigh scattering. Two important results have been obtained with this numerical simulation in the Mie regime:

i) The rate of depolarization is different for circular and linear incident polarization. In the large-sphere regime they differ from the Rayleigh regime, since the helicity of circular polarization needs more scatterings to be randomized. Contrary to what was claimed in reference 21, the difference between the circular and linear polarization degree (the parameter δ) is not strictly positive.

ii) The depolarization process is given by a continuous and progressive covering of the Poincaré sphere as a function of the polarization degree, which is a function of the slab length. Contrary to reference 13, elliptical states are the most probable ones and they are important in the depolarization process, especially for incident circular polarization. The helicity flip model[8] is oversimplified.

The present study pushes towards a separate class of "universality" for Mie and Rayleigh scatterings.

ACKNOWLEDGMENTS

We would like to thank F. Erbacher, R. Lenke and G. Maret for results prior to publication and for fruitful discussions as well as S. Alexander, and A. Dauchy for general assistance. One of us (A.S.M.) also wishes to thank C.A.P.E.S. for financial support.

REFERENCES

1. See, for instance: M.P. van Albada, M.B. van der Mark and A. Lagendijk, "Experiments on weak localization of light and their interpretation," *in: Scattering and Localization of Classical Waves in Random Media*, P. Sheng editor, World Scientific Publishing, Singapore (1990).
2. P.S. Theocaris and E.E. Gdoutos, *Matrix Theory of Photoelasticity*, SpringerVerlag, Berlin (1979).
3. E. Akkermans, P.E. Wolf and R. Maynard, Phys. Rev. Lett. **56**, 1471 (1986).
4. M.J. Stephen and G. Cwilich, Phys. Rev. **B34**, 7564 (1986).
5. E. Akkermans, P.E. Wolf, R. Maynard and G. Maret, J. Phys. (Paris) **49**, 77 (1988).
6. H.C. van de Hulst. *Light Scattering by Small Particles*, Dover Publications, New York (1981).
7. P.E. Wolf, G. Maret, E. Akkermans and R. Maynard, J. Phys. (Paris) **49**, 63 (1988).
8. F.C. MacKintosh, J.X. Zhu, D.J. Pine and D.A. Weitz, Phys. Rev. **B40**, 9342 (1989).
9. P.E. Wolf and G. Maret, "Dynamics of Brownian particles from strontly multiple light scattering," *in: Scattering in Volumes and Surfaces*, M. Nieto-Vesperino and J.C. Dainty editors, Elsevier Science Publishers B.V. (1990).

10. F.A. Erbacher, Ph.D. thesis, Constance University (1992).
11. A. Ishimaru, *Wave Propagation and Scattering in Random Media*, Academic Press, New York (1978).
12. J. Goodman, *Statistical Optics*, John Wiley & Sons, Inc., (1985).
13. S.M. Cohen, D. Eliyahu, I. Freund and M. Kaveh, Phys. Rev. **A43**, 5748 (1991).
14. R.L. Cheung and Ishimaru, Appl. Opt. **21**, 3792 (1982).
15. W.J. Lentz, Appl. Opt. **15**, 668 (1976).
16. G. Grehan and G. Gouesbet, Appl. Opt. **18**, 3489 (1979).
17. W.H. Press, B.P. Flannery, S.A. Teukolsky and W.T. Vetterling, *Numerical Recipes, The Art of Science Computing*, Cambridge University Press (1989).
18. E.A. Bucher, Appl. Opt. **12**, 2391 (1973).
19. K.E. Kunkel and J.A. Weinman, J. Atmos. Sci. **33**, 1772 (1976).
20. P. Bruscaglioni and G. Zaccanti, "Depolarization of radiation due to multiple scattering," *in: Topical Meeting on Atmospheric, Volume and Surface Scattering and Propagation*, Florence (1991).
21. I. Freund, Opt. Commun. **81**, 251 (1991).
22. D. Bicout, E. Akkermans and R. Maynard, J. Phys. (Paris) **I1**, 471 (1991).

DYNAMIC CORRELATIONS OF MULTIPLY SCATTERED LIGHT FROM STRONGLY INTERACTING SUSPENSIONS

J.X. Zhu,[1] D.A. Weitz[2] and R. Klein[3]

[1]Dept. of Chemical Engineering, Princeton University, Princeton, NJ USA
[2]Exxon Research and Engineering Co., Rt. 22E, Annandale, NJ 08801 USA
[3]Fakultät für Physik, Universität Konstanz, Konstanz, Germany

INTRODUCTION

The scattering of a coherent light source, such as a laser, from any random medium invariably results in a far field scattering pattern consisting of light and dark regions, called a speckle pattern. If the scattering medium changes in time, as for example will happen if the scattering particles move, then the speckle pattern also changes in time, reflecting this motion. The analysis of the intensity fluctuations of a single speckle spot can provide information about the dynamics of the scattering medium, and this form of light scattering is called dynamic light scattering (DLS), or quasielastic light scattering[1]. The traditional DLS experiment entails the measurement of the temporal autocorrelation function of the intensity fluctuations of a speckle spot, and for singly scattered light, the time constant of the decay of this correlation function can be related to the dynamics of the scattering system through knowledge of the scattering wave vector, q. This is a well developed form of light scattering spectroscopy, and traditional DLS has found many applications in the study of the dynamics of a wide variety of systems.

If the light is multiply scattered, the far-field scattering pattern is still comprised of speckle spots, and these still fluctuate in time again reflecting the dynamics of the scattering medium. The temporal correlation function of the intensity fluctuations can be measured in the same fashion as is done for traditional DLS. However, the interpretation of this correlation function is more difficult, and, until recently, has limited the applicability of DLS to singly scattered light.

In the limit of very strongly multiply scattered light, the interpretation of the measured temporal correlation functions of the scattered intensity again becomes relatively straightforward. This form of dynamic light scattering is called diffusing-wave spectroscopy (DWS).[2-5] It is based on the approximation that the propagation of light in very strongly scattering media can be described as a diffusion process.[6] The development of DWS has, in large measure, been stimulated by the progress made in our understanding of the propagation of classical waves, such as light, through strongly scattering random media. The observation of an enhancement of the light backscattered from strongly scattering media, and the identification of this enhancement as a manifestation of the weak localization of light,[7, 8] provided much of the initial stimulus for this research. In part, a focus of much of the subsequent work has been the search for strong localization of light. This has proven to be very elusive. The fundamental reason for this difficulty is that, while

Photonic Band Gaps and Localization, Edited by
C.M. Soukoulis, Plenum Press, New York, 1993

light can be scattered very strongly in many media, the scattering is still not sufficiently strong to result in the localization of light. Physically this is reflected in the very weak contribution made by any effects of interference of the light within the medium itself.[9, 10] Instead, the dominant contribution of interference effects arises from the interference of the light after it has exited the medium. The propagation of the light within the medium is instead very well described by the diffusion approximation, which completely ignores any interference effects. Thus, one of the most important conclusions of much of this work is that the diffusion approximation for the propagation of light in strongly scattering media is quite adequate in almost all cases. Diffusing-wave spectroscopy exploits this approximation, taking advantage of the generality of these results. Instead of addressing the nature of the propagation of light through random media, DWS seeks to obtain new information about the scattering medium itself.

There have been several detailed discussions about the theoretical underpinnings of DWS that have recently been published.[5, 11, 12] Consequently, only a short review of the underlying theory is presented here. Instead, we concentrate our attention on a description of one key limit that DWS must address: media that not only scatter light very strongly, but are themselves strongly interacting. In particular, we are concerned with very strongly interacting colloidal systems. Because DWS exploits the very strong multiple scattering of light to probe the dynamics of the system, it is ideally suited for the study of highly concentrated suspensions. However, a correct interpretation of the DWS data for these suspensions requires knowledge not only about the effects of the multiple scattering of light, but also about the consequences of the high particle concentration, and the concomitant strong particle interactions, on the multiple scattering of the light. The effects of these interactions must be incorporated into the theory of DWS to make it a generally useful technique. The effects of particle interactions on DWS have been developed in a somewhat *ad hoc,* but completely correct way, and have been used to successfully study the dynamics of colloidal suspensions as a function of volume fraction.[4, 13, 14] They have also been treated in a very formal way theoretically,[15] which yielded results in agreement with the simpler approaches. In this paper, our goal is to present a physical derivation of the theory for DWS from very strongly interacting particles. Our results are in agreement with the predictions derived previously on more formal theoretical grounds, and also provide a more detailed account of the underlying physics behind the more *ad hoc* approaches that have been presented in the past. In addition, we present a discussion of the description of the dynamics of the particles when time dependent hydrodynamic interactions become observable. These effects only become important at short times, but it is exactly here that DWS is most suitable.[16, 17] Thus they must also be considered. In this paper, they are considered in a somewhat formal fashion, representing the initial steps required in order to perform more detailed calculations.

The remainder of this paper is structured as follows: In the next section, we present a very brief account of the method for describing the average structure of a suspension of interacting particles, using the static structure factor. We follow this by a description of the dynamics of interacting particles in terms of their dynamic structure factor. Here we outline a possible method for formally calculating the time dependent hydrodynamic interactions that can be probed with DWS. We then discuss the derivation of the theory for DWS, beginning with a discussion of noninteracting particles to illustrate the methods used. This is followed by the generalization to interacting particles. A very brief concluding section finishes the paper.

STRUCTURE OF INTERACTING COLLOIDAL SUSPENSIONS

The colloidal suspensions that are most amenable to study with DWS are comprised of particles that are typically greater than about 0.1 μm in diameter up to several microns in diameter. These particles are large enough to provide sufficient scattering of the light, yet small enough to remain suspended by their Brownian motion. These colloidal particles will be noninteracting if there exist no correlations between either the positions or the velocities of neighboring particles. The particles will always be noninteracting if the volume fraction, ϕ, is sufficiently low that the particles are, on average, much farther apart than the extent of any potential interaction between them. However, as the volume fraction increases, the particles begin to interact with one another.[18] The simplest case to consider

is that of hard spheres, where the particles interact by a very short range repulsion due to volume exclusion: two particles can not occupy the same volume of space. This potential interaction has the shortest possible range, and is completely unavoidable. For hard sphere colloids, volume fractions of $\phi \leq 0.01$ are sufficiently low that particle interactions are generally negligible and the suspension can be viewed as a completely random dispersion of particles.

As the volume fraction increases, the positions of the particles become more correlated. This is because no two particles can occupy the same volume. As a consequence, there is a stronger likelihood of finding two particles separated by a particle diameter. These correlations can be described in real space by the two-particle correlation function. However, here it is more convenient to describe them in momentum space in terms of the particle structure factor, $S(q)$, defined as

$$S(q) = \frac{1}{N}\left\langle \sum_{i,j} e^{-i\mathbf{q}\cdot[\mathbf{r}_i - \mathbf{r}_j]} \right\rangle, \tag{1}$$

where $\mathbf{q}$ is the wave vector, $\mathbf{r}_i$ is the position of the i^{th} particle, and N the number of particles in the system. The brackets represent an ensemble average over all possible configurations of the system.

The correlations between the particles introduce an important new length scale into the description of the system. This new length scale is the correlation length, ξ, over which the particles are correlated. Particles within a correlation volume, ξ^3, are correlated, and the light scattering from them must reflect this fact. Particles separated by a distance greater than ξ are no longer correlated.

The structure factor of the particles reflects the correlations in their positions due to potential interactions between the particles. Hard sphere interactions are always present because volume exclusion is unavoidable. These interactions have the shortest range. There are other types of potential interactions with longer ranges. For example, Coulombic interactions result from the presence of charges on the surface of the particles and counterions in the solvent. If the density of counterions is low, then the range of the Coulombic interactions can be quite large. This will tend to keep the particles separated from one another by distances much greater than their diameters. This will lead to longer range positional correlations, which will be reflected in the particle structure factor.

DYNAMICS OF INTERACTING COLLOIDAL SUSPENSIONS

Diffusing wave spectroscopy is ultimately sensitive to the motion, or dynamics, of the scattering particles, and thus it is essential that we also consider the description of the dynamics of strongly interacting particles. For example, for a suspension of colloidal particles there is always one important type of dynamic correlations. This is due to the hydrodynamic interactions between the particles and arises because of the viscosity of the fluid. When one particle moves due to its Brownian motion, it establishes a flow field in the fluid. This fluid flow will cause the neighboring particles to move as well. Hence, the particle velocities can be correlated. In contrast to the potential interactions reflected by the structure factor, hydrodynamic interactions result solely from the motion of the particles. As such, they are not reflected in the structure factor, which is an ensemble averaged description of the system.[18] However, since DWS probes the dynamics of the colloidal particles, it is sensitive to hydrodynamic interactions, and they must also be considered.

The dynamics of strongly interacting particles can be described in terms of the dynamic structure factor,[18] which is the time dependent form of Eq. (1),

$$S(q,t) = \frac{1}{N}\left\langle \sum_{i,j} e^{-i\mathbf{q}\cdot[\mathbf{r}_i(t)-\mathbf{r}_j(0)]} \right\rangle \tag{2}$$

As $t \to 0$, $S(q,t) \to S(q)$, the static structure factor. Diffusing wave spectroscopy probes the very early time motion of the scattering particles. Thus, in order to interpret the DWS data, we require a short time expansion of the dynamic structure factor. We seek a form that, at least formally, will include all hydrodynamic interactions. To this end, we first express the first derivative of the dynamic structure factor,[19]

$$\frac{\partial S(q,t)}{\partial t} = -\frac{1}{N}\sum_{i,j}\left\langle \int_0^t dt' \mathbf{q}\cdot\mathbf{v}_i(t')\mathbf{v}_j(0)\cdot\mathbf{q} e^{-i\mathbf{q}\cdot[\mathbf{r}_i(t')-\mathbf{r}_j(0)]} \right\rangle \tag{3}$$

Typically, when using the Smoluchowski equation to describe the particle dynamics, the hydrodynamic interactions are approximated as instantaneous,[20] even at "short times." Within this approximation, on short-time scales we define an apparent diffusion coefficient,[18]

$$D_{app}(q) = \frac{D_0}{S(q)} H(q) \tag{4}$$

where

$$H(q) = \frac{1}{D_0 N}\sum_{i,j}\left\langle D_{ij}(R^N) e^{i\mathbf{q}\cdot\mathbf{r}_{ij}} \right\rangle \tag{5}$$

with $\mathbf{r}_{ij} = \mathbf{r}_i - \mathbf{r}_j$, and where $D_{ij}(R^N)$ is the diffusion tensor for a configuration of particles denoted by R^N. The self diffusion case is obtained for $q \to \infty$, so that

$$D_{app}(q \to \infty) = \left\langle D_{ii}(R^N) \right\rangle = D_s^s \tag{6}$$

where D_s^s is usually called the short-time self-diffusion coefficient.

We are interested in the behavior at even shorter time scales, on the order of $\tau_B \le \tau_R$, where $\tau_B = m/\zeta_0$ is the Brownian relaxation time, and τ_R is the structural relaxation time scale, or the time scale on which the configuration of particles changes appreciably.[18] We wish to describe the dynamics at times equal to and shorter than what is usually called "short times" in the description using the Smoluchowski equation. Thus, we are interested in the leading terms when one goes to times shorter than those at which Eqs. (4) and (6) are valid. These deviations from Eqs. (4) and (6) arise from retarded hydrodynamic interactions. Diffusing wave spectroscopy is sufficiently sensitive to probe these effects,[16, 17] and thus we must include them here.

The dynamics of the suspended, interacting particles are governed by coupled Langevin equations,[21]

$$m\frac{d\mathbf{u}_i(t)}{dt} = -\int_{-\infty}^{t} dt' \sum_{j=1}^{N} \underline{\underline{\zeta}}_{ij}(t-t';\mathbf{R}^N)\cdot\mathbf{u}_j(t') + \mathbf{F}_i(t) + \mathbf{F}_i^R(t) \tag{7}$$

Here, $\underline{\underline{\zeta}}_{ij}(t-t';\mathbf{R}^N)$ are time-dependent friction tensors which depend on the configurations, denoted by $\mathbf{R}^N \equiv \{\mathbf{r}_1,\ldots,\mathbf{r}_N\}$. The forces $\mathbf{F}_i(t)$ arise from potential interactions with neighboring particles and $\mathbf{F}_i^R(t)$ denotes the stochastic forces with properties given by

$$\left\langle \mathbf{F}_i^R(t) \right\rangle_F = 0 \tag{8}$$

$$\left\langle \mathbf{F}_i^R(t)\mathbf{F}_j^R(t') \right\rangle_F = k_B T \underline{\underline{\zeta}}_{ij}(t-t';\mathbf{R}^N) \tag{9}$$

It should be noted that the averages in Eqs. (8) and (9) are calculated by freezing the positions of the particles. Moreover, the process being described here by the Langevin equation, Eq. (7), is a non-Markov process, and therefore the random forces described in Eq. (9) are not delta function correlated as is normally the case.[22] Following earlier work by Mazur and Bedeaux,[23] Bonet Avalos *et al*[22] showed that the velocity $\mathbf{u}_i(t)$ of a particles consists of a rapidly fluctuating part, $\mathbf{u}_i^B(t)$, the "Brownian component" of the velocity and a systematic part, $\mathbf{u}_i^S(t)$,

$$\mathbf{u}_i(t) = \mathbf{u}_i^B(t) + \mathbf{u}_i^S(t) \tag{10}$$

where

$$\mathbf{u}_i^S(t) = -\int_{-\infty}^{t} dt' \sum_j \underline{\underline{\mu}}_{ij}(t-t';\mathbf{R}^N)\cdot\mathbf{F}_j^H(t') \tag{11}$$

Here, $\underline{\underline{\mu}}_{ij}$ are the mobility tensors, which are the reciprocals of the friction tensors, and $\mathbf{F}_j^H(t')$ is the fluctuating hydrodynamic drag force[21] exerted by the fluid on particle j. The Brownian component of the velocity, $\mathbf{u}_i^B(t)$, has the stochastic properties,

$$\left\langle \mathbf{u}_i^B(t) \right\rangle_F = 0 \tag{12}$$

$$\left\langle \mathbf{u}_i^B(t)\mathbf{u}_j^B(t') \right\rangle_F = k_B T \underline{\underline{\mu}}_{ij}(t-t';\mathbf{R}^N) = \underline{\underline{D}}_{ij}(t-t';\mathbf{R}^N) \tag{13}$$

Taking the time integral of the last equation, we obtain the usual expression for the time-dependent diffusion tensors

$$\int_0^{\infty} dt \left\langle \mathbf{u}_i^B(t)\mathbf{u}_j^B(0) \right\rangle_F = \underline{\underline{D}}_{ij}(\mathbf{R}^N) \tag{14}$$

Returning to the exact relation in Eq. (3), we now introduce approximations which restrict the results to short times. The first approximation is to replace $\mathbf{r}_i(t) - \mathbf{r}_j(0)$ in the exponent by $\mathbf{r}_i(0) - \mathbf{r}_j(0) \equiv \mathbf{r}_{ij}$. This approximation is reasonable because the particle configuration changes much more slowly than the time scales over which the motion is measured, since $t \ll \tau_R$. The second approximation is to split the total ensemble average into a "fast" velocity average and the usual configurational average,

$$\frac{\partial S(q,t)}{\partial t} \approx -\frac{q^2}{N}\sum_{i,j}\left\langle \hat{\mathbf{q}}\cdot\int_0^t dt' \underline{\underline{D}}_{ij}(t';R^N)\cdot\hat{\mathbf{q}} e^{i\mathbf{q}\cdot\mathbf{r}_{ij}} \right\rangle \tag{15}$$

where Eq. (13) has been used and $\hat{\mathbf{q}} = \mathbf{q}/q$. If the upper limit in the integral were $t = \infty$, we would obtain the usual short-time apparent diffusion coefficient as

$$D_{app}(q) = -\frac{1}{q^2 S(q)} \frac{\partial S(q,t)}{\partial t}$$
$$= \frac{1}{NS(q)} \sum_{i,j} \left\langle \hat{\mathbf{q}} \cdot \underline{\underline{D}}_{ij}(R^N) \cdot \hat{\mathbf{q}} e^{i\mathbf{q}\cdot\mathbf{r}_{ij}} \right\rangle \tag{16}$$

where Eq. (14) has been used. Equation (16) agrees with Eqs. (4) and (5).

Returning to Eq. (15), we can therefore introduce a time-dependent apparent diffusion coefficient,[24]

$$D_{app}(q,t) = D_{app}(q) - \frac{1}{NS(q,t)} \sum_{i,j} \left\langle \hat{\mathbf{k}} \cdot \int_t^\infty d\tau \underline{\underline{D}}_{ij}(\tau; R^N) \cdot \hat{\mathbf{k}} e^{i\mathbf{k}\cdot\mathbf{r}_{ij}} \right\rangle \tag{17}$$

The leading term for $\tau \to \infty$ of $\underline{\underline{D}}_{ij}(\tau; R^N)$ is proportional to $\tau^{-3/2}$. Ignoring the dependence of the diffusion tensors on the configuration, the second term in Eq. (17) is proportional to $\tau^{-1/2}$ and independent of the interactions on the system. This result has already been obtained by Pusey and Tough.[24] Using the more usual expressions by van Saarloos and Mazur,[25] the leading time dependence is still proportional to $\tau^{-1/2}$, but there will be a prefactor, which will be determined by the type of interactions, the particle volume fraction, among other parameters describing the system. This prefactor will also be different for collective and for self-diffusion. This power-law behavior is the well known "long-time" tail in the velocity correlation function, that results from the hydrodynamic interactions between any particle and the surrounding fluid.[26-28] This power-law behavior also persists to higher particle volume fractions.[17] Finally, we note that the fact that $\tau \to \infty$ here refers still to the short time limit for time scales much less than τ_R. It is on these time scales that the power-law behavior will be observed. Formally, the second term in Eq. (17) reflects the first correction due to the time dependent nature of the hydrodynamic interactions.

We can also express the apparent diffusion coefficient in terms of the mean square displacement of the particles, as is often done in interpreting DWS data. This can only be done in the limit that $q \to \infty$ in Eq. (17), when we can interpret the apparent time dependent diffusion coefficient as the time dependent self diffusion coefficient.[18] Then we have for the mean square displacement,

$$\left\langle \Delta r^2(t) \right\rangle = 6 \int_0^t dt' D_{app}(q \to \infty, t') \tag{18}$$

Thus, the first term of Eq. (17) is proportional to the "short-time" self diffusion coefficient, and gives $6D_s^S t$, while the second term will be proportional to $t^{-1/2}$.

We can now expand the dynamic structure factor at short times, similar to the expression in Eq. (4), but now including the time dependent hydrodynamic interactions,

$$S(q,t) = S(q)\left[1 - q^2 D_{app}(q,t)\right] \tag{19}$$

At somewhat longer times, if the transient hydrodynamic interactions are not considered, this takes the more familiar form,[18]

$$S(q,t) = S(q)\left[1 - q^2 D_0 \frac{H(q)}{S(q)} t\right] \tag{20}$$

These results, while formal in nature, form the basis required for further detailed calculations of the time dependent hydrodynamic interactions. These interactions have generally been considered to be instantaneous in most theoretical treatments to date. This has not presented a severe problem, as traditional dynamic light scattering can only resolve motion on relatively longer length scales, at time scales much greater than τ_B. At these time scales, all of the time dependence of these effects has decayed away, and need not be considered. It is only with the advent of DWS, with its power to resolve motion on extremely short length scales, that these effects must be considered.

DIFFUSING WAVE SPECTROSCOPY FROM NONINTERACTING PARTICLES

Before discussing the consequences of particle interactions, we briefly review the theory of DWS from noninteracting systems. This will allow us to outline the procedure followed without the complications of the particle interactions. We will then discuss the modifications that must be made to account for the effects of the particle interactions. In DWS, just as in conventional DLS, we measure the temporal fluctuations of the intensity in a single speckle spot of the scattered light, or a in single spatial coherence area. To parameterize these fluctuations, we determine the normalized temporal autocorrelation function of the scattered intensity,[1]

$$g_2(t) = \frac{\langle I(t)I(0)\rangle}{\langle I(0)I(0)\rangle}, \tag{21}$$

where $I(t)$ is the intensity in the speckle at time t, and the brackets represent an ensemble average, which for an ergodic system, is equivalent to an average over time. Rather than calculating the intensity autocorrelation function directly, it is more convenient to calculate the normalized field autocorrelation function,

$$g_1(t) = \frac{\langle E(t)E^*(0)\rangle}{\langle E(0)E^*(0)\rangle} \tag{22}$$

where $E(t)$ is the scattered field in the speckle spot. The normalized field autocorrelation is related to the normalized intensity correlation function by

$$g_2(t) = \beta g_1^2(t) - 1 \tag{23}$$

where β is a constant dependent on the optics used in the experiment and reflects the number of speckle spots measured at the detector.

For concreteness, we consider a colloidal suspension made up of identical, spherical particles, suspended in a fluid. In the limit of very low concentration the self diffusion coefficient of these particles is given by the Stokes-Einstein relationship,

$$D_0 = \frac{k_B T}{6\pi\eta a}, \tag{24}$$

where k_B is Boltzmann's constant, T is the temperature, η the viscosity of the fluid and a the particle radius. It is also convenient to define a characteristic time scale for diffusion of these particles by $\tau_0 = 1/k_0^2 D_0$, where $k_0 = 2\pi n/\lambda$, with n the index of refraction of the medium and λ the wavelength of the light in vacuum. This is the time it takes for a particle to diffuse by roughly the wavelength of light, and sets a characteristic time scale for diffusion.

To properly analyze the data obtained with DWS requires the calculation of the autocorrelation function of the multiply scattered light.[4, 5] To calculate this, the photons

are divided into separate, diffusive paths. The distribution of these paths, and the probability that a photon will follow a path of length, s, is determined though the use of the diffusion equation for the light. The contribution of each path to the total correlation function is calculated, taking advantage of the long length of the path, and the concomitant large number of scattering events.[29] Then the total correlation function is determined by summing the contributions of all possible paths, weighted by their probabilities. Since the scattering particles in each path are completely uncorrelated, we need consider only the contribution of an individual path, and then add these contributions, assuming that all interference that contributes to the final signal comes only outside the sample, at the detector.

The contribution to the total correlation function of a path consisting of n scattering events is given by its normalized correlation function,

$$g_1^n = \frac{\langle E^n(t)E^n*(0)\rangle}{\langle E^n(0)E^n*(0)\rangle} \tag{25}$$

where the normalized scattered field from an n^{th} order path is given by

$$\frac{E^n(t)}{E^n(o)} = \prod_{j=1}^{n} e^{i\mathbf{q}_j\cdot\mathbf{r}_j(t)} \tag{26}$$

where $\mathbf{q}_j$ is the scattering wave vector of the j^{th} scattering sequence in the path, from the particle at position $\mathbf{r}_j$. This is simply the sum of all the phase factors from each of n scattering sequences. However, since all the scattering particles are uncorrelated with each other, and since the scattering wave vectors are uncorrelated with the particle positions, when calculating the total correlation function for the paths, the only nonzero contributions are those from the particles in the same scattering sequence. Thus the normalized correlation function of the path is

$$g_1^n(t) = \left\langle \prod_{j=1}^{n} e^{-i\mathbf{q}_j\cdot\Delta\mathbf{r}_j(t)} \right\rangle. \tag{27}$$

where $\Delta\mathbf{r}_i(t) = \mathbf{r}_i(t) - \mathbf{r}_i(0)$. The phase factor in the exponent is the sum of all the individual phase factors of each scattering event in the path. The angular brackets reflect the ensemble average, which now also includes an average over different possible paths, all comprised of n scattering events. Since the number of scattering events is large, we approximate each event by an average scattering event, and neglect the conservation of momentum at each step. The scattering events are independent, so we can replace the summation in the phase factor by a product to obtain,

$$g_1^n(t) = \left\langle e^{-i\mathbf{q}\cdot\Delta\mathbf{r}(t)} \right\rangle_q^n \tag{28}$$

where the subscript q refers to an average over all scattering vectors, weighted by the scattering probability or form factor. This term is nothing more than the phase factor for a single scattering sequence, but averaged over q. At short times, we can use a cumulant expansion and bring the ensemble average to the exponent. Furthermore, for each scattering event the scattering vector is independent of the particle's mean square displacement, and each can be averaged independently, giving,

$$g_1^n(t) = e^{-n\langle q^2\rangle_q \langle \Delta r^2(t)/6\rangle} \tag{29}$$

where again the subscript q indicates an average over scattering vectors. Finally, we identify the path length as $s=nl$, where l is the scattering mean free path of the light. Then, we use the relationship,[2]

$$\frac{l}{l^*} = \frac{\langle q^2 \rangle}{2k_0^2} \tag{30}$$

for $\langle q^2 \rangle$, where l^* is the transport mean free path, the distance over which a photon must travel before its direction is randomized. For noninteracting, diffusing particles, $\langle \Delta r^2(t) \rangle = 6D_0 t$ and we can further simplify the expression by introducing the characteristic time scale, $\tau_0 = 1/k_0^2 D_0$, where we obtain

$$g_1^n(t) = e^{-2\left(\frac{t}{\tau_0}\right)\left(\frac{s}{l^*}\right)}. \tag{31}$$

The autocorrelation function does not depend on the scattering length, l, but only on the transport mean free path, l^*. This allows the diffusion equation for the light, which also depends only on l^*, to be used. The expression in Eq. (31) has a simple physical significance: The first part of the exponent, $2t/\tau_0$, reflects the decay of the correlation function due to a single scattering event, but averaged over all scattering vectors, weighted by the form factor of the particle. The additional quantity, s/l^*, reflects the effects of the multiple scattering. In following this diffusive path, the light is scattered through $n^*=s/l^*$ randomizing steps. It is only steps of order l^* that can lead to decay of the correlation function, as a single scattering step, l, is insufficient to change the direction of the light. Thus the decay rate of the total path is increased by a factor of n^*, because the light undergoes this number of randomizing events. Physically, this correlation function reflects the time it takes for the total path length to change by a wavelength. This change results from the cumulative motion of a large number of particles. Thus long paths decay more rapidly since they are scattered from a larger number of particles, and each individual particle must move a shorter distance, and hence take a shorter time, for the cumulative path length to change by a wavelength. By contrast, shorter paths decay more slowly as the light is scattered by fewer particles and each individual particle must move a relatively larger distance, and hence take a larger time, before the total path changes by a wavelength. We note, however, that the correlation function for each path has a linear dependence in the exponential on both the path length, s, and on time, t.

To obtain the full autocorrelation function, we sum over the contributions from all paths,

$$g_1(t) = \int_0^\infty P(s) e^{-2\left(\frac{t}{\tau_0}\right)\left(\frac{s}{l^*}\right)} ds \tag{32}$$

where $P(s)$ is the probability that the light travels a path of length s. With this expression, we implicitly assume that each path is uncorrelated with other paths and thus simply add the contributions of the different paths. The quantity $P(s)$ depends explicitly on the geometry of the experiment, but can be determined by the use of the diffusion equation for light. The method of its determination can be physically understood by considering what happens to a very narrow pulse of light incident on one side of the scattering medium. This light must travel roughly l^* into the medium before it has scattered a sufficient number of times that its transport becomes diffusive. The pulse exiting the other side will reflect the

distribution of paths followed by the diffusing photons. Some of the photons will follow very short paths and will exit the sample after a short time. Many more of the photons will follow longer paths and will be delayed before they exit. Some photons will follow very long paths and will exit much later. Thus, the pulse that exits the other side of the sample will exhibit a considerable amount of dispersion. Since the speed of light in the medium is known, the dispersion in time of the transmitted pulse directly reflects the distribution of paths the light takes in passing through the medium, allowing $P(s)$ to be determined.

The diffusion equation can be used to actually calculate the path distribution, $P(s)$. The diffusion equation is solved for the geometry of the experiment. Since it is a partial differential equation, the boundary and initial conditions must be specified. The simplest boundary conditions to choose are absorbing boundaries, so that any diffusing photon ceases to diffuse when it leaves the sample and can not re-enter the sample. While this choice is adequate, and provides the simplest results, more suitable boundary conditions are to assume that there is no flux of diffusing photons into the sample at the boundaries.[30, 31] This assumption leads to more complex boundary conditions as well as more complex expressions for the autocorrelation function, but these provide a better description of the data. As initial conditions, we choose a delta function in time, a distance l^* into the sample, on the side that the laser is incident. We then solve the diffusion equation to obtain the flux of diffusing photons emitted from the sample at the detector, and use the transformation, $s=ct$ to obtain $P(s)$. In fact the solution for the autocorrelation function is actually somewhat simplified by recognizing that Eq (32) is the Laplace transform of $P(s)$, so that we need only obtain the solution to the Laplace transform of the diffusion equation to obtain the autocorrelation function directly.

The correlation function measured with DWS can be calculated directly for several experimentally relevant geometries by solving Eq. (32). We do not discuss these solutions in detail here, but refer to other papers where this is done.[4, 5, 11, 12] Here, we simply quote the results. We consider only the case where the light is transmitted through the sample, which we take to be a slab of infinite extent and of thickness, L. Then, if the incident laser is focused to a point on one side of the sample, and the scattered light is collected from a point on the other side of the sample, on the same axis as the incident light, the normalized field correlation function is given by,

$$g_1(t) = \int_{\frac{L}{l^*}\sqrt{\frac{6t}{\tau_0}}}^{\infty} \left[A(s)\sinh s + e^{-s\left(1-\frac{4l^*}{3L}\right)} \right] ds \tag{33}$$

where

$$A(s) = \frac{\left(\frac{2l^*}{3L}s - 1\right)\left[\frac{2l^*}{3L}e^{\frac{4sl^*}{3L}} + \left(\sinh s + \frac{2sl^*}{3L}\cosh s\right)e^{s\left(1-\frac{4l^*}{3L}\right)}\right]}{\left(\sinh s + \frac{2sl^*}{3L}\cosh s\right)^2 - \left(\frac{2sl^*}{3L}\right)^2}. \tag{34}$$

While complicated, these expressions are readily evaluated, and provide excellent agreement with the data.

DIFFUSING WAVE SPECTROSCOPY FROM INTERACTING PARTICLES

In developing an expression for the temporal autocorrelation function of the intensity fluctuations of the light scattered from strongly interacting particles, we wish to

maintain as much of the simplicity of the derivation for noninteracting particles as is possible. In particular, we wish to again use the diffusion equation to describe the propagation of the light, and we wish to again express the correlation function in terms of a Laplace integral over the weighted contribution of paths. For interacting particles, however, the scattering from some of the particles is strongly correlated with that from other particles. Thus, we can no longer consider the contribution of each path to be totally uncorrelated with the contribution of all other paths. Moreover, even within a single set of paths, we must consider the possible correlations of different scattering particles. Thus we begin by considering the scattered electric field for an n^{th} order sequence,

$$E^n(t) = \sum_k E_k^n(t) = \sum_k \prod_\alpha^n b(\mathbf{q}^\alpha) e^{-i\mathbf{q}_k^\alpha \cdot \mathbf{r}_k^\alpha(t)} \tag{35}$$

Here, each path is assumed to consist of n distinct scattering events, 1, 2, ... n, with the subscript α denoting the scattering event. The α^{th} scattering event in the k^{th} path is from a particle at position $\mathbf{r}_k^\alpha$, and the scattering wave vector is $\mathbf{q}_k^\alpha$ and $b(\mathbf{q}^\alpha)$ is the scattering form amplitude from a single particle. Because of the strong interactions between the particles, many individual paths are strongly correlated with one another. In particular, paths following very nearly the same sequence of scattering events are correlated, resulting in some volume of correlated paths following a route through n scattering sequences. Thus, to calculate the correlated field, we must sum over the paths k, reflecting the number of paths within this correlated volume. Then, the normalized correlation function for n^{th} order scattering sequences is,

$$g_1^n(t) = \frac{\left\langle \sum_i E_i^n(t) \sum_j E_j^{n*}(0) \right\rangle}{\left\langle \left| \sum_i E_i^n(0) \right|^2 \right\rangle} \tag{36}$$

where i and j are indices which sum over distinct paths that are correlated with one another, and the brackets again indicate an ensemble average, which in this case also includes the average over all sequences of n scattering events. We consider the numerator of the expression in Eq. (17), which is the unnormalized field correlation function,

$$G_1^n(t) = \left\langle \sum_{i,j} E_i^n(t) E_j^n{}^*(0) \right\rangle = \left\langle \sum_{i,j} \prod_{\alpha,\beta}^n b(\mathbf{q}_i^\alpha) b(\mathbf{q}_j^\beta) e^{-i\mathbf{q}_i^\alpha \cdot \mathbf{r}_i^\alpha(t) + i\mathbf{q}_j^\beta \cdot \mathbf{r}_j^\beta(0)} \right\rangle \tag{37}$$

We assume that all the particles are identical and therefore have the same form amplitude factor. To simplify this expression further, we consider the scattering within a single scattering sequence. Since to remain fully correlated, the individual paths must follow very nearly the same route, we approximate the scattering wave vectors within the same scattering sequence but of different paths as being equal, setting $\mathbf{q}_k^\alpha = \mathbf{q}_k^\beta = \mathbf{q}_k$. Moreover, we assume that the scattering length is larger than the correlation length, $l > \xi$, so that only one scattering event can occur within each correlation volume. Thus particles from different scattering sequences are not correlated in time and terms with $\alpha \neq \beta$ average to zero, removing the summation over β in Eq. (37). Furthermore, the summation over i and j needs only to extend over the volume of the scattering sequence. This expression then simplifies to

$$G_1^n(t) = \left\langle \prod_{\alpha}^{n} \sum_{i,j} F(\mathbf{q}_i) e^{-i\mathbf{q}_i \cdot [\mathbf{r}_i^{\alpha}(t) - \mathbf{r}_j^{\alpha}(0)]} \right\rangle \tag{38}$$

where $F(\mathbf{q})$ is the particle scattering form factor. The indices i and j in the second summation now simply correspond to particle indices within the volume of a scattering sequence, or a single correlation volume. We can thus move the form factor outside of the second summation and identify this summation in terms of the dynamic structure factor,

$$N_\xi S(q,t) = \left\langle \sum_{i,j} e^{-i\mathbf{q}\cdot[\mathbf{r}_i(t) - \mathbf{r}_j(0)]} \right\rangle \tag{39}$$

where N_ξ is the number of particles within the correlation volume of the scattering sequence.

The correlations extend only over the region contained within ξ^3, and only a single scattering sequence occurs within this volume. Thus, the particles in different scattering sequences are separated by distances greater than ξ, and hence are statistically independent. We therefore make the further approximation that the total correlation function is the product of independent contributions from the n scattering sequences. This approximation is similar to that made in the derivation of the correlation function for the case of noninteracting particles in that it ignores the detailed conservation of momentum along the whole path, but should nevertheless be a reasonable approximation for long paths where n is large. To calculate the contribution from each of the independent scattering sequences, we note that the static structure factor multiplied by the form factor represents a properly intensity-weighted, q-dependent contribution to the correlation function. Thus the total contribution of this independent scattering volume is the sum over q of these contributions, and the unnormalized field correlation function of the n^{th} order scattering sequences is,

$$G_1^n(t) = \left[N_\xi \int dq\, qF(q)S(q,t) \right]^n \tag{40}$$

Since at $t = 0$, $S(q,t) = S(q)$, and we have for the normalized correlation function for n^{th} order scattering sequences,

$$g_1^n(t) = \frac{\left[\int dq\, qF(q)S(q,t) \right]^n}{\left[\int dq\, qF(q)S(q) \right]^n} \tag{41}$$

To proceed, we use the short time expansion for the dynamic structure factor discussed earlier. For simplicity, we begin with the simpler form, in Eq. (20), which does not explicitly include the time-dependent hydrodynamic interactions. Then we have,

$$g_1^n(t) = \left[\frac{\int dq\, qF(q)S(q) \left[1 - q^2 D_0 \frac{H(q)}{S(q)} t \right]}{\int dq\, qF(q)S(q)} \right]^n \tag{42}$$

Expanding this, we have

$$g_1^n(t) = \left[1 - \frac{D_0 t \int dq\, q^3 F(q) H(q)}{\int dq\, q F(q) S(q)}\right]^n, \tag{43}$$

which we can approximate as

$$g_1^n(t) \approx e^{-nD_0 \frac{[H]_3}{[S]_1} t} \tag{44}$$

Here, we have introduced the notation

$$[X]_m = \int dq\, q^m F(q) X(q) \tag{45}$$

To use the diffusion approximation for the light propagation through the medium, we must express the number of scattering sequences in terms of the path length, and we must describe the light propagation in terms of the transport mean free path. Since $n=s/l$, we have

$$n = \frac{s}{l^*}\frac{l^*}{l} \tag{46}$$

and from the definition of the transport mean free path,[2]

$$\frac{l^*}{l} = \frac{[S]_1}{[S]_3} \tag{47}$$

Thus, finally, the expression for the normalized field correlation function for the contribution from n scattering sequences is

$$g_1^n(t) = e^{-D_0 \frac{s}{l^*} \frac{[H]_3}{[S]_3} t} \tag{48}$$

We note that this form has exactly the same dependence on s, l^* and t as does the same contribution for the case of noninteracting particles. Thus, this form can be used directly in Eq. (32), and the same results hold for the case of interacting particles. Moreover, these results are in agreement with those obtained previously by MacKintosh and John,[15] Fraden and Maret,[13] and Qiu *et al.*[14]

Finally, we can, at least formally, use our more exact expression for the expansion of the dynamic structure factor, Eq. (21). To so this requires making the substitution,

$$D_0 t [H]_3 \rightarrow \int dq q^3 F(q) S(q) D_{app}(t) \tag{49}$$

in Eq. (48). From the expression for $D_{app}(t)$, Eq. (17), the first term, which corresponds to the limit where the transient hydrodynamic interactions no longer contribute, would yield exactly the same results as the simpler case above, Eq. (48). The second term in the expression would include the leading contributions of the hydrodynamic interactions, and for DWS measurements, these would be averaged over the form factor times q^3. Note that the $S(q)$ in the denominator of the second term in Eq. (17) would cancel with the $S(q)$ in the

integral in Eq. (49). The important physics for the DWS measurements is that, unlike traditional DLS, they average the dynamics over $q^3F(q)$. The additional factor of q^3 ensures that the average is dominated by the contributions at higher q. This tends to emphasize the contribution of self-diffusion for larger particles, greatly simplifying the interpretation of the results.

CONCLUSIONS

Our goal in this paper has been to present a physical picture to describe the quantities measured by DWS from interacting particles. We have considered a simple case by way of example: identical colloidal particles, interacting solely as hard spheres, where all the scattering is from the particles themselves. We describe the correlations of the particle positions in terms of their static structure factor, and the dynamics of the particles in terms of their dynamic structure factor. We show that the presence of the correlations between the particles requires that the correlations between some of the diffusive light paths be retained, unlike the case of noninteracting particles. However, if this is done, the correlation function then is expressed in terms of the dynamic structure factor. This can be formulated in a manner that is analogous to the case of noninteracting particles, allowing all the results derived for that case to be applied, with simple substitutions.

We have also presented some discussion of the dynamics of the interacting particles at very short time scales. This is required because DWS can probe the particle dynamics at much shorter time, and length, scales than has heretofore been possible. When the scatterers are colloidal particles, hydrodynamic interactions greatly affect their dynamics. Furthermore, at very short time scales, we must consider the time evolution of these hydrodynamic interactions. We have presented formal expressions for these, for interacting particles. Unfortunately, the evaluation of these formal expressions is quite difficult. However, the feasibility of making measurements of these effects using DWS provides greater incentive for their evaluation.

REFERENCES

1. B.J. Berne and R. Pecora. "Dynamic Light Scattering: with Applications to Chemistry, Biology and Physics," Wiley, New York (1976).
2. P.E. Wolf, G. Maret, E. Akkermans and R. Maynard, *J. Phys. France* 49:63 (1988).
3. D.J. Pine, D.A. Weitz, P.M. Chaikin and E. Herbolzheimer, Diffusing Wave Spectroscopy, *Phys. Rev. Lett.* 60:1134 (1988).
4. D.J. Pine, D.A. Weitz, J.X. Jhu and E. Herbolzheimer, Diffusing-Wave Spectroscopy: Dynamic Light Scattering in the Multiple Scattering Limit, *J. Phys. France* 51:2101 (1990).
5. D.J. Pine, D.A. Weitz, G. Maret, P.E. Wolf, P.M. Chaikin and E. Herbolzheimer, Dynamical Correlations of Multiply Scattered Light, *in*: "Scattering and Localization of Classical Waves in Random Media," P. Sheng, eds., World Scientific, Singapore (1990).
6. A. Ishimaru. "Wave Propagation and Scattering in Random Media," Academic, New York (1978).
7. P.E. Wolf and G. Maret, *Phys. Rev. Lett.* 55:2696 (1985).
8. M.P. van Albada and A. Lagendijk, Observation of Weak Localization of Light in a Random Medium, *Phys. Rev. Lett.* 55:2692 (1985).
9. M.P. van Albada, J.F. de Boer and A. Lagendijk, Observation of Long-Range Intensity Correlation in the Transport of Coherent Light through a Random Medium, *Phys. Rev. Lett.* 64:2787 (1990).
10. S. Feng, C. Kane, P.A. Lee and A.D. Stone, *Phys. Rev. Lett.* 61:834 (1988).
11. D.A. Weitz and D.J. Pine, Diffusing-Wave Spectroscopy, *in*: "Dynamic Light Scattering," W. Brown, eds., Oxford University Press, Oxford (1992).

12. D.A. Weitz, J.X. Zhu, D.J. Durian and D.J. Pine, Principles and Applications of Diffusing-Wave Spectroscopy, *in*: "Structure and Dynamics of Strongly Interacting Colloids and Supramolecular Aggregates in Solution," S.H. Chen, J.S. Huang and P. Tartaglia, eds., Kluwer, Dordrecht (1992).
13. S. Fraden and G. Maret, *Phys. Rev. Lett.* 65:512 (1990).
14. X. Qiu, X.L. Wu, J.Z. Xue, D.J. Pine, D.A. Weitz and P.M. Chaikin, Hydrodynamic Interactions in Concentrated Suspensions, *Phys. Rev. Lett.* 65:516 (1990).
15. F.C. MacKintosh and S. John, *Phys. Rev.* B40:2383 (1989).
16. D.A. Weitz, D.J. Pine, P.N. Pusey and R.J.A. Tough, Nondiffusive Brownian Motion Studied by Diffusing-Wave Spectroscopy, *Phys. Rev. Lett.* 63:1747 (1989).
17. J.X. Zhu, D.J. Durian, J. Muller, D.A. Weitz and D.J. Pine, Scaling of Transient Hydrodynamic Interactions in Concentrated Suspensions, *Phys. Rev. Lett.* 68:2559 (1992).
18. P.N. Pusey and R.J.A. Tough, Particle Interactions, *in*: "Dynamic Light Scattering: Applications of Photon Correlation Spectroscopy," R. Pecora, eds., Plenum, New York (1981).
19. P.N. Pusey, Colloidal Suspensions, *in*: "Liquids, Freezing and Glass Transition," J.P. Hansen, D. Levesque and J. Zinn-Justin, eds., Elsevier, Amsterdam (1991).
20. W. Hess and R. Klein, *Adv. Phys.* 32:173 (1983).
21. R. Klein, to be published.
22. J. Bonet Avalos, J.M. Rubi and D. Bedeaux, Dynamics of Polymers in Solution: The Role of Time-Dependent Hydrodynamic Interactions, *Macromolecules* 24:5997 (1991).
23. P. Mazur and D. Bedeaux, *Physica* A76:235 (1974).
24. P.N. Pusey and R.J.A. Tough, *Faraday Disc.* 76:123 (1983).
25. W. van Saarloos and P. Mazur, *Physica* 120A:77 (1983).
26. B.J. Alder and T.E. Wainwright, *Phys. Rev. Lett.* 18:988 (1967).
27. B.J. Alder and T.E. Wainwright, *Phys. Rev.* A1:18 (1970).
28. E.J. Hinch, *J. Fluid Mech.* 72:499 (1975).
29. G. Maret and P. Wolf, Multiple Light Scattering from Disordered Media. The Effect of Brownian Motion of Scatterers, *Z. Phys.* B65:409 (1987).
30. A. Lagendijk, R. Vreeker and P. DeVries, Influence of Internal Reflection on Diffusive Transport in Strongly Scattering Media, *Phys. Lette. A* 136:81 (1989).
31. J.X. Zhu, D.J. Pine and D.A. Weitz, Internal Reflection of Diffusive Light in Random Media, *Phys. Rev.* A44:3948 (1991).

FACTORS THAT INFLUENCE PHOTON TRANSPORT MEASUREMENTS IN DENSE RANDOM MEDIA

George H. Watson, Paul M. Saulnier,*
İ. İnanç Tarhan, and Martin P. Zinkin

Department of Physics and Astronomy
University of Delaware
Newark, DE 19716

INTRODUCTION

The possibility for study of localization effects in optically-disordered systems has spurred a renewed interest in the study of light scattering from dense random media, as evidenced by the numerous contributions to this volume. For several years, strong photon localization has been anticipated in composite materials possessing sufficiently high density of scatterers with sufficiently high cross sections for scattering photons.[1] Unfortunately, no unambiguous observation of strong photon localization in the visible or infrared wavelength range has yet been reported. Recent work has, however, indicated strong photon localization in the microwave regime for a randomly disordered system.[2] The difficulty in achieving localization of visible light arises from the lack of suitable materials possessing dielectric contrast sufficient to cause a localization transition in a completely random system. The conventional approach has been to rely on random suspensions of particles with large single-scattering Mie resonances, large cross-sections obtained for certain ratios of particle size to wavelength.[3] Determination of the optimal situation for realization of strong photon localization may be the most pressing theoretical challenge of classical wave localization.[4] Of particular interest is one theoretical approach that finds the presence of order underlying the disorder, such as in a disordered optical superlattice (*e.g.*, a colloidal crystal), will be beneficial in achieving photon localization.[5]

Experimental searches for strong photon localization have taken several routes in hope of observing non-diffusive photon transport. Toward this end, a complete understanding of photon transport in such optically dense systems is needed as well for the extended states in the diffusive regime. Measurements of photon transport in dense systems of relatively weak scatterers are presented here to highlight some of the

*Present address: Physics Department, Carroll College, Waukesha, WI 53186.

Photonic Band Gaps and Localization, Edited by
C.M. Soukoulis, Plenum Press, New York, 1993

factors that influence photon transport in dense (but not localizing) optically-disordered systems.

METHODS FOR PHOTON TRANSPORT MEASUREMENT

Observations of coherent backscattering (CBS) comprise most of the experimental work on photon localization to date; time-resolved techniques have also been applied with success. The advantages of each method are offset, of course, by certain disadvantages. CBS can be observed from nearly any sample surface using relatively inexpensive lasers, but primarily short path lengths are sampled because of the reflection geometry. Time-resolved work is easiest in transmission because of the long total path lengths (transit times) involved, but is made difficult by sample absorption and intense reflection.

Coherent Backscattering

Nearly all of the experimental evidence of photon localization comes from the observations of CBS made over the past few years. Observations of CBS, discussed in the context of weak localization of light, were first reported in 1985[6,7] from concentrated colloidal suspensions of sub-micron latex spheres in water.[8] Ensemble averaging of light backscattered from static suspensions was also found to exhibit CBS.[9,10] Theoretical work ensued to describe the observed features of CBS: peak shape,[11] polarization effects,[12] and changes in shape arising from truncated paths.[13] The differing contributions from long and short light paths to CBS were clarified experimentally with a novel difference technique[14] and via termination of light paths with absorbing dye.[15] Laboratory reviews of CBS have recently been published by the Amsterdam and CNRS groups.[16–18]

Observed features of CBS include an angular width inversely proportional to $k\ell$ (the photon wavevector and transport mean-free-path length), an enhancement over the incoherent backscattering by nearly a factor of two, and a rounding of the predicted triangular shape caused by finite angular resolution or absorption. The observed shape was found to be in good agreement with theories based on random-walk theory[10,11] and summation of ladder and maximally-crossed diagrams.[19]

Study of CBS in the time domain becomes possible when time resolution of several picoseconds is available. The angular dependence of enhancement in backscattering of light pulses from latex suspensions has been demonstrated using a streak camera having 15 ps resolution.[20] Short paths contribute most of the angular breadth of the CBS peaks observed to date; longer paths should make only narrow angular contributions to the peak. Direct observation of the time evolution of the CBS peak has been reported using a light-gating technique based on second-harmonic generation.[21]

Pulse Time-of-Flight

Our early experiments demonstrated that time-of-flight transmission measurements of short laser pulses could be used to determine optical diffusion coefficients precisely.[22] Time-resolved transmission can be used to measure the diffusion coefficient of light directly in terms of temporal delay and pulse shape (temporal distribution of diffusion paths). This method permits probing of the random medium on length scales from 10 up to 10^6 mean-free-path lengths in low absorbance samples and provides

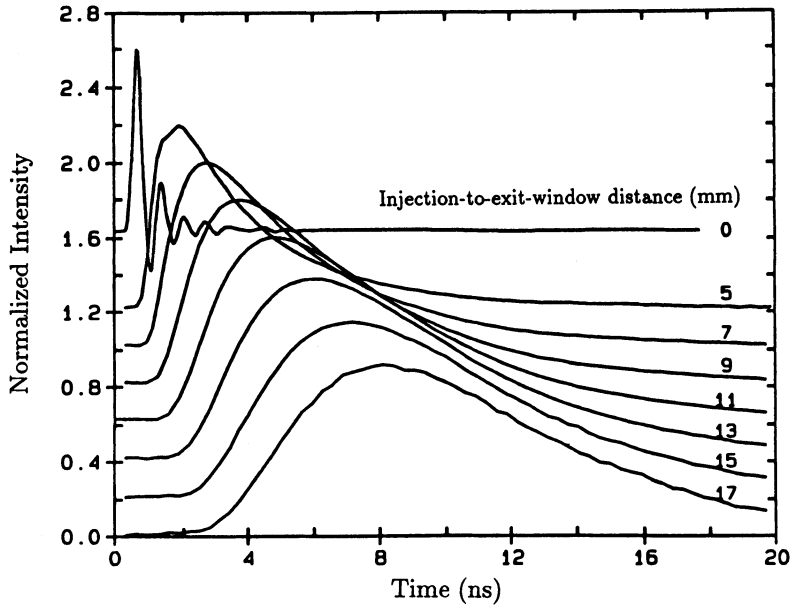

Figure 1. Time-Resolved Pulse Transmission Intensity Series.
The displayed data were obtained by injecting 0.5785 μm light into a 10% solution of 0.135 μm diameter polystyrene spheres. Curves are offset vertically and normalized by peak height for clarity.

a quantitative means for separation of elastic scattering and absorptive effects. The precision of this approach offers the possibility of detecting small departures from simple diffusion. Recent developments question the appropriateness of applying $D = c\ell^*/3$ without regard to possible renormalization of the velocity of energy transport;[23,24] these are discussed in detail elsewhere in this volume.

Improvement of time resolution by nearly two orders of magnitude over our earlier instrument[22] has been obtained by application of a synchronously pumped cavity-dumped dye laser and high-speed sampling techniques, thereby permitting study of smaller and more absorptive samples.[25] Similar resolution has also been demonstrated with excellent sensitivity by time-correlated single photon counting.[26] Additional resolution may be obtained by application of cross-correlation or Kerr gating techniques, limited only by the shortness of available laser pulses. In principle, these nonlinear optical techniques offer the highest temporal resolution and, in addition, the highest sensitivity with the use of conventional photomultiplier tubes and photon counting.

Transport parameters have been obtained using a time-resolved transmission technique optimized for fluid samples.[25] Pulses (10 ps duration, $\lambda_{\text{vac}} = 0.5785\,\mu$m) from a synchronously pumped dye laser were injected into each sample through an optical fiber; transmitted pulses were detected with a biplanar phototube and digital sampling oscilloscope for various values of effective sample thickness s, the distance between the launch point of the light (fiber tip) and the output window (See Fig. 1). Two parameters, the diffusion coefficient and an absorption parameter γ, as in $I(t) = e^{-\gamma t} I_D(t)$, were extracted from observed pulse shapes for all s by least-squares fitting of the solution of the diffusion equation with boundary conditions representing our experimental geometry.[22] Figure 2 shows the corresponding fit of the model to the data in Fig. 1 using the same diffusion coefficient and absorption parameter for each distance.

The time-of-flight approach has been applied to a thin, dense sample of titania, where the diffusion coefficient D was reported to be nearly a factor of three lower than

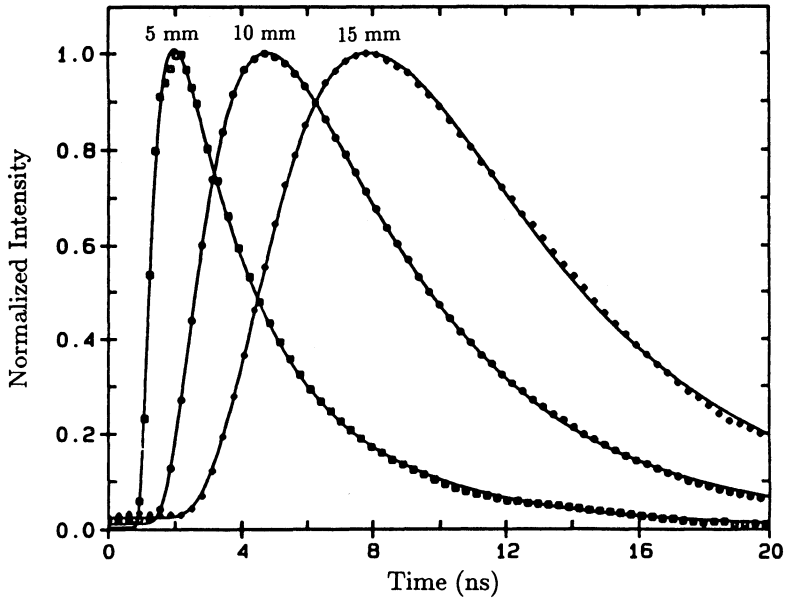

Figure 2. Pulse Transmission Data with Corresponding Diffusion Model Fits.
The diffusion model contains two physically significant parameters: the diffusion coefficient, D, and the absorption parameter, γ. The injection point to exit window distance, s, is indicated next to each curve.

that expected classically.[26] Similarly, transmission of femtosecond pulses have explicitly demonstrated failure of the diffusion approximation at short length scales.[27]

Speckle Autocorrelation Spectroscopy

The speckle observed in transmission can be used, in principle, to extract the same information about photon transport as is obtained from pulsed experiments. The scale dependence of the correlation frequency of intensity fluctuations transmitted through a small aperture in far field as laser frequency is swept was first examined by Genack.[28] The length dependence of the spectral correlation of intensity fluctuations in a coherence area was introduced to establish photon diffusion in titania samples with $\ell < 1\mu$m.[28] This work was extended to confirm the relationship between speckle fluctuations and pulse propagation.[29] We also applied this technique, with a sample and experimental configuration well-characterized by pulse transmission measurements, to evaluate its utility in determining transport in thin or absorptive samples where time domain measurements become difficult.[30] Suitable care in executing and interpreting speckle autocorrelation spectra is required as the effects of intrinsic absorption and finite aperture are important. Long range intensity correlations have been observed subsequently in the visible[31] and in the microwave regime[32] using this technique. Frequency-dependent speckle autocorrelation and pulse transmission have become widely used for determining the optical diffusion parameter in dense random media.

Additional Methods

Length dependence of cw transmission can also be used to determine the transport mean-free-path length; for systems exhibiting diffusive transport with insignificant absorption the total transmission is proportional to ℓ^*/L, where L is the

sample thickness. The dependence of transmission on L is modified in the presence of significant absorption.[28,33] The total transmission approach has been used to establish photon diffusion in titanium dioxide samples having mean-free-path lengths less than one micron[28] and has also been used to demonstrate the departure of the transport scattering cross section from simple density scaling discussed below.[16]

Multifrequency phasefluorometry, conventionally used to determine excited state lifetimes, has recently been extended to the determination of transport mean-free-path lengths.[34] In this technique, the photon time-of-flight through the random medium is measured as a phase-shift induced on the Fourier components of the ultrashort light pulse, and the transport parameter is extracted via the diffusion approximation.

FACTORS INFLUENCING PHOTON TRANSPORT MEASUREMENT

Correlation Effects

Photon transport in the diffusive regime can be characterized by the transport (or momentum-exchange) mean-free-path length,

$$\ell^* = (n\sigma^*)^{-1}, \tag{1}$$

where n is the number density of scatterers and

$$\sigma^* = \int \frac{d\sigma}{d\Omega}(1 - \cos\theta)\, d\Omega. \tag{2}$$

$d\sigma/d\Omega$ is the differential Mie cross section for scattering into $d\Omega$ at an angle θ, derived from Maxwell's equations for an isolated uniform dielectric sphere.[3] Equation (1) is accurate only in the limit of dilute scatterer concentration, however. As n increases, spatial correlation among scatterers leads to phase correlation among scattered waves and weakens the effective cross section for scattering below that of an individual scatterer.

Correlation effects may be introduced[17] by replacing σ^* with

$$\sigma_c^* = \int \frac{d\sigma}{d\Omega} S(\theta)(1 - \cos\theta)\, d\Omega, \tag{3}$$

where $S(\theta)$ is the static structure factor obtained from an appropriate radial distribution function, $g(r)$, by

$$S(\mathbf{q}) = 1 + n\int [g(r) - 1]\; e^{i\mathbf{q}\cdot\mathbf{r}}\, d^3\mathbf{r}. \tag{4}$$

$\mathbf{q}$ is the scattering vector of the elastically-scattered photon of wavevector $\mathbf{k}$ and is related to the scattering angle by $q = 2k\sin(\theta/2)$.

A systematic study of photon transport in well-characterized aqueous colloidal suspensions of monodisperse latex balls has been conducted over a range of densities spanning the dilute regime to the high-density regime, where correlations among particles become important.[25] Photon transport parameters were obtained for suspensions of 0.087, 0.135, and 0.198 μm diameter (d) latex balls with volume fractions f ranging from ~0.1 to 20%, obtained by successive dilution from the 10% stock suspension or by centrifuging for higher density.

In addition, extinction mean-free-path lengths†, ℓ, were obtained from the same samples for comparison with ℓ^*. A computer-controlled variable thickness cell was used

† $\ell = (n\sigma)^{-1}$, where σ is given by Eq. (2) or (3) without the $(1-\cos\theta)$ momentum-exchange factor.

in the usual extinction configuration to measure the relative intensity of transmitted, unscattered light with variation of sample thickness x: $I = I_0 \exp(-x/\ell)$. Extinction data were obtained primarily with $\lambda_{vac} = 0.5145\,\mu m$ from an argon ion laser because of its inherent stability and ease of operation; extinction measurements obtained using $\lambda_{vac} = 0.5785\,\mu m$ from the picosecond laser were observed to agree with the previous data after scaling for wavelength.

Observed values of ℓ^* and ℓ are shown in Fig. 3 over the accessible range of scatterer densities. To facilitate comparison of different ball sizes, dimensionless densities n' have been introduced as the number of scatterers per cubic wavelength, $n\lambda^3$, where $n = (6/\pi)\, f/d^3$ and λ is the wavelength *in water*. In all three samples, as the density is increased, departures from n^{-1} scaling of the mean-free-path lengths become apparent.

The hole correction model[35] provides the easiest introduction of particle correlations. Equation (4) can be evaluated analytically for the hole correction distribution function given by $g(r) = 0,\ r < d;\ = 1,\ r \geq d$. Good agreement with our observations is obtained for the larger diameter balls. Unfortunately, the hole correction model begins to diverge for f higher than about 10% for the 0.087 μm balls, arising from physically-inadmissible negative values calculated for $S(\theta)$ at small angles. The same limitation of the hole correction model was previously noted in an analysis of extinction measurements from similarly dense systems.[35]

The Percus-Yevick $g(r)$ can be used to provide a better approximation.[17] An exact solution of the Percus-Yevick integral equation for $g(r)$ for hard spheres is available[36] and has been used here for evaluation of Eq. (4).[37] The resulting corrections are shown as the curved lines in Fig. 3 which increasingly deviate from the n^{-1} scaling as density is increased. Agreement is favorable with both transport and extinction observations.

The experimental data have been reduced by least-squares fitting of straight lines in the dilute limit, with slope of -1 representing n^{-1} scaling, thereby removing possible systematic errors such as incorrectly-reported scatterer size. The observed high density values are reported relative to these best-fit lines as correlation correction factors $\Gamma(n') = \ell_c/\ell$ and shown in Fig. 4 for comparison with theoretical values. Correlation effects are capable of doubling observed mean-free-path lengths from the expected Mie-based lengths at the highest densities studied. Spatial correlation is observed to affect extinction more strongly than transport. The angular dependence of $S(\theta)$ is such that it deviates from unity mostly at small angles, deviating more strongly with increasing density. This angular dependence is somewhat similar to that of the factor $(1 - \cos\theta)$ already present in Eq. (2); each term serves to suppress the forward scattering contribution to the overall cross section. Thus, the correlation effect is correspondingly weaker for σ_c^* than σ_c.

For $n' < 1$ correlation effects on transport are relatively unimportant. Significant correction factors for extinction lengths can arise at lower values of n' however, especially for larger ball diameters. For a given actual density, say $f = 10\%$ (indicated by the arrows in Fig. 4), correlation effects are always stronger for smaller scatterers.

Previous studies[17,16] of CBS of light from colloidal latex suspensions have employed a comparison of observed backscattering widths with calculated ℓ^*. Correlation effects have been clearly observed in CBS at high densities[16] and have been included in the evaluation of transport calculations as described above.[17] We have shown by direct measurement of ℓ^* that this approach is indeed valid for these disordered systems. Clearly, correlation effects in photon transport cannot be ignored in the dense random systems currently being explored in localization studies, and in fact may tend to mask its observation.

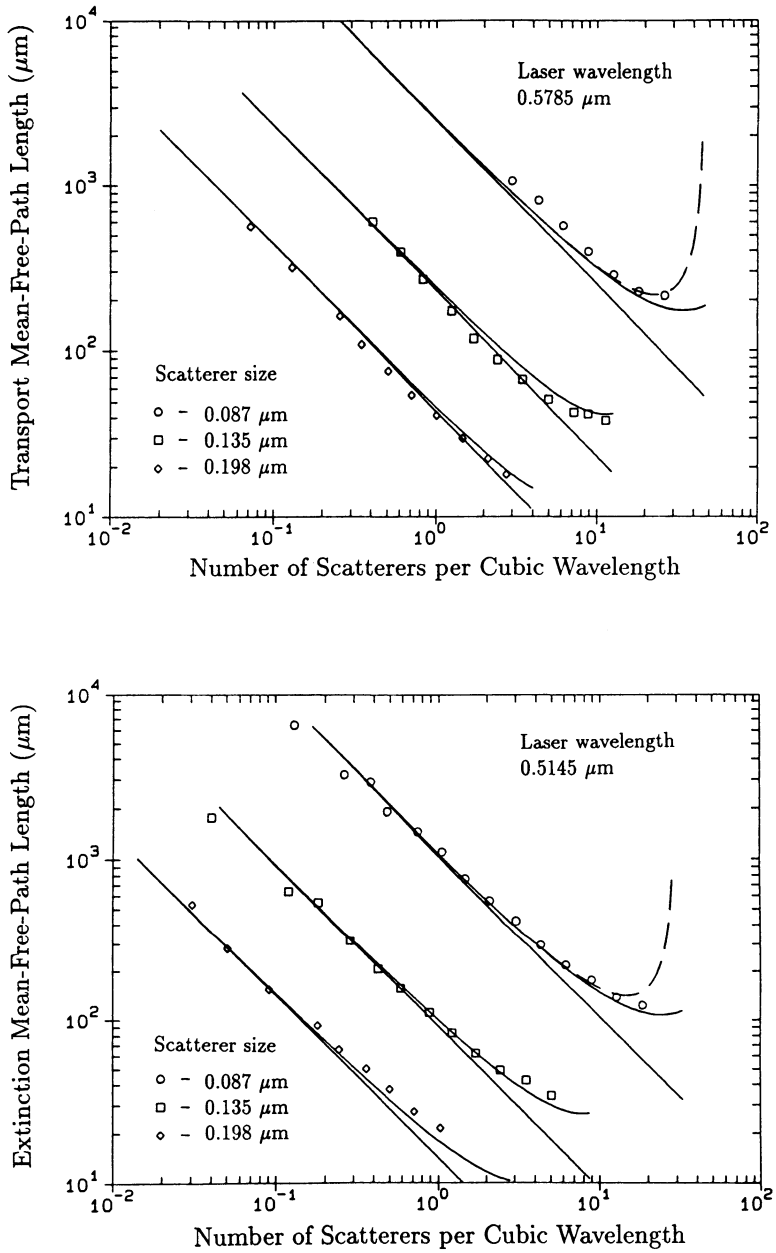

Figure 3. Observed Transport and Extinction Mean-Free-Path Lengths.
Departure from Mie theory without correlation correction (straight line) increases with increasing scatterer density. The correction from Percus-Yevick (PY) theory (solid curves) is compared to the Hole Correction (HC) model (dashed curve) for the 0.087 μm scatterers.

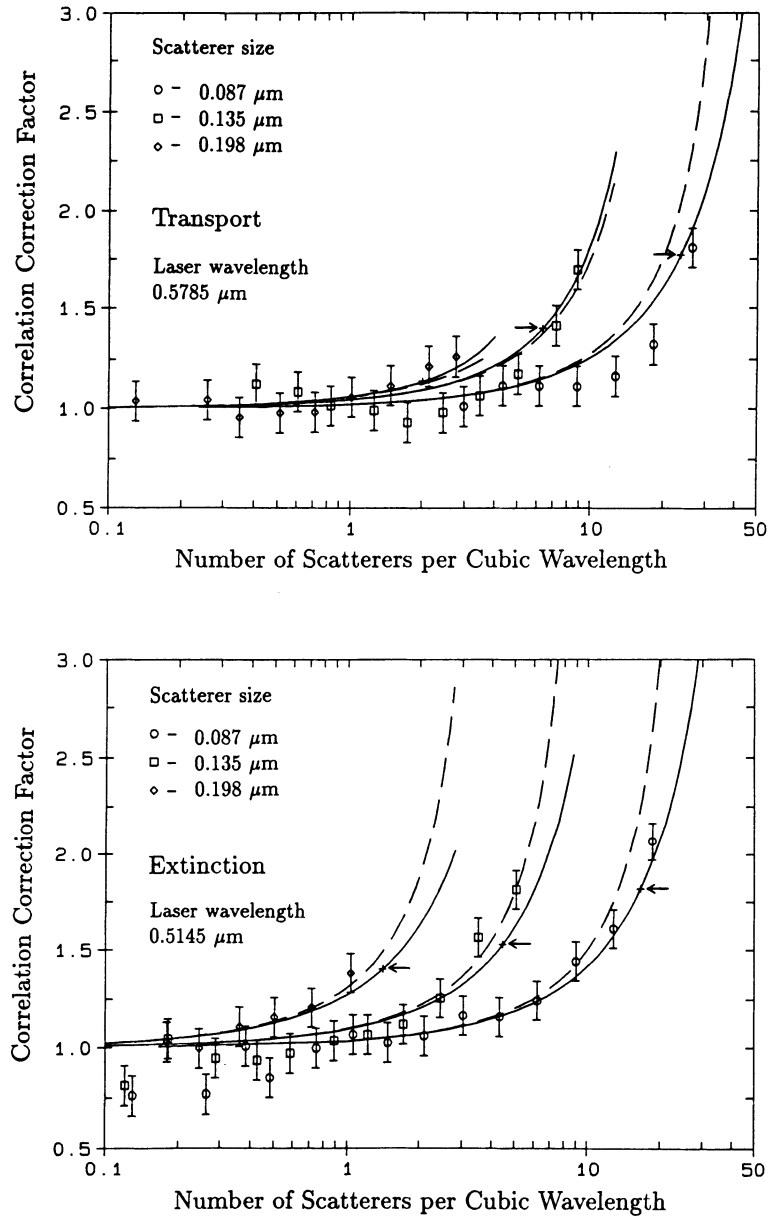

Figure 4. Correlation Correction Factors.
Departure from simple n^{-1} scaling of the path lengths is presented as the ratio of the observed to expected values, derived from best-fit n^{-1} scaling at low density. Percus-Yevick (solid curves) and Hole Correction (dashed curves) factors are shown for comparison. The arrows indicate scatterer densities of 10%.

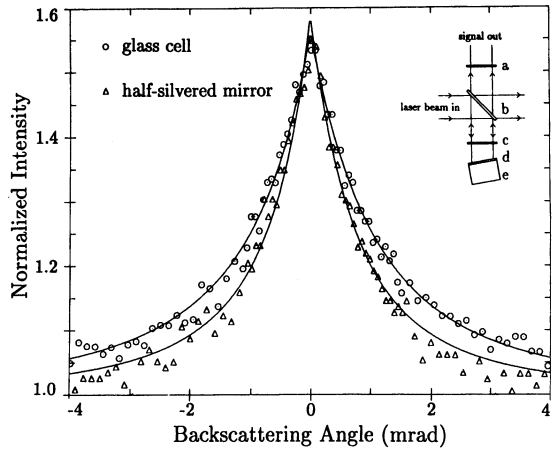

Figure 5. Coherent Backscattering Cone Narrowing with Increased Surface Reflectivity. Actual angular range was ±8 mrad; reduced here for clarity. Sample was 2.01 μm polystyrene balls, 10% volume fraction in water. INSET: Experimental geometry used: a, linear polarizer; b, beamsplitter; c, quarter-wave plate; d, partially-silvered mirror; e, sample cell.

Surface Reflectivity

Recently the effects of surface reflections on photon transport measurements in disordered systems have been considered.[38–41] Reflection from the sample surface of a photon attempting to escape a random medium has the effect of relaunching it and thereby increasing the average path length of photons injected into the sample. Photon transport measurements that are sensitive to the total photon path are thus influenced by the presence of strong surface reflectivity, typically encountered for large incidence angles, abundant after multiple scatterings. The severity of this effect was first noticed in the optical memory effect and accounted in large part for discrepancy with existing theory.[38] Subsequently, theoretical work considered the effects of surface reflections on CBS, pulse transmission, and frequency- and time-dependent speckle correlations.[39–41] The magnitude of these effects on CBS and their influence on transport parameter determination are reported here for observations in the presence of strong surface reflections.

The phase difference associated with a multiply-scattered path relative to its conjugate path is $\Delta\phi = (\mathbf{k}_i + \mathbf{k}_f)\cdot\mathbf{R}$, where $\mathbf{k}_{i,f}$ are the initial and final photon wavevectors and $\mathbf{R}$ is the separation between initial and final scatterers. In the diffusion approximation, the rms distance between first and last scatterers is $\mathcal{R} \sim \sqrt{s\ell^*}$ for path lengths s. For elastic multiple backscattering, phase coherence will be maintained (small $\Delta\phi$) within an angle given by $\theta_c k\sqrt{s\ell^*} < 1$. Longer paths thus predominately contribute to CBS within much smaller angles than low-order scattering. Surface reflectivity, which serves to reinject photons into the random medium, lengthens the average photon path and results in a narrowing of the CBS cone.

CBS measurements were made in a standard 45° beamsplitter geometry[16] using a polarized 5 mW HeNe laser and photon counting. A quarter-wave plate and linear polarizer were used in front of the sample as shown in the inset of Fig. 5 to eliminate single scattering and to select the helicity-preserving part of the multiply-scattered intensity in the backscattering direction.[15] The CBS peak shape calculated for scalar waves has been shown to be in good quantitative agreement with helicity-preserving CBS for vector waves such as light.[13] This experimental configuration facilitates comparison with the scalar wave calculations of Refs. 39 and 40.

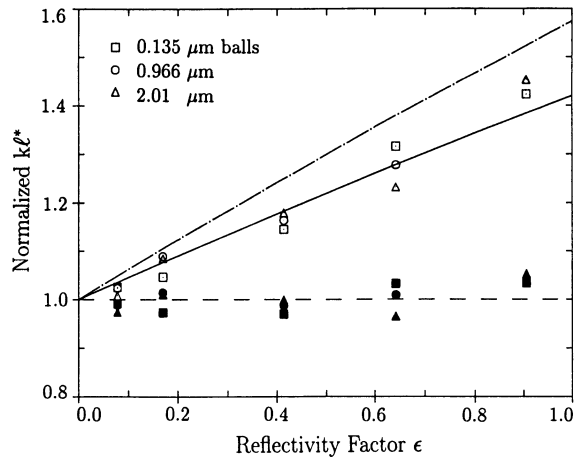

Figure 6. Effects of Surface Reflectivity on Transport Parameter $k\ell^*$ Obtained from CBS. Open symbols indicate the rising value of $k\ell^*$ obtained from Eq. (5) where surface reflectivity is ignored; the relatively flat closed symbols result when surface reflectivity is incorporated using Eq. (6). The solid curve shows the model of Ref. 39; the dashed curve, Ref. 40.

Surface reflectivity was varied by enclosing the suspension in cells constructed of various partially-silvered mirrors. Mirrors were used having normal reflectivities in air of 0.10, 0.25, 0.36 and 0.46, which dropped considerably in contact with the aqueous polyball suspension. When averaged over all incidence angles and both polarization states, using a standard treatment[42] for a silver mirror with a thin titania overcoat in contact with water, the effective surface reflectivities, r, were calculated and returned to 0.15, 0.30, 0.40, and 0.48, respectively. Reflections into the sample from the exterior glass-air interface were limited to $\sim 30°$ from normal by geometrical constraint, over which the reflectivity averaged over both polarizations does not deviate significantly from 0.04.

The decrease in CBS cone widths arising from increased surface reflectivity is evident in Fig. 5, where the width is seen to drop by $\sim 25\%$ on changing from a glass cell to one with a half-silvered mirror. Previous studies have determined that the full width at half maximum FWHM $\sim 0.7/(k\ell^*)$ in a glass cell.[16] Thus, elevated surface reflectivity clearly leads to overestimates in ℓ^* determined from CBS measurements. The CBS peaks were well fit by the following expression, derived for the case of no surface reflectivity following Refs. 16,17:

$$\begin{aligned} \gamma_0(\theta) &= \frac{1}{(1+2z_0)}\,\frac{1}{(\alpha+v)^2+u^2}\left\{\frac{1}{v}+\frac{1}{\alpha}[1-\exp(-2\alpha z_0)]\right\} \qquad (5)\\ u &= k\ell^*(1-\cos\theta)\\ v &= (1+\sec\theta)/2\\ \alpha &= k\ell^*|\sin\theta|, \end{aligned}$$

where $z_0 = .7104$ is the location of the trapping plane used in the diffusion model. Very slight cone rounding owing to sample absorption, finite sample size, and finite angular resolution did not significantly impair the fitting procedure. The resulting $k\ell^*$ parameters, indicated by the open symbols in Fig. 6, increase with increasing reflectivity. The parameters for the three ball sizes have been normalized by the average value of $k\ell^*$ as determined below.

Corrections to CBS from surface reflections were first considered through evaluation of the Green function for the case of finite reflectivity in the context of scalar diffusion.[39] Previous evaluation of CBS lineshapes based on diffusion relied on the simplifying assumption of $r = 0$ with Dirichlet boundary conditions accompanied by placement of a trapping plane at a distance $0.7104\ell^*$ outside the sample surface.[11] Surface reflectivity introduces mixed-type boundary conditions, complicating the evaluation of the Green function and necessitating reevaluation of z_0 for each value of r selected. The following model has been proposed for incorporating surface reflectivity into CBS:[39]

$$\gamma_\epsilon(\theta) = \frac{1}{1+2(\epsilon+z_0)} \frac{1}{(\alpha+v)^2+u^2} \left\{ \frac{1}{v} + \frac{1}{\alpha}\left[1 + \frac{\epsilon\alpha - 1}{\epsilon\alpha + 1} \exp(-2\alpha z_0)\right]\right\}, \quad (6)$$

where the reflectivity factor ϵ is related to the average surface reflectivity by $\epsilon = r/(1-r)$. The transport parameters extracted from the experimental CBS peaks using this model, with $z_0 = 0.7104$ throughout, are shown as solid symbols in Fig. 6. Clearly, this model accounts for the surface reflectivity and the transport parameter extracted from each cone remains constant, within the experimental noise, as the reflectivity is increased.

An alternative approach to incorporate surface reflectivity, which circumvents the issue of associated boundary conditions, has been based on the idea of treating reflection as a simple reinjection of light.[40] An important advantage gained is that a closed-form expression emerges based on the $r = 0$ results obtained previously. For CBS, the $r = 0$ cone shape γ_0 is modified in Ref. 40 to:

$$\gamma = (1-r)\gamma_0/(1-r\gamma_0). \quad (7)$$

The solid and dashed curves in Fig. 6 represent the values that would result from ignoring surface reflectivity, according to the two models above, Eqs. (6) and (7). These curves were constructed by evaluating each model at a given reflectivity and then by fitting Eq. (5), extracting the value of $k\ell^*$ that would be assigned were surface reflectivity ignored. Since the three resulting peak shapes are nearly identical, this procedure works surprisingly well. The model of Ref. 39 provides the best agreement with our observations, deviating somewhat at higher reflectivity, possibly owing to the failure of $z_0 = 0.7104$ to accurately represent the boundary condition. Further theoretical progress on this matter has been the subject of several recent papers.[43,44]

Intensity and Polarization Statistics

The speckle pattern formed by the interference of reflected or transmitted waves after propagating in random media can be described by the methods of statistics and is of great interest. Statistics are usually derived by considering waves comprised of random and statistically independent amplitudes leading to Rayleigh (negative exponential) statistics.[45] In the multiple scattering regime, non-Rayleigh statistics have been reported in CBS[10] and in microwave experiments[46,33] with restricted geometry and corrections have been introduced for this geometry.[47] Such studies have focused mainly on scalar waves, but recently the vector nature of light has attracted attention in experimental studies.[48,49] The study of polarization dependent fluctuations of a single speckle spot has led to a new kind of statistics, termed microstatistics,[48] which describes the polarization behavior of the many coherence areas comprising a speckle pattern.

As the polarization vector of the incoming laser beam is rotated, the intensity modulation at any point in the speckle pattern (with no output polarizer) can be

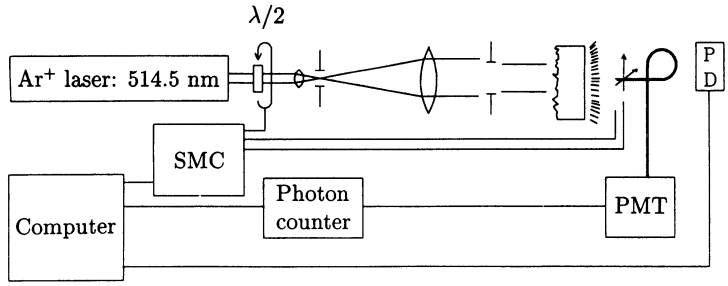

Figure 7. Experimental Set-up for Polarization Microstatistics.
SMC: Stepper motor controller, PD: Photodiode, λ/2: Half-wave plate.

described by

$$I(\theta) = a\cos^2(\theta - \varphi) + b \tag{8}$$

where θ is the polarization angle.[48] For each point in space this modulation can be represented by three parameters: amplitude a, baseline b, and relative phase φ.

Freund *et al.* examined microstatistics in reflection[48] and hypothesized that the main parameter needed to characterize these statistics both in reflection and transmission geometries is the depolarization ratio ρ. For long scattering paths involving point scatters, the additional parameters usually used to describe correlation of the scattered fields can be expressed in terms of the more easily determined ρ. Thus, the microstatistics of different samples, having different mean free pathlengths l^* but identical ρ, have been proposed to be similar, within this approximation.[48]

To test further the suggestion that microstatistics is a universal function of ρ, thin alumina membranes known as Anopore membranes,[‡] stacked to obtain higher ρ values and submerged in water for lower ρ values, have been used to span a wide range of depolarization. These membranes are available with thickness of 60 μm and nearly cylindrical pores of 0.1 μm or 0.2 μm in diameter with $\rho = 0.75$ and 0.90 in air, respectively. Details about the microstructure of these membranes can be obtained from Ref. 50. Extinction mean-free-path lengths were measured, as described in Ref. 25 to be $l = 33$ and 22 ± 1 μm for the above membranes in *water*, respectively.

Our experimental study aimed mainly to obtain microstatistics in transmission for a wide range of ρ values and compare the results for different samples having the same ρ.[51] The experimental set-up used to investigate microstatistics for the scattered field in transmission is shown in Fig. 7. Typically 20 mW of 514.5 nm Ar^+ laser radiation was incident on the sample with an illuminated area having a diameter of 6 mm. Polarization rotation was obtained by stepping a half wave plate with a resolution of 1.8°. The scattered intensity was collected by moving an optical fiber (0.28 m from the sample) to different points in a two dimensional grid, where the average size of a coherence area in the speckle pattern was about 80 times larger than the core of the optical fiber, having a core diameter of 3.7 μm. The dark count rate was at least three orders of magnitude smaller than the signal, detected with a cooled photomultiplier tube using conventional photon counting. Fluctuations in laser intensity were removed by normalizing the photon counter readings with the readings of a photodiode which averaged hundreds of coherence areas in the scattered field.

Individual probability density distributions, the microstatistics, for these parameters were obtained by sampling a large number of coherence areas ($\sim$ 2000–4000).

[‡]Anopore Inorganic Membrane Filter, Anotec Separations Ltd., U.K.

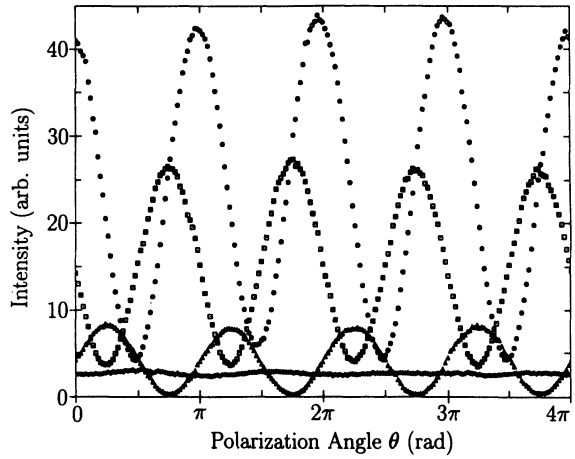

Figure 8. Typical Polarization-Dependent Intensity Modulations for a Sample with Unity ρ. Each curve represents the intensity modulation at a different point in the speckle pattern, demonstrating the range of parameters in Eq. (8).

Representative samples of our raw data are plotted in Fig. 8, where each curve was obtained at a different point in the speckle pattern. Modulation parameters have been normalized by the average intensity, *e.g.*, $\tilde{a} = a/\langle I \rangle$ for convenience.

In Fig. 9, the amplitude probability density distributions are shown for samples with $\rho = 0.044 \pm 0.002$ and $\rho = 1.00 \pm 0.02$, where $\int_0^\infty P_a(\tilde{a})\ d\tilde{a} = 1$. It is seen clearly that as $\rho \to 0$, the amplitude probability density distribution shifts toward the origin with a narrowing range of possible amplitude values. *i.e.*, a decreasing fullwidth for the distribution. For a sample with ρ=0, corresponding to no amplitude modulation, this distribution would be identically zero except at the origin.

A theoretical form for the amplitude probability density distribution for unity ρ has been derived by Freund *et al.*:[48]

$$\langle \tilde{a} \rangle P_a(\tilde{a}) = \frac{3\pi}{2} \tilde{a}^2 K_1(2\tilde{a}) \tag{9}$$

where K_1 is the first-order modified Bessel function. This model, with no adjustable parameters, and the data obtained from the scattered intensity in transmission are in excellent agreement as shown in Fig. 9.

The baseline statistics exhibit an asymptotic form $P_b(\tilde{b}) \sim \exp(-\alpha\tilde{b})$ as shown in Fig. 10. The baseline statistics revert to negative exponential statistics in the non-multiple scattering regime ($\alpha \to 1$ as $\rho \to 0$). The analysis of the asymptotic decay of $P_b(\tilde{b})$ ($0.5 < \tilde{b} < 1.5$) observed for unity ρ shows that $\alpha \approx 3 \pm 0.3$ compared to α=4 reported for the same interval of $\tilde{b}$ in Ref. 48. For large values of $\tilde{b}$, the asymptotic decay parameter for $P_b(\tilde{b})$ was predicted to be 4. This suggests that the theoretical predictions for the asymptotic decay of the baseline statistics might need some revision.

Probability density distributions for the intensity of laser speckle both in transmission and reflection have been obtained with a set-up similar to that used for the microstatistics measurement. As a speckle pattern becomes depolarized, the individual coherence areas become "smeared" and the contrast of the pattern is reduced; the intensity statistics start to deviate from the expected negative exponential statistics but can be retrieved by analyzing the pattern with a polarizer. The intensity statistics for a completely unpolarized speckle obtained from a $\rho = 1$ stack of Anopore membranes

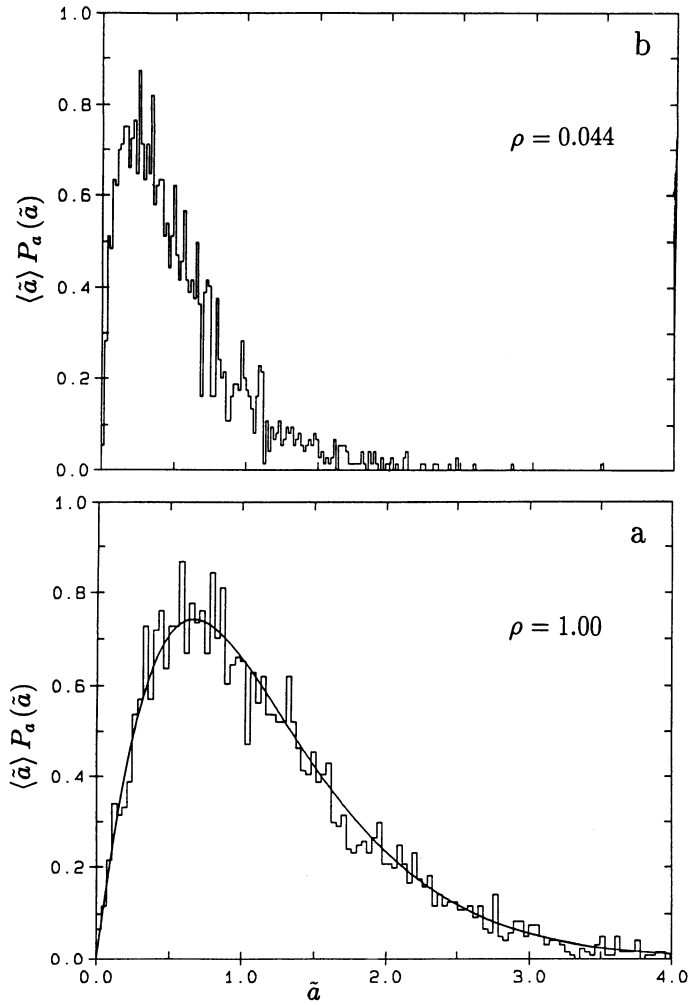

Figure 9. Amplitude Probability Density Distributions.
Curves are shown for (a) $\rho = 1.00$ and (b) $\rho = 0.044$. The solid line in (a) is the theoretical model of Ref. 48. Different bin sizes used for (a) and (b) result from sampling different ranges with a fixed resolution.

shows excellent agreement with the expected result:[52]

$$p_I^{\text{unpol}}(\tilde{I}) = 4\,\tilde{I}\,\exp\left[-2\tilde{I}\right], \tag{10}$$

where $\tilde{I} = I/\langle I \rangle$. After insertion of a polarizer between the scattering system and the optical fiber of the detector (See Fig. 7), intensity distributions were found to be in excellent agreement with negative exponential statistics. The resultant fits of

$$p_I^{\text{pol}}(\tilde{I}) = \exp\left[-(1+\delta)\tilde{I}\right], \tag{11}$$

summarized in Table 1, show that any possible departure from negative exponential statistics for this highly multiple scattering system is limited to less than 1%.

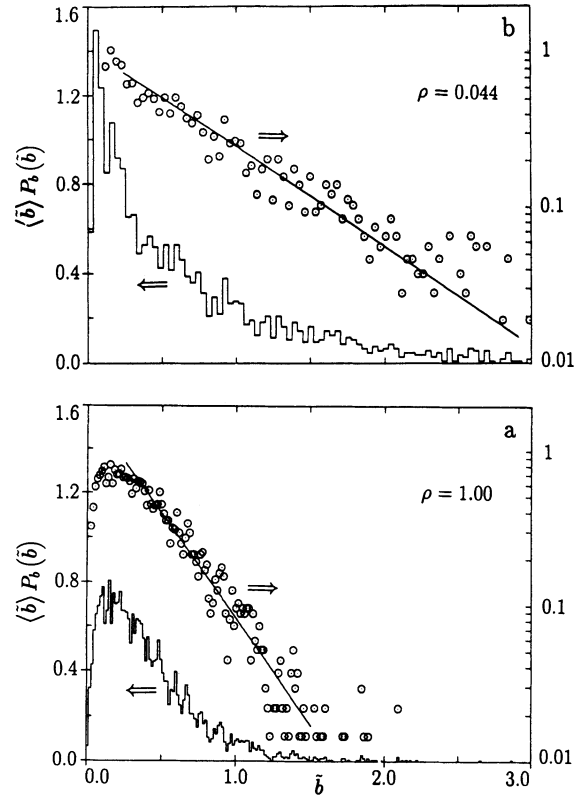

Figure 10. Baseline Probability Density Distributions.
The samples in (a) and (b) are the same as those in Fig. 9. The insets are the log plots of the same functions with fitted exponential decays. The slopes of these lines $(-\alpha)$ are (a) -3.11 and (b) -1.39.

Table 1. Fit Parameters for Negative Exponential Statistics of Polarized Speckle.

# of membranes	analyzer orientation	δ: Eq. (11)
1	$\parallel$, $\perp$	0.003, 0.008†
2	$\parallel$, $\perp$	0.005, 0.006
4	$\parallel$, $\perp$	0.009, 0.003
6	$\parallel$, $\perp$	0.010, 0.007

†The uncertainty in the determination of δ is ± 0.002.

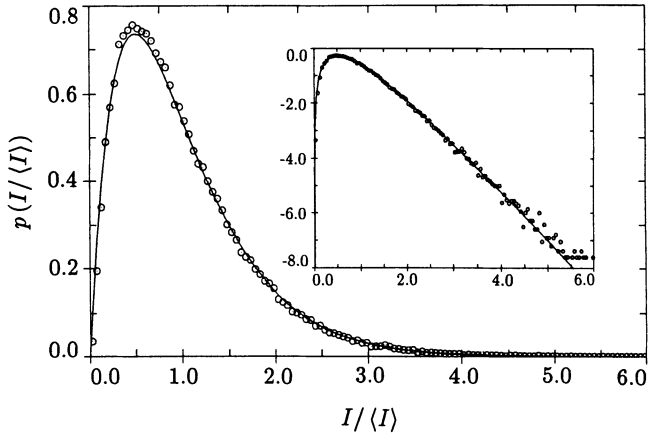

Figure 11. Intensity Statistics for Unpolarized Speckle.

The continuous curve is Eq. (10) (Inset: log plot).

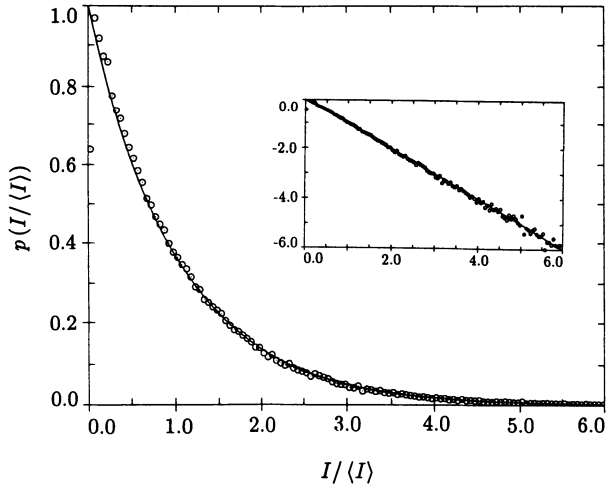

Figure 12. Intensity Statistics for Polarized Speckle.

The continuous curve is Eq. (11) (Inset: log plot).

CONCLUSIONS

Results of several experimental probes of photon transport in highly-multiple-scattering random media have been presented. The effects of spatial correlations among scatterers on the transport mean-free-path lengths obtained from time-resolved transmission of picosecond laser pulses compare favorably to corrections introduced into the Mie formalism via a static structure factor. Transport parameters determined from CBS have been improved significantly by current theoretical models for samples with high surface reflectivity. Finally, a new application of laser speckle to the study of dense random media has been discussed. The recent advances in this field, including improved understanding of photon transport probes, should facilitate the search for localization of light in disordered optical superlattices.

Acknowledgments

We are pleased to acknowledge previous support of this work by the University of Delaware Research Foundation and the Petroleum Research Fund, administered by the American Chemical Society. Current work is supported by Grant DMR9113618 from the National Science Foundation.

References

1. P. Sheng. *Scattering and Localization of Classical Waves in Random Media*, World Scientific, Singapore (1990).
2. A. Z. Genack and N. Garcia, "Observation of photon localization in a three-dimensional disordered system," *Phys. Rev. Lett.* 66:2064 (1991).
3. C. F. Bohren and D. R. Huftman. *Absorption and Scattering of Light by Small Particles*, Wiley, New York (1983).
4. E. N. Economou, "Classical localization," *Physica A* 167:215 (1990).
5. S. John, "Strong localization of photons in certain disordered dielectric superlattices," *Phys. Rev. Lett.* 58:2486 (1987).
6. M. P. van Albada and A. Lagendijk, "Observation of weak localization of light in a random medium," *Phys. Rev. Lett.* 55:2692 (1985).
7. P.-E. Wolf and G. Maret, "Weak localization and coherent backscattering of photons in disordered media," *Phys. Rev. Lett.* 55:2696 (1985).
8. Y. Kuga and A. Ishimaru, "Retroreflectance from a dense distribution of spherical particles," *J. Opt. Soc. Am. A* 1:831 (1984).
9. S. Etemad, R. Thompson, and M. J. Andrejco, "Weak localization of photons: Universal fluctuations and ensemble averaging," *Phys. Rev. Lett.* 57:575 (1986).
10. M. Kaveh, M. Rosenbluh, I. Edrei, and I. Freund, "Weak localization and light scattering from disordered solids," *Phys. Rev. Lett.* 57:2049 (1986).
11. E. Akkermans, P.-E. Wolf, and R. Maynard, "Coherent backscattering of light by disordered media: Analysis of the peak line shape," *Phys. Rev. Lett.* 56:1471 (1986).
12. M. J. Stephen, "Rayleigh scattering and weak localization," *Phys. Rev. Lett.* 56:1809 (1986). M. J. Stephen and G. Cwilich, "Rayleigh scattering and weak localization: Effects of polarization," *Phys. Rev. B* 34:7564 (1986). G. Cwilich and M. J. Stephen, "Rayleigh scattering and weak localization: Geometric effects and fluctuations," *Phys. Rev. B* 35:6517 (1987).
13. F. C. MacKintosh and S. John, "Coherent backscattering of light in the presence of time-reverse-noninvariant and parity-nonconserving media," *Phys. Rev. B* 37:1884 (1988).

14. M. P. van Albada, M. B. van der Mark, and A. Lagendijk, "Observation of weak localization of light in a finite slab: Anisotropy effects and light-path classification," *Phys. Rev. Lett.* 58:361 (1987).
15. S. Etemad, R. Thompson, M. J. Andrejco, S. John, and F. C. MacKintosh, "Weak localization of photons: Termination of coherent random walks by absorption and confined geometry," *Phys. Rev. Lett.* 59:1420 (1987).
16. M. B. van der Mark, M. P. van Albada, and A. Lagendijk, "Light scattering in strongly scattering media: Multiple scattering and weak localization," *Phys. Rev. B* 37:3575 (1988).
17. P. E. Wolf, G. Maret, E. Akkermans, and R. Maynard, "Optical coherent backscattering by random media: An experimental study," *J. Phys. France* 49:63 (1988).
18. E. Akkermans, P.-E. Wolf, R. Maynard, and G. Maret, "Theoretical study of the coherent backscattering of light by disordered media," *J. Phys. France* 49:77 (1988).
19. D. Shmeltzer and M. Kaveh, "Backscattering of electromagnetic waves by a random dielectric medium," *Phys. Rev. A* 35:2251 (1987).
20. K. M. Yoo, K. Arya, G. C. Tang, J. L. Birman, and R. R. Alfano, "Coherent backscattering of a picosecond pulse from a disordered medium: Analysis of the pulse shape in the time domain," *Phys. Rev. A* 39:3728 (1989).
21. R. Vreeker, M. P. van Albada, R. Sprik, and A. Lagendijk, "Femtosecond time-resolved measurements of weak localization of light," *Phys. Lett. A* 132:51 (1988).
22. G. H. Watson, P. A. Fleury, and S. L. McCall, "Search for photon localization in the time domain," *Phys. Rev. Lett.* 58:945 (1987).
23. M. P. van Albada, B. A. van Tiggelen, A. Lagendijk, and A. Tip, "Speed of propagation of classical waves in strongly scattering media," *Phys. Rev. Lett.* 66:3132 (1991).
24. B. A. van Tiggelen, A. Lagendijk, M. P. van Albada, and A. Tip, "Speed of light in random media," *Phys. Rev. B* 45:12233 (1992).
25. P. M. Saulnier, M. P. Zinkin, and G. H. Watson, "Scattering correlation effects on photon transport in dense random media," *Phys. Rev. B* 42:2621 (1990).
26. J. M. Drake and A. Z. Genack, "Observation of nonclassical optical diffusion," *Phy. Rev. Lett.* 63:259 (1989).
27. K. M. Yoo, F. Liu, and R. R. Alfano, "When does the diffusion approximation fail to describe photon transport in random media," *Phys. Rev. Lett.* 64:2647 (1990).
28. A. Z. Genack, "Optical transmission in disordered media," *Phys. Rev. Lett.* 58:2043 (1987).
29. A. Z. Genack and J. M. Drake, "Relationship between optical intensity, fluctuations and pulse propagation in random media," *Europhysics Lett.* 11:331 (1990).
30. G. H. Watson, S. L. McCall, P. A. Fleury, and K. B. Lyons, "Speckle autocorrelation spectroscopy and pulse transmission as probes of photon transport in strongly scattering random media," *Phys. Rev. B* 41:10947 (1990).
31. M. P. van Albada, J. F. de Boer, and A. Lagendijk, "Observation of long-range intensity correlation in the transport of coherent light through a random medium," *Phys. Rev. Lett.* 64:2787 (1990).
32. A. Z. Genack, N. Garcia, and W. Polkosnik, "Long-range intensity correlations in random media," *Phys. Rev. Lett.* 65:2129 (1990).
33. N. Garcia and A. Z. Genack, "Anomalous photon diffusion at the threshold of the Anderson localization transition," *Phys. Rev. Lett.* 66:1850 (1991).
34. K. Clays and A. Persoons, "Photon random walk in the frequency domain," *Opt. Comm.* 92:6 (1992).
35. A. Ishimaru and Y. Kuga, "Attenuation constant of a coherent field in a dense distribution of particles," *J. Opt. Soc. Am.* 72:1317 (1982).
36. M. S. Wertheim, "Exact solution of the Percus-Yevick integral equation for hard spheres," *Phys. Rev. Lett.* 10:321 (1963).

37. L. Tsang, J. A. Kong, and T. Habashy, "Multiple scattering of acoustic waves by random distribution of discrete spherical scatterers with the quasicrystalline and Percus-Yevick approximation," *J. Acoust. Soc. Am.* 71:552 (1982).
38. I. Freund, M. Rosenbluh, and R. Berkovits, "Geometric scaling of the optical memory effect in coherent-wave propagation through random media," *Phys. Rev. B* 39:12403 (1989).
39. A. Lagendijk, R. Vreeker, and P. De Vries, "Influence of internal reflections on diffusive transport in strongly scattering media," *Phys. Lett. A* 136:81 (1989).
40. I. Freund and R. Berkovits, "Surface reflections and optical transport through random media: Coherent backscattering, optical memory effect, frequency, and dynamical correlations," *Phys. Rev. B* 41:496 (1990).
41. J. X. Zhu, D. J. Pine, and D. A. Weitz, "Internal reflection of diffusive light in random media," *Phys. Rev. A* 44:3948 (1991).
42. M. Born and E. Wolf, *Principles of Optics*, Pergammon Press, Oxford (1980).
43. I. Freund and D. Eliyahu, "Surface correlations in multiple-scattering media," *Phys. Rev. A* 45:6133 (1992).
44. I. Freund, "Surface reflections and boundary conditions for diffusive photon transport," *Phys. Rev. A* 45:8854 (1992).
45. J. W. Goodman, "Some fundamental properties of speckle," *J. Opt. Soc. Am.* 66:1145 (1976).
46. N. Garcia and A. Z. Genack, "Crossover to strong intensity correlation for microwave radiation in random media," *Phys. Rev. Lett.* 63:1678 (1989).
47. N. Shnerb and M. Kaveh, "Non-Rayleigh statistics of waves in random systems," *Phys. Rev. B* 43:1279 (1991).
48. I. Freund, M. Kaveh, R. Berkovits, and M. Rosenbluh, "Universal polarization correlations and microstatistics of optical waves in random media," *Phys. Rev. B* 42:2613 (1990).
49. S. M. Cohen, D. Eliyahu, I. Freund and M. Kaveh, "Vector statistics of multiply scattered waves in random systems," *Phys. Rev. A* 43:5748 (1991).
50. R. C. Furneaux, W. R. Rigby and A. P. Davidson, "The formation of controlled-porosity membranes from anodically oxidized aluminum," *Nature* 337:147 (1989).
51. İ. İ Tarhan and G. H. Watson, "Polarization microstatistics of laser speckle," *Phys. Rev. A* 45:6013 (1992).
52. J. W. Goodman, *Statistical Optics*, Wiley-Interscience, New York (1985).

LIGHT PROPAGATION IN POROUS MEDIA

B. R. De[1] and D. Stroud[2]

[1] Chevron Oil Field Research Company
P. O. Box 446
La Habra, CA 90631

[2] Department of Physics
Ohio State University
Columbus, OH 43210

INTRODUCTION

Light propagation in composite media can be studied particularly conveniently in porous media. Such materials have the property that one of the components (the material in the pore space) can be chosen in a wide variety of ways. For example, it can be a suitable liquid, or a mixture of liquids. In addition, the composition can be a function of time. Thus, one can, by varying the composition of the pore space continuously, investigate a large number of different media in a single experiment.

In this paper, we discuss some basic concepts in light propagation in porous media, and illustrate by means of typical experiments how such media can be used conveniently for a range of both fundamental and applied investigations.

BASIC CONSIDERATIONS

In the study of light propagation in porous media, the most convenient quantity to measure is the transmission. Intuitively, one might expect this quantity to be immeasurably small in most porous media. Consider, for example, natural sandstone. This is a mechanical aggregate of irregularly-shaped quartz grains, and has porosity ϕ (i.e., pore volume divided by total volume) typically in the range 10% - 30%. Although the individual grains are transparent, a visual inspection of the composite rock suggests that it does not transmit light. Thus, it appears this most common naturally occurring optical composite is not amenable to study by visible light.

We have demonstrated recently, however, that when a sandstone is saturated with an appropriate fluid, there is a measurable transmission of visible light through macroscopic distances.[1] Our study, which was carried out in the short-wavelength limit ($\lambda << d$, where λ is the wavelength of the probing light and d is the typical grain size), leads to the following conclusions about the transmission T (Unless otherwise specified, the transmission T in this paper is defined as the total emergent power integrated over the exit face of a slab

Photonic Band Gaps and Localization, Edited by
C.M. Soukoulis, Plenum Press, New York, 1993

of porous medium corresponding to a collimated light beam incident normally at the entry face.):

(i). The smaller the contrast Δn between the refractive indices of the grains and the pore-filling fluid, the greater the transmission T.

(ii). The larger the grain size d (up to a certain limit), the greater the transmission T.

(iii). The more ordered the structure of the porous medium, the greater the transmission T.

It was also observed experimentally, and in numerical simulations, that the reflected power R at the entry face (the total power diffusely reflected from the entry face) shows the following correlation:

(iv). The smaller the grain size d or greater the contrast Δn, the greater the reflected power R.

Observation (i) suggests that porous media can be made to transmit visible light by introduction of an index-matching pore fluid. Observation (ii) suggests how the measurement of transmission can serve as a diagnostic probe of typical grain or pore size in a porous medium. Observation (iii) can be further developed through experiments in which a porous medium with an ordered structure can be made disordered by partial saturation with a contrasting pore fluid. Observation (iv) provides a qualitative understanding of the phenomenon of light-guiding in porous media.

DIFFUSIVE PROPAGATION IN POROUS MEDIA

Under certain circumstances, to be identified below, the propagation of light in porous media can be described by the diffusion approximation. Consider a monochromatic point source of light at the origin in a porous medium which is isotropic on a bulk scale. The average speed of light in the medium is $v = c/n$, where c is the velocity of light in free space and n is the appropriate effective refractive index of the medium.

We first assume there is no absorption in the medium. The propagation of light in the medium is then described by a photon "elastic mean free path" ℓ_{el}, defined by the condition that a photon travels a distance ℓ_{el}, on average, before being scattered. It has been shown that, approximately,[1]

$$\ell_{el} = \frac{4\epsilon_0^2 \ \zeta}{\langle(\delta\epsilon)^2\rangle \ln(2k^2\zeta^2)}, \qquad (1)$$

where ζ is an appropriate correlation length in the medium (assumed to be much smaller than the dimensions of the medium and much larger than the wavelength of light), ϵ_0 is the average dielectric constant of the medium, $\delta\epsilon$ is the dielectric contrast between the grain and the pore spaces, and $k = 2\pi\sqrt{\epsilon_0}/\lambda$ is the wave number. We expect ζ to be typically of the order of d. Using this fact, and neglecting logarithmic corrections, we find a simpler form of Eq. (1):

$$\ell_{el} \approx d\left[\frac{n\pi}{2\Delta n}\right]^2. \qquad (2)$$

If we assume isotropic elastic scattering, then after N scatterings a photon will have been scattered, on the average, $N/3$ times in each of the three Cartesian directions. Thus, it will travel a rms distance $r = \ell_{el}\sqrt{N/3}$ in a time $t = N\ell_{el}/v$, or

$$r^2 = Dt \qquad (3)$$

where

$$D = \frac{v\ell_{el}}{3} \qquad (4)$$

represents the *photon diffusion constant.*

We expect to see diffusive behavior for sample thicknesses $L >> \ell_{el}$. In thinner slabs, the photons are expected to propagate ballistically. Another requirement for diffusive behavior is that $\ell_{el} >> \lambda$. If this condition is not satisfied, interference between the electric fields scattered from different scattering centers will influence the transmission. In summary, the conditions for diffusive propagation are

$$L >> \ell_{el} >> \lambda. \qquad (5)$$

Next, consider how this picture is altered by weak absorption. The absorption mean free path ℓ_{abs} is defined by the statement that a photon traveling a distance dx has a probability dx/ℓ_{abs} of being absorbed. Thus, the probability that a photon is not absorbed in distance x is $\exp(-x/\ell_{abs})$. Now, what is the probability that a photon has been absorbed by the time it travels a distance r from the origin? This takes a time r^2/D, so that the total path length traveled is vr^2/D. When this path length equals ℓ_{abs}, the probability that the photon has not been absorbed is 1/e. We call this distance r_{abs}:

$$r_{abs} = \sqrt{D\ell_{abs}/v} \quad . \qquad (6)$$

Unless r_{abs} is less than the sample thickness L, the transmission of light through a porous medium is little affected by absorption.

CONTINUUM VIEW OF LIGHT DIFFUSION: ANALOGIES TO FLUID FLOW

Just as light diffuses more easily in porous media with larger grain sizes, so also fluids flow more readily in porous media with larger grains (and hence, larger pores). This latter dependence can be seen from the following empirical relation for the permeability k_f of a porous medium towards fluid flow:[2]

$$k_f = C_0\frac{\Phi^3}{S_0^2} \qquad (7)$$

where C_0 is an empirical constant, and S_0 is the specific surface area (the internal surface

area per unit bulk volume). Since $S_0 \propto d^{-1}$, the permeability increases with increasing grain size.

The correlation between light transmission and fluid flow has recently been observed in experiments carried out on sandstones of various pore sizes.[1] In the following, we further explore the formal basis of this analogy between light transmission and fluid flow in porous media.

The permeability of a porous medium is defined by the Darcy equation:[3]

$$\vec{J}_f = -\frac{k_f}{\eta}\vec{\nabla}p, \tag{8}$$

where $\vec{J}_f$ is the fluid (mass) current density, η is the fluid viscosity, and p is the pressure.

In a diffuse photon field, the quantity analogous to the pressure is the diffuse intensity (or local energy density) U (see e.g., Ref. 4), which obeys the conservation law

$$\frac{\partial U}{\partial t} = -\vec{\nabla}\cdot\vec{J}_U - \alpha U + Q, \tag{9}$$

where $\vec{J}_U$ is the energy current density, α represents the fraction of the local energy density which is absorbed per unit time, and Q represents any sources or sinks of energy in a given volume. The current density $\vec{J}_U$ may be assumed proportional to the local energy density gradient:

$$\vec{J}_U = -D\vec{\nabla}U, \tag{10}$$

where D is the photon diffusion constant defined earlier. (The minus sign appears because the photons diffuse in the direction of decreasing photon number, or energy, density.) Combining the preceding two equations gives

$$D\nabla^2 U - \alpha U + Q = \frac{\partial U}{\partial t}. \tag{11}$$

We now consider some limiting cases. In the steady state, with no sources or sinks, we get

$$\nabla^2 U - K^2 U = 0. \tag{12}$$

We identify K with the quantity $1/r_{abs}$ defined earlier in Eq. (6), so the above expression becomes

$$K^2 = \frac{\alpha}{D} = \frac{3}{\ell_{el}\ell_{abs}}. \tag{13}$$

In absence of absorption, with no sources or sinks, we get

$$D\nabla^2 U = \frac{\partial U}{\partial t} \tag{14}$$

which is simply the diffusion equation. We can now rewrite Eq. (10) as

$$\vec{J}_U = -\frac{k_{opt}}{n}\vec{\nabla}U. \tag{15}$$

Thus, in analogy with Eq. (8),

$$k_{opt} = c\ell_{el}/3 \tag{16}$$

is the "optical permeability" of the medium. The effective refractive index n is seen to be analogous to the viscosity η.

To explore the connection further, we examine the scaling of the optical permeability k_{opt} with grain size d. We compare this with the analogous scaling of the fluid permeability and the electrical conductivity of a porous medium consisting of non-conducting grains and a conducting pore fluid. Suppose that we expand such a medium isotropically, so that each linear dimension is increased by the same factor C. The electrical conductivity σ is scale-invariant, and remains unaffected by this transformation. The fluid permeability k_f will increase by a factor C^2, since the cross-section of each flow channel is increased by C^2, as is the Poiseuille flow through such a channel for a given pressure gradient and viscosity. Finally, the optical permeability k_{opt} is expected to increase by a factor C, since $k_{opt} \alpha \ell_{el}$ and we expect that $\ell_{el} \alpha C$. Summarizing the discussion, we have

$$\sigma(C) \ \alpha \ C^0 \tag{17}$$

$$k_{opt} \ \alpha \ C^1 \tag{18}$$

$$k_f \ \alpha \ C^2, \tag{19}$$

and hence, for a given class of porous media,

$$k_{opt}^2/k_f = \text{const.} \tag{20}$$

As one example of the above relationship, we may combine Eqs. (2), (7) and (16) to obtain (assuming spherical grains of diameter d)

$$\frac{k_{opt}^2}{k_f} = \frac{4c^2}{C_0\phi^3}\left[\frac{n\pi}{2\Delta n}\right]^4. \tag{21}$$

CONNECTION TO ELECTRICAL CONDUCTIVITY FOR NON-TRANSMISSIVE GRAIN SPACE

In the context of the above discussion, porous media may be divided into two categories: (i) both the grain space and the pore space transmit light (e.g., sandstone, glass bead pack); and (ii) only the pore space transmits light. In the latter class, e.g., in some limestones, the grains appear milky white, indicating perhaps there is considerable scattering within a single grain so light transmission occurs essentially through the pore space.

For such media, the scaling law (Eqs. 17-19) may be made somewhat more concrete by resorting to suitable models. As an example, we may consider the "shrinking tubes"

model,[5] which was originally introduced in an effort to connect the electrical conductivity and the permeability of a porous medium. The model starts from a single cubic multi-dimensional network of pores, all of the same length a and initially of the same radius r_p. Then, at each stage i, a particular pore is selected at random and its radius is shrunk by a factor $x < 1$. After a number of shrinkages, this process leads to a very wide distribution of pore radii - probably consistent with real porous media. On this basis, it has been shown that the electrical conductivity σ and the fluid permeability k_f vary as power laws in the porosity ϕ:

$$\sigma \propto \phi^m \tag{22}$$

$$k_f \propto \phi^{2m} \tag{23}$$

where m is an index related to the shrinkage parameter x by

$$m = \frac{\ln(x^2)}{x^2-1}. \tag{24}$$

A similar argument can be made for the optical permeability. In a medium where the grain is full of internal defects that the photon mean free path inside the grain is very short (but still much larger than the wavelength), essentially all the light trying to enter the grain is reflected diffusely back into the pore space. Assume, for simplicity, the pore space is a regular cubic network of pores, each of length a and radius r_p ($a >> r_p$). Thus, a photon travels a distance of the order of r_p in the pore space before being reflected. Since the reflection is diffuse, the reflected ray may come off at any angle. Since the photon, on reflection, is equally likely to travel in either direction along the pore, there will be required, on average, about $(a/r_p)^2 = N$ reflections for a photon to travel the length a of a pore. The time required to do this is $\tau = (a/r_p)^2 \, r_p/c'$, where c' is the speed of light in the pore. When the photon emerges from this pore, it is equally likely to go in any of six directions. Thus, by the usual random-walk argument, the photon requires $3\nu^2$ time steps τ to travel ν pore lengths away from its starting point in the x direction. Putting all these estimates together, we find the time required to travel a distance $x = \nu a$ is about $t = 3x^2/r_p \, c'$ or $x^2 = Dt$ with $D = c'r_p/3$. Comparing this with Eq. (4), we find that the mean free path of a photon is of the order of r_p.

Hence, the photon conductance (i.e., photon energy current per unit intensity gradient) varies as r_p^3. (The extra factor r_p^2 comes from the cross-section, which converts a conductivity into a conductance.) By the same arguments used in the shrinking-tubes model, this leads to the relation

$$k_{opt} \propto \phi^{3m/2}, \tag{25}$$

and hence to the fact that the ratio

$$R = \frac{k_{opt}^2}{k_f \sigma} \tag{26}$$

is independent of the porosity ϕ. Hence, knowledge of any two of these three quantities can lead to an estimate of the third, as a function of ϕ, at least in this shrinking tubes model.

Finally, we examine the scaling of the optical permeability within the shrinking-tubes model. Suppose we expand each linear dimension of the medium by a factor C. This leaves

the porosity and the electrical conductivity unchanged, but increases k_f by a factor C^2 and k_{opt} by a factor C. Thus, R remains scale-invariant in this process.

CONFINEMENT OF DIFFUSE LIGHT IN HIGH PERMEABILITY CHANNELS

The formal analogy developed above between light transmission and fluid flow in porous media leads directly to the following experimentally testable prediction: In a porous medium made of grains of a given size, if there exists a channel of larger size grains, then light will tend to propagate preferentially through that channel (since it is the higher permeability path).

This prediction is tested qualitatively in the experiment of Figure 1 where, in a continuous medium made of "small" spherical glass beads (refractive index $n_{glass} = 1.52$[6]) there is a layer of an intermediate-sized beads and a layer of large beads. These two layers are interconnected. The largest beads correspond to the highest permeability, the smallest to the lowest permeability. The dissimilar bead layers are simply deposited one above the other, without there being any artificial interfaces. In order to achieve light transmission over the macroscopic distances of the experiment, the entire medium is saturated with water ($n_{water} = 1.33$[6]).

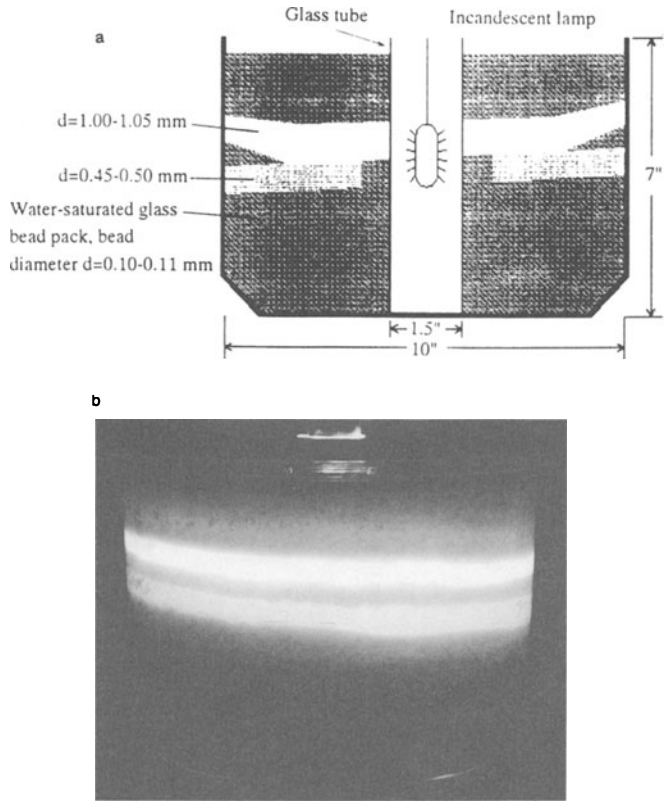

Figure 1. (a) A glass bead "reservoir" containing layers of different bead sizes, and an air-filled central glass "well" into which a light source can be lowered. The bead pack is saturated with water in order to achieve light transmission over macroscopic distances. (b) Photograph of the reservoir illuminated by a central light source (a 750 W tungsten-halogen lamp).

The results of the experiment [Figure 1(b)] illustrate the analogy: the maximum light transmission occurs through the layer with the largest bead size (the highest permeability layer). A somewhat weaker transmission occurs through the layer with the intermediate bead size (the intermediate permeability layer). Very little transmission occurs through the medium with the smallest beads, or the lowest permeability medium. Note how the light passes from the high permeability channel through to the intermediate permeability channel. (There is no direct path to the latter channel from the source.)

Apart from the analogy to fluid flow, the above experiment also illustrates the phenomenon of light-guiding in a porous medium. This will be discussed more generally in a following section.

MORPHOLOGICAL VIEW OF LIGHT DIFFUSION: ORDER-DISORDER TRANSITIONS

It was mentioned earlier that, in the short-wavelength limit, the transmission T is larger through an ordered medium than through a disordered medium, all other things being the same. This behavior is seen in transmission through close-packed aggregates of spherical glass beads and though such packs of irregularly-shaped quartz grains of comparable size. The former exhibit a far greater transmission. We now describe numerical simulations and experiments that further explore the connection between short-wavelength transmission of light through a porous medium, and the degree of order in the medium.

The degree of order in a porous medium may be discussed through the sketches in Figure 2. Figure 2(a) shows a periodic arrangement of spherical glass beads, and represents the highest degree of order. In Figure 2(b), this state is slightly disturbed, creating some disorder. Figure 2(c) shows a dense pack of irregularly-shaped quartz grains, and represents a structure of yet greater disorder.

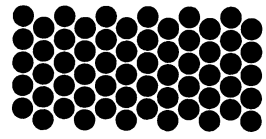

(a) Periodic Structure

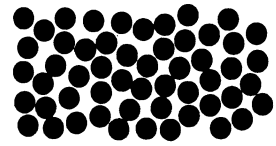

(b) Disordered Periodic Structure

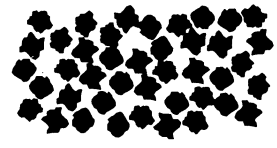

(c) Random Structure

Figure 2. Illustration of ordered and disordered structures in porous media.

The ideal arrangement in Figure 2(a) is difficult to materialize in practice. However, the difference in transmission between the cases in Figures 2(a) and 2(b) can be studied by means of numerical simulation calculations such as described in Ref. 1. It is found that the transmission T for the case (b) is higher. Thus, near perfect order, transmission may actually increase with the introduction of disorder, depending on how the disorder is created.

The difference between the cases in Figures 2(b) and 2(c) can be studied conveniently through experiments, such as shown in Figure 3, which also serve to investigate the effect of *time-dependent* disorder in each individual medium.

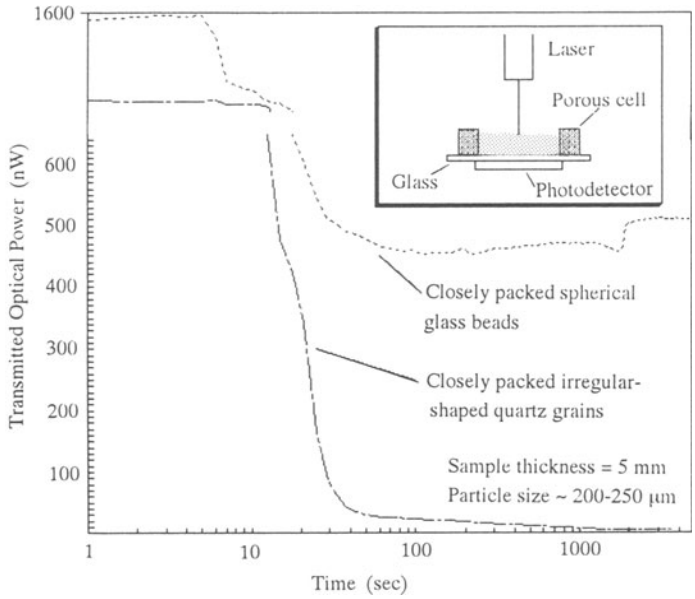

Figure 3. Time-traces of the transmission through toluene-saturated glass bead and sand grain packs, as they dry in open air. The experiment proceeds from the fully saturated state to the fully dry state. Inset: The experimental setup.

We now describe these experiments in detail. A 5 mm thick close-packed layer of glass beads (bead diameter = 250-300 μm) is kept fully immersed in toluene ($n_{\text{toluene}} = 1.49$[6]) in a compartment with porous wall. The transmission T of a He-Ne laser beam (red light; $\lambda = 0.63$ μm) through the layer is monitored as a function of time, as the bead pack dries through natural evaporation. The behavior of the transmission can be understood through the following characteristic stages. During the first stage, the bulk of the liquid is drawn into the porous cell wall, leaving the remaining liquid as a film adhering to the bead surfaces. The transmitted power decreases rapidly during this stage, as the contrast between the refractive indices of the beads and the pore space grows larger. In the next stage, the pore space dries more or less uniformly throughout the bead pack, and the transmission decreases monotonically but more slowly. We attribute the reduced transmission to an increase in disorder in the form of air/liquid interfaces in the pore space which contribute a great deal of surface area from which to scatter light. During the final stage, the transmission increases and then levels off. We attribute this increase to the gradual disappearance of the air/liquid interfaces (which, of course, must be absent when evaporation is complete), and hence to a transition from a disordered state back to a somewhat more ordered state.

Figure 3 also shows the results of the same experiment carried out in a close pack of irregularly-shaped sand grains (made of mineral quartz, $n_{quartz} = 1.55$[6]) with a size range and refractive index similar to the glass beads. Since the sand pack, unlike the bead pack, is highly disordered to begin with, the removal of a small additional disorder (in the form of air/liquid interfaces) at the last stage does not appreciably increase the transmission. Hence, in contrast to the glass bead pack, the transmission through the sand pack decreases monotonically with time to its fully dry value. It is also noted that in the fully-saturated or fully-dry state, the glass bead pack has a far greater transmission than the sand pack.

In summary, of the three configurations in Figure 2, the slightly disordered configuration has the highest value of the transmission T, and the random configuration has the lowest value. It is possible to cause a porous medium to pass to states of progressively increasing or decreasing order through the gradual introduction or removal of a pore fluid.

DEPENDENCE OF TRANSMISSION ON SAMPLE THICKNESS: STUDY OF OPACITY REGIMES

In a porous medium where neither the grain space nor the pore space absorbs light, the opacity is generally due to light diffusion, which is dependent on the pore size-scale r_p. Under this condition, the transmission T has a dependence on the thickness L of the sample slab. However, when the pore size r_p approaches the wavelength of light in a disordered medium, there is expected to arise another type of opacity: the localization opacity (see e.g., Ref. 7). In a simplified description of incipient localization of light (or of photons), we may view the pores and the grains as random waveguides near cutoff frequency and random resonators. Interference of light waves in this structure causes photons to be trapped in certain locations for a finite time. Since these photons are nearly prevented from reaching the detector, they give rise to an opacity. The waveguide effect requires the refractive index contrast Δn between the pore space and the grain space be large (a ratio of perhaps 2 to 3 between the two refractive indices for localization to occur[7]). When localization opacity is superimposed on diffusion, we expect the dependence of T on L to change. For this, and other reasons, it is useful to study the dependence of transmission on the sample thickness.

For this experiment we look for a porous medium with pore sizes comparable to the wavelength of visible light. Such a medium is natural chalk, or porous calcite. Calcite is optically birefringent,[8] with principal indices of refraction 1.49 and 1.67. Thus, for air-filled pores, the refractive index ratio is about 1.5 which may or may not be large enough to cause localization. Since natural chalk is often heterogeneous on a millimeter scale, and may contain impurities, a preferable alternative for this experiment is the familiar chalkboard chalk [Figure 4(a)]. We note that the pore sizes here bracket the wavelength of red light, 0.63 μm.

Figure 4(b) shows the dependence of the transmission T (normalized to the incident optical power T_0 ; T_0 = 10 mW) on the sample thickness L for dry chalk. The graph indicates a dependence of the type $T \alpha T_0 \exp(-\chi L)$, where the slope χ of the graph is an opacity-like quantity. This is indicative most likely of a single source of opacity (i.e., diffusive opacity) in the range of the measurement. The lowest power measured is 1.0 nW, below which we reach the noise floor of the measurement setup.

For comparison, we also show in Figure 4(b) the results for chalk samples soaked (i.e., nearly fully saturated) in acetone ($n_{acetone} = 1.37$[6]). The exponential dependence is again observed. As expected, the transmission is higher, and χ is lower.

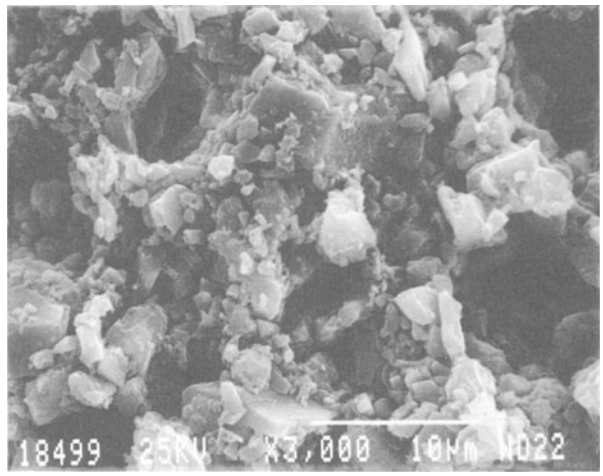

a

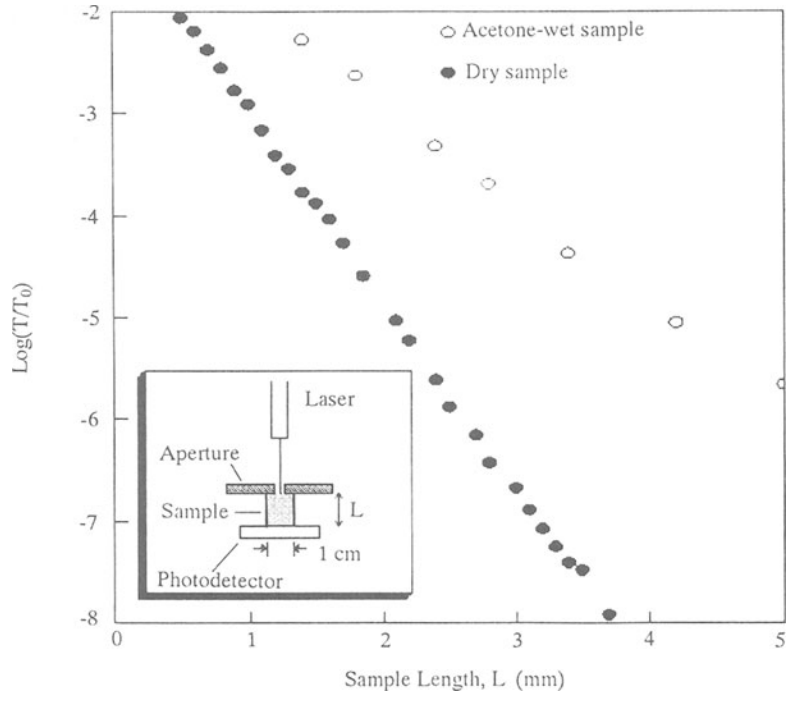

b

Figure 4. (a) SEM photograph of the pore structure of chalkboard chalk, with 10 μm scale shown. (b) The transmission as a function of the sample length for dry and acetone-wet samples of chalk. Inset: The experimental setup.

LIGHT-GUIDING IN POROUS MEDIA

The earlier observation of light confinement in high permeability channels is in fact a result of a "reflection" of diffuse light at the interface between two porous media with different values of the photon mean free path ℓ_{el}. As is evident from Eq. (2), this difference can arise due either to a difference in the pore/grain sizes (as in the above example) or to a difference in the pore fluid (as in the example below). Before describing an experiment that provides evidence for the latter case, we present a simple qualitative argument to support the concept of light-guiding in a porous medium.

We consider an imaginary surface dividing two porous media with mean free paths ℓ_{el1} and ℓ_{el2}, with $\ell_{el1} > \ell_{el2}$. Then, by observation (iv) mentioned at the outset, a photon starting at this surface and traveling into Medium 2 has a greater probability of being reflected into Medium 1 than *vice versa*. The overall effect of this is to cause confinement of light in Medium 1. A formal theory of light-guiding in porous media can be developed from these initial considerations.

Figure 5 shows the experiment supporting the idea of light-guiding in an initially homogeneous porous medium where a difference in ℓ_{el} is created by having different pore fluids. The sample is again chalkboard chalk, but now a portion T' of the transmitted light T is observed through an aperture. Initially, the sample is fully saturated with acetone. It is then allowed to dry by natural evaporation. The top and the bottom faces of the sample are sealed against evaporation with transparent seals, so a cylindrical drying front gradually moves towards the axis of the sample. The mean free path ℓ_{el} is longer inside the cylindrical front where the pores are acetone-filled, than outside, where the pores are air-filled [Cf. Eq. 2].

When the sample length L is small (here 4 mm) compared to the width (1 cm), the light passing through the aperture is not much affected by the progression of the drying front. Thus, the dominant effect observed is the reduction of T' due to the drying of the central parts of the sample. When L is comparable to the width (here L = 8 mm), the light intercepted by the aperture is dependent on the location of the drying front. Initially, as soon as the skin layer of liquid dries, there is a better index-matching to the free space so that more light escapes and T' decreases. Then, as the drying front moves inward, the light is guided more and more in narrower cylinders, so that T' increases. Eventually, the drying of the interior parts of the sample causes T' to decrease to its fully-dry value. This experiment thus provides further evidence of light-guiding in porous media.

SPEED OF LIGHT IN POROUS MEDIA

The distribution of transmission times of various ray paths through porous media has been studied through numerical simulations,[1] examples of which are shown in Figure 6. The figure shows the distribution of transmission times for photons incident at the entry face at the same instant of time. These examples are for a pack of quartz grains, 2.6 mm thick, of various grain sizes, and saturated with various fluids.

Figure 6 suggests some criteria for defining the "speed" of light: the first arrival time, the peak power, the steepest slope of the leading edge, etc. Clearly, as Δn decreases, all these definitions converge. For a given pore fluid, the smaller the grain size d, the smaller the speed of light. Referring back to observation (i) mentioned at the outset, we find that smaller the speed of light, the smaller the transmission T. In this way, the speed of light and the transmission in porous media are linked. A detailed analysis of the speed of light in random media may be found in Ref. 9.

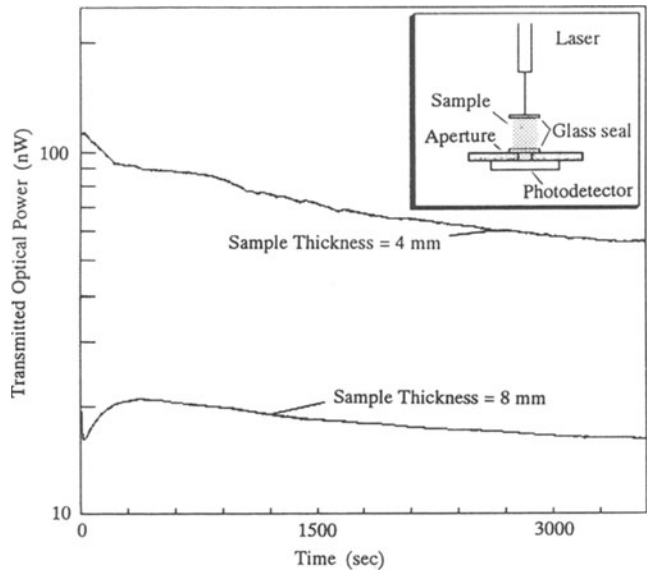

Figure 5. Time-traces of the transmission through acetone-saturated samples of chalk as they dry from the fully saturated state to the fully dry state. Inset: The experimental setup.

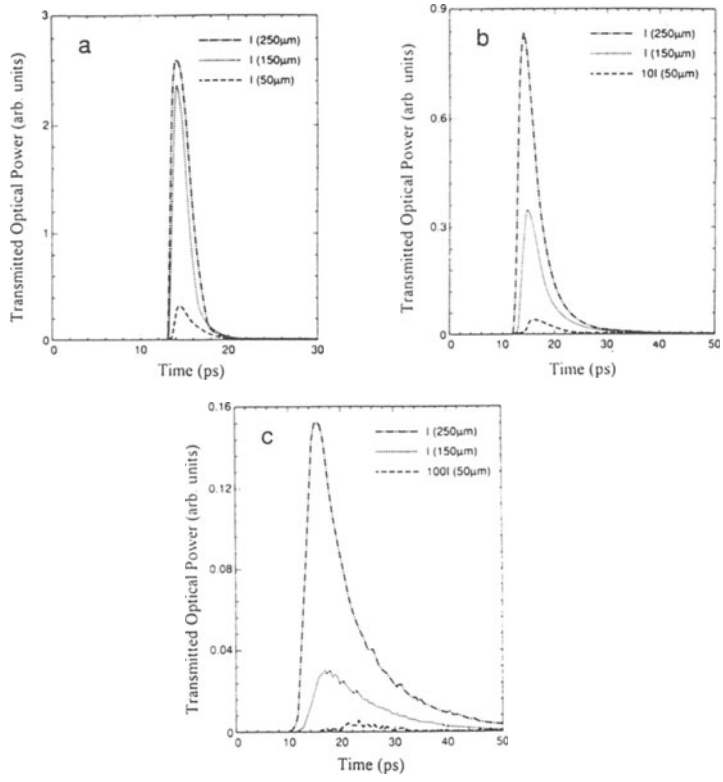

Figure 6. Numerical simulation of the distribution of the transmission times for quartz grain packs of various grain sizes (indicated in the figures), saturated with (a) toluene; (b) water; and (c) air. Normalization is such that for each saturating fluid, the area under a curve equals T/T_0 (T_0 = incident power). The absolute normalization is arbitrary but is the same for each of the three sets of curves (from Ref. 1).

REMARKS

We have discussed a variety of concepts and related experiments in light propagation in porous media. These are intended to serve as a general basis for the development of more detailed and more sophisticated theories and experimental designs. Future investigations in this field may also benefit from multi-wavelength and time-domain studies.

Acknowledgments

This work was supported in part by Chevron Oil Field Research Company and in part by NSF Grant No. DMR 90-20994.

REFERENCES

1. B. R. De, I. H. H. Zabel, D. Stroud and M. A. Nelson, Optical analog of the permeability of sandstones, *Phys. Rev. B* 45:196 (1992).
2. C. Carman. *Flow of Gases Through Porous Media*, Academic Press, New York (1956).
3. A. E. Scheidegger. *The Physics of Flow through Porous Media*, University of Toronto Press, Toronto (1974).
4. A. Ishimaru. *Wave Propagation and Scattering in Random Media*, Academic Press, New York (1978), Vol. 2.
5. P. Z. Wong, J. Koplik, and J. P. Tomanic, Conductivity and permeability of rocks, *Phys. Rev. B* 30:6606 (1984).
6. *Handbook of Chemistry and Physics*, 53rd ed., edited by R. C. Weast (Chemical Rubber Co., Cleveland, 1972).
7. P. W. Anderson, The question of classical localization: A theory of white paint?, *Phil. Mag.* B 52:505 (1985).
8. W. A. Deer, R. A. Howie, and J. Zussman. *An Introduction to the Rock-forming Minerals*, Longman, London (1966).
9. B. A. van Tiggelen, A. Lagendijk, M. P. van Albada, and A. Tip, Speed of light in random media, *Phys. Rev. B* 45:12233 (1992).

PRELIMINARY EXPERIMENTS ON THE TRANSMISSION OF LIGHT THROUGH NON-LINEAR DISORDERED MEDIA

Johannes F. de Boer[a], Rudolf Sprik[a], Ad Lagendijk[a,b]
and Shechao Feng[c]

(a) Van der Waals-Zeeman Laboratorium, University of Amsterdam
Valckenierstraat 65, 1018 XE Amsterdam, The Netherlands
(b) FOM-Institute for Atomic and Molecular Physics
Kruislaan 407, 1089 SJ Amsterdam, The Netherlands
(c) Department of Physics, University of California
Los Angeles, California 90024, USA

INTRODUCTION

Since the discovery of enhanced backscatter (weak localization) [1], light scattering in disordered media has drawn a lot of attention. In the pursuit of strong localization, a lot of interesting phenomena were discovered, such as fluctuations on the transmission of light through disordered slabs [2–7]. Recently, a new class of disordered media have come into focus, "non-linear disordered media." By non-linear in this context, a non-linear response of the constituting particles of the disordered medium to the electro-magnetic field is meant, e.g., particles with a second-harmonic susceptibility. Agranovich and Kravtsov predicted interesting phenomena that can be observed in non-linear disordered media [8]. They stated that enhanced backscatter can also be observed in the second-harmonic light generated in a non-linear disordered medium, although this is not yet experimentally verified.

Apart from enhanced backscatter, interference of multiple scattered waves manifests itself in the occurrence of fluctuations on the transmission and reflection of light in quenched disordered media. We present preliminary experimental results of the measurement of the fluctuations on the transmission of second-harmonic light generated *inside* the medium as a function of incoming and outgoing angles. There exists a short-range correlation in the fluctuating second-harmonic transmission patterns. As a non-linear medium, we used a thin layer of a non-linear crystal in a powder form ($LiNbO_3$).

Photonic Band Gaps and Localization, Edited by
C.M. Soukoulis, Plenum Press, New York, 1993

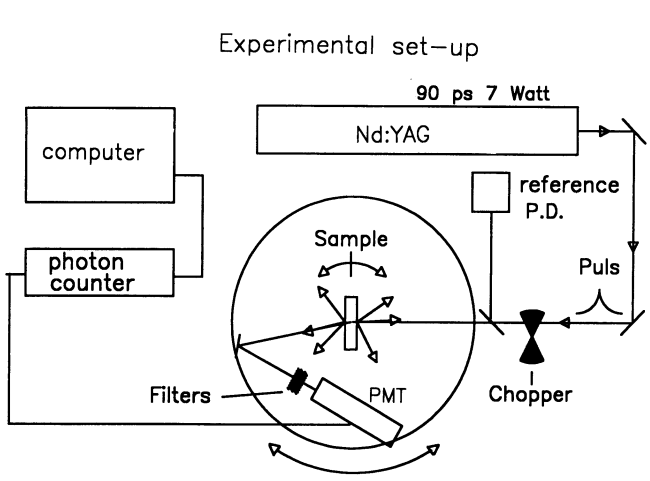

Figure 1. Experimental set up for measurement of the short-range correlation function. The fluctuating signal is recorded as a function of the angle rotation of the sample. Speckle is measured by rotating the PMT around the sample.

THEORY

An important theoretical paper on correlations in the transmission of light through disordered media was written by Feng *et al.* [4]. We briefly summarize the result. The volume occupied by the random sample is considered to be a waveguide, supporting N modes. The sample will mutually couple these modes in a random manner, and intensity transmission coefficients $T_{\alpha\beta}$ give the fraction of the power in the incoming mode α that is coupled into the outgoing mode β. For the correlator $C_{\alpha\beta\alpha'\beta'} \equiv \langle \delta T_{\alpha\beta} \delta T_{\alpha'\beta'} \rangle$ (triangular brackets stand for averaging over the disorder) Feng *et al.* [4] obtained the expression $C = C^{(1)} + C^{(2)} + C^{(3)}$ with

$$
\begin{aligned}
C^{(1)}_{\alpha\beta\alpha'\beta'} &\equiv D_1 \langle T_{\alpha\beta} \rangle \langle T_{\alpha'\beta'} \rangle \delta_{\Delta \mathbf{q}_\alpha, \Delta \mathbf{q}_\beta} F_1(\Delta \mathbf{q}_\alpha L), \\
C^{(2)}_{\alpha\beta\alpha'\beta'} &\equiv D_2 g^{-1} \langle T_{\alpha\beta} \rangle \langle T_{\alpha'\beta'} \rangle [F_2(\Delta \mathbf{q}_\alpha L) + F_2(\Delta \mathbf{q}_\beta L)], \\
C^{(3)}_{\alpha\beta\alpha'\beta'} &\equiv D_3 g^{-2} \langle T_{\alpha\beta} \rangle \langle T_{\alpha'\beta'} \rangle,
\end{aligned}
$$

where the D's are constants of order unity and where F_1 and F_2 are form functions. The magnitude of the $C^{(1)}$-part is of order 1 if $\alpha = \alpha'$ *and* $\beta = \beta'$, and decays exponentially with increasing $\Delta \mathbf{q} \equiv \mathbf{q}_\alpha - \mathbf{q}_{\alpha'} = \mathbf{q}_\beta - \mathbf{q}_{\beta'}$ ("memory effect"), and is zero if $\Delta \mathbf{q}_\alpha \neq \Delta \mathbf{q}_\beta$, with $\mathbf{q}$ the transverse wave vector. The magnitude of the $C^{(2)}$-part is of order g^{-1} (with g the dimensionless conductivity $N\ell/L$, where ℓ is the mean-free path and L the sample-thickness) if *either* $\Delta \mathbf{q}_\alpha$ *or* $\Delta \mathbf{q}_\beta = 0$, and shows the power-law decay with increasing $\Delta \mathbf{q}$. Finally, the magnitude of the $C^{(3)}$-part is of order g^{-2} and does not depend on either $\Delta \mathbf{q}_\alpha$ or $\Delta \mathbf{q}_\beta$. The results predict that if, in an experiment on a sample with $g \gg 1$, just one incoming mode is excited, the $C^{(1)}$ and the $C^{(2)}$ correlations will be present in the signal of just one outgoing mode and of the total transmission, respectively. If all incoming modes are excited by mutually uncorrelated signals and the total transmission is measured for different sample-realizations (we then have a situation analogous to that in an electronic conduction experiment) the $C^{(3)}$-term (Universal Conductance Fluctuations) would be found.

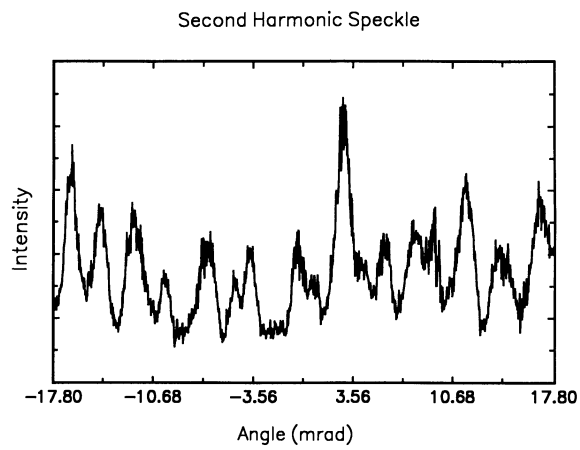

Figure 2. Fluctuating transmitted intensity (speckle) of second-harmonic light as a function of angle of rotation around the sample.

The short-range correlation function $C^{(1)}$ has been studied by varying the angle of incidence [5] and by varying the wave length [6,7], and good agreement between theory and experiment was found. In the present experiment, the short-range correlation is studied for second harmonic light generated by the scattering particles and the result is compared with the correlation that exists for linear scattering particles.

EXPERIMENT

The experimental set-up is shown schematically in Fig. (1). A Spectra Physics 3800 Nd:YAG laser was used, giving 90 ps. pulses at 1064 nm. The beam was chopped and focused to 560 μm on the sample. The sample was prepared by suspending $LiNbO_3$ powder, obtained through milling a single crystal, in chloroform. Particle sizes were between 0.1 and 5 μm. The suspension was then spread on a transparent substrate, and after evaporation of the chloroform, its thickness was determined microscopically. A reference beam was split off and doubled in a $LiNbO_3$ crystal. The infra-red contributions to the second-harmonic signals were blocked by absorption filters. Second-harmonic signals were divided by the reference signal to correct for power fluctuations on the fundamental beam. A photon counter was used to detect the second-harmonic light, giving about 25 cps. At each point the counts were accumulated for 5 sec., using digital lock-in detection to eliminate any contributions of ambient light to the signal. The speckle patterns for the fundamental wave length were measured after replacing the photon counter by a photodiode. First, the existence of speckle in the second-harmonic and fundamental light was verified by rotating a detector around the sample while measuring the transmitted intensity. Then, the fluctuating intensity in transmission was recorded as a function of the angle of rotation of the sample. The sample was rotated over an angle of 180 mrad for each scan. From these scans the short-range correlation in transmission was calculated.

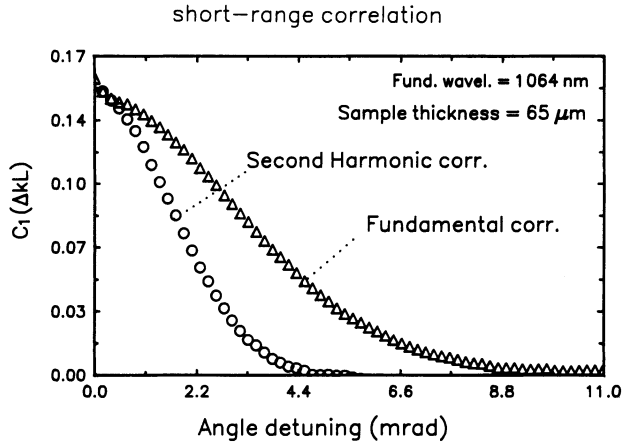

Figure 3. ○: Measured correlation function of second harmonic light.
△: Measured correlation function of fundamental light.

CONCLUSION

The existence of speckle in the second harmonic light is shown in Fig. (2) The measured correlation functions for both the second harmonic and fundamental light are shown in Fig. (3) for the same sample of 65 μm thickness. The shown correlation functions are averages of three scans. The correlation function for the fundamental wave length is scaled to make the top of the fundamental and the second harmonic correlation function coincide.

In conclusion, we have verified the existence of speckle in the second harmonic light generated in a disordered medium with a non-linear susceptibility. Secondly, we find that the halfwidth of the short-range correlation function in transmission for the second harmonic light is half the halfwidth of the fundamental light. Further experiments will have to confirm these preliminary results.

ACKNOWLEDGMENT

The authors acknowledge M.P. van Albada, P.N. den Outer, M. van Hoften and Th.M. Nieuwenhuizen for discussions, Ad Wijkstra and F. de Leeuw for technical support, and B. Nesti of Inrad for supplying the $LiNbO_3$ crystals. This work is supported in part by the Stichting voor Fundamenteel Onderzoek der Materie (FOM), which is a part of the Nederlandse Organisatie voor Wetenschappelijk Onderzoek (NWO).

References

[1] M.P. van Albada and A. Lagendijk, Phys. Rev. Lett. 55, 2692 (1985); P.E. Wolf and G. Maret, Phys. Rev. Lett. 55, 2696 (1985).

[2] For recent reviews, see *Classical Wave Localization*, ed. P. Sheng (World Scientific, Singapore, 1990); *Analogies in Optics and Micro Electronics*, ed. W. van Haeringen and D. Lenstra (Kluwer, 1990).

[3] N. Garcia and A.Z. Genack, Phys. Rev. Lett. **63**, 1678 (1989).

[4] S. Feng, C. Kane, P.A. Lee, and A.D. Stone, Phys. Rev. Lett. **61**, 834 (1988).

[5] I. Freund, M. Rosenbluh, and S. Feng, Phys. Rev. Lett. **61**, 2328 (1988).

[6] A. Z. Genack and J. M. Drake, Europhys. Lett. **11**, 331 (1990)

[7] M.P. van Albada, J.F. de Boer and A. Lagendijk, Phys. Rev. Lett. **64**, 2787 (1990).

[8] V.M. Agranovich and V.E. Kravtsov, Phys. Lett. A **131**, 378 (1988).

PHOTON DIFFUSION AND INTERNAL REFLECTIVITY

A.A Lisyansky, J.H. Li, D. Livdan, N. Garcia, T.D. Cheung, and A.Z. Genack
Department of Physics, Queens College of CUNY, Flushing, NY 11367

INTRODUCTION

The particle diffusion model is widely used to describe the propagation of waves in multiply scattering random media [1-3]. It has been used to calculate the functional form of key aspects of electromagnetic propagation such as surface intensity profiles [2], which determine the shape of the coherent backscattering cone [4,5], angular correlation functions [6,7] the thickness dependence [8] and temporal distribution of reflection [9], and transmission [10], spatial [11-15], spectral [8,11-16], and temporal [17] correlation functions. Though qualitative agreement is obtained between experiment and theory, these observations do not give quantitative values for spatial transport parameters such as the transport mean free path ℓ, the distance in which the direction of propagation is randomized inside the medium, or for the coherent penetration depth z_p [3], the distance from the surface at which the placement of a source of diffusive flux faithfully mimics the randomization of the coherent incident beam. Recently it has been realized that in order to achieve good agreement between theory and experiment and to extract microscopic scattering parameters from measurements, it is necessary to include reflection at the boundaries in the analysis of the experiment [18-21]. In the present study we perform experiments which critically test the photon diffusion theory. We show, that with proper choice of boundary conditions, diffusion theory is in excellent agreement with measurements of the microwave intensity distribution inside the sample and of the optical intensity profile on the surface of the sample. We also show that internal reflection can dramatically change long-range spatial and spectral intensity-intensity correlation functions.

Photonic Band Gaps and Localization, Edited by
C.M. Soukoulis, Plenum Press, New York, 1993

In Sec. 2 we present calculations of the intensity distribution as a function of transverse, ρ, and longitudinal, z, displacements $I(\rho,z)$ using diffusion theory and show how internal reflectivity can be incorporated in these calculations. The effect of internal reflection on the spatial and spectral intensity-intensity correlation functions is considered in Sec. 3. Comparison of optical measurements of $I(\rho,z)$ and total transmission $T(L)$ for a point source and of microwave measurements of $I(z)$ and $T(L)$ for a plane wave source with the predictions of the theory developed in Sec. 2 are reported in Secs. 4 and 5, respectively. The excellent agreement between experiment and theory allows us to determine z_p and ℓ. From measurements of the diffusion coefficient, we are able to determine the transport velocity v.

INTENSITY DISTRIBUTION IN THE PRESENCE OF INTERNAL REFLECTION. THEORETICAL RESULTS

We first consider the propagation of the electromagnetic radiation through a slab of a random medium of infinite extent in the x, y directions situated between $0 < z < L$. We assume that we are in the weak scattering regime in which $k\ell \gg 1$, where k is the magnitude of the photon wave vector, so that wave interference does not influence average transport. The intensity distribution inside a slab obeys the diffusion equation,

$$\nabla^2 I(\boldsymbol{r}) - \alpha^2 I(\boldsymbol{r}) = -\frac{1}{D} Q(\boldsymbol{r}), \tag{1}$$

where α is the absorption coefficient, D is the diffusion coefficient and $Q(\boldsymbol{r})$ is a source function. We replace the incoming coherent flux by a source of diffusive radiation at a plane $z = z_p$, with a strength equal to the incident flux. In this case, the source function has cylindrical symmetry with respect to the z-axis and can be written as $Q(\boldsymbol{r}) = Q(\rho)\delta(z-z_p)$. Since the source is assumed to lie inside the sample, the only flux incident from a boundary towards the interior of the slab is the reflected part of the outgoing flux. This results in the following boundary conditions for Eq. (1) [20,21],

$$\left[\frac{1}{z_{0l}} I(\boldsymbol{r}) - \frac{d}{dz} I(\boldsymbol{r})\right]_{z=0^+} = 0; \qquad \left[\frac{1}{z_{0r}} I(\boldsymbol{r}) + \frac{d}{dz} I(\boldsymbol{r})\right]_{z=L^-} = 0, \tag{2}$$

where $z_{0l,r} = 2\ell(1+R_{l,r})/3(1-R_{l,r})$ and R_l and R_r are the reflection coefficients of the left (input) and right (output) boundaries, respectively.

Solving Eq. (1) with the boundary conditions, (2) we obtain,

$$I(\rho, z) = \int_0^\infty \frac{d\lambda\,\lambda}{k(\lambda)} J_0(\lambda\rho) \int_0^\infty dx\, x J_0(\lambda x)\, Q(x,z) \left\{ \left[1 + z_{0l} k(\lambda) z_{0r} k(\lambda)\right] \sinh[k(\lambda)L] \right.$$

$$\left. + \left[z_{0l} k(\lambda) + z_{0r} k(\lambda)\right] \cosh[k(\lambda)L] \right\}^{-1} \begin{cases} P_\lambda^{(l)}(z)\, P_\lambda^{(r)}(L - z_p); & z < z_p \\ P_\lambda^{(l)}(z_p)\, P_\lambda^{(r)}(L - z). & z > z_p \end{cases} \tag{3}$$

Here $k^2(\lambda) = \lambda^2 + \alpha^2$ and $P_\lambda^{(l,\,r)}(x) = \sinh[k(\lambda)x] + \alpha z_{0l,\,r} \cosh[k(\lambda)x]$ and $J_0(x)$ is the Bessel function of zero order.

For the case of coherent flux focused on the slab surface, $Q(\rho) = q\delta(\rho)/\rho$, where q is a constant, whereas for a plane wave incident on a slab, $Q(\rho) = q$. In the latter case we obtain a simplified expression for the intensity distribution,

$$I(z) = \frac{q}{\alpha D} \left[\left(1 + \alpha^2 z_{0l} z_{0r}\right) \sinh(\alpha L) + \alpha (z_{0l} + z_{0r}) \cosh(\alpha L) \right]^{-1}$$

$$\times \begin{cases} P_\lambda^{(l)}(z) P_\lambda^{(r)}(L - z_p); & z < z_p \\ P_\lambda^{(l)}(z_p) P_\lambda^{(r)}(L - z). & z > z_p \end{cases} \tag{4}$$

Using the relationship between the intensity and the flux of diffusing photons, and the boundary conditions given by Eqs. (2), the normalized transmitted flux can be expressed as,

$$T(L) = \frac{J_{transmitted}(L)}{J_{incident}} = \frac{1 - R}{q} J_+(L^-) = \frac{I D z_{0r}}{q}. \tag{5}$$

If absorption is weak, $\alpha L \ll 1$ and $\alpha z_{0l,r} \ll 1$, we have,

$$T(L) = (z_{0r} + z_p)/(L + z_{0l} + z_{0r}). \tag{6}$$

In the case of a plane wave incident on a weakly absorbing slab, $z_{0l,r}$ corresponds to the length beyond the boundary at which the intensity extrapolates to zero. In the absence of absorption and reflection at the boundaries, diffusion theory gives $z_{0l,r} = 2\ell/3$, whereas transport theory gives the Milne result, $z_{0l,r} = 0.7104\ell$ [1]. We will incorporate this correction below in Secs. 4 and 5 when finding the transport mean free path from the fit of Eqs. (3) and (4) to optical and microwave measurements, respectively.

LONG-RANGE INTENSITY CORRELATION FUNCTION IN RANDOM MEDIA WITH STRONGLY REFLECTING BOUNDARIES

Internal reflection strongly affects the spectral and the spatial intensity-intensity correlation functions. We calculate these correlation functions for tube geometry assuming that the fluctuating part of the intensity $\delta I = I - \langle I \rangle$ satisfies the diffusion equation with a Langevin source [14,15] and with the boundary conditions given by Eqs. (2) [22]. We find that the fluctuations at the surface, which are usually neglected [14,15], become important when the surface reflectivity is large. As a result, the correlation function with frequency shift $\Delta\omega = \omega - \omega'$, at points $\boldsymbol{r}_1$ and $\boldsymbol{r}_2$, $C_{\omega\omega'}(\boldsymbol{r}_1,\boldsymbol{r}_2) = \langle I_\omega(\boldsymbol{r}_1) I_{\omega'}(\boldsymbol{r}_2)\rangle$, splits into surface and volume terms:

$$C_{\omega\omega'}(z_1; z_2) = C^{(S)}_{\omega\omega'}(z_1; z_2) + C^{(V)}_{\omega\omega'}(z_1; z_2); \tag{7a}$$

$$C^{(S)}_{\omega\omega'}(z_1; z_2) = -\frac{\pi \ell c^2}{3q^2k^2A}\frac{d}{dz}\left\{\left[I(z_1; z)\, I(z_2; L) + I(z_1; L)\, I(z_2; z)\right]_{z=L}\left|\langle I_{\omega\omega'}(L)\rangle\right|^2\right.$$
$$\left. + \left[I(z_1; 0)\, I(z_2; z) + I(z_1; z)\, I(z_2; 0)\right]_{z=0}\left|\langle I_{\omega\omega'}(0)\rangle\right|^2\right\}; \tag{7b}$$

$$C^{(V)}_{\omega\omega'}(z_1; z_2) = -\frac{\pi \ell c^2}{3q^2k^2A}\int_0^L dz \left|\langle I_{\omega\omega'}(z)\rangle\right|^2 \frac{dI(z_1; z)}{dz}\frac{dI(z_2; z)}{dz}, \tag{7c}$$

where A is a cross-section of a tube, $\langle I_{\omega\omega'}(z)\rangle$ is the field-field correlation function [14,15] and $I(z)$ is given by Eq. (4). In Eqs. (7 b,c), only terms corresponding to long-range correlation are taken into account. Equations (7) are general expressions for the dependence of the correlation function upon the separation and frequency. In the limiting cases of low surface reflectivity or strong absorption, the surface term is small compared with the volume term and Eqs. (7) give the well-established results [14,15] for the correlation functions. But when internal reflectivity is strong, $z_0 \gg L$ and $z_0(\Delta\omega/2D)^{1/2} \gg 1$, the surface term dominates both the spectral and the spatial correlation functions,

$$C^{(S)}_{\Delta\omega}(z_1 = L; z_2 = L) \approx \frac{6\pi D^2}{k^2 \ell A\, \Delta\omega}; \quad C^{(S)}_{\Delta\omega=0}(z_1 = L; z_2 = L - \Delta r) \approx \frac{3\pi z_0}{k^2 \ell A}\left(1 + \frac{L - \Delta r}{z_0}\right) \tag{8}$$

As a result, the spectral correlation function falls-off as $(\Delta\omega)^{-1}$ rather than as $(\Delta\omega)^{-1/2}$ as occurs in the case of low reflectivity and the spatial correlation function falls-off linearly instead of quadratically. We also find that the degree of correlation for the spatial correlation function is enhanced by a factor of z_0 / L.

OPTICAL MEASUREMENTS

Optical measurements of total transmission versus thickness for a random alumina wedge sample in air are shown in Fig. 1. For $L > 100$ μm, $T(L)^{-1}$ is a straight line in agreement with the prediction of diffusion theory [Eq. (6)]. Fitting Eq. (6) to the linear portion of the curve gives $z_p = 24.8 \pm 0.1$ μm and $z_{0r} = 190.9 \pm 0.3$ μm. The mean free path can only be determined from the measurement of z_{0r} once the reflectivity is known. To eliminate internal reflectivity at the boundaries, we have measured the relative transmission with the sample immersed in index matching fluid. These measurements are shown in Fig. 1. Although in this case we do not measure the absolute transmission, from the x-intercept we obtain $z_{0r} = 22.3 \pm 1.5$ μm. Since $z_{0r} = 0.7104\ell$ in this case, we find $\ell = 31.4 \pm 1.5$ μm.

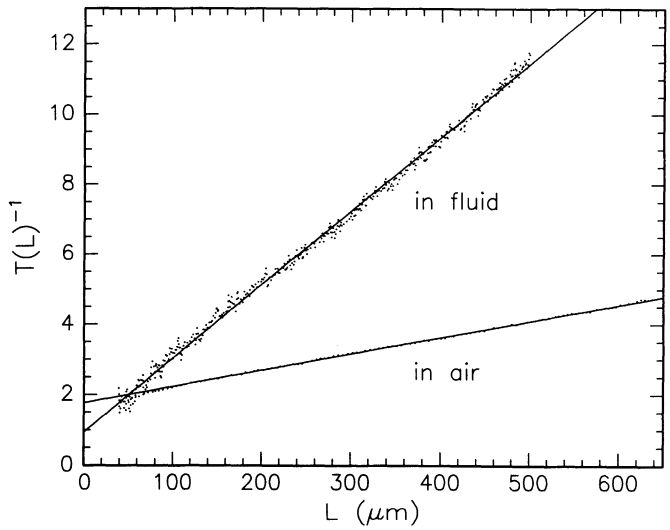

Figure 1. Scale dependence of the inverse of the transmission coefficient for the alumina slab in air and in index matching fluid.

An independent test of the adequacy of diffusion theory and the accuracy of values of the scattering parameters is whether the parameters found in measurements of transmission can be used to predict the surface intensity distributions using Eq. (3). A comparison of the measured $I(\rho; L = 280$ μm) for a sample in air and in index matching fluid to the predictions of Eq. (3), using the values of z_0 and z_p found from the transmission measurements of Fig. 1, is shown in Fig. 2. We find good agreement with diffusion theory whenever $L \geq 150$ μm.

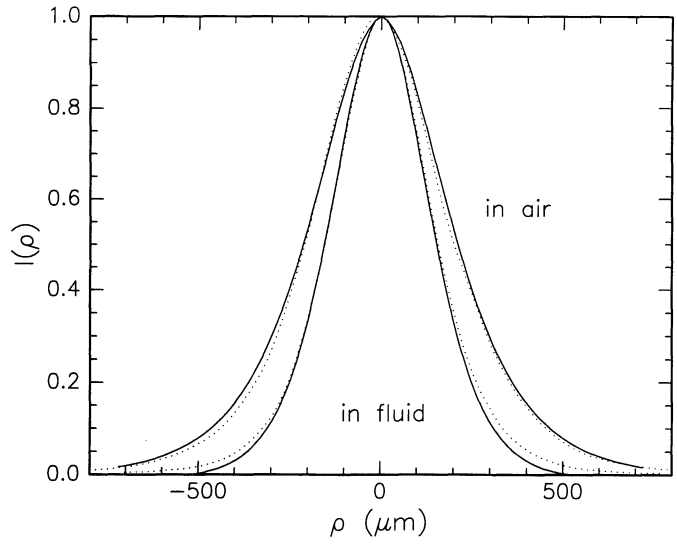

Figure 2. Intensity profiles on the output surface for the L = 280 μm sample in air and in index matching liquid. The solid lines are calculated from Eq. (3).

MICROVAWE MEASUREMENTS

The validity of the diffusion theory has also been independently tested in measurements of the microwave intensity distribution inside and of the transmission through an ensemble of configurations of ½-in polystyrene spheres. These results allow us to determine ℓ, R, and the transport velocity v without any assumptions regarding the nature of scattering.

The medium is 150 cm long and is contained between 1/16-in-thick plastic disks in a copper tube of the diameter of 7.3 cm. The tubes are rotated in order to tumble the sample to facilitate configuration averaging. Intensity measurements are made using Schottky diode detectors in the sample without (R_1) and with additional reflecting copper plates placed in contact with the plastic disk at the output of the sample. These plates contain regularly spaced holes of 0.50" (R_2) and 0.25" (R_3) diameter which cover approximately 55% and 42% of the plate area, respectively. Measurements were made at 18.5 Ghz. The intensity measurements are shown in Fig. 3. The curves in the figure are the fit of Eq. (4) to the data with z_{0r} and α as a fitting parameters. In order to obtain the mean free path, however, the reflection coefficient must be known. To determine the reflection coefficient we have measured the relative transmission for the three different reflectors. The reflection coefficients can be obtained by comparing the values of z_{0r} and of the relative values of the total transmission for two different reflectors using the following system of equations [23]

$$\frac{z_{0r}^{(i)}}{z_{0r}^{(j)}} = \frac{(1+R_r^{(i)})(1-R_r^{(j)})}{(1-R_r^{(i)})(1+R_r^{(j)})}; \qquad \frac{T^{(i)}/J_+^{(i)}(L^-)}{T^{(j)}/J_+^{(j)}(L^-)} = \frac{1-R_r^{(i)}}{1-R_r^{(j)}}. \tag{9}$$

Here the indices i, j correspond to the reflection coefficients $R^{(i,j)}$. The comparison of data for any pair of reflectors allows us to find their reflectivities using Eqs. (9). Then, using values of z_{0r} obtained from the fit of Eq. (4) to the data, we can determine the mean free path. Since there are three combinations of pairs of reflection coefficients to be used in Eqs. (9), we have three separate determinations of the mean free path. The average of which is found to be $\ell = 6.5 \pm 0.3$ cm. The transport velocity is found from a determination of the diffusion coefficient obtained by fitting the photon diffusion model to measurements of the intensity autocorrelation function with a frequency shift in the 18-19 Ghz range. The theoretical expressions for the correlation functions include the field factorization term and the leading order correction found using the Langevin approach [16,17]. The fit gives $D = 4.7 \pm 0.3 \times 10^{10}$ cm^2/s at 18.5 Ghz. This gives $v = 3D/\ell = 2.16 \pm 0.2 \times 10^{10}$ cm/s. This value of v is 15% less than the effective medium approximation, indicating that microscopic resonances in the sample retard energy transport even in the present high density limit. An independent check of the applicability of photon diffusion theory near the output surface is

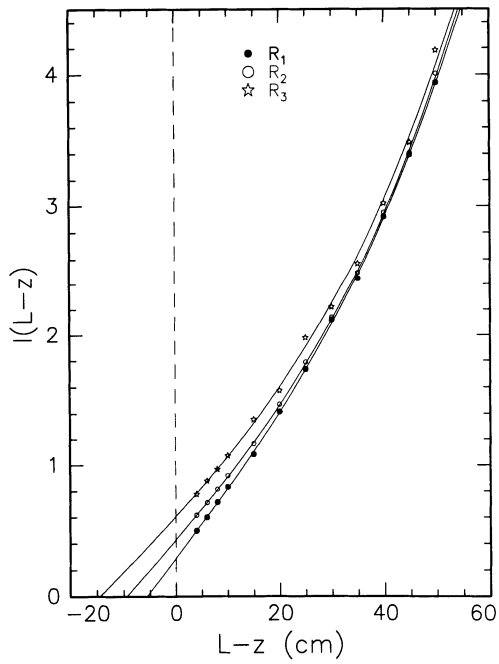

Figure 3. Intensity variation inside a sample of randomly distributed ½-inch polystyrene spheres for three different reflectivities at the output of the sample. The solid line is a fit of Eqs. (4) to the data.

obtained by relating intensity values at the sample surface to the transmission for the three reflectors. From Eq. (5) it follows that the ratio between the total transmission and the intensity at the output boundary is independent of the surface reflectivity $T(L)z_{0r}/I(L^-)=D/q$. $I(L^-)$ is obtained from the extrapolation of the lines in Fig. 3 to $L - z = 0$. The consistency of our experiments with the predictions of diffusion theory can be verified by taking $T(L)$, $I(L^-)$ and z_{0r} and checking to see if the ratio given above is constant for the three reflectors. Our results show that within 3% the ratio does not depend on internal reflection for the three output reflection conditions as predicted by diffusion theory.

The results presented here show that diffusion theory gives a *quantitative* description of transmission through and of intensity inside a random media. These measurements allow us to determine the transport mean free path and the internal reflectivity. Comparison of these results with the value of the diffusion coefficient obtained from measurements of the autocorrelation function with frequency shift allows us to determine the phenomenological transport velocity, which gives the connection between dynamic and static transport parameters.

ACKNOWLEDGEMENTS

This work was supported by the NSF under grant DMR-9001335, by the Petroleum Research Fund of the ACS under grant 22800-AC,7, and by several PSC-CUNY awards.

REFERENCES

1. S. Glasstone and M.C. Edlund. "The Elements of Nuclear Reactor Theory," Van Nostrand, New York (1952); P.M. Morse and H. Feshbach "Methods of Theoretical Physics," McGraw-Hill, New York (1953).
2. E. Akkermans, P.E. Wolf, and R. Maynard, Phys. Rev. Lett. 56:1471 (1986).
3. F.C. MacKintosh and S. John, Phys. Rev. B 40:2383 (1989).
4. M.P. van Albada and A. Lagendijk, Phys. Rev. Lett. 55:2692 (1985).
5. P.E. Wolf and G. Maret, Phys. Rev. Lett. 55:2696 (1985).
6. S. Feng, C. Kane, P.A. Lee, and A.D. Stone, Phys. Rev. Lett. 61:834 (1988).
7. I. Freund, M. Rosenbluh, and S. Feng, Phys. Rev. Lett. 61:2328 (1988).
8. A.Z. Genack, Phys. Rev. Lett. 58:2043 (1987).
9. R. Vreeker, M.P. van Albada, R. Sprik, and A. Lagendijk, Phys. Lett. A 132:51 (1988).
10. J.M. Drake and A.Z. Genack, Phys. Rev. Lett. 63:259 (1989).
11. B. Shapiro, Phys. Rev. Lett. 57:2168 (1986).
12. M.J. Stephen and G. Cwilich, Phys. Rev. Lett. 59:285 (1987).
13. A.Z. Genack, N. Garcia, and W. Polkosnik, Phys. Rev. Lett. 65:2129 (1990).
14. R. Pnini and B. Shapiro, Phys. Lett. A 157:265 (1991).
15. E. Kogan and M. Kaveh, Phys. Rev B 45:1049 (1992).
16. M.P. van Albada, J.F. de Boer, and A. Lagendijk, Phys. Rev. Lett. 64:2787 (1990).

11. B. Shapiro, Phys. Rev. Lett. 57:2168 (1986).
12. M.J. Stephen and G. Cwilich, Phys. Rev. Lett. 59:285 (1987).
13. A.Z. Genack, N. Garcia, and W. Polkosnik, Phys. Rev. Lett. 65:2129 (1990).
14. R. Pnini and B. Shapiro, Phys. Lett. A 157:265 (1991).
15. E. Kogan and M. Kaveh, Phys. Rev B 45:1049 (1992).
16. M.P. van Albada, J.F. de Boer, and A. Lagendijk, Phys. Rev. Lett. 64:2787 (1990).
17. G. Maret and P.E. Wolf, Z. Phys. B 65:409 (1987); D.J. Pine, D.A. Weitz, G. Maret, P.E. Wolf, E. Herbolzhmeimer, P.M. Chaikin, *in* : "The Scattering and Localization of Classical Waves," P. Sheng, ed., World Scientific Press, Singapore (1990).
18. A. Lagendijk, R. Vreeker, and P. de Vries, Phys. Lett. A 136:81 (1989).
19. I. Freund and R. Berkovits, Phys. Rev. B 41:496 (1990).
20. N. Garcia, J.H. Li, W. Polkosnik, T.D. Cheung, P. Tsang, A.A. Lisyansky, and A.Z. Genack, Physica B 175:9 (1991).
21. J.X. Zhu, D.J. Pine, and D.A. Weitz, Phys. Rev. A 44:3948 (1991).
22. A.A. Lisyansky and D. Livdan, Phys. Lett A, 170:53 (1992).
23. N. Garcia, A.Z. Genack, and A.A. Lisyansky, Phys. Rev. B 46:14475 (1992).

INTERNAL REFLECTIONS IN DIFFUSIVE MEDIA

Th. M. Nieuwenhuizen

Van der Waals-Zeeman Laboratorium
University of Amsterdam
Valckenierstraat 65
1018 XE Amsterdam
The Netherlands

INTRODUCTION

The study of light propagation through turbid media has been an intensive field of research for many decades. Many aspects of the transport of light in such media are well described by the so-called *radiative transfer equation.* This transport equation, which was derived long ago by astrophysicists, is equivalent to a diffusion equation, as far as long-distance properties are concerned. This diffusive behavior can also be obtained by summing the dominant scattering processes, the so-called ladder diagrams.

Near the boundaries of a diffusive medium, however, the diffusion approximation breaks down, for the simple reason that light undergoes too few scattering events. In the *skin layers*, i.e., when the distance to the boundary is of the order of a few times the mean free path, diffusive transport crosses over to free propagation, or vice versa. In practical situations, the optical index of the scattering medium is usually different from that of the surrounding medium (air or glass). This causes the additional problem of reflections at the interface.

The aim of the present work is to discuss a microscopic description of the effects of internal reflections on the diffuse transport of waves through thick slabs. We restrict the analysis to scalar waves, and to the regime where the mean free path is much larger than the wavelength. Indeed, internal reflections have effects which are of order unity, and thus overshadow many weak localization effects.

THEORY

We study the propagation of scalar waves in a slab with thickness L. It contains a small density of isotropic scatterers, which lead to a scattering mean free path ℓ, much larger than the wavelength of light inside the medium, λ_0. The optical index is equal to n_0 inside the diffusive medium ($0 < z < L$), and to $n_1 \equiv n_0/m$ outside ($z < 0$; $z > L$).

Photonic Band Gaps and Localization, Edited by
C.M. Soukoulis, Plenum Press, New York, 1993

After averaging over the uncorrelated random positions of the scatterers, the mean amplitude Green's function inside the medium obeys the equation

$$\left[\frac{d^2}{dz^2} - q^2 + \left(k_0 + \frac{i}{2\ell}\right)^2\right] G(z,z';q) = -\delta(z-z') \qquad (0 < z < L) \tag{1}$$

where q is the transversal wavevector.

We consider the scattering of a plane wave, with unit amplitude, and transversal wavevector q_a, incident from the left ($z = -\infty$). Throughout the following, the index a (respectively, b) will refer to the incoming (respectively, the outgoing) beam.

The starting point of our analysis is the following observation. For $L \to \infty$, the solution of eq. (1) inside the medium ($z, z' > 0$) consists of a "charge" term and a "mirror charge" term

$$G(z,z';q) = \frac{i}{2P}\left[e^{iP|z-z'|} + \frac{P-p}{P+p}e^{iP(z+z')}\right] \qquad (z > 0, \quad z' > 0) \tag{2}$$

where $p = \sqrt{k_1^2 - q^2}$ and $P = \sqrt{k_0^2 - q^2 + ik_0/\ell}$. The prefactor of the second term in eq. (2) is the Fresnel reflection amplitude.

The diffuse intensity is of special interest. We restrict the analysis to the ladder approximation to the Bethe-Salpeter equation, which amounts to summing the ladder diagrams. Inserting the result (2) and neglecting the oscillating cross terms, we are led to the following generalized Schwartzschild-Milne equation

$$\Gamma(\tau) = e^{-\tau/\mu_a} + \int_0^b M(\tau,\tau')\Gamma(\tau')d\tau' \tag{3}$$

$\Gamma(\tau)$ represents the normalized diffuse intensity, scattered at a depth $z = \ell\tau$, arising from a normalized plane wave, incident under an angle θ_a. $b = L/\ell$ is the optical thickness. The source term $\exp(-\tau/\mu_a)$ describes the decay of the unscattered incoming beam entering the random medium at $z = 0$, expressing the Lambert-Beer law. Here $\mu_a = \cos\theta_a'$ is related to the angle $\theta_a' = \arcsin(m\sin\theta_a)$ of the incoming beam inside the medium. The kernel $M(\tau,\tau')$ has a bulk contribution M_B, coming from the "charge" term in the expression (2) of the Green's function G, which is already present in the absence of internal reflections, and a layer contribution M_L, which originates in the "mirror charge" term. For isotropic point scatterers, we find

$$M(\tau,\tau') = M_B(\tau,\tau') + M_L(\tau,\tau') \tag{4}$$

$$M_B(\tau,\tau') = \int_0^1 \frac{d\mu}{2\mu} e^{-|\tau-\tau'|/\mu} \tag{5}$$

$$M_L(\tau,\tau') = \int_0^1 \frac{d\mu}{2\mu} R(\mu) e^{-(\tau+\tau')/\mu} \tag{6}$$

where $R(\mu) = |\mu - \sqrt{\mu^2 - 1 + m^{-2}}|^2 / |\mu + \sqrt{\mu^2 - 1 + m^{-2}}|^2$ is the intensity reflection coefficient at the angle such that $\mu = \cos\theta'$. For the case $m > 1$ there are angles for which $R = 1$, describing total internal reflection. The layer kernel M_L decays exponentially away from the boundary; it therefore represents a surface effect, which is only important in the skin layers ($z \sim \ell$, and $L - z \sim \ell$). However, internal reflections lead, via the layer kernel M_L, to effects of order unity even in the limit where $k_0\ell \to \infty$.

In the limit $b \to \infty$, eq. (3) has a homogeneous solution with the asymptotic behavior $\Gamma_H(\tau) \to \tau + \tau_0$ for large τ and some τ_0, and a special solution that approaches

a constant, $\Gamma_S \to \tau_1$. Using this, we obtain the following prediction for the reflected intensity per solid angle element $d\Omega_b$

$$dR(a \to b) = A^R(\theta_a, \theta_b) d\Omega_b \tag{7}$$

with

$$A^R(\theta_a, \theta_b) = \frac{\cos\theta_a}{4\pi m^2} \frac{T_a T_b}{\mu_a \mu_b} \int_0^\infty \Gamma_S(\mu_a; \tau) e^{-\tau/\mu_b} d\tau \tag{8}$$

where $T_a = T(\mu_a) = 1 - R(\mu_a)$. Equation (7) obeys a sum rule expressing conservation of flux in the z-direction.

The diffuse transmitted intensity can be evaluated in analogy with eq. (7),

$$dT(a \to b) = \frac{A^T(\theta_a, \theta_b)}{b + 2\tau_0} d\Omega_b = \frac{\cos\theta_a}{12\pi m^2} \frac{T_a T_b}{\mu_a \mu_b} \frac{\tau_1(\mu_a)\tau_1(\mu_b)}{b + 2\tau_0} d\Omega_b \tag{9}$$

The above result exhibits the simple ℓ/L decay law, characteristic of diffusive, or Ohmic, behavior, which is present e.g. in the conductance of a one-dimensional conductor.

The enhanced backscattering cone can also be evaluated. Restricting to the situation of normal incidence ($q_a = 0$), we set $q_b = Q/\ell$. For a normalized incident plane wave, the diffusive intensity in the vicinity of the exact backscattering direction consists of $A^R + A^C(Q)$ with

$$A^C(Q) = \frac{T(1)^2}{4\pi m^2} \left[\gamma_C(Q) - \frac{1}{2}\right] \tag{10}$$

In the exact backscatter direction, the term involving $\gamma_C(0)$ coincides with the background contribution A^R. The factor $1/2$ corrects for double counting of single scattering events. It holds that

$$\gamma_C(Q) = \int_0^\infty \Gamma_C(\tau; Q) e^{-\tau} d\tau \tag{11}$$

and $\Gamma_C(\tau; Q)$ is the solution of the Milne equation (3), (4) with Q-dependent kernels

$$\begin{aligned} M_B(\tau, \tau'; Q) &= \int_0^1 \frac{d\mu}{2\mu} J_0\left(Q|\tau - \tau'|\sqrt{1-\mu^2}/\mu\right) e^{-|\tau-\tau'|/\mu} \\ M_L(\tau, \tau'; Q) &= \int_0^1 \frac{d\mu}{2\mu} J_0\left(Q(\tau + \tau')\sqrt{1-\mu^2}/\mu\right) R(\mu) e^{-(\tau+\tau')/\mu} \end{aligned} \tag{12}$$

where $J_0(z)$ is the Bessel function of order 0.

THE REGIME OF LARGE INDEX MISMATCH

In this section, we discuss an accurate approximate analytical scheme, which yields predictions concerning the behavior of physical quantities in the regime where the optical indices n_0 and n_1 are very different from each other, i.e., when their ratio m goes to zero, or to infinity.

It will turn out that they provide satisfactory estimates for all quantities related to the long-distance physics of the problem over the entire range of values of the index ratio m, and especially for $m > 1$, i.e., in the usual situation where the refractive index of the random medium (a liquid or a solid) is larger than that of the outside (air).

The analytical analysis now shows that physical quantities depend in leading order only on the *mean flux transmission coefficient* $\mathcal{T}$

$$\mathcal{T} = \int_0^1 2\mu\, T(\mu)\, d\mu. \tag{13}$$

This quantity depends only on the ratio m of optical indices and it falls off for small and large m, according to $\mathcal{T} \approx 8m/3$ for $m \to 0$ and $\mathcal{T} \approx 8/3m^3$ for $m \to \infty$.

As far as reflection and transmission properties are concerned, we obtain the simple expressions

$$\tau_0 \approx \frac{4}{3\mathcal{T}}, \qquad \tau_1(\mu) \approx \frac{4\mu}{\mathcal{T}}. \tag{14}$$

As a consequence, our predictions in the $m \to \infty$ limit are as follows

$$\begin{aligned} A^R(\theta_a, \theta_b) &\approx \frac{6}{\pi m} \cos^2\theta_a \cos\theta_b \\ \frac{A^T(\theta_a, \theta_b)}{b + 2\tau_0} &\approx \frac{3m^2}{\pi} \frac{\cos^2\theta_a \cos\theta_b}{b + m^3}. \end{aligned} \tag{15}$$

The estimate concerning transmission shows an interesting crossover phenomenon when the optical thickness b and the index ratio m are simultaneously large. Indeed b is to be compared with the effective thickness of the skin layers which grows as m^3.

The amplitude of the backscattering cone at normal incidence can also be determined analytically, for $m \to 0$, or $m \to \infty$, in the regime where enhanced backscattering is dominated by long distance effects, i.e., for small values of the reduced wavevector Q. We find the following scaling form

$$\gamma_C(Q) \approx \frac{1}{\mathcal{T}/4 + Q/3} \qquad (Q \to 0;\ \mathcal{T} \to 0) \tag{16}$$

This indicates in particular that the backscattering cone becomes very narrow for a large index mismatch, with an inverse slope of the peak vanishing according to $\Delta Q \approx \frac{3\mathcal{T}}{4}$.

In Figure 1 we compare the quantities $3\tau_0$, $\tau_1(\mu = 1)$ and $\gamma_C(0)$, obtained by numerically solving the Milne equation, with their asymptotic behavior $4/\mathcal{T}$. For m not much larger than unity, $\tau_1(1)$ and $\gamma_C(0)$ are already very close to their asymptotic value.

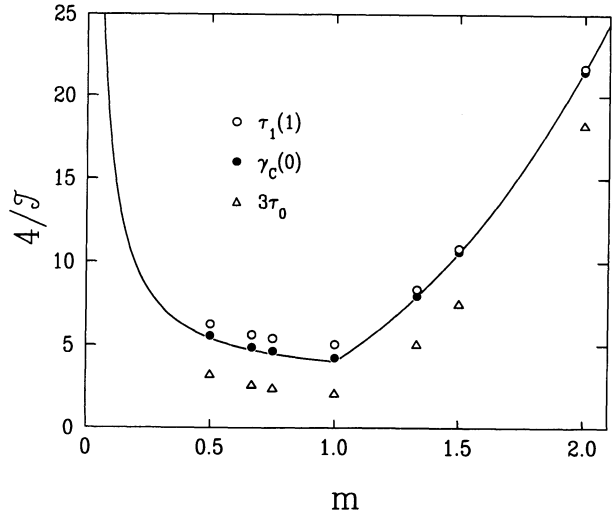

Figure 1: The effective thickness of the skinlayer τ_0 and the related quantities τ_1 and $\gamma_C(0)$ as function of the ratio of optical indices m. Full line: the asymptotic limit $4/\mathcal{T}$.

DISCUSSION

We have presented the theoretical framework for the description of internal reflections in diffusive media. In the limit of large index mismatch, the transport quantities only depend on a mean flux transmission coefficient $\mathcal{T}$. This explains to some extent the success of a heuristic approach, initiated by Lagendijk et al. [1], where the effects of internal reflections are studied by means of an improved diffusion approximation. One common step of such studies consists in introducing a surface reflectivity $\mathcal{R}_S$, which represents the angular average of the ratio of the flux coming to the interface from inside the medium, to the flux reflected into the medium. The work by Zhu et al. [2] can be directly compared to ours. These authors consider the case of vector waves, which we can adapt to scalar waves by neglecting the polarization dependence of the reflectivities. We find that the quantity $1 - \mathcal{R}_S$ of ref. [2] coincides with $\mathcal{T}$, defined in eq. (13), to leading order as $m \to \infty$. This implies their prediction for τ_0 reads $\tau_0 \approx 4/(3\mathcal{T}) - 1$. The leading term is in exact agreement with our result (14), whereas the finite correction has the right sign, and takes a reasonable but incorrect value.

The present framework can be used to evaluate other quantities concerning the diffusive transport of light, such as, e.g., various speckle correlation functions. The influence of internal reflections on the relative fluctuations in the angle-resolved reflected and transmitted intensities can be evaluated within the present framework. For thick slabs ($b \gg \tau_0$), and fixed incoming and outgoing directions, the speckle correlation functions will exhibit the same dependence w.r.t. the index ratio m as the average reflection and transmission, considered in this work.

The case of vector electromagnetic waves can also be dealt with in a similar fashion. In the regime considered here ($k_0 \ell \gg 1$), the propagation between scatterers will involve only nearly on-shell transversal photons. However, for a moderate disorder, the longitudinal component of the electromagnetic field will also contribute to transport. This will also make the analysis more difficult. This effect has been studied in the closely related situation of resonant atoms [3].

Detailed derivations and further aspects of the work discussed here can be found in reference [4].

Acknowledgments

This work has been performed in collaboration with Jean-Marc Luck, and gained much from discussions with Ad Lagendijk. The research has been made possible by a fellowship of the Royal Netherlands Academy of Arts and Sciences (KNAW).

6. K.M. Ho, C.T. Chan, and C. M. Soukoulis, Existence of a photonic gap in periodic dielectric structures

References

[1] A. Lagendijk, R. Vreeker, and P. de Vries, Phys. Lett. A **136**, 81 (1989).

[2] J.X. Zhu, D.J. Pine, and D.A. Weitz, Phys. Rev. A **44**, 3948 (1991).

[3] Th.M. Nieuwenhuizen and G.V. Shlyapnikov, to appear (1992).

[4] Th.M. Nieuwenhuizen and J.M. Luck, *The skinlayer of diffusive media*, Saclay preprint 1992.

FUNDAMENTAL DIFFERENC EBETWEEN THE ROLE OF ABSORPTION AND INELASTIC SCATTERING IN RANDOM SYSTEM

Moshe Kaveh and Eugene Kogan

The Jack and Pearl Resnick Institute of Advanced Technology
Department of Physics, Bar-Ilan University
Ramat - Gan 5290, Israel

INTRODUCTION

A few years ago a new interest[1-9] in propagation of classical waves in random systems took place, mainly due to the possibility of weak[3-6] and strong[1,2] localization effects. Many of the ideas that were developed in solid state physics for transport of electrons in random materials found[8,10] their counterpart in optical waves. In the spirit of finding analogies between quantum (electron) waves and classical waves, it was generally assumed[2,7,11,12] that absorption for classical waves plays a similar role to inelastic scattering for electrons. It is the purpose of this paper to examine this assumption and to demonstrate that it is unjustified. The role of absorption is fundamentally different from the role of inelastic scattering. The difference arises from the simple fact that absorption is an amplitude effect whereas inelastic scattering affects the phase of the wave. This leads to fundamentally different effects in almost all observed phenomena such as: transmission, coherent backscattering, spectral auto correlation function, renormalization of the diffusion constant near resonance and the optical Anderson transition.

EFFECT OF ABSORPTION ON TRANSMISSION

The most obvious and immediate difference between inelastic scattering and absorption is manifested in the average transmission coefficient $< T >$ for electrons and optical waves. An inelastic scattering event takes place over a distance $L_i = (D\tau_i)^{1/2}$, where τ_i is the inelastic scattering time and D is the diffusion constant (determined by elastic scattering due to disorder). Suppose now that we inject an electron on one side of the sample and look for the signal on the other side. In mesoscopic regime

Photonic Band Gaps and Localization, Edited by
C.M. Soukoulis, Plenum Press, New York, 1993

where $\tau_i \gg \tau$ (where τ is the elastic scattering time)

$$< T >= \ell/L, \tag{1}$$

where ℓ is the elastic transport mean free path. Thus L_i does not affect $< T >$, because inelastic scattering simply adds random phases (we neglect corrections of the order $\tau/\tau_i \ll 1$).

We now turn to the analogous effect of absorption. Here L_a replaces L_i, where $L_a = (D\tau_a)^{1/2}$ is the absorption length over which the wave is absorbed over the absorption time τ_a). This is an amplitude effect which reduces $< T >$ by an exponential factor $\exp[-L/L_a]$ for a slab of width L. In contrast to Eq. (1) we get

$$< T >= \frac{\ell}{L_a}\, exp[-L/L_a]. \tag{2}$$

This simple example demonstrates that inelastic scattering events affect the phase, whereas absorption affects the amplitude of the wave. This is the starting point of our analysis and discussion of the role of absorption on interference, correlation and localization of classical waves.

COHERENT BACKSCATTERING

The shape of the coherent backscattering depends[3-6] on the distribution of Feynman trajectories caused by multiple scattering. This shape was calculated for optical waves [13] and electrons[14]. For electrons an inelastic scattering destroys the time reversal symmetry over a distance L_i. Thus, trajectories longer than L_i contribute to the intensity of the reflected wave but destroy the constructive interference for such trajectories. Therefore, the maximum enhancement is less than a factor of two. For shorter τ_i the time reversal symmetry breaks down for shorter trajectories and the enhancement of the coherent backscattering is reduced until it is destroyed when $\ell_i = \ell$. On the other hand, absorption affects the coherent backscattering peak in a different way. Trajectories longer than L_a are simply cut down and do not contribute to the intensity of the backscattered wave. Nevertheless, the remaining shorter trajectories preserve the time reversal symmetry. This means that although the enhanced coherent backscattering peak is very much broadened[15], it preserves the time reversal property that the maximum enhancement remains always independent of the degree of absorption. We now turn to more sophisticated phenomena in which again the role of absorption is very much different from inelastic scattering.

SPECTRAL INTENSITY-INTENSITY AUTOCORRELATION FUNCTION

The spectral intensity autocorrelation function $C(\Delta\omega) =< I(\omega)I(\omega+\Delta\omega) >_c$ was intensively measured [7,11,16,17] and analized[18-22] for optical waves. The basic physics was first put forward by Thouless[23] for electrons. The main idea is that it needs a change in the electron energy by $\Delta E_c = \hbar/t_D$ in order to dephase the wave, where t_D is the time it takes for electron to diffuse across the sample. Thus, if one measures the conductance $G(E_F)$ at the Fermi energy E_F and the conductance at $E_F + \Delta E_c$,

they will turn out to be uncorrelated. In other words, $< G(E_F)G(E_F + \Delta E) >_c$ falls down [24] as ΔE increases with a half width $\Delta E_{1/2} = \Delta E_c$. Since the averaged time to diffuse through a random system is $t_D = L^2/D$, it follows that $\Delta E_{1/2} = \hbar D/L^2$, and the half width frequency is given by $\Delta\omega_{1/2} = \Delta E_{1/2}/\hbar = D/L^2$. This argument holds only for a mesoscopic system for which $L_i > L$. For short inelastic scattering times such as $L_i \ll L$, the dephasing energy is $\Delta E_c = \hbar/\tau_i$ or $\Delta\omega_{1/2} = \tau_i^{-1}$. For the case where both times t_D and τ_i are of the same order $\Delta\omega_{1/2} = t_D^{-1} + \tau_i^{-1}$, which leads to

$$\Delta\omega_{1/2} = D[L^{-2} + L_i^{-2}]. \tag{3}$$

The main property to notice is that when L becomes larger than L_i, $\Delta\omega_{1/2}$ saturates until it becomes independent of $L(\Delta\omega_{1/2} = D/L_i^2)$. We have now demonstrated that for the case of absorption one can not replace L_i by L_a in Eq. (3). Without absorption the relation $\Delta\omega_{1/2} = D/L^2$ holds for classical waves as well as for quantum waves. It is simply the property of dephasing the wave due to its frequency change. The given phase acquired by a Feynman trajectory of length S is $\Phi = kS$, where k is the wavenumber. Changing the frequency leads to $\Delta\Phi = \Delta kS$. Using the fact that the averaged trajectory length is given by $< S >= L^2/\ell$, it follows that when $\Delta\omega_{1/2} = D/L^2$ the phase is changed by 2ϕ. What happens when absorption is taken into account? For simplicity, let us consider a point source in an infinite disordered medium. The intensity at a distance R after a time t is given by

$$I = \frac{1}{(Dt)^{3/2}} \exp[-\frac{R^2}{Dt}] \exp[-\frac{t}{t_a}]. \tag{4}$$

We see that including absorption changes the profile of the wave front. The effect of absorption is twofold. Firstly, it shifts the maximum of the intensity to much smaller times and secondly it narrows dramatically the width of the line shape. Without absorption the maximum of $I(t)$ is at $t_m = R^2/D$. For strong absorption ($R \gg L_a$) the maximum appears at $t_m = (RL_a)/D$; the time now reduced by a factor L_a/R. The width of the lineshape $I(t)$ in the absence of absorption is very broad. This is the characteristic property of diffusion. The fall-off of $I(t)$ goes like $t^{-3/2}$. In the case of absorption the width is much reduced and is given by $\Delta t = (RL_a)^{1/2}L_a/D$. Thus Δt is reduced by $(L_a/R)^{3/2}$ for $R > L_a$. We see that the amplitude effect of absorption as described by Eq. (4) changes drastically the lineshape of I(t), and hence the spectral intensity autocorrelation function becomes much broader. In particular, for a slab of width L the width of I(t) is given by

$$\Delta t = (LL_a)^{1/2}L_a/D; \qquad L_a < L. \tag{5}$$

Since the half width $\Delta\omega_{1/2}$ is approximately given by$\Delta\omega_{1/2} \sim \Delta t^{-1}$, it follows that

$$\Delta\omega_{1/2} \sim D/(LL_a)^{1/2}L_a. \tag{6}$$

We see that in contrast to electrons $\Delta\omega_{1/2}$ never saturates, it rather decays as $L^{-1/2}$. This means that the intensity autocorrelation function $C(\Delta\omega)$ depends always on the width of the slab L, even for $L_a \ll L$. This difference between $C(\Delta\omega)$ and $< G(E_F)G(E_F + \Delta E) >_c$ arises from the fact that the inelastic scattering is a dephasing effect, whereas absorption is an amplitude effect. This is demonstrated in Fig. 1, where we plot $\Delta\omega_{1/2}$ as a function of L/L_a.

A similar effect[22] of absorption occurs for long-range intensity spectral correlations $C_2(\Delta\omega)$. The half-width $\Delta\omega_{1/2}$ is similar to that of the short range. Namely, without absorption $\Delta\omega_{1/2} \sim D/L_i^2$ and absorption changes it to $\Delta\omega_{1/2} \sim D/(LL_a)^{1/2}L_a$. For$\Delta\omega \gg \Delta\omega_{1/2}$ the long-range charecter results in power law behavior $C_2(\Delta\omega) = 1/(\Delta\omega)^{1/2}$. This behavior is independent of absorption since $\Delta\omega \to \infty$ coresponds to short times where $t \ll \tau_a$, and in this regime diffusion is unaffected by absorption which did not yet take place.

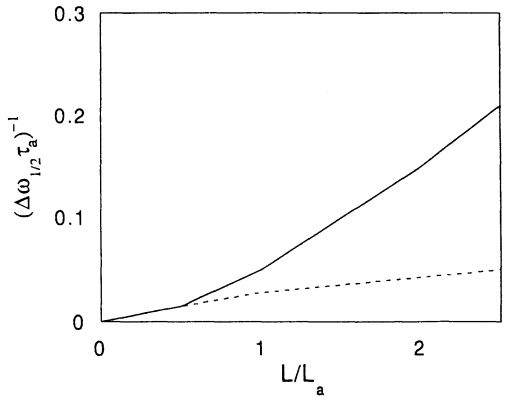

Figure 1. The half-width $\Delta\omega_{1/2}$ as a function of L/L_a. The dashed curve represents the half-width for electrons, where L_a is replaced by L_i.

EFFECT OF ABSORPTION ON THE DIFFUSION CONSTANT

We now examine the role of absorption on two different effects which change the diffusion constant. The first is effect in which the diffusion constant is drastically reduced near the resonance[25]. The second effect is the weak localization phenomenon and scaling prediction near the Anderson transition.

We claim that the absorption does not affect D in both cases. The general argument for this is as follows. From Eq. (4) it is clear that the absorption time τ_a is decoupled from D. In Fig. 2 we plot $< R^2 >$ as a function of t. Due to the presence of absorption it decays to zero exponentially for $t > \tau_a$. But if we renormalize it and plot $< R^2 > / < I >$, this remains linear (see dashed line in Fig. 2) as a function of time and independent of absorption. This property is independent of the geometry of the boundary conditions. The consequences of the above conclusion are very important. We now discuss two cases.

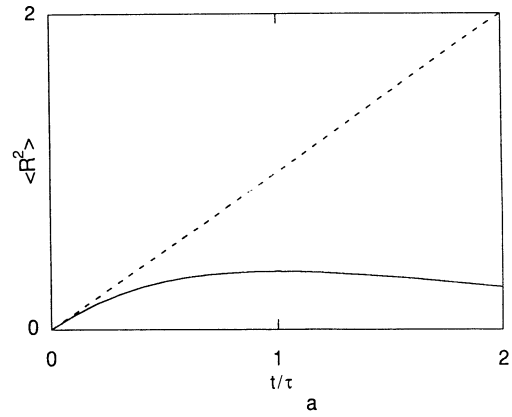

Figure 2. The averaged square of the displacement $< R^2 >$ as a function of the time t. The dashed line represents $< R^2 > / < I >$ as a function of time.

Effect of Resonances on the Diffusion Constant

We have recently modified[26] Boltzmann equation to include the delay time caused by a resonance scattering. The delay time being taken into account it leads to a reduction of the diffusion constant D according to the equation $D = D_0/(1 + \tau_d/\tau)$, where D_0 is the diffusion constant calculated on the basis of Boltzmann equation and τ_d is the scattering delay time. In Fig. 3 we plot the results of a detailed calculation [26] which confirms the prediction first given by the Netherlands group[25].

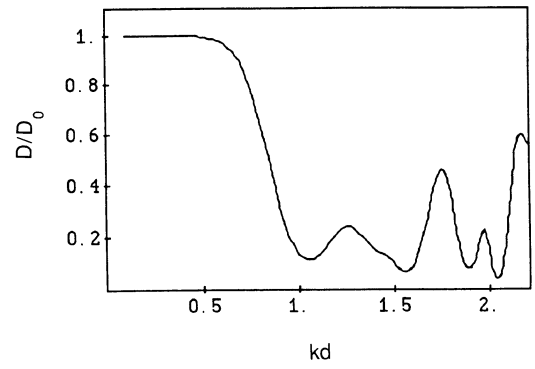

Figure 3. The diffusion constant as a function of kd, where k is the wave number and d is the radius of the scatterer.

We have then included the absorption time τ_a in the calculations and have found that D is unaffected by the existence of absorption (up to corrections of the order τ_a/τ). This is important since it predicts that oscillatory dependence of D and its minima are not smeared out due to absorption. It is interesting to test this prediction experimentally.

Effect of Absorption on the Localization Transition

One of the important predictions of the scaling theory for the diffusion constant of electrons near the Anderson transition is that $D = D_0(\ell/L)$, where $D_0 = c\ell/3$. In the presence of inelastic scattering L is replaced by L_{eff}, where L_{eff} is given by

$$L_{eff} = [L^{-2} + L_i^{-2}]^{-1/2}. \tag{7}$$

For $L_i \ll L$ Eq. (7) predicts $L_{eff} = L_i$ and at finite temperatures we get a "minimum diffusion constant" which is given by $D = D_0(\ell/L_i)$. After the pioneering work of John[1], who mapped the scalar Maxwell equation to the Scroedinger equation and predicted that optical waves may be localized. It was generally assumed that absorption plays the same role as inelastic scattering. In fact, it was generally assumed that L_a replaces L_i exactly at the Anderson transition and just above it $L_{eff} = [L^{-2} + L_a^{-2} + \xi^{-2}]^{-1/2}$, where$\xi$ is the correlation length. A detailed calculation[27] demonstrates clearly that this assumption is incorrect, and in fact D is independent of L_a. Thus using the one-parameter scaling theory for optical waves leads to

$$D = D_0\ell[L^{-2} + \xi^{-2}]^{-2} \tag{8}$$

even in the presence of absorption. The difference between the role of absorption for classical waves and inelastic scattering for electrons is demonstrated in Fig. 4.

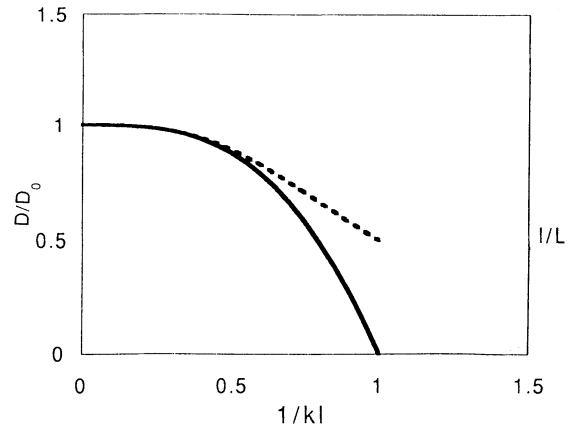

Figure 4. A schematic plot of the diffusion constant as a function of the disorder parameter 1/kl. The dashed curve represents electrons, whereas the solid curve represents optical waves.

The logic behind this conclusion relies on Eq. (4) and Fig. 2, which demonstrate that D is decoupled from τ_a. It is correct that absorption cuts the long trajectories, but the wave that escapes absorption undergoes the same constructive interference (that leads to weak localization) independent of the part of the trajectories that were eliminated due to absorption. This is manifested by the existence of the enhanced coherent backscattering even in the presence of absorption with a maximum enhancement of a factor two due to the perseverance of time reversal symmetry for the trajectories that were not cut down. The prediction that D is unaffected by the presence of absorption is extremely important for experimental studies of the optical Anderson transition. In particular, Eq. (8) suggests a direct measurement of correlation length x and its critical behavior at the transition.

SUMMARY

We have demonstrated that absorption for classical waves is fundamentally different from inelastic scattering for quantum waves (electrons). Inelastic scattering affects the phase of the wave, whereas absorption is an amplitude effect. This results in a major different influence on the transport properties. In particular, the correlation frequency $\Delta\omega_{1/2}$ for electrons saturates $\Delta\omega_{1/2} \sim \tau_i^{-1}$ for $L_i < L$, whereas $\Delta\omega_{1/2}$ never saturates for classical waves, but is given by $\Delta\omega_{1/2} \sim D/(LL_a)^{1/2}L_a$. The diffusion constant for electrons when $L_i < L$ depends explicitly on L_i (due to weak localization), whereas for classical waves D is independent of $L_a < L$. This is especially important near the Anderson transition, where it turns out that absorption helps to observe the transition rather than presents an obstacle.

ACKNOWLEDGEMENTS

We are grateful for important discussions with D. Khmelnitskii and M. Yosefin. M. K. acknowledges SERC Fellowship during his stay at the Cavendish laboratory where this work eas initiated.

REFERENCES

1. S. John, Phys. Rev. Lett. 53:2169 (1984).
2. P.W. Anderson, Phil. Mag. B 52:502 (1985).
3. Y.Kuga and A. Ishimaru, J. Opt. Soc. Am. A1:831 (1984).
4. M.P. van Albada and A. Lagendijk, Phys. Rev. Lett. 55:2692 (1985).
5. P.E. Wolf and G. Maret, Phys. Rev. Lett. 55:2696 (1985).
6. M. Kaveh, M. Rosenbluh, I. Edrei, and I. Freund, Phys. Rev. Lett. 57:2049 (1986).
7. A.Z. Genack, Phys. Rev. Lett. 58:2043 (1987).
8. "Analogies in Optics and Micro-Electronics," W. van Itaeringen and D. Lestra ed., North Holland, Amsterdam (1990).
9. "Scattering and Localization of Classical Waves in Random Media," P. Sheng, ed., World Scientific, Singapore (1990).

10. M. Kaveh, in: "Analogies in Optics and Micro-Electronics," W. van Itaeringen and D. Lestra ed., North Holland, Amsterdam (1990); M. Kaveh, Waves in Random Media 3:5121 (1991).
11. J.M. Drake and A.Z. Genack, Phys. Rev. Lett. 63:259 (1989).
12. R. Berkovits and M. Kaveh, J. Phys. Condensed Matter 2:307 (1990).
13. E. Akkermans, P.E. Wolf, and R. Maynard, Phys. Rev. Lett. 56:1471 (1986).
14. R. Berkovits and M. Kaveh, Phys. Rev. B 37:584 (1988); R. Berkovits, D.Eliyahu, and M. Kaveh, Phys. Rev. B 41:401 (1990).
15. M. Rosenbluh, I. Freund, I. Edrei, and M. Kaveh, Phys. Rev. A 35:4458 (1987); S. Etemad, R. Thompson, M.J. Anndrejco, S. John, and F. Mackintosh, Phys. Rev. B 37:3575 (1988); P.E. Wolf, E. Akkermans, and R. Maynard, J. Physique 49:63 (1988).
16. N.A. Garcia and A.Z. Genack, Phys. Rev. Lett. 63:1678 (1989).
17. M.P. van Albada, J.F. de Boer, and A. Lagendijk, Phys. Rev. Lett. 64:2787 (1990).
18. B. Shapiro, Phys. Rev. Lett. 57:2168 (1986).
19. M.J. Stephen and G. Cwilich, Phys. Rev. Lett. 59:285 (1987).
20. I. Edrei, and M. Kaveh, Phys. Rev. B 38:950 (1988); ibid 40:9419 (1989).
21. A.Z. Genack, Europhys. Lett. 11:733 (1990).
22. E.Kogan and M. Kaveh, Phys. Rev. B 45:1049 (1992).
23. D.J. Thouless, Phys. Rep. 13:93 (1974).
24. P.A. Lee and A.D. Stone, Phys. Rev. Lett. 55:162 (1985).
25. M.P. van Albada, B.A. van Tiggelen, A. Lagendijk, and A. Tipp, Phys. Rev. Lett. 67:3132 (1991).
26. E.Kogan and M. Kaveh, Phys. Rev. B 46:10636 (1992).
27. M. Yosefin, Phys. Rev. Lett., submitted for publication.

HIGHER ORDER INTERFERENCE EFFECTS IN THE REFLECTION OF COHERENT WAVES FROM RANDOM MEDIA

M. Nieto-Vesperinas and J.A. Sanchez-Gil

Instituto de Optica, C.S.I.C.
Serrano 121
Madrid 28006, Spain

INTRODUCTION

The propagation of classical waves from disordered media has been a subject of intense study in recent years.[1-3] This has been due to the discovery of coherent effects associated with multiple scattering, like the phenomenon of enhanced backscattering, related with the weak localization of waves, and found both in dense media[4-9] and rough surfaces;[10-13] and also with the prediction and observation of intensity correlations in light and other classical waves both reflected and transmitted in dense media.[14-24]

We study here the angular correlation of the speckle pattern of coherent scalar waves *reflected* from a random medium under two different directions of propagation of the incident wave. We consider a sample so small that the wavefield diffusely reflected has no circular Gaussian joint probability density; namely, the *factorization approximation* is not valid. In this case, corrections to the so-called *memory effect* obtained under the factorization approximation have predicted the existence of long-range correlations both in reflected and transmitted waves.[15,17,22,23] Also, we predict a new kind of long-range angular correlation of the intensity, different to the one studied in previous works, and that has an analogy with the phenomenon of enhanced backscattering as it arises from constructive interference between waves travelling in paths in the random medium which are the reverse of each other.

PHENOMENOLOGICAL MODEL

We consider a plane wave with wavevector $\mathbf{k}_i$, incident on a sample of the random medium. The speckle pattern resulting from the wave reflected is considered at a generic scattering direction characterized by the wavevector $\mathbf{k}_f$. Then, we consider

Photonic Band Gaps and Localization, Edited by
C.M. Soukoulis, Plenum Press, New York, 1993

another speckle pattern in the generic direction $\mathbf{k}'_f$ produced on reflection of a second plane wave incident with wavevector $\mathbf{k}'_i$. The intensity correlation function is then given by:

$$C(\mathbf{k}_i, \mathbf{k}_f; \mathbf{k}'_i, \mathbf{k}'_f) = \frac{< \delta I(\mathbf{k}_i, \mathbf{k}_f) \delta I(\mathbf{k}'_i, \mathbf{k}'_f) >}{< I(\mathbf{k}_i, \mathbf{k}_f) >< I(\mathbf{k}'_i, \mathbf{k}'_f) >}, \tag{1}$$

where $\delta I = I - < I >$, and $< ... >$ denotes ensemble average.

The numerator of Eq.(1) is obtained as follows: Let A_{lm} be the complex amplitude from the initial scattering point $\mathbf{r}_l$ to the terminal scattering point $\mathbf{r}_m$. The incident and emerging wavevectors being $\mathbf{k}_i$ and $\mathbf{k}_f$, respectively. In the multiple scattering model one must consider also the time-reversed path from $\mathbf{r}_m$ to $\mathbf{r}_l$ whose corresponding complex amplitude is A_{ml}. Then the scattered field given by all of these pairs of paths is

$$A(\mathbf{k}_i, \mathbf{k}_f) = \frac{1}{2} \sum_{l,m} [A_{lm} exp[i(\mathbf{k}_i \cdot \mathbf{r}_l - \mathbf{k}_f \cdot \mathbf{r}_m)] + A_{ml} exp[i(\mathbf{k}_i \cdot \mathbf{r}_m - \mathbf{k}_f \cdot \mathbf{r}_l)]]. \tag{2}$$

And the intensity of the reflected wave is therefore:

$$I(\mathbf{k}_i, \mathbf{k}_f) = I_0 + \sum_{l,m} |A_{lm}|^2 \cos(\mathbf{k}_i + \mathbf{k}_f) \cdot (\mathbf{r}_l - \mathbf{r}_m) + F(\mathbf{k}_i, \mathbf{k}_f), \tag{3}$$

where $I_0 = \sum_{lm} |A_{lm}|^2$. The second, diagonal, term of Eq.(3) leads on averaging over several realizations of the random medium to the effect of enhanced backscattering, and the third, off-diagonal, term is:

$$F(\mathbf{k}_i, \mathbf{k}_f) = \frac{1}{4} \sum_{(l,m) \neq (l',m')} A_{lm} A^*_{l'm'} exp[i\mathbf{k}_i \cdot (\mathbf{r}_l - \mathbf{r}_{l'})] exp[-i\mathbf{k}_f \cdot (\mathbf{r}_m - \mathbf{r}_{m'})], \tag{4}$$

which represents the speckle fluctuations and is zero on averaging.

From Eq.(3) one obtains:

$$\begin{aligned} < \delta I(\mathbf{k}_i, \mathbf{k}_f) \delta I(\mathbf{k}'_i, \mathbf{k}'_f) > = \\ \frac{1}{2} \sum_{l,m;j,k} < \delta I_{lm} \delta I_{jk} > [\cos[(\mathbf{k}_i + \mathbf{k}_f) \cdot (\mathbf{r}_l - \mathbf{r}_m) + (\mathbf{k}'_i + \mathbf{k}'_f) \cdot (\mathbf{r}_j - \mathbf{r}_k)] + \\ \cos[(\mathbf{k}_i + \mathbf{k}_f) \cdot (\mathbf{r}_l - \mathbf{r}_m) - (\mathbf{k}'_i + \mathbf{k}'_f) \cdot (\mathbf{r}_j - \mathbf{r}_k)]] + \\ \sum_{jk} < F(\mathbf{k}_i, \mathbf{k}_f) I_{jk} > \cos(\mathbf{k}'_i + \mathbf{k}'_f) \cdot (\mathbf{r}_j - \mathbf{r}_k) + \\ \sum_{lm} < F(\mathbf{k}'_i, \mathbf{k}'_f) I_{lm} > \cos(\mathbf{k}_i + \mathbf{k}_f) \cdot (\mathbf{r}_l - \mathbf{r}_m) + \\ < F(\mathbf{k}_i, \mathbf{k}_f) F(\mathbf{k}'_i, \mathbf{k}'_f) >, \end{aligned} \tag{5}$$

where $I_{lm} = |A_{lm}|^2$ and $\delta I_{lm} = I_{lm} - < I_{lm} >$.

The diagonal elements $l = j$, $m = k$, or $l = k$, $m = j$, of the first term of Eq.(5) lead to:

$$\begin{aligned} \sum_{l,m} < \delta I^2_{lm} > [\cos[(\mathbf{k}_i + \mathbf{k}_f) + (\mathbf{k}'_i + \mathbf{k}'_f)] \cdot (\mathbf{r}_l - \mathbf{r}_m) \\ + \cos[(\mathbf{k}_i + \mathbf{k}_f) - (\mathbf{k}'_i + \mathbf{k}'_f)] \cdot (\mathbf{r}_l - \mathbf{r}_m)]. \end{aligned} \tag{6}$$

Equation (6) represents two peaks, centered at values:

$$\mathbf{q}_i + \mathbf{q}_f = \pm(\mathbf{q}'_i + \mathbf{q}'_f), \tag{7}$$

where $\mathbf{q}$ represents the transversal component of $\mathbf{k}$. An argument analogous to that used for the analysis of the enhanced backscattering lineshape (cf. e.g., Ref. 7 on using a continuous approach) gives a width of these peaks of the order of λ/l, where l is the transport mean free path. For fixed $\mathbf{q}'_i$, $\mathbf{q}'_f$ and $\mathbf{q}_i$, these two peaks represent *enhanced long-range correlations* (ELRC) around the two values of $\mathbf{q}_f$ given by Eq.(7).

Also, it is worth observing that on writing

$$< I(\mathbf{k}_i, \mathbf{k}_f) I(\mathbf{k}'_i, \mathbf{k}'_f) > = < (A(\mathbf{k}_i, \mathbf{k}_f) A^*(\mathbf{k}'_i, \mathbf{k}'_f))(A^*(\mathbf{k}_i, \mathbf{k}_f) A(\mathbf{k}'_i, \mathbf{k}'_f)) > \tag{8}$$

one can see that the term described by Eq.(6) arises from interference of terms of the form $|A_{lm}|^2 exp[i(\mathbf{k}_i - \mathbf{k}'_i)\cdot\mathbf{r}_l] exp[-i(\mathbf{k}_f - \mathbf{k}'_f)\cdot\mathbf{r}_m]$ and their time-reversed counterparts, and also of terms $|A_{lm}|^2 exp[i(\mathbf{k}_i + \mathbf{k}'_f)\cdot\mathbf{r}_l] exp[-i(\mathbf{k}'_i + \mathbf{k}_f)\cdot\mathbf{r}_m]$ and their time-reversed counterparts. Observe also that the usual factorization approximation does not allow for this interference effect and, hence, leads to the memory effect (ME) only. In this sense, the ME is a "specular" phenomenon in $\Delta\mathbf{k}_i = \mathbf{k}_i - \mathbf{k}'_i$ and $\Delta\mathbf{k}_f = \mathbf{k}_f - \mathbf{k}'_f$, and so is the time-reversed ME in $\mathbf{k}_i + \mathbf{k}'_f$ and $\mathbf{k}'_i + \mathbf{k}_f$.

Concerning the other terms of Eq.(5), the averages in the second and third terms are zero, whereas the fourth term is zero for $j = l$, $k = m$, $j' = l'$, $k' = m'$, or $j = m$, $j' = m'$, $k = l$, $k' = l'$, and leads to the ME (terms with $j = l'$, $k = m'$, $j' = l$, $k' = m$) and its time-reversed (terms with $j = m'$, $k = l'$, $j' = m$, $k' = l$).

The other long-range correlations, addressed in Ref. 17, should be included in the other surviving elements of Eq.(5).

The ratio of the peak values of the ELRC and the ME is $\sum_{lm} < \delta I_{lm}^2 > / [\sum_{lm} < I_{lm} >]^2$. The ELRC effect should be observed in speckle patterns corresponding to a scattered field on reflection that does not have a Gaussian joint probability density for its random values at two pairs of arguments $(\mathbf{k}_i, \mathbf{k}_f)$ and $(\mathbf{k}'_i, \mathbf{k}'_f)$, and hence, for which the factorization approximation does not hold.

NUMERICAL RESULTS

We have done a numerical experiment in which we have computed the correlation Eq.(1) in the numerical simulation of the scattering of electromagnetic waves, s or p polarized from a one-dimensional random rough surface, of profile $z = D(x)$, separating vacuum from a perfect conductor, (the surface thus being constant in the y direction). The plane of incidence is OXZ. It is well-known after Refs. 11-13 and 25 the analogy of rough surfaces with dense media in producing multiple scattering effects like e.g., enhanced backscattering.

Following the procedure of Refs. 12 and 13, we generate random profiles with Gaussian statistics, zero mean, r.m.s. height $\sigma = 1.9\lambda$, a Gaussian correlation function of the random heights, and a correlation length $T = 3.16\lambda$. Each realization of the illuminated surface is sampled with 300 sampling points and has a length $L \approx 30\lambda$. This involves 10 sampling points per wavelength, which is accurate enough. Averages are made over 4000 realizations. Two Gaussian beams, (chosen instead of plane waves in order to get smoother results), of width $W = L\cos\theta_0/4$, propagating in the directions $\mathbf{k}_i$ and $\mathbf{k}'_i$, are incident at an angles θ_0 and θ'_0 with the OZ axis, respectively; namely, with the surface mean plane normal. Let θ and θ' represent the angles of $\mathbf{k}_f$ and $\mathbf{k}'_f$ with the OZ axis, respectively.

Figure 1 shows the function $C(\theta)$, Eq.(1) for $\mathbf{k}_i$, $\mathbf{k}'_i$ and $\mathbf{k}'_f$ fixed at $\theta_0 = 2^0$, $\theta'_0 = 5^0$, $\theta' = 9^0$. The peak at $\theta_0 = 6^0$ corresponds to the memory effect and has a width of the order of $\lambda \cos\theta_0 / W$. On the other hand, the two additional peaks, predicted by Eq.(6) are also present at $\theta \approx 12^0$ and $\theta \approx -16^0$; they have a width λ/T approximately, as l is of the order of T in this case.

The coherent effect addressed in this paper and the phenomenon of enhanced backscattering should be both special cases for the lower statistical moments of the reflected intensity of a general class of coherent phenomena present in the moments of arbitrary order of non-Gaussian speckle patterns.

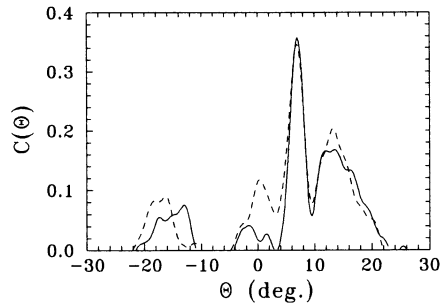

Figure 1. Angular correlation versus θ, with $\theta_0 = 2^0$, $\theta'_0 = 5^0$ and $\theta' = 9^0$. $T = 3.16\lambda$ and $\sigma = 1.9\lambda$. Broken line: s-polarization. Solid line: p-polarization.

ACKNOWLEDGMENTS

Work supported by the CICYT under grant PB0278. JA S-G acknowledges a grant from the MEC. Discussions with J.C. Dainty and A.A. Maradudin supported by a NATO travel grant are also acknowledged.

REFERENCES

1. P. Sheng, ed., *Scattering and Localization of Classical Waves in Random Media*, World Scientific, Singapore, 1990.
2. W. Van Haeringen and D. Lestra, eds., *Analogies in Optics and Micro Electronics*, Kluwer Academic, The Netherlands, 1990.
3. M. Nieto-Vesperinas and J.C. Dainty, eds., *Scattering in Volumes and Surfaces*, North-Holland, Amsterdam, 1990.
4. Y. Kuga and A. Ishimaru, *J. Opt. Soc. Am. A* **1**, 831 (1984); L. Tsang and A. Ishimaru, *J. Opt. Soc. Am. A* **1**, 836 (1984).
5. H.P. Van Alvada and A. Lagendijk, *Phys. Rev. Lett.* **55**, 2692 (1985).
6. P.E. Wolf and G. Maret, *Phys. Rev. Lett.* **55**, 2696 (1985).

7. E. Akkermans, P.E. Wolf and R. Maynard, *Phys. Rev. Lett.* **56**, 1471 (1986); E. Akkermans, P.E. Wolf, R. Maynard and G. Maret, *J. Phys. France* **49**, 77 (1988).
8. M. Kaveh, M. Rosenbluth, M. Edrei and I. Freund, *Phys. Rev. Lett.* **57**, 2049 (1986).
9. S. Etemand, R. Thompson and M.J. Andrejco, *Phys. Rev. Lett.* **57**, 575 (1986).
10. V. Celli, A.A. Maradudin, A.M. Marvin and A.R. McGurn, *J. Opt. Soc. Am. A* **2**, 2225 (1985).
11. K.A. O'Donnell and E.R. Mendez, J. Opt. Soc. Am. A **4**, 1194 (1987).
12. M. Nieto-Vesperinas and J.M. Soto-Crespo, *Opt. Lett.* **12**, 979 (1987); J.M. Soto-Crespo and M. Nieto-Vesperinas, *J. Opt. Soc. Am. A* **6**, 367 (1989).
13. A.A. Maradudin, E.R. Mendez and T. Michel, *Opt. Lett.* **14**, 151 (1989); A.A. Maradudin, T. Michel, A.R. McGurn and E.R. Mendez, *Ann. Phys. NY* **203**, 255 (1990).
14. B. Shapiro, *Phys. Rev. Lett.* **57**, 2168 (1986).
15. M. Stephen and G. Cwilich, *Phys. Rev. Lett.* **59**, 285 (1987).
16. A.Z. Genack, *Phys. Rev. Lett.* **58**, 2043 (1987).
17. S. Feng, C. Kane, P.A. Lee and D. Stone, *Phys. Rev. Lett.* **61**, 834 (1988).
18. I. Freund, M. Rosenbluth and S. Feng, *Phys. Rev. Lett.* **61**, 2328 (1988).
19. R. Berkovits, M. Kaveh and S. Feng, *Phys. Rev. B* **40**, 737 (1989).
20. N. Garcia and A.Z. Genack, *Phys. Rev. Lett.* **63**, 1678 (1989).
21. R. Berkovits and M. Kaveh, *Phys. Rev. B* **41**, 2635 (1990).
22. R. Berkovits, *Phys. Rev. B* **42**, 10750 (1990).
23. M.P. Van Albada, J.F. de Boer and A. Lagendijk, *Phys. Rev. Lett.* **64**, 2787 (1990).
24. D. Eliyahu, R. Berkovits and M. Kaveh, *Phys. Rev. B* **43**, 13501 (1991).
25. M.J. Kim, J.C. Dainty, A.T. Friberg and A.J. Sant, *J. Opt. Soc. Am. A* **7**, 569 (1990).

DISORDERED FABRY-PEROT INTERFEROMETER: DIFFUSIVE WAVE SPECTROSCOPY

Richard Berkovits

Department of Physics
Bar-Ilan University
Ramat-Gan 52900, Israel

INTRODUCTION

A theoretical study of correlation phenomena in an optical Fabry-Perot Interferometer (FPI) containing random elastic scatterers between the mirrors is presented. Among the correlation effects, we find a Lorentzian shaped correlation function between incident waves of different frequencies. For an FPI which contains moving scatterers between the mirrors (for example, scatterers embedded in a liquid), we calculated the intensity correlations between different times. Generally, the calculated intensity correlations are much broader than the corresponding correlations for bulk systems.

FABRY-PEROT INTERFEROMETER

The study of double-barrier resonant-tunneling structures has a long and fruitful history.[1] Recently, the effects of elastic scattering, due to irregularities in the barriers or the presence of impurities between the barriers, have attracted much interest.[2,3,4] In the context of electronic systems, one of the interesting realizations of these systems is the double-barrier quantum-well device (DBQW). The DBQW is usually made from molecular beam epitaxy grown heterostructures. The effect of elastic scattering in this system is manifested by the temperature independent broadening of the resonant peak observed experimentally at low temperatures.[2]

Lately, Fertig and Das Sarma,[3] and Leo and MacDonald[4] have calculated the effect of elastic scattering on resonant tunneling, using the Born approximation up to

Photonic Band Gaps and Localization, Edited by
C.M. Soukoulis, Plenum Press, New York, 1993

second-order impurity scattering, and found, among other effects, the broadening of the resonant peak. This broadening effects the conductance of the system, which is experimentally measurable.

The optical analogy to the electronic DBQW is the well-known FPI. While the conductance of the DBQW is determined by all incoming and outgoing electronic waves, in the case of the FPI one is able to measure specific incoming and outgoing wave intensity transmission coefficients. Therefore, the FPI has, from the experimental point of view, a wealth of measurable features. Some of these features, such as an enhanced *transmission* peak due to weak localization in the mirror direction whose hight is exactly a factor of 2, the "memory effect" for angular correlations, and the extreme sensitivity of the transmission intensity to the motion of a single scatterer, were already discussed.[5]

In this paper we will expand our previous discussion to include the subject of correlations between transmission coefficients of different frequencies. A further point of interest, which we shall refer to, is the application of the standard diffusive wave spectroscopy[6] (DWS) to the FPI. For the case of scatterers suspended in a solution placed between the mirrors, the scatterers will execute a random Brownian motion. Measurement of the correlations between transmission intensities at different times should enable us to obtain useful information on the nature of the Brownian motion in the solution.

FREQUENCY CORRELATION

The correlation between incident waves of different frequencies (or wave vectors) is defined in the following way:

$$\langle \delta T(\vec{q}_a, \vec{q}_b, k_0) \delta T(\vec{q}_{a'}, \vec{q}_{b'}, k_{0'}) \rangle = \tag{1}$$

$$\langle \{ T(\vec{q}_a, \vec{q}_b, k_0) - \langle T(\vec{q}_a, \vec{q}_b, k_0) \rangle \} \{ \langle T(\vec{q}_{a'}, \vec{q}_{b'}, k_{0'}) - \langle T(\vec{q}_{a'}, \vec{q}_{b'}, k_{0'}) \rangle \} \rangle,$$

where $T(\vec{q}_a, \vec{q}_b, k_0)$ is the intensity transmission coefficient for a coherent wave incident onto the left of the FPI in a direction characterized by the transverse wavevector $\vec{q}_a$, and leaving the device on the right in direction $\vec{q}_b$ (see Fig. 1). Here $(\vec{q}_a)^2 + k_a^2 = k_0^2$, with k_a being the z-component of the wavevector (similarly for $\vec{q}_b$). The transverse wavevectors are quantized according to $q_a^x = \frac{2\pi n_x}{L_x}$, where L_x is the width of the sample in the x-direction (similarly for the y-direction). $\langle ... \rangle$ denotes an ensemble average.

It is possible to calculate the frequency correlations defined in Eq. (1) by using a diagrammatic expansion similar to the method used in Ref. 5 to calculate angular correlations. As in Ref. 5 we assume the FPI has resonant wave vectors $k^* = \frac{m\pi}{d}$ (d is the distance between the mirrors). The transmission coefficient of the mirrors T is chosen to be small (*i.e.*, $T \ll 1$) to ensure sharp resonance levels. Due to the presence of scatterers between the mirrors, the wave undergoes multiple scattering between the

mirrors characterized by an elastic mean free path l_{el}. Up to first order in $1/k_{2D}l_{el}$ (where $k_{2D} = \sqrt{k_0^2 - k^{*2}}$), one may calculate the frequency correlation by taking into account the Feynman diagrams given in Fig. 2. Performing the explicit calculation, we obtain the following result:

$$\langle \delta T(\vec{q}_a, \vec{q}_b, k_0) \delta T(\vec{q}_{a'}, \vec{q}_{b'}, k_{0'}) \rangle = \delta_{\Delta\vec{q}_a, \Delta\vec{q}_b} \left(\frac{Tk^*}{d} \right)^4 \tag{2}$$

$$|G_{k_0}(\vec{q}_a) G_{k_0}(\vec{q}_b) G_{k_{0'}}(\vec{q}_{a'}) G_{k_{0'}}(\vec{q}_{b'})|^2 |B(\Delta\vec{q}_a, \Delta k_0) + B(\vec{q}_a + \vec{q}_b + \Delta\vec{q}_a, \Delta k_0)|^2,$$

where $\Delta\vec{q}_a = \vec{q}_{a'} - \vec{q}_a$, $\Delta\vec{q}_b = \vec{q}_{b'} - \vec{q}_b$, and $\Delta k_0 = k_{0'} - k_0$. The averaged Green function is given by:

$$G_{k_0}(\vec{q}) = \frac{1}{(k_0^2 - q^2 - k^{*2})^2 - ik_0(1/l_{el} + 1/l_\phi)/2}. \tag{3}$$

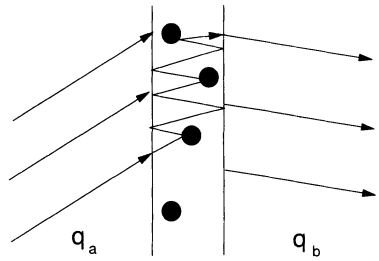

Fig 1. (a) Schematic drawing of a Fabry-Perot interferometer (FPI). The incoming plane wave approaches the FPI in direction $\vec{q}_a$. It is transmitted through the mirror, undergoes multiple scattering due to the presence of scatterers between the mirrors, and part of it emerges on the other side of the FPI in direction $\vec{q}_b$.

The total path length inside the FPI, before the wave decays due to transmission, is $l_\phi = d/2T$. Our calculations assume multiple scattering within the FPI, i.e., $l_\phi \gg l_{el}$. The correlation propagator $B(\vec{q}, \Delta k_0)$ in Eq. (2) may be expressed in the following way:

$$B(\vec{q}, \Delta k_0) = \frac{4k_0/l_{el}L^2}{l_{el}/l_\phi + (k_{2D}^2/k_0^2)(q^2 + i\gamma^2(\Delta k_0))l_{el}^2}, \tag{4}$$

where $\gamma(\Delta k_0) = \sqrt{3\Delta k_0/l_{el}}$. The first B dependence in Eq. (2) is the result of the diffusion propagator (see Fig. 2), while the second term is the result of the maximal crossed propagator, which results from the interference between time-reversed multiple-scattering paths. In the derivation of all the above results, we assumed that the wave vector difference is small, i.e., $\Delta k_0 l_{el} \ll 1$.

It would be instructive to consider the case of correlations between waves for which the incoming and outgoing directions are identical. Further simplification may

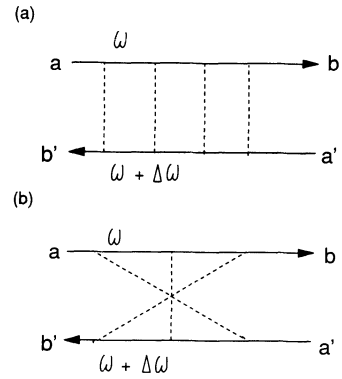

Fig 2. Feynman diagrams for frequency correlations: (a) the diffusion propagator, (b) the maximally crossed propagator.

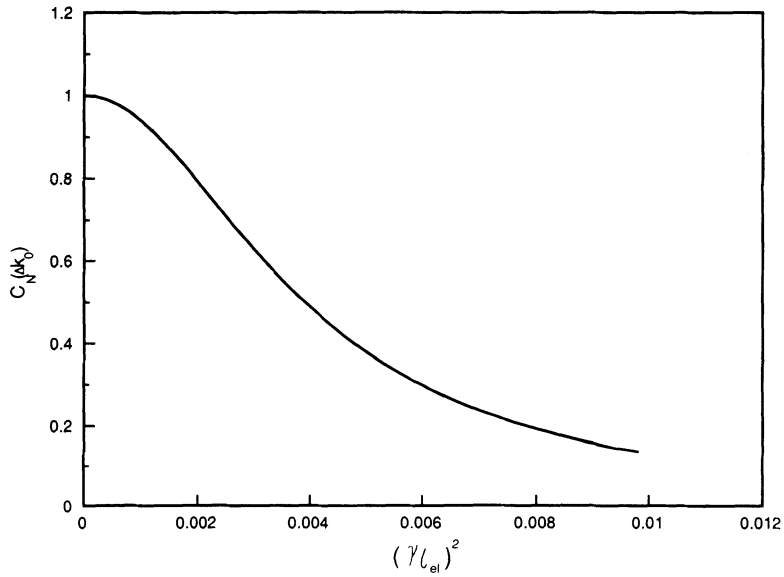

Fig 3. The line shape of the frequency (wave vector) correlations $C_N(\Delta k_0)$ as a function of the difference in the incoming wave vector Δk_0 (where $(\gamma l_{el})^2 = 3\Delta k_0$) given in Eq. (5).

be obtained by assuming that $|\vec{q}_a + \vec{q}_b| > 1/l_{el}$. Under these conditions one may write the normalized correlations as:

$$C_N(\Delta k_0) = \frac{\langle \delta T(\vec{q}_a, \vec{q}_b, k_0) \delta T(\vec{q}_a, \vec{q}_b, k_0\prime) \rangle}{\langle T(\vec{q}_a, \vec{q}_b, k_0) \rangle \langle T(\vec{q}_a, \vec{q}_b, k_0\prime) \rangle} = \frac{(l_{el}/l_\phi)^2}{(l_{el}/l_\phi)^2 + (k_{2D}^4/k_0^4)(\gamma^4(\Delta k_0)) l_{el}^4}. \quad (5)$$

As is shown in Fig. 3, the normalized correlation has a Lorentzian shape. This type of power-law decay for the first-order (in $k_{2D} l_{el}$) correlation is quite different from the behavior of similar frequency correlations for bulk systems. It has been shown that the first order frequency correlations for bulk systems (such as a slab of width bigger

than a mean free path) decay exponentially.[7] Only the second order correlations (which are usually of much smaller magnitude) exhibit a power-law decay. In Fig. 3 one can see that the line shape of the correlation is rounded for small frequency differences, and reaches its half width at $\Delta k_0 \sim (k_{2D}/k_0)^2 1/l_\phi$.

DIFFUSIVE WAVE SPECTROSCOPY

Another correlation of interest is the correlation between transmission intensities at different times for an FPI which has moving scatterers. An example for such a system is an FPI where between the mirrors there are scatterers suspended in a solution. These scatterers perform a random motion in the solution known as Brownian motion, which influences the transmitted intensity. By studying the autocorrelation of the transmitted intensity, one is able to study properties regarding the motion of the scatterers in the solution. This is known as diffusive wave spectroscopy. The Brownian motion of the scatterers is characterized by the time constant $\tau_s = 1/D_s k_0^2$, where D_s is the particle diffusion constant in the solution. Using the results of Stephen,[8] we calculated the transmission intensity correlation between different times, and obtained:

$$\langle \delta T_t(\vec{q}_a, \vec{q}_b, k_0) \delta T_{t'}(\vec{q}_{a'}, \vec{q}_{b'}, k_0) \rangle = \delta_{\Delta\vec{q}_a, \Delta\vec{q}_b} \left(\frac{Tk^*}{d} \right)^4 \tag{6}$$

$$|G_{k_0}(\vec{q}_a) G_{k_0}(\vec{q}_b) G_{k_{0'}}(\vec{q}_{a'}) G_{k_{0'}}(\vec{q}_{b'})|^2 |B(\Delta\vec{q}_a, \Delta t) + B(\vec{q}_a + \vec{q}_b + \Delta\vec{q}_a, \Delta t)|^2,$$

where $\Delta t = t' - t$, and

$$B(\vec{q}, \Delta t) = \frac{4k_0/l_{el}L^2}{l_{el}/l_\phi + (k_{2D}^2/k_0^2)(q^2 + F^2(\Delta t))l_{el}^2}, \tag{7}$$

where $F^2(t) = 3[1 - f(t)]/f(t)$, and

$$f(t) = \frac{\tau_s}{t}(1 - e^{-|t|/\tau_s}).$$

One can see that $F^2(t)$ has a monotonous dependence on t, which may be written as $F^2(t) \sim |t|/\tau_s$. The main difference, between the expression we have obtained for the frequency correlation (Eq. (2)) and the one we have obtained for DWS correlation (Eq. (6)), is that for the frequency correlation the correlation propagator B has an imaginary part, while for the DWS correlation B has no imaginary part. Therefore, the normalized time dependent correlation, for the same conditions as in Eq. (5), is:

$$C_N(\Delta t) = \frac{\langle \delta T_t(\vec{q}_a, \vec{q}_b, k_0) \delta T_{t'}(\vec{q}_a, \vec{q}_b, k_0) \rangle}{\langle T(\vec{q}_a, \vec{q}_b, k_0) \rangle \langle T(\vec{q}_a, \vec{q}_b, k_0) \rangle} = \frac{(l_{el}/l_\phi)^2}{(l_{el}/l_\phi + (k_{2D}^2/k_0^2)(F^2(\Delta t))l_{el}^2)^2}, \tag{8}$$

which has no Lorentzian line shape, although it still decays as a power-law with respect to Δt. As in the case of the frequency correlations, the DWS correlations decay much slower than for bulk systems.[6,8]

The FPI experimental set-up is especially suitable for the study of the motion of particles in a quasi-two dimensional liquid. By measuring the line shape of the correlation function of the transmitted intensity at different times for a liquid between the mirrors of an FPI, one can study different properties of the scatterer motion such as the diffusion constant of the particles D_s, and the short and long time motions of the scatterers,

In summary, we have discussed frequency and time dependent correlations for an FPI. We have shown these correlations are quite different from the equivalent correlations for wide samples. The first order correlations exhibit a power law decay as function of the frequency or time difference. The possible application of these correlations to the study of motions of particles in quasi-two dimensional solutions was also discussed.

Many useful discussions with S. Feng on various aspects of FPI are greatfully acknowledged.

REFERENCES

1. R. Tsu and L. Esaki, **Appl. Lett. 22**, 562 (1973); B. Ricco and M. Ya. Azbel, **Phys. Rev. B 29**, 1970 (1984); F. Capasso, K. Mohammed, and Y. O. Cho, **IEEE J. Quantum Electron. 22**, 1853 (1986); V. J. Goldman, D. C. Tsui, and J. E. Cunningham, **Phys. Rev. Lett. 58**, 1256 (1987); E. E. Mendez, **J. Phys. (Paris) Colloq. 48**, C5 (1987); S. Luryi, **Superlattices Microstruct. 5**, 375 (1989).

2. P. Gueret, C. Rossel, E. Marclay, and H. Meier, **J. Appl. Phys. 66**, 278 (1989).

3. H. A. Fertig and S. Das Sarma, **Phys. Rev. B 40**, 7410 (1989); H. A. Fertig, Song He, and S. Das Sarma, **Phys. Rev. B 41**, 3596 (1990).

4. J. Leo and A. H. MacDonald, **Phys. Rev. Lett. 64**, 817 (1990).

5. R. Berkovits and S. Feng, **Phys. Rev. B 45**, 97 (1992).

6. D. J. Pine et al., in *Scattering and Localization of Classical Waves in Random Media*, edited by P. Sheng, (World Scientific, Singapore, 1990).

7. B. Shapiro, **Phys. Rev. Lett. 57**, 2168 (1986); I. Edrei and M. Kaveh, **Phys. Rev. B 38**, 950 (1988); A. Z. Genack, **Phys. Rev. Lett. 58**, 2043 (1987).

8. M.J. Stephen, **Phys. Rev. B 37**, 1 (1988).

PHOTONIC BAND STRUCTURE

E. Yablonovitch

Bell Communications Research
Navesink Research Center
Red Bank, NJ 07701-7040

ABSTRACT

The analogy between electromagnetic wave propagation in multi-dimensionally periodic structures and electron wave propagation in real crystals has proven to be a very fruitful one. Initial efforts were motivated by the prospect, of a photonic bandgap; a frequency band in 3-dimensional dielectric structures, in which electromagnetic waves are forbidden, irrespective of propagation direction in space. Today, many new ideas and applications are being pursued in 2 and 3 dimensions, and in metallic, dielectric, and acoustic structures, etc.

In this paper, we review the early motivations for this work which were derived from the need for a photonic bandgap in quantum optics. This led to a series of experimental and theoretical searches for the elusive photonic bandgap structures; those 3-dimensionally periodic dielectric structures which are to photon waves, as semiconductor crystals are to electron waves. Then we describe how the photonic semiconductor can be "doped" producing tiny electromagnetic cavities. Finally, we will summarize some of the anticipated implications of photonic band structure for quantum electronics and for other areas of physics and electrical engineering.

INTRODUCTION

In this paper we will pursue the rather appealing analogy[1,2] between the behavior of electromagnetic waves in artificial, 3-dimensionally periodic, dielectric structures, and the rather more familiar behavior of electron waves in natural crystals.

These artificial 2- and 3-dimensionally periodic structures we will call "photonic crystals". The familiar nomenclature of real crystals will be

Photonic Band Gaps and Localization, Edited by
C.M. Soukoulis, Plenum Press, New York, 1993

carried over to the electromagnetic case. This means that the concepts of Reciprocal Space, Brillouin Zones, Dispersion Relations, Bloch Wave functions, Van Hove Singularities, etc., must now be applied to photon waves. It makes sense then to speak of photonic band structure and of a photonic reciprocal space which has a Brillouin zone approximately 1000 times smaller than the Brillouin zone of the electrons. Due to the periodicity, photons can develop an effective mass, but this is in no way unusual, since it occurs even in 1-dimensionally periodic, optically layered, structures. We will frequently leap back and forth between the conventional meaning of a familiar concept like "conduction band", and its new meaning in the context of photonic band structure.

Under favorable circumstances, a "Photonic Bandgap" can open up; a frequency band in which electromagnetic waves are forbidden, irrespective of propagation direction in space. Inside a photonic bandgap, optical modes, spontaneous emission, and zero point fluctuations are all absent. Because of its promised ability to control spontaneous emission of light in quantum optics, the pursuit of a photonic bandgap has been a major motivation for studying photonic band structure.

MOTIVATION

Spontaneous emission of light is a major natural phenomenon, which is of great practical and commercial importance. For example, in semiconductor lasers, spontaneous emission is the major sink for threshold current, which must be surmounted in order to initiate lasing. In heterojunction bipolar transistors (HBrs), which are non-optical devices, spontaneous emission nevertheless rears its head. In some regions of the transistor current-voltage characteristic, spontaneous optical recombination of electrons and holes determines the HBT current gain. In solar cells, surprisingly, spontaneous emission fundamentally determines the maximum available output voltage. We will also see that spontaneous emission determines the degree of photon number state squeezing, an important new phenomenon[3] in the quantum optics of semiconductor lasers. Thus the ability to control spontaneous emission of light is expected to have a major impact on technology.

The easiest way to understand the effect of a photonic bandgap on spontaneous emission is to take note of Fermi's Golden Rule. Consider the spontaneous emission event illustrated in Fig. 1. The downward transition transition rate, w, between the filled and empty atomic levels is given by:

$$w = \frac{2\pi}{\hbar} |V|^2 \rho(E), \qquad (1)$$

where $|V|$ is sometimes called the zero-point Rabi matrix element and $\rho(E)$ is the density of final states per unit energy. In spontaneous emission, the density of final states is the density of optical modes available to the photon emitted in Fig. 1. If there are no optical modes available, there will be no spontaneous emission.

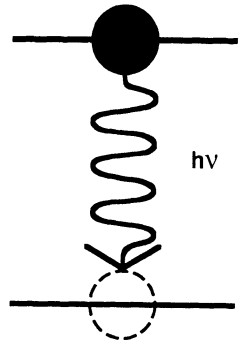

Figure 1. A spontaneous emission event from a filled upper level to an empty lower level. The density of final states is the available mode density for photons.

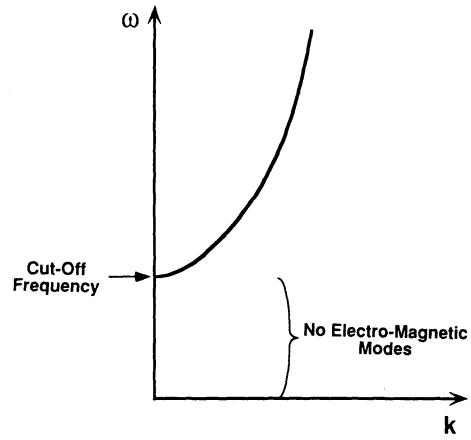

Figure 2. Electromagnetic wave dispersion between a pair of metal plates. The waveguide dispersion has a cut-off frequency below which there are no electromagnetic modes, and there is no spontaneous emission allowed.

Before the 1980s, spontaneous emission was often regarded as a natural and inescapable phenomenon, one over which no control was possible. In spectroscopy it gave rise to the term "natural linewidth". However in 1946, an overlooked note by Purcell[4] on nuclear spin levels, had already indicated that spontaneous emission could be controlled. In the early '70s, interest in this phenomenon was re-awakened by the surface-adsorbed dye molecule fluorescence studies[5] of Drexhage. Indeed during the mid-'70s, Bykov proposed[6] that 1-dimensional periodicity inside a co-axial line could influence spontaneous emission. The modern era of inhibited spontaneous emission dates from the Rydberg atom experiments of Kleppner. A pair of metal plates acts as a wave-guide, with a cut-off frequency for one of the two polarizations, as shown in Fig. 2. Rydberg atoms are atoms in very high lying principal quantum number states, which can spontaneously emit in the microwave region of wavelengths. Kleppner et al[7] showed that Rydberg atoms in a metallic waveguide could be prevented from undergoing spontaneous decay. There were no modes available below the wave-guide cut-off.

There is a problem with metallic waveguides however. They do not scale well into optical frequencies. At high frequencies, metals become more and more lossy. These dissipative losses allow for virtual modes, even at frequencies which would normally be forbidden. Therefore it makes sense to consider structures made of positive dielectric constant materials such as glasses and insulators, rather than metals. These can have very low dissipation, even all the way up to optical frequencies. This is ultimately exemplified by optical fibers which allow light propagation over many kilometers, with negligible losses. Such positive dielectric constant materials can have an almost purely real dielectric response with low resistive losses. If arrayed into a 3-dimensionally periodic dielectric structure, a photonic bandgap should be possible, employing a purely real, reactive, dielectric response.

The benefits of such a photonic bandgap for direct gap semiconductors are illustrated in Fig. 3. On the right side of the figure is a plot of the photon dispersion, (frequency versus wave-vector). On the left side of Fig. 3, sharing the same frequency axis, is a plot of the electron dispersion, showing conduction and valence bands appropriate to a direct gap semiconductor. Since atomic spacings are 1000 times shorter than optical wavelengths, the electron wave-vector must be divided by 1000 in order to fit on the same graph with the photon wave-vectors. The dots in the electron conduction and valence bands are meant to represent electrons and holes, respectively. If an electron were to recombine with a hole, they would produce a photon at the electronic band edge energy. As illustrated in Fig. 3, if a photonic bandgap straddles the electronic band edge, then the photon produced by electron-hole recombination would have no place to go. The spontaneous radiative recombination of electrons and holes would be inhibited. As can be imagined, this has far-reaching implications for semiconductor photonic devices.

One of the most important applications of inhibited spontaneous emission is likely to be the enhancement of photon number state squeezing, which has been playing an increasing role in quantum optics lately. The form of squeezing introduced by Yamamoto[3] is particularly appealing, in that the active element producing the squeezing effect is none other than the common resistor, as shown in Fig. 4. When an

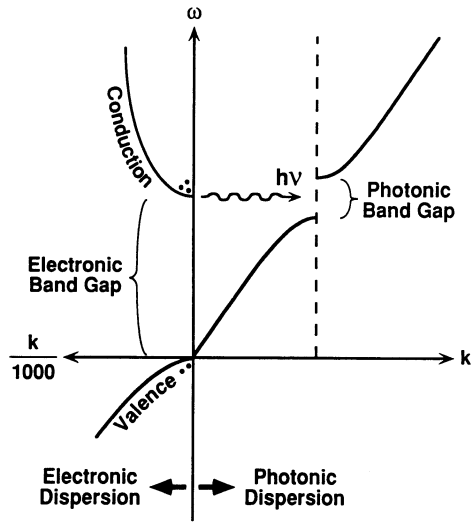

Figure 3. On the right side is the electromagnetic dispersion, with a forbidden gap at the wave vector of the periodicity. On the left side is the electron wave dispersion typical of a direct gap semiconductor, the dots representing electrons and holes. Since the photonic bandgap straddles the electronic band edge, electron-hole recombination into photons is inhibited. The photons have no place to go.

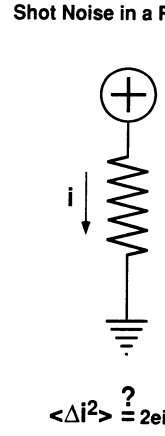

Figure 4. In a good quality metallic resistors, the current flow is quite regular, producing negligible amounts of shot noise.

electrical current flows, it generally carries the noise associated with the graininess of the electron charge, called shot noise. The corresponding mean square current fluctuations are:

$$\langle(\Delta i)^2\rangle = 2ei\Delta f \qquad (2)$$

where i is the average current flow, e is the electronic charge and Δf is the noise bandwidth. While Eq. (2) applies to many types of random physical processes, it is far from universal. Equation(2) requires that the passage of electrons in the current flow be a random Poissonian process. As early as 1954, Van der Ziel[8], in an authoritative book called *Noise*, pointed out that good quality metal film resistors, when carrying a current, generally exhibit much less noise than given by Eq. (2). Apparently, the flow of electrons in the Fermi sea of a metallic resistor represents a highly correlated process. Far from being a random process, the electrons apparently sense one another, producing shot noise far below Eq. (2); (so low as to be difficult to measure and to distinguish from thermal or Johnson noise). Sub-Poissonian shot noise has the following meaning: Suppose the average flow consists of 10 electrons per nanosecond. Under random flow, the count in successive nanoseconds could sometimes vary from 8 to 12 electrons. With good quality metal film resistors, the electron count would be 10 for each and every nanosecond.

Yamamoto[3] put this property to good use by driving a high quantum efficiency laser diode with such a resistor as shown in Fig. 5. Suppose the laser diode quantum efficiency in the cavity mode were 100%. Then, for each electron passing through the resistor there would be one photon into the laser cavity mode. A correlated stream of photons are produced whose statistical properties are unprecedented since Einstein's photo-electric effect. If the photons are used for optical communication, then a receiver would detect exactly 10 photo-electrons each nanosecond. If 11 photons were detected, it would be no mere random fluctuation, but would represent an intentional signal. Thus, information in an optical communications signal could be encoded at the level of individual photons. The name photon-number-state squeezing is associated with the fixed photon number per unit time interval. Expressed differently, the bit-error rate in optical communication can be diminished by squeezing.

There is a limitation to the squeezing, however. The quantum efficiency in into the lasing mode is not 100%. The 4π steradians outside the cavity mode can capture a significant amount of random spontaneous emission. If unwanted electromagnetic modes captured 50% of the excitation, then the maximum noise reduction in squeezing would be only 3dB. Therefore it is necessary to minimize the spontaneous recombination of electrons and holes into modes other than the lasing mode. If such random spontaneous events were reduced to 1% allowing 99% quantum efficiency into the lasing mode, the corresponding noise reduction would be 20dB, well worth fighting for. Thus we see that control of spontaneous emission is essential for deriving the full benefit from photonnumber-state squeezing.

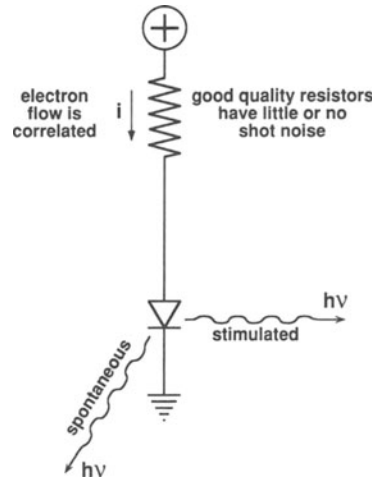

Figure 5. A high quantum efficiency laser diode converts the correlated flow of electrons from a low-shot-noise resistor into photon-number-state squeezed light. Random spontaneous emission outside the desired cavity mode limits the attainable noise reduction.

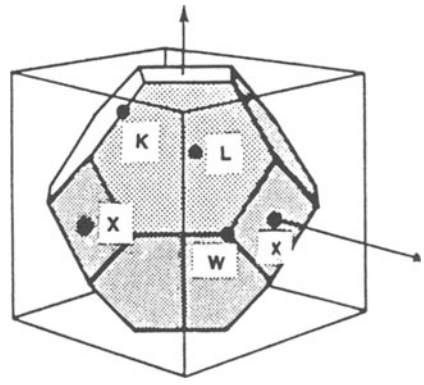

Figure 6. The face-centered-cubic Brillouin Zone in reciprocal space.

We have motivated the study of photonic band structure for its applications in quantum optics and optical communications. Positive dielectric constants and fully 3-dimensional forbidden gaps were emphasized. It is now clear that the generality of artificial, multi-dimensional, band structure concepts allows for other types of waves, other materials, and various lower dimensional geometries, limited only by imagination and need.

SEARCH FOR THE PHOTONIC BANDGAP

Having decided create a photonic bandgap in three dimensions, we need to settle on a particular 3-dimensionally periodic geometry. For electrons, the 3-dimensional crystal structures come from nature. Several hundred years of mineralogy and crystallography have classified the naturally occurring 3-dimensionally periodic lattices. For photonic bandgaps, we must create an artificial structure using our imagination.

The face-centered-cubic (fcc) lattice appears to be favored for photonic bandgaps, and was suggested independently by Yablonovitch[1] and John[2] in their initial proposals. Let us consider the fcc Brillouin Zone (BZ) as illustrated in Fig. 6. Various special points on the surface of the BZ are marked. Closest to the center is the L-point oriented toward the body diagonal of the cube. Farthest away is the W-point, a vertex where 4 plane waves are degenerate, (which will cause problems later on). In the cubic directions are the familiar X-points.

Consider a plane wave in the X-direction. It will sense the periodicity in the cubic direction, forming a standing wave, opening up a forbidden gap as indicated by the shading in Fig. 7. Suppose, on the other hand, the plane wave is going in the L direction. It will sense the periodicity along the cubic-body-diagonal, and a gap will form in that direction as well. But the wave vector to the L-point is about 14% smaller than the wave-vector to the X-point. Therefore, the gap at L is likely to be centered at a 14% smaller frequency than the gap at X. If the two gaps are not wide enough, they are unlikely to overlap in frequency. In Fig. 7 as shown, the two gaps barely overlap. This is the main problem in achieving a photonic bandgap. It is difficult to ensure that a common frequency overlap is assured for all possible directions in reciprocal space.

The lesson from Fig. 7 is that the Brillouin Zone should most closely resemble a sphere in order to increase the likelihood of a common frequency overlap in all directions of space. Therefore, let us look at the two common Brillouin Zones in Fig. 8, the fcc BZ and the body-centered-cubic (bcc) BZ. The bcc BZ has pointy vertices which make it difficult to achieve a common frequency overlap in all directions. Likewise most other common BZ's deviate even farther from a spherical shape. Among all the common BZ's the fcc has the least percentage deviation from a sphere. Therefore, up until now all photonic bandgaps in 3 dimensions have been based[9] on the fcc lattice.

The photonic bandgap is different from the idea of a 1-dimensional stop band as understood in electrical engineering. Rather, the photonic bandgap should be regarded as a stop band with a common frequency

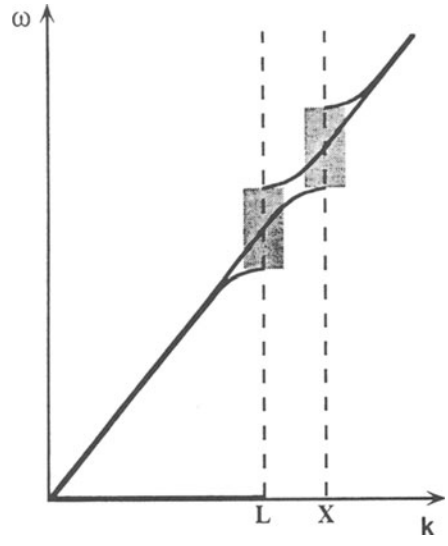

Figure 7. The forbidden gap (shaded) at the L-point is centered at a frequency ~14% lower than the X-point forbidden gap. Therefore it is difficult to create a forbidden frequency band overlapping all points along the surface of the Brillouin Zone.

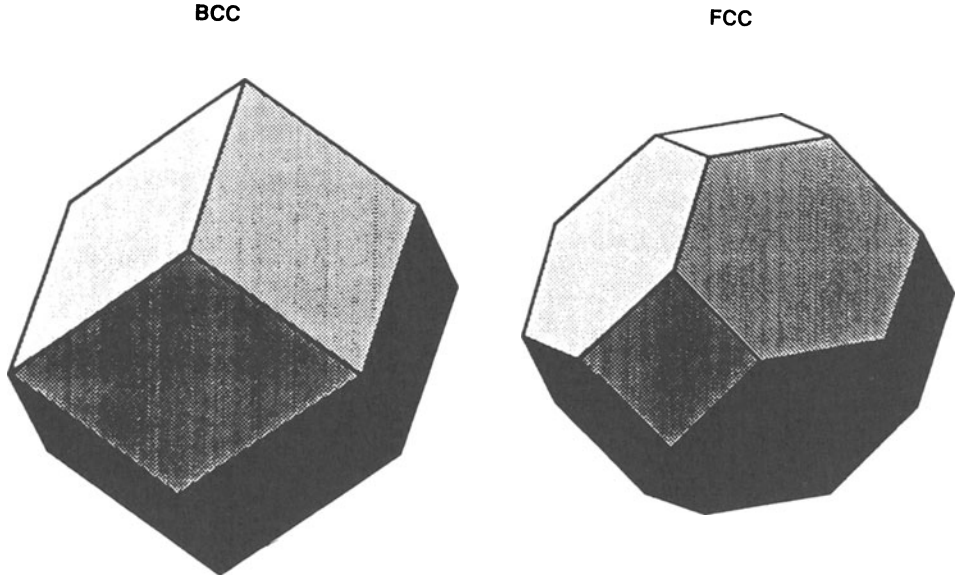

Figure 8. Two common Brillouin Zones for body-centered and face-centered cubic. The fcc case deviates least from a sphere, favoring a common overlapping band in all directions of space.

overlap in all 4π steradians of space. The earliest antecedent to photonic band structure, dating[10] back to 1914 and Sir Lawrence Bragg, is the Dynamical Theory of X-ray Diffraction. Nature gives us face-centered-cubic crystals and X-rays are bona fide electromagnetic waves. As early as 1914, narrow stop bands were known to open up. Therefore, what was missing?

The refractive index contrast for X-rays is tiny, generally 1 part in 10^4. The forbidden X-ray stop bands form extremely narrow rings on the facets of the BZ. As the index contrast is increased, the narrow forbidden rings open up, eventually covering an entire facet of a BZ and ultimately all directions in reciprocal space. We will see that this requires an index contrast $\gtrsim 2$ to 1. The high index contrast is the main new feature of photonic band structure beyond dynamical X-ray diffraction. In addition, we will see that electromagnetic wave polarization, which is frequently overlooked for X-rays, will play a major role in photonic band structure.

In approaching this subject, we adopted an empirical view-point. We decided to make photonic crystals on the scale of microwaves, and then we tested them using sophisticated coherent microwave instruments. The test setup, shown in Fig. 9, is what we would call in optics a Mach-Zender interferometer. It is capable of measuring phase and amplitude in transmission through the microwave scale photonic crystal. In principle, one can determine the frequency versus wave-vector dispersion relations from such coherent measurements. Later on we used a powerful commercial instrument for this purpose, the HP8510 Network Analyzer. The philosophy of the experiments was to measure the forbidden gap in all possible internal directions in reciprocal space. Accordingly, the photonic crystal was rotated and the transmission measurements repeated. Due to wave vector matching along the surface of the photonic crystal, some internal angles could not be accessed. To overcome this, large microwave prisms, made out of polymethyl-methacrylate, were placed on either side of the test crystal in Fig. 9.

Early on the question arose, of what material should the photonic crystal be made? The larger the refractive index contrast, the easier it would be to find a photonic bandgap. In optics however, the largest practical index contrast is that of the common semiconductors, Si and GaAs, with a refractive index n= 3.6. If that index was inadequate, then photonic crystals would probably never fulfill the goal of being useful in optics. Therefore, we decided to restrict the microwave refractive index to 3.6, and the microwave dielectric constant to $n^2 = 12$. A commercial microwave material, Emerson & Cumming Stycast 12 was particularly suited to the task, since it was machinable with carbide tool bits. Any photonic band structure that was found in this material could simply be scaled down in size and would have the identical dispersion relations at optical frequencies and optical wavelengths.

With regard to the geometry of the photonic crystal, there are a universe of possibilities. So far, the only restriction we have made is toward face-centered-cubic lattices. It turns out that a crystal, with an fcc BZ in reciprocal space, as shown in Fig. 6, is composed of fcc Wigner-Seitz unit cells in real space as shown in Fig. 10. The problem of

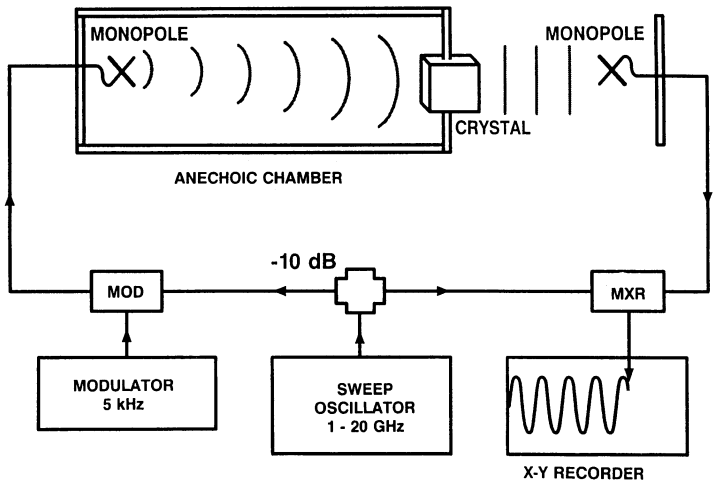

Figure 9. A homodyne detection system for measuring phase and amplitude in transmission through the photonic crystal under test. A sweep oscillator feeds a 10dB splitter. Part of the signal is modulated (MOD) and then propagated as a plane wave through the test crystal. The other part of the signal is used as local oscillator for the mixer (MXR) to measure the amplitude change and phase shift in the crystal. Between the mixer and the X-Y recorder is a lock-in amplifier (not shown).

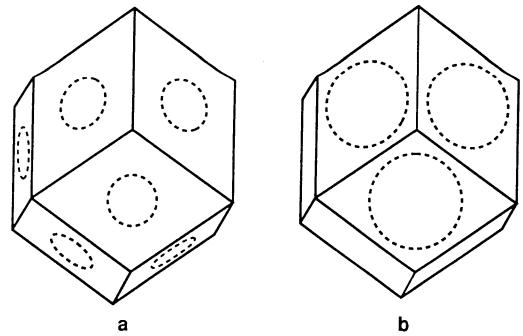

Figure 10. The Wigner-Seitz real-space-unit-cell of the fcc lattice is a rhombic dodecahedron. (a) Slightly oversized spherical voids are inscribed into the unit cell, breaking through the faces, as illustrated by dashed circles. (b) W-S cell structure possessing a photonic bandgap. Cylindrical holes are drilled through the top 3 facets of the rhombic dodecahedron and exit through the bottom 3 facets. The resulting atoms are roughly cylindrical, and have a preferred axis in the vertical direction.

creating an arbitrary fcc dielectric structure reduces to the problem of filling the fcc W-S real-space-unit-cell with an arbitrary spatial distribution of dielectric material. Real space is then filled by repeated translation and close-packing of the W-S unit cells. The decision before us is what to put inside the fcc Wigner-Seitz cells. There are an infinite number of possible fcc lattices since anything can be put inside the fundamental repeating unit. The problem before us is: What do we put inside the fcc W-S unit cell in Fig. 10? In X-ray language, we had to find a "Form Factor" for the W-S unit cell which would produce a crystal with a photonic bandgap.

This question provoked strenuous difficulties and false starts over a period of several years before finally being solved. In the first years of this research, we were unaware of how difficult the search for a photonic bandgap would be. A number of fcc crystal structures were proposed, each representing a different choice for filling the rhombic dodecahedron fcc W-S cells in real space. For example the very first suggestion[1], was to make a 3-dimensional "checkerboard" as in Fig. 11, in which cubes were inscribed inside the fcc W-S real space cells in Fig. 10. Later on, the experiments[11] adopted spherical "atoms" centered inside the fcc W-S cell composed of precision Al_2O_3 spheres, n~3.06, each ~6mm in diameter. This structure was tested at a number of filling ratios from close-packing to very dilute. Nevertheless, it always failed to produce a photonic bandgap!

Then, we tested the inverse structure in which spherical voids were inscribed inside the fcc W-S real space cell. These could be easily fabricated by drilling hemispheres onto the opposite faces of a dielectric sheet with a spherical drill bit as shown in Fig. 12. When the sheets were stacked up so that the hemispheres faced one another, the result was an fcc array of spherical voids inside a dielectric block. These were also tested over a wide range of filling ratios by progressively increasing the diameter of the hemispheres. These also failed to produce a photonic bandgap!

The typical failure mode is illustrated in Fig. 13. As expected, the "conduction band" at the L-point falls at a low frequency, while the "valence band" at the W-point falls at a high frequency. The overlap of the bands at L and W results in a band structure which is best described as "semi-metallic".

The empirical search for a photonic bandgap led nowhere until we tested a spherical void structure with oversized voids breaking through the walls of the W-S unit cell as shown in Fig. 10(a). For the first time, the measurements seemed to indicate a photonic bandgap, and we published[11] the band structure shown in Fig. 14. There appeared to be a narrow gap, centered at 15GHz, and forbidden for both possible polarizations. Unknown to us, however, Fig. 14 harbored a serious error. Instead of a gap at the W-point, the conduction and valence bands crossed at that point allowing the bands to touch. This produced a pseudo-gap with zero density of states but *no* frequency width. The error arose due to the limited size of the crystal. The construction of crystals with ~10^4 atoms required tens of thousands of holes to be drilled. Such a 3-dimensional crystal was still only 12 cubic units wide, limiting the wave-vector resolution, and restricting the dynamic range in

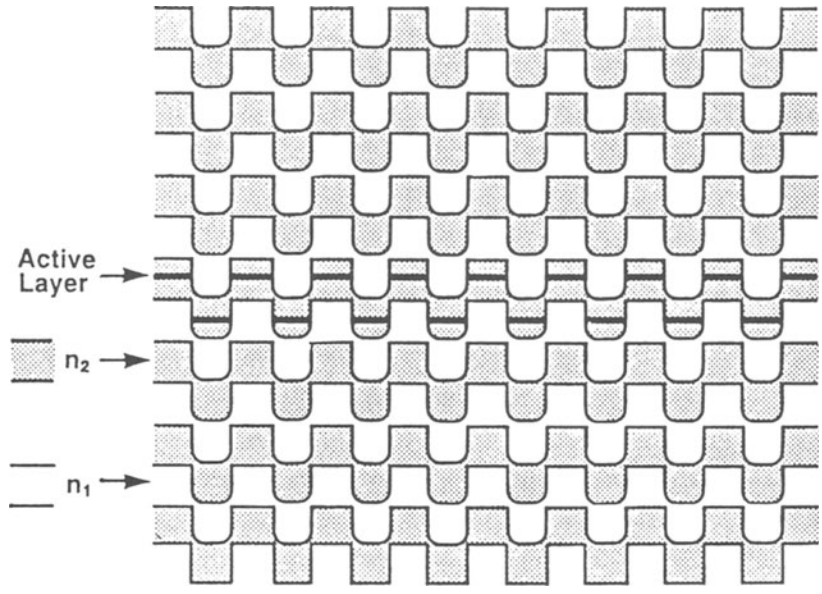

Figure 11. A face-centered-cubic crystal in which the individual W-S cells are inscribed with cubes stacked in a 3-dimensional "checkerboard" .

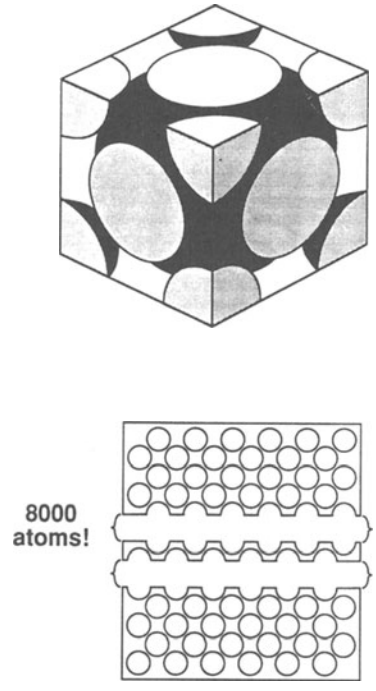

Figure 12. Construction of fcc crystals consisting of spherical voids. Hemispherical holes are drilled on both faces of a dielectric sheet. When the sheets are stacked up, the hemispheres meet producing an fcc crystal.

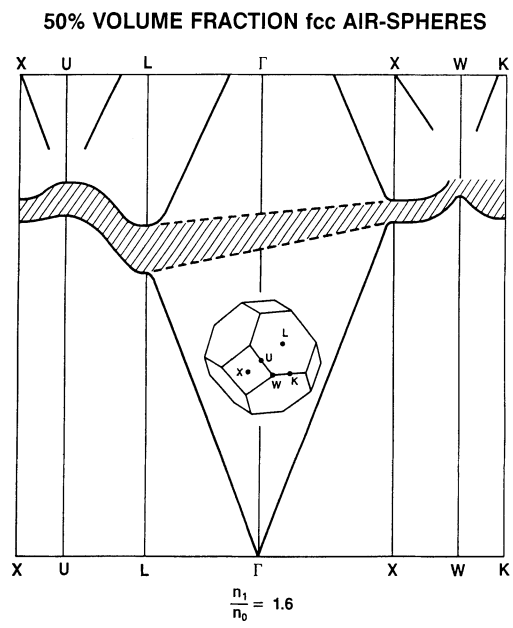

Figure 13. Typical semi-metallic band structure for a photonic crystal with no photonic bandgap. An overlap exists between the conduction band at L and the valence band at W.

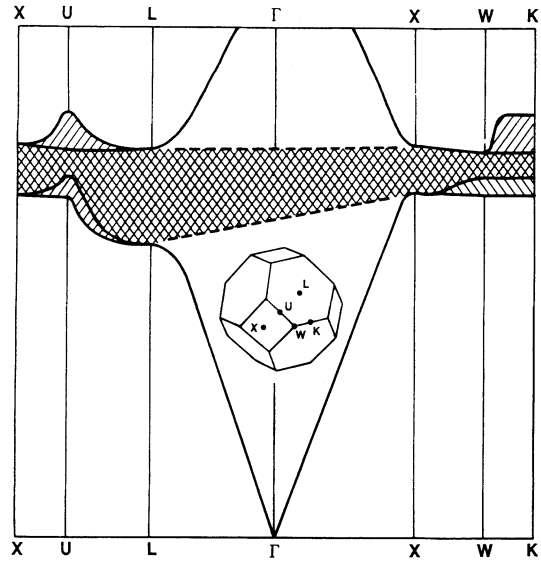

Figure 14. The purported photonic band structure of the spherical void structure shown in Fig. 10(a). The right sloping lines represent polarization parallel to the X-plane, while the left sloping lines represent the orthogonal polarization which has a partial component out of the X-plane. The cross hatched region is the reported photonic bandgap. This figure fails to show the crossing of the valence and conduction bands at the W-point which was first discovered by theory.

transmission. Under these conditions, it was experimentally difficult to notice a conduction-valence band degeneracy which occurred at an isolated point in k-space, such as the W-point.

While we were busy with the empirical search, theorists began serious efforts to calculate photonic band structure. The most rapid progress was made not by specialists in electromagnetic theory, but by electronic band structure theorists who were accustomed to solving Schrödinger's equation in 3-dimensionally periodic potentials. The early calculations[12-15] were unsuccessful however. As a short cut, they treated the electromagnetic field as a scalar, much as is done for electron waves in Schrödinger's equation. The scalar wave theory of photonic band structure did not agree well with experiment. For example, it predicted photonic bandgaps in the dielectric sphere structure, where none were observed experimentally. The approximation of Maxwell's equations as a scalar wave equation was not working. Finally, incorporating the full vector Maxwell's equations, theory began to agree with experiment. Leung and Liu[16] were probably the first to publish a successful vector wave calculation in photonic band structure, followed by others[17-18] with substantially similar results. The theorists agreed well with one another, and they agreed well with experiment[11] except at the high degeneracy points U and particularly W. What the experiment failed to see was the degenerate crossing of valence and conduction bands at those points.

The unexpected pseudo-gap in the fcc crystal triggered concern and a search for a way to overcome the problem. A worried editorial[19] was published in *Nature*. But even before the editorial appeared, the problem had already been solved by the Iowa State group of Ho, Chan, and Soukoulis.[18] The degenerate crossing at the W-point was very susceptible to changes in symmetry of the structure. If the symmetry was lowered by filling the W-S unit cell not by a single spherical atom, but by two atoms positioned along the <111> direction, as in diamond structure, then a full photonic bandgap opened up. Their discovery of a photonic bandgap using a diamond "form factor" is particularly significant, since diamond geometry seems to be favored by Maxwell's equations. A form of diamond structure[20] gives the widest photonic bandgaps requiring the least index contrast, n~1.87.

More generally, the spherical void symmetry in Fig. 10(a) can be lowered by distorting the spheres along the <111> direction, lifting the degeneracy at the W-point. The W-S unit cell in Fig. 10(b) has great merit for this purpose. Holes are drilled through the top 3 facets of the rhombic dodecahedron and exit through the bottom 3 facets. The beauty of the structure in Fig. 10(b) is that a stacking of W-S unit cells results in straight holes which pass clear through the entire "crystal"! The "atoms" are odd-shaped, roughly cylindrical voids centered in the W-S unit cell, with a preferred axis pointing to the top vertex, <111>. An operational illustration of the construction which produces an fcc " crystal" of such W-S unit cells is shown in Fig. 15.

A slab of material is covered by a mask containing a triangular array of holes. Three drilling operations are conducted through each hole, 35.26° off normal incidence and spread out 120° on the azimuth. The resulting criss-cross of holes below the surface of the slab produces a fully 3-dimensionally periodic fcc structure, with W-S unit cells given by

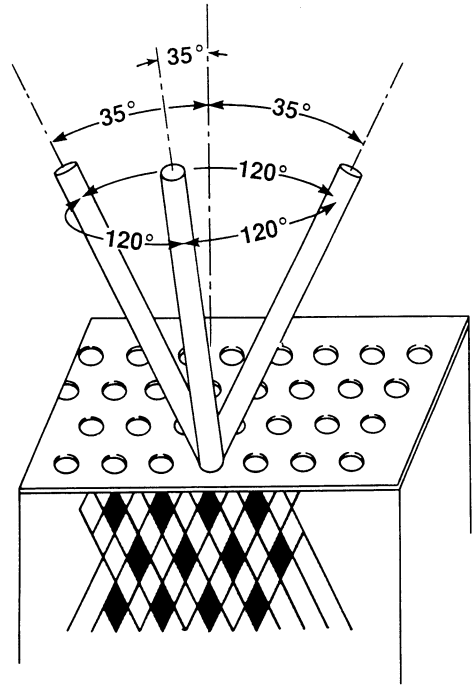

Figure 15. The method of constructing an fcc lattice of the Wigner-Seitz cells as shown in Fig. 10(b). A slab of material is covered by a mask consisting of a triangular array of holes. Each hole is drilled through 3 times, at an angle 35.26° away from normal, and spread out 120° on the azimuth. The resulting criss-cross of holes below the surface of the slab, suggested by the cross-hatching shown here, produces a fully 3-dimensionally periodic fcc structure, with unit cells as given by Fig. 10(b). The drilling can be done by a real drill bit for microwave work or by reactive ion etching to create an fcc structure at optical wavelengths.

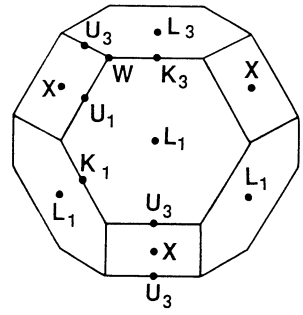

Figure 16. The Brillouin Zone of an fcc structure incorporating non-spherical atoms, as in Fig. 10(b). Since the space lattice is not distorted, this is simply the standard fcc Brillouin Zone lying on a hexagonal face rather than the usual cubic face. Only the L-points on the top and bottom hexagons are 3-fold symmetry axes. Therefore they are labeled L_3. The L-points on the other 6 hexagons are labeled L_1. The U_3-K_3 points are equivalent since they are a reciprocal lattice vector apart. Likewise the U_1-K_1points are equivalent.

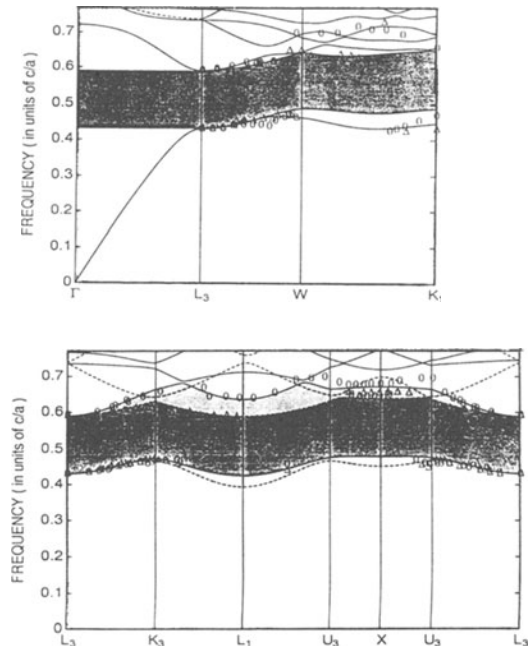

Figure 17. Frequency versus wave-vector, ω–vs- k, dispersion along the surface of the Brillouin Zone shown in Fig. 16, where c/a is the speed of light divided by the fcc cube length. The ovals and triangles are the experimental points for s and p polarization respectively. The solid and dashed lines are the calculations for s and p polarization respectively. The dark shaded band is the totally forbidden bandgap. The lighter shaded stripes above and below the dark band are forbidden only for s and p polarization respectively.

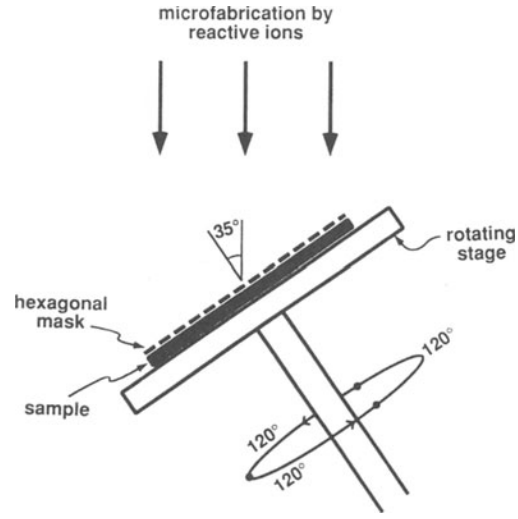

Figure 18. Construction of the non-spherical void photonic crystal of Fig. 10(b) and Figs. 15-17 by reactive ion etching.

Fig. 10(b)! The drilling can be done by a real drill bit for microwave work or by reactive ion etching to create an fcc structure at optical wavelengths.

In spite of non-spherical atoms in Fig. 10(b), the Brillouin Zone (BZ) is identical to the standard fcc BZ shown in textbooks. Nevertheless, we have chosen an unusual perspective from which to view the Brillouin Zone in Fig. 16. Instead of having the fcc BZ resting on one of its diamond-shaped facets as is usually done, we have chosen in Fig. 16, to present it resting on a hexagonal face. Since there is a preferred axis for the atoms, the distinctive L,points centered in the top and bottom hexagons are 3-fold symmetry axes, and are labeled L_3. The L-points centered in the other 6 hexagons are symmetric only under a 360° rotation, and are labeled L_1. It is helpful to know that the U_3-K_3 points are equivalent since they are a reciprocal lattice vector apart. Likewise, the U_1-K_1 points are equivalent.

Figure 17 shows the dispersion relations along different meridians for our primary experimental sample of normalized hole diameter d/a= 0.469 and 78% volume fraction removed, (where a is the unit cube length). The oval points represent experimental data with s-polarization ($\perp$ to the plane of incidence, $\parallel$ to the slab surface), while the triangular points represent p-polarization ($\parallel$ to the plane of incidence, partially $\perp$ to the slab surface). The horizontal abscissa in the lower graph of Fig. 20, L_3-K_3-L_1-U_3-X-U_3-L_3 represents a full meridian from the North pole to the South pole of the BZ. Along this meridian the Bloch wave functions separate neatly into s and p polarizations. The s and p polarized theory curves are the solid and dashed lines, respectively. The dark shaded band is the totally forbidden photonic bandgap. The lighter shaded stripes above and below the dark band are forbidden only for s and p polarization, respectively.

At a typical semiconductor refractive index, n= 3.6, the 3-d forbidden gap width is 19% of its center frequency. Calculations[21] indicate that the gap remains open for refractive indices as low as n=2.1 using circular holes. We have also measured the imaginary wave vector dispersion within the forbidden gap. At mid-gap we find an attenuation of 10dB per unit cube length a. Therefore, the photonic crystal need not be very many layers thick to effectively expel the zero-point electromagnetic field. The construction of Fig. 15 can be implemented by reactive ion etching as shown in Fig. 18. In reactive ion etching, the projection of circular mask openings at 35° leaves oval holes in the material, which might not perform as well. Fortunately it was found,[21] defying Murphy's Law, that the forbidden gap width for oval holes is actually improved, fully 21.7% of its center frequency.

DOPING THE PHOTONIC CRYSTAL

The perfect semiconductor crystal is quite elegant and beautiful, but it becomes ever more useful when it is doped. Likewise, the perfect photonic crystal can become of even greater value when a defect[22] is introduced.

Lasers, for example, require that the perfect 3-d translational symmetry should be broken. Even while spontaneous emission into all 4π steradians should be inhibited, a local electromagnetic mode, linked to a defect, is still necessary to accept the stimulated emission. In 1-dimensional distributed feedback lasers,[23] a quarter wavelength defect is introduced, forming effectively a Fabry-Perot cavity as shown in Fig. 19. In 3-dimensional photonic band structure a local defect-induced structure resembles a Fabry-Perot cavity, except that it reflects radiation back upon itself in all 4π spatial directions.

The perfect 3-dimensional translational symmetry of a dielectric structure can be lifted in either one of two ways: (1) Extra dielectric material may be added to one of the unit cells. We find that such a defect behaves very much like a donor atom in a semiconductor. It gives rise to donor modes which have their origin at the bottom of the conduction band. (2) Conversely, translational symmetry can be broken by removing some dielectric material from one of the unit cells. Such defects resemble acceptor atoms in semiconductors. The associated acceptor modes have their origin at the top of the valence band. We will find that acceptor modes are particularly well-suited to act as laser microresonator cavities. Indeed it appears that photonic crystals made of sapphire or other lowloss dielectrics, will make the highest-Q single-mode cavities (of modal volume $\sim 1\ \lambda^3$) covering electromagnetic frequencies above the useful working range of superconducting metallic cavities. The short wavelength limit in the ultraviolet, is set by the availability of optical materials with refractive index $\gtrsim 2$, the threshold index[18,21] for the existence of a photonic bandgap.

Figure 20 is a $\langle 1,\bar{1},0\rangle$ cross-section of our photonic crystal of Fig. 10(b) and Figs. 15-17, cutting through the center of a unit cube. Shading represents dielectric material. The large dots are centered on the air-atoms and the rectangular dashed line is a face-diagonal cross-section of the unit cube. Since we could design the structure at will, donor defects were chosen to consist of a single dielectric sphere centered in an air-atom. Likewise, by breaking one of the inter-connecting ribs, it is easy to create acceptor modes. We selected an acceptor defect as shown in Fig. 20 centered in the unit cube. It comprises a vertical rib which has a missing horizontal slice.

The heart of our experimental apparatus is a photonic crystal embedded in microwave absorbing pads as shown in Fig. 21. The photonic crystals were 8-10 atomic layers thick in the $\langle 1,1,1\rangle$ direction. Monopole antennas, consisting of 6 mm pins, coupled radiation to the defect mode. The HP 8510 Network Analyzer was set up to measure transmission between the antennas. Figure 22(a) shows the transmission amplitude in the absence of a defect. There is very strong attenuation ($\sim 10^{-5}$) between 13GHz and 16GHz marking the valence and conduction band edges of the forbidden gap. This is a tribute to both the dynamic range of the network analyzer, and the sizable imaginary wavevector in the forbidden gap.

A transmission spectrum in the presence of an acceptor defect is shown in Fig. 22(b). Most of the spectrum is unaffected, except at the

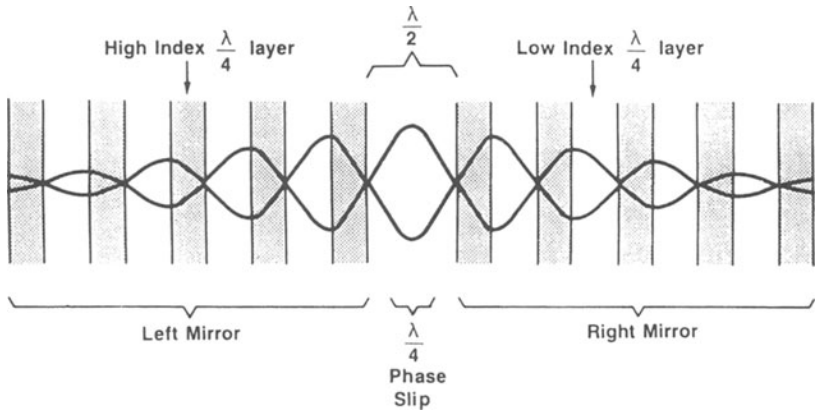

Figure 19. A 1-dimensional Fabry-Perot resonator made of multilayer dielectric mirrors with a space of one-half wavelength between the left and right mirrors. The net effect is to introduce a quarter wavelength phase slip defect into the overall periodic structure. A defect mode is introduced at mid-gap.

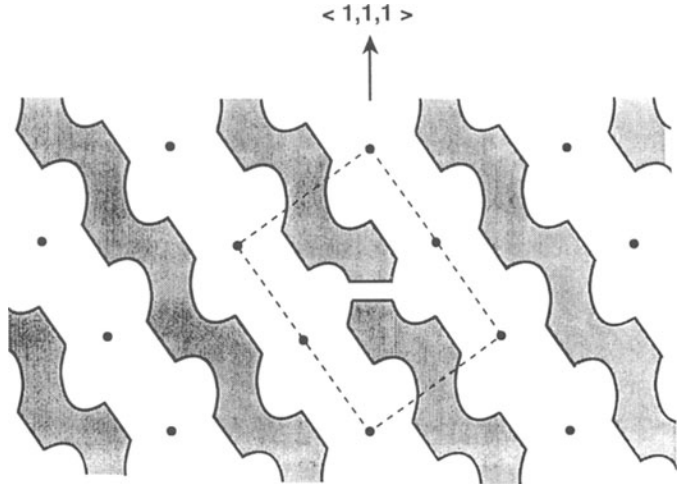

Figure 20. A <1,$\bar{1}$,0> cross-sectional view of our face-centered-cubic photonic crystal consisting of non-spherical "air-atoms" centered on the large dots. Dielectric material is represented by the shaded area. The rectangular dashed line is a face-diagonal crosssection of the unit cube. Donor defects consisted of a dielectric sphere centered on an atom. We selected an acceptor defect as shown, centered in the unit cube. It consists of a missing horizontal slice in a single vertical rib.

electromagnetic frequency marked Deep Acceptor within the forbidden gap. At that precise frequency, radiation "hops" from the transmitting antenna to the acceptor mode and then to the receiving antenna The acceptor level frequency, within the forbidden gap, is dependent on the volume of material removed. Figure 26 shows the acceptor level frequency as a function of defect volume removed from one unit cell. When a relatively large volume of material is removed, the acceptor level is deep as shown in Fig. 22(b). A smaller amount of material removed results in a shallow acceptor level, nearer the valence band. If the removed material volume falls below a threshold volume, the acceptor level falls within the continuum of levels below the top of the valence band, becoming metastable.

On an expanded frequency scale we can measure the resonator Q of the deep acceptor mode, which is Q~1000, as limited by the loss tangent of the Emerson & Cumming Stycast material of which the photonic crystal was made.

The behavior of an off-center donor defect is shown in Fig. 22(c). In this case, the donor volume was only slightly above the required threshold for forming bound donor modes. Already two shallow donor modes can be seen in Fig. 22(c). When the donor is centered in the Wigner-Seitz unit cell, the two modes merge to form a doubly degenerate donor level as in Fig. 23. Single donor defects seem to produce multiple donor levels. Figure 23 gives the donor level frequency as a function of donor volume. As in the case of acceptors, there is a threshold defect volume required for the creation of bound modes below the conduction band edge. However, the threshold volume for donor defects is almost ten times larger than the acceptor threshold volume. Apparently this is due to the electric field concentration in the dielectric ribs at the top of the valence band. Bloch wave functions at the top of the valence band are rather easily disrupted by the missing rib segment.

We have chosen in Fig. 23 to normalize the defect volume to a natural volume of the physical system, $[\lambda/2n]^3$, which is basically a cubic half-wavelength in the dielectric medium. More specifically, λ is the vacuum wavelength at the midgap frequency, and n is the refractive index of the dielectric medium. Since we are measuring a dielectric volume, it makes sense to normalize to a half-wavelength cube as measured at the dielectric refractive index. Based on the reasonable scaling of Fig. 23, our choice of volume normalization would seem justified.

The vertical rib with a missing horizontal slice, as in Fig. 20, can be readily microfabricated. It should be possible to create it in III-V materials by growing an aluminum-rich epitaxial layer and lithographically patterning it down to a single dot the size of one of the vertical ribs. After regrowth of the original III-V composition and reactive ion etching of the photonic crystal, HF acid etching, whose[24] selectivity $\geq 10^8$, will be used to remove the Al-rich horizontal slice from the one rib containing such a layer. The resonant frequency of the micro-cavity can be controlled by the thickness of the Al-rich sacrificial layer.

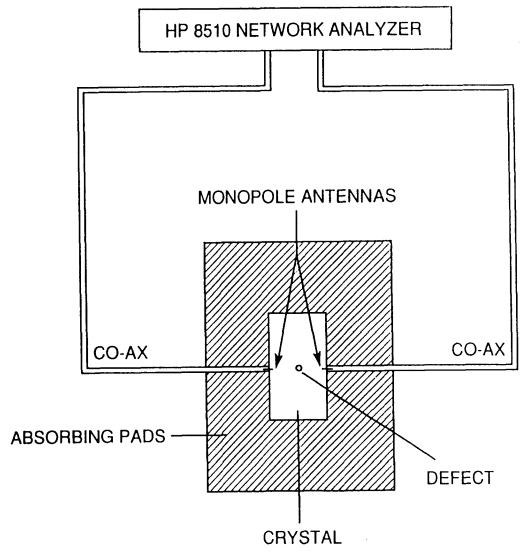

Figure 21. Experimental configuration for the detection of local electromagnetic modes in the vicinity of a lattice defect. Transmission amplitude attenuation from one antenna to the other is measured. At the local mode frequency the signal hops by means of the local mode in the center of the photonic crystal producing a local transmission peak. The signal propagates in the < 1,1,1> direction through 8-10 atomic layers.

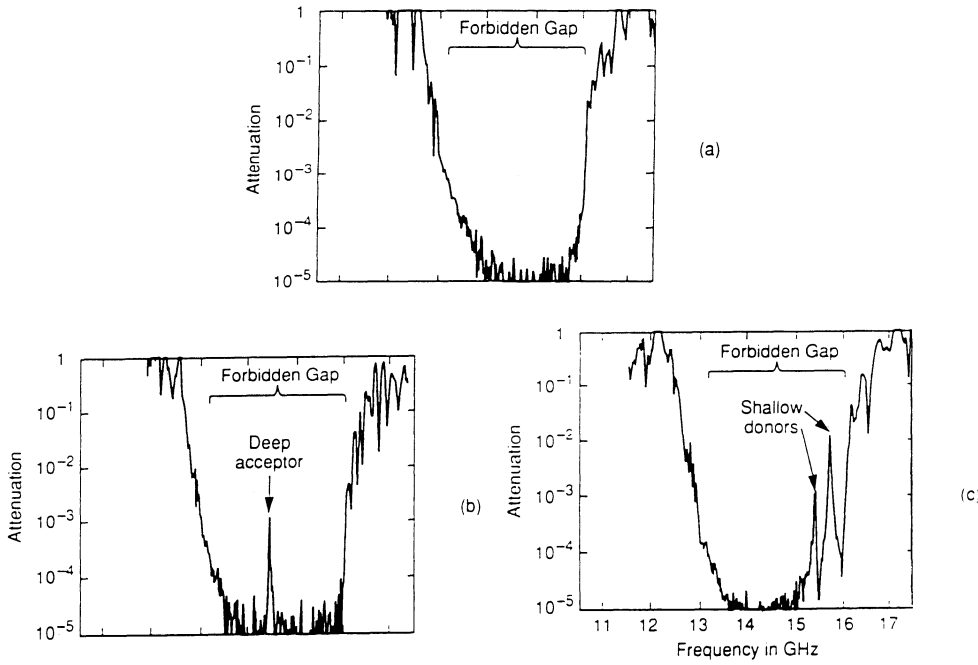

Figure 22. (a) Transmission attenuation through a defect-free photonic crystal, as a function of microwave frequency. The forbidden gap falls between 13GHz and 16GHz. (b) Attenuation through a photonic crystal with a single acceptor in the center. The large acceptor defect volume shifted its frequency near mid-gap. The electromagnetic resonator Q was ~1000, limited only by the loss tangent of the dielectric material. (c) Attenuation through a photonic crystal with a single donor defect, an uncentered dielectric sphere, leading to two shallow donor modes.

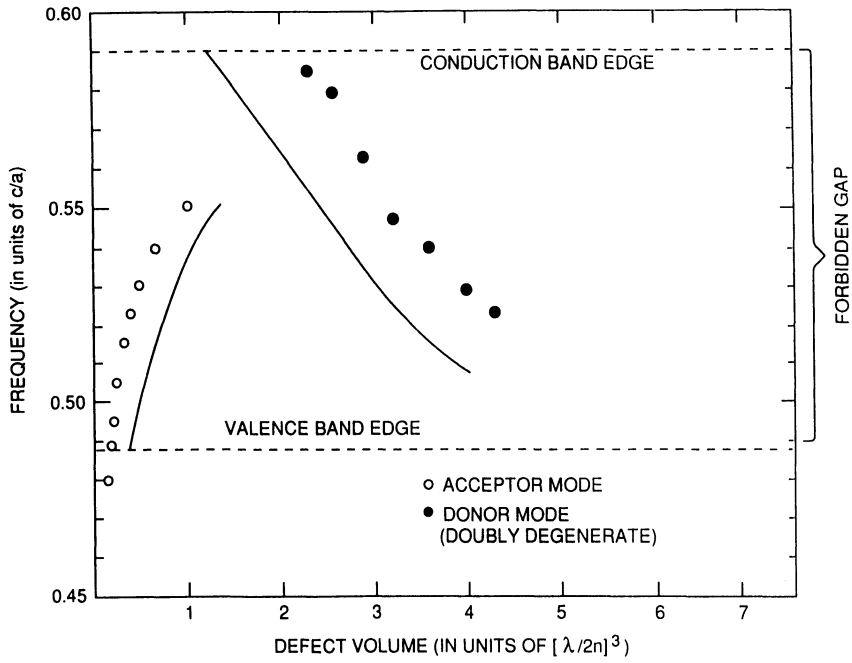

Figure 23. Donor and acceptor mode frequencies as a function of normalized donor and acceptor defect volume. The points are experimental and the corresponding lines are calculated. Defect volume is normalized to $[\lambda/2n]^3$ where λ is the mid-gap vacuum wavelength and n is the refractive index. A finite defect volume is required to bind a mode in the forbidden gap.

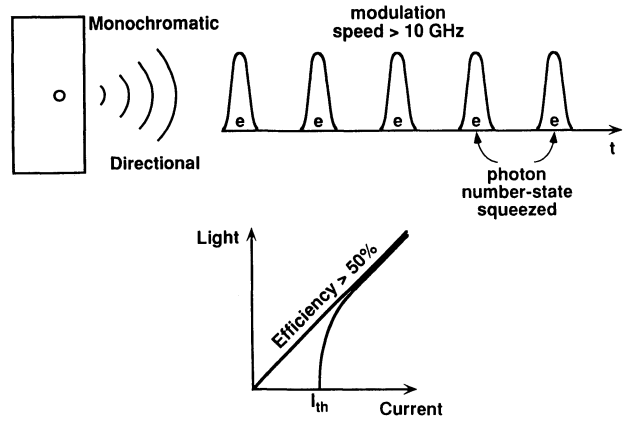

Figure 24. An illustration of the properties of the single-mode light-emitting-diode, (SM-LED), whose cavity is represented by the small circle inside the rectangular photonic crystal, at left. The words monochromatic and directional represent the temporal and spatial coherence of the SM-LED output as explained in the text. The modulation speed can be > 10GHz, and the differential quantum efficiency can be > 50%, competitive with laser diodes. But there is no threshold current for the SM-LED as indicated by the L-I curves at the bottom. The regular stream of photo-electrons, e, are meant to represent photon number state squeezing, which can be produced by the SM-LED if the spontaneous emission factor, β, of the cavity is high enough.

Therefore, by doping the photonic crystal, it is possible to create high-Q electromagnetic cavities whose modal volume is less than a half-wavelength cubed. These doped photonic crystals would be similar to metallic microwave cavities, except that they would be usable at higher frequencies where metal cavity walls would become lossy. Using sapphire as a dielectric, for example, it should be possible to make a millimeter wave cavity with $Q \gtrsim 10^9$. The idea is not to compete directly with superconducting cavities, but rather to operate at higher frequencies where the superconductors become lossy. Given the requirement for refractive index > 2, doped photonic crystals should work well up to ultraviolet wavelengths where diamond crystals and TiO_2 are still transparent.

APPLICATIONS

The forthcoming availability of single-mode micro-cavities at optical frequencies will lead to a new situation in quantum electronics. Of course, microwave cavities containing a single electromagnetic mode have been known for a long time. At microwave frequencies, however, spontaneous emission of electromagnetic radiation is a weak and unimportant process. At optical frequencies, spontaneous emission comes into its own. Now we can combine the physics and technology of spontaneous emission with the capability for single mode micro-cavities at optical frequencies where spontaneous emission is important. This combination is fundamentally a new regime in quantum electronics.

The major example of this new type of device is the single-mode light-emitting-diode (SM-LED), which can have many of the favorable coherence properties of lasers, while being a more reliable, and threshold less device. Progress in electromagnetic microcavities, allows all the spontaneous emission of an LED to be funneled into a single electromagnetic mode.

As the interest in low-threshold semiconductor laser diodes has grown, e.g., for optical interconnects, its spontaneously luminescent half-brother, the light-emitting-diode has begun to re-emerge in a new form. In this new form, the LED is surrounded by an optical cavity. The idea is for the optical cavity to make available only a single electromagnetic mode for the output spontaneous emission from the semiconductor diode. In fact, the Figure-of-Merit for such a cavity is β, the fraction of spontaneous emission which is being funneled into the desired mode. What is new for this application is the prospective ability to make high β cavities at optical frequencies employing photonic crystals. The 3-dimensional character of the cavities ensures that spontaneous emission will not seek out those neglected modes which are found propagating in a direction away from the optical confinement.

With all the spontaneous emission funneled into a single optical mode, the SM-LED can begin to have many of the coherence and statistical properties normally associated with above-threshold lasing. The essential point is that the spontaneous emission factor, β, should approach unity. (A closely related concept is that of the "zero-threshold

laser", in which the high spontaneous emission factor produces a very soft and indistinct threshold characteristic in the light output-versus-current input curve of laser diodes.) The idea is to combine the advantages of the LED which is thresholdless and highly reliable, with those of the semiconductor laser which is coherent and very efficient.

The coherence properties of the single-mode LED (SM-LED) are illustrated in Fig. 24. In a laser, single mode emission is the result of gain saturation and mode competition. In the SM-LED, there is no gain and therefore no gain saturation, but the output is still single-mode, because only one mode is available for emission. Since a single spatial mode can always be mode converted into a plane wave, the SM-LED can be regarded as having spatial coherence.

What about temporal coherence? The spectral linewidth of the SM-LED is narrower than the luminescence band of the semiconductor. All the radiation is funneled into the narrow spectral band determined by the micro-cavity Q. Thus SM-LED's have both spatial and temporal coherence as represented by words " directional" and " monochromatic" in Fig. 24.

What about the modulation speed of SM-LED's in comparison to laser diodes under direct current modulation? Generally, the modulation speed depends on the carrier's lifetime. Since electron-hole pairs in laser diodes experience both spontaneous and stimulated recombination, they have an advantage. However, single-mode cavities concentrate zero-point electric field fluctuations into a smaller volume creating a stronger matrix element for spontaneous emission. Detailed calculations indicate that spontaneous emission can be speeded up by a factor ~10 due to this cavity quantum electro-dynamic (QED) effect. On Fig. 24, we indicate that a modulation speed > 10GHz should be possible for SM-LED's.

The same cavity QED effects can enhance the spontaneous emission efficiency of SM-LED's since the radiative rate can then compete more successfully with non-radiative rates. External efficiency should exceed 50%, but this can come most easily from intelligent LED design[25] rather than cavity QED effects.

Shown at the bottom of Fig. 24 is the light output versus current input curve of SM-LED's and laser diodes. SM-LED's can compete with laser diodes in terms of differential external efficiency, but the SM-LED's can have the advantage by not demanding any threshold current. Lack of threshold behavior makes the output power and the operating wavelength of an SM-LED relatively insensitive to ambient temperature. Combined with the inherent reliability of an LED, this should produce many systems advantages for the SM-LED concept.

The final SM-LED property illustrated in Fig. 24 is photon number state squeezing, as suggested by the regular sequence of photo-electrons on the horizontal line. Stimulated emission is *not* required for these exotic squeezing effects. The critical variable is absolute quantum efficiency. If the quantum efficiency of the SM-LED is high, then these useful correlations will exist in the spontaneous output of the single-mode LED. This requires, most of all, a high spontaneous emission factor, β, our overall Figure-of-Merit for microcavities.

There are many other applications for photonic crystals, particularly in the microwave and millimeter wave regime. They are very imaginative and have gone far beyond our initial goals for using photonic crystals in quantum optics.

CONCLUSIONS

It is worthwhile to summarize the similarities and the differences between photonic band structure (PBS) and electronic band structure (EBS). This is best done by reference to Table I.

Electrons are massive and so the underlying dispersion relation for electrons in crystals is parabolic. Photons have no mass, so the underlying dispersion relation is linear. But as a result of the periodicity, the photons develop an effective mass in PBS and this should come as very little surprise.

Electrons have spin 1/2, but frequently this is ignored and Schrödinger's equation is treated in a scalar wave approximation. In electronic band theory, the spin 1/2 is occasionally important, however. In contrast, photons have spin 1, but it is generally never a good approximation to neglect polarization in PBS calculations.

Finally, we come to the accuracy of band theory. It is sometimes believed that band theory is always a good approximation in electronic

TABLE I. A summary of the differences and similarities between photonic band structure and electronic band structure.

	Electronic Band Structure	Photonic Band Structure
Underlying Dispersion Relation	parabolic	linear
Angular Momentum	Spin 1/2 scalar wave approximation	Spin 1 vector wave character
Accuracy of Band Theory	approximate due to electron-electron interactions	essentially exact

structure. This is not really true. When there are strong correlations, as in the high T_c superconductors, band theory is not even a good zeroth order approximation. Photons are highly non-interacting, so if anything, band theory makes more sense for photons than for electrons.

The final point to make about photonic crystals is they are very empty structures, consisting of about 78% empty space. But in a sense they are much emptier. They are emptier and quieter than even the vacuum, since they contain not even zero point fluctuation within the forbidden frequency band.

ACKNOWLEDGEMENTS

I would like to thank John Gural for drilling all the holes and Tom Gmitter for making the measurements. Thanks are also due to Ming Leung and Bob Meade for their collaborative work. The Iowa State group is thanked for making me aware of their diamond structure results prior to publication.

REFERENCES

1. E. Yablonovitch, *Phys. Rev. Lett.* **58**, 2059 (1987).
2. S. John, *Phys. Rev. Lett.* **58**, 2486 (1987).
3. Y. Yamamoto, S. Machida, and W. H. Richardson, *Science* **255**, 1219 (1992).
4. E. M. Purcell, *Phys. Rev.* **69**, 681(1946).
5. K H. Drexhage in *Progress in Optics, vol.* 12, ed. by E. Wolf (North-Holland, Amsterdam, 1974), see p. 165.
6. V. P. Bykov, Sov. *J. Quant. Elec.* **4**, 861(1975)
7. R. G. Hulet, E. S. Hilfer, and D. Kleppner, *Phys. Rev. Lett.* **55**, 2137 (1985).
8. A. Van der Ziel, *Noise,* (Prentice-Hall, N. Y., 1954). see pp. 208-209.
9. There has been a report recently, of a photonic bandgap in a simple cubic geometry. H. S. Sozuer, J. W. Haus, and R. Inguva, *Phys. Rev. B* **45**, 13962 (1992); The Iowa State group also has non fcc structures with photonic bandgaps.
10. C. G. Darwin, *Phil. Mag.* **27**, 675 (1914)
11. E. Yablonovitch and T. J. Gmitter, *Phys. Rev. Lett.* **63**, 1950 (1989).
12. S. Satpathy, Z. Zhang and M. R. Salehpour, *Phys. Rev. Lett.* **64**,1239 (1990).
13. K M. Leung and Y. F. Liu, *Phys. Rev. B***41**, 10188 (1990).
14. S. John and R. Rangarajan, *Phys. Rev. B***38**, 10101(1988).
15. E. N. Economou and A. Zdetsis, *Phys. Rev. B***40**, 1334 (1989).
16. K M. Leung and Y. F. Liu, *Phys. Rev. Lett.* **65**, 2646 (1990).
17. Z. Zhang and S. Satpathy, *Phys. Rev. Lett.* **65**, 2650 (1990).
18. K M. Ho, C. T. Chan and C. M. Soukoulis, *Phys. Rev. Lett.* **65**, 3152 (1990).
19. J. Maddox, *Nature* **348**, 481(1990).
20. C. T. Chan, K M. Ho, and C. M. Soukoulis, *Europhys. Lett.* **16**, 563 (1991).
21. E. Yablonovitch, T. J. Gmitter and K M. Leung, *Phys. Rev. Lett.* **67**, 2295 (1991).

22. E. Yablonovitch, T. J. Gmitter, R. D. Meade, A. M. Rappe, K D. Brommer and J. D. Joannopoulos, *Phys. Rev. Lett.* **67**, 3380 (1991).
23. H. A. Haus and C. V. Shank *IEEE J. Quant. Elec.* **QE-12**, 532 (1976). S. L McCall and P. M. Platzman, *IEEE J. Quant. Elec.* **QE-21**, 1899 (1985).
24. E. Yablonovitch, T. Gmitter, J. P. Harbison, R. Bhat, *Appl. Phys. Lett.* **51**, 2222 (1987).
25. I. Schnitzer, E. Yablonovitch, C. Caneau, and T. J. Gmitter, submitted to *Appl. Phys. Lett.*

PHOTONIC GAPS FOR ELECTROMAGNETIC WAVES IN PERIODIC DIELECTRIC STRUCTURES: DISCOVERY OF THE DIAMOND STRUCTURE

K. M. Ho, C. T. Chan, and C. M. Soukoulis

Ames Laboratory and
Department of Physics & Astronomy
Iowa State University
Ames, Iowa 50011, USA

INTRODUCTION

Electron waves traveling in the periodic potential of a crystal are arranged into energy bands separated by gaps in which propagating states are prohibited.[1] It is interesting to see if analogous band gaps exist when electromagnetic (EM) waves propagate in a periodic dielectric structure (e.g., a periodic lattice of dielectric spheres of dielectric constant ε_a embedded in a uniform dielectric background ε_b). If such a band gap or frequency gap exists, EM waves with frequencies inside the gap cannot propagate in any direction inside the material. These frequency gaps are referred to as "photonic band gaps."

Photonic band gaps can have a profound impact on many areas in pure and applied physics.[2,3] Due to the absence of optical modes in the gap, spontaneous emission is suppressed for photons with frequencies in the forbidden region.[4,5] It has been suggested that, by tuning the photonic band gap to overlap with the electronic band edge, the electron-hole recombination process can be controlled in a photonic band gap material, leading to enhanced efficiency and reduced noise in the operation of semiconductor lasers and other solid state devices.[5] The suppression of spontaneous emission in can also be used to prolong the lifetime of selected chemical species in catalytic processes.[6] Photonic band gap materials can also find applications in frequency-selective mirrors, band-pass filters, and resonators. Besides technical applications in various areas, scientists are interested in the possibility of observing the localization of EM waves by the introduction of defects and disorder in a photonic band gap material.[7-9] This will be an ideal realization of the phenomenon of localization uncomplicated by many-body effects present in the case of electron localization. Another interesting effect is that, zero-point fluctuations, which are present even in vacuum, are absent for frequencies inside a photonic gap. Electromagnetic interaction governs many properties of atoms, molecules, and solids. The absence of EM modes and zero point fluctuations inside the photonic gap can lead to unusual physical phenomena.[7-12] For example, atoms or molecules embedded in such a

Photonic Band Gaps and Localization, Edited by
C.M. Soukoulis, Plenum Press, New York, 1993

material can be locked in excited states if the photons to be emitted to release the excess energy have frequency within the forbidden gap. All the aforementioned ideas about new physics and new technology hinges upon the assumption of the existence of material with photonic gaps.

To search for the appropriate structures, scientists at Bellcore employed a "cut-and-try" approach in which various periodic dielectric structures were fabricated in the microwave regime and the dispersion of EM waves were measured to see if a frequency gap existed.[13] The process turned out to be time consuming and not very successful. After dozens of structures tried over a period of two years, they identified only one structure with a photonic band gap. This structure consists of a periodic array of overlapping spherical holes inside a dielectric block. The centers of the holes are arranged in a face-centered-cubic (fcc) lattice and the holes occupy 86% of the volume of the block.

PLANE WAVE METHOD

Stimulated by the experimental work, theorists became interested in the solution of the photonic band problem and in the search for structures with photonic band gaps. Early work in this area employed the "scalar wave approximation" which assumed that the two polarizations of the EM waves can be treated separately, thus decoupling the problem into the solution of two scalar wave equations. When we first became involved with the photon band problem, calculations had already been completed for the experimental structure in the scalar wave approximation.[14,15] The results showed the existence of a gap but the position and size of the gap were not in quantitative agreement with the experiment, indicating the need for a full vector wave treatment. It turned out from subsequent calculations that the errors made in neglecting the vector nature of the EM wave are more serious than initially anticipated, and the scalar wave calculations actually give qualitatively wrong results.

The vector wave solution of Maxwell's equations for a periodic dielectric system was carried out independently by several groups shortly after the appearance of the scalar wave results.[16-18] All of the methods employ a plane wave expansion of the electromagnetic fields and use Bloch's theorem to reduce the problem to the solution of a set of linear equations. In this article, we will concentrate mainly on the methods developed in our group.

For EM waves with frequency ω, the Maxwell equations can be written as

$$\nabla \cdot \mathbf{D} = 0 \tag{1a}$$

$$\nabla \times \mathbf{H} = -i\frac{\omega}{c}\mathbf{D} \tag{1b}$$

$$\nabla \times \mathbf{E} = i\frac{\omega}{c}\mathbf{H} \tag{1c}$$

$$\nabla \cdot \mathbf{H} = 0 \tag{1d}$$

and,

$$\mathbf{D}(\mathbf{r}) = \varepsilon(\mathbf{r})\,\mathbf{E}(\mathbf{r}) \tag{1e}$$

where $\varepsilon(\mathbf{r})$ is a real and periodic function of $\mathbf{r}$ and frequency independent in the range of frequency under consideration. We also take the magnetic permeability $\mu = 1$. Since $\varepsilon(\mathbf{r})$ is periodic, we can use Bloch's theorem to expand the **H**, **E**, and **D** fields, for example:

$$\mathbf{H}(\mathbf{r}) = \sum_{\mathbf{K}} \mathbf{H}_{\mathbf{K}}\, e^{i\mathbf{K}\cdot\mathbf{r}} \tag{2}$$

where $\mathbf{K} = \mathbf{k} + \mathbf{G}$, with $\mathbf{k}$ being a wave vector (in the Brillouin zone) that determines the propagation direction and wavelength of the EM wave, and $\mathbf{G}$ is a reciprocal lattice vector. Equation (2) and the corresponding expansions for **E** and **D** transform the Maxwell equations 1(a)-(d) into

$$\mathbf{K}\cdot\mathbf{D}_{\mathbf{K}} = 0 \tag{3a}$$

$$\mathbf{K}\times\mathbf{H}_{\mathbf{K}} = -\frac{\omega}{c}\mathbf{D}_{\mathbf{K}} \tag{3b}$$

$$\mathbf{K}\times\mathbf{E}_{\mathbf{K}} = \frac{\omega}{c}\mathbf{H}_{\mathbf{K}} \tag{3c}$$

$$\mathbf{K}\cdot\mathbf{H}_{\mathbf{K}} = 0. \tag{3d}$$

We can now eliminate the **E** field in terms of the **H** field, and get

$$\sum_{\mathbf{K}'} \mathbf{K}\times\varepsilon^{-1}_{\mathbf{K}\mathbf{K}'}\left(\mathbf{K}'\times\mathbf{H}_{\mathbf{K}'}\right) = -\frac{\omega^2}{c^2}\mathbf{H}_{\mathbf{K}}, \tag{4a}$$

where $\mathbf{K}' = \mathbf{k} + \mathbf{G}'$, and $\varepsilon_{\mathbf{K},\mathbf{K}'} = \varepsilon(\mathbf{K}-\mathbf{K}') = \varepsilon(\mathbf{G}-\mathbf{G}')$ is the Fourier transform of the $\varepsilon(\mathbf{r})$.

Using Eq. (3), we can also eliminate the H field in terms of E and obtain

$$\mathbf{K}\times\mathbf{K}\times\mathbf{E}_{\mathbf{K}} + \frac{\omega^2}{c^2}\sum_{\mathbf{K}'} \varepsilon_{\mathbf{K},\mathbf{K}'}\,\mathbf{E}_{\mathbf{K}'} = 0. \tag{4b}$$

Equation 3(d) shows that **H** is transverse, so we can write:

$$\mathbf{H}_{\mathbf{K}} = \mathbf{h}_{\mathbf{K},1}\hat{\mathbf{x}}_1 + \mathbf{h}_{\mathbf{K},2}\hat{\mathbf{x}}_2, \tag{5}$$

where $(\hat{\mathbf{x}}_1, \hat{\mathbf{x}}_2, \hat{\mathbf{K}})$ forms an orthogonal triad. Equation (5) and some vector algebra reduce Eq. (4a) to

$$\sum_{\mathbf{K}',\lambda} M^{\lambda\lambda}_{\mathbf{K},\mathbf{K}'} h_{\mathbf{K}'\lambda} = \left(\frac{\omega}{c}\right)^2 h_{\mathbf{K},\lambda} \tag{6}$$

where

$$M_{\mathbf{K},\mathbf{K}'} = |\mathbf{K}||\mathbf{K}'|\varepsilon^{-1}_{\mathbf{K},\mathbf{K}'} \begin{bmatrix} \hat{x}_2 \cdot \hat{x}_{2'} & -\hat{x}_2 \cdot \hat{x}_{1'} \\ -\hat{x}_{1'} \cdot \hat{x}_2 & \hat{x}_1 \cdot \hat{x}_{1'} \end{bmatrix}.$$

Thus, Eq. (4a) can be reduced to a set of 2N linear equations where N is the number of plane waves used to expand the electromagnetic fields. On the other hand, the E field is not a transverse field in the present problem, thus Eq. (4b) reduces to a set of 3N linear equations. There is an extra N roots corresponding to zero-frequency longitudinal wave solution which must be projected out of the problem to reduce the number of equations from 3N to 2N. The E field formulation offers some insights on the photon band dispersion in the long wavelength limit. However, it can be shown mathematically that it gives the same eigenvalues as the H field formulation. Thus, in this article, we will concentrate on solving the H field equations.

Diagonalization of the Hermitian matrix M for each k-point solves the photon band problem, with the eigenvalues giving the square of the frequencies of the eigenmodes and the eigenvectors giving the components of the field intensities. This approach has the unique advantage of being applicable to all forms of periodic structures, irrespective of the shape and size of the "objects" under consideration.

When we solved the photon band structure for the experimental structure of 86% air spheres in a dielectric matrix, we got a big surprise! While the calculated bands and the experimental results agree quite well in most regions of the Brillouin zone, there is an essential difference between the calculated and the experimental results. Contrary to the results reported by experiment, the calculation showed that the structure does not have a photonic band gap. The photon band structure of the fcc structure is shown in Fig. 1, while the corresponding density-of-states (DOS) is shown in Fig. 2. Even though the fcc structure does not have a complete photonic gap for the lowest-lying bands, a very large depletion of DOS is found, called a "pseudo-gap." Actually, this result was also obtained earlier by two other groups,[16-17] although at that time we were not aware of their results.

Initially, we thought our computer code was in error, and we investigated different ways to solve the problem to check the convergence and accuracy of our calculations (see Appendix). However, after careful examination, we are confident of the accuracy of our results, so the reason for the discrepancy must lie in the interpretation of the experimental data. Furthermore, we performed an analysis of the characters of the photon bands in the wavevector regions at the W point and near the K point in the Brillouin zone where the discrepancies occurred and found that these wave vectors lie on a reflection plane so that the modes can be divided into even symmetry modes which couples to p-polarized incident EM waves only and odd modes which couples only to s-polarized incident waves (see Fig. 2). Thus, if the photon bands are measured with s- and p-polarized waves separately as was done in the experiment, the calculations indicated gaps would be observed for the individual polarizations, but the top of the p-gap would coincide with the bottom of the s-gap. Detailed discussions with Yabolonovitch confirmed the above picture: due to the finite size of the experimental crystal, the experimental data did not have sufficient wavevector resolution and dynamic range for the experimentalist to resolve the overlap of the two gaps in the regions near W and K.

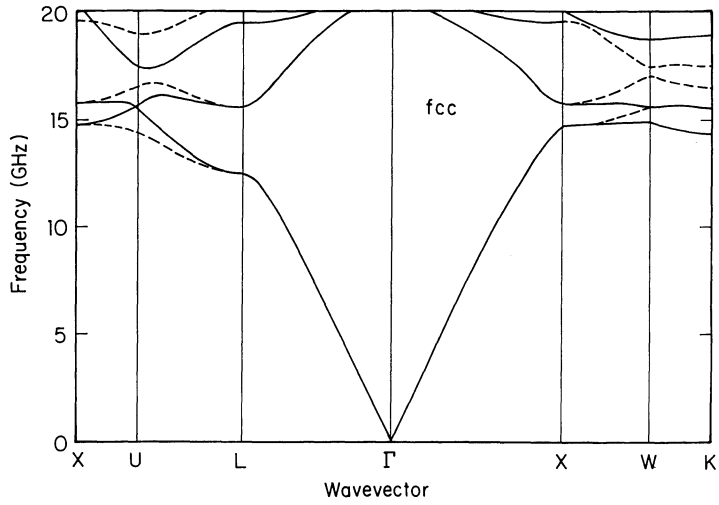

Figure 1. Calculated photonic band structure along symmetry lines in the Brillouin zone for a fcc dielectric structure composing of air spheres in a dielectric background of refractive index 3.5. The filling ratio is 86% air and 14% dielectric material. Along X-U-L and X-W-K, the dotted and solid line indicate bands which couple only an s and p polarized light, respectively, in the experiment of Ref. 13.

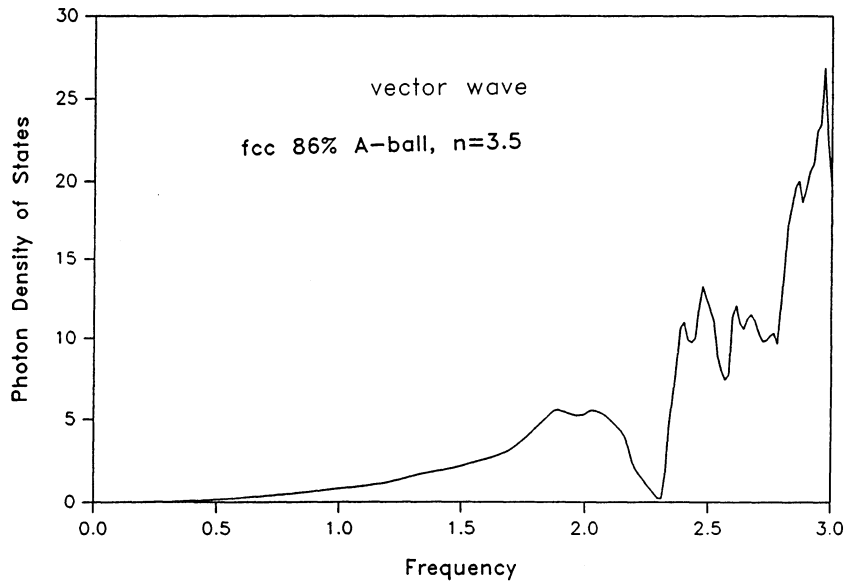

Figure 2. The density-of-states of the photon modes for the fcc dielectric structure, whose band structure is shown to Fig. 1.

At this point, the existence of photonic gap materials was seriously doubted.[2] However, since we found that the method developed can solve the photon band problem so efficiently and so much faster than the experimental "cut-and-try" method, we used it to investigate whether other structures can succeed where the fcc air sphere structure has failed. Motivated by the geometry of the electronic semiconducting family of diamond, silicon, and germanium, the first structure we tried was the diamond structure.[19] As luck would have it, we found the most favorable structure for creating a photonic band gap. We initially tried the diamond structure with dielectric spheres and air spheres centered on the lattice sites and found that both types of structures support full photonic band gaps. For example, Fig. 3 displays the photonic band structure calculated for an air sphere diamond lattice with refractive index contrast of 3.6 and air filling ratio of 81%. The density of states for a similar case, with cylindrical rods joining nearest neighbor sites in a diamond lattice, are shown in Fig. 4. For a given filling fraction and refractive index contrast, the frequencies of a selected structure are inversely proportional to the lattice constant. Thus, the size of the gap can be measured by a dimensionless quantity which is the ratio of the gap to the midgap frequency (gap/midgap ratio). For the case of air spheres on a diamond lattice in a dielectric matrix (refractive index contrast=3.6), the filling fraction of the dielectric can be optimized to yield a maximum gap/midgap ratio of 29%, while for the case of dielectric spheres, the performance is not as good, the maximum gap achieved is only 14%.

We were quite excited with our findings and communicated them to Yablonovitch, who, very quickly devised an ingenious way of constructing a diamond lattice. He noted that the diamond lattice is a very open structure characterized by open channels along the [110] directions. Thus, by drilling cylindrical holes through a dielectric block, a structure with the symmetry of the diamond structure can be created. Since there are 6 sets of equivalent [110] directions in the lattice, there are 6 set of holes to be drilled. If the crystal is oriented such that the [111] surface is exposed, then three sets of these holes will be slanted at angles of 35.26 degrees with respect to the normal [111] direction. The remaining three sets of holes have their axes parallel to the [111] surface and are harder to make on a thin film oriented in the [111] direction. Thus, in the end, the experimentalist decided to abandon the second three sets of holes and construct a structure with only the first three set of holes (see Fig. 15, in the article by Yablonovitch in this book) which became the first experimental structure that demonstrates the existence of a photonic band gap.[20]

We repeated our calculations for several variations on the diamond lattice.[21] One is the diamond lattice generated by 6 set of air cylinders or dielectric cylinders in the [110] directions. The other is a diamond rod lattice in which, instead of putting spheres at the lattice sites, we joined them together by nearest-neighbor rods. We also tested the effects on the photon band gap when 3 sets of cylinders are omitted in the 6-cylinder diamond structure. The results are summarized in Fig. 5. All of these structures exhibit photonic band gaps, with the best performance coming from a diamond rod lattice, which achieves a maximum gap of 30% for a refractive index contrast of 3.6.

In summary, we have developed a method for solving the problem of the propagation of EM waves in a periodic dielectric medium and from our

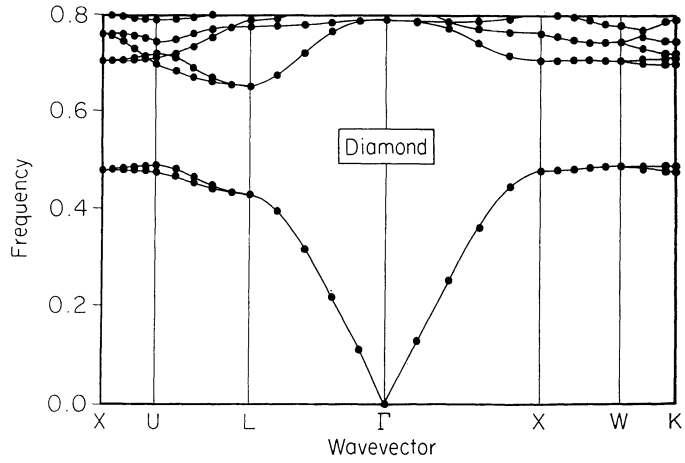

Figure 3. Calculated photonic band structure for a diamond dielectric structure consisting of overlapping air spheres in a material of refractive index 3.6. The filling ratio of the empty sphere is 81%. The frequency is given units of c/a, where a is the cubic lattice constant of the diamond lattice, and c is the velocity of light.

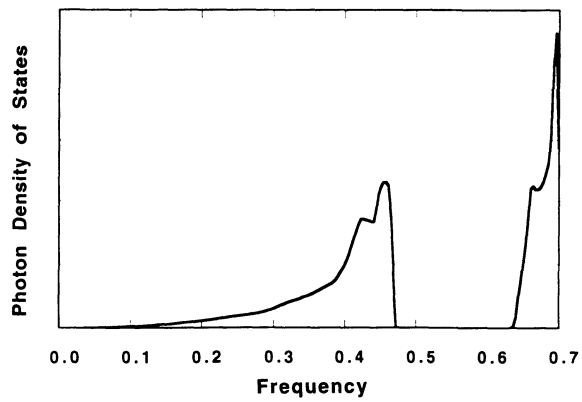

Figure 4. The density-of-states of the photon modes for the diamond dielectric structure, with dielectric rods (of n=3.6) joining nearest neighbor sites in a diamond lattice. The filling ratio of the rods are about 21%. The frequency unit is the same as Fig. 3.

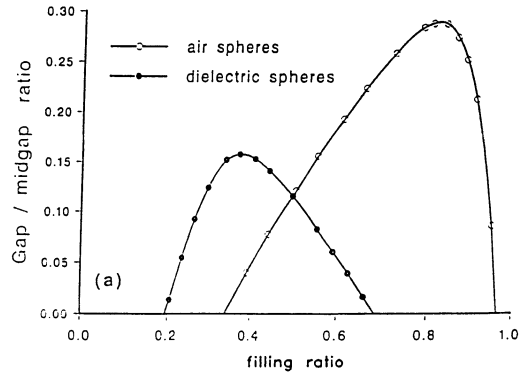

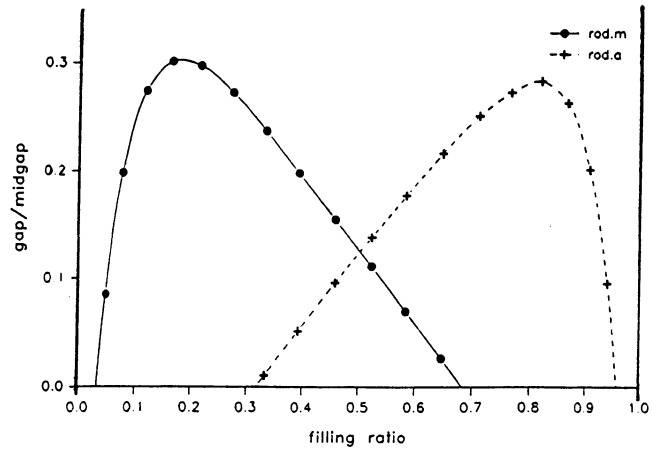

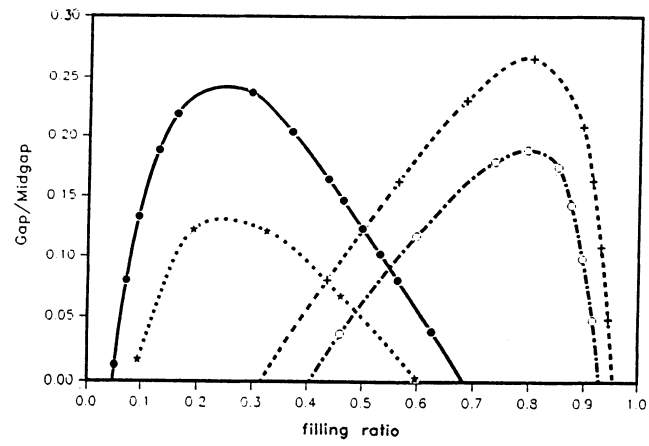

Figure 5. (a) Gap-to-midgap frequency ratio ($\Delta\omega/\omega_g$) as a function of filling ratio for dielectric spheres n air (solid circles) in air and air spheres (open circles) in dielectric.

(b) Gap-to-midgap frequency ratios ($\Delta\omega/\omega_g$) as a function of filling ratio for "material" rods (solid circles) and "air" (empty) rods (crosses) joining nearest-neighbors sites in a diamond lattice.

(c) Gap-to-midgap frequency ratios for the case of 6- and 3-cylinder arrangements. Solid circles and stars are 6 sets and 3 sets of "material" cylinders, respectively, while crosses and empty circles are for 6 and 3 sets of "air" (empty) cylinders, respectively.

In all cases the refractive index of the material is chosen to be 3.6.

calculations, discovered the first structure to exhibit a photonic band gap. We have demonstrated that a systematic search for the structures that possess optimal photonic gaps can be conducted via theoretical calculations. Practical three-dimensional periodic arrangements of dielectric structures were proposed. These dielectric structures possess a full photonic gap, with refractive-index contrasts as low as 1.9, and are much easier to fabricate than dielectric spheres arranged in a diamond lattice. While there is no simple explanation as to the exact conditions photonic band gaps appear, our findings suggest that the existence or not of gaps is related with the connectivity of the high dielectric material and the symmetry of the resulting structure. We are quite excited about the future applications of photonic band gaps and the prospects of using our calculational techniques to design and help the fabrication of these photonic band gap materials.

ACKNOWLEDGMENTS

Ames Laboratory is operated by the U.S. Department of Energy by Iowa State University under contract No. W-7405-Eng 82. This work was supported by the Director for Energy Research, Office of Basic Energy Sciences, including a grant of computer time on the Cray computer at the Lawrence Livermore Laboratory.

APPENDIX: CONVERGENCE AND ACCURACY TESTS

One important detail which has been left out in the above discussion on the plane wave method is the representation of $\varepsilon_{\mathbf{K},\mathbf{K}'}$ in Eqs. (4a) and (4b). There are actually two choices: one is to represent $\varepsilon(r)$ on a grid in real space, Fourier transform to obtain $\varepsilon_{\mathbf{K},\mathbf{K}'}$ in reciprocal space, and perform a matrix inversion to get $\varepsilon^{-1}_{\mathbf{K},\mathbf{K}'}$, the other is to represent $(1/\varepsilon(r))$ in real space, Fourier transform to obtain $\varepsilon^{-1}_{\mathbf{K},\mathbf{K}'}$ and perform the matrix inversion to obtain $\varepsilon_{\mathbf{K},\mathbf{K}'}$. While the two choices produce the same results in the limit of an infinite plane wave basis set for a finite plane wave expansion, they give different answers when truncated to a finite basis. We will refer to the first choice as the ε inverse method and the second choice as the $(1/\varepsilon)$ method. For many cases, we found that the two methods have different convergence behavior as the size of the plane wave basis is increased. For example, in the case of the fcc 86% air spheres structure, the dependence of the eigenvalues obtained by the two methods are shown in Fig. 6, where we plot the eigenvalues of some selected modes as a function of basis size. To obtain the results for some of the larger basis sets, we found it necessary to use an iterative solution of the matrix problem (the block Davidson scheme) instead of the traditional diagonalization method we used for the smaller matrices. For the first method, the eigenvalues increase as the number of plane waves is increased while the second method has just the opposite behavior. Thus, by solving the problem using two methods, we obtain an upper and a lower bound on the fully converged result, giving us a very good estimate of the convergence of our calculations. We also note that, in Fig. 6, the convergence of the second method is much slower than the first method, so that for moderate basis sets, there is a big difference in the numeric results one obtains from the two methods. In the two earliest vector wave photonic band structure calculations,[16,17] one used the first method and one used the second method. The difference in the numbers obtained from the two calculations initially caused some doubts about the

accuracies of the calculations. For the case of the fcc 86% air sphere geometry, the ε inverse method converges much faster than the (1/ε) method. We have examined many other geometries. We found that, in general, when the high dielectric material forms an interlinked, continuous, infinite network, the method we employed converges much better than the H method. We found that the structures with large photonic gaps belong to this class of geometries. When the big dielectric constant material forms a discontinuous array of isolated scatterers, both methods have trouble with convergence. In this regime, the convergence of different bands are also quite uneven; for the same structure, some bands converge more rapidly for one method, while other bands behave in just the opposite manner. We also observed that results obtained by the (1/ε) method are more sensitive to the sharpness of the boundary between the air region and the dielectric region in the photonic crystal. Most of the time, this sensitivity is an artifact of the method and does not reflect the real behavior of the system. Therefore, in most work in exploring the behavior of candidate structures, we employed the ε inverse method. However, near the point of transition between the two classes of structures, that is, when the isolated scatterers get close to touching each other, the second method seems to perform better than the first method. The case of dielectric spheres in a diamond lattice with filling ratio close to but less than 34% falls into this category. Sozuer and Haus[22] were the first to point out that the results published in our first paper overestimate the gap for non-touching dielectric spheres because these geometries are highly sensitive to the high Fourier components of the structure. Our original calculations did not contain enough plane waves to obtain converged results for sharp dielectric spheres. The unconverged results from the ε inverse method correspond to a system where the sharp boundaries are replaced by smooth ones.

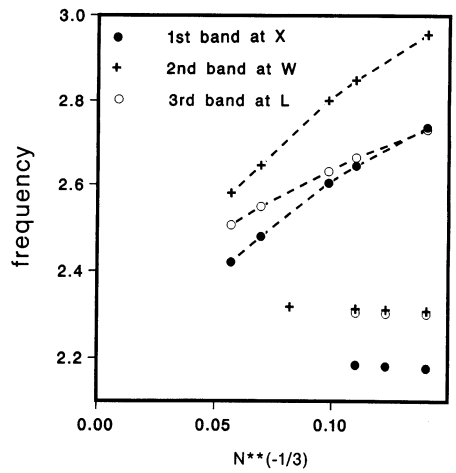

Figure 6. Frequencies of selected bands at high symmetry points in the Brillouin zone for the case of a fcc lattice of air spheres in a dielectric medium of refractive index n=3.5 are plotted as function of the inverse one-third power of the number of plane waves in the basis set. The points linked by dashed lines are the results from the second method (1/ε), the other points are the results from the first method (inverse matrix method).

REFERENCES

1. See e.g., C. Kittel, *Introduction to Solid State Physics*, (5th Edition, Wiley, 1976) Ch.7.

2. J. Maddox, *Nature* **348**, 481 (1990).

3. E. Yablonovitch, review article in this volume.

4. E. M. Purcell, *Phys. Rev.* **69**, 681 (1946).

5. E. Yablonovitch, *Phys. Rev. Lett.* **58**, 2059 (1987).

6. N. Lawandy, article in this volume.

7. S. John, *Phys. Rev. Lett.* **58**, 2486 (1987); S. John, *Comments Cond. Mat. Phys.* **14**, 193 (1988); S. John *Physics Today* **32**, 33 (1991).

8. *Scattering and Localization of Classical Waves in Random Media*, edited by P. Sheng (World Scientific, Singapore, (1990).

9. J. M. Drake and A. Z. Genack, *Phys. Rev. Lett.* **63**, 259 (1989).

10. C. A. Condat and T. R. Kirkpatrick, *Phys. Rev. B* **36**, 6783 (1987).

11. J. Martorell and N. M. Lawandy, *Phys. Rev. Lett.* **65**, 1877 (1990).

12. G. Kurizki and A. Z. Genack, *Phys. Rev. Lett.* **66**, 1850 (1991).

13. E. Yablonovitch and T. J. Gmitter, *Phys. Rev. Lett.* **63**, 1950 (1989).

14. S. Satpathy, Z. Zhang, and M. R. Salehpour, *Phys. Rev. Lett.* **64**, 1239 (1990).

15. K. M. Leung and Y. F. Liu, *Phys. Rev. B* **41**, 10188 (1990).

16. K. M. Leung and Y. F. Liu, *Phys. Rev. Lett.* **65**, 2646 (1990).

17. Z. Zhang and S. Satpathy, *Phys. Rev. Lett.* **65**, 2650 (1990).

18. K. M. Ho, C. T. Chan, and C. M. Soukoulis, *Phys. Rev. Lett.* **65**, 3152 (1990).

19. Subsequent developments actually indicate that the relationship between electronic band structures and photonic band structures for a given crystal lattice is actually much weaker than we initially thought it would be. The electronic band structure problem (since the spin interactions of electrons are quite a bit weaker than their interactions with the lattice potential). At the time we thought of the diamond structure, we were still not fully aware of the serious errors of scalar waves calculations for the photonic band problem.

20. E. Yablonovitch, T. J. Gmitter, and K. M. Leung, *Phys. Rev. Lett.* **67**, 2295 (1991); E. Yablonovitch and K. M. Leung, *Nature* **351**, 278 (1991).

21. C. T. Chan, K. M. Ho, and C. M. Soukoulis, *Europhys. Lett.* **16**, 563 (1991).

22. H. S. Sözuer and J. W. Haus, *J. Opt. Soc. Am. B*, in press 1993.

PHOTONIC BAND STRUCTURES OF TWO-DIMENSIONAL DIELECTRIC MEDIA

Alexei A. Maradudin[1] and Arthur R. McGurn[2]
[1]Department of Physics
University of California
Irvine, CA 92717, USA
[2]Department of Physics
Western Michigan University
Kalamazoo, MI 49008, USA

1. INTRODUCTION

When a quantum or a classical wave propagates in a periodic structure in any number of spatial dimensions, the dispersion curves that relate the frequencies of the wave to the wave vector characterizing its propagation possess an infinite number of branches. These branches form bands that are separated by frequency gaps at points of symmetry in the corresponding Brillouin zones. In some cases an absolute gap occurs, viz. a frequency range in which no waves can propagate that exists for all values of the wave vector in the Brillouin zone , and gives rise to a gap in the density of states of the waves propagating through these structures.

In recent years a great interest has arisen in the band structures of electromagnetic waves propagating in three-dimensional, periodic, dielectric structures. These band structures have been named *photonic band structures.* The reasons for this interest are both fundamental and practical. It has been suggested[1] that if the three dimensional, periodic, dielectric structure is disordered in such a way that it remains periodic on average, it may be easier to observe in it the Anderson localization of light whose frequency is close to an edge of an absolute band gap of the corresponding periodic structure than it would be in a disordered dielectric structure that is homogeneous on average. It has also been suggested[2,3] that since electromagnetic waves with frequencies in absolute band gaps are totally absent, spontaneous emission is forbidden in situations in which the band gap overlaps the electronic band edge. The suppression of spontaneous emission can improve the performance of many optical and electronic devices. The absence of electromagnetic modes in a certain frequency range can also modify the basic properties of many atomic, molecular, and excitonic systems.[4]

Photonic Band Gaps and Localization, Edited by
C.M. Soukoulis, Plenum Press, New York, 1993

The earliest theoretical studies of the photonic band structures of three-dimensional, periodic, dielectric structures were carried out on the basis of a scalar wave approximation for the electromagnetic field in these structures.[2,5–8] However, it was soon found that the band structures obtained on the basis of this approximation were not in agreement with those obtained on the basis of a full vector treatment of the electromagnetic field.[9,10] Since that time all calculations of the photonic band structures of three-dimensional, periodic, dielectric structures have been based on the full set of Maxwell's equations for electromagnetic waves in a material medium.[11,12]

The object of the earliest investigations was finding structures that possess absolute band gaps.[9–12] Subsequently, attention was directed toward the surface electromagnetic states that can exist at the planar surface of a semi-infinite, three-dimensional, periodic, dielectric structure formed, e.g. by cutting an infinite, three-dimensional, periodic structure along some plane.[13] In addition, the spatially localized defect modes that can arise in the vicinity of a perturbation of a periodic dielectric structure have also been investigated.[14] Finally, quantum electrodynamic effects associated with the introduction of atoms and molecules into photonic band gap structures have been studied theoretically.[15,16]

In addition to these theoretical investigations of three-dimensional photonic band structures, several experimental investigations of the propagation of electromagnetic waves in three-dimensional, periodic, dielectric structures have been carried out[12,17,18].

Recently, the photonic band structures of two-dimensional, periodic, dielectric structures, have begun to be investigated, both theoretically[19–23] and experimentally[22–25]. The motivations for such studies are the same as for the corresponding studies of the photonic band structures of three-dimensional systems. In addition, two-dimensional periodic structures are often easier to fabricate than the three-dimensional structures that have been investigated until now[12,17,18]. Moreover, the localization of light in a disordered two-dimensional structure that is periodic on average, whose frequency is close to an edge of an absolute band gap of the corresponding periodic structure, may be easier to achieve than in the case of a disordered three-dimensional, dielectric structure.

In this chapter we outline a theory of the calculation of the photonic band structures of dielectric structures that are periodic in two orthogonal directions, and infinite in a third orthogonal direction, and investigate how the results are changed when the dielectric structure is made finite in the direction normal to the plane in which the medium is periodic, and when a defect is introduced into an otherwise periodic, infinite, dielectric structure. In each case the treatment is based on the use of a position-dependent dielectric constant, and expansions of the electromagnetic field components in two-dimensional plane waves, an approach that had been found to be effective in earlier calculations of this type.[26,27]

The outline of this chapter is as follows. In Section 2 we present a method for the calculation of the photonic band structure for electromagnetic waves propagating in the x_1x_2-plane in a dielectric medium whose dielectric constant is periodic in the x_1- and x_2-directions and is infinite in the x_3-direction. Two polarizations of the electromagnetic field are considered, viz. H-polarization, in which the magnetic vector is parallel to the x_3-axis, and E-polarization, in which the electric vector is parallel to the x_3-axis. In Section 3 we investigate the photonic band structure for electromagnetic waves in a dielectric medium whose dielectric constant retains its periodicity in the x_1- and x_2-directions, but is no longer infinite in the x_3-direction. Specifically, we assume that the dielectric medium occupies the region between two perfectly conducting plates at $x_3 = 0$ and $x_3 = d$, and study how the photonic band structure of the electromagnetic

waves in this system depends on the distance d between the plates. In Section 4 we present a Green's function approach to the determination of the frequencies of the spatially localized electromagnetic modes that arise in an infinite dielectric medium whose dielectric constant is periodic in the x_1- and x_2-directions, when that periodicity is perturbed by an infinite line defect whose axis is parallel to the x_3-direction. A brief discussion of some directions for further work in this field, in Section 5, concludes this chapter.

2. PHOTONIC BAND STRUCTURES OF INFINITE TWO-DIMENSIONAL DIELECTRIC SYSTEMS[19,20]

In this section we present a theory of the photonic band structure of a system that consists of a periodic array of infinitely long, parallel, identical dielectric rods, characterized by a dielectric constant ϵ_a, embedded in a background dielectric material characterized by a dielectric constant ϵ_b. The rods are assumed to be parallel to the x_3-axis. The intersections of their axes with the x_1x_2-plane form a periodic two-dimensional structure. In the present chapter this periodic structure will be assumed to be one of the five two-dimensional Bravais lattices. However, the generalization of the theory presented here to more complex, periodic, two-dimensional structures is straightforward.

The sites of the two-dimensional Bravais lattice underlying the dielectric systems to be studied here are given by the vectors

$$\vec{x}_{||}(\ell) = \ell_1\vec{a_1} + \ell_1\vec{a_2}, \tag{2.1}$$

where $\vec{a}_1$ and $\vec{a}_2$ are the two noncollinear primitive translation vectors of the lattice, while ℓ_1 and ℓ_2 run over all the integers, positive, negative, and zero, and are denoted collectively by ℓ. The area of the primitive unit cell of this lattice or, equivalently, of the corresponding Wigner-Seitz cell, is

$$a_c = |\vec{a}_1 \times \vec{a}_2|, \tag{2.2}$$

if $\vec{a}_1$ and $\vec{a}_2$ are defined in such a way that $\vec{a}_1$ is rotated into $\vec{a}_2$ by a positive rotation about the x_3-axis through an angle smaller than π.

It is convenient to introduce the lattice reciprocal to the one defined by the vectors $\{\vec{x}_{||}(\ell)\}$. The sites of this lattice are given by the vectors

$$\vec{G}_{||}(h) = h_1\vec{b}_1 + h_2\vec{b}_2, \tag{2.3}$$

where the primitive translation vectors $\vec{b}_1$ and $\vec{b}_2$ are defined by the equations

$$\vec{a}_i \cdot \vec{b}_j = 2\pi\delta_{ij} \quad i,j = 1,2, \tag{2.4}$$

while h_1 and h_2 run over all the positive and negative integers and zero, and are denoted collectively by h. If we write the primitive translation vectors $\vec{a}_1$ and $\vec{a}_2$ as

$$\vec{a}_1 = (a_1^{(1)}, a_2^{(1)}), \quad \vec{a}_2 = (a_1^{(2)}, a_2^{(2)}), \tag{2.5}$$

the primitive translation vectors $\vec{b}_1$ and $\vec{b}_2$ are given explicitly by

$$\vec{b}_1 = (2\pi/a_c)(a_2^{(2)}, -a_1^{(2)}), \ \vec{b}_2 = (2\pi/a_c)(-a_2^{(1)}, a_1^{(1)}). \tag{2.6}$$

The dielectric constant of the systems we investigate is clearly position-dependent, and we denote it by $\epsilon(\vec{x}_{||})$. Here $\vec{x}_{||} = \hat{x}_1x_1 + \hat{x}_2x_2$, where $\hat{x}_1$ and $\hat{x}_2$ are unit vectors along

the x_1- and x_2-axes, respectively, is a position vector in the x_1x_2-plane. The dielectric constant $\epsilon(\vec{x}_{||})$ is a periodic function of $\vec{x}_{||}$ and satisfies the relation $\epsilon(\vec{x}_{||}+\vec{x}_{||}(\ell)) = \epsilon(\vec{x}_{||})$. More important for the analysis that follows is that the reciprocal of the dielectric constant is also a periodic function of $\vec{x}_{||}$, $\epsilon^{-1}(\vec{x}_{||} + \vec{x}_{||}(\ell)) = \epsilon^{-1}(\vec{x}_{||})$.

In this section we study the photonic band structures for electromagnetic waves propagating in these structures in a plane perpendicular to the axes of the dielectric rods, i.e. in the x_1x_2-plane. We consider two different polarizations of the electromagnetic waves.

A. H-Polarization

In this case we seek solutions of Maxwell's equations which have the forms

$$\vec{H}(\vec{x};t) = (0,0,H_3(\vec{x}_{||}|\omega))exp(-i\omega t) \tag{2.7a}$$

$$\vec{E}(\vec{x};t) = (E_1(\vec{x}_{||}|\omega), E_2(\vec{x}_{||}|\omega), 0)exp(-i\omega t). \tag{2.7b}$$

The Maxwell "curl" equations for the three nonzero field components are

$$\frac{\partial E_2}{\partial x_1} - \frac{\partial E_1}{\partial x_2} = \frac{i\omega}{c} H_3 \tag{2.8a}$$

$$\frac{\partial H_3}{\partial x_1} = \frac{i\omega}{c} D_2 = \frac{i\omega}{c}\epsilon(\vec{x}_{||})E_2 \tag{2.8b}$$

$$\frac{\partial H_3}{\partial x_2} = -\frac{i\omega}{c} D_1 = -\frac{i\omega}{c}\epsilon(\vec{x}_{||})E_1. \tag{2.8c}$$

The equation for H_3, obtained by eliminating E_1 and E_2 from these equations, can be written in the form

$$\frac{\partial}{\partial x_1}\left(\frac{1}{\epsilon(\vec{x}_{||})}\frac{\partial H_3}{\partial x_1}\right) + \frac{\partial}{\partial x_2}\left(\frac{1}{\epsilon(\vec{x}_{||})}\frac{\partial H_3}{\partial x_2}\right) + \frac{w^2}{c^2} H_3 = 0. \tag{2.9}$$

To solve Eq. (2.9) we expand the periodic function $\epsilon^{-1}(\vec{x}_{||})$ according to

$$\frac{1}{\epsilon(\vec{x}_{||})} = \sum_{\vec{G}_{||}} \hat{\kappa}(\vec{G}_{||}) e^{i\vec{G}_{||}\cdot\vec{x}_{||}}, \tag{2.10}$$

and $H_3(\vec{x}_{||}|\omega)$ in a form that satisfies the Bloch-Floquet theorem, dictated by the two-dimensional periodicity of the system being studied,

$$H_3(\vec{x}_{||}|\omega) = \sum_{\vec{G}_{||}} A(\vec{k}_{||} + \vec{G}_{||}) e^{i(\vec{k}_{||}+\vec{G}_{||})\cdot\vec{x}_{||}}, \tag{2.11}$$

where $\vec{k}_{||} = \hat{x}_1 k_1 + \hat{x}_2 k_2$ is the two-dimensional wave vector of the wave. When these expansions are substituted into Eq. (2.9) we obtain as the equation for the coefficients $\{A(\vec{k}_{||} + \vec{G}_{||})\}$

$$\sum_{\vec{G}_{||}'} (\vec{k}_{||} + \vec{G}_{||}) \cdot (\vec{k}_{||} + \vec{G}'_{||}) \hat{\kappa}(\vec{G}_{||} - \vec{G}'_{||}) A(\vec{k}_{||} + \vec{G}'_{||}) = \frac{\omega^2}{c^2} A(\vec{k}_{||} + \vec{G}_{||}), \tag{2.12}$$

which has the form of a standard eigenvalue problem for a symmetric matrix.

B. E-Polarization

In this case we seek solutions of Maxwell's equations which have the forms

$$\vec{E}(\vec{x};t) = (0,0,E_3(\vec{x}_{||}|\omega))exp(-i\omega t) \tag{2.13a}$$

$$\vec{H}(\vec{x};t) = (H_1(\vec{x}_{||}|\omega),H_2(\vec{x}_{||}|\omega),0)exp(-i\omega t). \tag{2.13b}$$

The Maxwell "curl" equations in this case are

$$\frac{\partial H_2}{\partial x_1} - \frac{\partial H_1}{\partial x_2} = -\frac{i\omega}{c}D_3 = -\frac{i\omega}{c}\epsilon(\vec{x}_{||})E_3 \tag{2.14a}$$

$$\frac{\partial E_3}{\partial x_1} = -\frac{i\omega}{c}H_2 \tag{2.14b}$$

$$\frac{\partial E_3}{\partial x_2} = \frac{i\omega}{c}H_1. \tag{2.14c}$$

The equation for E_3 obtained by eliminating H_1 and H_2 from these equations can be written in the form

$$\frac{1}{\epsilon(\vec{x}_{||})}\left(\frac{\partial^2}{\partial x_1^2}+\frac{\partial^2}{\partial x_2^2}\right)E_3 + \frac{\omega^2}{c^2}E_3 = 0. \tag{2.15}$$

To solve Eq. (2.15) we again use the expansion (2.10) and write $E_3(\vec{x}_{||}|\omega)$ in the form

$$E_3(\vec{x}_{||}|\omega) = \sum_{\vec{G}_{||}} B(\vec{k}_{||}+\vec{G}_{||})e^{i(\vec{k}_{||}+\vec{G}_{||})\cdot\vec{x}_{||}}. \tag{2.16}$$

The equation satisfied by the coefficients $\{B(\vec{k}_{||}+\vec{G}_{||})\}$ is

$$\sum_{\vec{G}'_{||}} \hat{\kappa}(\vec{G}_{||}-\vec{G}'_{||})(\vec{k}_{||}+\vec{G}'_{||})^2 B(\vec{k}_{||}+\vec{G}'_{||}) = \frac{\omega^2}{c^2}B(\vec{k}_{||}+\vec{G}_{||}). \tag{2.17}$$

A more convenient equation is obtained if we make the replacement

$$B(\vec{k}_{||}+\vec{G}_{||}) = \frac{C(\vec{k}_{||}+\vec{G}_{||})}{|\vec{k}_{||}+\vec{G}_{||}|}. \tag{2.18}$$

The equation for the $\{C(\vec{k}_{||}+\vec{G}_{||})\}$,

$$\sum_{\vec{G}'_{||}} |\vec{k}_{||}+\vec{G}_{||}|\hat{\kappa}(\vec{G}_{||}-\vec{G}'_{||})|\vec{k}_{||}+\vec{G}'_{||}|C(\vec{k}_{||}+\vec{G}'_{||}) = \frac{\omega^2}{c^2}C(\vec{k}_{||}+\vec{G}_{||}), \tag{2.19}$$

is a standard eigenvalue problem for a symmetric matrix.

If we denote by R the region of the x_1x_2-plane intercepted by the dielectric rod whose axis intersects that plane at $\vec{x}_{||}=0$, we can write $\epsilon^{-1}(\vec{x}_{||})$ in the form

$$\frac{1}{\epsilon(\vec{x}_{||})} = \frac{1}{\epsilon_b} + \left(\frac{1}{\epsilon_a}-\frac{1}{\epsilon_b}\right)\sum_{\ell} S(\vec{x}_{||}-\vec{x}_{||}(\ell)), \tag{2.20}$$

where

$$S(\vec{x}_{||}) = 1 \quad \vec{x}_{||} \text{ inside } R \tag{2.21a}$$

$$= 0 \quad \vec{x}_{||} \text{ outside } R. \tag{2.21b}$$

The Fourier coefficient $\hat{\kappa}(\vec{G}_{\|})$ is then given by

$$\hat{\kappa}(\vec{G}_{\|}) = \frac{1}{a_c}\int_{a_c} d^2x_{\|}\frac{e^{-i\vec{G}_{\|}\cdot\vec{x}_{\|}}}{\epsilon(\vec{x}_{\|})} \tag{2.22a}$$

$$= \frac{1}{\epsilon_b}\delta_{\vec{G}_{\|},\vec{0}} + \left(\frac{1}{\epsilon_a}-\frac{1}{\epsilon_b}\right)\frac{1}{a_c}\int d^2x_{\|}e^{-i\vec{G}_{\|}\cdot\vec{x}_{\|}}S(\vec{x}_{\|}), \tag{2.22b}$$

where the integration in the second line is over the entire x_1x_2-plane. When we take into account the definition of the function $S(\vec{x}_{\|})$, Eq. (2.21), we obtain

$$\hat{\kappa}(\vec{G}_{\|}) = \frac{1}{\epsilon_a}f + \frac{1}{\epsilon_b}(1-f) \qquad \vec{G}_{\|}=0 \tag{2.23a}$$

$$= \left(\frac{1}{\epsilon_a}-\frac{1}{\epsilon_b}\right)\frac{1}{a_c}\int_R d^2x_{\|}e^{-i\vec{G}_{\|}\cdot\vec{x}_{\|}} \qquad \vec{G}_{\|}\neq 0, \tag{2.23b}$$

where f is the filling fraction, i.e. the fraction of the total volume occupied by the rods. It is given by $f = a_R/a_c$, where a_R is the area of the region R, i.e. the cross sectional area of a rod. Although the result given by Eq. (2.23) is valid only for a structure consisting of nonoverlapping, identical, dielectric rods of arbitrary cross section, embedded in a different dielectric medium, the determination of the Fourier coefficients $\{\hat{\kappa}(\vec{G}_{\|})\}$ for more complex structures poses no significant problems. In some of these cases the integral in Eq. (2.22a) may have to be evaluated numerically, however.

To illustrate the preceding results we consider the case in which the intersections of the axes of the dielectric rods with the x_1x_2-plane form a triangular lattice, for which the primitive translation vectors are given by

$$\vec{a}_1 = a(1,0),\ \vec{a}_2 = a(\frac{1}{2},\frac{\sqrt{3}}{2}). \tag{2.24}$$

The primitive translation vectors of the reciprocal lattice, obtained from Eq. (2.6), are then

$$\vec{b}_1 = \frac{2\pi}{a}\left(1,-\frac{\sqrt{3}}{3}\right), \quad \vec{b}_2 = \frac{2\pi}{a}\left(0,\frac{2\sqrt{3}}{3}\right). \tag{2.25}$$

The rods are assumed to have a circular cross section of radius R. The Fourier coefficients $\{\hat{\kappa}(\vec{G}_{\|})\}$ in this case are given by

$$\hat{\kappa}(\vec{G}_{\|}) = \frac{1}{\epsilon_a}f + \frac{1}{\epsilon_b}(1-f) \qquad \vec{G}_{\|}=0 \tag{2.26a}$$

$$= \left(\frac{1}{\epsilon_a}-\frac{1}{\epsilon_b}\right)f\frac{2J_1(G_{\|}R)}{(G_{\|}R)} \qquad \vec{G}_{\|}\neq 0, \tag{2.26b}$$

where the filling fraction is $f = (2\pi/\sqrt{3})(R^2/a^2)$, and $J_1(x)$ is a Bessel function.

In Fig. 1a we present the photonic band structure for the case of E-polarization when $\epsilon_a = 1$, $\epsilon_b = 13$, and the filling fraction $f = 0.8358$. A total of 691 plane waves was used in solving Eq. (2.19) to obtain this result. An absolute band gap occurs in this band structure in the frequency range $0.450 < \omega a/2\pi c < 0.564$. In Fig. 1b we present the photonic band structure for the same dielectric structure, but now for the case of H-polarization. Again, a total of 691 plane waves was used in solving Eq. (2.12) to obtain this result. An absolute band gap occurs in this band structure in the frequency range $0.427 < \omega a/2\pi c < 0.536$. Consequently, the triangular lattice characterized

by the dielectric constants $\epsilon_a = 1$ and $\epsilon_b = 13$, and a filling fraction $f = 0.8358$ has a common absolute band gap in its photonic band structure for electromagnetic waves of E-polarization and of H-polarization propagating in a plane perpendicular to the rods, in the frequency range $0.450 < \omega a/2\pi c < 0.536$. The existence of this common absolute band gap was first pointed out by Meade *et al.*[23]. There are some small quantitative differences between the band structures depicted in Figs. 1a and 1b and the corresponding results of Meade *et al.* This is because the convergence of the photonic band structure calculations for the triangular lattice is slow, and we have used significantly more plane waves in our calculations than were used in the work of Meade *et al.*

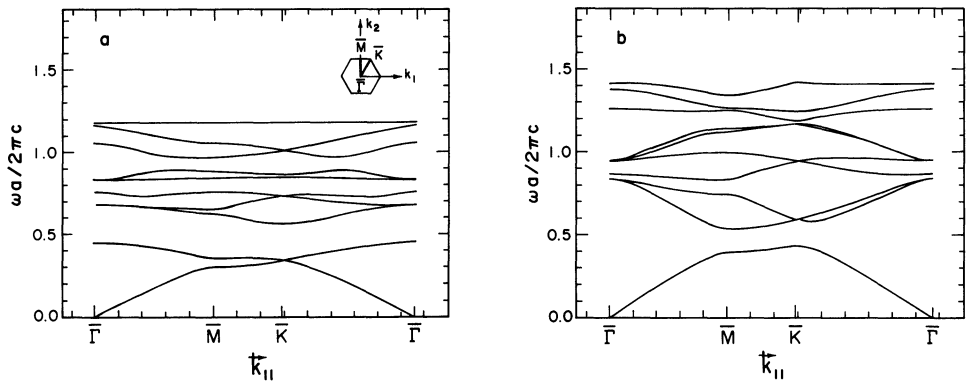

Figure 1. a) The photonic band structure for E-polarized waves in a triangular lattice of infinite rods of circular cross section with $\epsilon_a = 1, \epsilon_b = 13$, and $f = 0.8358$. The inset shows the first Brillouin zone for the triangular lattice with the symmetry points indicated. b) The photonic band structure for H-polarized waves in a triangular lattice of infinite rods of circular cross section with $\epsilon_a = 1, \epsilon_b = 13$ and$f = 0.8358$.

Photonic band structures for other triangular lattices can be found in Ref. 20; those for square lattices can be found in Refs. 19 and 22.

We end this section with a cautionary note. The safest way to demonstrate the existence of an absolute band gap in a photonic band structure is by calculating the photonic density of states and showing that a gap exists in it. This is because the existence of an absolute band gap in the dispersion curves calculated along the symmetry direction in the irreducible element of the two-dimensional first Brillouin zone does not guarantee that the dispersion curves do not close up the gap at some off-symmetry point or points. Densities of photonic states for several triangular lattices together with the corresponding band structures have been calculated in Ref. 20. In each case that the existence of an absolute band gap could be inferred from the photonic band structure, a gap in the same frequency range was observed in the photonic density of states.

3. Photonic Band Structures of a Two-Dimensional Planar Waveguide Structure[28]

The assumption, made in the preceding section, of a periodic, two-dimensional, dielectric structure consisting of infinitely long, parallel, identical, dielectric rods embedded in a background dielectric material with a different dielectric constant, is an idealization. This is because any periodic, two-dimensional, dielectric structure used in the experimental study of photonic band structures will, of necessity, be finite along all three coordinate axes. Indeed, the periodic, two-dimensional, dielectric structure that was employed in a recent experimental study[22] of the propagation of electromagnetic waves at microwave frequencies through it, consisted of an array of identical, parallel, dielectric rods, of finite length, confined to the region between two parallel metal plates that are parallel to the rods. The electromagnetic waves propagated in directions parallel to the metal plates, and their electric vector was oriented parallel to the rods.

In this section we study theoretically the photonic band structure for the propagation of electromagnetic waves in dielectric structures of this type. We retain a degree of idealization in this study by assuming that the structures we investigate are of infinite extent in the directions parallel to the metal plates. In addition, in view of the comparatively low frequencies of the electromagnetic waves used in the experiments described in Ref. 22 (GHz), in the present study we will model the metal plates by perfectly conducting plates. Of particular interest will be the manner in which the photonic band structures for electromagnetic waves propagating in dielectric structures of this type change as the separation between the perfectly conducting plates changes.

The physical system we consider in this section is depicted schematically in Fig. 2. It consists of an infinite array of parallel, identical, dielectric rods of arbitrary cross section and characterized by a dielectric constant ϵ_a, embedded in a background

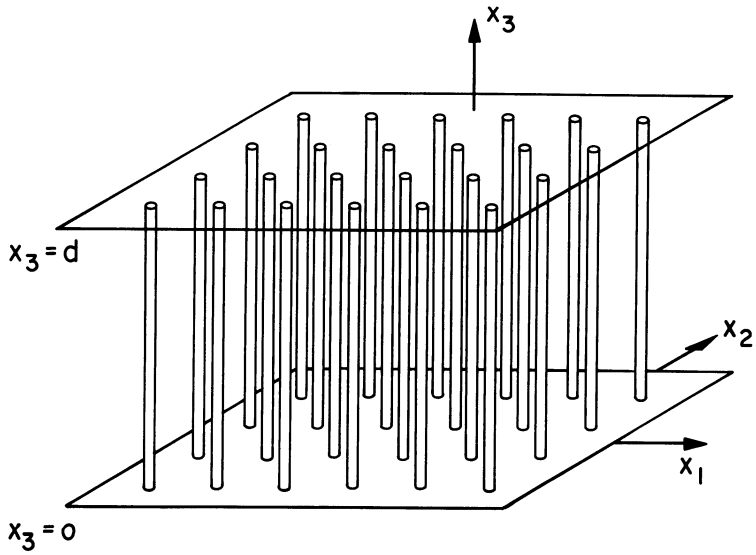

Figure 2. A two-dimensional, periodic, structure consisting of parallel, indentical, dielectric rods of finite length embedded in a medium with a different dielectric constant, that is confined to the region between two perfectly conducting plates that are perpendicular to the rods.

dielectric medium whose dielectric constant is ϵ_b. The resulting spatially inhomogeneous dielectric medium fills the region between two parallel, perfectly conducting plates at $x_3 = 0$ and $x_3 = d$. The intersections of the dielectric rods with these perfectly conducting plates form a two-dimensional Bravais lattice. The sites of this lattice are given by Eq. (2.1), and the lattice vectors of the reciprocal lattice are given by Eq. (2.3). The dielectric constant of the system depicted in Fig. 2, $\epsilon(\vec{x}_\parallel)$, is a periodic function of $\vec{x}_\parallel$, with the periodicity of the Bravais lattice, as is $\epsilon^{-1}(\vec{x}_\parallel)$.

To obtain the photonic band structure for the system depicted in Fig. 2 it is convenient to work with the electric field in the region between the conducting plates. This is because the boundary conditions at the perfectly conducting plates are particularly easy to satisfy in this case. We write the electric field in the form

$$\vec{E}(\vec{x};t) = \vec{E}(\vec{x}|\omega)exp(-i\omega t), \tag{3.1}$$

and the Maxwell equations satisfied by the components of the amplitude vector $\vec{E}(\vec{x}|\omega)$ as

$$\frac{1}{\epsilon(\vec{x}_\parallel)}\left(-\frac{\partial^2 E_1}{\partial x_2^2} - \frac{\partial^2 E_1}{\partial x_3^2} + \frac{\partial^2 E_2}{\partial x_1 \partial x_2} + \frac{\partial^2 E_3}{\partial x_1 \partial x_3}\right) = \frac{\omega^2}{c^2}E_1 \tag{3.2a}$$

$$\frac{1}{\epsilon(\vec{x}_\parallel)}\left(\frac{\partial^2 E_1}{\partial x_2 \partial x_1} - \frac{\partial^2 E_2}{\partial x_3^2} - \frac{\partial^2 E_2}{\partial x_1^2} + \frac{\partial^2 E_3}{\partial x_2 \partial x_3}\right) = \frac{\omega^2}{c^2}E_2 \tag{3.2b}$$

$$\frac{1}{\epsilon(\vec{x}_\parallel)}\left(\frac{\partial^2 E_1}{\partial x_3 \partial x_1} + \frac{\partial^2 E_2}{\partial x_3 \partial x_2} - \frac{\partial^2 E_3}{\partial x_1^2} - \frac{\partial^2 E_3}{\partial x_2^2}\right) = \frac{\omega^2}{c^2}E_3. \tag{3.2c}$$

The boundary conditions satisfied by the electric field are that its tangential components should vanish at the perfectly conducting surfaces. These conditions are automatically satisfied if we expand the components of $\vec{E}(\vec{x}|\omega)$ according to

$$E_1(\vec{x}|\omega) = \sum_{\vec{G}_\parallel}\sum_{n=1}^{\infty} a_1^{(n)}(\vec{k}_\parallel + \vec{G}_\parallel)e^{i(\vec{k}_\parallel+\vec{G}_\parallel)\cdot\vec{x}_\parallel}\sin\frac{n\pi x_3}{d} \tag{3.3a}$$

$$E_2(\vec{x}|\omega) = \sum_{\vec{G}_\parallel}\sum_{n=1}^{\infty} a_2^{(n)}(\vec{k}_\parallel + \vec{G}_\parallel)e^{i(\vec{k}_\parallel+\vec{G}_\parallel)\cdot\vec{x}_\parallel}\sin\frac{n\pi x_3}{d} \tag{3.3b}$$

$$E_3(\vec{x}|\omega) = i\sum_{\vec{G}_\parallel}\sum_{n=0}^{\infty} \epsilon_n a_3^{(n)}(\vec{k}_\parallel + \vec{G}_\parallel)e^{i(\vec{k}_\parallel+\vec{G}_\parallel)\cdot\vec{x}_\parallel}\cos\frac{n\pi x_3}{d}, \tag{3.3c}$$

where $\epsilon_0 = \frac{1}{2}$ and $\epsilon_n = 1$ for $n \geq 1$. We also expand $\epsilon^{-1}(\vec{x}_\parallel)$ as in Eq. (2.10).

The equations for the coefficients $\{a_\alpha^{(n)}(\vec{k}_\parallel + \vec{G}_\parallel)\}$ ($\alpha = 1, 2, 3$; $n = 0, 1, 2,...$) for different n decouple, which is an attractive feature of the expansions (3.3). For $n = 0$ we obtain the single equation

$$\sum_{\vec{G}'_\parallel}\hat{\kappa}(\vec{G}_\parallel - \vec{G}'_\parallel)(\vec{k}_\parallel + \vec{G}'_\parallel)^2 a_3^{(0)}(\vec{k}_\parallel + \vec{G}'_\parallel) = \frac{\omega^2}{c^2}a_3^{(0)}(\vec{k}_\parallel + \vec{G}_\parallel). \tag{3.4}$$

This is just Eq. (2.17) which yields the photonic band structure for electromagnetic waves of E-polarization propagating in the x_1x_2-plane of a two-dimensional dielectric structure that is periodic in x_1 and x_2 and is of infinite extent along x_3. The resulting modes are *bona fide* solutions of the present problem as well, because $E_1(\vec{x}|\omega)$ and $E_2(\vec{x}|\omega)$ are identically zero, while $E_3(\vec{x}|\omega)$ is independent of x_3, so that the boundary

conditions at the perfectly conducting plates are automatically satisfied, as are the Maxwell equations (3.2).

For each value of $n \geq 1$ the coefficients $\{a_\alpha^{(n)}(\vec{k}_\parallel + \vec{G}_\parallel)\}$ satisfy a set of three coupled matrix equations,

$$\sum_{\vec{G}'_\parallel} \hat{\kappa}(\vec{G}_\parallel - \vec{G}'_\parallel)\{[(k_2 + G'_2)^2 + \left(\frac{n\pi}{d}\right)^2]a_1^{(n)}(\vec{k}_\parallel + \vec{G}'_\parallel) -$$
$$-(k_1 + G'_1)(k_2 + G'_2)a_2^{(n)}(\vec{k}_\parallel + \vec{G}'_\parallel) + (k_1 + G'_1)\left(\frac{n\pi}{d}\right)a_3^{(n)}(\vec{k}_\parallel + \vec{G}'_\parallel)\}$$
$$= \frac{\omega^2}{c^2}a_1^{(n)}(\vec{k}_\parallel + \vec{G}_\parallel) \tag{3.5a}$$
$$\sum_{\vec{G}'_\parallel} \hat{\kappa}(\vec{G}_\parallel - \vec{G}'_\parallel)\{-(k_2 + G'_2)(k_1 + G'_1)a_1^{(n)}(\vec{k}_\parallel + \vec{G}'_\parallel) +$$
$$+[(k_1 + G'_1)^2 + \left(\frac{n\pi}{d}\right)^2]a_2^{(n)}(\vec{k}_\parallel + \vec{G}'_\parallel) +$$
$$+(k_2 + G'_2)\left(\frac{n\pi}{d}\right)a_3^{(n)}(\vec{k}_\parallel + \vec{G}'_\parallel)\} = \frac{\omega^2}{c^2}a_2^{(n)}(\vec{k}_\parallel + \vec{G}_\parallel) \tag{3.5b}$$
$$\sum_{\vec{G}'_\parallel} \hat{\kappa}(\vec{G}_\parallel - \vec{G}'_\parallel)\{(k_1 + G'_1)\left(\frac{n\pi}{d}\right)a_1^{(n)}(\vec{k}_\parallel + \vec{G}'_\parallel) +$$
$$+(k_2 + G'_2)\left(\frac{n\pi}{d}\right)a_2^{(n)}(\vec{k}_\parallel + \vec{G}'_\parallel) +$$
$$+(\vec{k}_\parallel + \vec{G}'_\parallel)^2 a_3^{(n)}(\vec{k}_\parallel + \vec{G}'_\parallel)\} = \frac{\omega^2}{c^2}a_3^{(n)}(\vec{k}_\parallel + \vec{G}_\parallel). \tag{3.5c}$$

Equations (3.5) constitute a standard eigenvalue problem.

In the limit as the separation d between the perfectly conducting plates tends to infinity, the set of equations (3.5) decouples into a pair of equations for $a_1^{(n)}(\vec{k}_\parallel + \vec{G}_\parallel)$ and $a_2^{(n)}(\vec{k}_\parallel + \vec{G}_\parallel)$,

$$\sum_{\vec{G}'_\parallel} \hat{\kappa}(\vec{G}_\parallel - \vec{G}'_\parallel)[(k_2 + G'_2)^2 a_1^{(n)}(\vec{k}_\parallel + \vec{G}'_\parallel) -$$
$$-(k_1 + G'_1)(k_2 + G'_2)a_2^{(n)}(\vec{k}_\parallel + \vec{G}'_\parallel)] = \frac{\omega^2}{c^2}a_1^{(n)}(\vec{k}_\parallel + \vec{G}_\parallel) \tag{3.6a}$$
$$\sum_{\vec{G}'_\parallel} \hat{\kappa}(\vec{G}_\parallel - \vec{G}'_\parallel)[-(k_2 + G'_2)(k_1 + G'_1)a_1^{(n)}(\vec{k}_\parallel + \vec{G}'_\parallel) +$$
$$+(k_1 + G'_1)^2 a_2^{(n)}(\vec{k}_\parallel + \vec{G}'_\parallel)] = \frac{\omega^2}{c^2}a_2^{(n)}(\vec{k}_\parallel + \vec{G}_\parallel), \tag{3.6b}$$

and a single equation for $a_3^{(n)}(\vec{k}_\parallel + \vec{G}_\parallel)$,

$$\sum_{\vec{G}'_\parallel} \hat{\kappa}(\vec{G}_\parallel - \vec{G}'_\parallel)(\vec{k}_\parallel + \vec{G}'_\parallel)^2 a_3^{(n)}(\vec{k}_\parallel + \vec{G}'_\parallel) = \frac{\omega^2}{c^2}a_3^{(n)}(\vec{k}_\parallel + \vec{G}_\parallel). \tag{3.7}$$

By comparison with Eqs. (10) of Ref.19, Eqs. (3.6) are seen to be the equations describing the propagation of electromagnetic waves of H-polarization in the x_1x_2-plane in a system that is infinite along x_3. Similarly, Eq. (3.7) is just Eq. (2.17), which describes the propagation of electromagnetic waves of E-polarization in the same plane, in the same system. Thus in the limit as $d \to \infty$ the resulting photonic band structure is the

superposition of the photonic band structures for waves of pure H- and E-polarization propagating in the plane perpendicular to the dielectric rods in a system that is infinite in the direction parallel to the rods.

In the opposite limit as $d \to 0$, Eqs. (3.5) for $n \geq 1$ reduce to

$$\sum_{\vec{G}'_{\|}} \hat{\kappa}(\vec{G}_{\|} - \vec{G}'_{\|}) a_1^{(n)}(\vec{k}_{\|} + \vec{G}'_{\|}) = \left(\frac{\omega d}{n\pi c}\right)^2 a_1^{(n)}(\vec{k}_{\|} + \vec{G}_{\|}) \tag{3.8a}$$

$$\sum_{\vec{G}'_{\|}} \hat{\kappa}(\vec{G}_{\|} - \vec{G}'_{\|}) a_2^{(n)}(\vec{k}_{\|} + \vec{G}'_{\|}) = \left(\frac{\omega d}{n\pi c}\right)^2 a_2^{(n)}(\vec{k}_{\|} + \vec{G}_{\|}) \tag{3.8b}$$

$$a_3^{(n)}(\vec{k}_{\|} + \vec{G}_{\|}) = 0. \tag{3.8c}$$

The eigenvalues of this system of equations take two distinct values, which we write as

$$\frac{\omega d}{2\pi^2 nc} = \frac{1}{2\pi\sqrt{\epsilon_a}}, \ \frac{1}{2\pi\sqrt{\epsilon_b}}, \tag{3.9}$$

each of which is infinitely degenerate. Thus, in the limit as $d \to 0$ the photonic band structure of the system we study here degenerates into two dispersionless bands for each value of $n \geq 1$, whose frequencies are given by Eq. (3.9). They are the frequencies of electromagnetic waves of H-polarization that propagate in the x_1x_2-plane.

However, although the equations describing the propagation of waves of H- and E-polarization are decoupled in both limits as $d \to \infty$ and as $d \to 0$, for finite, nonzero values of d they are coupled, and the solutions of Eqs. (3.5) represent waves of mixed H- and E-polarization.

We illustrate the preceding results for a square lattice of dielectric rods of circular cross section of radius R and dielectric constant $\epsilon_a = 9$, embedded in air, so that $\epsilon_b = 1$. The filling fraction is $f = 0.4488$. These parameters correspond to those of the system studied experimentally in Ref. 22. The primitive translation vectors of this structure are given by

$$\vec{a}_1 = a(1,0), \ \vec{a}_2 = a(0,1). \tag{3.10}$$

The primitive translation vectors of the reciprocal lattice, obtained from Eq. (2.6), are then

$$\vec{b}_1 = \frac{2\pi}{a}(1,0), \ \vec{b}_2 = \frac{2\pi}{a}(0,1). \tag{3.11}$$

The Fourier coefficients $\{\hat{\kappa}(\vec{G}_{\|})\}$ in this case are again given by Eqs. (2.26).

In Fig. 3, we present a plot of $\omega a/2\pi c$ versus wave vector $\vec{k}_{\|}$ along directions of high symmetry in the two-dimensional first Brillouin zone for $n = 0$. Dispersion curves for the ten lowest frequency bands are shown. The curves were obtained from the matrix eigenvalue problem represented by Eq. (2.19), which is equivalent to Eq. (3.4), by using the 377 shortest reciprocal lattice vectors $\vec{G}_{\|}$ to generate a finite matrix representation of this equation. The band structure presented in Fig. 3 is independent of d and agrees with the band structure for waves of E-polarization in the lattice of infinite rods presented in Fig. 1b of Ref. 22. It possesses three absolute band gaps in the frequency range considered.

In Figs. 4a, 4b, and 4c we present plots of $\omega a/2\pi c$ versus $\vec{k}_{\|}$ for $n = 1$ and $d/a = 0.5$, 1, and 5, respectively. Results are shown for the ten lowest frequency bands plotted

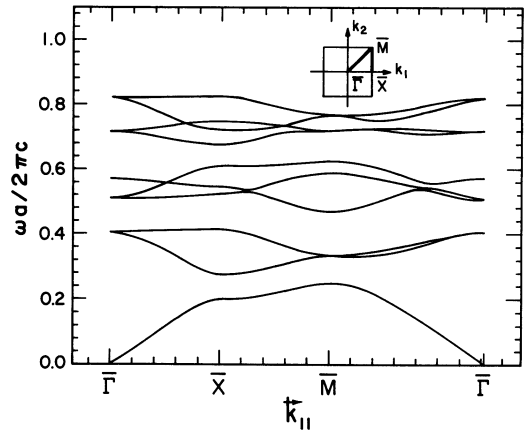

Figure 3. The photonic band structure for the $n = 0$ modes of a square lattice of lattice constant a of parallel, identical rods of circular cross section and finite length d, characterized by a dielectric constant $\epsilon_a = 9$ embedded in air between parallel, perfectly conducting plates, so that $\epsilon_b = 1$. The filling fraction is $f = 0.4488$. The band structure is independent of ratio d/a. The inset shows the first Brillouin zone for the square lattice, with the symmetry points indicated.

along the same symmetry directions as in Fig. 3. The 173 smallest reciprocal lattice vectors $\vec{G}_{||}$ were used in solving Eqs. (3.5). The results presented in Fig. 4a show that for $d/a = 0.5$ the $n = 1$ bands overlap the $n = 0$ bands depicted in Fig. 3 in such a way that the three absolute gaps present in the latter band structure are not closed up. Similarly, the results presented in Fig. 4b show that for $d/a = 1$ the $n = 1$ bands overlap the $n = 0$ bands in Fig. 3 in such a way that the lowest frequency absolute gap present in the latter band structure is not closed up, but the two higher frequency gaps are. By the time the ratio d/a has reached a value of 5, the overlap of the $n = 1$ and $n = 0$ bands is such that the lowest frequency absolute gap present in the latter band structure is also closed.

In Figs. 5a, 5b, and 5c we present results for $\omega a/2\pi c$ versus wavevector for $n = 2$ and $d/a = 0.5$, 1, and 5, respectively. Results are shown for the ten lowest frequency bands, plotted along the same symmetry directions as in Figs. 3 and 4. The smallest 173 reciprocal lattice vectors $\vec{G}_{||}$ were used in the solution of Eqs. (3.5) to obtain these results. The $n = 2$ bands for $d/a = 0.5$, together with the $n = 1$ bands for the same value of this ratio, do not close up the three absolute band gaps in the band structure of the $n = 0$ modes depicted in Fig. 3. For $d/a = 1$ the overlap of the $n = 2$ and $n = 1$ bands with the $n = 0$ bands closes up the two higher frequency absolute band gaps present in the band structure of the $n = 0$ modes, but leaves the lowest frequency absolute band gap open. However, the lowest frequency absolute band gap in the band structure of the $n = 0$ modes is closed by the overlap of the $n = 2$ and $n = 1$ bands with the $n = 0$ bands when $d/a = 5$.

The results of this section indicate that if it is desired to use a structure of the kind depicted in Fig. 2 to reproduce the low frequency band structure of the electromagnetic

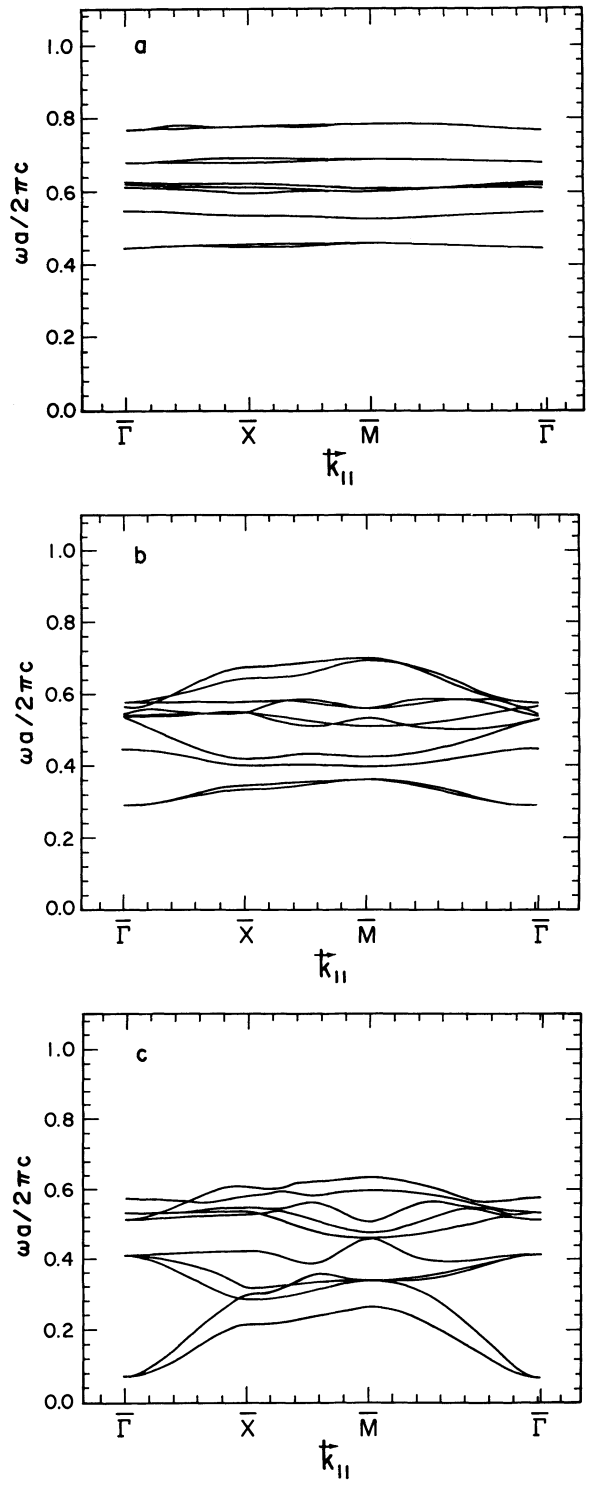

Figure 4. The photonic band structure for the $n = 1$ modes of a square lattice of lattice constant a of parallel, identical rods of circular cross section and finite length d characterized by a dielectric constant $\epsilon_a = 9$ embedded in air between parallel, perfectly conducting plates, so that $\epsilon_b = 1$. The filling fraction is $f = 0.4488$. Results are shown for a) $d/a = 0.5$, b) $d/a = 1$, and c) $d/a = 5$.

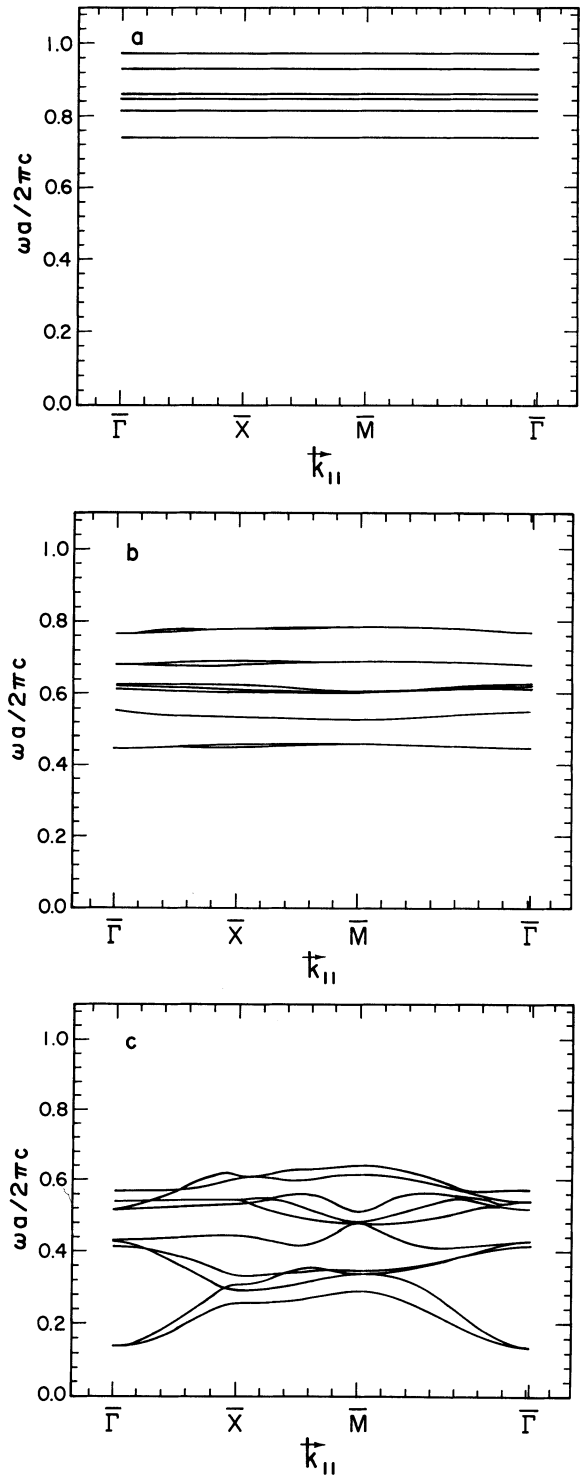

Figure 5. The photonic band structure for the $n = 2$ modes of a square lattice of lattice constant a of parallel, identical rods of circular cross section and finite length d characterized by a dielectric constant $\epsilon_a = 9$ embedded in air between parallel, perfecting conducting plates, so that $\epsilon_b = 1$. The filling fraction is $f = 0.4488$. Results are shown for a) $d/a = 0.5$, b) $d/a = 1$, and c) $d/a = 5$.

waves of E-polarization in the corresponding structure that is infinite in the x_3-direction, it is necessary to make d/a small enough that the lowest frequency $n = 1$ bands lie above the frequencies of the $n = 0$ bands that it is desired to reproduce. For the square lattice studied here a value of $d/a = 1$ appears to be small enough to leave the lowest frequency absolute gap unaffected, and even the next higher frequency absolute band gap is not closed by the modes with $n \geq 1$ if $d/a = 0.5$. It is in fact a value of d/a in this range that was used in the experimental work described in Ref. 22, viz. $d/a = 0.787$.

The results of this section also indicate that the additional degree of freedom provided by the finite separation of the parallel, perfectly conducting plates in the structure studied here, allows the resulting photonic band structures to be modified by varying this parameter. This feature could be useful in designing periodic, two-dimensional, dielectric structures for specific applications.

4. Defect Modes

Up to this point we have considered only the dispersion curves (band structures) for electromagnetic waves in perfectly periodic, two-dimensional, dielectric structures. The introduction of a defect, or defects, into such a structure can give rise to states of the electromagnetic field that are localized in space about the defect site(s). Such localized states, or defect modes, are the analogues for electromagnetic excitations in otherwise perfectly periodic dielectric structures of the localized donor or acceptor levels associated with impurities in semiconductors[29], or of the localized and gap vibrational modes associated with substitutional or interstitial defects in crystals[30] . We conclude this discussion of electromagnetic states in periodic, two-dimensional, dielectric structures by sketching out a theory of the defect modes that can occur in such structures when a localized defect is introduced into them. For this purpose we examine the particular case of defect states of E-polarization. A theory of defect modes of H-polarization can be constructed along similar lines, but will not be discussed here.

The system we study is characterized by a position-dependent dielectric constant of the form

$$\epsilon(\vec{x}_{||}) = \epsilon_0(\vec{x}_{||}) + \delta\epsilon(\vec{x}_{||}), \tag{4.1}$$

where $\epsilon_0(\vec{x}_{||})$ is a periodic function of $\vec{x}_{||}$,

$$\epsilon_0(\vec{x}_{||} + \vec{x}_{||}(\ell)) = \epsilon_0(\vec{x}_{||}), \tag{4.2}$$

where $\vec{x}_{||}(\ell)$ is a translation vector of one of the five two-dimensional Bravais lattices, while $\delta\epsilon(\vec{x}_{||})$ is nonzero in only a small region of the x_1x_2-plane. In this structure the electric vector in a state of E-polarization is given by

$$\vec{E}(\vec{x};t) = (0, 0, E_3(\vec{x}_{||}|\omega))exp(-i\omega t), \tag{4.3}$$

where the amplitude function $E_3(\vec{x}_{||}|\omega)$ is the solution of the equation

$$\left(\frac{\partial^2}{\partial x_1^2} + \frac{\partial^2}{\partial x_2^2} + \frac{\omega^2}{c^2}\epsilon(\vec{x}_{||})\right) E_3(\vec{x}_{||}|\omega) = 0. \tag{4.4}$$

In view of Eq. (4.1) we can rewrite this equation in the form

$$\left(L(\vec{x}_{||}) + \frac{\omega^2}{c^2}\right) E_3(\vec{x}_{||}|\omega) = -\frac{\omega^2}{c^2}\frac{\delta\epsilon(\vec{x}_{||})}{\epsilon_0(\vec{x}_{||})} E_3(\vec{x}_{||}|\omega), \tag{4.5}$$

where the differential operator $L(\vec{x}_\parallel)$ is defined by

$$L(\vec{x}_\parallel) = \frac{1}{\epsilon_0(\vec{x}_\parallel)} \left(\frac{\partial^2}{\partial x_1^2} + \frac{\partial^2}{\partial x_2^2} \right). \tag{4.6}$$

It is Eqs. (4.5)-(4.6) that we must solve.

The eigenfunctions and eigenvalues of the operator $L(\vec{x}_\parallel)$ have already been obtained in Section 2. Thus if we define the function $\psi_{n\vec{k}_\parallel}(\vec{x}_\parallel)$ by

$$\psi_{n\vec{k}_\parallel}(\vec{x}_\parallel) = \frac{1}{2\pi} \sum_{\vec{G}_\parallel} \frac{C_n(\vec{k}_\parallel + \vec{G}_\parallel)}{|\vec{k}_\parallel + \vec{G}_\parallel|} e^{i(\vec{k}_\parallel + \vec{G}_\parallel)\cdot\vec{x}_\parallel}, \tag{4.7}$$

where the $\{C_n(\vec{k}_\parallel + \vec{G}_\parallel)\}$ are the eigenvectors of the matrix eigenvalue problem,

$$\sum_{\vec{G}'_\parallel} M(\vec{k}_\parallel + \vec{G}_\parallel, \vec{k}_\parallel + \vec{G}'_\parallel) C_n(\vec{k}_\parallel + \vec{G}'_\parallel) = \lambda_n(\vec{k}) C_n(\vec{k}_\parallel + \vec{G}_\parallel), \tag{4.8}$$

with

$$M(\vec{k}_\parallel + \vec{G}_\parallel, \vec{k}_\parallel + \vec{G}'_\parallel) = |\vec{k}_\parallel + \vec{G}_\parallel| \hat{\kappa}(\vec{G}_\parallel - \vec{G}'_\parallel) |\vec{k}_\parallel + \vec{G}'_\parallel|, \tag{4.9}$$

we find by applying the operator $L(\vec{x}_\parallel)$ to $\psi_{n\vec{k}_\parallel}(\vec{x}_\parallel)$ that

$$L(\vec{x}_\parallel)\psi_{n\vec{k}_\parallel}(\vec{x}_\parallel) = -\lambda_n(\vec{k}_\parallel)\psi_{n\vec{k}_\parallel}(\vec{x}_\parallel). \tag{4.10}$$

For the cases in which we are interested in this chapter the matrix $M(\vec{k}_\parallel + \vec{G}_\parallel, \vec{k}_\parallel + \vec{G}'_\parallel)$ is real and symmetric. The eigenvectors $\{C_n(\vec{k}_\parallel + \vec{G}_\parallel)\}$ can then be chosen to be real, with no loss of generality. We can then impose the following orthonormality and completeness conditions on them:

$$\sum_{\vec{G}_\parallel} C_n(\vec{k}_\parallel + \vec{G}_\parallel) C_{n'}(\vec{k}_\parallel + \vec{G}_\parallel) = \delta_{nn'} \tag{4.11a}$$

$$\sum_{n} C_n(\vec{k}_\parallel + \vec{G}_\parallel) C_n(\vec{k}_\parallel + \vec{G}'_\parallel) = \delta_{\vec{G}_\parallel, \vec{G}'_\parallel}. \tag{4.11b}$$

If we use the result that

$$\epsilon_0(\vec{x}_\parallel) L(\vec{x}_\parallel) = \left(\frac{\partial^2}{\partial x_1^2} + \frac{\partial^2}{\partial x_2^2} \right), \tag{4.12}$$

and the result that follows from Eq. (4.10),

$$\epsilon_0(\vec{x}_\parallel) L(\vec{x}_\parallel) \psi_{n\vec{k}_\parallel}(\vec{x}_\parallel) = -\lambda_n(\vec{k}_\parallel)\epsilon_0(\vec{x}_\parallel)\psi_{n\vec{k}_\parallel}(\vec{x}_\parallel), \tag{4.13}$$

we find that

$$\begin{aligned} &\int d^2x_\parallel \psi^*_{m\vec{q}_\parallel}(\vec{x}_\parallel) \left(\frac{\partial^2}{\partial x_1^2} + \frac{\partial^2}{\partial x_2^2} \right) \psi_{n\vec{k}_\parallel}(\vec{x}_\parallel) \\ &= -\lambda_n(\vec{k}_\parallel) \int d^2x_\parallel \epsilon_0(\vec{x}_\parallel) \psi^*_{m\vec{q}_\parallel}(\vec{x}_\parallel) \psi_{n\vec{k}_\parallel}(\vec{x}_\parallel), \end{aligned} \tag{4.14}$$

where the integrals are taken over the entire x_1x_2-plane. The use of Eqs. (4.7) and (4.11a), and the fact that $\vec{q}_\parallel$ and $\vec{k}_\parallel$ are both restricted to lie in the two-dimensional

first Brillouin zone defined by the vectors $\{\vec{G}_{\|}\}$, yields the result that the left hand side of Eq. (4.14) equals $-\delta(\vec{q}_{\|}-\vec{k}_{\|})\delta_{mn}$. Thus, we obtain the orthonormality condition satisfied by the $\{\psi_{n\vec{k}_{\|}}(\vec{x}_{\|})\}$:

$$\int d^2x_{\|}\epsilon_0(\vec{x}_{\|})\psi^*_{m\vec{q}_{\|}}(\vec{x}_{\|})\psi_{n\vec{k}_{\|}}(\vec{x}_{\|}) = \frac{1}{\lambda_n(\vec{k})}\delta(\vec{q}_{\|}-\vec{k}_{\|})\delta_{mn}. \tag{4.15a}$$

From this result we are led directly to the completeness condition satisfied by the $\{\psi_{n\vec{k}_{\|}}(\vec{x}_{\|})\}$:

$$\sum_n \int_{BZ} d^2k_{\|}\lambda_n(\vec{k}_{\|})\psi^*_{n\vec{k}_{\|}}(\vec{x}_{\|})\psi_{n\vec{k}_{\|}}(\vec{x}\,'_{\|}) = \frac{1}{\epsilon_0(\vec{x}_{\|})}\delta(\vec{x}_{\|}-\vec{x}\,'_{\|}). \tag{4.15b}$$

With these results in hand we can now proceed to the solution of Eq.(4.5).

We begin by expanding $E_3(\vec{x}_{\|}|\omega)$ in terms of the $\psi_{n\vec{k}_{\|}}(\vec{x}_{\|})$,

$$E_3(\vec{x}_{\|}|\omega) = \sum_n \int_{BZ} \frac{d^2k_{\|}}{(2\pi)^2} a_{n\vec{k}_{\|}}\psi_{n\vec{k}_{\|}}(\vec{x}_{\|}). \tag{4.16}$$

On substituting this expansion into the left hand side of Eq. (4.5), and using the eigenvalue equation (4.10) and the orthonormality condition (4.15a), we obtain the coefficient $a_{n\vec{k}_{\|}}$ in the form

$$a_{n\vec{k}_{\|}} = (2\pi)^2\frac{\omega^2}{c^2}\frac{\lambda_n(\vec{k}_{\|})}{\lambda_n(\vec{k}_{\|})-\frac{\omega^2}{c^2}}\int d^2x_{\|}\psi^*_{n\vec{k}_{\|}}(\vec{x}_{\|})\delta\epsilon(\vec{x}_{\|})E_3(\vec{x}_{\|}|\omega). \tag{4.17}$$

When this result is substituted into the right hand side of Eq. (4.16) we obtain the relation

$$E_3(\vec{x}_{\|}|\omega) = \frac{\omega^2}{c^2}\int d^2x'_{\|}G(\vec{x}_{\|};\vec{x}\,'_{\|}|\omega^2)\delta\epsilon(\vec{x}'_{\|})E_3(\vec{x}'_{\|}|\omega), \tag{4.18}$$

where the Green's function $G(\vec{x}_{\|};\vec{x}\,'_{\|}|\omega^2)$ is given by

$$G(\vec{x}_{\|};\vec{x}\,'_{\|}|\omega^2) = \sum_n \int_{BZ} d^2k_{\|}\frac{\psi_{n\vec{k}_{\|}}(\vec{x}_{\|})\lambda_n(\vec{k}_{\|})\psi^*_{n\vec{k}_{\|}}(\vec{x}\,'_{\|})}{\lambda_n(\vec{k}_{\|})-\frac{\omega^2}{c^2}}. \tag{4.19}$$

In Eq. (4.18) the electric field component $E_3(\vec{x}_{\|}|\omega)$ at any point in the x_1x_2-plane is given in terms of its values within that region of the x_1x_2-plane in which $\delta\epsilon(\vec{x}_{\|})$ is nonzero. Thus, if we denote the latter region by R, and define the function $f(\vec{x}_{\|}|\omega)$ by

$$f(\vec{x}_{\|}|\omega) = E_3(\vec{x}_{\|}|\omega) \qquad \vec{x}_{\|} \text{ inside } R \tag{4.20a}$$

$$= 0 \qquad \vec{x}_{\|} \text{ outside } R, \tag{4.20b}$$

then $f(\vec{x}_{\|}|\omega)$ is the solution of the homogeneous integral equation

$$f(\vec{x}_{\|}|\omega) = \frac{\omega^2}{c^2}\int_R d^2x'_{\|}G(\vec{x}_{\|};\vec{x}\,'_{\|}|\omega^2)\delta\epsilon(\vec{x}'_{\|})f(\vec{x}'_{\|}|\omega). \tag{4.21}$$

The solvability condition for this equation yields the frequencies of the defect modes associated with the perturbation $\delta\epsilon(\vec{x}_{\|})$. Once these frequencies and $f(\vec{x}_{\|}|\omega)$ have been

obtained, the electric field component $E_3(\vec{x}_\parallel|\omega)$ in the region $\vec{x}_\parallel$ outside R can be obtained from Eq. (4.18).

An alternative approach to the determination of these frequencies is provided by returning to Eq. (4.17) and substituting Eq. (4.16) into the right hand side of it:

$$\frac{\lambda_n(\vec{k}_\parallel) - \frac{\omega^2}{c^2}}{\lambda_n(\vec{k}_\parallel)} a_{n\vec{k}_\parallel} = \frac{\omega^2}{c^2} \sum_{n'} \int_{BZ} d^2k'_\parallel \widehat{\delta\epsilon}(n\vec{k}_\parallel|n'\vec{k}'_\parallel) a_{n'\vec{k}'_\parallel}, \tag{4.22}$$

where

$$\widehat{\delta\epsilon}(n\vec{k}_\parallel|n'\vec{k}'_\parallel) = \int_R d^2x_\parallel \psi^*_{n\vec{k}_\parallel}(\vec{x}_\parallel)\delta\epsilon(\vec{x}_\parallel)\psi_{n'\vec{k}'_\parallel}(\vec{x}_\parallel). \tag{4.23}$$

The solvability condition for Eq. (4.22) yields the frequencies of the defect modes. Once they and $a_{n\vec{k}_\parallel}$ have been determined the electric field component $E_3(\vec{x}_\parallel|\omega)$ can be obtained from Eq. (4.16).

As an initial study of the defect modes given by the solutions of Eq. (4.20) we have considered the case, studied experimentally by Schultz *et al.*[22], of a square lattice of dielectric rods from which one of the rods has been removed. Specifically, these authors considered a square lattice formed of cylindrical rods of dielectric constant $\epsilon_a = 9$ and filling fraction $f = 0.4488$. The rods were placed in a background whose dielectric constant is $\epsilon_b = 1$, and a single rod was removed from the system. This array of rods was placed in a microwave chamber, so that a square array of infinite rods is only a rough approximation to the real experimental set up. A better approximation to the experimental set up is the set of rods between two parallel, perfectly conducting plates that was studied in Section 3 in connection with another experiment performed by Schultz *et al.*[22] The $n = 0$ parallel plate solution (corresponding to the E-polarization case for the infinite rod system), however, is not affected by the finite separation of the plates in the experimental system, as we have seen above, so the infinite rod system we consider theoretically here should correctly portray the gross properties of the single impurity experiments conducted by Schultz *et al.*[22]

Schultz *et al.* found that removing a rod from the system gives rise to an impurity mode whose frequency falls in the second band gap. No mode is reported to have been found in the lower first band gap of the system. Preliminary results from our study of Eq. (4.21) for the system of infinite rods of dielectric constant $\epsilon_a = 9$ and filling fraction $f = 0.4488$ agree with these experimental observations.

Equation (4.21) was studied numerically by converting it into a matrix equation. A Gauss-Legendre quadrature scheme was used to evaluate the integral in terms of r and θ variables, defined by

$$\vec{x}_\parallel(i,j) = (r_i \cos\theta_j, r_i \sin\theta_j) \tag{4.24}$$

for

$$r_i = R[q_i + 1]/2 \tag{4.25a}$$

$$\theta_j = \pi[q_j + 1], \tag{4.25b}$$

where R is the radius of a dielectric cylinder and $-1 \leq q_i \leq 1$ for i = 1,2,...P are the Gauss-Legendre quadrature abscissas corresponding to quadrature weights w_i. In terms of $\vec{x}_\parallel(i,j)$ and w_i the integral equation in Eq. (4.21) becomes

$$f(\vec{x}_\parallel(i,j)|w) - \frac{\pi R^2}{4}\frac{\omega^2}{c^2} \sum_{m,n} [w_m w_n G(\vec{x}_\parallel(i,j), \vec{x}_\parallel(m,n)|w^2) \times \delta\epsilon(\vec{x}_\parallel(m,n)) f(\vec{x}_\parallel(m,n)|w) = 0. \tag{4.26}$$

For the results presented below we have taken $P = 10$ so that Eq. (4.26) represents a 100x100 matrix equation. The frequencies of the impurity modes of our system are the zeros of the determinant of the 100x100 matrix of the coefficients in Eq. (4.26).

We have computed the Green's function, Eq. (4.19), by using a Gauss-Legendre quadrature scheme to perform the $\vec{k}_{||}$ integration in the first Brillouin zone. Results for $\psi_{n\vec{k}_{||}}(\vec{x}_{||})$and $\lambda_n(\vec{k}_{||})$ used in evaluating Eq. (4.19) were obtained by numerically solving the eigenvalue problem in Eqs. (4.8)-(4.9) for an $N \times N$ matrix. To obtain the results presented below we have taken 100 $\vec{k}_{||}$ points in the first Brillouin zone, and the $N =$ 101, 185, 241, or 305 smallest reciprocal lattice vectors $\vec{G}_{||}$ in the calculation of Eq. (4.19) for use in computing the determinant of Eq. (4.26).

When 100 $\vec{k}_{||}$ points in the first Brillouin zone are used the upper and lower edges of the second band gap for $N = 101$ are found to occur at $\omega a/2\pi c = 0.483$ (11.41 GHz) and 0.419 (9.90 GHz), respectively. For $N = 305$ the upper and lower edges occur at $\omega a/2\pi c = 0.470$ (11.1 GHz) and 0.413 (9.76 Ghz), respectively. By using $N = 101$, 185, 241, and 305, we find frequencies of the impurity mode given by $\omega a/2\pi c = 0.469$, 0.454, 0.449, and 0.445, respectively, each of which is well within the gap. These results give us confidence that an impurity mode frequency given by $\omega a/2\pi c = 0.45$ is in error by no more than about 1% . This value translates into a frequency of 10.63 GHz, which is a bit lower than the impurity mode frequency of 11.2 GHz measured by Schultz *et al.*[22] The difference between these two results may be due to the fact that the experiments reported in Ref. 22 were carried out in the dielectric structure of finite extent along the x_3-axis depicted schematically in Fig. 2.

Currently, calculations using more $\vec{k}_{||}$-points in the first Brillouin zone and a larger number of reciprocal lattice vectors $\vec{G}_{||}$ in the determination of the Green's function $G(\vec{x}_{||}; \vec{x}'_{||}|\omega^2)$ are being carried out to determine the impurity mode frequency more precisely.

5. SOME DIRECTIONS FOR FUTURE WORK

It would be worthwhile to carry out a systematic study of the photonic band structures of two-dimensional, periodic, dielectric structures that are more general than the square and triangular structures studied until now. An aim of this study would be finding a structure, or structures, possessing the largest, common, absolute band gap for the propagation of electromagnetic waves of both H- and E-polarization in the plane perpendicular to the generators of the structures. Ideally, the results of this investigation should also demonstrate the dependence of the position and width of such absolute band gaps on the connectivity of the dielectric portion of the structure, the filling fraction, and the dielectric contrast. They should also incorporate the consequences of the space group symmetry of a structure which, for example, can give rise to the degeneracy of bands at symmetry points in its two-dimensional first Brillouin zone that close up band gaps that would occur in structures of lower symmetry. One would then have some basis for predicting the kinds of structures that are most favorable for possessing large, common, absolute band gaps.

The development of computational approaches to the calculation of photonic band structures of two-dimensional, periodic dielectric structures that converge more rapidly than the plane wave method, particularly in the case of large dielectric contrast and complex unit cells, would be very desirable.

The discussion in Section 2 of the propagation of electromagnetic waves in the infinite structure consisting of a lattice of parallel dielectric rods embedded in a medium

with a different dielectric constant was limited to the case in which the propagation occurred in a plane perpendicular to the rods. In this case electromagnetic waves of pure H-polarization and pure E-polarization exist. A straightforward, but worthwhile, extension of this work is the study of the photonic band structures associated with out-of-plane propagation, in which case waves of pure H- and E-polarization no longer exist. In particular, it would be of interest to determine how far out of the plane perpendicular to the rods the waves in the triangular lattice studied in Section 2, that possesses a common absolute band gap for waves of both H- and E-polarization, can propagate before that absolute band gap closes up. This result could be useful in the context of practical applications of two-dimensional photonic band gap structures.

In the study of the localized modes introduced into an otherwise doubly periodic, infinite dielectric structure by the presence of a substitutional or interstitial line defect of the kind considered in Section 4, it would be of interest to study the modes associated with pairs or clusters of such defects whose symmetries are lower than that of an isolated defect. It may be possible to excite such defect modes preferentially by external fields of suitably chosen polarization and direction of propagation.

Perhaps even more interesting would be the study of defect modes in the structure considered in Section 3, which is of finite extent in the x_3-direction. Here, the ability to modify the photonic band structure of the unperturbed dielectric structure by varying the distance between the perfectly conducting plates could be exploited to facilitate the occurrence of localized defect modes, or to hinder it.

The preceding examples hardly exhaust the possibilities for interesting work that can be done in the area of electromagnetic wave propagation in two-dimensional, periodic or perturbed, dielectric structures. But they serve to indicate the existence of such possibilities and, it may be hoped, will serve to suggest other fruitful directions for future work in this field.

Acknowledgments

This work was supported in part by NSF Grant No. DMR 89-18184. It was also supported by the University of California, Irvine, through the allocation of computer time. We would like to acknowledge useful discussions with Professor S. Schultz and Mr. D. Smith concerning the topics discussed in Sections 3 and 4, respectively.

References

1. S. John, "Strong Localization of Photons in Certain Disordered Dielectric Superlattices," Phys. Rev. Lett. 58:2486 (1987).

2. E. Yablonovitch, "Inhibited Spontaneous Emission in Solid-State Physics and Electronics," Phys. Rev. Lett. 58:2059 (1987).

3. E. Yablonovitch, T. J. Gmitter, and R. Bhat, "Inhibited and Enhanced Spontaneous Emission From Optically Thin AlGaAs/GaAs Double Heterostructures," Phys. Rev. Lett. 61:2546 (1988).

4. G. Kurizki and A. Z. Genack, "Suppression of Molecular Interactions in Periodic Dielectric Structures," Phys. Rev. Lett. 61:2269 (1988).

5. S. John and R. Rangarajan, "Optimal Structures for Classical Wave Localization: An Alternative to the Ioffe-Regel Criterion," Phys. Rev. B38:10101 (1988).

6. E. N. Economou and A. Zdetsis, "Classical Wave Propagation in Periodic Structures," Phys. Rev. B40:1334 (1989).

7. S. Satpathy, Ze Zhang, and M. R. Salehpour, "Theory of Photon Bands in Three-Dimensional Periodic Dielectric Structures," Phys. Rev. Lett. 64:1239 (1990); 65:2478(E) (1990).

8. K. M. Leung and Y. F. Liu, "Photon Band Structures: The Plane Wave Method," Phys. Rev. B41:10188 (1990).

9. K. M. Leung and Y. F. Liu, "Full Vector Wave Calculation of Photonic Band Structures in Face-Centered-Cubic Dielectric Media," Phys. Rev. Lett. 65:2646 (1990).

10. Z. Zhang and S. Satpathy, "Electromagnetic Wave Propagation in Periodic Structures: Bloch Wave Solution of Maxwell's Equations," Phys. Rev. Lett. 65:2650 (1990).

11. K. M. Ho, C. T. Chan, and C. M. Soukoulis, "Existence of a Photonic Gap in Periodic Dielectric Structures," Phys. Rev. Lett. 65:3152 (1990).

12. E. Yablonovitch, T. J. Gmitter, and K. M. Leung, "Photonic Band Structure: The Face-Centered Cubic Case Employing Nonspherical Atoms," Phys. Rev. Lett. 67:2295 (1991).

13. R. D. Meade, K. D. Brommer, A. M. Rappe, and J. D. Joannopoulos, "Electromagnetic Bloch Waves at the Surface of a Photonic Crystal," Phys. Rev. B44:10961 (1991).

14. E. Yablonovitch, T. J. Gmitter, R. D. Meade, A. M. Rappe, K. D. Brommer, and J. D. Joannopoulos, "Donor and Acceptor Modes in Photonic Band Structure," Phys. Rev. Lett. 67:3380 (1991).

15. S. John and J. Wang, "Quantum Electrodynamics Near a Photonic Band Gap: Photon Bound States and Dressed Atoms," Phys. Rev. Lett. 64:2418 (1990).

16. S. John and J. Wang, "Quantum Optics of Light in a Photonic Band Gap," Phys. Rev. B43:12772 (1991).

17. E. Yablonovitch and T. J. Gmitter, "Photonic Band Structure: The Face-Centered Cubic Case," Phys. Rev. Lett. 63:1950 (1989).

18. E. Yablonovitch and T. J. Gmitter, "Photonic Band Structure: The Face-Centered Cubic Case," J. Opt. Soc. Am. A7:1792 (1990).

19. M. Plihal, A. Shambrook, A. A. Maradudin, and P. Sheng, "Two-Dimensional Photonic Band Structures," Opt. Comm. 80:199 (1991).

20. M. Plihal and A. A. Maradudin, "Photonic Band Structures of Two-Dimensional Systems: The Triangular Lattice," Phys. Rev. B44:8565 (1991).

21. P. R. Villeneuve and M. Piché, "Photonic Band Gaps of Transverse-Electric Modes in Two-Dimensionally Periodic Media," J. Opt. Soc. Am. A8:1296 (1991).

22. S. L. McCall, P. M. Platzman, R. Dalichaouch, D. Smith and S. Schultz, "Microwave Propagation in Two-Dimensional Dielectric Lattices," Phys. Rev. Lett. 67: 2017 (1991).

23. R. D. Meade, K. D. Brommer, A. M. Rappe, and J. D. Joannopoulos, "The Existence of a Photonic Bandgap in Two Dimensions," Appl. Phys. Lett. (to appear).

24. W. M. Robertson, G. Arjavalingam, R. D. Meade, K. D. Brommer, A. M. Rappe, and J. D. Joannopoulos, "Measurement of Photonic Band Structure in a Two-Dimensional Periodic Dielectric Array," Phys. Rev. Lett. 68:2023 (1992).

25. W. M. Robertson, G. Arjavalingam, R. D. Meade, K. D. Brommer, A. M. Rappe, and J. D. Joannopoulos, "Measurement of the Photon Dispersion Relation in 2D Ordered Dielectric Arrays," J. Opt. Soc. Am. B (to appear).

26. N. E. Glass and A. A. Maradudin, "Diffraction of Light by a Periodically Modulated Dielectric Half-Space," Phys. Rev. B29:1840 (1984).

27. B. A. Auld, Y. A. Shui, and Y. Wang, "Elastic Wave Propagation in Three-Dimensional Periodic Composite Materials," J. de Physique, Colloque No. 5, Supplément au No. 4, 45:C5-159 (1984).

28. A. A. Maradudin and A. R. McGurn, "The Photonic Band Structure of a Truncated, Two-Dimensional, Periodic Dielectric Medium," J. Opt. Soc. Am. B (to appear).

29. See, for example, J. Callaway, *Quantum Theory of the Solid State*, 2nd ed. (Academic Press, New York, 1991). pp. 418-423.

30. See, for example, A. A. Maradudin, E. W. Montroll, G. H. Weiss, and I. P. Ipatova, *Theory of Lattice Dynamics in the Harmonic Approximation*, 2nd ed. (Academic Press, New York, 1971), Chap. VIII.

PLANE-WAVE CALCULATION OF PHOTONIC BAND STRUCTURE

K. M. Leung

Department of Physics
Polytechnic University
Brooklyn, NY 11201

INTRODUCTION

The new class of artificial periodic dielectric media called the photonic crystals, originally proposed by Yablonovitch[1] and John[2] a few years ago, has been attracting a great deal of research interests because of its highly unusual properties which offer exciting and challenging new problems, and because of its broad potentials for device applications from the mm to the uv wavelengths. Recently photonic crystals which have a full photonic bandgap have been discovered.[3] [4] Surface states as well as defect modes[5] in these crystals have now also been studied.

The experimental study on the photonic band structure of fcc arrays of spherical "atoms"[6] attracted a number of subsequent theoretical studies. At the beginning the studies were all based on the use of the scalar wave equation,[7] [8] [9] [10] which for good reasons did not yield results that can be compared with the real physical situation. These studies were soon followed by realistic photonic band calculations based on the use of the Maxwell's equations.[11] [3] Unlike the corresponding electron band calculations, which are only approximate because of many-body effects, photonic band calculations using Maxwell's equations are in principle exact, unless the medium is nonlinear and the electromagnetic fields are strong. Therefore these calculations can be directly compared with experimental data. and have been rather helpful in understanding and guiding experiments efforts. The methods used were all based on the plane-wave (PW) expansion, although there were variations in the way in which the expansion was actually implemented. To the best of our knowledge, all the computed results on the photonic band structure for vector waves thus far have all been done with the help of the PW method.

There are also PW calculations of two dimensional photonic crystals.[12] They are also interesting and have potential device applications. The interested reader should consult the article by Maradudin in this NATO conference proceeding.

Photonic Band Gaps and Localization, Edited by
C.M. Soukoulis, Plenum Press, New York, 1993

The PW method has several important advantages. (1) With the exception of a single known pathological case,[3] the PW method yields reasonably rapidly convergent results. Calculations are usually done with a hundred to a few hundred PWs, depending on the strength of the dielectric contrast. The band structure can be obtained by diagonalizing matrices on the order of two hundred to a few hundred in sizes, which can easily be handled with todays computers. (2) The method is quite simple to implement and does not require writing lengthy computer programs. (3) The method is also very versatile and can be applied to handle all forms of dielectric modulations. This is an especially important advantage because some of the interesting photonic crystals have "atoms" of rather odd shapes.

We will discuss three variations of the PW method in detailed here, and present a new result on the frequency dependence of the attenuation length in the Yablonovitch photonic bandgap crystal.[4]

We start by considering monochromatic wave of frequency ω in an inhomogeneous dielectric medium which is described by the Maxwell's equations

$$\nabla \times \mathbf{E} = \frac{i\omega\mu}{c}\mathbf{H}, \qquad \nabla \times \mathbf{H} = \frac{-i\omega\varepsilon}{c}\mathbf{E},$$
$$\nabla \cdot (\varepsilon \mathbf{E}) = 0, \qquad \nabla \cdot (\mu \mathbf{H}) = 0. \tag{1}$$

If we eliminate **H** from these equations and assume that $\mu = 1$, we have the following equation for the electric field

$$\nabla \times \nabla \times \mathbf{E} = k_b^2 \varepsilon \mathbf{E}, \tag{2}$$

where $k_b^2 \equiv \varepsilon_b \mu \omega^2 / c^2$, $\varepsilon \equiv \varepsilon(\mathbf{r})/\varepsilon_b$, and ε_b is the dielectric constant of a background host medium. Equation (2) can also be written as

$$\nabla(\nabla \cdot \mathbf{E}) - \nabla^2 \mathbf{E} = k_b^2 \varepsilon \mathbf{E}. \tag{3}$$

Now if the term $\nabla(\nabla \cdot \mathbf{E})$ is neglected then each component of **E** obeys the so-called scalar wave equation:

$$-\nabla^2 \psi - k_b^2 \varepsilon \psi = 0, \tag{4}$$

which is sometimes used in optics instead of the full set of Maxwell's equations. This aproximation is valid if the magnitude of the neglected term is small. One can make use of the vector identity

$$\nabla \cdot \left(\varepsilon \mathbf{E} \right) = \varepsilon \nabla \cdot \mathbf{E} + \mathbf{E} \cdot \nabla \varepsilon = 0 \tag{5}$$

to rewrite the neglected term as

$$\nabla \left(\nabla \cdot \mathbf{E} \right) = -\nabla \left(\mathbf{E} \cdot \nabla \ln \varepsilon \right). \tag{6}$$

It is clear that this term vanishes inside a homogeneous medium and in general may be neglected if the variation in ε is small on the scale of a wavelength. However, in photonic bandgap crystals the size of the photonic unit cell must be comparable to the wavelength which corresponds to a frequency within the bandgap. In order to have a sizable forbidden bandgap, the refractive index must vary considerably within the unit cell. Therefore this term cannot be neglected in photonic bandgap materials. Results obtained based on the scalar wave equation are not only quantitatively but qualitatively far from the actual physical reality, contrary to the claim made in one study.[10]

However, it was not an unreasonable equation to start investigating photonic band structure three years ago. First, there was no calculation based on the full Maxwell's equations at that time. Second, because of the resemblance of the scalar wave equation with the Schrödinger's equation of a spinless electron, one can readily make use of the knowledge gained and computational techniques developed for the electron problem. Third, any computational method intended for Maxwell's equations should also work with certain modifications for the scalar wave equation. This does not mean that if a method works for the scalar wave equation then it will necessarily work for the Maxwell's equations. But rather, if a method fails when it is used for the scalar wave equation then we cannot expect that it will work for the electromagnetic waves. It was primarily because of this last reason that we did a calculation for scalar waves.[9]

PLANE-WAVE EXPANSION FOR SCALAR WAVE

We work with the scalar wave equation in Eq. (3). Our major finding was that the PW expansion method, at least in the case of scalar wave, can be used with no convergence problem to calculate photonic band structure.[9] This conclusion was arrived at by calculating the photonic band structure using separately the PW expansion method and the Korringa-Kohn-Rostoker (KKR) method.[13]

In the PW method, we use the expansions

$$\psi(\mathbf{r}) = \sum_{\mathbf{G}} c_{\mathbf{k}+\mathbf{G}}\, e^{i(\mathbf{k}+\mathbf{G})\cdot\mathbf{r}}, \tag{7}$$

for the scalar field $\psi(\mathbf{r})$, and

$$\varepsilon(\mathbf{r}) = \sum_{\mathbf{G}} \varepsilon_{\mathbf{G}}\, e^{i\mathbf{G}\cdot\mathbf{r}}, \tag{8}$$

for the dielectric function, where $\mathbf{k}$ is a wave vector and $\mathbf{G}$ is a reciprocal lattice vector. Eq. (8) is appropriate since $\varepsilon(\mathbf{r})$ is a periodic function of $\mathbf{r}$, *i.e.* $\varepsilon(\mathbf{r}+\mathbf{R}) = \varepsilon(\mathbf{r})$ for any lattice vector $\mathbf{R}$. The Fourier coefficients are given by

$$\varepsilon_{\mathbf{G}} = \int_{cell} \frac{d\mathbf{r}}{\Omega}\, e^{-i\mathbf{G}\cdot\mathbf{r}}\, \varepsilon(\mathbf{r}), \tag{9}$$

where the integral extends over the real space primitive cell whose volume is denoted by Ω. The expansions in Eqs. (7) and (8) are used in the scalar wave equation to obtain the result

$$k_b^2 \sum_{\mathbf{G}} \varepsilon_{\mathbf{G}'-\mathbf{G}}\, c_{\mathbf{k}+\mathbf{G}'} - |\mathbf{k}+\mathbf{G}|^2 c_{\mathbf{k}+\mathbf{G}} = 0. \tag{10}$$

This result can be cast into a standard matrix eigenvalue problem:

$$\frac{1}{|\mathbf{k}+\mathbf{G}|} \sum_{\mathbf{G}'} \frac{\varepsilon_{\mathbf{G}'-\mathbf{G}}}{|\mathbf{k}+\mathbf{G}'|}\, d_{\mathbf{k}+\mathbf{G}'} - \frac{1}{k_b^2} d_{\mathbf{k}+\mathbf{G}} = 0, \tag{11}$$

for a real and symmetric matrix. The eigenvalues are identified as k_b^{-2} and the new eigenvectors are given in terms of the original ones by the relation $d_{\mathbf{k}+\mathbf{G}} = |\mathbf{k}+\mathbf{G}|\, c_{\mathbf{k}+\mathbf{G}}$.

The KKR method for scalar wave follows very closely the original works of Korringa, Kohn and Rostoker, and will not be given here. A detailed account of the

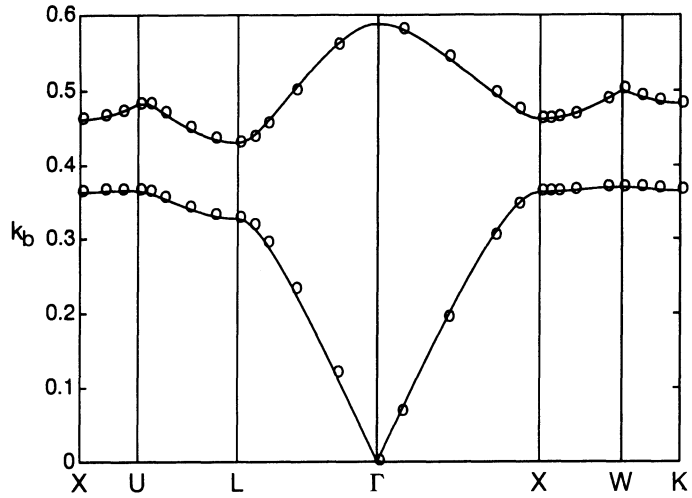

Figure 1. The solid curves show the band structure of a fcc lattice of dielectric spheres calculated with the PW expansion. The circles are the results calculated with the KKR method. The volume-filling fraction of spheres is 0.375 and the dielectric ratio is 12.25.

method for photonic band structure calculation, together with numerical results have in fact already been made by John and Rangarajan.[7]

Using Eq. (11) we calculated the photonic band structure for a fcc lattice of dielectric spheres of refractive index 3.6 in a host medium of refractive index 1. For the case of dielectric spheres considered here, we have

$$\varepsilon_{\mathbf{G}} = \delta(\mathbf{G}) - 3f(1-\frac{\varepsilon_a}{\varepsilon_b})g(Ga), \tag{12}$$

where the function $g(x) = (\sin x - x\cos x)/x^3$, a is the radius and f is the volume fraction of the spheres. This result applies as long as the spheres are not overlapping. The solid curves give the results computed using the PW method with 67 PWs, and the ovals denote those obtained by the KKR method with an angular momentum truncation of $l_{\max}=3$. The results agree with each other reasonable well. There was no noticeable change in the result by using a larger number of PWs for the PW calculation, or a larger $l_{\max}$ in the case of the KKR calculation. Our results are basically identical with those reported by Satpathy et al., [10] who also use the PW method, but did not reduce the eigenvalue problem into the standard form. However, our results are different than those given by John and Rangarajan [7] who used the KKR method, and by Economou and Zdetsis[8] who used the augmented PW method. We believe that our results are indeed correct because they were obtained by two independent methods.

We should also mention that for scalar waves, because the two different states of polarization are ignored, the lowest common gap, if it exist at all, is expected to lie between the first and second allowed bands. This situation is very different from the actual vector wave case where the lowest common gap is expected to lie between the second and third allowed bands. However, as we discussed earlier there is no reason to expect the results calculated based on the scalar wave equation to have any bearing on the real physical situation.

PLANE-WAVE EXPANSION FOR VECTOR WAVE

We now consider the electromagnetic case.[11] In our original work we chose to work with the electric field, which obeys Eq. (2). Using the PW expansion of the electric field in the form

$$\mathbf{E}(\mathbf{r}) = \sum_{\mathbf{G}} \mathbf{E}_{\mathbf{k}+\mathbf{G}} \, e^{i(\mathbf{k}+\mathbf{G})\cdot\mathbf{r}} , \tag{13}$$

Eq. (2) becomes

$$\left[\, |\, \mathbf{k}+\mathbf{G} \,|^2 \mathbf{I} - (\mathbf{k}+\mathbf{G})(\mathbf{k}+\mathbf{G}) \right] \cdot \mathbf{E}_{\mathbf{k}+\mathbf{G}} - k_b^2 \sum_{\mathbf{G}'} \varepsilon_{\mathbf{G}'-\mathbf{G}} \, \mathbf{E}_{\mathbf{k}+\mathbf{G}'} = 0 , \tag{14}$$

where $\varepsilon_{\mathbf{G}}$ is defined as in Eq. (8). This equation has a standard matrix form $(A - \lambda B)v = 0$, where A and B are both symmetric matrices.

Eq. (14) gives an infinite number of linear equations which could only be solved by truncation. If we keep N PWs then there are $3N$ eigenvectors and eigenvalues. However N of those correspond to zero-frequency longitudinal modes. This can be seen by setting $k_b^2 = 0$ which gives

$$\left[\, |\, \mathbf{k}+\mathbf{G} \,|^2 \mathbf{I} - (\mathbf{k}+\mathbf{G})(\mathbf{k}+\mathbf{G}) \right] \cdot \mathbf{E}_{\mathbf{k}+\mathbf{G}} = 0 . \tag{15}$$

It can be shown that the matrix involved in the above equation is indeed singular and so there are non-trivial solutions. This becomes more obvious if one works in a coordinate system in which the z-axis is parallel to the vector $(\mathbf{k}+\mathbf{G})$. For then Eq. (15) becomes

$$\begin{pmatrix} |\, \mathbf{k}+\mathbf{G} \,|^2 & 0 & 0 \\ 0 & |\, \mathbf{k}+\mathbf{G} \,|^2 & 0 \\ 0 & 0 & 0 \end{pmatrix} \begin{pmatrix} E^x_{\mathbf{k}+\mathbf{G}} \\ E^y_{\mathbf{k}+\mathbf{G}} \\ E^z_{\mathbf{k}+\mathbf{G}} \end{pmatrix} = 0 . \tag{16}$$

The eigenvectors are clearly given by $E^x_{\mathbf{k}+\mathbf{G}} = E^y_{\mathbf{k}+\mathbf{G}} = 0$, and $E^z_{\mathbf{k}+\mathbf{G}} \neq 0$. This means that these N zero-frequency modes are in fact longitudinal.

One could get rid of these zero modes by imposing the $\nabla \cdot \mathbf{D} = 0$ condition explicitly. This condition gives the equation

$$(\mathbf{k}+\mathbf{G}) \cdot \sum_{\mathbf{G}'} \varepsilon_{\mathbf{G}-\mathbf{G}'} \, \mathbf{E}_{\mathbf{k}+\mathbf{G}'} = 0 . \tag{17}$$

At this point, it is convenient to use matrix notation so that:

$$(E_x)_i = (\mathbf{E}_{\mathbf{k}+\mathbf{G}_i})_x \qquad (E_y)_i = (\mathbf{E}_{\mathbf{k}+\mathbf{G}_i})_y \qquad (E_z)_i = (\mathbf{E}_{\mathbf{k}+\mathbf{G}_i})_z$$

$$(G)_{ij} = \delta_{ij} \, |\, \mathbf{k}+\mathbf{G}_i \,| \qquad (\varepsilon)_{ij} = \varepsilon_{\mathbf{G}_j - \mathbf{G}_i} \tag{18}$$

$$(X)_{ij} = (\mathbf{k}+\mathbf{G}_i)_x \qquad (Y)_{ij} = (\mathbf{k}+\mathbf{G}_i)_y \qquad (Z)_{ij} = (\mathbf{k}+\mathbf{G}_i)_z . \tag{19}$$

The eigenvalue equation in Eq. (14) can then be rewritten as

$$\begin{aligned} G^2 E_x - k_b^2 \, \varepsilon \, E_x - X(XE_x + YE_y + ZE_z) = 0 , \\ G^2 E_y - k_b^2 \, \varepsilon \, E_y - Y(XE_x + YE_y + ZE_z) = 0 , \end{aligned} \tag{20}$$

$$G^2 E_z - k_b^2 \varepsilon E_z - Z(XE_x + YE_y + ZE_z) = 0 .$$

The $\nabla \cdot \mathbf{D} = 0$ equation becomes

$$X \varepsilon E_x + Y \varepsilon E_y + Z \varepsilon E_z = 0 , \tag{21}$$

We can now use Eq. (21) to eliminate the N zero-frequency modes, and to reduce the $3N$ by $3N$ matrix problem to a $2N$ by $2N$ one. This can be accomplished in many ways. For example, using Eq. (21) E_z can be expressed in terms of the other two components as

$$E_z = -\varepsilon^{-1} Z^{-1} (XE_x + YE_y) . \tag{22}$$

Using this result in Eqs. (20) yields the standard matrix eigenproblem of the form:

$$\begin{bmatrix} (Y^2+Z^2)\varepsilon^{-1} + XZ\varepsilon^{-1}Z^{-1}X & -XY\varepsilon^{-1} + XZ\varepsilon^{-1}Z^{-1}Y \\ -YX\varepsilon^{-1} + YZ\varepsilon^{-1}Z^{-1}X & (X^2+Z^2)\varepsilon^{-1} + YZ\varepsilon^{-1}Z^{-1}Y \end{bmatrix} \begin{bmatrix} D_x \\ D_y \end{bmatrix} = k_b^2 \begin{bmatrix} D_x \\ D_y \end{bmatrix} , \tag{23}$$

where $D_\alpha = \varepsilon E_\alpha$ for $\alpha = x,y,z$. This equation can be written in many other equivalent forms. In addition, there are numerous other ways to impose the $\nabla \cdot \mathbf{D} = 0$ condition, and we can also interchange the role of the background and the "atom".

We note that matrix in Eq. (23) contains the factor ε^{-1}. However this factor can be obtained, at least in principle, without first computing ε from the equation

$$\varepsilon_{\mathbf{G}'-\mathbf{G}} = \int_{cell} \frac{d\mathbf{r}}{\Omega} e^{-i(\mathbf{G}'-\mathbf{G})\cdot\mathbf{r}} \left\{ 1 - [1 - \varepsilon(\mathbf{r})] \right\} = \delta_{\mathbf{G},\mathbf{G}'} - \left(1 - \frac{\varepsilon_a}{\varepsilon_b} \right) \int_{atom} \frac{d\mathbf{r}}{\Omega} e^{-i(\mathbf{G}'-\mathbf{G})\cdot\mathbf{r}} , \tag{24}$$

and then invert this matrix to find its inverse. This is because

$$\varepsilon^{-1}_{\mathbf{G}'-\mathbf{G}} = \int_{cell} \frac{d\mathbf{r}}{\Omega} e^{-i(\mathbf{G}'-\mathbf{G})\cdot\mathbf{r}} \frac{1}{\varepsilon(\mathbf{r})} = \delta_{\mathbf{G},\mathbf{G}'} - \left(1 - \frac{\varepsilon_b}{\varepsilon_a} \right) \int_{atom} \frac{d\mathbf{r}}{\Omega} e^{-i(\mathbf{G}'-\mathbf{G})\cdot\mathbf{r}} . \tag{25}$$

In reality because we keep only a finite number of PWs, ε and ε^{-1} calculated as shown in Eqs. (24) and (25) do not satisfy the relation $\varepsilon\varepsilon^{-1} = 1$ with sufficient accuracy. Consequently calculations that involve computing this inverse have different convergence rates compared with calculations that do not involve computing this inverse. From our experience we found that much faster convergence can be obtained by using a calculation that involves inverting a matrix containing ε.

Results calculated from Eq. (23) are shown in Fig. (2), which shows the photonic band structure of a fcc lattice of spherical voids. The volume fraction of air is 0.86, which is larger than the close-pack value. Thus the atoms are actually overlapping and we therefore cannot use Eq.(12) to compute the matrix ε. Instead the triple integral for ε in Eq. (8) was first reduced to a single integral, which was then computed numerical using qaussian quadrature. We considered this particular case because it was explored experimentally and seemed to have a common photonic bandgap.[6] Our results in Fig. 2 however do not exactly have a full gap because of the closing up of the bandgap at the U- and W-points. The closing of the bandgap at the U-point (or equivalent the K-point) turned out to be purely accidental. This is confirmed by computing the results for a different volume fraction. An example is shown in Fig. 3, where the volume fraction is 0.96. [14] We see that the bandgap at the U-point now opens up. On the other hand, the closing up of the bandgap at the W-point is due to symmetry, which persists for any volume fraction. However, this degeneracy can be lifted, for example, by suitably distorting the shape of the "atoms".

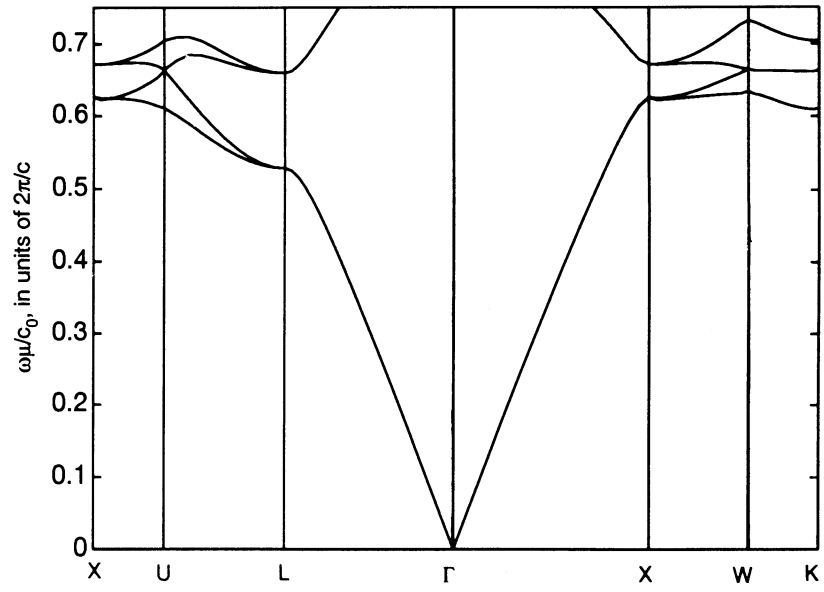

Figure 2. The computed photonic band structure for a 0.86 volume fraction of spherical voids on a fcc lattice embedded in a dielectric material with a refactive index of 3.5. The voids are closer than close-packed, and are overlapping.

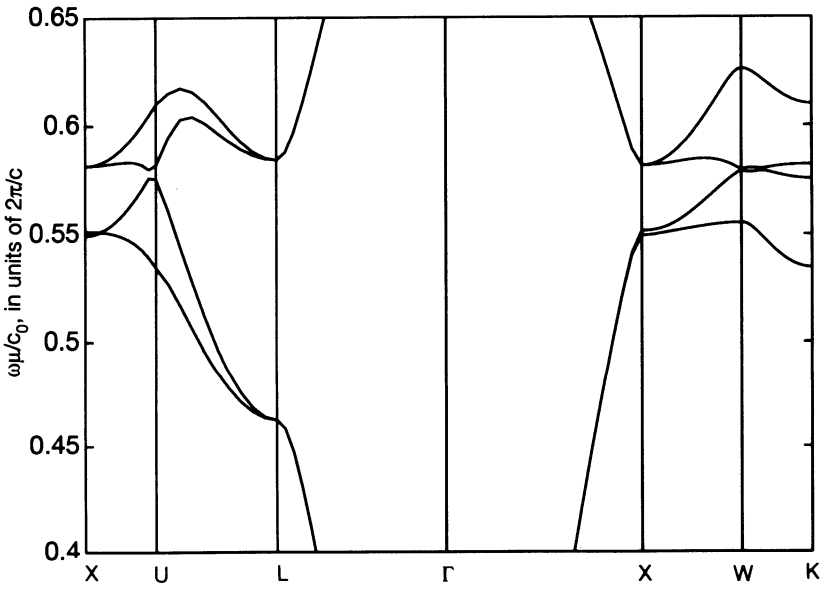

Figure 3. The computed photonic band structure for a 0.96 volume fraction of spherical voids on a fcc lattice embedded in a dielectric material with a refactive index of 3.5.

This was successfully accomplished by going to a structure proposed by Yablonovitch.[4] Details can be found in the article by Yablonovitch in this proceeding. We will only report our result for the attenuation length as a function of the frequency for the Yablonovich structure, which is shown in Fig. 4. We see that the attenuation length goes from zero at the forbidden band edges to about $9.0\,dB/a$ at midgap. This result for the attenuation length is very close to the experimental value. [4] Information on the attenuation length within the bandgap is very useful. For example

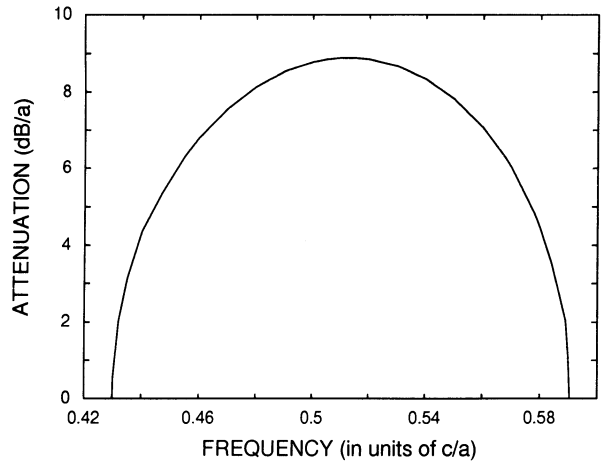

Figure 4. The attenuation length as a function of the frequency for propagation along the L_3 direction in the Yablonovitch structure.

this means that at midgap frequency, a crystal of about 10 unit cells on a side will behave almost like an infinite crystal.

We should also mention an alternate formulation of the PW method for electromagnetic waves by Ho, Chan and Soukoulis.[3] Starting with Maxwell's equations in Eq. (1), if the electric field is eliminated then the following equation for the magnetic field is obtained

$$\nabla\times\frac{1}{\varepsilon(\mathbf{r})}\nabla\times\mathbf{H}(\mathbf{r}) = \frac{\omega^2}{c^2}\mathbf{H}(\mathbf{r})\,. \tag{26}$$

Because $\mathbf{H}(\mathbf{r})$ obeys Bloch's theorem and also the condition $\nabla\cdot\mathbf{H}(\mathbf{r}) = 0$, it can be expanded in the form

$$\mathbf{H}(\mathbf{r}) = \mathbf{H}_n(\mathbf{k},\mathbf{r}) = \sum_{\mathbf{G}}\sum_{\lambda=1}^{2} h_{n,\lambda}(\mathbf{k}+\mathbf{G})\,\hat{e}_\lambda(\mathbf{k}+\mathbf{G})\,e^{i(\mathbf{k}+\mathbf{G})\cdot\mathbf{r}}\,, \tag{27}$$

where $\hat{e}_1(\mathbf{k}+\mathbf{G})$ and $\hat{e}_2(\mathbf{k}+\mathbf{G})$ are polarization unit vectors chosen in order that the three vectors $\hat{e}_1(\mathbf{k}+\mathbf{G})$, $\hat{e}_2(\mathbf{k}+\mathbf{G})$ and $\mathbf{k}+\mathbf{G}$ form a triad. Using this expansion for $\mathbf{H}(\mathbf{r})$, they obtained the following eigenvalue equation:

$$\sum_{\mathbf{G}'} |\,\mathbf{k}+\mathbf{G}\,|\;|\,\mathbf{k}+\mathbf{G}'\,|\,\varepsilon^{-1}_{\mathbf{G},\mathbf{G}'}\begin{pmatrix} \hat{e}_2(\mathbf{k}+\mathbf{G})\cdot\hat{\mathbf{e}}_2(\mathbf{k}+\mathbf{G}') & -\hat{e}_2(\mathbf{k}+\mathbf{G})\cdot\hat{\mathbf{e}}_1(\mathbf{k}+\mathbf{G}') \\ -\hat{e}_1(\mathbf{k}+\mathbf{G})\cdot\hat{\mathbf{e}}_2(\mathbf{k}+\mathbf{G}') & \hat{e}_1(\mathbf{k}+\mathbf{G})\cdot\hat{\mathbf{e}}_1(\mathbf{k}+\mathbf{G}') \end{pmatrix}$$
$$\times\begin{pmatrix} h_{n,1}(\mathbf{k}+\mathbf{G}') \\ h_{n,2}(\mathbf{k}+\mathbf{G}') \end{pmatrix} = \frac{\omega_n^2(\mathbf{k})}{c^2}\begin{pmatrix} h_{n,1}(\mathbf{k}+\mathbf{G}) \\ h_{n,2}(\mathbf{k}+\mathbf{G}) \end{pmatrix}. \tag{28}$$

This form for the matrix eigenproblem is the most convenient, since the matrix involved is naturally real and symmetric, and so this method is often adopted in many PW calculations. However, results obtained by this method are identical to within several significant figures with those based on our method. Thus, we believe the two methods are totally equivalent, although we have not yet been able to find the precise connection between these methods.

THE CASE OF OVAL HOLES

For experiment in the microwave regime, the Yablonovitch structure was made by direct drilling three sets of holes at polar angles $\theta_0 = \cos^{-1}\sqrt{2/3}$ off normal and with azimuthal angles ϕ = 120° apart into the the top surface of a dielectric slab. Besides having a sizable bandgap, this basic structure is also interesting in that it lends itself readily to microfabrication on the scale of optical wavelengths by techniques such as reactive ion etching.[15] However, as a result of the fabrication process, the cylinders will have an oval rather than circular cross-section. If a very thin mask is used in the fabrication process of this structure, then the eccentricity of the oval holes is given by $1/\sqrt{3}$.

We have also computed the photonic bands for this structure with oval holes using the PW method.[16] In our calculation, a fine mesh was set up within the Wigner-Seitz cell to represent the structure in real space. Its Fourier transform was then computed to obtain the dielectric function in reciprocal space. The number of PWs used in our calculation was varied from 113, to 169, 259 and then to 531 to test for convergence. The results reported below were obtained using 169 PWs, which we found to be a suitable compromise between accuracy and the required amount of computational time. The largest change in the lowest several eigenvalues was less than one percent, as compared with the corresponding results obtained using 531 PWs. That only happened for the largest value of refractive index ratio of 5 which we have studied, and for a few **k**-points within the Brillouin zone.

We have computed the photonic bands for a host refractive index n between 1.9 to 5, and for the ratio of the diameter of the holes in the mask to the length of the conventional unit cube, d/a, between 0.30 to 0.58. We found no true bandgap for $n < 2.05$. Due to the lack of suitable non-absorbing optical material whose refractive index is larger than 5, we have not explored the region $n > 5$. For values of d/a above 0.58, the structure becomes more and more fragile as it is getting close to becoming non self-supporting.

In Fig. 5, we show the photonic bands for n = 3.6 and for $d/a = 0.53$, which is the optimal ratio for this refractive index contrast. We have adopted the same labeling of the symmetry points in the Brillouin zone as in the previous work.[4] In Fig. 5b, **k** varies within a mirror plane and the electric field can be classified as either s-polarized (**E** is perpendicular to the mirror plane) or p-polarized (**E** lies within the mirror plane). The s-polarized bands and the p-polarized bands are shown by the solid and dashed lines, respectively. In Fig. 5a, there is no separation into s- and p-polarized bands. These bands of mixed polarizations are shown by solid lines. In both plots, the darker shaded regions denote the absolute bandgap for any polarization. The lighter shaded regions either above or below the absolute gap in Fig. 5a represent forbidden gaps for the s-polarized wave only. The gap size to midgap frequency ratio, Δ, is found to be 21.3%, which is about 12% larger than the optimal value in the case of circular holes for this value of n. The volume filling fraction of air here is 80.5%, which is very close to the corresponding optimal fraction for the case of circular holes. The top of the valence band occurs close to W, and the bottom of the conduction band occurs at L_1. This is exactly the same as that found for circular holes. The overall band structure is also quite similar as compared to that of circular holes. The most

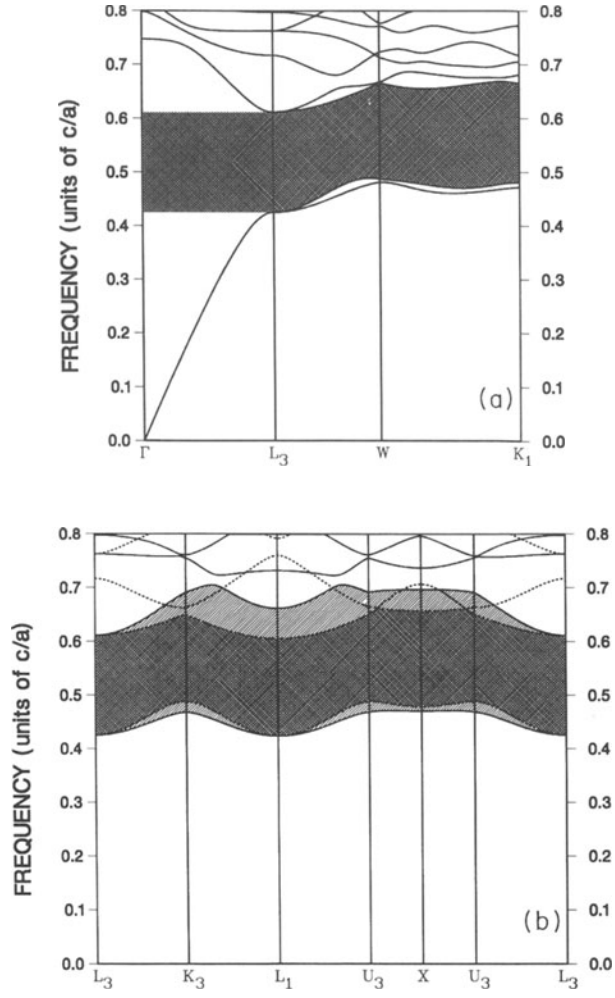

Figure 5. The photonic bands for the Yablonovitch structure with oval holes. The refractive index contrast is 3.6 and the major diameter of the holes is 0.53 in units of the length of the conventional unit cube, a.

noticeable difference is in the ordering of the two valence bands. The s-polarized band is actually lower than the p-polarized band here. However, the frequency at the top of the valence remains almost identical in both cases. It is the bottom of the conduction band situated at L_1 which is pushed slightly upward and this accounts for the 12% improvement in the gap size to mid-gap frequency ratio.

The variation of the gap size to mid-gap frequency ratio as a function of d/a for $n = 3.6$ is shown in Fig. 6. In general, for all the values of n and d/a that we have computed, the top of the valence band occurs either at K_3, or near U_3 or W. In any case we find these eigenvalues are very close to each other. The bottom of the conduction band is located either at L_3 or L_1. Again, the eigenvalues differ only very slightly in either case.

In Fig. 7, we show a contour plot of Δ and the mid-gap frequency as a function of n and d/a. The minimum threshold value of n for the present structure to exhibit a

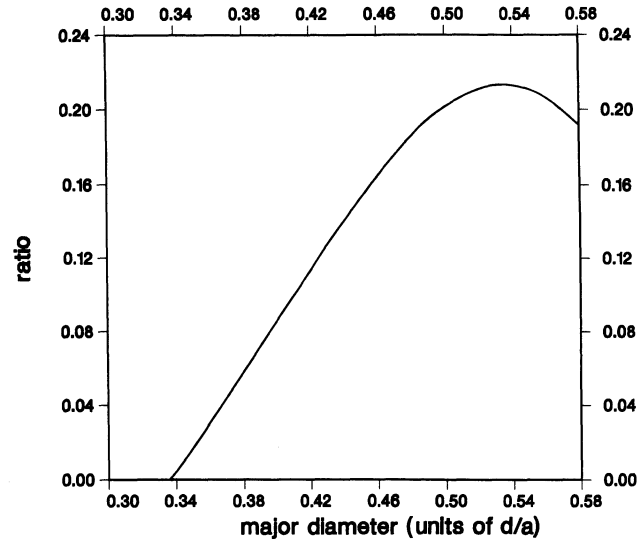

Figure 6. The bandgap size to mid-gap frequency ratio as a function of the major diameter of the oval holes at a refractive index contrast of 3.6.

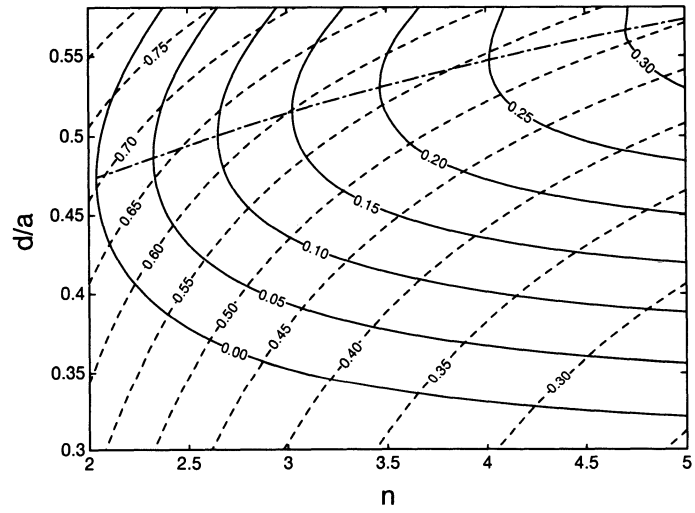

Figure 7. Contour plot showing the gap size to mid-gap frequency ratio and the mid-gap frequency in reduced unit as a function of both the refractive index contrast and the major diameter of the oval holes.

true bandgap is found to be 2.05, and this occurs at an optimal value of d/a of about 0.47. The optimal value of d/a is seen to shift monotonically upward with increasing n, while the optimal value of Δ also increases monotonically. For $n=5$, the optimal values of Δ is about 32.2%, and that occurs when d/a is about 0.58.

The results given above assume an eccentricity of $1/\sqrt{3}$. In the fabrication of the material, by using a thicker mask during the etching process, it is possible to increase the eccentricity of the oval holes to values larger than $1/\sqrt{3}$. It turns out that

it is not profitable to do so because the optimal values for Δ actually decrease with increasing eccentricity.

CONCLUSION

The PW method has now been fully established as a very useful way in computing the band structure in photonic band crystals. Although other methods for calculating photonic band structure will be developed, because of the advantages of the PW method, it will no doubt continue to be used by many theorists in finding newer types of photonic crystals in the future. Already, by employing the supercell method, one can extend the PW method to calculate surface modes as well as defect properties.

ACKNOWLEDGMENTS

The author wishes to thank Prof. Eli Yablonovitch for stimulating discussions and constant encouragements. He is also grateful to Prof. Alex Maradudin for suggesting to him the use of the PW method, and to NATO for sponsoring this very important conference. This work is supported by NSF, under grant No. ECS-9113953, and the Pittsburgh Supercomputing Center.

REFERENCES

1. E. Yablonovitch, Phys. Rev. Lett. **58**, 2059 (1987).
2. S. John, Phys. Rev. Lett. **58**, 2486 (1987).
3. K. M. Ho, C. T. Chan, and C. M. Soukoulis, Phys. Rev. Lett. **65**, 3152 (1990).
4. E. Yablonovitch, T. J. Gmitter, and K. M. Leung, Phys. Rev. Lett. **67**, 2295 (1991); E. Yablonovitch and K. M. Leung, Nature, **351**, 278 (1991).
5. R. D. Meade, K. D. Brommer, A. M. Rappe, and J. D. Joannopoulos, Phys. Rev. B **44**, 10961 (1991); S. L. McCall, P. M. Platzman, R. Dalichaouch, D. Smith, and S. Schultz, Phys. Rev. Lett. **67**, 2017 (1991); E. Yablonovitch, T. J. Gmitter, R. D. Meade, K. D. Brommer, A. M. Rappe, and J. D. Joannopoulos, Phys. Rev. Lett. **67**, 3380 (1991); R. D. Meade, K. D. Brommer, A. M. Rappe, and J. D. Joannopoulos, Phys. Rev. B **44**, 13772 (1991).
6. E. Yablonovitch, and T. J. Gmitter, Phys. Rev. Lett. **63**, 1950 (1989).
7. S. John and R. Rangarajan, Phys. Rev. B, **38**, 10101 (1988).
8. E. N. Economou and A Zdetsis, Phys. Rev. B, **40**, 1334 (1989).
9. K. M. Leung and Y. F. Liu, Phys. Rev. B, **41**, 10188, (1990).
10. S. Satpathy, Z. Zhang, and M. R. Salehpour, Phys. Rev. Lett. **64**, 1239 (1990).
11. K.M. Leung and Y.F. Liu, Phys. Rev. Lett. **65**, 2646 (1990).
12. M. Plihal, A Shambrook, A. A. Maradudin, and P. Sheng, Opt. Commun. **80**, 199 (1991); M. Plihal and A. A. Maradudin, Phys. Rev. B **44**, 8565 (1991).

13. J. Korringa, Physica (Amsterdam) **13**, 392 (1947); W. Kohn and N. Rostoker, Phys. Rev. **94**, 1111 (1954).

14. For a 0.96 volume fraction of air, the structure is not self-supporting. The results were intended to show that the degenaracy at the U-point is purely accidental.

15. A. Scherer, B. P. van der Gaag, E. D. Beebe, and P. S. D. Lin, J. Vac. Sci. Technol. B**8**, 28 (1990).

16. G. X. Qian and K. M. Leung, Phys. Rev. B **44**, 11482 (1991).

PHOTONIC BAND GAPS IN TWO-DIMENSIONAL SQUARE AND TRIANGULAR LATTICES

Pierre R. Villeneuve and Michel Piché

Physics Department
Université Laval
Québec (Québec) G1K 7P4
Canada

ABSTRACT

While three-dimensional lattices can generate complete band gaps between the first and second bands for both orthogonal polarizations p and s, the overlap of the p and s gaps in two-dimensional lattices occurs between low s bands and higher p bands. This leads to significant differences between two- and three-dimensional lattices. Dielectric grids with cylindrical air holes located at the corners of a square or triangle can yield photonic band gaps common to p and s polarizations. The cross-sectional geometry of the cylindrical holes plays a vital role in determining the conditions to open a gap. Dielectric grids with holes of circular cross section located at the corners of a triangle or square require a similar index contrast to generate a band gap. Dielectric grids with holes of square cross section located at the corners of a square require a much larger index contrast to generate a band gap. Any defect in the cross-sectional symmetry of the cylindrical air holes can significantly affect the gap size in a square lattice with square holes, while the consequences are moderate in a triangular lattice with circular holes.

INTRODUCTION

It has been proposed[1,2] that dielectric structures with a periodic index of refraction could give rise to photonic band gaps for which propagation of electromagnetic waves would be forbidden in the structure. Such band gaps could give rise, for example, to fundamental changes of atomic and molecular radiative properties. A search for periodic structures with three-dimensional[3–6] and two-dimensional[7–11] lattices yielding

Photonic Band Gaps and Localization, Edited by
C.M. Soukoulis, Plenum Press, New York, 1993

such band gaps has been carried out. The features of two-dimensional lattices are: (i) the bandgaps for p and s polarizations are not as likely to overlap as in three-dimensional lattices, (ii) the experimental fabrication of three-dimensional lattices at optical wavelengths remains a challenge, and (iii) there are possible applications in thin film optics.

We have performed a systematic study of band gaps in two-dimensional triangular and square lattices. We have studied both cases of high dielectric grids with low dielectric holes and arrays of high dielectric rods in a low dielectric background. In the case of square lattices, we have considered rods with either square or circular cross section; when the cross section of the rods is circular, the rods are just touching when their filling fraction is 79%. This corresponds to the close-packed condition. In the case of triangular lattices, we have considered rods with circular cross section; the close-packed condition is reached when the filling fraction of the rods is 91%.

Our objective is to find a structure yielding the largest band gap for both orthogonal polarizations with the smallest index contrast. Furthermore, we want to study the effects on the gap size from defects in the cross-sectional symmetry of the rods.

THEORY

We start from the complete wave equation for the electric field, and use the plane wave expansion method. By separating the field into two orthogonal polarizations, the problem can be reduced to solving two standard eigenvalue equations. When the electric field is parallel to the rods (p polarization), the wave equation becomes:

$$\sum_{\mathbf{G}'} (\mathbf{k}+\mathbf{G})\cdot(\mathbf{k}+\mathbf{G})\, d_{\mathbf{G}-\mathbf{G}'}\, A_{\mathbf{G}'} - \omega^2 A_{\mathbf{G}} = 0; \tag{1}$$

when the electric field is perpendicular to the rods (s polarization), the wave equation becomes:

$$\sum_{\mathbf{G}'} (\mathbf{k}+\mathbf{G})\cdot(\mathbf{k}+\mathbf{G}')\, d_{\mathbf{G}-\mathbf{G}'}\, A_{\mathbf{G}'} - \omega^2 A_{\mathbf{G}} = 0, \tag{2}$$

where $\mathbf{k}$ is the wave vector and $\mathbf{G}$ is the reciprocal lattice vector. The coefficients $d_{\mathbf{G}-\mathbf{G}'}$ carry all the information about the periodic structure such as the lattice shape, the index contrast and the filling fraction. The wave frequency is normalized with respect to $2\pi c/a$ where a is the length of the unit cell. The dispersion relations for p and s polarizations can be found from Eqs. (1) and (2), respectively. We have solved these equations using standard matrix diagonalization methods. The results that follow were obtained with matrices of dimensions 225×225 and the gap sizes were estimated to be accurate to within 1% for the index contrasts considered in this paper.

SQUARE LATTICE

We first investigate dielectric grids with cylindrical air holes of either square or circular cross section located at the corners of a square. Figure 1(a) shows the dispersion relation for a grid with square holes. While three-dimensional lattices generate complete band gaps from an overlap of the gaps between the first and second bands for both p and s polarizations, band gaps in two-dimensional square lattices occur from an overlap of the gaps between the first and second s bands and third and fourth p bands. The lower p bands are very similar for either square or circular holes, except for a degeneracy of the second and third p bands at the Γ symmetry point in the structure with circular

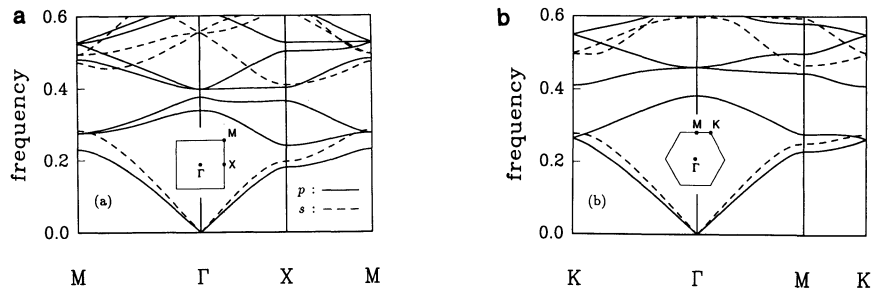

Figure 1. Photonic band structure of (a) a square lattice of air holes with square cross section in a dielectric material of refraction index 4, and (b) a hexagonal lattice of air holes with circular cross section in a dielectric material of index 3.5. The filling fraction of the air holes is 65% in both cases. The insets show the first Brillouin zones. From Ref. 9; reprinted with permission.

holes; both structures yield a p gap across all symmetry points between the first and second bands and third and fourth bands, the larger p gap occurring in the grid with circular holes. In the case of the lower s bands, there is a significant difference in the two structures; the grid with square holes yields an s gap between the first and second bands while the grid with circular holes yields an s gap between the second and third bands (and can also yield a gap between the first and second bands for another set of parameters). The larger s gap occurs in the grid with square holes. The aforementioned observations will play an important role in finding the conditions to generate a band gap since the overlap of p and s gaps will not occur between the same bands in grids with square holes and circular holes.

By changing the index contrast and/or the filling fraction, the p and s gaps can be made to shift and change in size. The largest overlap generated in a square lattice is shown in Fig. 2 as a function of the index contrast. The largest gap is taken over all filling fractions, thus each point corresponds to a different filling fraction. A grid with circular holes requires a significantly lower index contrast to generate a band gap than a grid with square holes. Indeed, the minimum index contrast required for the p and s gaps to overlap is 2.70 in a grid with circular holes and 3.51 in a grid with square holes. Although a grid with circular holes requires a lower index contrast to generate a band gap than a grid with square holes, Fig. 2 shows that the latter gives rise to a larger band gap when the index contrast is greater than 4.3. For example, when the index contrast is 5, the largest gap is 13.8% in a grid with square holes and 11.4% in a grid with circular holes. Furthermore, there seems to exist a maximum gap width that can be generated in a grid with circular holes. The small drop of the gap width at index 5.0 with respect to the value at 4.75 is probably due to an increasing numerical error of the gap width as the index contrast increases.

TRIANGULAR LATTICE

Next, we investigate dielectric grids with cylindrical air holes of circular cross section located at the corners of a regular triangle — see Fig. 1(b). A complete gap occurs between the second and third p bands and first and second s bands. The minimum index contrast required for p and s gaps to overlap is 2.66 when the filling fraction of the air rods is 66%. A triangular lattice can generate a larger gap than a square lattice, even for a smaller index contrast. Since the triangular lattice has a

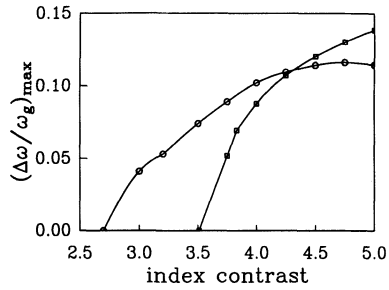

Figure 2. Maximum gap width to midgap frequency ratio in a square lattice as a function of the index contrast. The circles correspond to holes with circular cross section and the squares correspond to holes with square cross section. From Ref. 10; reprinted with permission.

more circlelike Brillouin zone than the square lattice, the gaps should be more likely to overlap across all symmetry points. However, the similarity between the minimum index contrast required to generate a gap in either square (2.70) or triangular (2.66) lattices with circular rods seems to suggest that the shape of the lattice is not the dominant parameter in trying to open a gap common to p and s polarizations in a two dimensionally periodic structure, since p and s bands are not degenerate at the symmetry points. Rather, the shape of the rods seems to play an important role in determining the conditions to open a gap in a square lattice. However, triangular lattices can give rise to significantly larger gaps than square lattices.

ASYMMETRY

Since the bands for p and s polarizations are not degenerate at the symmetry points, the gaps are not likely to overlap. Indeed, when the index contrast is sufficiently large to open the gap between the first and second p bands in a square lattice, the p gap does not overlap the s gap. In the case of a triangular lattice, the degeneracy at the K symmetry point inhibits the gap between the first and second p bands from opening — see Fig. 1(b). This symmetry induced degeneracy can be lifted by introducing an asymmetry in the structure. If the cross section of the cylinders is elliptical and if the ellipses are parallel and still located at the corners of a regular triangle, the degeneracy of the first and second p bands is lifted. We have performed numerous calculations with a wide range of parameters, but we have not been able to generate an overlap of the gaps between the first and second bands for both p and s polarizations in an asymmetric structure with an index contrast lower than 4. In the best of cases, the conduction band edge of p waves and the valence band edge of s waves were equal within our numerical error.

We have performed a systematic study of the effect of asymmetry on the gap size in square lattices with square holes and triangular lattices with circular holes. We have found that a defect in the cross-sectional symmetry of the square holes leads to a significant reduction (and even the disappearance) of the gaps while the gaps in triangular lattices with circular holes undergo small changes. We have defined an asymmetry coefficient α in the square lattice as the ratio of the sides of the rectangular rods, and in the triangular lattice as the ratio of the two semi-axes of the elliptical rods. For both lattices, the largest (over all filling fractions) gap width to midgap ratio is generated in structures with symmetric holes. The gap width to midgap ratio is

shown in Fig. 3 as a function of the filling fraction of the holes for several asymmetric structures. In a square lattice, a small degree of asymmetry gives rise to a significant reduction of the gap width. When the index contrast is 4 and $\alpha = 0.96$, the largest gap is close to 3 times smaller than the largest gap in a symmetric structure; the gap completely disappears when the asymmetry coefficient is less than 0.92. On the other hand, a triangular lattice of asymmetric holes gives rise to large gaps. When the index contrast is 3.5 and $\alpha = 0.70$, the largest gap is only 18% smaller than that of a symmetric structure. Figure 3(b) shows that for some filling fractions, the gap width is larger in an asymmetric structure than in a symmetric structure. As the asymmetry coefficient decreases, the filling fractions of the holes for which a band gap exists decrease. In addition, we have performed numerous calculations to find the structure that would require the lowest index contrast to generate a band gap. We found that for both lattices, an asymmetric structure will require a larger index contrast than a symmetric structure to generate a complete band gap.

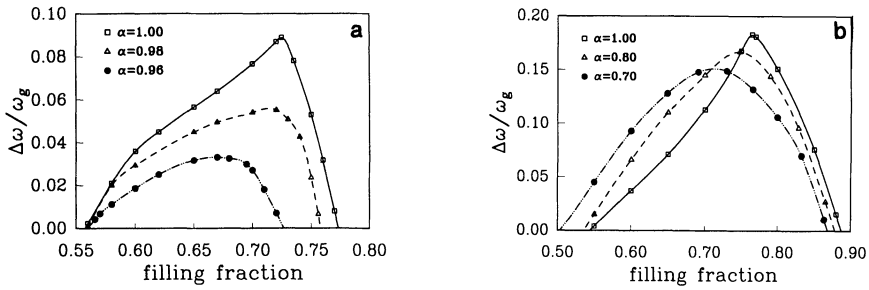

Figure 3. Ratio of the gap width to the midgap frequency as a function of the filling fraction of the air holes in (a) a square lattice of index 4, and (b) a triangular lattice of index 3.5. From Ref. 9; reprinted with permission.

DIELECTRIC RODS

We now investigate arrays of dielectric rods in air. In these structures, the dispersion relations for square and triangular lattices are similar. The arrays can give rise to band gaps for p and s polarizations, but degeneracies of the bands at symmetry points do not allow for a complete gap to open. By introducing asymmetry in the cross-sectional geometry of the rods, the degeneracies can be lifted but we were unable to open a complete gap across all symmetry points.

Since dielectric grids can give rise to complete band gaps while band gaps cannot be opened in arrays of dielectric rods, it seems that the connectedness of the dielectric material in the periodic structure is necessary for the generation of band gaps. However, this is not a sufficient condition, and further, three-dimensional band gaps have been predicted in disconnected three-dimensional periodic structures.[6] One could probably get some insight on the role of the connectedness of the dielectric material by calculating the field in the structure for the modes in the vicinity of the gap. By calculating the field, one could see whether it is located in the dielectric material of high index and if it undergoes a significant change from modes under the gap to modes above the gap.

CONCLUSION

We have shown that periodic arrays of cylindrical air holes with either square or circular cross section located on a square or triangular lattice in a dielectric material of higher index exhibit photonic band gaps common to p and s polarizations. Dielectric grids with holes of circular cross section located at the corners of a triangle or square require a similar index contrast to generate a band gap (2.66 and 2.70, respectively). On the other hand, dielectric grids with holes of square cross section located at the corners of a square require a much larger index contrast of 3.51 to generate a band gap. However, in square lattices, when the index contrast is greater than 4.3, a grid with square holes can give rise to larger gaps than a grid with circular holes.

We have also shown that the choice of lattice is not the only important parameter in trying to open a full gap. Indeed, the cross-sectional geometry of the cylindrical holes plays a vital role in determining the conditions to open a gap. However, the array of cylindrical air holes in a triangular dielectric lattice remains the best overall two-dimensional structure to open the largest gap for the smallest index contrast.

Finally, it is possible, as expected, to lift the degeneracies of p and s bands at symmetry points simply by introducing a defect in the cross-sectional geometry of the holes. These defects can significantly affect the gap size in square lattices with square holes, while the consequences are moderate in triangular lattices with circular holes.

REFERENCES

1. E. Yablonovitch, Phys. Rev. Lett. **58**, 2059 (1987).
2. S. John, Phys. Rev. Lett. **58**, 2486 (1987).
3. E. Yablonovitch, T. J. Gmitter and K. M. Leung, Phys. Rev. Lett. **67**, 2295 (1991).
4. K. M. Leung and Y. F. Liu, Phys. Rev. Lett. **65**, 2646 (1990).
5. Z. Zhang and S. Satpathy, Phys. Rev. Lett. **65**, 2650 (1990).
6. K. M. Ho, C. T. Chan and C. M. Soukoulis, Phys. Rev. Lett. **65**, 3152 (1990).
7. M. Plihal and A. A. Maradudin, Phys. Rev. B **44**, 8565 (1991).
8. S. L. McCall, P. M. Platzman, R. Dalichaouch, D. Smith and S. Schultz, Phys. Rev. Lett. **67**, 2017 (1991).
9. P. R. Villeneuve and M. Piché, Phys. Rev. B **46**, 4969 (1992).
10. P. R. Villeneuve and M. Piché, Phys. Rev. B **46**, 4973 (1992).
11. W. M. Robertson, G. Arjavalingam, R. D. Meade, K. D. Brommer, A. M. Rappe and J. D. Joannopoulos, Phys. Rev. Lett. **68**, 2023 (1992).

PHOTONIC BAND GAPS IN PERIODIC DIELECTRIC STRUCTURES: RELATION TO THE SINGLE-SCATTERER MIE RESONANCES

S. Datta[1], C.T. Chan[1], K.M. Ho[1], C.M. Soukoulis[1], and E.N. Economou[2]

[1] Ames Laboratory and Department of Physics and Astronomy
Iowa State University, Ames, Iowa 50011, USA
[2] Research Center of Crete-FORTH and Department of Physics
University of Crete, 71110 Heraklion, Crete, Greece

INTRODUCTION

A lot of theoretical and experimental work is being done in the area of propagation of classical waves in periodic and disordered structures. The interest in this subject has grown, particularly in the last several years, due to a variety of fundamental and practical reasons. The possibility of the observation[1] of Anderson localization of EM waves in disordered dielectric structures and frequency gaps in periodic structures, in analogy to the electron waves, is of fundamental interest. The very large number of potential practical applications[2] of such photonic band gaps, such as the enhanced performance of semiconductor lasers, has also spurred interest in this topic. Studies have been done using scalar waves[3-7], EM waves[8-10] and elastic waves[11]. The existence of band gaps and localized states have been reported in a variety of cases, particularly in periodic and disordered arrays of spherical scatterers. However, the relative importance of the roles of two differrent mechanisms, single scatterer resonances and macroscopic Bragg-like resonances, in the formation of gaps and localized states is still being debated. The resolution of this question is of interest for the following reason. Most theoretical treatments of the problem involve a lot of complicated calculations. In the plane wave expansion method[7-8] that we have used, a large number of plane waves have to be used to ensure accuracy necessitating the diagonalization of large matrices and the expending of a lot of computational effort. Therefore, it would be extremely helpful to know to what extent a single scatterer in an array maintains its individual identity so that, qualitatively at least, by looking at the simple case of a single scatterer, we can extract some initial information about the whole system with less effort. Also, using that information, it would be possible to formulate the problem in a simpler way, similar to the tight-binding formulation of the electronic problem.

Photonic Band Gaps and Localization, Edited by
C.M. Soukoulis, Plenum Press, New York, 1993

In this paper we have attempted to find out how much the Mie resonances of a single sphere influence the formation of gaps by comparing them with the results that we have obtained[7-8] by studying the propagation of scalar and EM waves in periodic arrays of spheres using the plane wave expansion method.

Apart from our own studies, which show a distinct correspondence between the gaps observed and the Mie resonances of a sphere, several other investigations have also indicated a similar correspondence. Calculations based on the coherent potential approximation (CPA) and the potential-well analogy (PWA) done by Soukoulis et al.[12,13] show that the single sphere Mie resonances persist in strongly influencing the transport properties even for rather high values of the filling ratio, which, for the CPA-PWA approximate results, can reach up to the close-packing limit. Also, Economou and Zdetsis[4] have found that band gaps in periodic dielectric structures can be associated with the Mie resonance frequencies. The corresponding gap disappeared when they omitted a particular partial wave in their augmented plane wave calculation, providing convincing support for the view that the appearance of gaps is due to strong resonant scattering by each sphere. Sheng and Zhang[14] have related the occurrence of localization with the higher Mie resonances.

RESULTS FOR SCALAR AND VECTOR WAVES COMPARED WITH MIE RESONANCES

Using a plane wave expansion method, we made a systematic examination[7-8] of the photonic band structures for dielectric spheres and air spheres for the simple cubic, bcc, fcc, and diamond lattices as a function of the filling ratio and the dielctric constant ratio. In our method, we made use of the periodicity of the dielectric function by expanding it in terms of its Fourier coefficients in the reciprocal lattice vectors. The wave function was also expanded in terms of plane waves following the standard Bloch theorem. This enabled us to cast the wave equation in the form of an eigenvalue equation and reduce the problem to one of diagonalizing a matrix. Our results were obtained with matrix sizes of the order of 750 and the frequencies converged to better than 1%. We have made a systematic examination of the photonic band structure for scalar waves[7] propagating in periodic lattices of dielectric spheres (dielectric constant ϵ_a) in a uniform dielectric background (ϵ_b). All of the lattices studied (simple cubic, bcc, fcc, and diamond) do possess a full band gap. The optimal values of the filling ratio f of the spheres and of the relative dielectric contrast for the existence of a gap are obtained. The minimum value of the relative dielectric constant for creating a gap is also obtained. For vector waves[8], we observed a gap in the lower bands only for the diamond structure. In Fig. 1 (scalar case) and Fig. 2 (vector case), we plot the threshold value of the dielectric constant ratio $\mu = \epsilon_a/\epsilon_b$ needed to first open up a gap as a function of the filling ratio f for all the lattices we have studied. We observe that in all the cases a threshold value of the dielectric constant ratio $\mu = 3$ to 4 is necessary to open up a gap. In particular, comparing the diamond lattice case where we have results for both the scalar case (Fig. 1d) and the vector case (Fig. 2, solid curve), we notice that the threshold value of μ is roughly the same, i.e., equal to 4, for the two cases. The only difference is that the optimum value of f, $f_{opt} \simeq 0.15$ for the first gap of the scalar case, while $f_{opt} \simeq 0.35$ for the first gap of the vector case. But this is expected, since for the vector case there are no s waves ($l = 0$, where l is the magnitude of the angular momentum) and therefore one has to compare the second gap of the scalar

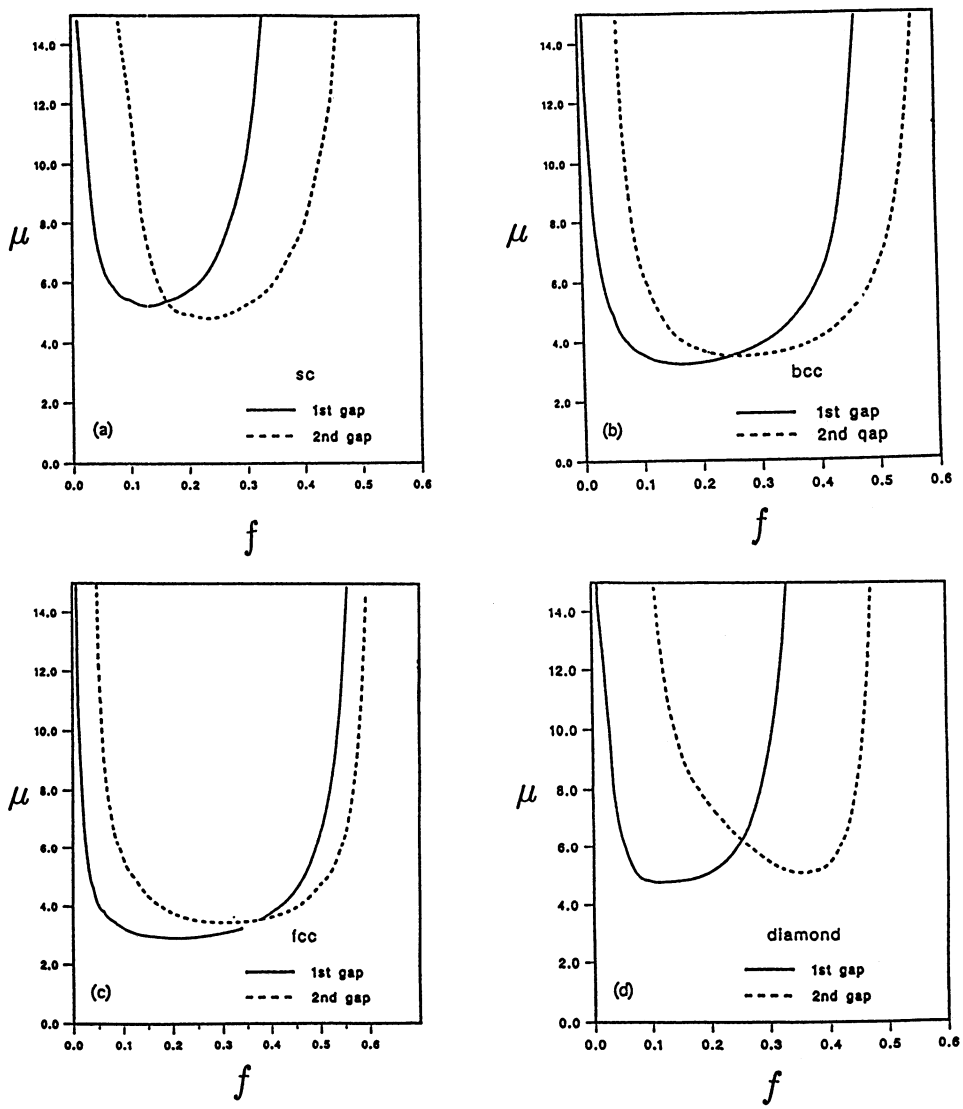

Figure 1. The threshold value of the dielectric constant ratio $\mu = \epsilon_a/\epsilon_b$. The point at which the band gap just opens up, for the scalar case is plotted as a function of the filling ratio f for the (a) sc, (b) bcc, (c) fcc, and (d) diamond lattices composed of dielectric spheres in air background.

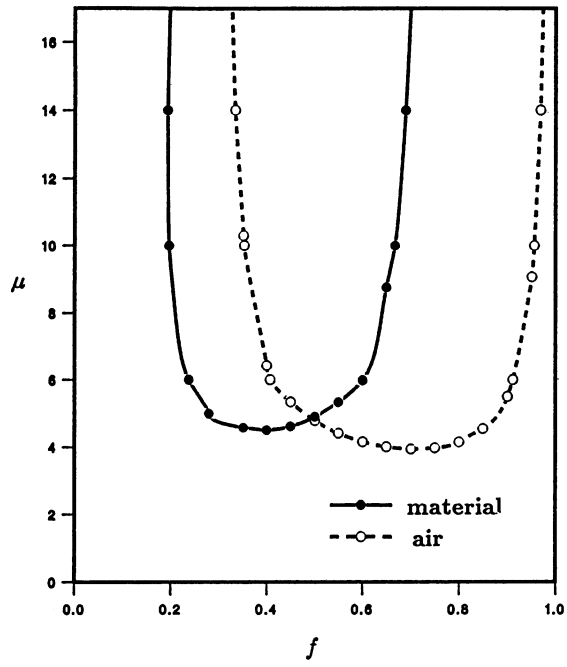

Figure 2. The threshold value of the dielectric constant ratio $\mu = \epsilon_a/\epsilon_b$. The point at which a band gap just opens up, for the vector case, is plotted as a function of the filling ratio f for the diamond lattice composed of dielectric spheres in air background and also air spheres in dielectric background.

case (p waves) with the first gap of the vector case (again a p wave). Indeed, then $f_{opt} \simeq 0.35$, for both the second gap of the scalar wave and the first gap of the vector wave of the diamond lattice. Can the behavior of the band gaps be interpreted by the Mie resonant scattering from a single sphere? For a single sphere of dielectric constant ϵ_a in a dielectric background ϵ_b, there are an infinite number of resonance frequencies ω. In all of our numerical studies we have set $\epsilon_b = 1$. If ϵ_a is much larger than ϵ_b, very strong resonances appear in the total scattering cross-section roughly when

$$\frac{d}{\lambda_a} = \frac{n+1}{2} \quad , \tag{1}$$

where λ_a, the wavelength inside the sphere, is related with the frequency ω by $\lambda_a = 2\pi c/\omega\sqrt{\epsilon_a}$, d is the diameter of the sphere, $n = 0, 1, 2, 3, \cdots$ for the scalar case, and $n = 1, 2, 3, \cdots$ for the vector case. In Fig. 3 we plot the total scattering cross-section for scalar waves from a single sphere of dielectric constant ϵ_a versus d/λ_a, for different values of ϵ_a. Notice that for large dielectric constants, $\epsilon_a = 50$ and 13, the total scattering cross-section shows strong peaks when $d/\lambda_a = (n+1)/2$. However, as ϵ_a is decreased, one starts losing the strong resonances and by the time $\epsilon_a \simeq 3$, the resonances are no longer distinct. Therefore, no band gap will be created if one has a lattice of dielectric spheres with this low value of ϵ_a. Similar behavior for the total scattering cross-section is obtained for the vector case too (see Fig. 4). Again, we note that the resonances become distinct only at dielectric constant ratios greater than 3. We can, therefore, say that there is a qualitative agreement in the threshold value of the dielectric constant ratio in the two cases. Here, it is necessary to mention that we are only comparing the results for the material spheres and not the air spheres with the Mie theory, since only in the case of material spheres are the scatterers spherical. For air spheres in a dielectric

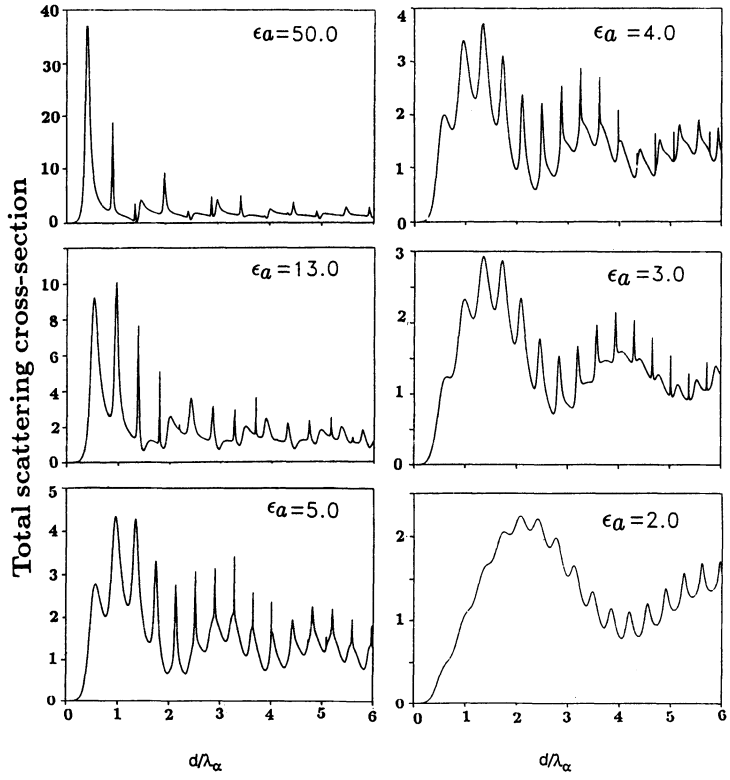

Figure 3. Total scattering cross-section of an isolated sphere versus d/λ_a for scalar waves for different values of the dielectric constant ϵ_a (d is the diameter of the sphere and $\lambda_a = 2\pi c/\omega\sqrt{\epsilon_a}$ is the wavelength inside the sphere).

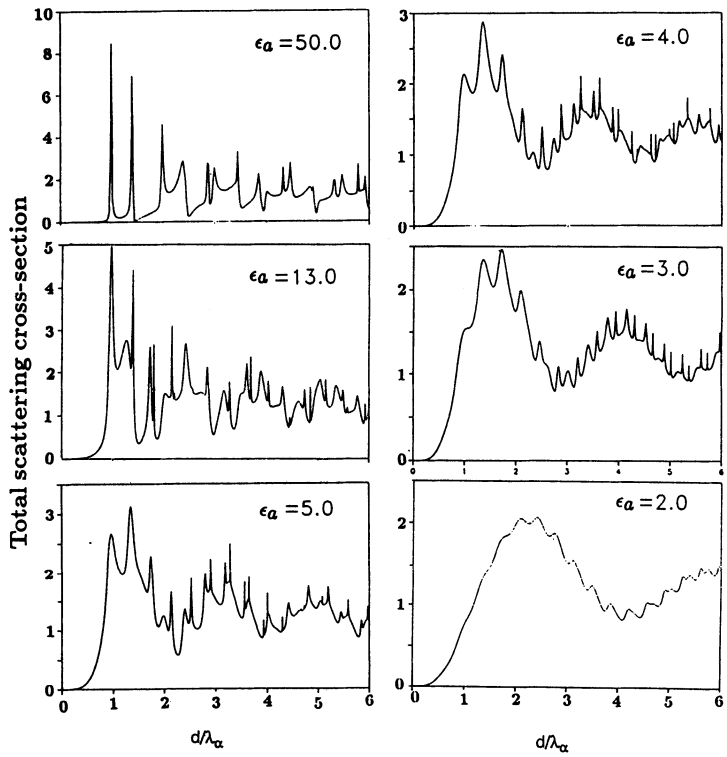

Figure 4. Total scattering cross-section of an isolated sphere versus d/λ_a for vector waves for different values of the dielectric constant ϵ_a (d is the diameter of the sphere and $\lambda_a = 2\pi c/\omega\sqrt{\epsilon_a}$ is the wavelength inside the sphere).

medium the low velocity and high dielectric constant scatterers have a complicated geometry and therefore, Mie theory for a sphere will not be applicable.

Apart from the threshold values of the dielectric contrast, we have also compared the frequencies at which the gaps are found with the resonance frequencies of a single scatterer (see Fig. 5 for the scalar case and Fig. 6 for the vector case). This comparison is more revealing for the scalar case (Fig. 5) where indeed there is a strong correlation between the resonance frequencies of a single scatterer and the frequencies at which gaps appear. In Fig. 5, we plot the midgap frequency for the first two gaps versus the filling ratio f for all the lattices we have examined. We have presented the midgap frequency as d/λ_a, where d is the diameter of the sphere and $\lambda_a = 2\pi c/\omega\sqrt{\epsilon_a}$ is the wavelength inside the sphere. The first few Mie resonances in these units are

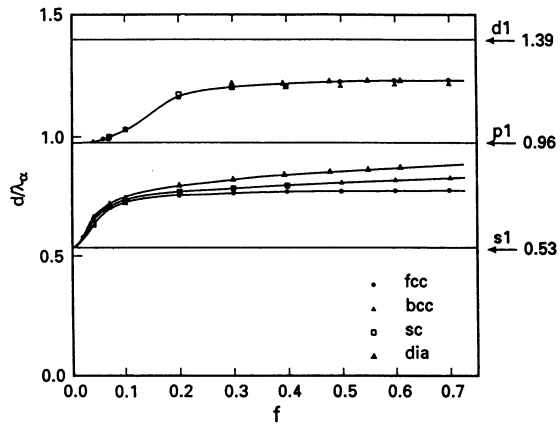

Figure 5. The midgap frequency, for scalar waves, of the first two gaps versus the filling ratio f for the sc, bcc, fcc, and diamond lattices composed of dielectric spheres of $\epsilon_a = 13$ in air background.

given by $d/\lambda_a = 0.53$, 0.96 and 1.39 for the case of $\epsilon_a = 13$ and $\epsilon_b = 1$. We find that at low filling ratios, the frequencies at which gaps are found are close to the values of d/λ_a for which Mie resonances appear. For a low concentration of scatterers f, the propagation of the waves takes place through the background material ($\epsilon_b = 1$) and the isolated scatterers obstruct the propagation; thus, the position of the Mie resonance (strong scattering) is expected to almost coincide with the gap (or would be gap). As the filling ratio increases, we may expect the resonances to mix and broaden into bands and we find (Fig. 5) that the gaps tend to be located in between the resonances. This behavior can be understood from the following argument. For a high concentration of scatterers, the propagation of waves is taking place by hopping from scatterer to scatterer through the overlap of the local resonance states (the analog of a band made up from a linear combination of atomic orbitals in the electronic case). Therefore, for high f, it is expected that the positions of the resonances would approximately coincide with the center of the bands. Thus, in the scalar case, the correspondence between the

gaps and the resonances is quite clear. Such a clear correspondence does not emerge in the vector case as is evident from Fig. 6. For the vector case, since the resonances are close to each other (see Fig. 4 for the case of $\epsilon_a = 13$), a hybridization is expected and there will be no simple *a priori* relation between the position of the resonances and the midgaps (or midbands).

CONCLUSION

We compared our band structure results for the propagation of scalar and EM waves in various cubic periodic arrangements of spheres with the information available from the total scattering cross-section of a single sphere. We found that the appearance and location of the resonances of a single sphere can throw some light on the threshold

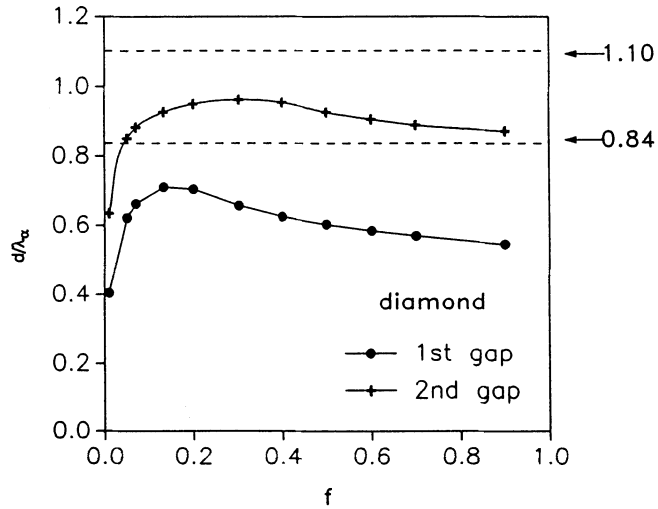

Figure 6. The midgap frequency, for vector waves, of the first two gaps versus the filling ratio f for the diamond lattice composed of dielectric spheres of $\epsilon_a = 13$ in an air background.

dielectric contrast and the position of the gaps in a periodic array. It is surprising that the positions of the bands in periodic dielectric structures are in any way related to the positions of the isolated Mie resonances as our results indicate. One possible reason for the dominant role played by Mie resonances in determining the band gaps may be that the scatterers we have considered are spherical and as opposed, e.g., to cubic scatterers, cannot form new well connected shapes by clustering together. The Mie resonances of an isolated scatterer can be said to play the role of the energy levels of an isolated atom in a crystal. By carrying this analogy further, we may be able to understand more clearly exactly how the Mie resonances influence the formation of gaps and also explain the differences between the scalar and EM cases.

ACKNOWLEDGMENTS

Ames Laboratory is operated for the USDOE by Iowa State University under contract # W-7405-Eng-82. This work is supported by the Director for Energy Research, Office of Basic Energy Sciences including a grant of computer time on the Cray computer at the Lawrence Livermore Laboratory, NATO Grant No. RV911010 and NSF Grant No. INT-9117356.

REFERENCES

[1] S. John, *Phys. Rev. Lett.* **58**, 2486 (1987); S. John, *Comments Cond. Mat. Phys.* **14**, 193 (1988); S. John, *Phys. Today* **32**, 33 (1991).
[2] E. Yablonovitch, *Phys. Rev. Lett.* **58**, 2059 (1987); Review article in this volume.
[3] S. John and R. Rangarajan, *Phys. Rev. B* **38**, 10101 (1988).
[4] E.N. Economou and A.D. Zdetsis, *Phys. Rev. B* **40**, 1334 (1989).
[5] K.M. Leung and Y.F. Liu, *Phys. Rev. B* **41**, 10188 (1990).
[6] S. Sathpathy, Z. Zhang and M.R. Salehpour, *Phys. Rev. Lett.* **64**, 1239 (1990).
[7] S. Datta, C.T. Chan, K.M. Ho, and C.M. Soukoulis, *Phys. Rev. B* **46**, 10650 (1992).
[8] K.M. Ho, C.T. Chan, and C.M. Soukoulis, *Phys. Rev. Lett.* **65**, 3152 (1990); *Europhys Lett.* **16**, 563 (1991).
[9] K.M. Leung and Y.F. Liu, *Phys. Rev. Lett.* **65**, 2646 (1990).
[10] Z. Zhang and S. Sathpathy, *Phys. Rev. Lett.* **65**, 2650 (1990).
[11] M. Sigalas and E.N. Economou, *Journal of Sound Vibr.* **158**, 377 (1992).
[12] C.M. Soukoulis, E.N. Economou, G.S. Grest, and M.H. Cohen, *Phys. Rev. Lett.* **62**, 575 (1989).
[13] E.N. Economou and C.M. Soukoulis, *Phys. Rev. B* **40**, 7977 (1989).
[14] P. Sheng and Z.Q. Zhang, *Phys. Rev. Lett.* **57** 1879 (1986).
[15] M. Kerker, *The Scattering of Light and Other Electromagnetic Radiation*, Academic Press (New York and London, 1969).

PERIODIC DIELECTRIC STRUCTURES: THE LONG WAVELENGTH EFFECTIVE DIELECTRIC CONSTANT

C.T. Chan, S. Datta, K.M. Ho, and C.M. Soukoulis

Ames Laboratory and Department of Physics and Astronomy
Iowa State University, Ames, Iowa 50011

INTRODUCTION

The study of the electromagnetic properties of heterogeneous media is an old but still very active subject. Initially, various effective medium approaches [1] like the Maxwell-Garnet approximation were used to determine the dielectric constant and other properties in the long wavelength limit. It was later realized that these were inadequate and the microgeometry of the medium needs to be taken into account even though it is on a much smaller scale than the probing wavelength. Several such studies were made by McPhedran and McKenzie [2] and others for periodic systems using the boundary-matching approach. The efficacy of this approach is limited to special shapes like spheres and cubes which do not overlap. In recent years, several [3-5] groups have used Fourier expansion techniques which can be used to study any periodic microgeometry and are much wider in scope than the previous efforts. We have also used a Fourier expansion technique to study this problem and our method will be applied to find the effective dielectric constant of several classes of "photonic band gap" (PBG) materials. The PBG materials are basically periodic arrangements of one type of material embedded in another. It is interesting to note that besides the possibility of possessing photonic gaps, some of these materials are also anisotropic and thus will exhibit birefringence.

THE LONG WAVELENGTH LIMIT

For the class of PBG materials we are interested in, the most straightforward approach to study the electromagnetic (EM) spectrum is to operate in the Fourier space, where the periodic boundary condition can be put in trivially by imposing Bloch's theorem. There is no restriction on the shape of the structural units as long as they

Photonic Band Gaps and Localization, Edited by
C.M. Soukoulis, Plenum Press, New York, 1993

are in a periodic formation. We solve the wave equation by expanding the dielectric constant in plane waves of the form $\exp(i\vec{G}.\vec{r})$ where the $\vec{G}$'s are the reciprocal lattice vectors as determined by the periodicity of the system. This transforms the Maxwell equations into a matrix equation which, upon diagonalization, gives the frequency and the eigenvectors of the EM wave eigen-modes. This has recently been, with slight variations, the favorite approach of many authors[6-11]. The same approach can also be used to find the long wavelength limit of the EM dispersion curves and thus determine the effective dielectric constant of periodic composite materials. One obvious way is simply to use finite differences, where the effective dielectric constant can be deduced from the slope of the EM wave dispersion curves as $|k| \to 0$. What we are presenting here is an alternate approach in which we deduce the effective dielectric constant via second order perturbation theory, which leads us to the expression:

$$\tilde{\epsilon}_{k\to 0} = \left[\begin{pmatrix} \epsilon_{TT}^{xx} & \epsilon_{TT}^{xy} \\ \epsilon_{TT}^{yx} & \epsilon_{TT}^{yy} \end{pmatrix} - \begin{pmatrix} \epsilon_{TL}^{x}\epsilon_{LL}^{-1}\epsilon_{LT}^{x} & \epsilon_{TL}^{x}\epsilon_{LL}^{-1}\epsilon_{LT}^{y} \\ \epsilon_{TL}^{y}\epsilon_{LL}^{-1}\epsilon_{LT}^{x} & \epsilon_{TL}^{y}\epsilon_{LL}^{-1}\epsilon_{LT}^{y} \end{pmatrix} \right]_{\vec{G}=0,\vec{G}'=0} \tag{1}$$

where $(\epsilon_{TT}^{\alpha\beta})_{kk'} = \epsilon_{kk'}\hat{\alpha}_k.\hat{\beta}_{k'}$, $(\epsilon_{LL})_{kk'} = \epsilon_{kk'}(\hat{k}.\hat{k}')$, $(\epsilon_{TL}^{x})_{kk'} = (\epsilon_{kk'})(\hat{x}_k.\hat{k}')$ and $(\hat{\alpha}_k, \hat{\beta}_k, \hat{k})$ form an orthogonal triad.

$\epsilon_{kk'}$ is the Fourier transform of the dielectric function. The first term at $\vec{G} = 0$ and $\vec{G}' = 0$ becomes

$$\begin{pmatrix} \epsilon_{TT}^{xx} & \epsilon_{TT}^{xy} \\ \epsilon_{TT}^{yx} & \epsilon_{TT}^{yy} \end{pmatrix} = \begin{pmatrix} \langle\epsilon\rangle & 0 \\ 0 & \langle\epsilon\rangle \end{pmatrix} \tag{2}$$

where

$$\langle\epsilon\rangle = (1-f)\epsilon_1 + f\epsilon_2 = \epsilon_1[1 + (\Delta\epsilon/\epsilon_1)f] \tag{3}$$

which is the scalar wave result for a periodic array of material of dielectric constant ϵ_2 embedded in material of dielectric constant ϵ_1 with a filling ratio f. The diagonalization of the second term gives the correction to the scalar wave result.

For a cubic crystal, Eq. (1) reduces to

$$\tilde{\epsilon}_{\infty} = \begin{pmatrix} \langle\epsilon\rangle & 0 \\ 0 & \langle\epsilon\rangle \end{pmatrix} + \begin{pmatrix} \alpha & 0 \\ 0 & \alpha \end{pmatrix} \tag{4}$$

where $\alpha = \epsilon_{TL}^{x}\epsilon_{LL}^{-1}\epsilon_{LT}^{x}$; $\hat{x}$ is any axis.

NUMERICAL RESULTS

Using the above method, we have calculated the effective dielectric constant in the long wavelength limit for a few prototypical PBG materials, including structures that have spheres arrayed in face-centered cubic, simple cubic, and diamond structures. We considered the case with material spheres embedded in air and the conjugate configuration of air spheres embedded in materials of high refractive index. Different filling ratios are considered. The dielectric contrast is set at 13, which is roughly that of Si in air at optical wavelengths. The results for the material spheres are compared (Fig. 1) with the scalar wave results (which ignore the vector nature of light) and the Maxwell-Garnet theory (basically a Clausius-Mosotti relation), which is given by

$$\epsilon = \epsilon_1 \left(\frac{2\epsilon_1 + \epsilon_2 + 2f(\epsilon_2 - \epsilon_1)}{2\epsilon_1 + \epsilon_2 - f(\epsilon_2 - \epsilon_1)} \right) \quad . \tag{5}$$

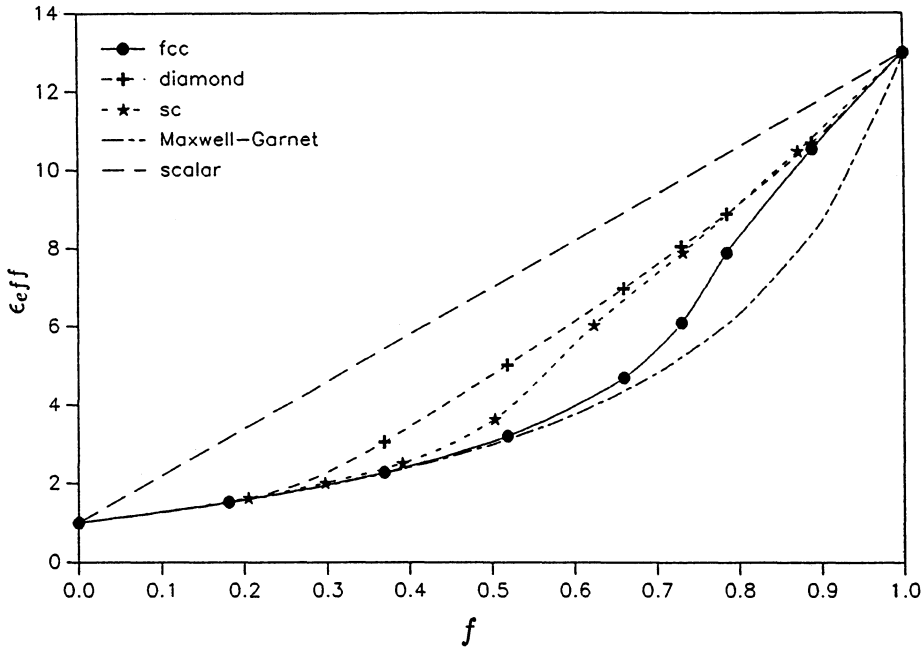

Figure 1. The effective dielectric constant ϵ_{eff} for the fcc, sc, and diamond structures composed of material spheres (dielectric constant $\epsilon = 13$) in air background as a function of the filling ratio f compared with the scalar and Maxwell-Garnet results.

We observe that the effective dielectric constant is smaller than the scalar wave result in all cases and also that it is different for different structures. For the scalar wave result, the effective dielectric constant is independent of the microstructure of the media, and is determined entirely by the average dielectric constant of the media. What this means is the scalar wave provides no information whatever about the structure in the long wavelength limit. However, the vector nature of the EM waves allows some sensitivity to the microstructure of the media, even as $|k| \to 0$, so that for the same filling ratio, the effective dielectric constant changes with the structure factor of the material under consideration. We note that the term α in Eq. (4) can be written such that it is a series expansion in $\Delta\epsilon/\epsilon_1$. Then

$$\tilde{\epsilon}_{k\to 0} = \epsilon_1[1 + (\Delta\epsilon/\epsilon_1)f - (\Delta\epsilon/\epsilon_1)^2 \sum_{\vec{G}} \mathcal{S}^2(\vec{G})(\hat{x}.\vec{G})^2 + \cdots] \tag{6}$$

where $\mathcal{S}(\vec{G}) = \frac{1}{\Omega}\sum_{\vec{r}} \exp(i\vec{G}.\vec{r}) f(\vec{G})$ is the structure factor. We note that the term up to $\Delta\epsilon/\epsilon_1$ is precisely the scalar wave result. The leading $(\Delta\epsilon/\epsilon_1)^2$ correction term to the scalar result is negative definite, so it is quite natural that all the effective dielectric constants are smaller than the scalar wave results. The structure factor and the vector nature of EM waves enter at this order.

The optical properties of crystals in nature can be classified into three groups: isotropic, uniaxial, and biaxial, depending on the symmetry of the crystal. As far as optical properties are concerned, the PBG materials can be viewed as man-made crystals. Cubic PBG systems, like the fcc, sc, and diamond structures we have considered,

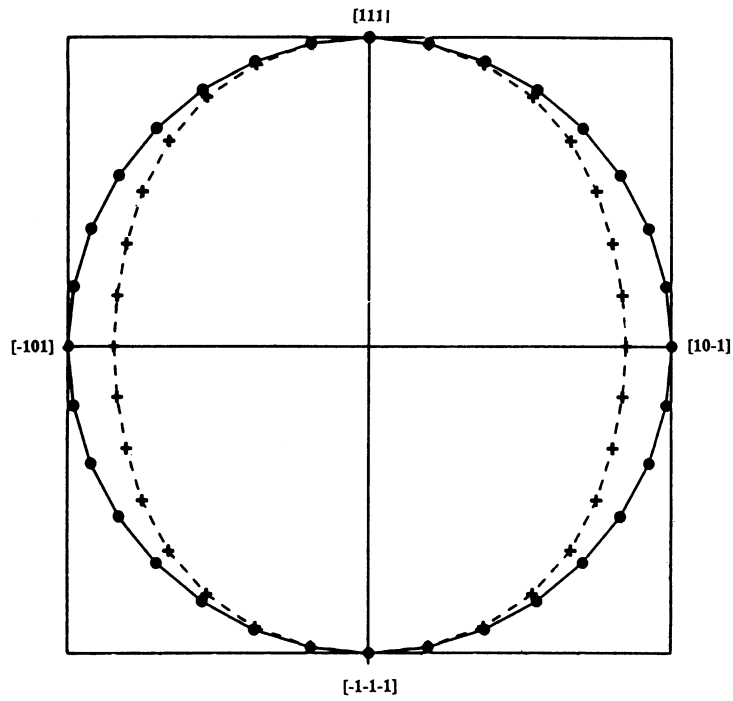

Figure 2. The effective velocities $1/\sqrt{\epsilon_1}$ and $1/\sqrt{\epsilon_2}$ for material cylinders (dielectric constant ratio $\epsilon = 13$) in the "3-cylinder" structure as a function of the propagation direction in the [111] – [10$\bar{1}$] plane.

are isotropic. There is only one effective dielectric constant (the index ellipsoid is a sphere) and the effective wave velocities in all directions are the same.

The "3-cylinder" structure [12,13] that has been fabricated by Bell-Core is anisotropic and has the preferred axis in the [111] direction. (The structure is fabricated by drilling three cylinders through each hole of a triangular array at an angle of 35.26 degrees away from the normal and spread out 120 degrees on the azimuth.)

In Fig. 2 we have plotted $1/\sqrt{\epsilon_1}$ and $1/\sqrt{\epsilon_2}$, i.e., the effective velocities, as a function of propagation direction in the [111] – [10$\bar{1}$] plane for material cylinders in the "3-cylinder" structure with a dielectric constant ratio of 13.0 and a filling ratio of 0.32. We find that the two velocities coincide in the [111] direction and that the anisotropy is maximum in a direction perpendicular to it. The structure behaves like a uniaxial crystal. An interesting aspect of PBG materials is that the anisotropy in the refractive index of natural crystals is dictated by nature and is usually small, while that of PBG materials can be engineered to a certain extent by man as far as technological capabilities permit. The maximum anisotropy in the refractive index $\sqrt{\epsilon}$ of a " 3-cylinder" structure is plotted as a function of the filling ratio (Fig. 3) for a fairly modest dielectric constant ratio of 7 for both material and air cylinders and we see that quite a large anisotropy can arise by optimizing the structure. We have considered both "material" cylinders and "air" cylinders in the "3-cylinder" structure. The commonly practiced fabrication processes involve drilling or etching and thus give "air" cylinder configurations.

CONCLUSIONS

We have calculated the long wavelength effective dielectric constants of a few PBG composite materials using a Fourier space technique. The method can be applied to any structure as long as it is periodic and the dielectric constant is not too high (otherwise the number of plane waves required would be prohibitive). The latter is not a serious problem in the optical frequency regime, since the dielectric constant is rarely a large number.

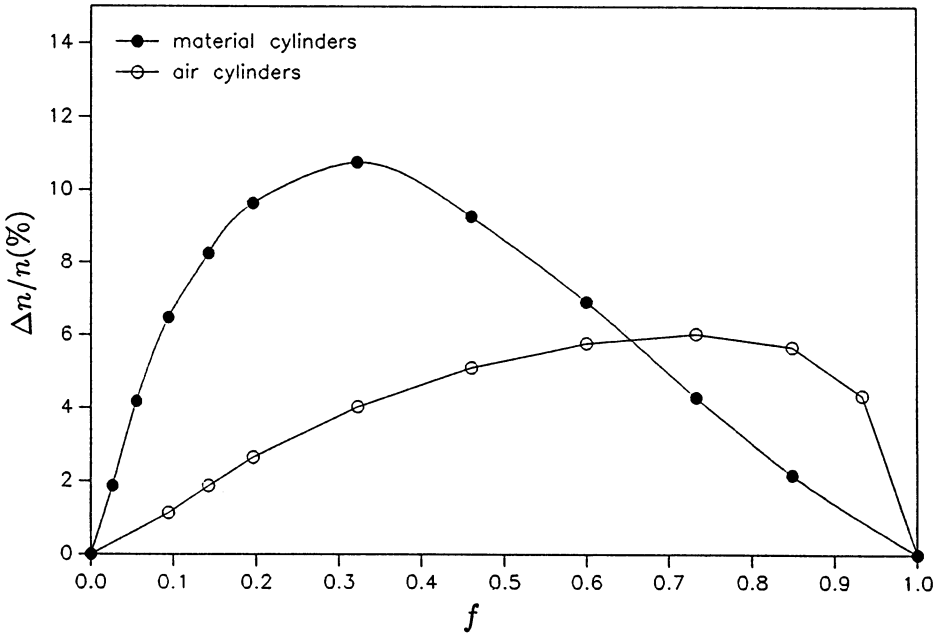

Figure 3. The maximum anisotropy $\Delta n/n$ in the effective refractive index $n = \sqrt{\epsilon}$ of a "3-cylinder" structure plotted as a function of the filling ratio f for both material and air cylinders for material of dielectric constant $\epsilon = 7$.

ACKNOWLEDGMENTS

Ames Laboratory is operated for the U.S. Department of Energy by Iowa State University under contract No. W-7405-ENG-82. This work is supported by the Director of Energy Research, Office of Basic Energy Sciences, including a grant for computer time on the Cray computers at NERSC at the Lawrence Livermore Laboratory.

REFERENCES

[1] W. Lamb, D.M. Wood, and N.W. Ashcroft, *Phys. Rev. B* **21**, 2248 (1980).
[2] R.C. McPhedran and D.R. McKenzie, *Proc. R. Soc. London Ser. A* **359**, 45 (1978).
[3] R. Tao, Z. Chen, and P. Sheng, *Phys. Rev. B* **41**, 2417 (1990).
[4] L.C. Shen, C. Liu, J. Korringa, and K.J. Dunn, *J. Appl. Phys.* **67**, 7071 (1990).
[5] D.J. Bergman and K.J. Dunn, *Phys. Rev. B* **45**, 13262 (1992).
[6] S. Satpathy, Z. Zhang, and M.R. Salehpour, *Phys. Rev. Lett.* **64**, 1239(1990).
[7] K.M. Leung and Y.F. Liu, *Phys. Rev. B* **41**, 10188 (1990).
[8] K.M. Ho, C.T. Chan, and C.M. Soukoulis, *Phys. Rev. Lett.* **65**, 3152 (1990).
[9] M. Plihal, A. Shambrook, A.A. Maradudin, and P. Sheng, *Opt. Commun.* **80**, 199 (1991).
[10] R.D. Meade, K.D. Brommer, A.M. Rappe, and J.D. Joannopoulos, *Phys. Rev. B* **44**, 10961 (1991).
[11] H.S. Sözuer, J.W. Haus and R. Inguva, *Phys. Rev. B* **45**, 13962 (1992).
[12] E. Yablonovitch, T. Gmitter, and K.M. Leung, *Phys. Rev. Lett.* **67**, 2295 (1991).
[13] C.T. Chan, K.M. Ho and C.M. Soukoulis, *Europhys. Lett.* **16**, 563 (1991).

MEASUREMENTS OF LOCALIZATION AND PHOTONIC BAND GAP SYSTEMS IN TWO-DIMENSIONS

S. Schultz and D. R. Smith

Department of Physics
University of California, San Diego
9500 Gilman Drive
La Jolla, California 92093-0319

ABSTRACT

We report the results of experimental investigations of two dimensional periodic and random scattering systems. The systems consist of arrays of dielectric cylindrical scatterers bounded on top and bottom by conducting sheets. We present the results of measurements made on defect modes created by removing part or all of a scatterer from an otherwise perfect lattice. We also present a series of measurements made on localized modes created by randomly removing an increasing number of scatterers. Discussion of applications for photonic band gap structures is included.

INTRODUCTION

The basic properties of waves, whether representing a classical or quantum mechanical system, explicitly give rise to the possibility of exhibiting the phenomenon of strong localization (SL). These properties are elastic scattering, superposition, and interference. The phenomenon of SL occurs when waves traveling in a strongly scattering medium interfere in such a way as to produce a bound mode centered at some location in the medium. This localized mode is generally characterized by a rapid (usually exponential) fall off of the energy density in all directions away from the central point. Whether SL occurs or not for a given situation depends on the strength and configuration of the scattering potential, and critically depends on the dimension of the system. The lower the dimension of the system, the easier it is to achieve localization. In this work, we focus on structures which are effectively two-dimensional.

One approach to understanding SL as it occurs in more complicated situations is to begin with the simplest system available which exhibits the essential properties. When the elastic scatterers are arranged in a periodic lattice, it becomes much easier to understand the behavior of the system, because we have the history of experience for solutions of many examples of wave propagation in a periodic lattice; ranging from Bragg scattering for x-rays,

Photonic Band Gaps and Localization, Edited by
C.M. Soukoulis, Plenum Press, New York, 1993

to the detailed electronic band structure of solids. If we neglect the complications of many body effects due to particle-particle interactions, any quantum mechanical particle or classical wave system can be represented in terms of its appropriate wave equation, and the full power of the well-developed band structure formalism may be utilized to determine the dispersion relations, i.e., the frequency k-vector relationship as a function of all parameters. When the wave system consists of electomagnetic waves, Maxwell's equations of course describe the system, and the full set of dispersion relations have been termed "photonic band structure".[1,2] It should be clear that as this term is generally used, there is nothing specifically photon-related to the subject. Using "photonic" reflects a growing usage whenever systems or devices are examined in the range of optical frequencies, and has become the accepted terminology for electromagnetic band structure systems. We also adopt this language, even when our work is in the microwave region of the spectrum, since the conceptual results are directly scalable to optical frequencies.

When one examines the bandstructure for an infinite system composed of periodically placed potential scatterers, one finds bands of frequencies corresponding to normalizable propagating modes, as well as regions of frequencies where no propagating modes exist, i.e., band gaps. If it happens that the band structure for a system has a continuous band of frequencies for which there is no propagating mode in any direction, the system is said to have a Photonic Band Gap (PBG). If one breaks the translational symmetry of the lattice by either terminating the system or introducing a local perturbation, then modes with frequencies in the band gap do occur, corresponding to eigenfunctions which grow or decay exponentially. If we create a defect in the lattice by, for example, altering the strength or shape of just one of the sites, then we introduce the possiblity of a mode occurring in the band gap region with a wavefunction which decays exponentially away in all directions from the defect site. This is a defect mode, and is the simplest example of SL.

The term localization, however, as it is generally used applies to systems where the scattering potential strengths and/or positions are distributed randomly throughout the medium. Because of the difficulty in analyzing random scattering systems analytically or numerically, it is difficult to determine (especially in higher dimensions) for what parameters SL will occur, or even if it will occur at all. Nevertheless, we can still imagine a region of frequency in which eigenfunctions for a given random system must either grow or decay (not necessarily with exponential dependence), and thus any mode for such a system would again be required to be a bound, localized mode. In one- and two-dimensional random configurations it is believed that all modes are localized, and that in higher dimensions localized modes only occur for certain ranges of frequencies, if at all.[3]

We have performed experiments at microwave frequencies for both random and periodic two dimensional arrays of cylindrical dielectric scatterers, in which we demostrate SL modes and PBG states, respectively. By creating single defects in a PBG system we also demonstrate the corresponding defect states. Studies of random scattering systems are of interest to determine properties such as the dependence of the ensemble average localization length on scattering parameters. Studies of PBG and defect systems are of interest for their potential application in devices. In this paper we report on a study whereby we follow the evolution of the defect states created by randomly removing an increasing number of cylinders from a square lattice until we have 50% occupancy.

EXPERIMENTAL TECHNIQUE

Our experiments[4] were carried out at microwave frequencies (~6-20 GHz) in a waveguide scattering chamber (Fig. 1), 1 cm high, 46 cm wide, and 51 cm long. The bottom and side walls of the chamber are machined out of a solid aluminum plate. On both ends of the chamber are standard 8-12 GHz waveguide fittings which can be used to detect or inject microwaves in the chamber via a tapered region integrally machined into the main plate. An aluminum cover plate, free to translate laterally, completes the chamber. The scatterers inside the chamber are typically cylinders with height of 1 cm and of various radii and dielectric constants. Accurate lattices can be constructed by placing the cylinders into a precision drilled styrofoam (ε=1.04) template. Finally, a thick layer of low density absorber

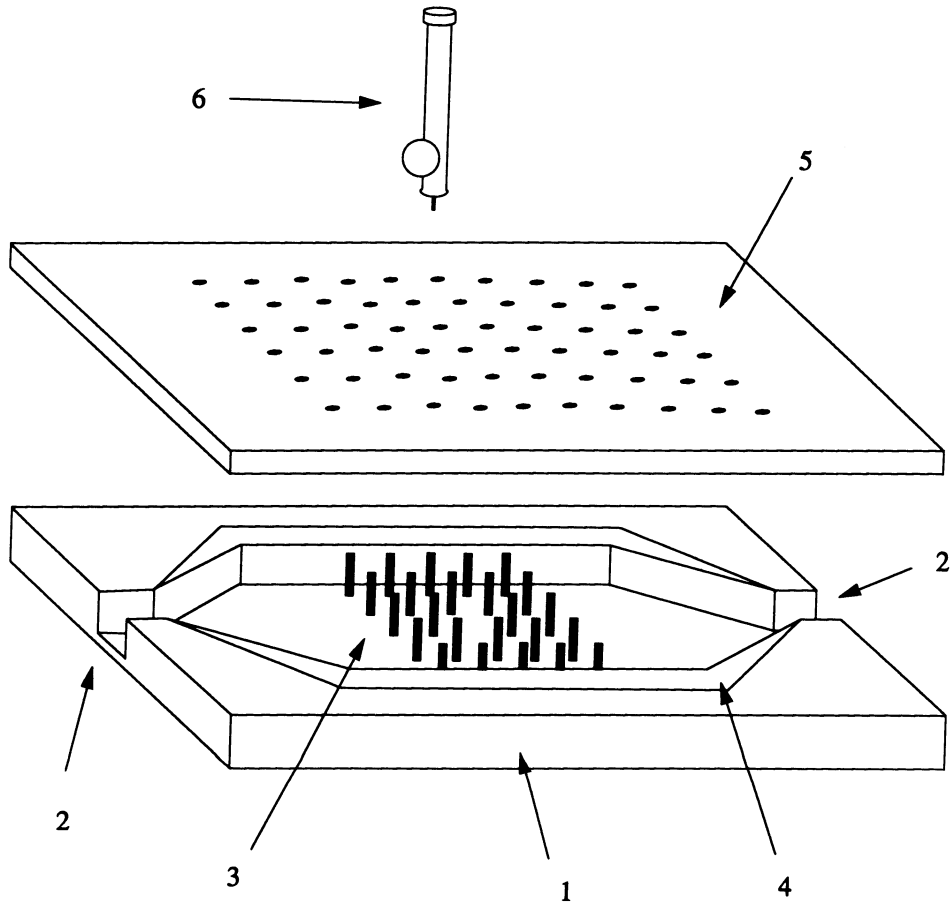

Figure 1. Schematic representation of the scattering system (not to scale). (1) Bottom and sides of scattering chamber (made as one piece), (2) inlet and outlet waveguide ports, (3) dielectric cylinders placed on a square lattice, (4) microwave absorber, (5) cover plate with holes for sampling electric energy density, and (6) a tuned microwave probe which is placed in the sampling holes in the coverplate, and whose output is measured by a homodyne detector at two phases 90° apart.

is placed between the interior chamber side walls and the styrofoam template which serves to minimize reflection.

The cylinders, styrofoam template, and absorber constitute a system of a finite array of scatterers (up to 900) with "free" boundary conditions. Furthermore, if the wavelength of the microwaves is larger than the spacing between the upper and lower metal boundaries (1 cm), our system is effectively two-dimensional (i.e., the electric field has no dependence along the direction of the cylinder axes).

In conjunction with an HP network analyzer we are able to sweep the microwave frequency and make measurements of the power transmitted through the scattering region. We are also able to map the spatial structure of standing wave modes (e.g., defect modes) by weakly coupling to a tuned probe through any of a lattice of small holes in the cover plate. Using standard homodyne techniques, we can measure both the phase and amplitudes of the fields sampled by the probe. By mapping the Mie resonances[4] associated with scattering from a single cylinder, we have found that the probe does not significantly perturb the system and the chamber is adequately terminated.

RESULTS

Fig. 2(a) shows the transmission for the case of a single cylinder completely removed from a square lattice of dielectric cylinders. By mapping the phase of the electric field as a function of position in a region around the defect, we have determined that the defect mode has fourfold symmetry.[5] In Fig. 2(b) we show the transmission data for a defect consisting of a cylinder with radius about 25% smaller than the radii of the cylinders composing the lattice. In this case we also observe a defect mode in the gap, but at a different frequency; also, measurements of the phases at select points indicate the mode is a dipole. The frequencies and symmetries of the defect modes agree with a numerical calculation completed by Meade et al.[6]

In Figs. 3(a) and 3(b) we have removed two cylinders from the positions indicated in the insets. In Fig. 3(a) the defects are far enough apart spatially so the defect mode overlap is negligible. The frequency of each mode is thus the same and we see only one resonance in the bandgap. When the defects are closer together as in Fig. 3(b), the modes begin to interact and we see a splitting of the defect frequencies in the band gap; if the interaction is small we may presume the modes are only slightly perturbed and couple symmetrically and antisymmetrically.

In Figs. 4(a)-(d) we present a sequence of transmission measurements of a periodic lattice with 162 sites (9 X 18) with increasing numbers of cylinders randomly removed. In Fig. 4(a) we have removed 3 (1.9%) cylinders. As shown in the inset, these cylinders happen to be distant both from each other and from the lattice boundary; thus, the transmission shows only one mode unperturbed within the gap, although this mode is actually triply degenerate. In Fig. 4(b) we have removed an additional 4 cylinders for a total of 7 (4.3%) defects. This time the defect modes have coupled, mainly through interaction with the boundary, and spread into an impurity band within the gap. In Fig. 4(c) we have removed a total of 20 (12.3%) cylinders from the lattice, as shown in the inset. Note that in addition to the broadening of the defect band in the band gap, there is an overall decrease in transmission for the entire spectrum; this suggests that the randomness in the lattice is sufficient to cause diffusive scattering in the pass band regions. This effect is even more noticeable in Fig. 4(d), which shows the transmission spectrum for a lattice with 30 (18.5%) cylinders removed.

Finally, in Fig. 5 we show the transmission spectra taken by R. Dalichaouch of a much larger square lattice [36 x 27 cylinders] from which 50% of the cylinders have been removed. The underlying modulation due to the bandstructure is evident, despite the randomness of the configuration. A spatial map of the electric field energy density for a localized mode corresponding to one of the peaks in the transmission spectrum is presented in Fig. 3 of Ref. 7, where the localized nature of the mode was demonstrated. We turn now to a discussion of applications of photonic band gap and defect structures.

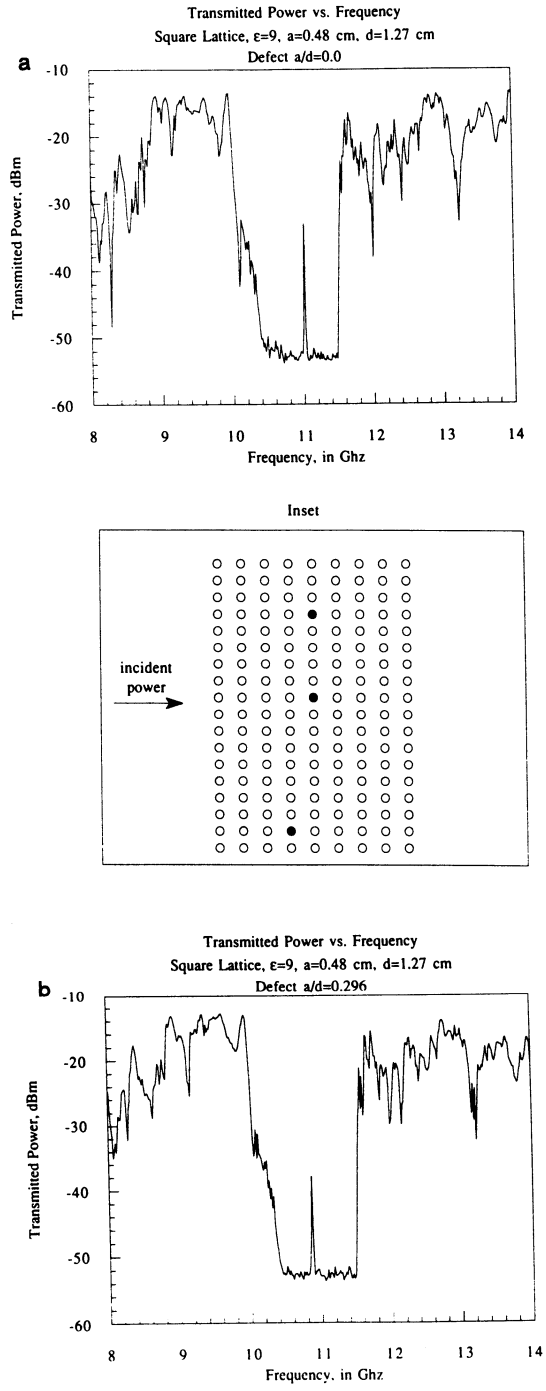

Figure 2. The transmitted power vs. frequency for a square array (9 x 18) of dielectric cylinders of ε=9 embedded in a styrofoam (ε=1.04) template. A single cylinder has been removed in Fig. 2(a), while a cylinder of 25% smaller radius has replaced a lattice cylinder in Fig. 2(b).

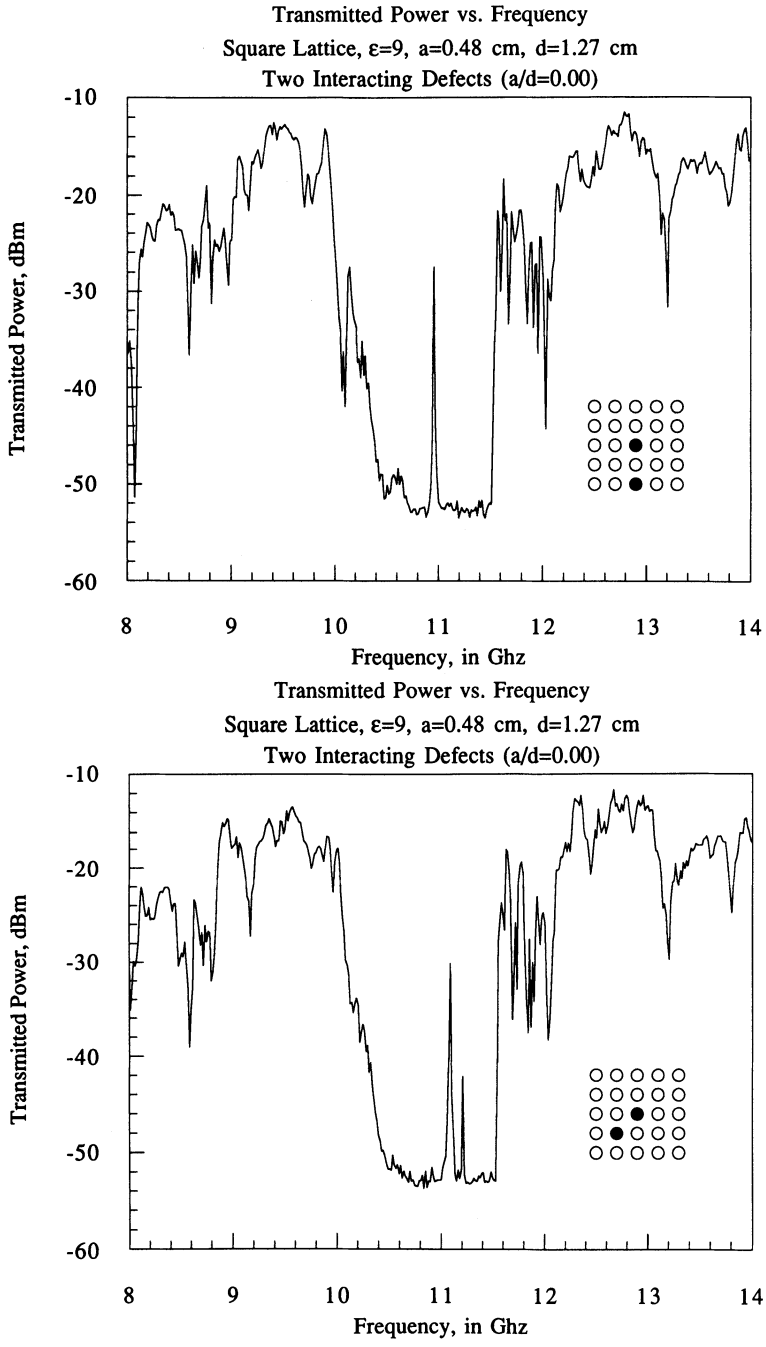

Figure 3. A spectrum for the same lattice used in Fig. 2. We have removed two cylinders from near the center of the lattice (to avoid interaction with the boundary). The darkened circles in the insets represent the relative orientation of the defects with respect to each other.

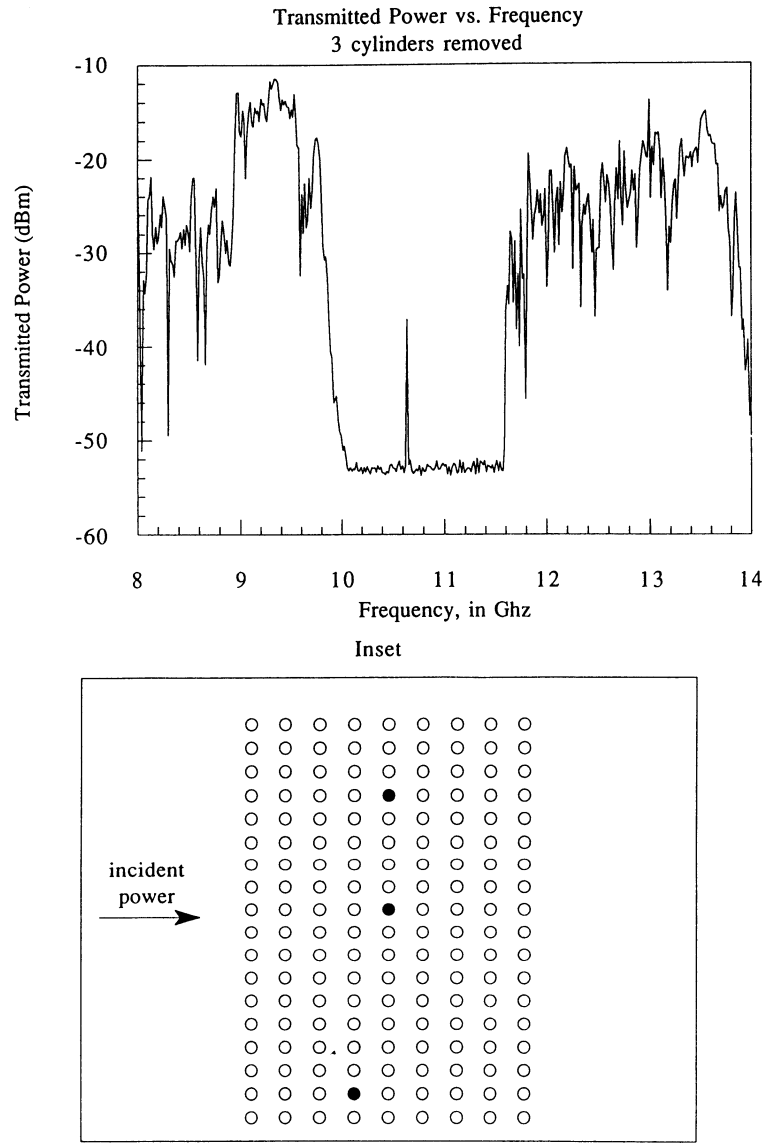

Figure 4(a): Transmitted power versus frequency for the lattice shown in the inset (3 cylinders removed).

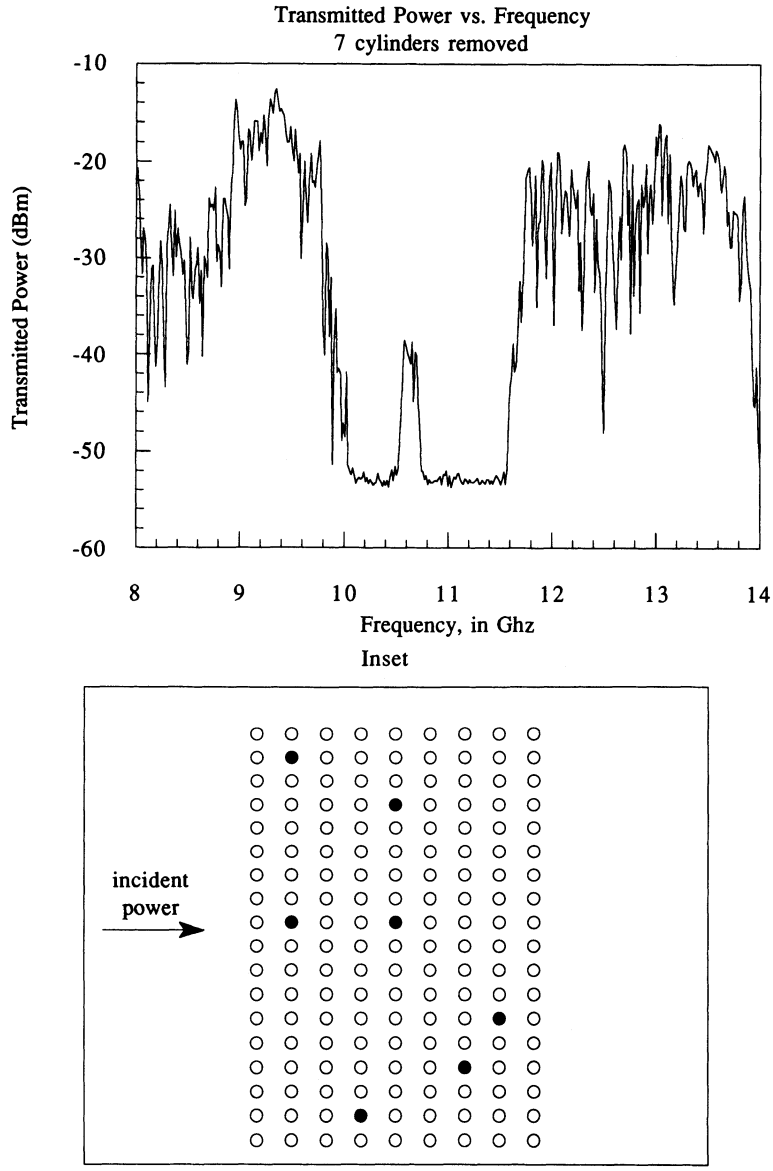

Figure 4(b). Transmitted power versus frequency for the lattice shown in the inset (7 cylinders removed).

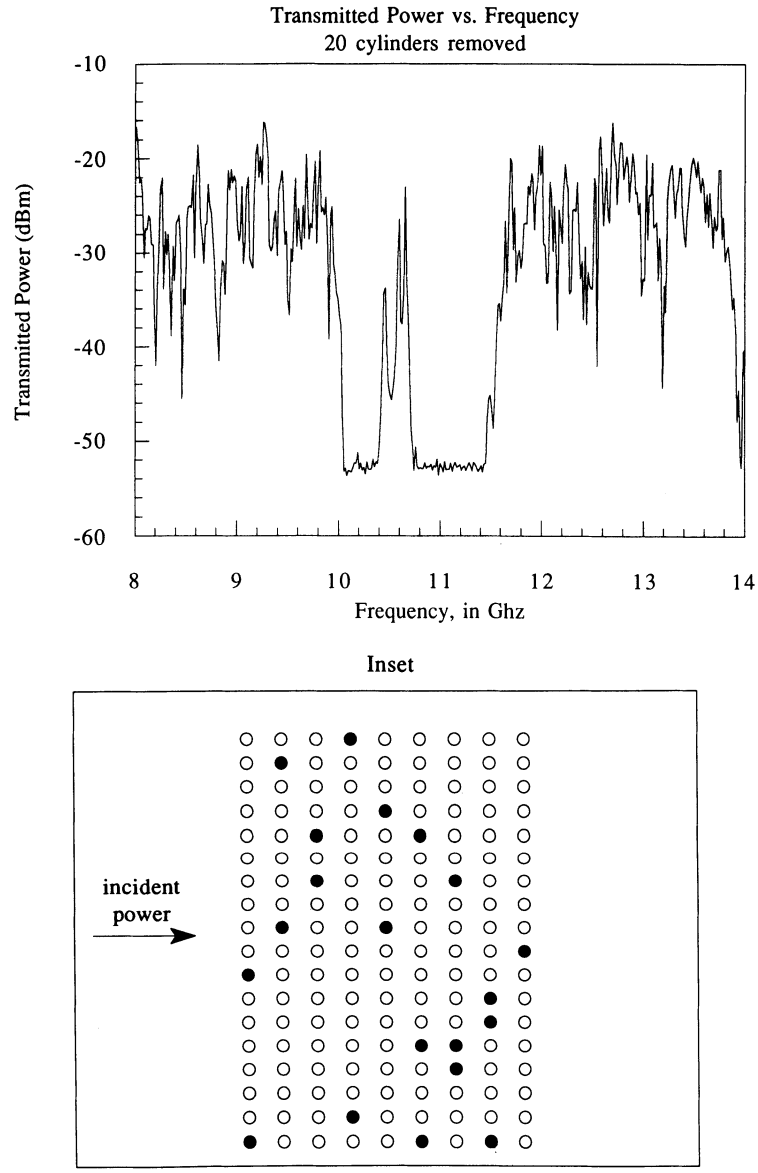

Figure 4(c). Transmitted power versus frequency for the lattice shown in the inset (20 cylinders removed).

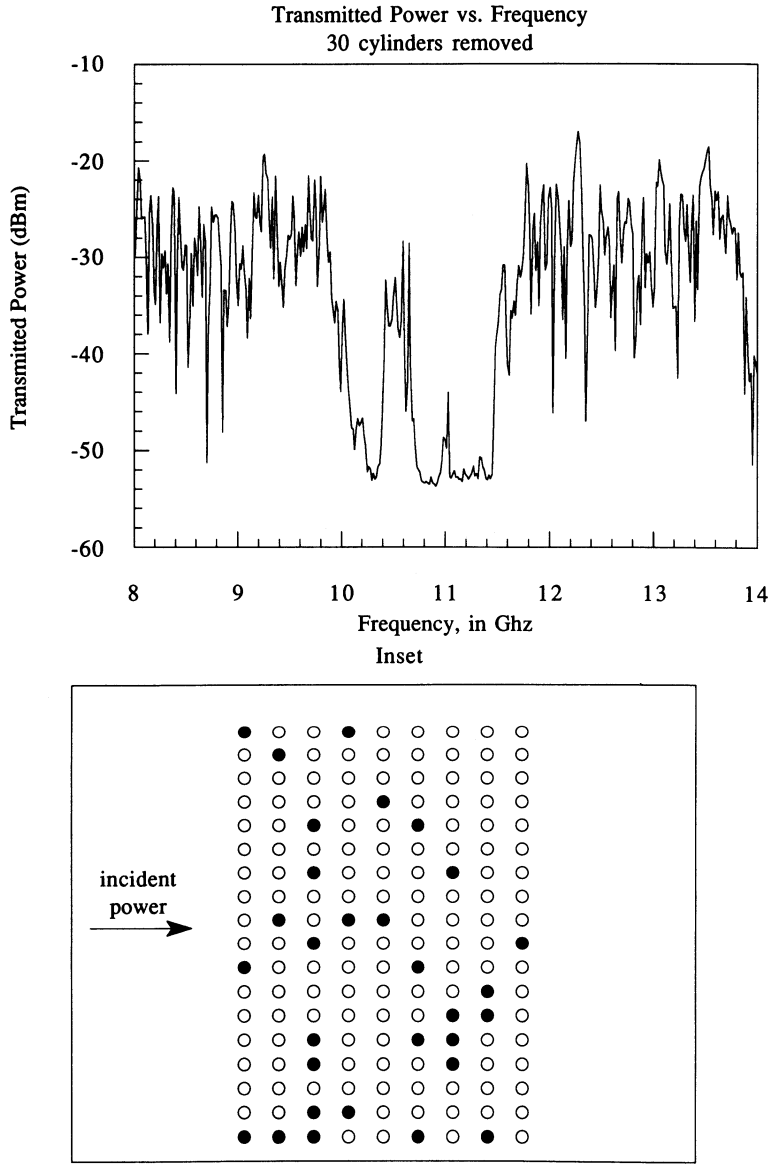

Figure 4(d). Transmitted power versus frequency for the lattice shown in the inset (30 cylinders removed).

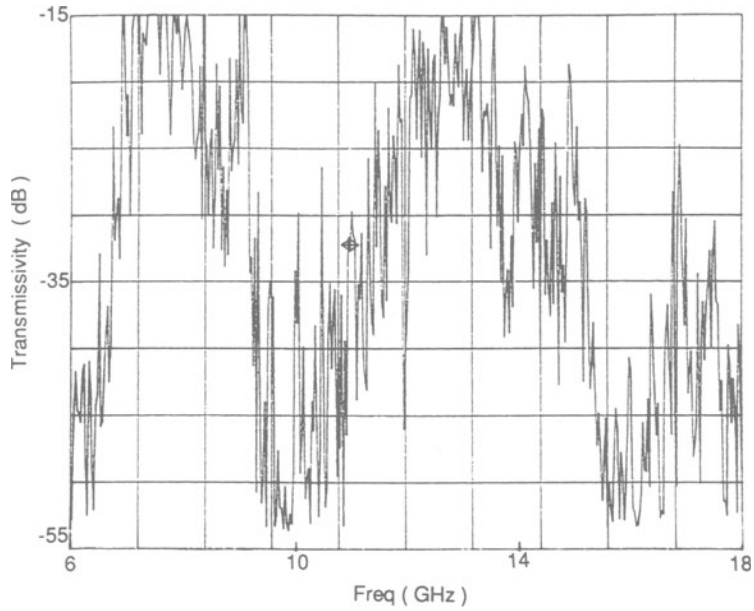

Figure 5. The ratio of the transmitted to incident power as a function of frequency for a set of dielectric cylinders ($\varepsilon = 9$), of radius 0.98 cm, placed randomly with 50% probability on a square lattice of spacing a_0 =1.27 cm. (a) an extended sweep range of 6-18 GHz. The sharp peaks are attributed to excitation of localized modes. The superimposed modulation with width of ~4GHz is attributed to vestiges of the stop and pass bands of the underlying lattice.

DISCUSSION

In general, one finds satisfactory agreement between experimental results and numerical simulations for photonic band structures, which supports the expectation that one should be able to model PBG systems in two-dimensions over a broad range of frequencies and material parameters. Of course, there are additional effects to take into account if one wishes to include the finite conductivity of the metal plates, the loss tangent of the dielectrics, etc. In addition, in some applications the finite distance between the plates may have to be explicitly modeled, and this can also be done.[8,9] A more difficult class of problem is perturbation due to holes in the metal plates, inclusion of coupling antennae, etc. However, given the powerful techniques for addressing finite boundary value problems that are now available, it is likely that numerical solutions will be available, if it is decided they are worth the computational effort.

There is a large range of devices and applications for which PBG structures may play a new and important role. It should be appreciated that by using superconducting end plates, and going to cryogenic temperatures, very high Q values for the defect resonances should be readily available. Thus, with currently available high T_c wafer material, one should get Q~10^6 at 77K, and with classical superconductors at 4 K, Q's up to ~10^{10}. In many respects the localized mode, or resonance state associated with a defect may be regarded as comparable to the familiar resonant modes in metal walled cavities. However, there are important differences, and these may prove particularly useful for certain applications. For example, the series of resonant modes in a rectangular box (or other geometrical form) can be specified in terms of a set of integer valued indices. There are no comparable simple sets of formulas for PBG structures, and the nature of the mode spacings is completely different. In some cases it may be possible to select parameters to have only one true PBG-defect state, or a selected finite set. Another difference is that one can design PBG-defect systems that have multiple defects, and those with varying geometrical and material structure. By placing defects regularly spaced, one can create the equivalent of supercells. Meade et al.[10] have reported a numerical investigation of investigated surface wave modes of the PBG structure,

and the effects of varying the choice of the termination plane at the interface between a 3-D PBG structure and that of a constant dielectric medium.

Since the localized mode around a defect state in a PBG structure does have many features in common with resonant cavities, they can be considered for all the applications where resonant cavities are utilized. Thus, they may prove useful for filters, impedance matching structures, masers, lasers, experiments in QED, etc. We have been investigating the applicability of PBG structures for replacing resonant cavities in linear accelerators, where their different mode properties may make them uniquely useful.[8]

In the introduction, we mentioned that we have focused on PBG structures in 2-D (as opposed to 3-D) because we felt they were equally useful, but much easier to implement. The reason they are easier to implemement in 2-D than 3-D is not only the inherent simplicity of a lower dimension, but because there is a much broader range of geometric and material parameters for which true PBG states exist. As illustration, consider that the only lattice found for a PBG stucture in 3-D is diamond,[11] with a minimum dielectric constant ~9, whereas in 2-D we have also utilized a triangular lattice[12] to get data similar to that shown here for a triangular lattice, and that the numerical simulations by Plihal et al.[13] for the H_{rf} field polarization parallel to the cylinder axis show that the minimum dielectric constant for a PBG can be as small as 2.

We believe that extension of our experiments up to the infrared regime is reasonably straightforward provided that one utilizes a dielectric scattering material with an adequate index and loss factor at the frequencies of interest. The reflecting plates could either be first surface silver mirrors, or even dielectric layers optimized for reflection at band gap frequencies. Experiments along these lines are in progress and will be reported separately.

Acknowledgments

Our prior work,[4,5,8,12] was completed in collaboration with R. Dalichaouch, S. L. McCall, P. M. Platzman, and N. Kroll, whom we thank for very helpful conversations. We thank John Armstrong for his help in implementing computer simulations and experimental data acquisition. This research has been supported by the National Science Foundation, grant #DMR-89-15815.

REFERENCES

1. E. Yablonovitch, *Phys. Rev. Lett.* 58:2059 (1987).
2 S. John, Phys. *Rev. Lett.* 58:2486 (1987).
3. P. A. Lee, and T. V. Ramakrishnam, *Rev. Mod. Phys.* 57:287 (1985).
4. Rachida Dalichaouch, Thesis, University of California, San Diego; (1991) unpublished
5. S. L. McCall, P. M. Platzman, R. Dalichaouch, David Smith, S. Schultz, *Phys. Rev. Lett.* 67:2017 (1991).
6. R. D. Meade, A. M. Rappe, K. D. Brommer, J. D. Joannopoulos, "Accurate Theoretical Analysis of Photonic Band-Gap Materials", preprint, submitted to *Phys. Rev. Lett.*
7. R. Dalichaouch, J. P. Armstrong, S. Schultz, P. M. Platzman, S. L. McCall, *Nature* 354:53 (1991).
8. N. Kroll, D. R. Smith, S. Schultz, "Photonic Band Gap Structures: A New Approach to Accelerator Cavities", submitted to *Proc. of Advanced Accelerator Concepts Workshop,* Port Jefferson, June, 1992.
9. A. A. Maradudin, private communication.
10. R. D. Meade, K. D. Brommer, A. M. Rappe, J. D. Joannopoulos, *Phys. Rev. B* 44:10961 (1991).
11. E. Yablonovitch, T. J. Gmitter, K. M. Leung, *Phys. Rev. Lett.* 67:2295 (1991).
12. D. R. Smith, Rachida Dalichaouch, N. Kroll, S. Schultz, S. L. McCall, and P. M. Platzman, "Photonic band structure and defects in one- and two-dimensions", accepted for special issue of *J. Op. Soc. of America B,* (JOSA B) (1992).
13. M. Plihal, A. Shambrook, A. A. Maradudin, Ping Sheng, *Optics Communications* 80:199 (1991).

SPECTRAL GAPS FOR CLASSICAL WAVES IN PERIODIC STRUCTURES

E. N. Economou[1,2] and M. Sigalas[1,*]

[1]Research Center of Crete-Forth
P.O. Box 1527, 71110 Heraklion Crete,
[2]Department of Physics,
University of Crete, 71409 Heraklion, Crete
Greece

INTRODUCTION

Recently, the problem of a classical wave (CW), such as electromagnetic (EM), acoustic scalar (AS), or elastic (EL), propagating in composite media, has received increasing interest (Sheng, 1990). In these media, problems, such as electron-electron and electron-phonon interactions which occur in the electronic case, do not exist. For this reason, it is easier to understand and study phenomena of localization. Also, future useful devices may be based on the problem of classical wave propagation (John, 1988; Yablonovitch, 1987; John, 1991).

John and Rangarajan (1988) and Economou and Zdetsis (1989) have pointed out the connection between the possible localization of classical waves in disordered media and the possible existence of band gaps or regions of very low density of states (DOS) in periodic structures. Actually the band gaps will become, at least partially, regions of localized states as a disordering process is gradually introduced in the periodic structure. As a result of this, the question of band structure of classical waves has received increased attention.

The scalar wave (SW) equation has been studied (only in fcc structure) by several authors using the augmented plane wave (APW) (Economou and Zdetsis, 1989), the Korringa Kohn Rostoker (John and Rangarajan, 1988; Leung and Liu, 1990a) and plane wave (PW) (Leung and Liu, 1990a; Satpathy et al., 1990) methods. Also, the EM wave equation has been studied (in fcc and diamond structures) using the PW method (Ho et al., 1990; Leung and Liu, 1990b; Zhang and Satpathy, 1990). A disordered elastic

Photonic Band Gaps and Localization, Edited by
C.M. Soukoulis, Plenum Press, New York, 1993

discrete medium has been studied by John et al. (1983). They found that all finite phonons in one and two dimensions are localized and that a mobility edge separating low frequency extended states from high frequency localized states exist above two dimensions. More recently the EL and AS wave equation in the continuum have been examined (Sigalas and Economou, 1992a). Yablonovitch and Gmitter (1989) did the first experimental work for microwaves propagating in periodic fcc dielectric structures.

In this paper, we comment first on some general points regarding all types of classical waves: simple scalar waves (SSW), scalar acoustic waves propagating in a composite periodic medium where the mass density (as well as the sound velocity) varies in space (ASW), electromagnetic waves (EMW), and elastic waves (ELW) in a composite periodic solid. Then, we present some results for SSW, ASW, EMW and ELW.

GENERAL REMARKS

In this section, we point out some general features of wave propagation in inhomogeneous media, we raise some yet unanswered questions, and we present arguments favoring the study of ASW and ELW.

Connection Between Spectral and Mobility Gaps

Spectral gaps in periodic media as well as mobility gaps (i.e., spectral regions where the eigenstates are localized or non-propagating) in random systems are both due to *strong multiple-scattering and interference.* Thus, there is an intimate connection between the two. A particular, but very common case, which shows explicity this connection emerges when we gradually disorder a periodic medium possessing spectral gaps. The disordering process creates bandtails (Urbach tails), which consist of *localized* states and which tend to fill in the gaps. As a result, the regions of localized states in the weakly disordered system almost coincide with the gaps of the unperturbed periodic medium. Consequently, the determination of the gaps in a periodic medium (an extensively studied problem for which many accurate techniques have been developed) allows one to approximately locate the regions of localized states in a random system, provided that a corresponding periodic medium can be found from which the random one can be generated by a weak disordering procedure.

Bragg vs Mie

In order to create a spectral gap, it is necessary to have a destructive interference of a similar nature as in the Bragg diffraction. This implies that the wavelength, λ, must be comparable to twice the linear dimension, a, of the fundamental cell of the periodic structure. However, a genuine spectral gap (i.e., one existing for all directions of propagation in a 2D or 3D system) requires also wide gaps for each direction (otherwise as the wave vector $\vec{k}$ is rotated, the gap will be wiped out). But, a wide gap in each direction implies strong scattering from each individual scattering center (or more correctly from each unit cell). We were thus led to the conclusion that a genuine gap will be associated with strong *resonance* scattering from each unit cell. A classical case of such resonance scattering has been studied by Mie for the case of electromagnetic waves impinging upon a spherical dielectric. A review of resonance scattering can be found in a recent paper by Flax et al. (1981). If the dielectric constant of the sphere is very large (in comparison to that of the surrounding medium) very strong resonances appear in the total cross section approximately when $\lambda_i(n+1) = 2d$, where λ_i is the wavelength inside the sphere ($\lambda_i = 2\pi c/\omega\sqrt{\epsilon_i}$), n=1,2,3,... and d is the diameter

of the sphere. Thus, to satisfy both the Bragg condition and the Mie-type resonance condition, d must be comparable to a, which implies that the volume fraction of the scatterers, x, must be appreciable on the order of at least 10 %.

How one can make a rough estimate about the optimum values of the parameters for the appearance of a gap? If the individual scatterer's resonance structure is the dominant factor, one would expect that the most important parameter would be the ratio d/λ_i . Indeed, at least for SSW and ASW, there is strong correlation between the resonance structure from an individual sphere and the appearance of gaps (see Fig. 1,2 as well as Fig. 5 in the paper of Datta et al. in this book). The values of d/λ_i, for which resonances appear, almost coincide with the positions of the midgaps (or the deeps in the density of states) for small x, and with the position of the middle of the bands for large x ! The reason for this behavior is the following: For low x (low concentration of scatterers), the propagation is taking place through the host material and the scatterers impede the propagation; thus the position of the resonance is expected to almost coincide with the gap (or the would be gap). On the contrary, for a high concentration of scatterers the propagation takes place by hopping from scatterer to scatterer through the overlap of the local resonance states (the analog of a band made up from a linear combination of atomic orbitals in the electronic case); thus, for high x, it is expected that the position of the resonances would approximately coincide with the center of the bands (see Fig. 5 in the paper of Datta et al. in this book). When two or more resonances are close to each other, a hybridization is expected and there will be no simple a priori relation between the position of the resonances and the midgap (or midband). It seems this is the case for EMW.

The dominance of the resonances for the creation of gaps would also imply that the ratio ϵ_i/ϵ_o must be large (ϵ_o is the dielectric constant of the host, high velocity material). Indeed, a large value of ϵ_i/ϵ_o would produce strong resonances and, hence, gaps. Analysis of the numerical data show that the ratio ϵ_i/ϵ_o must exceed a critical value for a gap to appear; beyond this critical value the width of the gap grows linearly with ϵ_i/ϵ_o and then seems to saturate. Another feature of the band structure, which supports the dominant role of the resonances, is the observed flatness of many "optical" branches (see Figs. 6, 7, 8, 10, 11, 12, 13 and 17). Furthermore, the data show that the results are not so sensitive to the value of x, provided that x is in a region around its optimum value; this feature tends to imply a not so sensitive dependence on the exact satisfaction of the Bragg condition. It may even be possible that a strong short range order of sufficiently large range is enough to create a gap and that a perfect periodic long range order is not really necessary. On the other hand, the data in the electromagnetic case seem to indicate that gap formation is strongly enhanced if the scatterer(s) in each unit cell are connected to form a continuous network running through the entire system. This feature suggests that one cannot analyze the basic properties-at least for the EM case-in terms of what is happening at an isolated individual scatterer.

Classical Waves vs Electron Waves

The wave equation satisfied by an SSW ψ is given by:

$$\nabla^2\psi - \frac{\epsilon(\vec{r})}{c^2}\frac{\partial^2\psi}{\partial t^2} = 0 \quad or \quad \nabla^2\psi + \frac{\omega^2}{c^2}\epsilon(\vec{r})\psi = 0. \tag{1}$$

The corresponding equations for the electronic case are :

$$\nabla^2\psi - \frac{2m}{\hbar^2}V(\vec{r})\psi + \frac{2mi}{\hbar}\frac{\partial\psi}{\partial t} = 0 \qquad \text{or}$$

$$\nabla^2\psi + \frac{2m}{\hbar^2}(E - V(\vec{r}))\psi \quad = 0 \quad . \tag{2}$$

In the time domain the electronic and the classical wave equations are not equivalent; as a result, time dependent processes such as the diffusion of an initially localized pulse cannot be carried over from the electronic to classical wave case without further analysis. On the other hand, in the frequency domain the two equations are equivalent. Since $\epsilon(\vec{r})$ and m are positive quantities, it follows that the obvious inequality $\omega^2 \geq 0$ implies for the electronic problem that

$$E \geq V_{max}, \tag{3}$$

i.e., the CW problem is mapped onto the electronic problem for energies larger than the maximum value of the potential. The gaps in the CW problem are equivalent to gaps for $E \geq V_{max}$ in the electronic problem. The existence of gaps *in this region of energy* for 2D and 3D periodic systems is not a priori guaranteed. As a matter of fact, only under rather extreme conditions do gaps above V_{max} appear.

In the CW case, the disorder (which is incorporated in $\epsilon(\vec{r})$) is multiplied by ω^2; as a result of this in the $\omega \to 0$ limit, we have always free-like propagation. Note also that the regions of low velocity, $c/\sqrt{\epsilon(\vec{r})}$, i.e., of high $\epsilon(\vec{r})$, correspond to regions of potential wells; since a potential well is a stronger scatterer than a potential bump (because the potential well as opposed to the potential bump may develop resonances), we shall consider the high $\epsilon(\vec{r})$, low velocity regions, as the scatterers and the rest as the host material; x always denotes the volume fraction occupied by the low velocity component, which may be disjoint or may be joined together to form a continuous network.

For EMW and ELW we have vector fields, where their cartesian components are coupled together. This is somehow analogous to the spin-orbit coupling in the electronic case. It is well-known that the presence of spin-orbit creates a new universality class as far as the electronic localization is concerned. Thus, it would be of interest to make a comparative study of SSW, EMW, and ELW aiming at checking out whether or not the above cases belong to different universality classes.

Acoustic and Elastic Waves

Acoustic scalar waves, in an inhomogeneous fluid medium, show a richer behavior than the SSW described by Eq. (1). The reason is that we have two independent quantities, i.e., the elastic constant $\lambda(\vec{r})$ and the mass density $\rho(\vec{r})$, entering the acoustic wave equation:

$$\frac{\partial^2 p}{\partial t^2} = \lambda\vec{\nabla}(\frac{\vec{\nabla}p}{\rho}), \tag{4}$$

where $p(\vec{r})$ is the pressure, and $c^2 = \lambda(\vec{r})/\rho(\vec{r})$ is the square of the local speed of sound. If the mass density is constant, Eq. (3) reduces to the simple wave equation (1). In other words, the propagation of the sound wave faces, in general, both velocity mismatch as well as impedance mismatch.

For elastic waves the physics is even richer, because we have a full vector field (both longitudinal and transverse with quite different velocities, c_ℓ, and c_t, respectively) encountering in its propagation transverse and longitudinal velocity mismatch as well as impedance mismatch. Given the fact that the two-component EMW develops gaps under more extreme conditions than the one-component SSW, one expects the three-component ELW would require even more extreme conditions for the opening of gaps. It is conceivable, that under realistic conditions we may have always a no gap situation.

THE SCALAR CASE

We have solved Eq. (2) (or its equivalent (1)) in the case where we have non-overlapping spheres of potential $V(\vec{r}) = -\delta$ (or of dielectric constant ϵ_i) arranged in a periodic way within a host material of potential $V(\vec{r}) = 0$ (or of dielectric constant ϵ_o). For the numerical solution, we have employed both the unsymmetrized APW method (Mattheiss et al., 1968; Papaconstantopoulos, 1986) and the plane wave method (John and Rangarajan, 1988; Leung and Liu, 1990a). In the APW method, it is necessary to limit the infinite sum over ℓ to a finite number of terms (Mattheiss et al., 1968). In all the calculations, 10 terms in this sum are sufficient to yield results which are accurate to a few mRy. The number of reciprocal vectors, KMAX, required in order to obtain convergent results, depends on three factors: (a) the structure; (b) the value of δ; and (c) the value of x. For the same values of δ and x, it is easier to find a convergence of a few mRy for an fcc structure than for a bcc structure, and it is more difficult for simple cubic (sc) structure. For fixed δ and x, we have scanned the positive energy E semiaxis to find the gap positions (parallel solid line in Fig. 1).

Our results for the muffin tin electronic problem are directly applicable to the SSW equation (Eq. (1)). Indeed each E and δ point in Fig. 1 mapped to an ω, r ($\equiv \sqrt{\epsilon_i/\epsilon_o}$) point by the equations (Economou and Zdetsis, 1989; Soukoulis et al., 1989; Economou and Soukoulis, 1989):

$$r^2 \equiv \frac{\epsilon_i}{\epsilon_o} = 1 + \frac{\delta}{E}, \quad \frac{\omega^2 \epsilon_o R^2}{c^2} = \frac{E}{E_0}, \tag{5}$$

where $E_o = \hbar^2/2mR^2$, R is the radius of the muffin tin sphere, and ϵ_i is the high and ϵ_o the low dielectric constant.

The case where $\delta \geq 0$, correspond to attractive potentials and the opposite case to repulsive potentials. We expect that an arrangement of attractive potentials (for nonoverlapping spheres) form more easily gaps; thus, we choose to work only for $\delta \geq 0$; this corresponds to $0 < \epsilon_o < \epsilon_i$ in the SSW.

Within the framework of the plane wave method, we recast Eq. (1) as follows:

$$-\nabla^2\psi + T\psi = k_b^2\psi, \quad T = k_b^2[1 - \frac{\epsilon}{\epsilon_o}], \quad k_b^2 = \omega^2\epsilon_0/c^2. \tag{6}$$

For a periodic dielectric structure, T can be expanded in terms of its Fourier components $T(\vec{G})$, $\vec{G}$ being a reciprocal lattice vector. The wave function ψ which satisfies Bloch's theorem can be expanded in terms of the plane waves:

$$\psi(\vec{r}) = e^{i\vec{k}\vec{r}} \sum_{\vec{G}} C_{\vec{k}+\vec{G}} e^{i\vec{G}\vec{r}}. \tag{7}$$

Equation (6) can then be expressed in the form (Leung and Liu, 1990a):

$$\frac{1}{|\vec{k}+\vec{G}|} \sum_{\vec{G}'} \frac{\delta(\vec{G}-\vec{G}') - U_{\vec{G}-\vec{G}'}}{|\vec{k}+\vec{G}'|} d_{\vec{k}+\vec{G}'} = \frac{1}{k_b^2} d_{\vec{k}+\vec{G}}, \tag{8}$$

where $U = T/k_b^2$ and $d_{\vec{k}+\vec{G}} = |\vec{k}+\vec{G}|C_{\vec{k}+\vec{G}}$. For the case of non overlapping dielectric spheres, we have $U_{\vec{G}} = 3x(1-r^2)g(|\vec{G}|R)$ where $g(y) = (\sin y - y\cos y)/y^3$. The SSW band structure is then obtained by solving Eq. (8) for the eigenvalues k_b^2 for each value of $\vec{k}$. The APW results are in good agreement with those obtained by the PW method.

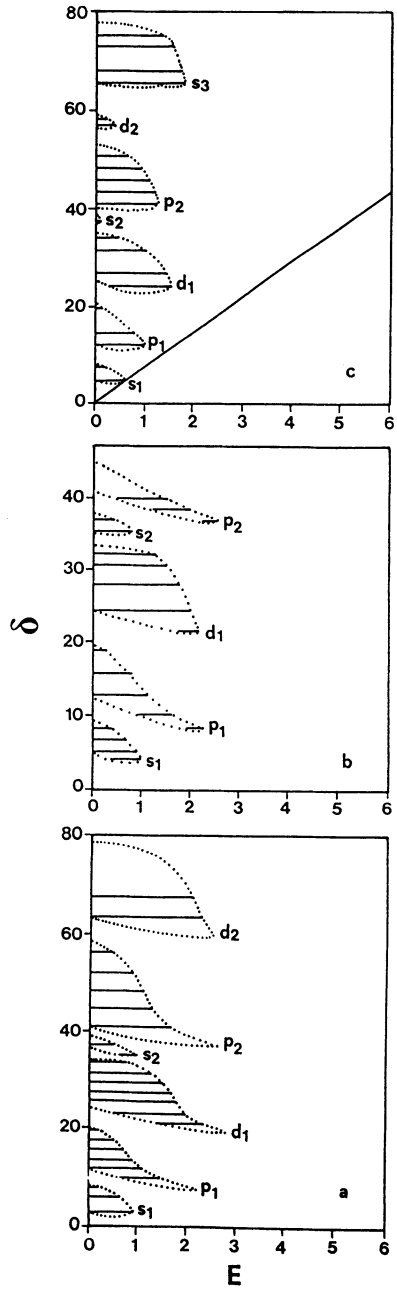

Figure 1. Position of the gaps (solid horizontal lines) in fcc (a), bcc (b) and sc (c) muffin-tin periodic potential (-δ inside the spheres, zero inside the interstitial region) for volume fraction x=0.144. The energy E and the depth δ are measured in units of $\hbar^2/2mR^2$ where R is the muffin-tin radius. The dotted line passing through the ends of the horizontal lines is a guide to the eye, roughly indicating the trajectories of the all band edges for positive E. The symbols indicate the dominant resonant scatterings responsible for the corresponding gap. No gap exists at higher energy E.

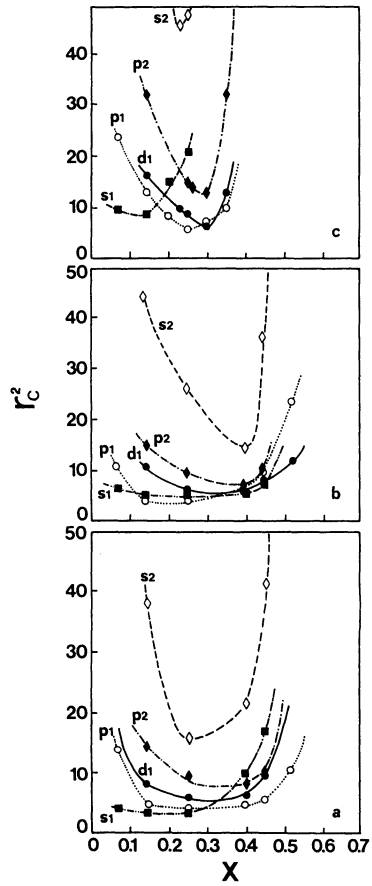

Figure 2. Each curve represents the threshold value of the contrast r_c^2 for which a frequency gap of a specific type just opens plotted against x for various lattices: (a) fcc ; (b) bcc ; (c) sc. The type of the gap (and consequently the corresponding curve) is characterized by the dominant resonance responsible for its existence.

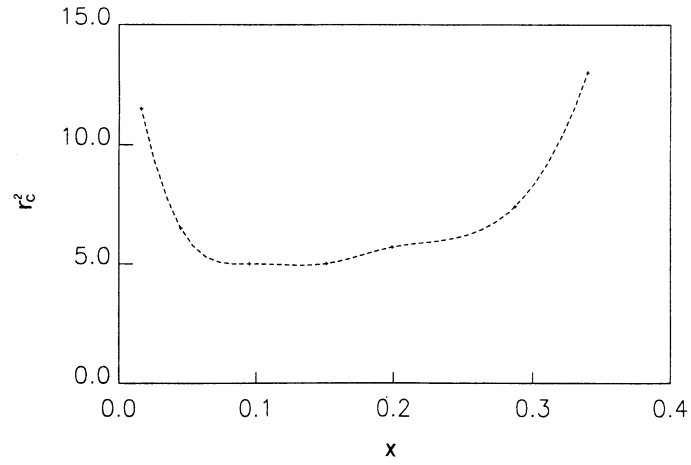

Figure 3. The threshold value, r_c^2, of the contrast $r^2 \equiv (c_o/c_i)^2$ for which the p1 gap just opens plotted against x, the volume fraction of the low velocity component, for scalar waves in a diamond structure.

Results

Using the APW method we find for each x and δ the position of the gap(s) and we display them as horizontal solid lines in the E vs δ plane as shown in Fig. 1 for various lattices (fcc, bcc, and sc) and for $x = 0.144$. In the problem of scattering from a single sphere, it is well-known (Economou and Zdetsis, 1989; Soukoulis et al., 1989) that when δ increases, the cross-section has an oscillatory variation; thus, for some values of δ the scattering cross-section has a maximum. These are the so-called resonance scatterings which are associated with those critical values of δ for which a new bound state appears in the single potential well. For a given value of ℓ, there are infinite critical values of δ denoted by $\delta_{\ell n}$ $(n = 1, 2, \ldots)$. These values are related to the values of δ for which gaps appear in the periodic case considered here and plotted in Fig. 1.

The absolute threshold contrast, r_c^2, for which a frequency gap in SSW case just appears is obtained from Fig. 1 by drawing the minimum slope straight line through the origin which intersects a gap segment as shown in Fig. 1c for the s1 gap, which is associated with the first $\ell = 0$ resonance scattering from a single sphere. We can also find from our data and Eq. (5) the threshold value of r_c^2 for each particular resonance structure of Fig. 1 (s1, p1, d1, s2, p2). These various threshold values of r_c^2 relative to the volume fraction x are plotted in Fig. 2a,b,c for fcc, bcc, sc structures, respectively. For a particular gap it appears that there is a threshold value of x, x_i, immediately above of which this gap appears for very large value of r_c. As x increases beyond x_i, r_c decreases and reaches a minimum, r_c^m, for an optimum value of x, x_m. As x increases further beyond x_m, r_c increases slowly and approaches infinity for an upper cut off value of x, x_u. Thus, the particular gap appears only for $x_i \leq x \leq x_u$.

Comparing our results in Figs. 1a and 2a with those of Economou and Zdetsis (1989), we find a nearly perfect agreement for small values of δ (i.e., for r_c near its

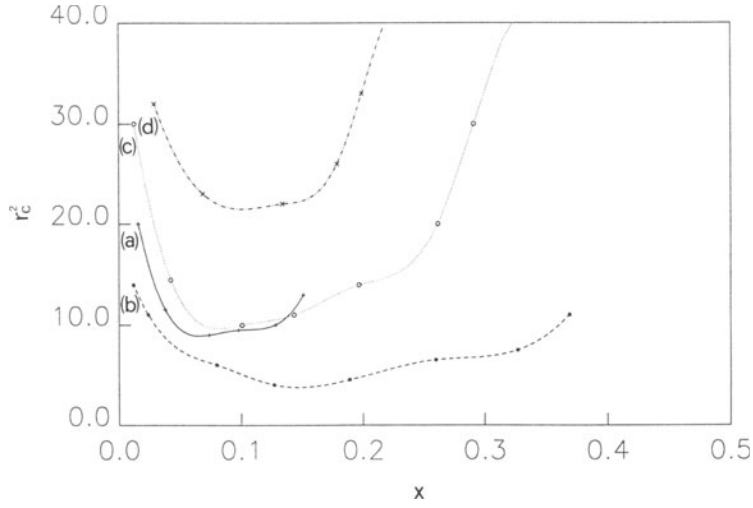

Figure 4. r_c^2 as a function of x, the volume fraction of the low velocity component, for s1 gap and scalar waves in an sh structure with c/a=0.5 (a), 0.8 (b), 1.5 (c), 2.2 (d).

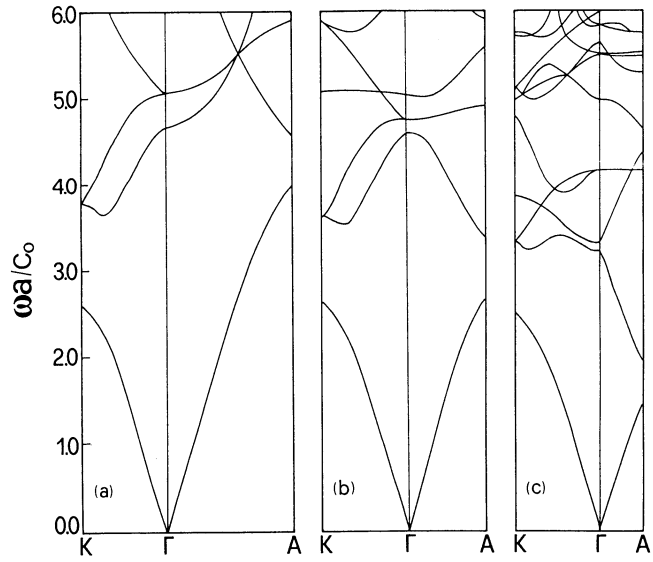

Figure 5. Calculated band structure across K-Γ-A axes for scalar waves in an sh structure with c/a= 0.5 (a), 0.8 (b), 1.5 (c) and x=0.144, $r^2 = 5$; a and c are the lattice constants.

minimum). But for very large values of δ (which corresponds to large values of r_c^2, as implied by Eq. (5)), there are some discrepancies as we can see by comparing our Fig. 1a with Fig. 1a of Economou and Zdetsis (1989). Our present results are more convergent than those of Economou and Zdetsis (1989) and are more reliable. In general, we found no disconnected closed loops in the band edge trajectories. Furthermore, the x_u for the p3 gap is smaller than that of Economou and Zdetsis (1989).

The fcc results (Figs. 1a, 2a) are similar to bcc results (Figs. 1b, 2b) and in both structures there is a region ($10\% \leq x \leq 30\%$) where the r_c for the s1 gap is almost constant. For the sc structure the gaps appear for lower values of x_u and greater values of r_c^m (Figs. 1c, 2c). The higher gaps appear for greater values of x_m (for example, the p1 gap appears for $x_m \approx 0.25$ in all the structures) and the value of r_c^m depends on the particular structure. Note that the r_c^m of p1 gaps are smaller than the r_c^m of s1 gaps for both bcc and sc structures but they are nearly the same for fcc structureS. Also, the r_c^m of s2 and p2 gaps have greater values than the r_c^m of s1 and p1 gaps. Our results for s1 gaps of fcc structures are in good agreement with the results of Satpathy et al. (1990) who found $x_m \approx 0.1 - 0.15$ and $r_c^m \approx 1.7$ using the PW method, and those of Leung and Liu (1990a) who found $r_c^m \approx 1.7$ using both the KKR and the PW methods. On the contrary, John and Rangarajan (1988) found $r_c^m \approx 2.8$ using the KKR method.

Using the PW method, we considered diamond, simple hexagonal (sh) and hcp structures. It is already known (Ho et al., 1990; Sigalas and Economou, 1992a) that for diamond structures the first band is doubly degenerate across the W - X (Z) axis, so it is impossible to find the first gap, which is associated with the lowest s-wave resonance. However, there is a pseudogap in the same region of frequencies. In the diamond structure, the p1 gap appears for $x_m \approx 0.1 - 0.15$ and $r_c^m \approx 2.2$ as shown in Fig. 3. So, the p1 gap for a diamond structure appears for greater values of r_c^m and lower values of x compared with the p1 gap for both fcc and bcc structures.

In Fig. 4 we show the r_c^2 relative to x diagrams for sh lattice and different ratios of the lattice constants c/a. For $c/a \approx 3/4$, the results are quite similar with the fcc results and this is the optimum ratio (Sigalas and Economou, 1992a). When the ratio c/a departs from this value (either to lower or higher values), the appearance of gaps becomes more difficult. Comparing the band structures across $K - \Gamma - A$ axes for the same values of x, r, and c/a = 0.5, 0.8, 1.5 (Fig. 5), we can see that the bands at the A point [π/c(0, 0, 1)] are lower for c/a = 1.5; thus, it is not easy to find a gap in any direction. For c/a= 0.5, the bands at K point [π/a(4/3, 0, 0)] are lower than the bands at the A point. We can also see from Fig. 5 that the band structure for c/a= 1.5 has a more complicated form because some bands go down to lower values of frequency due to the smaller value of π/c.

For the hcp structure, the first band is doubly degenerate across the P axis for every value of x and r. Thus, it is impossible to find the first gap, which is associated with the lowest s-wave resonance.

THE ELECTROMAGNETIC CASE

Maxwell's equations for EM waves can be written as:

$$\vec{\nabla} \times \vec{H} = -i\frac{\omega}{c}\epsilon\vec{E} \tag{9}$$

$$\vec{\nabla} \times \vec{E} = i\frac{\omega}{c}\vec{H} \tag{10}$$

$$\vec{\nabla}\vec{H} = 0. \tag{11}$$

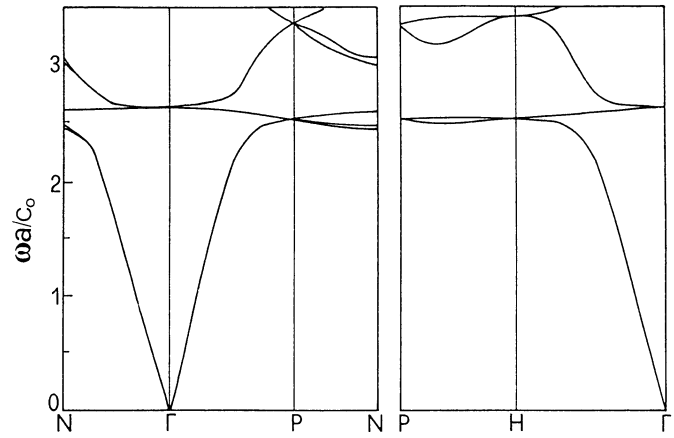

Figure 6. Calculated band structure for EM waves in a bcc structure x=0.144 and $r^2 = 29.92$; a is the lattice constant.

Substituting Eq. (9) into (10) we obtain:

$$\vec{\nabla} \times (\epsilon^{-1}\vec{\nabla} \times \vec{H}) = \frac{\omega^2}{c^2}\vec{H}. \tag{12}$$

Following previous work by Ho et al. (1990), we expand the $\vec{H}$ field into plane waves:

$$\vec{H}(\vec{r}) = \sum_{\vec{K}} \vec{H}_{\vec{K}} e^{i\vec{K}\vec{r}}, \tag{13}$$

where $\vec{K} = \vec{k} + \vec{G}$ and the sum is over $\vec{G}$. Substituting Eq. (13) into Eq. (12) and using Eq. (11), we obtain the following eigenvalue equation:

$$\frac{\omega^2}{c^2}\vec{H}_K = \sum_{K'} \epsilon^{-1}_{K-K'} |\vec{K}||\vec{K'}| \begin{pmatrix} \hat{y}_K\hat{y}_{K'} & -\hat{y}_K\hat{x}_{K'} \\ -\hat{x}_K\hat{y}_{K'} & \hat{x}_K\hat{x}_{K'} \end{pmatrix} \vec{H}_{K'}, \tag{14}$$

where $\hat{x}_K \cdot \vec{K} = 0$, $\hat{y}_K \cdot \vec{K} = 0$, $\hat{x}_K \cdot \hat{y}_K = 0$, and $\hat{x}_K$, $\hat{y}_K$ are unit vectors.

If the infinite series is approximated by a sum of N reciprocal vectors, Eq. (14) is reduced to a $2N \times 2N$ matrix eigenvalue problem. For $r = \epsilon_i/\epsilon_o$ up to 6 and for an accuracy 3% in the lower lying eigenmodes, we retained $N \approx 300$ for all the structures considered here except diamond in which $N \approx 450$.

Our results are in good agreement with the previous results (Ho et al., 1990; Leung and Liu, 1990b; Zhang and Satpathy, 1990). For the fcc structure, it was found that a true gap does not exist due to a degeneracy of the second band at the W point. But, a pseudogap develops in the photon spectrum for moderate values of the dielectric contrast and it optimizes generally for $x \approx 0.3 - 0.4$ (Zhang and Satpathy, 1990). For similar reason a true band gap is absent in bcc structures, as we can see in Fig. 6, due to a degeneracy of the second band at H and P points. Also, the third and fourth bands

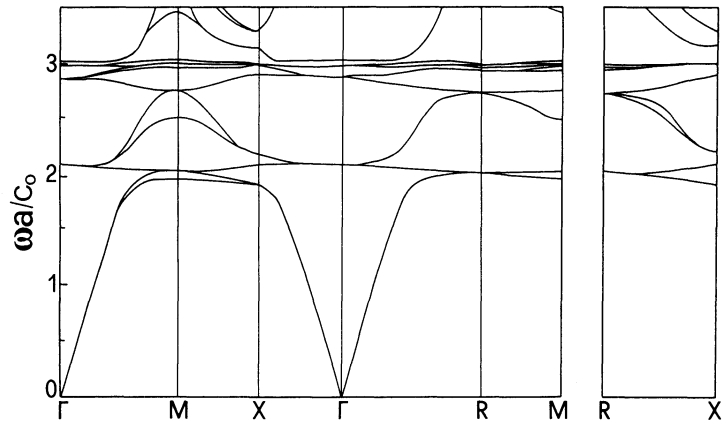

Figure 7. Calculated band structure for EM waves in an sc structure ; x=0.144, r^2 = 29.92 ; a is the lattice constant.

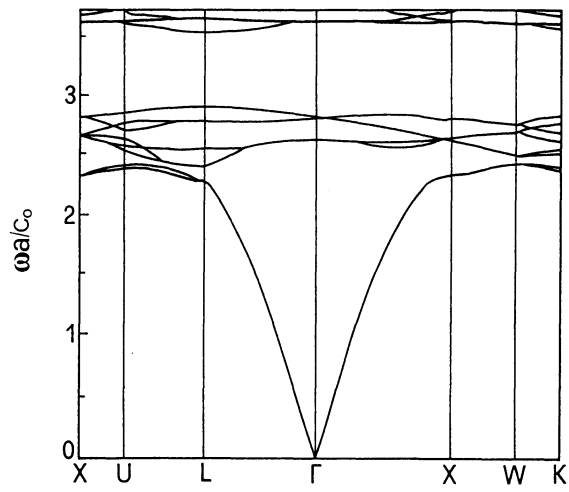

Figure 8. Preliminary calculations for the band structure of EM waves in a diamond structure; x=0.34, r^2 = 38.12; a is the lattice constant.

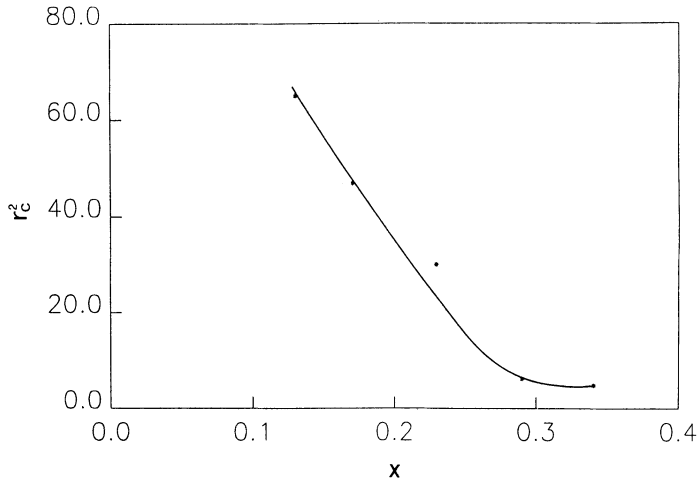

Figure 9. r_c^2 as a function of x, the volume fraction of the low velocity component, for the first frequency gap of EM waves in a diamond structure.

have a crossing only at Γ point so a second sharp pseudogap appears in the DOS. In the sc structure a band gap is also absent due to a degeneracy of second band at the R and M points (Fig. 7).

On the contrary, a true photonic band gap does exist in a diamond structure for easily obtainable dielectric constants (Ho et al., 1990). In Fig. 8 we present preliminary results for the band structure of EMW for a diamond structure and very large dielectric contrast. Because of very large contrast and the relatively high frequency, the accuracy of these results is low as witnessed by the fact that the first gap (between second and third bands) does not appear in this particular case as it should. Thus, we must consider the large wide gap, (between eighth and ninth band) as doubtful until more accurate calculations are performed. In Fig. 9 we plot the r_c^2 vs x for the first gap of the diamond structure and we find $x^m \geq 0.34$, $r_c^m \leq 2.2$ and $x^i \geq 0.1$. So comparing with the corresponding scalar results (Fig. 3), it is obvious there is a considerable difference in the optimum value of x but the values of the optimum r_c are nearly the same.

Finally, in the sh structure and for EM waves, the second band is doubly degenerate at the L point so it is impossible to find a true band gap, but the magnitude of the pseudogap is optimized for $c/a \approx 3/4$ as in the scalar case.

ACOUSTIC AND ELASTIC CASES

From the theory of elasticity it is well-known (Landau and Lifshitz, 1959; Lai et al., 1978) that the equation which relates the stress tensor, T_{ij}, and the strain tensor (neglecting second order terms),

$$u_{ik} = \frac{1}{2}\left(\frac{\partial u^i}{\partial x_j} + \frac{\partial u^j}{\partial x_i}\right), \tag{15}$$

is given by:

$$T_{ij} = C_{ijk\ell} u_{k\ell}, \tag{16}$$

where $C_{ijk\ell}$ is the elasticity tensor and u^i is the i-th component of the displacement vector $\vec{u}(\vec{r})$. For isotropic materials:

$$T_{ij} = \lambda u_{\ell\ell}\delta_{ij} + 2\mu u_{ij}, \tag{17}$$

where λ and μ are the so-called Lamé coefficients (Landau and Lifshitz, 1959; Lai et al., 1978).

The equation describing elastic waves in inhomogeneous solids is given by:

$$\frac{\partial^2 u^i}{\partial t^2} = \frac{1}{\rho}\frac{\partial T_{ij}}{\partial x_j}, \tag{18}$$

where $\rho \equiv \rho(\vec{r})$ is the density. Using Eqs (15), (17) and (18) we obtain:

$$\frac{\partial^2 u^i}{\partial t^2} = \frac{1}{\rho}\{\frac{\partial}{\partial x_i}(\lambda\frac{\partial u^\ell}{\partial x_\ell}) + \frac{\partial}{\partial x_\ell}[\mu(\frac{\partial u^i}{\partial x_\ell} + \frac{\partial u^\ell}{\partial x_i})]\}. \tag{19}$$

Equation (17), for an homogeneous material, gives rise to uncoupled longitudinal and transverse waves of velocities c_ℓ and c_t respectively, where $c_\ell^2 = (\lambda + 2\mu)/\rho$, $c_t^2 = \mu/\rho$. It must be pointed out that the reduction of Eq. (19) into two independent equations can be done only in the homogeneous case where λ, μ and ρ = constants. For fluids $\mu = 0$ and by introducing the pressure $p = -\lambda\vec{\nabla}\vec{u}$, Eq. (19) is reduced to Eq. (4).

For periodic media $f(\vec{r})$ ($f \equiv \mu, \lambda$ or ρ^{-1}) can be expanded in terms of its Fourier components f_G. In the case considered here, the periodic medium consists of identical spheres of radius R with sound velocities $c_{\ell i}$ and c_{ti} placed periodically within a host homogeneous material with sound velocities $c_{\ell o}$ and c_{to}, $f_G = f_o\delta(\vec{G}) + 3x(f_i - f_o)g(|\vec{G}|R)$, where $g(y) = (\sin y - y\cos y)/y^3$. The displacement vector $\vec{u}(\vec{r})$ which satisfies Bloch's theorem can be expanded in terms of the plane waves: $\vec{u}(\vec{r}) = \sum_{\vec{K}} \vec{u}_{\vec{K}} e^{i\vec{K}\vec{r}}$ where $\vec{K} = \vec{k} + \vec{G}$, and the summation is over $\vec{G}$. Substituting in Eq. (19) we obtain:

$$\begin{aligned}\omega^2 u^i_{\vec{k}+\vec{G}} \;=\; & \sum_{\vec{G}'}\{\sum_{\ell,\vec{G}''} \rho^{-1}_{\vec{G}-\vec{G}''}[\lambda_{\vec{G}''-\vec{G}'}(\vec{k}+\vec{G}')_\ell(\vec{k}+\vec{G}'')_i \\ & + \mu_{\vec{G}''-\vec{G}'}(\vec{k}+\vec{G}')_i(\vec{k}+\vec{G}'')_\ell]u^\ell_{\vec{k}+\vec{G}'} \\ & + \sum_{\vec{G}''}[\rho^{-1}_{\vec{G}-\vec{G}''}\mu_{\vec{G}''-\vec{G}'}\sum_j(\vec{k}+\vec{G}')_j(\vec{k}+\vec{G}'')_j]u^i_{\vec{k}+\vec{G}'}\}.\end{aligned} \tag{20}$$

If the infinite series is approximated by a sum of N reciprocal vectors, Eq. (20) is reduced to a $3N \times 3N$ matrix eigenvalue equation which can be solved numerically. In all the cases considered here, N did not exceed 350. The accuracy of the results is better than 2%. In the full elastic case ($\mu \neq 0$), the N must be greater compared with the N used in the scalar case, for the same contrast of velocities and the same accuracy. For ρ constant, Eq. (21) is reduced to a symmetric matrix; on the contrary if $\rho_i \neq \rho_o$ Eq. (20) is of a general matrix form.

Results

We have examined the effects of a non constant density (Eq. (4)) in a recent paper (Sigalas and Economou, 1992a) and the main conclusion was that by increasing $y \equiv \rho_i/\rho_o$ from one, the gaps tend to disappear; however, when y becomes smaller than

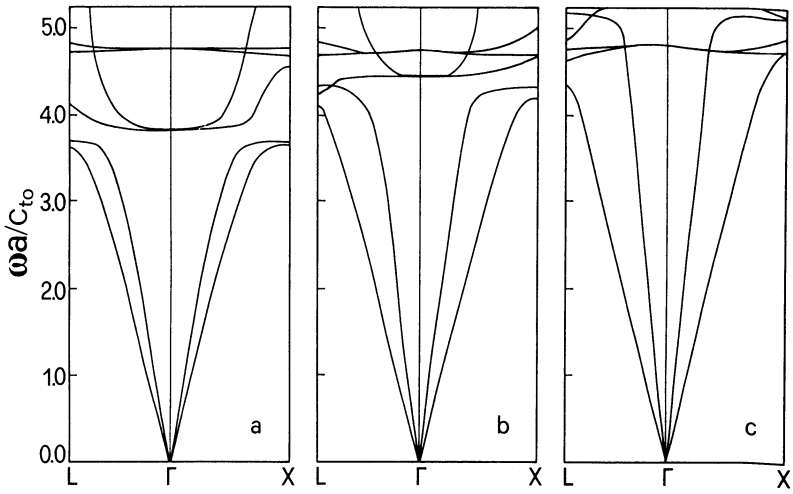

Figure 10. The band structure across L-Γ-X axes for EL waves in an fcc lattice with x=0.144, $\rho_i/\rho_o = 1$, $c_{to}/c_{ti} = 5.48$ and $c_\ell/c_t = \sqrt{2}$ (a), 2 (b), 2.83 (c) everywhere; a is the lattice constant.

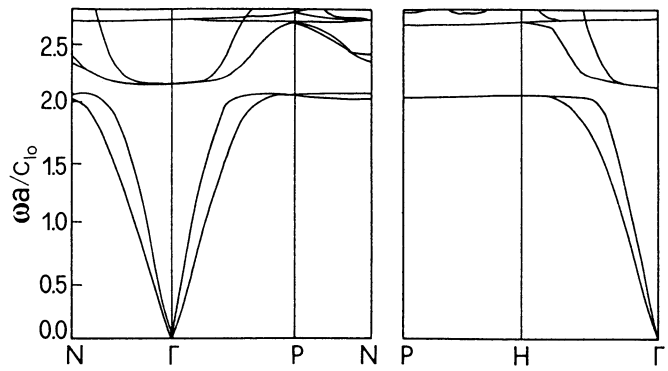

Figure 11. The band structure for EL waves in a bcc lattice with x=0.144, $\rho_i/\rho_o = 1$, $c_{to}/c_{ti} = 5.48$ and $c_\ell/c_t = \sqrt{2}$ everywhere; a is the lattice constant.

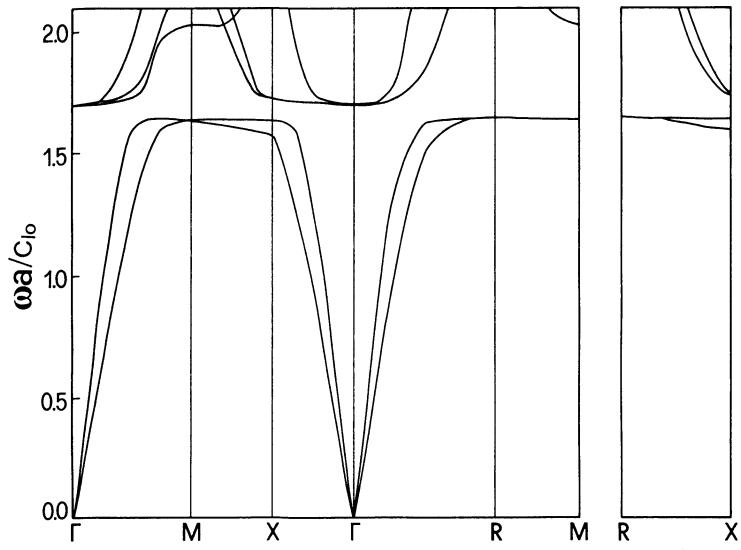

Figure 12. The band structure for EL waves in an sc lattice with x=0.144, $\rho_i/\rho_o = 1$, $c_{to}/c_{ti} = 5.48$ and $c_\ell/c_t = \sqrt{2}$ everywhere; a is the lattice constant.

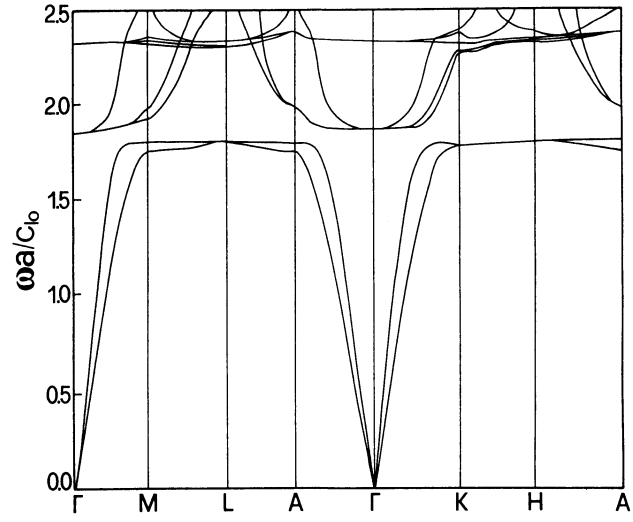

Figure 13. The band structure for EL waves in an sh lattice with $c/a = 3/4$, x=0.144, $\rho_i/\rho_o = 1$, $c_{to}/c_{ti} = 5.48$ and $c_\ell/c_t = \sqrt{2}$ everywhere; a and c are the lattice constants.

one, the bands tend to be narrower and the gaps gets wider. Hereafter, we consider the full elastic case ($\mu, \lambda \neq 0$, Eq. (19)), first for y=1 and then for y$\neq$1.

We checked first the limiting "empty lattice" case (λ, μ, ρ = constants). We found numerically that the band structure are fully separated into transverse (T) and longitudinal (L) modes which have a free plane wave structure in perfect agreement with our theoretical results; also the T modes are double degenerate. For $\lambda_i \neq \lambda_o$ and μ, ρ are constant everywhere the T bands remains free plane waves-like but the L bands are qualitatively similar (but not identical) with that obtained from the SSW equation. For $\lambda_i \neq \lambda_o$ and $\mu_i \neq \mu_o$ the band structure for both T and L modes departs from free plane wave structure. By increasing the contrasts $c_{\ell o}/c_{\ell i}$ and c_{to}/c_{ti}, it is more difficult to separate the bands into T and L parts.

In Fig. 10 we plot the band structure across L-Γ-X axis for the fcc structure. In the first panel (Fig. 10a), the case $c_{\ell o}/c_{to} = c_{\ell i}/c_{ti} = \sqrt{2}$ (which is the lowest possible realistic value of the ratio c_ℓ/c_t (Landau and Lifshitz, 1959)) is shown in which the first gap is already present. There are a single and a double degenerate bands below as well as just above the gap; two nearly flat bands are located at higher frequencies (Fig. 10a). By increasing the ratio c_ℓ/c_t (Figs. 10b,c) the bands go up to higher frequencies except the flat bands which remain nearly unchanged; also, the single band below the gap rises more rapidly than the double degenerate bands. Thus, the gap disappears. So the extreme $c_\ell/c_t = \sqrt{2}$ (both inside and outside the sphere) case, in which the L and T bands have the strongest mixing, seems to provide the most favorable condition for gaps to appear.

In Figs. 11, 12 and 13, we plot the band structures for bcc, sc, and sh structures, respectively, for characteristic cases in which the first gap has already appeared. In all these band structures there is a single and a double degenerate band below the gap; these bands become flat near the edge of the Brillouin zone; thus, a sharp peak appears in the DOS as we can see from the DOS of the bcc structure. Also, for frequencies just above the gap we find a single and a double degenerate band; these bands coincide and become flat near the center of the Brillouin zone, so another sharp peak appear in the DOS. For higher frequencies the bands have a more complicated form which depends on the structure. In lattices with a base such as diamond there are six bands below the gap (Sigalas and Economou, 1992a).

We examine now the effect of increasing the contrast $r \equiv c_{to}/c_{ti}$ on the band structure, especially on the appearance of gaps. In particular, for the bcc structure and x=0.144, $c_\ell/c_t = \sqrt{2}$ we found the gap along $\Gamma - N$ (Σ) axis is more difficult to appear as compared with $\Gamma - H$ (Δ), $\Gamma - P$ (Λ) axis. For r just below 4.6, for which the first gap just opens, the single band below the gap has a crossing point across the Σ axis with the first double band just above the gap. So at the N point, this single band has a greater value than the double band which also splits into two bands (Fig. 11); in contrast, the first gap has already appeared in all the other axes.

For r just above 4.6, the first gap has appeared in all the directions but has the smaller size at the N point; also, the double band just above the gap has a minimum at N point so this gap is direct. For higher r, the double band above the gap has a minimum at Γ point, as for example in Fig. (11), so the gap is indirect; also, the single and the double degenerate bands below the gap coincide at the P and H points, but not at the N point (Fig. 11). Similar behavior exists in the other lattices considered here. For sc (Fig. 12) and sh (Fig. 13) structures, it is more difficult to find gap across $\Gamma - X$ and $\Gamma - A$ axis, respectively. In Fig. 12 we present a case where the double band just above the gap is nearly flat across $\Gamma - X$ axis of the sc structure, thus by increasing the contrast r above 5.5, the gap changed from direct to indirect.

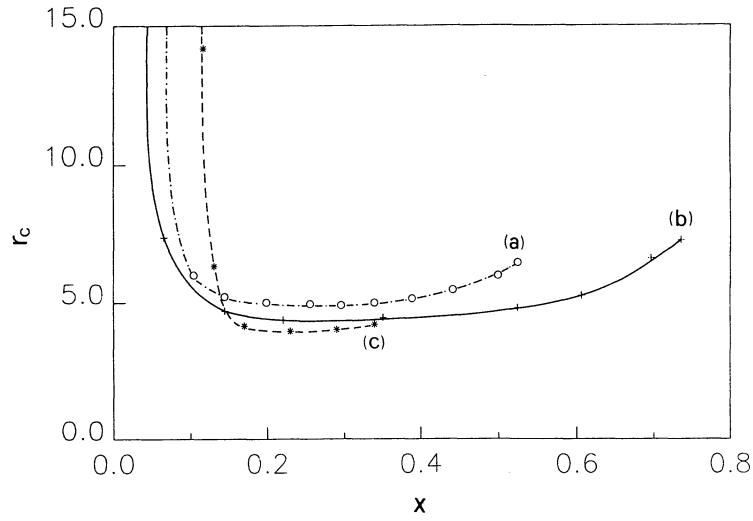

Figure 14. The threshold value, r_c, of the contrast $r = c_{\ell o}/c_{\ell i}$ for which the first frequency gap just opens plotted against the volume fraction x for elastic waves in an sc (a), fcc (b), and diamond (c) lattice with $\rho_i/\rho_o = 1$ and $c_\ell/c_t = \sqrt{2}$ everywhere.

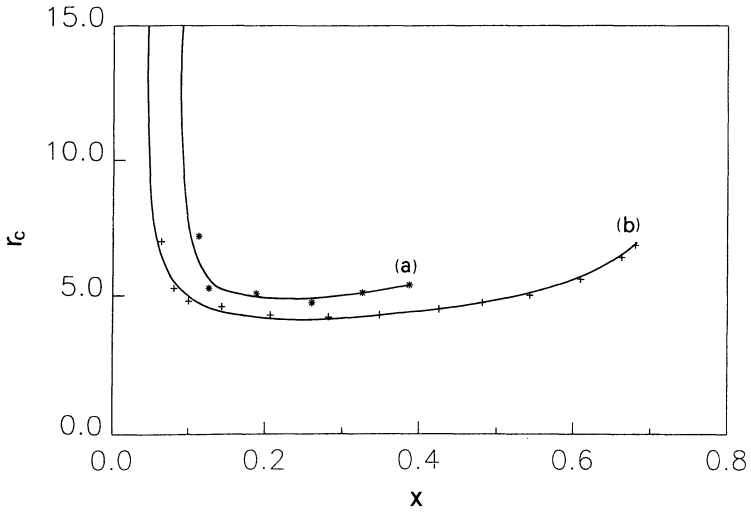

Figure 15. r_c vs x diagrams for EL waves in sh with $c/a = 3/4$ (a) and bcc (b) lattice with $\rho_i/\rho_o = 1$ and $c_\ell/c_t = \sqrt{2}$ everywhere; a and c are the lattice constants.

The threshold value, r_c, of the ratio r for which the first gap just opens as a function of the filling fraction x is shown in Figs. 14 and 15 for different lattices. We remind the reader there is no gap for x smaller than x_i and greater than x_u. The r_c vs x curve has a minimum at $x = x_m$ for which $r_c = r_c^m$. The value of x_i (Figs. 14 and 15) range from 0.05 (in fcc structure) to 0.11 (in diamond structure). We have not considered the case of overlapping spheres, so we do not know the exact values of x_u. It is difficult to pinpoint the exact value of x_m because the r_c is nearly constant for $x \approx 0.2 - 0.4$ for all the structures considered here; nevertheless, the values of x_m seem to be in the range from 0.20 to 0.30. The value of r_c^m is minimum in diamond ($r_c^m \approx 4$) and maximum in sc and sh structures ($r_c^m \approx 5$). In fcc and bcc structures $r_c^m \approx 4.2$. For the sh structure the optimum value of c/a is about 0.8 for reasons similar to those described in the scalar case (section II).

We have also considered the case where the spheres are the high velocity material surrounded by the low velocity material for the fcc structure (Fig. 16). Due to the fact that we considered only cases with non overlapping spheres, our fcc's results are restricted to $x \geq 0.26$. From Fig. 16 we can see there is no gap for x larger than about 0.5 and that r_c is nearly the same for x=0.3 and 0.26, so we expect that x_m will not be much smaller than 0.25 and r_c^m is not much below 7.5; this contrast is greater from that found in the opposite case where the high velocity material surrounds the low velocity spheres. Similar behavior appears in the scalar waves while in the EMW case gaps are found more easily when the scatterers (i.e., the low velocity material) are simply connected to form a network running through the entire composite system.

Comparing the ELW case with the SSW and EMW case, we find the x_m for ELW is much greater than x_m for SSW waves but it is nearly the same with the corresponding x_m for EMW. However, the values of r_c^m for elastic waves are at least twice as large as the r_c^m for SSW and EMW. The reason seems to be related with the well-known fact (Economou and Zdetsis, 1989) that the gaps are due to destructive multiple scattering interference. In the EL case we have both T and L waves mixed together in the interference process which makes the proper conditions for destructive interference more difficult to satisfy. Furthermore, the velocity ratio of L and T waves cannot become, in practice, smaller than $\sqrt{2}$; the resulting frequency mismatch makes the destructive interference more difficult. For the same reason, the ratio $\delta\omega/\omega_g$ (where $\delta\omega$ is the size of the gap and ω_g is the midgap frequency) for elastic waves is at least by a factor of two smaller as compared with SSW (Leung and Liu, 1990a) and EMW (Ho et al., 1990) case ($\delta\omega/\omega_g$ has a maximum of about 0.06 for ELW waves and 0.2 for both SSW and EMW). If we plot the ratio $\delta\omega/\omega_g$ relative to $r \equiv c_{to}/c_{ti}$ for constant value of x, we find that $\delta\omega/\omega_g$ is zero for $r < r_c$ (r_c is the value of r for which the first gap just opens), $\delta\omega/\omega_g$ increases rapidly for r just above r_c and $\delta\omega/\omega_g$ becomes nearly constant for higher values of r.

Finally, we consider the effects of the non-constant density. In Fig. 17b we plot the band structure across the L-Γ-X axis for the fcc lattice and $y \equiv \rho_i/\rho_o = 1$. In that case a narrow gap has already appeared. For smaller values of y (Fig. 17a) all the bands go to higher frequencies but the bands below the gap rise more rapidly; thus the gap tends to disappear. On the contrary, by increasing y (Fig 17c), the bands bellow the gap go down to smaller frequencies but the minimum of the bands above the gap remain at about the same frequency while these bands become flatter, so the gap becomes wider. If $\delta\omega_1$ and $\delta\omega_2$ are the size of the gaps for y=1, 4, respectively, the ratio $\delta\omega_2/\delta\omega_1 \approx 3$. As discussed in the beginning of this section, the ASW exhibit completely opposite dependence on y. We have no simple physical interpretation for this unexpected result.

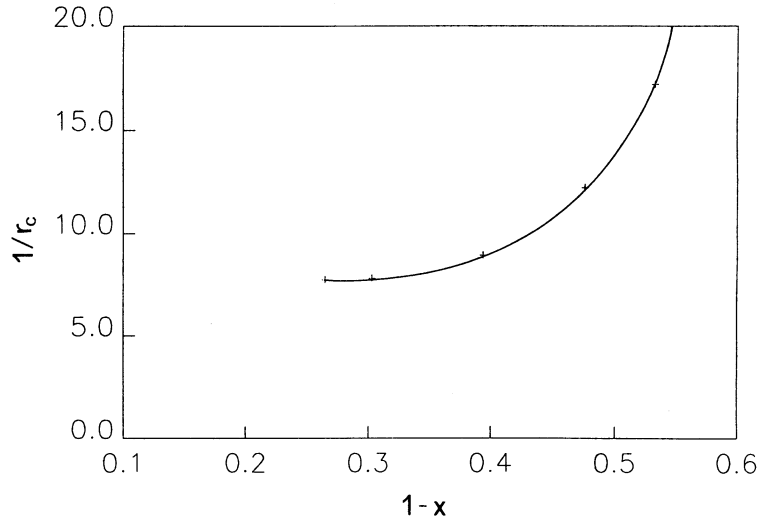

Figure 16. The critical contrast $r_c \equiv (c_{lo}/c_{li})_c$ vs the volume fraction, x, of the low sound velocity material for EL waves in the fcc lattice with $\rho_i/\rho_o = 1$ and $c_\ell/c_t = \sqrt{2}$ everywhere. The sphere in this case is the high sound velocity material.

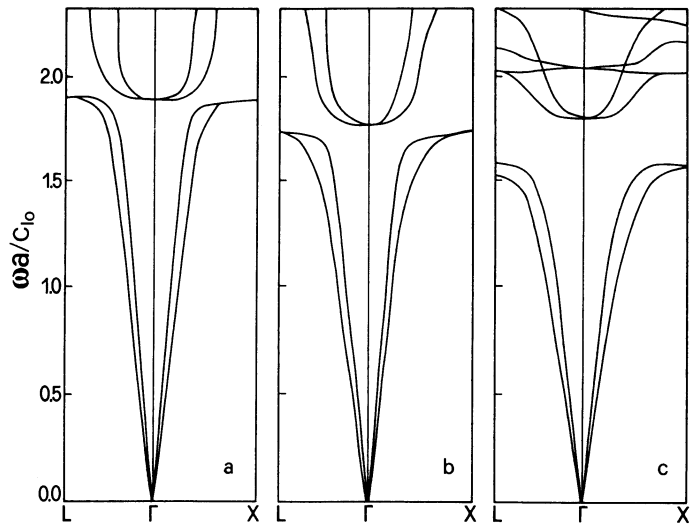

Figure 17. The band structure across L-Γ-X axis for EL waves in the fcc lattice with x=0.144, $c_{to}/c_{ti} = 8.66$, $c_\ell/c_t = \sqrt{2}$ everywhere and ρ_i/ρ_o =0.25 (a), 1 (b), 4 (c).

CONCLUSIONS

We reported results of a systematically comparative study of classical wave (CW) propagation in periodic structures consisting of spheres placed in a host material. We considered simple scalar waves (SSW), acoustic scalar waves (ASW), electromagnetic waves (EMW), and elastic waves (ELW) propagating in fcc, bcc, sc, diamond, sh, and hcp structures. We used both the APW and PW methods. Although both methods gave the same results, the PW approach is preferable because of its simplicity and its ability to go beyond the muffin-tin scheme. We focus our attention to the question of the appearance of frequency gaps. Frequency gaps in CW correspond to gaps above the maximum value of the potential for the electronic case. As a result of this, frequency gaps in CW are more difficult to obtain, they tend to be narrower and easier to eliminate through a disordering procedure.

The only case where wide gaps and narrow bands (reminiscent of a tight binding electronic case) appear is for ASW propagating in a liquid with periodically placed bubbles (i.e., $\mu = 0$, $\rho_i/\rho_o \ll 1$). In all of the other cases, especially ELW, one must go to rather extreme conditions to obtain gaps.

For SSW the appearance of the first gap requires, under optimum conditions ($x_m \approx 0.1 - 0.15$), a velocity ratio, r, of about 2 or larger for fcc, bcc, sh (for $c/a \approx 0.8$) structures. For sc and sh (c/a either smaller or greater than 0.8) the minimum value of r is larger. In lattices with a base (as diamond and hcp), the first gap does not exist because the first zone is doubly degenerate at certain high symmetry k-points.

For EMW we found gaps only in the diamond lattice. In all the other structures considered here, it was not possible to find a true gap at least in the frequency ranges we studied, because there are crossings of the bands at certain high symmetry k-points in frequency regions where the gaps could be open. However, pseudogaps developed at the frequencies of crossings. In the diamond lattice, under optimum conditions ($x_m \geq 0.34$), the minimum velocity ratio is about 2.2, which is nearly the same as the corresponding value in the scalar case, but x_m is considerable greater than the corresponding value in the scalar case. So the scalar wave equation cannot accurately describe the propagation of EMW in the dielectric structure (Ho et al., 1990; Leung and Liu, 1990b; Zhang and Satpathy, 1990).

Our results for the propagation of elastic waves in a periodic arrangement of spheres of radius R, density ρ_i, and sound velocities c_{ti} and $c_{\ell i}$ embedded in a medium of density ρ_o and sound velocities c_{to}, $c_{\ell o}$ show that extreme conditions are required for the appearance of gaps. Under optimum conditions ($x_m \approx 0.2 - 0.3$, $c_\ell/c_t = \sqrt{2}$ both inside and outside the spheres) the minimum required ratio of velocities is a little over 4 for diamond, 4.2 for fcc and bcc, and about 5 for sc and sh. Increasing the ratio ρ_i/ρ_o above one improves the chances for the appearance of gaps. Thus, in order to obtain gaps in ELW propagation, we need sphere and host materials with c_ℓ/c_t as close as possible to $\sqrt{2}$ (which is the minimum realistic value of c_ℓ/c_t). The sphere material must be a high density, low velocity material while the host material must have a low density, high velocity. Possible candidates for sphere material are Bi ($c_\ell = 2.27\,Km/sec$, $c_\ell/c_t = 2$, $\rho = 9.8\,gm/cm^2$), RbI ($c_\ell = 2.245\,Km/sec$, $c_\ell/c_t = 1.87$, $\rho = 3.55\,gm/cm^2$), etc (Anderson 1965). As host materials one may consider: Be ($c_\ell = 13.11\,Km/sec$, $c_\ell/c_t = 1.44$, $\rho = 1.85\,gm/cm^2$), Al_2O_3 ($c_\ell = 10.85\,Km/sec$, $c_\ell/c_t = 1.69$, $\rho = 3.97\,gm/cm^2$), TiO_2 ($c_\ell = 9.27\,Km/sec$, $c_\ell/c_t = 1.8$, $\rho = 4.26\,gm/cm^2$), Si ($c_\ell = 8.94\,Km/sec$, $c_\ell/c_t = 1.67$, $\rho = 2.33\,gm/cm^2$), MgO ($c_\ell = 9.59\,Km/sec$, $c_\ell/c_t = 1.59$, $\rho = 3.59\,gm/cm^2$), etc (Anderson, 1965). From the above examples one can see that the experimental realization of frequency gaps in EL waves will be rather

difficult but not impossible. As a matter of fact we found that lead or gold spheres in a silicon host do produce gaps (Sigalas and Economou, 1992b).

We conclude by pointing out that the introduction of a gradual disordering procedure in the periodic structures studied here will produce the following effects: Tails of localized states will appear in the gaps; these tails will eventually fill up the gaps giving rise to regions of localized states. A further increase of the disorder will increase the DOS in the regions (where the gaps were) while the eigenstates there will probably become delocalized. In the regions of pseudogaps or very low DOS, the introduction of disorder at the beginning may possibly lead to the appearance of narrow regions of localized states, which will most probably become delocalized as the disorder increases further.

Acknowledgments

This work was partially supported by NATO Grant No.RG769/87.

REFERENCES

* present address: Ames Laboratory, Physics Department, Iowa State University, Ames Iowa 50011-3020.

Anderson, O. L., 1965, in: "Physical Acoustics III," W. P. Mason, ed., Academic Press, New York.

Economou, E. N., and Soukoulis, C. M., 1989, *Phys. Rev.* B40:7977.

Economou, E. N., and Zdetsis, A., 1989, *Phys. Rev.* B40:1334.

Flax, L., Gaunaurd, G., and Uberall, H., 1981, in: "Physical Acoustic XV," Mason, W.P.,and Thurston, R.N., eds, Academic,New York.

Ho, K. M., Chan, C. T., and Soukoulis, C. M., 1990, *Phys. Rev. Lett.* 65:3152.

John, S., Sompolinsky, H., and Stephen, M. J, 1983, *Phys. Rev.* B27:5592.

John, S., 1988, *Comments Cond. Matt. Phys.* 14:193.

John, S., 1991, *Physics Today* 40:32.

John, S., and Rangarajan, R., 1988, *Phys. Rev.* B38:10101.

Lai, W. M., Rubin, D., and Krempl, E., 1978, "Introduction to Continuum Mechanics," Pergamon Press,Oxford.

Landau, L. D., and Lifshitz, E. M., 1959, "Theory of Elasticity," Pergamon, London.

Leung, K. M., and Liu, Y. F., 1990a, *Phys. Rev.* B41:10188.

Leung, K. M., and Liu, Y. F., 1990b, *Phys. Rev. Lett.* 65:2646.

Mattheiss, L. F., Wood, J. F., and Switendick, A. C., 1968, *Methods Comput. Phys.* 8:63.

Papaconstantopoulos, D. A., 1986, "The Band Structure of Elemental Solids," Plenum Press, New York.

Satpathy, S., Zhang, Z., and Salehpour, M. R., 1990, *Phys. Rev. Lett.* 64:1239.

Sheng, P. , ed., 1990, "Scattering and Localization of Classical Waves in Random Media," World Scient., Singapore.

Sigalas, M., and Economou, E. N., 1992a, *Journal Sound Vibr.* 158:377.

Sigalas, M., and Economou, E. N., 1992b, unpublished.

Soukoulis, C. M., Economou, E. N., Grest, G. S., Cohen, M. H., 1989, *Phys. Rev. Lett.* 65:575.

Yablonovitch, E., 1987, *Phys. Rev. Lett.* 58:2059.

Yablonovitch, E., and Gmitter, T. J., 1989, *Phys. Rev. Lett.* 63:1950.

Zhang, Z., and Satpathy, S., 1990, *Phys. Rev. Lett.* 65:2650.

EXPERIMENTAL OBSERVATION OF BENDING WAVE LOCALIZATION

George Cody,[1] Ling Ye,[1] Minyao Zhou,[1] Ping Sheng,[1]
and Andrew N. Norris[2]

[1]Exxon Research & Engineering Co., Rt. 22 East, Annandale, NJ 08801

[2]Department of Mechanical & Aerospace Engineering,
Rutgers University, P. O. Box 909, Piscataway, NJ 08855

ABSTRACT

Localization of bending waves has been observed for the first time for two-dimensional (2-D) acoustic wave propagation in an inhomogeneous (rough) composite system consisting of a steel plate decorated with Lucite blocks. A significant experimental feature of the localized modes is an exponential decay of the mode intensity from their peaked centers, with a decay length that increases as $(f_0 - f)^{-1}$ when the mode frequency f approaches a quasi-mobility edge f_0. The minimum attenuation length is of the order of a block diagonal and is about 40% of the bending wave's wavelength. The experimental data, as well as results of finite-element calculations, suggest that the source of the localization phenomenon is strong scattering of the bending wave by shear resonances of the Lucite blocks. This result supports the theoretical prediction that resonant scattering enhances localization. It suggests that the bending-wave regime of a composite plate is particularly convenient for the study of classical localization in 2-D and at higher frequencies in 3-D. Finally, the generic nature of the localization phenomenon suggests its potential use as a tunable attenuation mechanism for bending waves.

INTRODUCTION

We report on the first direct observation of localized elastic waves in a composite two-dimensional system - propagation of bending waves of a steel plate decorated with Lucite blocks. Bending waves,[1-3] or flexural waves, are a hybrid between shear and longitudinal waves where the top and the bottom of a plate, beam, or rod undergo compressional and extensional deformations. The bending wave is governed by the full compressional and shear wave equations,[3] but its properties can also be derived by a simple bending wave theory.[4] The critical assumption of this theory is that the plate (beam or rod) cross section remains rigid during the bending wave deformation. This condition is realized when the plate (beam or rod) thickness is much less than the wavelength of the bending wave. For plate (beam or rod) thicknesses comparable to the wavelength of either the shear, longitudinal, or bending wave wavelength, a full 3-D calculation is required.

The propagation of elastic waves in an infinite homogeneous plate has been extensively studied, and a number papers can be found on the calculation of both bending

Photonic Band Gaps and Localization, Edited by
C.M. Soukoulis, Plenum Press, New York, 1993

wave dispersion and wave propagation in thick and thin plates.[1-5] Wave propagation in either the thin or thick plate regimes for layered composite plates has received less attention - experimentally and theoretically. Indeed, the present experiments were motivated by recent experimental observations on wave propagation in rough, inhomogeneous steel-refractory composite walls[6] at frequencies well above the bending wave regime where the wall thickness was comparable to the longitudinal wavelength. In these experiments, the vibrational signals measured were found to attenuate exponentially with distance away from the excitation point and in addition, localized resonances were observed. These result disagree with the classical theory for smooth composite walls,[7] and suggested to us that random roughness of the wall might play an important role on the observed wave behavior. The present experiments on bending wave propagation in a rough steel plate-Lucite Composite system were designed to explore localization phenomena in both the thin (2-D, and thick (3-D) regimes. We report here on the first stage of this study.

The concept of wave localization was first proposed by Anderson in the context of electronic transport in disordered materials.[8] In its general outline, the theory of localization[9] predicts that no wave, quantum or classical, can be transported indefinitely in a one- or two-dimensional disordered system. In contrast, for a three-dimensional random medium, waves can be localized in some frequency regimes but delocalized outside of these regimes. The frequencies separating the localized from the delocalized regimes are usually denoted as the "mobility edges." Over the past three decades, the importance of the localization concept in the physics of electronic transport and metal-insulator transition has been extensively documented.[10] However, as a phenomenon in itself, Anderson localization has eluded direct observation in electronic systems. This is due to both the difficulty in mapping electronic wave functions, as well as the difficulty in isolating Anderson localization from ever-present electron-electron interaction and consequent many-body effects. The fact that such intrinsic difficulties are absent in classical wave systems is one reason why the study of both elastic wave and light localization has received so much experimental and theoretical attention in recent years.[11-13]

Our experiments on the steel-Lucite system have led to the discovery that strong resonant scattering of bending waves leads to spatial localization of the bending wave over a broad frequency range. The localized mode of the bending wave is characterized by a peaked center, with an exponentially-decaying intensity envelope away from the center. Spatial orthogonality of the localized mode has been demonstrated using a point excitation with a broad frequency band, and it has been shown that the excited localized state is insensitive to the outside boundary conditions. Measurement of the frequency dependence of the decay length yields evidence for a "quasi mobility edge" which separates the strongly localized modes from the more extended modes, with the decay length increasing as $(f_o - f)^{-1}$ when the mode frequency f approaches the quasi mobility edge frequency f_o.

Both the experimental and theoretical results indicate that the mechanism of strong bending wave scattering by Lucite block resonances is the source of the observed localization phenomenon. The frequency spectrum of the intensity of the velocity transfer function for bending waves exhibits a pronounced frequency gap with a width of 1 kHz, and a gap attenuation of almost three orders of magnitude. The measured frequency gap and the resonance frequencies of Lucite-steel modes are coincident and can be calculated by finite element analysis or by corrections to simple quarter-wave shear and flexural resonances of the Lucite block. The gap can thus be tuned by changing the block height and this suggests its potential use as a frequency-tunable attenuation mechanism for bending waves propagating in structural walls.

MEASUREMENTS

The properties of the wave excitation generated in a homogeneous thin plate can be well understood by the classical theory of bending waves. If we define w(x,y,t) as the local vertical displacement of the plate vibration, the governing bending wave equation is[4]

$$D\nabla^4 w(x,y,t) + \rho h \frac{\partial w^2(x,y,t)}{\partial t^2} = q(x,y,t), \quad (1)$$

where ρ is the density of the plate, h is the thickness, $D = Eh^3/12(1-\sigma^2)$, and E is Young's modulus, σ is Poisson ratio, and q(x,y,t) is the excitation force. The biharmonic operator in the bending wave equation reflects both the compression and the extension characters of the plate bending deformation. The general dispersion relation for bending waves in a thin plate ($h \rightarrow 0$) can be obtained from the above equation as $\omega = k^2 \sqrt{\frac{D}{\rho h}}$.

The excitations of an elastic plate with a finite thickness can, in general, be divided into two frequency regimes.[14] Due to the finite thickness of the plate, excitations in the vertical direction have a discrete spectrum, with a non-zero minimum frequency, f_L , given by f_L = (shear wave speed)/2h for the plate. For $f \leq f_L$ the excitation modes may be regarded as two-dimensional, both in the sense that $h/\lambda < 1$, and more importantly, that wave transport occurs only in the two directions parallel to the plate. For $f \geq f_L$, plate excitations acquire an increasingly 3D character. For a one-inch steel plate, f_L = 65kHz. In the frequency range, from 0 - 6 kHz, of the present experiment only two circularly-symmetric modes exist: the bending wave, the displacement of which is transverse in nature and perpendicular to the plate, and a longitudinal wave, where the displacement is compressional and in the plane of the plate. In the present experiment, unless otherwise noted, only the bending wave is excited by the impact source, as well as measured by the detector.

The experimental system consists of a 1.83m x1.83m x 2.54 cm (6 ft. x 6 ft. x 1 inch) steel plate set on four vibration-isolation supports. To reduce edge reflections, a 2.54 cm x 2.54 cm (1 inch x 1 inch) glass bar was glued around the four sides of the steel plate, and the exposed sides of the glass bar were sealed with a flexible viscoelastic damping material (GP-3 manufactured by Soundcoat Co.). This treatment reduces the edge reflection coefficient for $f \geq 2$ kHz to ≈ 0.5 as estimated from the quality factor of the finite-plate resonances; it has little effect on the edge reflections below 2 kHz. If necessary, a suitable graded interface on the boundary can reduce the reflection coefficient well below 0.5. The effect of edge reflections on the processed data can be reduced by appropriate windowing in the time domain.

The excitation source used in the experiment is a B&K force transducer (#8203), which produces a pulse 0.025 - 0.04 ms in duration in an area less than 1 mm^2 . The frequency content of the pulse is flat within 10% from 0 to 6 kHz. The detector is a B&K accelerometer (#4384), which is magnetically attached to the plate and measures the local vertical acceleration. Due to the highly polished contact surfaces of the accelerometer magnet and the plate, no contact, or mounting, resonance is found up to 25 kHz. The signals from both the force transducer and the accelerometer are analyzed with a Dual Channel Signal Processor (B&K 2032), whose output is the transfer function $H(f) = \langle a(f)*F(f)\rangle / \langle F(f)*F(f)\rangle$, where a(f) denotes the Fourier transform of measured acceleration, F(f) is the Fourier transform of the excitation force, * denotes complex conjugation, and the angular brackets denote averaging over repeated excitation-detection measurements under the same condition (synchronous time averaging). H(f), in units of inverse mass, expresses the acceleration response of the system as a function of frequency for a given source-receiver configuration. A comparison of the experimental spatial intensity distribution of the transfer function in the bare steel plate excitation at 1.5 kHz with bending wave calculations[15] shows excellent quantitative agreement, including the separation between the intensity maxima of 39 cm.

Two sets of Lucite blocks, two hundred for each set (8.89 cm x 8.89 cm x 7.62 cm (x 6.35 cm)), were solidly bonded to the steel plate in either a periodic checkerboard pattern or a random arrangement. The solid bond between the Lucite and steel was made by locally heating the plate above the melting point of Salol.[16] Salol was chosen as a low melting point solid contact to eliminate absorption due to viscoelasiticity of the interface. The Salol contact is visibly non-uniform because Salol does not wet Lucite when it is in the liquid state. Thus,

even with a periodic arrangement of blocks, there remains significant randomness in the steel-Lucite contacts.

Measurements of the composite system excitations were carried out with two types of source-receiver configurations. In each, both the hammer and accelerometer are on the side of the steel plate opposite to the bonded Lucite blocks. The first type of measurement configuration (Type I) is a point source-point detector arrangement. The second type (Type II) is a line source-line detector where the average defining the transfer function includes the coherent addition of point source excitations along a line, with detectors also placed along a line parallel to the excitation line. Type II measurements smooth the fluctuation of the frequency spectrum of the transfer function for point measurements resulted from the reverberation of the bending wave propagation in the finite plate. In addition, for Lucite blocks arranged in the checkerboard pattern, the Type II measurements represent an average over different **k** vectors.

DATA AND DISCUSSION

In this section, we present the experimental results on bending wave localization and compare these results to a finite-element calculation of the resonance modes of the Lucite/steel unit. We also discuss the effects of the periodicity in the Lucite block arrangement, as well as the effects of energy dissipation due to the vibrational damping of Lucite blocks.

Figure 1 displays the frequency response of the composite system displacement velocity (displayed[17] as $|H(f)|^2/f^2$) in the case where the Lucite blocks are arranged in a periodic "checker-board" configuration, and where the measurements were made with the Type II method with the source and detector "lines" parallel to one side of the plate and separated by 160 cm. The data shown have been "windowed" to remove the effect of edge reflections. Three frequency regimes are seen in Fig. 1. For $f < 2$ kHz and $f > 3.5$ kHz, the response is characterized by broad frequency continuum, where the response of the block loaded plate is roughly comparable to the response of the bare steel plate shown by the dotted line. The most striking feature of Fig. 1 is the third regime, the frequency band between 2 kHz $< f <$ 3.5 kHz. In this frequency band, the bending wavelength is on the order of two to four Lucite blocks, and the square of the transfer function is two to three orders of magnitude smaller (essentially indistinguishable from noise) than the response in the other two regimes. The same frequency gap exhibited in Fig. 1 is found when the source-detector lines are rotated 45°. Furthermore, the observed frequency gap is not affected by reflections from the boundary of the finite steel plate. This has been shown by noting the change in $|H(f)|/f$ when the time window is removed. Only minor changes occur in the transmission bands and there is no change in the gap. The gap shown in Fig. 1 is thus isotropic and independent of boundary reflections.

The spatial intensity distributions of the modes at five different frequencies are also exhibited in Fig. 1. These distributions were mapped with a fine mesh of detector locations (Type I measurement configuration for a fixed source located at the plate center). For $f = 1.5$ kHz and $f = 4.4$ kHz, the mode configurations are essentially identical to those for the bare steel plate. The intensity patterns of the modes at these two frequencies show that the attenuation length of the composite system is at least the size of the system, since the effect of boundary reflection in establishing the modal structure is easily seen.

In contrast, within the gap region (2 kHz - 3.5 kHz) the wave modes are clearly localized, with each of the localized modes characterized by a high peak, the position of which is independent of the source position (as long as the source remains inside the spatial domain where the mode has significant amplitude), with an isotropic exponentially decaying envelope. In terms of amplitude, the decay length is as small as 12 cm at 2.8 kHz, of the order of the Lucite block diagonal. This surprisingly small localization length, 40% of the bending wavelength at 2.8 kHz, can only be understood on the basis that the strong interaction between the Lucite blocks and the steel plate has completely altered the character of the bending wave. Furthermore, excitation of the plate outside the localized

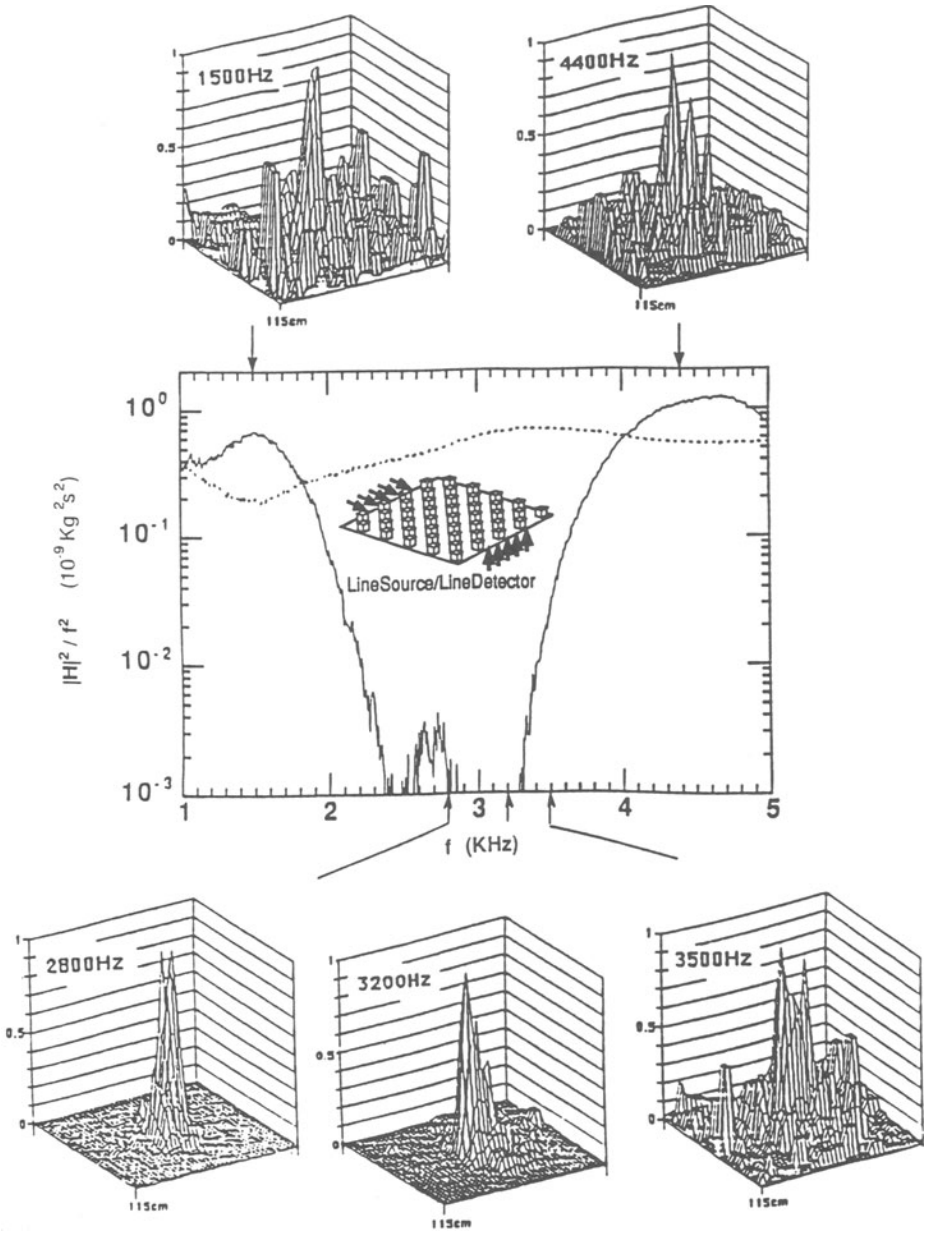

Figure 1. The square of the magnitude of the velocity transfer function, expressed as $|H(f)|^2/f^2$, for the Type II measurement configuration with a line source line detector separation of 160 cm. The inset is a schematic drawing of the measurement configuration - two hundred Lucite blocks (8.89 x 8.89 x 7.62 cm) bonded to the steel plate in a checkerboard pattern. $|H(f)|^2/f^2$ is obtained from time domain data filtered by a 3.5 ms time window to minimize residual edge reflections. The measured bare steel plate response is shown by the dashed line for comparison. Localized modes are clearly seen in the frequency gap extending from 2.2 kHz $\rightarrow$ 3.5 kHz. as shown in the 3D plots which show the measured bending wave intensity patterns produced by a point source at the center of the plate at five different frequencies.

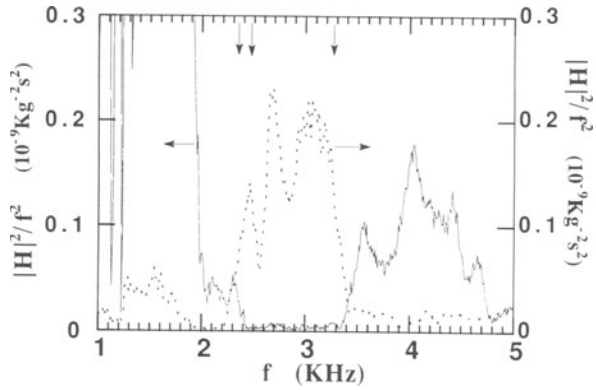

Figure 2. The solid line denotes the square of the magnitude of the velocity transfer function, $|H(f)|^2/f^2$, for the Type I measurement configuration at a source detector separation of 160 cm where the same Lucite blocks as in Fig. 1 are randomly bonded to the steel plate, as illustrated in the inset. Fig. 2 exhibits the same gap as in Fig. 1, but the response outside the frequency gap is different as would be expected from effect of the lack of periodicity on the extended states. The dashed line and the righthand scale denote the square of the magnitude of the block horizontal velocity transfer function for the point source-point detector configuration at a separation of 80 cm when the source is present on the steel plate and the detector is on the side of a Lucite block. The three peaks delineated by the dashed line represent resonance modes of the Lucite block. The vertical arrows indicate the frequency positions of flexural resonances obtained by finite element calculations as discussed in the text.

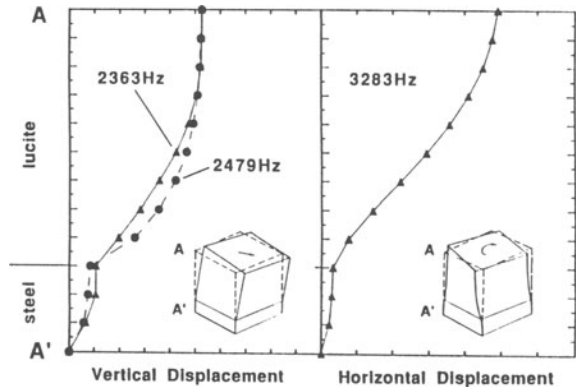

Figure 3. The vibrational configurations of the three flexural resonance modes calculated by the finite-element method. In the lefthand figure, the vertical displacement is plotted, in arbitrary units, along the line AA'. For the two lower-frequency modes, at 2.363 kHz and 2.479 kHz, the dominant motion is represented by the relative flexure of the upper Lucite block surface relative to the steel plate along the diagonal direction, accompanied by a slight relative vertical shift of the two corners. In the righthand figure, the configuration of the higher frequency resonance at 3.28 kHz is shown. For this torsional/shear mode, the horizontal displacement along the line AA' is exhibited.

domain displays a "quiescent state" of the system where the vertical displacement and horizontal displacement of the Lucite blocks (as measured by detectors placed on top and side) fall below background and system noise.

Figure 1 displays the system response with the Lucite blocks arranged periodically in a checkerboard array, and it is tempting to associate the frequency gap with coherent scattering due to periodicity. This association is easily shown to be false. In Fig. 2 the solid line gives the frequency response of the system, measured with the Type I arrangement, where the Lucite blocks are not in a checkerboard array, but randomly arranged. The frequency gap observed in Fig. 1 for a periodic array is identical to that shown in Fig. 2 for the random array. The frequency response outside the gap in the extended state regime does exhibit differences for the random configuration compared to the periodic case. This difference is expected, since for extended states the frequency response is a function both of the coherent reflections from the Lucite blocks as well as boundary reflections.

Inside the frequency gap, localized modes on the Lucite blocks are found for the random arrangement as in the periodic case. However, the profiles of the localized modes are more varied, with some exhibiting multiple intensity peaks. The presence of the frequency gap in both periodic and random configurations demonstrates that coherent scattering due to block periodicity is not the source of the gap and implies that random resonant scattering due to the imperfect and random Salol bonds is sufficient to localize the bending wave. The random contacts are also the source of the observed variability in the localized modes.

We also exhibit in Fig. 2, by the dashed line, the measured horizontal displacement velocity of a Lucite block on the steel plate, when it is excited by a point impact on the steel plate 80 cm away. The three "shear" response peaks at 2.4 kHz, 2.6 kHz, and 3.1 kHz coincide remarkably well with the position of the observed frequency gap and are also in excellent agreement with the three calculated resonance frequencies using a finite element method which is described below. The width of the observed resonance modes also agrees well with the measured lifetime of the localized modes ($\approx$2 ms). We conclude that resonant scattering by the resonances of the Lucite blocks is responsible for the observed bending wave localization.

The significant role of resonant scattering in enhancing localization has been the prediction of numerous theoretical calculations.[9,18] To further explore this phenomenon, a finite-element calculation was carried out for a Lucite block bonded on the steel plate by dividing the single Lucite block into 8 x 8 x 9 elements, with traction-free boundary conditions on five sides with the sixth side, the 8.89 cm x 8.89 cm side, joined on to an 8.89 cm x 8.89 cm x 2.54 cm steel plate, where the bottom of the steel plate is fixed at four corners. The steel plate, in turn, is divided into 8x8x3 elements. A Young's modulus of 4×10^9 N/m^2, and a Poisson's ratio of 0.4, were taken for Lucite in the calculation. The three lowest vibrational eigenstates have the character of flexure and shear/torsional resonances with frequencies of 2.36 kHz, 2.48 kHz, and 3.28 kHz. These three resonances are separated by more than 1 kHz from the next higher resonance mode and span the observed frequency gap of Figs. 1 and 2.

The effect of varying the boundary condition at the Lucite-steel interface was also examined by the finite-element calculation. By changing the usual displacement and traction continuity condition to traction free at four sides of the surface but zero displacement elsewhere on the surface, it was found that all three resonances are shifted only slightly to 2.37 kHz, 2.40 kHz, and 3.22 kHz. However, the shifts can increase to as large as four hundred Hertz, that is, to 2.77 kHz, 2.79 kHz, and 3.43 kHz, if the zero displacement condition is applied to the whole surface. These shifts offer an estimate on the effect of the randomness at the Lucite-steel bonding interfaces.

The finite-element calculation gives not only the three lowest resonance frequencies, but also the resonance eigenstates. Figure 3 shows the configuration of the three resonance modes: two nearly degenerate flexural modes and one shear/torsional mode. The two lower-frequency modes at 2.36 kHz and 2.48 kHz are a consequence of the coupling between the

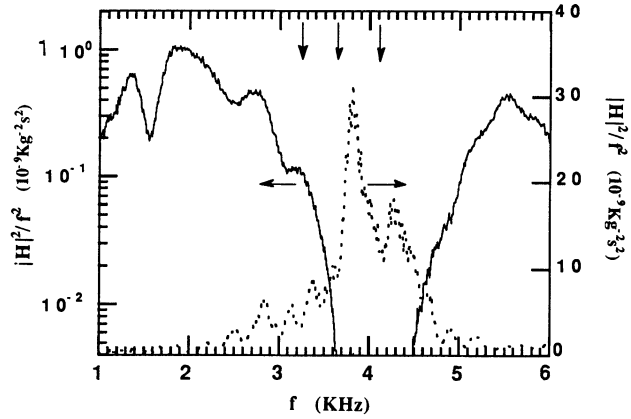

Figure 4. The square of the magnitude of the velocity transfer function, $|H(f)|^2/f^2$, for the Type II measurement configuration at a line source point detector separation of 160 cm, for smaller Lucite blocks (8.89 x 8.89 x 6.35 cm). Two hundred Lucite blocks are bonded to the steel plate in a checkerboard pattern and $|H(f)|^2/f^2$ is obtained from time domain data filtered by a 3.5 ms time window to minimize residual edge reflections. The measured bare steel plate response is also shown by the dashed line for comparison. The scale of the velocity transfer function for the plate is given by the lefthand logarithmic coordinate. The thick solid line, whose scale is given by the righthand linear coordinate, is the square of the magnitude of the horizontal velocity transfer function of the Lucite block. The vertical arrows indicate the positions of the resonance frequencies calculated by finite element analysis as described in the text.

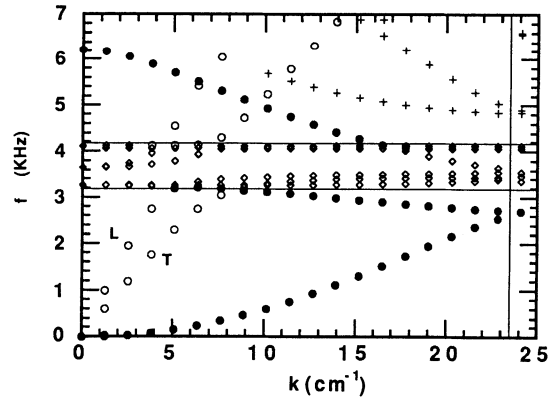

Figure 5. Dispersion relations for the excitations of an infinite steel plate decorated with a periodic array of 8.89 x 8.89 x 6.35 cm Lucite blocks in a checkerboard pattern (see Fig. 4). The Bloch wave vector k is along the [11] direction. The modes noted as T and L involve only displacements parallel to the steel plate which are not excited or detected in the present experiment. The excited bending wave is denoted by the solid circles. The solid horizontal lines indicate the region dominated by coupled Lucite resonance/bending wave modes with very low group velocity (the diamond symbols). The crosses denote bending waves from higher Brillouin zones. The vertical line corresponds to the 2D Brillouin zone and the intersection of this zone with the bending bave mode (solid circles) indicates the small acoustic gap produced by mass defect scattering.

flexural mode of the block and bending waves of the steel plate. They are split by the small vertical displacement common to the two modes, and the resulting modes involve the relative shear of the upper block surface with respect to the bottom in the diagonal directions. At the Lucite-steel interface for all three modes, the vertical displacement is in fact 8-10 times larger than the small horizontal displacement.

In the absence of coupling to the steel plate, the flexural mode of the block varies inversely with the square of the block height, L. In the limit of D/L << 1 where D denotes the block side (D = 3.5"), the flexural resonance frequency is given by the standard formula[19] for a rod flexural resonance,

$$f(n) = C_n K_m (\frac{r}{L^2}) \times 10^4. \quad (2)$$

In Eq. (2), n denotes the number of the resonance mode, C_n is the constant for the nth mode (C_1 = 11.3, C_2 = 70.85 and C_3 = 198.3), K_m is the ratio of sound extensional velocity between that of Lucite and steel (K_m = 0.35) and r is the radius of gyration of a cross-sectional area of the beam ($r=D/2\sqrt{3}$). For D/L < 1, Eq. (2) has been verified by the finite-element calculation. For D/L ~ 1, on the other hand, the thin rod approximation is no longer valid and the calculated, as well as the measured, resonance frequency of the flexural modes are about a factor of 1.8 smaller than the thin rod formula. The height dependence, however, remains approximately $1/L^2$. The higher frequency resonance of Fig. 3 (3.28 kHz) is about 10% higher than the quarter wave shear resonance of the Lucite block ($\approx C_{shear}/4L$) and varies inversely with height L.

To verify the connection between the Lucite block shear resonances, the localized states, and the location of the gap, we have repeated all the experiments with Lucite blocks which have only 5/6 the original height (L=2.5 inches) so that the measured shear resonances shift to about 3.5 - 4.5 kHz. Figure 4 gives the results. As expected, the frequency response gap is now at higher frequencies. Again, the measured Lucite resonances coincide with the observed gap. Comparison of Fig. 4 with Fig. 1 and Fig. 2 demonstrates the predictive power of the resonant scattering mechanism.

To further clarify the interaction between the propagating bending wave and the resonances of the coupling block/plate mode, a finite-element calculation was carried out by dividing a single Lucite block into 8x8x12 elements, with traction-free boundary conditions on five sides and the sixth side joined on to the steel plate, which is, in turn, divided into 16x16x4 elements within the unit cell. Bloch boundary conditions are applied at four sides of the unit cell. Young's moduli of 4×10^9 N/m^2 and 2.07×10^{11} N/m^2, Poisson's ratios of 0.4 and 0.286, and densities of 1.18 g/cm^3 and 7.84 g/cm^3 were taken for Lucite and steel, respectively. The results of the finite element calculation for the 2.5" high Lucite blocks are shown in Fig. 5 for wave propagation in the [11] direction. The following points should be noted: (1) The calculated gap at the Bloch wave vector $\mathbf{k}$ = 23.5 cm^{-1} corresponding to the edge of the first Brillouin zone in this direction is not only small (less than 100 Hz), but also shows directionality outside the gap shown in Fig. 3. Both observations rule out periodicity as the source of the observed gap of Fig. 1. (2) Three resonance ($\mathbf{k}$ = 0) modes introduced by the Lucite blocks are evident at frequencies of 3.26, 3.65, and 4.12 kHz. For finite $\mathbf{k}$, these modes exhibit nearly flat dispersions, indicating a low group velocity that makes them waiting to be localized. (3) The high frequency Lucite resonance is predominantly a shear resonance whose frequency is lowered and whose characteristics are modified by coupling to the steel plate. On the other hand, the two lower modes have predominantly flexural characteristics. All three modes exhibit vertical displacement that are ~ 10% of the overall horizontal displacement.

The localized mode should be insensitive to boundary conditions outside its localization length. This conclusion was verified in a separate experiment by removing successive layers of Lucite blocks centered at the intensity peak of a localized mode. It is found that the mode at f = 2.8 kHz does not alter its configuration up to the removal of the third layer from the center, as shown in the top figure of Fig. 6(a). Placing the source on

the steel plate outside the third layer is also seen not to excite the localized mode, as expected from the spatial orthogonality property of a localized mode. With the removal of the third layer, however, the intensity peak of the localized state drops abruptly (by 40%), together with the appearance of bending wave amplitude everywhere on the plate, as shown in the bottom figure of Fig. 6(a). This last observation confirms that the observed localization is not due to dissipation. Dissipation is local in nature, hence it cannot be the cause of the observed large non-local effect. All the observations can be understood in terms of wave interference resulting from scattering between the blocks. Indeed, no localized mode is found when only a single block is present on the steel plate.

The spatial orthogonality of the localized mode to the extended modes is strikingly illustrated by the fact that when the source is outside the localized region, the excitation seems to go around the domain of the localized state, leaving it an island of quietude. This is demonstrated in Fig. 6(b), where the 3D plot shows the spatial distribution of bending wave when only four Lucite blocks are bonded off the center of the plate. In the top figure of Fig. 6(b), impact excitation is under the center of the four-block area. The local intensity maximum of the velocity displacement in the block area is the response to excitation of the local bending wave/block resonance which is the source of the localized state. In the bottom figure of Fig. 6(b), impact excitation at this case is near the center of the plate and not under the four-block area. With this excitation the system exhibits a propagating bending wave which extends to the edges of the plate. It also exhibits a near zero intensity distribution observed in the block area. Figure 6(b) demonstrates that the local localized state of the bending mode is indeed an exponentially decaying function of position. When the excitation is outside the decay length, the local vibrational mode cannot be excited.

QUASI-MOBILITY EDGE

The transition between localized and extended states in a two-dimensional disordered system is a question of considerable interest.[12,20-22] For two dimensions as noted earlier, waves of every frequency are localized in the presence of disorder and there cannot be a true mobility edge. Nevertheless, it has been conjectured that there could be "quasi mobility edge(s)" in two-dimensional disordered systems[20,21,23] which separate the strongly localized states from those whose localization lengths may be transcendentally large, or even power-law localized, instead of exponentially localized. In the present experimental system, although the perturbation introduced by the Lucite blocks appears the third dimension, the dominant scattering mechanism of resonant coupling to the bending waves means that the block/plate system is two-dimensional.

We have measured the exponential decay length of the amplitude as a function of frequency in both source-detector configurations, and found it to vary as $|H| = |H_0| e^{-r/L_d}$ and $|H| = |H_0| e^{-r/L_d}/\sqrt{r}$ for the Type II and Type I measurement configurations, respectively. Measurement of L_d shows that it increases rapidly as the edge of the frequency gap is approached. In Fig. 7, the inverse of the measured amplitude decay length, $1/L_d$, is plotted as a function of frequency for the upper halves of the frequency gaps shown in Figs. 1 and 3. The error bars are estimated from the spatial resolution in the measurement of a fine mesh of detector locations. A linear relationship is found up to $L_d \sim 100$ cm, which is about half the size of the system. A linear fit to the data yields $L_d = \alpha(f_o - f)^{-1}$ cm, where f and f_o are expressed in kHz, α =13cm and 18cm, and $f_o \approx 3.5$ kHz and 4.8 kHz for the two cases shown in Figs. 1 and 4. This behavior suggests a "quasi mobility edge" at $f = f_o$. Furthermore, coincidence of the upper end of the Lucite shear resonance spectrum, 3.5 kHz and 4.8 kHz, with the quasi mobility edge f_o suggests that the physics of the quasi-mobility edge lies in the change of the localization mechanism from resonant to non-resonant scattering below and above f_o. Since at a fixed measurement distance we have $\log(|H(f)|/f) \sim -1/L_d(f)$, the frequency dependence of L_d directly translates into the frequency dependence of the $|H(f)|^2/f^2$ gaps in Figs. 1 and 4. Therefore, the observed gap symmetry in Fig. 1 implies similar behavior for the lower halves of the gaps. This is shown in Fig. 8. Due to the finite size of the system, the nature of the states for $f > f_o$ are difficult to ascertain in the present experiment.

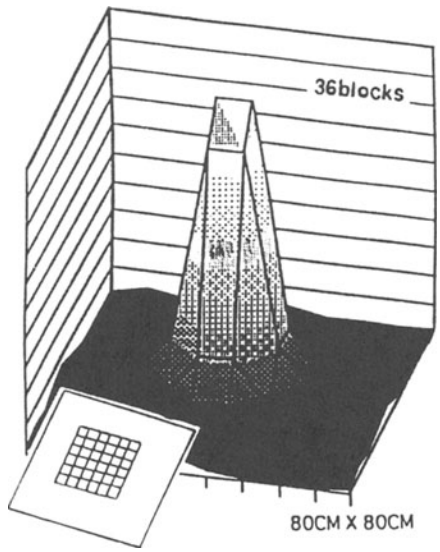

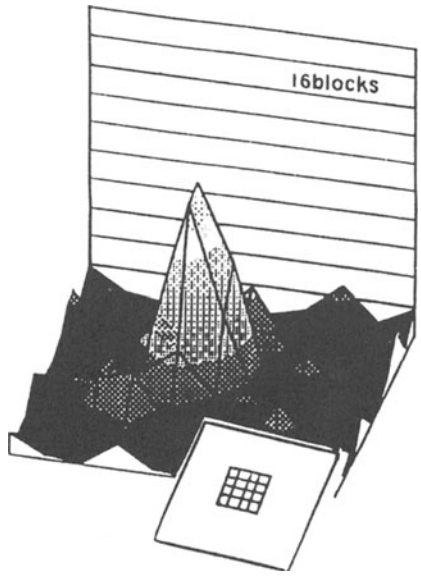

Figure 6(a). The spatial dependence of $|H|^2(f)/f^2$ at the frequency of 2.8 kHz measured from the center area (80cm x 80cm) of the steel plate as a function of the number of blocks in the array. The top figure corresponds to measurements with the point source located in the center of the plate with a thirty-six block bonded array, as indicated by the inset. The bottom figure corresponds to measurements with the point source located in the center of the plate with a sixteen block bonded array, The 40% drop in the intensity and the appearance of bending wave intensity over the plate with the removal of the outside layers of the thirty-six block bonded array confirms the conclusion that the observed localization in the lefthand figure is not due to dissipation in the bonds between the Lucite blocks and the steel plate.

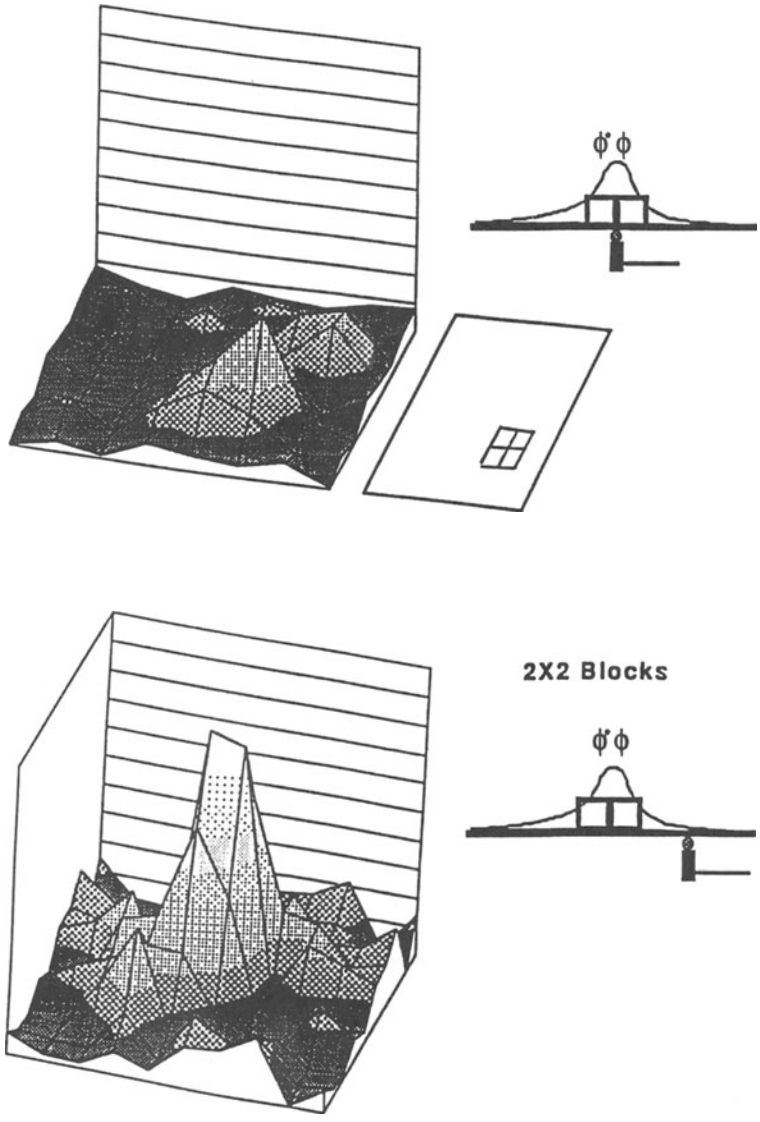

Figure 6(b). The spatial dependence of $|H|^2(f)/f^2$ at the frequency of 2.8 kHz measured for the system where only four Lucite blocks are bonded in an array located off-center of the steel plate. The top figure was obtained from measurements with the point source located in the center of the blocks as indicated by the insert. For this configuration of block array and source, a localized mode in the block area is observed. The bottom figure was obtained from measurements with the point source located in the center of the plate and outside the block area as indicated by the insert. For this configuration of block array and source, we note that the localized mode is not excited and that the bending wave travels around the block area.

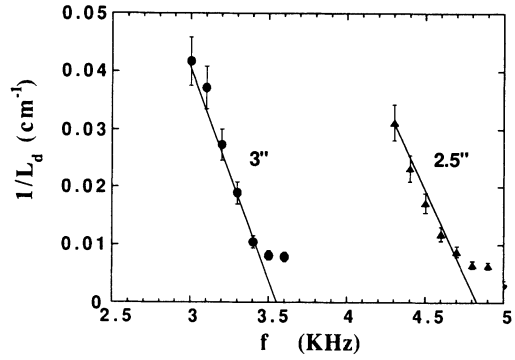

Figure 7. The inverse exponential decay length, $1/L_d$, for the magnitude of $|H(f)|$ plotted as a function of frequency for the two block sizes shown in Fig. 1 and Fig. 3 (8.89 x 8.89 x 7.62 (6.35) cm). The decay length was measured in the Type II configuration through variation of the line source- line detector separation. The solid line is linear fit given by $1/L_d = \alpha^{-1} (f-f_0)$ where α=13 and 18 and f_0 =3.5 and 4.8kHz for the two block heights (7.62 and 6.35 cm).

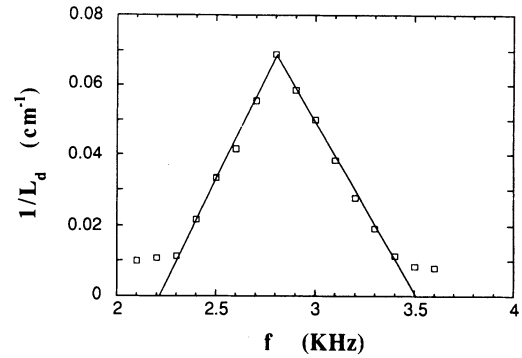

Figure 8. The inverse exponential decay length, $1/L_d$ for the amplitude plotted as a function of frequency for the case shown in Fig. 1 (8.89 x 8.89 x 7.62 cm). The extrapolated mobility edges at the low and high sides of the gap are at 2.2 kHz and 3.5 kHz. The symmetry of the frequency dependence of $1/L_d$ with respect to the localization gap shown in Fig. 1 should be noted.

SUMMARY

We have observed the first spatial localization of bending waves in a composite system over a relatively broad frequency range of ~ 1 kHz. The spatial intensity mappings of the localized states allow us to demonstrate graphically not only the effect of localization, but also the spatial orthogonality between the localized modes and the extended states. The physical mechanism for localization is found to be resonance scattering of bending waves by the three resonances of the coupled Lucite blocks-steel plate system. The character of the three resonances are also classified, whereas the two lower-frequency resonances are flexural in nature, the highest frequency one is torsion/shear in nature. Since the position of the attenuation gap varies inversely with the block height to a power between 1 and 2, the present phenomenon is thus potentially useful as a frequency-tunable attenuation mechanism for bending waves propagating in structural walls.

Our experimental results show a linear frequency dependence of the inverse exponential decay length, and indicate the existence of a "quasi-mobility edge". Further experimental and theoretical work are required to understand quantitatively the relationship between the localization length and parameters such as the block distribution density and the coupling strength between the block resonance and bending waves. The present experimental system, with the addition of an additional smooth layer of Lucite, is capable of extending the present studies into the frequency range $f \approx f_L$ and hence the regime of 3-D localization.

REFERENCES

1. L. Rayleigh, Proc. Lond. Math. Soc. 17, 4 (1887).
2. H. Lamb, Phil. Trans. R. Soc. A203, 1 (1904).
3. L. Cremer and M. Heckl, Structure-Borne Sound Spring-Verlag, Berlin, (1988).
4. L. D. Landau and E. M. Lifshitz, Theory of Elasticity, 3rd Ed. Pergamon Press, (1986), p103.
5. R. L. Weaver and Y. H. Pao, J. Appl. Mech. 49, 821 (1982).
6. George Cody, to be published.
7. Andrew Norris, to be published.
8. P. W. Anderson, Phys. Rev. 109, 1492 (1958).
9. P. Sheng, Ed., Scattering and Localization of Classical Waves in Random Media, World Scientific Publishing Co., Singapore, (1990).
10. P. A. Lee and T. V. Ramakrishnan, Rev. Mod. Phys. 51, 287 (1985).
11. S. He and J. D. Maynard, Phys. Rev. Lett. 37, 3171 (1986) present experimental data on a 2D network of coupled tuning forks. R. L. Weaver, Wave Motion, 12, 129 (1990) presents recent experiments on Anderson localization of ultrasound as does I. S. Graham, L. Piche, and M. Grant (Phys. Rev. Lett. 64, 3135 (1990).
12. D. Sornette, revews the general area of acoustic waves in random media including Anderson localization in three papers (D. Sornette, ACUSTICA 67, 199 (1989), ACUSTICA 67, 251 (1989), ACUSTICA 68, 199 (1989))
13. For light localization, see B. Levi in Search & Discovery, 17 (1991) and Sajeev John (Physics Today, May Issue p. 32 (1991))
14. R. L. Weaver and Y. H. Pao, J. of App. Mech. 49, 821 (1982); see L. Cremer and M. Heckl, Structure-Borne Sound, Spring-Verlag, Berlin, (1988) for a detailed derivation of the bending wave equation in which some effects of a blocking mass on bending waves have been considered in a 1D geometry.
15. L. D. Landau and E. M. Lifshitz, Theory of Elasticity, 3rd Edition (Pergamon Press, 1986), p. 103. The solution with a "changed boundary conditions" is used.
16. Salol is a short name for the chemical compound phenyl salicylate. Its melting point is 45C.

17. At the excitation point, the quantity |H(f)/f| is proportional to the "input conductance" of the plate. For a detailed consideration of the input conductance of infinite and finite plates in the bending wave regime see chapter 2 of R. Lyon, Statistical Energy Analysis of Dynamical Systems: Theory and Applications, MIT Press,Cambridge (1975).
18. The effect of resonant scattering on localization is discussed in P. Sheng and Z. Q. Zhang, Phys. Rev. Lett. 57, 1879 (1986).
19. H. A. Rothbart, Mechanical Design and Systems Handbook, McGraw Hill, New York (1960) p. 6-56
20. Y. Meir, A. Aharony, and A. B. Harris, Europhys. Lett. 10, 275 (1989).
21. M. Kaveh, Philos. Mag. B52, 521 (1985).
22. C. M. Soukoulis and G. S. Grest, Phys. Rev. B44, 4685 (1991).
23. The Koslowski and W. von Niessen, Phys. Rev. B42, 10342 (1990).

MOLECULAR AND FREE ELECTRON SPONTANEOUS EMISSION IN PERIODIC THREE DIMENSIONAL DIELECTRIC STRUCTURES

N. M. Lawandy and Gyeong-il Kweon

Division of Engineering and Department of Physics
Brown University
Providence, RI 02912, USA

INTRODUCTION

Since the prediction by Purcell in 1946 that the spontaneous emission rate of an atom could be enhanced by placing it in a resonantly tuned high-Q cavity, a great deal of theoretical and experimental work has been performed in this area.(1) In particular, Klepner was able to extend Purcell's observation to both predict and observe the inhibition of spontaneous emission.(2,3) This effect relies on the opposite extreme of placing the excited atom in a structure which has no modes available at the atomic radiation frequency. The inhibition of spontaneous emission was elegantly demonstrated using high Rydberg state transitions and parallel plate structures in a molecular beam experiment. The use of high Rydberg state transitions was necessitated by the requirement of a long wavelength emission where a structure could be fabricated. The molecular beam was required because the transition energies involved are of the order of 10^{-2}eV and the excited states would be quickly collisionally quenched in an environment with enough atoms to directly obtain a fluorescence signal.

Since this pioneering work, other experiments using trapped electrons and dye monolayers have also been employed to study the spontaneous emission process.(4) The experiments on dye monolayers showed the effect of placing a spontaneously radiating molecule in front of a mirror.(5,6) These experiments were among the first to bring the work closer to the visible-UV region of the spectrum where spontaneous emission plays an important role in many chemical and physical processes.

The problems of experimentally studying the spontaneous emission process in the important visible-UV region are primarily related to the original issues of a structure encountered in the experiments referred to earlier. The two primary problems are scale

Photonic Band Gaps and Localization, Edited by
C.M. Soukoulis, Plenum Press, New York, 1993

and losses. The 3-D structures required would have to be on the scale of several hundred nanometers and be lossless at frequencies of 10^{14} - 10^{16}sec.$^{-1}$

A recently proposed structure for tailoring the electromagnetic vacuum mode spectrum is the electromagnetic analogue of a 3-D lattice for electrons. This structure is a periodic scattering structure which produces a gap in photon propagation and density-of-states over a certain frequency range in all directions of space.[7,8] The understanding of the basic electromagnetic material properties and structure symmetries required to open this 3-D gap has generated a great deal of excitement but its fabrication at optical scales from suitable lossless materials is far from being realized.

In this paper I will review recent experimental work performed at Brown University on molecular spontaneous emission in 3-D periodic dielectric structures. These structures do not have a large enough index of refraction contrast to produce forbidden photon propagation bands in all directions of space, but they provide the first direct experimental evidence that 3-D Bragg scattering can alter the spontaneous emission process. In addition, I will briefly discuss the potential ramifications of using a periodic structure with a photonic bandgap for the suppression of spontaneous emission in photo-catalysis applications. Finally, a simple model of a photonic crystal is used to show that the Cerenkov emission by relativistic electrons can take place efficiently in these materials with the near complete removal of material energy loss processes, such as ionization.

MOLECULAR SPONTANEOUS EMISSION IN A 3-D PERIODIC DIELECTRIC STRUCTURE

The ideal photonic bandgap material briefly discussed in the introduction produces a gap in the photon density-of-states in all directions. To date many calculations of this photonic band structure have been undertaken, resulting in relatively well-defined criteria for the occurrence of a 3-D bandgap. The minimum index contrasts required are in the range $n \geq 2$ and it is now well established that spherical atoms in an fcc structure will not suffice when electromagnetic polarization considerations are taken into account. This latter point results in band crossings which destroy the gap in certain well-defined directions. Even in this limit however, a strong suppression of the direction averaged density-of-states is expected.. This limit has been studied for air and dielectric spheres in an fcc structure with a gap near the Mie resonances by Satpathy et al.[9,10] Their results for a structure with a 30% volume fraction reveal that the density-of-states is strongly suppressed just above the Mie resonance and exhibits the expected sharp increase at the point analogous to van Hove singularity on each side of the gap. Based on this qualitative picture of an infinite size fcc structure, we would expect that atoms or molecules whose spontaneous emission frequency falls within the pseudo-gap would find a greatly diminished density of final photon states and by Fermi's golden rule radiate more slowly

than in free space.[8] In addition, we expect that an excited molecule whose emission frequency was at one of the van Hove singularity points on either side of the gap might exhibit an enhanced radiation rate compared to free space. This may or may not be true, since plane transverse electromagnetic modes are no longer the correct field states in a medium with a space dependent dielectric constant. This deviation could, in principle, change the field atom-coupling for a given electromagnetic mode and possibly off-set the increase in density of final states.

The experimental measurement of the spontaneous emission rate of an atom or molecule in a 3-D fcc dielectric structure poses many challenges, even beyond the fabrication of a periodic structure with hundreds of nanometer spacings between planes. The suitable structure must be readily impregnated by the radiating molecules, which, in turn, must be kept away from surfaces in order to avoid nonradiative relaxation. In addition, the scattering properties of the structure must be controllable in terms of the strength of the scattering as well as the position of the Bragg resonance. Finally, an experimental approach capable of yielding unambiguous information about the time evolution of the excited state is required to probe the system dynamics. This latter point is important because direct temporal measurements of spontaneously emitted light can be flawed by internal scattering and radiation rates which vary with direction.

The approach we have taken to partially solve the problems at hand relies on a novel structure comprised of charged polystyrene spheres in water (or CH_3OH) ordered in an fcc lattice with (111) plane spacings having sub-optical dimensions.[11] This structure, called a colloidal crystal, results when a high density (~10^{14} particles/cm^3) collection of charged spheres lower their free energy by self-organizing into a lattice. The spheres have a narrow size distribution (5% coefficient of variation), are typically 100 nm in diameter, and carry about 10^3 negatively (-1) charged groups. In the presence of counter ions from the dissociated groups on the spheres, as well as the natural pH of the water, the electric potential from the spheres surface has a screened Coulomb behavior given by:

$$U \sim \frac{e^{-\kappa R}}{R} \qquad (1)$$

where κ^2 is proportional to the ion concentration. In terms of this approximate solution of the Poisson-Boltzman equation, one can view the crystalization as a hard sphere transition (Kirkwood-Adler) with a sphere radius of $R \sim \kappa^{-1}$.[12] This view shows that it is actually the electrical radius which is responsible for lattice formation so that other systems using materials other than polystyrene may be possibly used in the future. Figure 1a shows a polycrystalline colloidal crystal with different density bands towards the top of the container. This illustrates how this structure's lattice spacing can be controlled by dilution or concentration of the spheres. In addition, the scattering strength can be controlled by either index matching the solution closer to the index of refraction of polystyrene or by using smaller or larger spheres.[11,13]

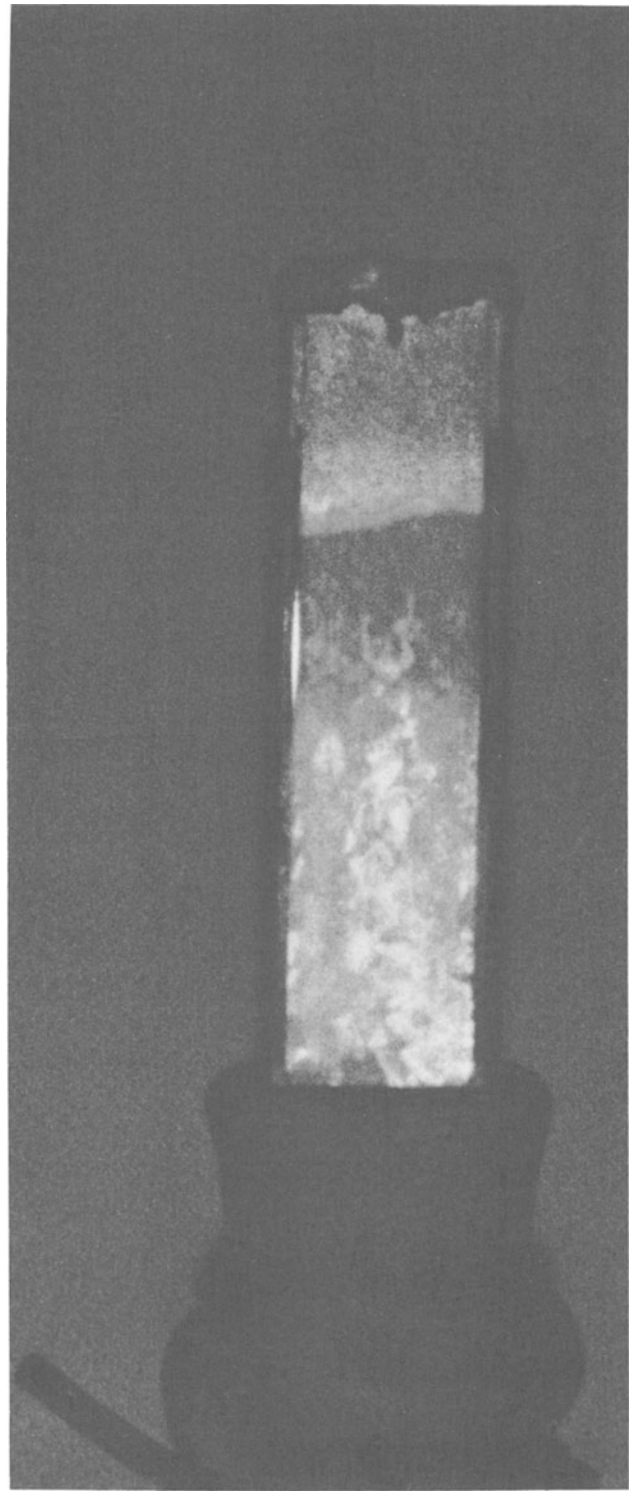

Figure 1a

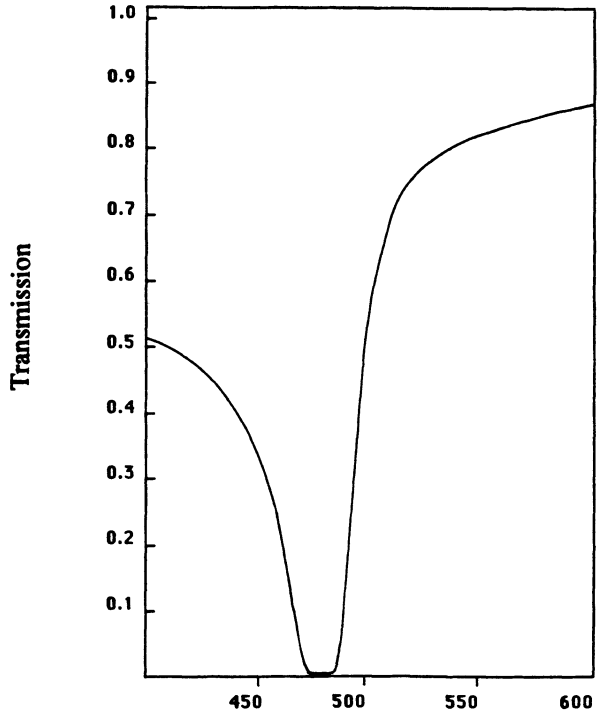

Figure 1b

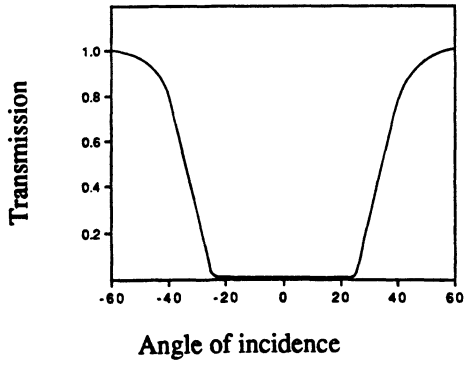

Figure 1c

These crystals are in many ways ideal for the experimental studies we propose, but they do fall short with respect to the amount of k-space over which the Bragg scattering modifies the density-of-states. This is due to the low index of refraction ratio of polystyrene to water (n = 1.17). In this regime of scattering, each of the four sets of (111) planes of the fcc crystal blocks photon propagation over a narrow solid angle and these solid angles do not overlap to form a full photonic bandgap.

Figure 1b shows the transmission of a 100 μm thick colloidal single crystal measured normal to the (111) plane direction. The transmission at the minimum of the Bragg notch was measured to be $\sim 10^{-7}$. Figure 1c shows the results of angling the crystal with a fixed frequency of illumination. These measurements can be used to estimate the total solid angle inhibited by one set of planes and result in about ~0.9 steradians/plane set.

The crystals can be well characterized by light-scattering analogues of x-ray crystallography and offer a unique structure for incorporating a high quantum efficiency atomic or molecular system to study the periodic dielectric effects on spontaneous emission. The ideal molecular systems which are naturally compatible with the colloidal crystal host are dye chromophores. These molecules are typically used as laser dyes and have strongly allowed singlet absorption and fluorescence bands in the visible region where the colloidal crystal structure can be manipulated. The ideal molecular dye would be water soluble, have a high quantum efficiency, and would possess a negatively charged chromophore so that it is electrically repelled by the sphere surface. These criteria were found to be well satisfied by the sulforhodamine molecule which could be incorporated into the crystals at concentrations as high as 10^{-4}M.

The combined sulforhodamine doped colloidal crystal was studied using a dual wavelength picosecond pump-probe system. This technique uses picosecond pulses from two synchronously pumped dye lasers operating at the singlet absorption (590 nm) and singlet fluorescence (620 nm) bands, respectively, to excite and probe the population of the upper singlet state. The principle of measurement relies on the gain experienced by the probe after excitation, which is proportional to the remaining excited state population. Thus, by measuring this gain in the small signal limit as a function of the delay after excitation, we can measure the temporal decay of the excited state. Figure 2 shows the experimental set-up used in the experiments.

Experiments were performed to measure the lifetime of the dye doped colloidal crystal. The measurements were performed at different lattice spacings corresponding to the position of the Bragg notch position above and below the transition wavelength. When the transition wavelength is longer than the Bragg position wavelength for propagation normal to the planes, the spontaneous emission is expected to be essentially unaffected since Bragg scattering cannot occur. If, however, the emission wavelength is shorter, then at some angle relative to any one of the four sets of (111) planes, Bragg scattering occurs and the photon density-of-states for the spontaneously emitting molecule should be affected. The results of the experiments measuring the decay of the upper singlet state are

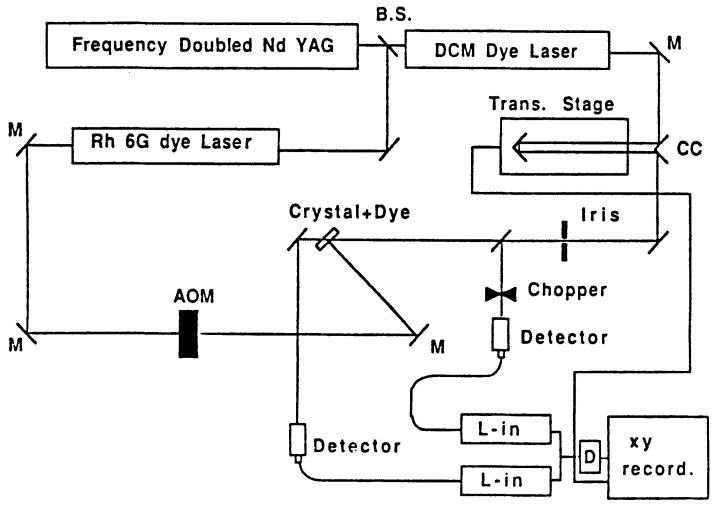

Figure 2

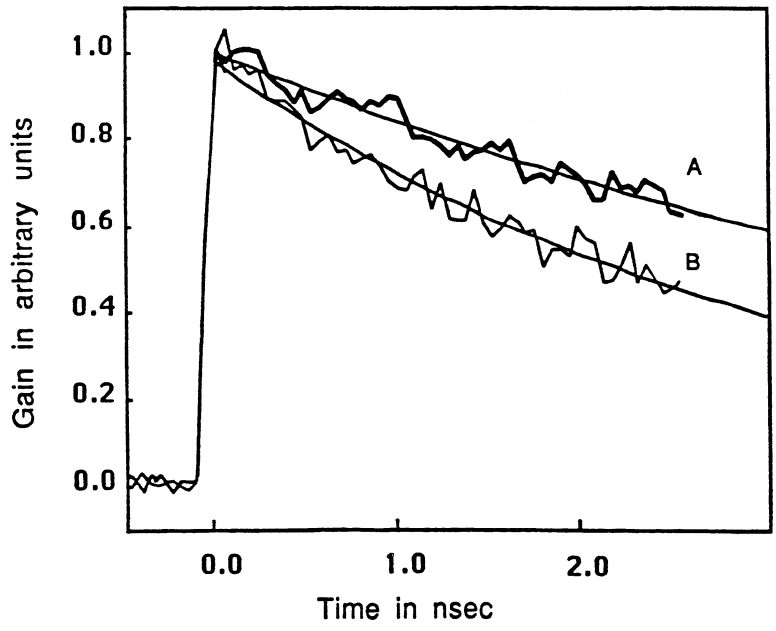

Figure 3

shown in Figure 3. The top curve corresponds to a normal incidence scattering wavelength longer than the emission wavelength in water and the lower curve corresponds to the case of the emission wavelength being the longer of the two. The measured liftetimes fit to exponential decays for the two cases were found to be 5.6 ns and 3.2 ns. In addition, when the plane spacing was set for the spontaneous inhibition position but the sphere size was reduced, the lifetime returned to the value in water within the allowed error of our measurements. These results provide the first experimental test of inhibited molecular spontaneous emission in a 3-D fcc dielectric crystal.(14)

The experimental findings can be understood by a treatment which estimates the vacuum mode amplitudes in the structure and uses the Wigner-Weisskopf formulation.(15) This calculation leads to a radiative rate suppression factor of ~1.5 which is in good agreement with the values measured. A simple method to estimate the expected suppression is to simply consider the amount of solid angle of space over which the radiation channels are blocked. The previous estimate of 0.9 steradians per set of (111) planes as measured from the angular rejection of the Bragg notch leads to a total solid angle of inhibition about 3.6 steradians for all four (111) planes. Since in free space 4π steradians are available, the rate should be suppressed by the ratio of the available solid angle to the free space value. This estimate results in an inhibition factor of about 1.4, which is also in reasonable agreement with our findings.

Photonic Bandgap Substrates for Photo-catalysis

It has been known for many decades now that the reaction pathways, products, and rates of chemical reactions can be drastically influenced by photo-excitation of the reactants. One of the simplest examples is atomic oxygen which is relatively benign in its ^3P state and several orders of magnitude more reactive in its ^1D state, the latter being responsible for the chemical pumping of the OH laser. Another class of important reactions are photo-catalytic processes. In these systems the reaction rate for a process is enhanced by many orders of magnitude in the presence of a catalytic species in an excited electronic state. The field of photo-catalysis is very large and impacts various areas of chemical synthesis and applications in biochemistry, fuels development, and solar energy conversion. It is also important to note that the most common catalyst supports are semiconducting and insulating materials with bandgaps comparable to typical redox potentials.

The catalytic reaction rate enhancements are related to the catalyst band structure, the available number of catalyst surface sites, and the detailed electronic orbital structure of the responsible electron/hole state. Since all solid state catalysts require as much surface area as possible, the catalyst supports are used in the form of ultra small particles, typically a fraction of a micron. In this configuration, a given volume of catalyst presents a large surface area and many sites for catalytic action to occur. In some catalyst reactions, the

excited state is quenched during the catalytic step, while in others it is not and the catalyst can participate in other reactions. In either case, the de-excitation of the catalyst by any other channel represents a loss of valuable excitation energy which does not produce products. Since photo-catalysis often takes place with UV excitation (1900-3000Å), where emission lifetimes are typically short (~100 psec), spontaneous emission can be the dominant loss channel for de-excitation of the catalyst. This loss mechanism can determine the efficiency and cost of these processes which require expensive pump photons to produce catalytic action.

The simplest considerations we have discussed lead to the ideal photo-catalytic material as one which

(1) has an extremely large internal surface area,

(2) allows for the efficient transport of reactants and products, and

(3) exhibits no scattering at the excitation wavelength.

(4) has essentially no spontaneous emission leading to catalyst de-excitation.

All of these points are achievable using **photonic bandgap crystals made of or coated with photo-catalytic materials such as semiconducting or insulating materials.**(16) The theoretical calculations of photonic band structure have shown that regardless of the crystal's symmetry, fcc or diamond, bandgaps are only present for void fractions of 80%-90%, resulting in an intrinsically large surface area. Furthermore, since the photonic crystals exceed the close packing volume fraction limit of 74%, they necessarily have connected channels which allow transport through the material. In addition, since the crystals have a zero density of photon states within the gap in all directions of space, they will inhibit spontaneous emission when the photon energy is within the gap. Finally, an additional improvement results in the process due to the removal of random scattering at the excitation band used to pump the catalyst. This results from the periodic crystal's structure factor, which now is centered at the fluorescence emission band. The removal of scattering at the pump band will result in more efficient excitation of the catalytic material.

CERENKOV EMISSION IN A PHOTONIC BANDGAP CRYSTAL

In this section a simple model of the interaction of a "free" electron with a periodic structure with a 3-D photonic bandgap is presented. Although it is well-known and easily shown that free electrons do not emit or absorb photons, electrons traversing polarizable media do radiate. This effect, known as Cerenkov emission, occurs because momentum and energy can be conserved when material polarization is possible.(17) Thus, the use of the term "free" is not exact, since the electron interacts with the material via the polarization it induces. Cerenkov emission further requires that the electron or any other charged particle move with a velocity faster than the speed of light in the medium. Because of this, the effect has been often cast as an electromagnetic analogue of a sonic

boom. In a typical situation where a relativistic electron traverses a low Z (proton number) material such as glass (n = 1.5) or water (n = 1.33), about 90% of the electron energy is lost to ionization events and about 10% to Cerenkov emission. This emission typically peaks in the blue-green region of the spectrum and is responsible for the light often seen in the pool of nuclear reactors.

The process of Cerenkov emission can be treated classically as well as in the context of quantum mechanics. The latter is the approach taken here, since its connection with the density of photon states concept, familiar to the light localization and photonic bandgap community, is more transparent. The treatment presented follows closely the work of Marcuse and begins with the description of the electron with the Klein-Gordon equation describing relativistic spinless particles.(18).

The electron wavefunction Ψ can be found as a solution of:

$$\nabla^2\Psi - \frac{1}{c^2}\frac{\partial^2\Psi}{\partial t^2} = \frac{m_0^2}{\hbar^2}\Psi \qquad (2)$$

where m_0 is the electron rest mass. In an electromagnetic field, the canonical momentum is required and results in the field coupled equation for the electron:

$$[c^2(\vec{p} - e\vec{A})^2 + m_0^2 c^4]\,|\Psi\rangle = w^2\,|\Psi\rangle \qquad (3)$$

where A is the vector potential and w is the electron energy given by:

$$w^2 = \frac{m_0^2 c^4\,[1 - (v/c)^2] + m_0^2 c^2 v^2}{1 - (v/c)^2} \quad . \qquad (4)$$

Because the Hamiltonian appears in a quadratic form, no direct separation of an interaction Hamiltonian, H_{int}, is possible. This situation does not pose a problem, since what we are really interested in is the matrix element of H_{int}. After some detailed manipulations, it can be shown that:

$$\langle \psi_f\,|H_{int}|\,\psi_i\rangle = \frac{-2ec^2}{w_i + w_f}\langle\phi_f|\,p \bullet A\,|\psi_i\rangle \qquad (5)$$

where ψ_i and ψ_f are the initial and final electron wavefunctions and w_i and w_f are their respective energies.

The process of Cerenkov emission requires that momentum be conserved when the electron radiates a photon into the material. The momentum conservation condition can be found using the reference diagram shown below:

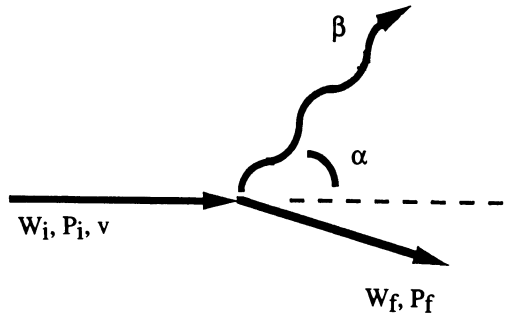

In terms of the incident momentum, velocity, and the angle of photon emission α, momentum conservation requires that

$$\cos\alpha = \frac{c}{\sqrt{\varepsilon_r}\,V} + \frac{\varepsilon_r - 1}{2\varepsilon_r}\frac{\hbar\beta}{p_i} \quad . \tag{6}$$

This condition serves to act as a constraint on the available density of final photon states for Cerenkov emission. Thus, the effective density-of-states for this process, unlike spontaneous emission by atoms and molecules, is not the usual photon density-of-states.

The precise description of the Cerenkov process in a photonic crystal requires a detailed knowledge of the form of the vector potential solutions as well as a detailed 3-D dispersion relation for the crystal. This calculation would require the use of numerical solutions using the computer-generated bandstructure of one of the photonic crystal lattices such as the diamond or nonspherical atom fcc structures. In order to capture the essential physics of the process in an analytically tractable model, we will assume that the form of the electromagnetic modes is weakly affected and that it is primarily the density-of-states and the dispersion relation which capture the salient features of Cerenkov emission in a photonic crystal.

The dispersion relation we use is that of a 1-D dielectric array with extension to three dimensions. In the limit that the 1-D Mie resonance matches the Bragg condition, the dispersion relation is given by:

$$\omega_k = \frac{c}{4na}\arccos\left(\frac{4n\cos(kL)+(1-n)^2}{(1+n)^2}\right) \tag{7}$$

where 2a is the scattering well size and n is the index of refraction ratio. This dispersion relation has been used previously to study various QED phenomena in photonic bandgaps by John and Wang.[19] Care must be taken, however, since this 1-D relation exhibits unphysical density-of-states singularities at the band edges. In order to remedy this problem, the calculations are cut off at frequencies where the density-of-states reaches peak values comparable to those found in numerical bandstructure calculations. For example, in the case of the fcc structure with spherical Mie resonances, the density-of-states grows to a peak value about ten times that of free space.[11] Thus, in using the isotropic 1-D model, we truncate the dispersion relation at the frequency point where the density-of-states was similarly enhanced over the free space density-of-states.

Figure 4 shows the Cerenkov density-of-states (DOS) using the isotropic 1-D dispersion relation for the case, where a single scattering resonance occurs at the Bragg condition (λ_0 = 500 nm) and the dielectric material response is not a function of frequency. In the uniform (no structure) dispersionless dielectric, the conventional DOS is proportional to ω^2 while the Cerenkov DOS is proportional to ω.

Using the constrained density-of-states, we can examine the frequency dependence of the radiated power. In the case of a dispersionless uniform dielectric, the frequency of Cerenkov emission increases monotonically towards higher frequencies. For this dispersionless case, a uniform dielectric slab would emit all the frequencies in a cone with the same angle. When a photonic bandgap is present, the emission wavelength becomes a strong function of the angle. In the case of a more realistic photonic bandgap calculation, the multivalley structure of the bands would result in a more complicated but symmetric chromatic emission pattern with different colors being emitted along characteristic directions. A comparison of the frequency dependence of the radiated power for an isotropic photonic bandgap and the uniform dielectric is shown in Figure 5.

Using the assumption of a weakly perturbed functional form for the vector potential, we can estimate the radiated power of an electron traversing a photonic bandgap material. This calculation again must be terminated before the density-of-states diverges due to the 1-D dispersion relation. Calculations were performed for a 15% filling fraction crystal with a peak density-of-states corresponding to an index of refraction ratio 3.5. In this case, an enhancement of about a factor of ten in the DOS is expected from numerical bandstructure calculations.[11] Figure 6 gives a comparison between the total power radiated per unit length as a function of free space wavelength for an electron with v = 0.7c traversing the photonic crystal (n = 3.5) and the solid dielectric.

The main results which we draw from this simple model of Cerenkov radiation in photonic crystal is that the peak radiated power scales at the bandedge density-of-states and that this can be comparable or exceed the power radiated by a uniform dielectric. This latter point presents a particularly interesting possibility for slowing down charged particle beams by purely radiative means. This could be accomplished using the photonic structure described by Yablonovitch et al. which is formed by the intersection of channels which

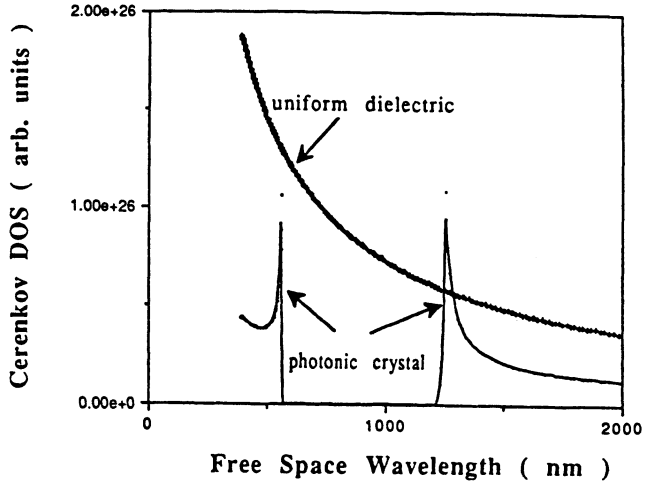

Figure 4

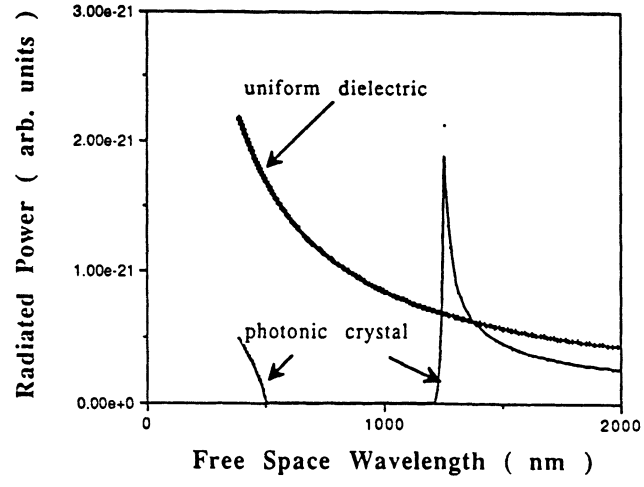

Figure 5

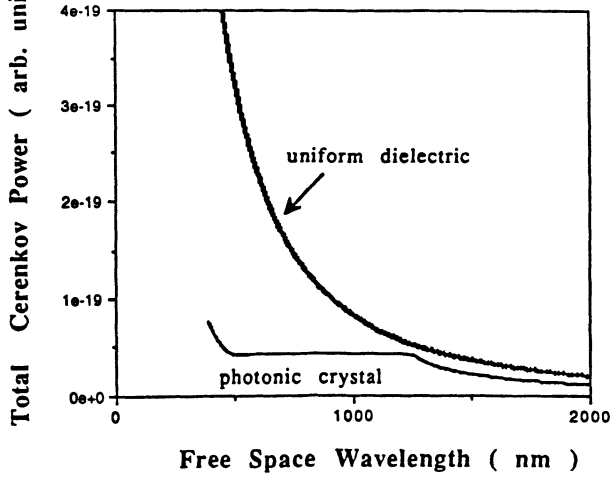

Figure 6

extend through the entire crystal.[20] In the visible region, the channels would be of the order of 100 nm in diameter allowing for the unimpeded passage of a collimated electron beam. This concept may prove useful for particle detectors, reactor moderators, and stimulated Cerenkov lasers.

ACKNOWLEDGMENTS

The author is grateful to the Air Force Office of Scientific Research for funding the research described in this paper.

REFERENCES

(1) E. M. Purcell, Phys. Rev. 69, 681 (1946).
(2) D. Klepner, Phys. Rev. Lett. 47, 233 (1981).
(3) R. G. Hulet, E. S. Hilfner, and D. Klepner, Phys. Rev. Lett. 55, 67 (1985).
(4) G. Gabrielse and H. Dehmelt, Phys. Rev. Lett. 55, 67 (1985).
(5) K. H. Drexhage, J. Lumin. 1-2, 693 (1970).
(6) H. Kuhn, J. Chem. Phys. 55, 101 (1970).
(7) S. John, Phys. Rev. Lett. 58, 2486 (1987).
(8) E. Yablonovitch, Phys. Rev. Lett. 58, 2059 (1987).
(9) S. Satpathy, Ze Zhang, and M. R. Salehpour, Phys. Rev. Lett. 64, 1239 (1990).
(10) S. Satpathy, Ze Zhang, and M. R. Salehpour, Phys. Rev. Lett. 65, 2478 (1990).
(11) J. Martorell and N. M. Lawandy, Optics Comm. 78, 169 (1990).
(12) J. G. Kirkwood, J. Chem. Phys. 3, 300 (1935).
(13) R. J. Spry and D. J. Kosan, Appl. Spectrosc. 40, 782 (1986).
(14) J. Martorell and N. M. Lawandy, Phys. Rev. Lett. 65, 1877 (1990).
(15) W. H. Louisell, *Quantum Statistical Properties of Light* (Wiley, New York, 1973), p. 285.
(16) N. M. Lawandy, APS March Meeting, Indianapolis, IN, Vol. 37(1), Paper G53, 1992.
(17) J. V. Jelley, *Cerenkov Radiation and Its Application* (Pergamon Press, New York, 1958).
(18) D. Marcuse, *Engineering Quantum Electrodynamics* (Harcourt Brace and World Inc., New York, 1980), pp. 53-57.
(19) S. John and J. Wang, Phys. Rev. B 43, 12772 (1991).
(20) E. Yablonovitch, T. J. Gmitter and K. M. Leung, Phys. Rev. Lett. 67, 2295 (1991).

THE SINGLE-MODE LIGHT-EMITTING-DIODE

I. Schnitzer, E. Yablonovitch, A. Scherer, and T. J. Gmitter

Bellcore
331 Newman Springs Rd.
Red Bank, NJ 07701-7040, USA

ABSTRACT

A single-mode light-emitting-diode (LED) can have many of the favorable coherence properties of lasers, while being a more reliable, threshold-less, device. Progress in electromagnetic micro-cavities, such as those formed by photonic band structure, allow all the spontaneous emission (of an LED) to be funneled into a single electromagnetic mode. It is shown that the internal spontaneous emission quantum efficiency in GaAs/AlGaAs double heterostructures can be as high as 99.7%, and consequently, the external quantum efficiency and the shot-noise suppression in such single-mode LEDs can be comparable to those of semiconductor lasers, but at much lower injection level.

INTRODUCTION

As the interest in low-threshold semiconductor laser diodes has grown, e.g., for optical interconnects, its spontaneously luminescent half-brother, the light-emitting-diode (LED) has begun to re-emerge in a new form. In this new form, the LED is surrounded by a specially designed optical cavity. The idea is for the optical cavity to make available only a single electromagnetic mode for the output spontaneous emission from the semiconductor diode.

With all the spontaneous emission funneled into a single optical mode, the LED can begin to have many of the coherence and statistical properties normally associated with above-threshold lasing. The essential point is that the spontaneous emission factor, β, which measures the proportion of spontaneous emission going into the preferred electromagnetic mode, should approach unity. (A closely related concept is that of the "zero-threshold laser,"[1,2] in which the high spontaneous emission factor produces a very soft and indistinct threshold characteristic in the light output-versus-current input curve of laser diodes.)

Photonic Band Gaps and Localization, Edited by
C.M. Soukoulis, Plenum Press, New York, 1993

The idea behind the new concept of the single-mode LED is to combine the advantages of the LED which is threshold-less and highly reliable, with those of the semiconductor laser which is coherent, highly efficient, and capable of producing sub-Poissonian light (shot-noise suppressed) into a specified electromagnetic mode.

It becomes clear now[2-4] that in addition to the spontaneous emission factor, β, also the internal quantum efficiency, η, need to be as close to unity as possible, in order to produce a photon stream with sub-Poissonian shot noise (called photon number-state squeezing). That is because carrier injection noise is determined by $(1-\eta)$, while photon-number partition noise is measured by $(1-\beta)$. Typically, in semiconductor light emitting devices, $\beta << 1$ while $\eta > 90\%$. Therefore, most of the attention in this field is given to micro-resonator structures in which a high β factor (> 0.1) is achievable. In this paper, we will discuss these two limiting factors, with emphasis given this time to an accurate measurement of η. Our purpose is to show that a single mode LED can be realized in a III-V semiconductor in the near future.

β: THE SPONTANEOUS EMISSION FACTOR

The essential ingredient for the concept of single-mode LED is a single mode electromagnetic micro-resonator which captures all the spontaneous emission from the LED active region. There has been great progress recently, in designing and making dielectric resonators employing the concepts of photonic band structure.[5-8] A photonic bandgap can occur in a 3-dimensionally periodic structure (a photonic crystal), which does to photon waves what a semiconductor crystal does to electron waves; it creates a forbidden band of energies irrespective of propagation direction in space.[5] By introducing a defect into the otherwise perfect photonic crystal, a local electromagnetic mode forms in the forbidden gap region. In keeping with electronic analogy, the defect mode can be either acceptor-type or donor-type. This subject is further clarified in another paper in this volume.[6]

Recent progress in microfabrication of photonic bandgap structures in GaAs/AlGaAs semiconductors[7,8] shows that a wide gap may be opened up, similar to the photonic bandgap that was demonstrated in the microwave regime. The idea is to fabricate a perfect f.c.c. photonic crystal by reactive ion beam etching and then to create a local defect in the center of that "crystal" which accommodates a single localized electromagnetic mode that strongly overlaps with the emitting region. The preferred defect mode would be of the acceptor type since it supports a non-degenerate mode (unlike the donor type defect), does not have a threshold volume, and, most importantly, it can be created relatively easy. The acceptor defect type, a missing tiny slice in one of the structure's ribs, can be created in III-V semiconductors by growing an Al rich epitaxial layer and lithographically patterning it down to a single dot the size of the acceptor defect. After regrowth of the original III-V composition and reactive ion etching of the photonic crystal, HF acid etching, whose[9] selectivity $> 10^8$, will be used to remove the Al rich horizontal slice from the one rib containing such a layer.

The quality factor (Q) of a localized mode decreases in the presence of losses. Therefore, the feasible β factor is limited by the loss tangent of the semiconductor from which the photonic crystal is made. Since photon localization is expected to be more susceptible to weak disorder than electron localization, high β factor would require improved nanofabrication techniques.

η: THE SPONTANEOUS EMISSION INTERNAL QUANTUM EFFICIENCY

In terms of luminescent quantum efficiency at room temperature, the direct gap III-V semiconductors are rather unique substances. It has been known[10] for almost 20 years that good quality III-V double heterostructures can have high internal quantum yields, well over 90% efficient. When combined with direct electrical injection, these high quantum yields form the basis for opto-electronics. This has led to important applications such as light-emitting diodes (LED's), semiconductor lasers and solar cells, for each the utmost quantum yield is desirable.

In this section, we will examine experimentally the absolute luminescent quantum yield of some good quality AlGaAs/GaAs/AlGaAs double heterostructures. We will find that the internal luminescent yield can be even higher than expected. Moreover, the high *internal* yield can be converted into an impressive *external* quantum efficiency by means of a simple geometrical configuration: III-V thin films are floated off their substrates by the epitaxial liftoff technique[9] and then mounted on various high reflectivity surfaces. We will show how this geometry allows most of the internal luminescence to escape externally, which can make LED efficiency competitive with the best laser diodes. In the race for low-threshold laser arrays, we consider such LED's to be a significant development since they require *no* threshold current.

The Cavity

In LED's the external quantum efficiency is rather poor, generally only a few percent. The reason for this poor efficiency is the semiconductor refractive index is rather high, $n \sim 3.54$ in GaAs for example, leading to a very narrow escape cone for the isotropic spontaneous emission. The 16° cone angle imposed by Snell's Law covers a solid angle of only $\approx (1/4n^2) \times 4\pi$ steradians. Because the refractive index is so high, $4n^2 \gtrsim 50$ and the *external* efficiency is only $\approx 2\%$ in commonplace LED's, even when the *internal* efficiency happens to be close to unity. This problem has been addressed by incorporating a hemispherical semiconductor dome[11] over the LED, allowing most of the internal luminescence to escape at normal incidence. We will show that semiconductor hemispheres are unnecessary and that a simple thin film geometry, as illustrated in Fig. 1, will also allow most of the light to escape externally.

A conventional n^+-AlGaAs/p-GaAs/p^+-AlGaAs double heterostructure is grown over a 500Å thick AlAs release layer by organo-metallic chemical vapor deposition, where $n^+ \approx 3 \times 10^{18} cm^{-3}$, $p \approx 3 \times 10^{17} cm^{-3}$, and $p^+ \approx 3 \times 10^{18} cm^{-3}$. The heterostructure is then separated from the GaAs substrate by epitaxial liftoff[9] (ELO), using HF acid selective etching of the AlAs release layer. Following the ELO procedure, the thin film, supported from above by a thick wax layer, is Van der Waals bonded by surface tension forces onto a reflecting substrate. As shown in Fig. 1, this substrate reflects the emitted photons back into the GaAs where they may be absorbed and possibly re-emitted into the escape cone. As a substrate, we use high reflectivity metal mirrors coated with a low index transparent layer, which offers, when angle averaged, a higher effective reflectivity than a multilayer AlAs/GaAs Bragg reflectors.[12] In principle, bonding the heterostructure thin film on a perfect diffuser (a white surface) may produce the best result since it offers the highest angle averaged reflectivity.

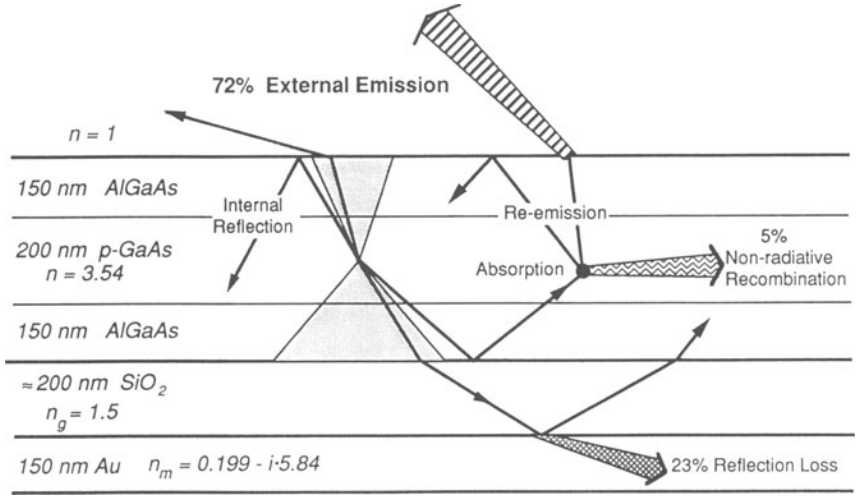

Figure 1. Schematic cross section of epi-liftoff heterostructure, Van der Waals bonded onto a glass coated metallic reflector. The upper and lower escape cones are depicted by the shaded area. The partition among external emission, reflection loss, and non-radiative recombination processes, is indicated by percentages. Refractive indices are given by n, n_g, and n_m.

Once a luminescent photon is emitted internally, it will have one of several possible destinies: (a) It can escape through the escape cone at the top of the double heterostructure; (b) It can be re-absorbed by the parasitic optical losses in the structure, in the bottom reflector for example; (c) It can be re-absorbed in the active layer and experience re-incarnation as a photon, since the internal luminescent quantum yield is quite high. If there were no parasitic optical losses, and if the internal quantum efficiency, η, were high enough, the photon would be re-incarnated many times, having a 4% probability of finding the escape cone each time. To achieve a high external quantum efficiency, as we have done, requires 25 or more re-incarnations of the photon! This is illustrated in Fig. 2. Therefore, the external efficiency, η_{ext}, is a sensitive function of the small parasitic optical losses and the small non-radiative loss channel $(1-\eta)$.

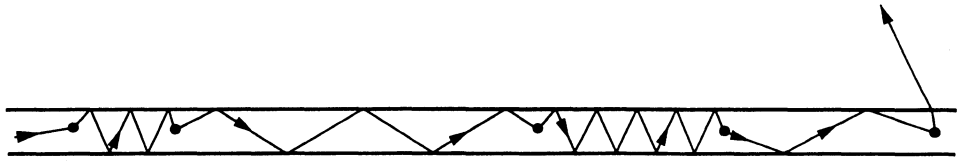

Figure 2. Typical photon trajectory in the heterostructure shown in Fig. 1. Dots represent absorption/emission events. High external efficiency demands $\gtrsim 25$ such events before a photon finds the escape cone.

The Model

To model the behavior of the photoluminescence in our GaAs films, we will invoke a statistical approach[13] which was first introduced to explain the ergodic behavior of light in solar cells. We justify this statistical model by averaging over internal angle, polarization, over volume or the depth of luminescent material, over the wavelength band, and over thickness fluctuations or surface roughness. Therefore, coherent effects are ignored. Let B_{int} be the brightness (in photons/sec per cm^2 per steradian) of the trapped luminescent radiation inside the thin film. The internal luminescence will generally be re-absorbed by surface absorption or volume absorption. The parasitic absorption at the surface of the reflector is:

$$(1) \qquad \int_0^{\pi/2} B_{int} A\,[1-R(\theta)]\cos\theta\, 2\pi\sin\theta d\theta = \frac{4\pi B_{int} A\,[1-\bar{R}]}{4} \quad ,$$

where θ is the polar angle, A is the surface area, and $\bar{R}$ is the angle averaged reflectivity. The volume integrated absorption within the bulk is:

$$(2) \qquad \int \alpha(z)\, B_{int}\, dV\, d\Omega = 4\pi B_{int} A \sum_i \alpha_i d_i \quad ,$$

where dV is the volume element, $d\Omega$ is the internal solid-angle element, $\alpha(z)$ is the local absorption co-efficient and α_i and d_i are the absorptivity and thickness of the *i*th layer, respectively. The active layer re-absorbs radiation right at the band edge, while in the other layers there can be parasitic bulk absorption mechanisms. We assume one typical wavelength for each absorption coefficient α_i, instead of a careful spectral averaging.

The band-to-band absorption in the active layer, α_o, produces electron-hole pairs, which may be sub-divided into a portion $\eta\alpha_o$ which leads to re-radiation and a portion $[1-\eta]\alpha_o$ which leads to non-radiative recombination and heat. The radiative part may itself be further sub-divided into a fraction which falls within the forward or backward going escape cone, $2\times(1/4n^2)$, and a remaining portion which re-joins the trapped internal radiation. Therefore, the internal bulk absorption in Eq. (2) may actually be divided into 4 terms; parasitic bulk absorption, band-to-band absorption leading to non-radiative recombination of electron-hole pairs, band edge absorption leading to external escape of the photons, and band edge absorption which contributes to the trapped pool of photons:

$$(3) \qquad 4\pi B_{int} A \left[\sum_j \alpha_j d_j + (1-\eta)\alpha_o d_o + \frac{\eta\alpha_o d_o}{2n^2} + \eta\alpha_o d_o \left(1 - \frac{1}{2n^2}\right)\right] \quad ,$$

where d_o is the thickness of the active layer, and $\alpha_j d_j$ represents parasitic bulk absorption.

In steady state, the pump rate and the loss rates balance. The final term in Eq. (3), $\eta\alpha_o d_o(1-1/2n^2)$, is irrelevant, since it merely represents re-emission into the pool of trapped luminescent photons and produces no net gain or loss. The external efficiency, η_{ext}, is the escape rate divided by the sum of all the rates in

Eqs. (1) and (3):

$$\eta_{ext} = \frac{\eta\alpha_o d_o / 2n^2}{\left[\eta\alpha_o d_o / 2n^2 + (1-\eta)\alpha_o d_o + \sum_j \alpha_j d_j + (1-\bar{R})/4\right]} \quad (4)$$

This may be further simplified by collecting all parasitic absorption into a loss term L representing the double pass parasitic absorption.

$$\eta_{ext} = \frac{\eta / 2n^2}{\left[\eta / 2n^2 + (1-\eta) + L/4\alpha_o d_o\right]} \quad (5)$$

where the double pass parasitic absorption is: $L \equiv (1-\bar{R}) + \sum 4\alpha_j d_j$.

Experimental

The heterostructures were optically pumped using a continuous wave 780nm AlGaAs laser, focused down to a 300μm spot. Taking into account the laser power (15mW), the pump photon energy, the Fresnel transmission into the heterostructure (68%), and the absorption fraction at the pump wavelength ($0.27 \leq A_p \lesssim 0.55$), we estimate the carrier injection rate to be equivalent to a current density between 2.5 Amp/cm^2 and 5 Amp/cm^2. This low level injection is, nevertheless, well into the radiative diffusion current regime (diode quality factor = 1) and about an order of magnitude above the recombination current dominated injection[14] regime, (diode quality factor = 2). We note that we are near the injection level at which highly efficient GaAs LED's are expected to operate.

The luminescence was collected by an *f*/0.3 lens, focused through an 830nm long-wave-pass optical filter which blocked the pump, and onto a biased Si photodiode. The photodiode output was fed to a lock-in amplifier tuned to the chopping frequency of the pump beam. In all cases, the photoluminescence signal was found to be linear in pump intensity (down to 20% of maximum intensity) as expected in our low-level-injection, but radiative diffusion current dominated, regime. Due to substantial statistical averaging under our experimental conditions as discussed earlier, a Lambertian angular distribution was always observed.

The absolute external quantum efficiency, η_{ext}, was measured by referencing the 880nm photoluminescence signals to elastically scattered light at 780nm from a white surface substituted for the sample in the identical optical setup. A minor correction was made for the difference in Si photodiode sensitivity between 780nm and 880nm wavelength. The signal ratio was then divided by the calculated pump absorption fraction to yield the true value for external quantum yield, η_{ext}.

In estimating the pump absorption, we note that the $Al_{0.3}Ga_{0.7}As$ cladding layers are transparent at the pump wavelength, while the 200nm p-GaAs active layer has an absorption coefficient[15,16] of $\alpha_p = 1.5 \times 10^4$ cm^{-1}. The sample absorption was calculated using a multiple reflection model which takes into account the reflectivity of the metallic substrate and that of the air/semiconductor interface at the 40° incidence angle. We determined a pump absorption fraction $A_p \approx 0.54$ for good reflectors, $A_p \approx 0.3$ on glass, and $A_p = 0.27$ on the wafer before ELO.

The integrated photoluminescence was measured in four different types of specially prepared thin film structures. The four cases, (a)-(d), in Fig. 3 represent different amounts of parasitic optical absorption in the thin film structure:

a. In case (a), only the Au metallic reflector absorbs light. The $Al_{0.3}Ga_{0.7}As$ layers were intentionally left undoped to eliminate free-carrier absorption. We calculated the absorption using the complex refractive index[17] $n_m = 0.199 - 5.84i$ for Au at 880nm, near the luminescence wavelength. This would lead to an air-Au reflectivity $R(0) = 97.8\%$, and an SiO_2-Au reflectivity $R(0) = 96.8\%$. The effective reflectivity is much higher, however. Due to the narrow 25° escape cone entering the SiO_2 layer from the semiconductor, most of the light is totally internally reflected, and only a small portion actually suffers parasitic absorption in the metal. We have calculated the angle and polarization averaged reflectivity to be $\bar{R} = 99.2\%$ for the geometry in Fig. 1.

b. In case (b), the 150nm $Al_{0.3}Ga_{0.7}As$ layers were doped to $3 \times 10^{18}cm^{-3}$, as would be needed for electrical pumping. Assuming the free-carrier absorption cross-sections[16] for electron and hole sum to $1.1 \times 10^{-16}cm^2$, the additional double-pass parasitic optical loss is $L = 2\%$.

c. In case (c), an additional layer of GaAs, 40nm thick, was added in Fig. 1 between the AlGaAs layer and the SiO_2 layer, intentionally for the purpose of contributing parasitic optical absorption. Since the 40nm thick GaAs layer was unpassivated on one side, rapid surface recombination ensured that all absorbed optical energy would degrade rapidly to heat. An averaged band-edge[15] absorption $\alpha_o = 5 \times 10^3 cm^{-1}$ was assumed for the luminescent wavelengths. This implied an additional double pass parasitic loss $L = 8\%$.

d. In case (d), a Palladium mirror was substituted for the the SiO_2-Au mirror. The doped heterostructure, including the 40nm GaAs dead layer, was Van der Waals bonded onto Pd, a procedure which results[18] in a metallurgical reaction and a robust bond. The GaAs-Pd mirror had a measured reflectivity $R(0) = 70\%$, which when combined with the bulk losses resulted in a total double pass parasitic loss $L = 40\%$.

Analysis

The curves in Fig. 3, external yield η_{ext} versus parasitic loss L, represent Eq. (5) with the internal yield η as a parameter. The best fit implies an internal quantum efficiency $\eta = 99.7\%$! Therefore, we can estimate a non-radiative minority carrier lifetime, which is 300 times longer than the radiative time. The internal rate of spontaneous emission is expressed as Bnp, where B is the electron-hole radiative co-efficient and np is the product of electron and hole densities. B is most accurately determined by the Shockley-van Roosbroeck relation[15] which gives[19] $B = 13 \times 10^{-10}cm^{-3}sec^{-1}$, considerably larger than the usually accepted value. At our doping level $p = 3 \times 10^{17}cm^{-3}$ and carrier injection flux of 5 Amp/cm^2, the minority carrier density (n) is roughly 10 times smaller than the hole density (p). Hence, the internal spontaneous emission lifetime per electron is 2.6 nsec, which imply a non-radiative electron lifetime of 0.85 μsec, similar to recent measurements[20] in moderately doped n-GaAs. Moreover, assuming the carrier lifetime is bounded by the GaAs/AlGaAs interfacial recombination processes, we arrive at the conclusion that the interfacial recombination velocity is lower than $d_o/2\tau < 12$ cm/s![20]

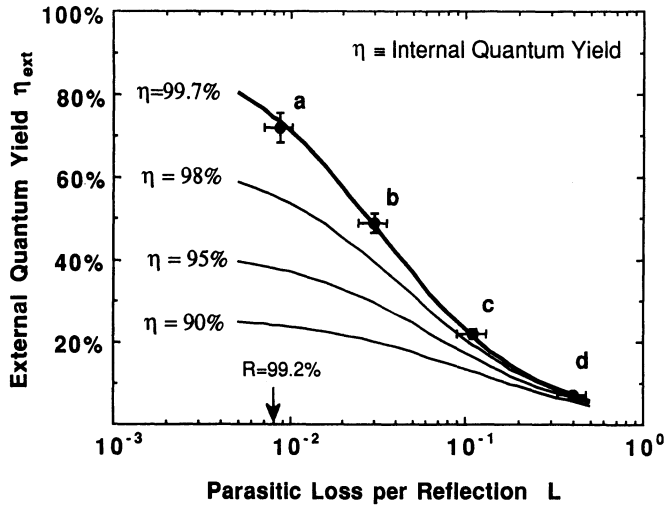

Figure 3. The dependence of external quantum efficiency on double-pass parasitic optical absorption. The theoretical curves are plots of Eq. (5), with internal quantum yield as an adjustable parameter.

CONCLUSIONS

The remarkable internal quantum efficiency and the high self absorption that we have demonstrated are tributes to the electronic quality of doped GaAs double heterostructures. These make it undoubtedly the most suitable material from which single mode spontaneous light sources can be made. It was shown that simple, non resonant, cavity effects can lead to a spontaneous emission external quantum efficiency that was believed to be achievable only by stimulated emission (above some threshold). It was also argued that the spontaneous emission factor β in III-V-based photonic structures can be made close to unity. In that case, we conclude that the shot noise in a single-mode LED can be suppressed to about -25dB [$= 10\log(1-\eta)$] below the standard quantum limit. This possibility is especially attractive for low carrier injection levels (below threshold) where optical systems are truly shot noise limited.

Acknowledgments

This work was partially sponsored by DARPA and ONR under contract N0014-90-C-0048.

REFERENCES

1. T. Kobayashi, T. Segawa, A. Morimoto, and T. Sueta, Technical Digest of the 43rd Fall Meeting of the Japanese Applied Physics Society, Sept. 1982, Proceedings No. 29a-B-6, (in Japanese).

2. Y. Yamamoto, S. Machida, and G. Bjork, Micro-cavity semiconductor lasers with controlled spontaneous emission, *Optical and Quantum Electronics* 24:S215 (1992); H. Yokoyama, K. Nishi, T. Anan, Y. Nambu, S. D. Brorson, E. P. Ippen, and M. Suzuki, Controlling spontaneous emission and threshol-less laser oscillation with optical microcavities, same issue 24:S245; see also other papers in that recent special issue.

3. R. E. Slusher and B. Yurke, Squeezed light for coherent communications, *J. Lightwave Tech* 8:466 (1990).

4. Y. Yamamoto, S. Machida, and W. H. Richardson, Photon number squeezed states in semiconductor lasers, *Science* March 6 issue: 1219 (1992).

5. E. Yablonovitch, T. J. Gmitter, and K. M. Leung, Photonic band structure: the face-centered-cubic case employing nonspherical atoms, *Phys. Rev. Lett.* 67:2295 (1991).

6. E. Yablonovitch, T. J. Gmitter, R. D. Meade, A. M. Rappe, K. D. Brommer, and J. D. Joannopoulos, Donor and acceptor modes in photonic band structure, *Phys. Rev. Lett.* 67:3380 (1991); see also in this volume.

7. E. Yablonovitch, I. Schnitzer, and A. Scherer, Microfabrication of a photonic bandgap structure, Paper No. QWG2 in the Technical Digest of the Quantum Electronics and Laser Science Conf. held at Anaheim CA, May 1992.

8. A. Scherer, E. Yablonovitch, I. Schnitzer, J. L. Jewell, B. P. Van der Gaag, and E. D. Beebe, Microfabrication of ultra-small optical cavities, in this volume.

9. E. Yablonovitch, T. J. Gmitter, J. P. Harbison, and R. Bhat, Extreme selectivity in the lift-off of epitaxial GaAs films, *Appl. Phys. Lett.* 51:2222 (1987).

10. R. J. Nelson and R. G. Sobers, Minority-carrier lifetime and internal quantum efficiency of surface-free GaAs, *J. Appl. Phys.* 49:6103 (1978).

11. W. N. Carr and G. E. Pittman, One-watt GaAs p-n junction infrared source, *Appl. Phys. Lett.* 3:173 (1963).

12. E. F. Schubert, Y.-H. Wang, A. Y. Cho, L.-W. Tu, and G. J. Zydzik, Resonant cavity light-emitting diode, *Appl. Phys. Lett.* 60:921 (1992).

13. E. Yablonovitch, Statistical ray optics, *J. Opt. Soc. Am* 72:899 (1982).

14. For our double heterostructures the cross-over point in injection level from diode quality factor=2 to diode quality factor=1 is estimated to be at $\lesssim$ 1Amp/cm^2, relying on parameters from: E. Yablonovitch, T. J. Gmitter, and B. G. Bagley, As_2S_3/GaAs, a new amorphous/crystalline heterojunction for the III-V semiconductors, *Appl. Phys. Lett.* 57:2241 (1990).

15. J. I. Pankove, *Optical Processes in Semiconductors*, Prentice-Hall, NJ (1971).

16. H. C. Casey, Jr. and M. B. Panish, *Heterostructure Lasers*, Academic Press, NY (1978).

17. M. A. Ordal, R. J. Bell, R. W. Alexander, L. L. Long, and M. R. Querry, Optical properties of Au, Ni, and Pb at submillimeter wavelengths, *Appl. Opt.* 26:744 (1987).

18. E. Yablonovitch, T. Sands, D. M. Hwang, I. Schnitzer, T. J. Gmitter, S. K. Shastry, D. S. Hill, and J. C. C. Fan, Van der Waals bonding of GaAs on Pd leads to a permanent, solid-phase-topotaxial, metallurgical bond, *Appl. Phys. Lett.* 59:3159 (1991).

19. E. Yablonovitch, T. J. Gmitter, and R. Bhat, Inhibited and enhanced spontaneous emission from optically thin AlGaAs/GaAs double heterostructures, *Phys. Rev. Lett.* 61:2546 (1988).

20. G. B. Lush, D. H. Levi, H. F. MacMillan, R. K. Ahrenkiel, M. R. Melloch, and M. S. Lundstrom, Microsecond lifetime and low interface recombination velocities in moderately doped n-GaAs thin films, *Appl. Phys. Lett.* 61:2440 (1992).

LOCALIZATION TRANSITION IN ANISOTROPIC AND INHOMOGENEOUS SYSTEMS

Ping Sheng and Zhao-Qing Zhang+

Exxon Research and Engineering Co.
Rt. 22 East, Annandale, New Jersey 08801
+Also at Bartol Research Institute, University of Delaware
Newark, DE 19716 and
Institute of Physics, Academia Sinica
Beijing, China

I. INTRODUCTION

The Anderson Hamiltonian[1]

$$H = \sum_{\alpha} \varepsilon_{\alpha} a_{\alpha}^{+} a_{\alpha} + t \sum_{nn} a_{\alpha}^{+} a_{\beta} \tag{1}$$

has been the prevalent model for the investigation of localization phenomena during the past few decades. Here $a_{\alpha}^{+}, a_{\alpha}$ are the creation and annihilation operators, respectively, α,β are the indices for sites on a lattice, nn denotes nearest neighbors, t is the hopping matrix element, and ε_{α} is the potential energy at site α, with a distribution $P(\varepsilon_{\alpha})$ for its value. $P(\varepsilon_{\alpha})$ can be either a flat distribution with width W or a Gaussian distribution with a variance W.

From the results of extensive investigations based on Eq. (1), it is now widely accepted that the marginal spatial dimension for localization is two,[2] i.e., all waves are localized in random media with dimensionality two or one. However, an important assumption underlying these investigations is the geometric correlation length of the inhomogeneities is finite, so the medium is macroscopically homogeneous and isotropic. This assumption does not exclude the case where the correlation of the site energies ε_{α} is algebraic. In fact, it has been shown[3,4] that if $<\varepsilon_{\alpha}\varepsilon_{\beta}>$ = constant

Photonic Band Gaps and Localization, Edited by
C.M. Soukoulis, Plenum Press, New York, 1993

$|R_\alpha - R_\beta|^{-\gamma}$, where < > denotes ensemble averaging and R_α, R_β denote the impurity sites, then the localization behavior in 1D and 2D does depend strongly on the value of γ, yet the overall localization characteristics still conform to the prediction of the scaling theory of localization. This is because the impurity energies are algebraically correlated, yet their spatial distribution is still macroscopically homogeneous and isotropic.

In this paper, we consider two different models of long-range correlations where the assumption of isotropy and macroscopic homogeneity is violated. The first model is anisotropic so it breaks the isotropy symmetry. The second model is a fractal impurity model which breaks the property of macroscopic homogeneity. We show here these two models exhibit novel localization characteristics distinct from those considered previously.

2. DESCRIPTION OF MODELS

In this section, we describe the anisotropic model and the fractal model separately and delineate some of their salient localization features.

2a. Anisotropic Model

Consider a three-dimensional randomly layered system with lateral inhomogeneity in each layer. The value of ε_α in Eq. (1) can be written to model such a system as a sum of two components, one purely layered component γ_k and another purely isotropic component η_{ik}:

$$\varepsilon_\alpha = \theta\eta_{ik} + (1-\theta)\gamma_k$$

with

$$P(\gamma_k) = P(\eta_{ik}) = P(x) = \begin{cases} \frac{1}{W}, |x| \le \frac{W}{2} \\ 0, \text{ otherwise} \end{cases}, \qquad (2)$$

where k denotes the anisotropy axis z, i denotes the transverse directions x and y, γ and η are random variables with a flat distribution P of width W, and θ is an anisotropy parameter, varying between 0 and 1. The function of the θ parameter is to interpolate the randomness between a 1D layered (θ=0) and a 3D isotropic (θ=1) system. From (2), it is easy to see that, for any $\theta < 1$, an infinite-range correlation (of amount $(1-\theta)\gamma_k$) in the site energy is introduced in each layer k. The numerical and analytic approaches used to analyze this model will be described in Sections 3 and 4. The most salient features of the results are as follows. First, there exists a Fermi-energy-dependent

critical θ_c below which the wave function is localized for arbitrarily small randomness, and above which the system acquires three-dimensional characteristics. An interesting reentry phenomenon is found in the localization phase diagram near the band edge, where the density of states is small. Expressions for the localization lengths are obtained analytically in the localized regime when the randomness is small. The behavior of the localization length in the layering direction is found to follow the simple one-dimensional result, while in the transverse direction the localization length behaves differently from the standard two-dimensional result. The physical reasons underlying these behaviors will be given in Section 3. Here, we only note that our anisotropic model should be contrasted with that arising from an isotropic dispersion of anisotropic scatterers (or locally anisotropic environments), usually modeled by an anisotropic hopping matrix element t, where the system delocalizes for small W as soon as the scattering deviates from strict one dimensionality.[6] In this case, the interpolation between 1D and 3D is smooth and does not have a critical value of anisotropy.

2b. Fractal Impurity Model

In the fractal impurity model, the impurity correlation length ζ is larger than the sample size. For instance, if the impurity is a single fractal of infinite size, there exists no scale in the sample above which the system is homogeneous. Geometrically, this model is complementary to systems where the electron or the wave is confined on the fractal objects, where it has been suggested that the localized wave function may decay faster than exponential, i.e., superlocalized.[7] Here, instead of confining the electron or the wave, the fractally-correlated impurities are embedded in an otherwise homogeneous host medium and act as wave scatterers.

In the fractal impurity model,[8] the site energy ε_α in Eq. (1) is assigned as

$$\varepsilon_\alpha = \begin{cases} W_0 & \text{for the impurity site} \\ 0 & \text{for the host site} \end{cases} . \qquad (3)$$

Here, W_0 denotes the barrier height of an impurity atom. This problem has been studied both numerically and diagrammatically in two dimensions, which is the marginal dimension of localization for the homogeneously disordered systems. What is shown is contrary to the conventional conclusion that all waves are localized in 2D, here the 2D fractal impurity model exhibits a metal-insulator transition. This transition is accessible through the variation of either the Fermi energy or the impurity scattering strength W_0. Moreover, in the metallic regime the electronic transport is shown to be superdiffusive in nature, i.e., faster than diffusion but slower than ballistic.

The numerical method we use to study both the anisotropic and the fractal-impurity models is the standard finite-size scaling approach. The analytic method used here is based on the diagrammatical theory of Vollhardt and Wolfle,[9] with some generalizations. Below, we describe these methods separately for each model, along with the presentation of the results. For convenience, we set both the hopping matrix t and the lattice constant to one.

3. THE ANISOTROPIC MODEL

3a. Analytic Approach

The self-consistent diagrammatical theory of Vollhardt and Wolfle[9] is generalized to the anisotropic model of Eqs. (1) and (2). Schematically, the general procedure may be described as follows. Starting with the Kubo formula,[10] we first evaluate the conductivity tensor by including the ladder and maximally-crossed diagrams. The ladder diagrams give the bare conductivity tensor, while the maximally cross diagrams account for the localization effect. By summing these diagrams and using the Einstein relation, a set of two coupled self-consistent equations for the two diffusion constants, perpendicular ($D_\perp$) and parallel ($D_\parallel$) to the layers, are obtained. The condition of vanishing diffusion constants then determines the mobility edge. In the localized regime, the frequency dependence of these two diffusion constants give the localization lengths in directions perpendicular ($\zeta_\perp$) and parallel ($\zeta_\parallel$) to the layers. Below, we give a more detailed description of the approach.[6]

The Hamiltonian given by Eq. (1) can be rewritten in the momentum representation as,

$$H = H_0 + H_1 = \sum_p \varepsilon(p) a_p^+ a_p + \sum_{p,q} v(q) a_{p+q}^+ a_p \ , \qquad (4)$$

with $\varepsilon(p) = \Sigma_\delta \exp(-ip.\delta)$, and $v(q) = N^{-1} \Sigma_\alpha \varepsilon_\alpha \exp(iq.r_\alpha)$. Here, δ denotes the vector pointing from a site to one of its nearest neighbors, N is the total number of sites, and r_α is the spatial coordinate of site α. The averaged single-particle Green's function has the form

$$R_p = \langle G_p \rangle = 1/[z - \varepsilon(p) - \Sigma_p] \ , \qquad (5)$$

where z is the complete energy and Σ_p is the self-energy. Within the self-consistent Born approximation,[5] the form of ε_α in Eq. (2) gives following equation for the self-energy Σ_p,

$$\Sigma_p = \sum_q \langle v(q)v(-q)\rangle R_{p+q} = \frac{W^2}{12}\theta^2 \frac{1}{N}\sum_{p'} \frac{1}{z-\varepsilon(p)-\Sigma_{p_\parallel}} + \frac{W^2}{12}(1-\theta)^2 \frac{1}{N_\perp}$$

$$\sum_{q_\perp} \frac{1}{z-\varepsilon\left(p_\parallel + q_\perp\right)-\Sigma_{p_\parallel}}, \tag{6}$$

where $N_\perp$ is the number of layers and $\parallel$, $\perp$ denote components of the vector that are parallel or perpendicular to the layers, respectively. The term proportional to θ^2 in Eq. (6) represents contributions from isotropic scattering, whereas the term proportional to $(1-\theta)^2$ represents contributions from scattering in the layering, or the z direction. The self-energy is noted to depend only on $p_\parallel$. The zero-temperature Kubo formula[10] for the conductivity tensor has the form

$$\sigma_{ik}(E,\omega) = -\frac{2\pi e^2}{N}\left(\phi_{ik}^{RA} + \phi_{ik}^{AR}\right), \tag{7a}$$

with

$$\phi_{ik}^{AR}(E,\omega) = \frac{1}{4\pi^2}\sum_{p_1 p_2} v_1(p_1) \langle\langle p_1 | G^-(E_+) | p_2 \rangle v_k(p_2) \langle p_2 | G^+(E_-) | p_1 \rangle\rangle, \tag{7b}$$

where $E_\pm = E \pm \omega/2$, E is the Fermi energy, ω is the exciting frequency, $v_i(p) = \partial p_i \varepsilon(p)$ is the velocity matrix element, AR denotes averaged advanced (-) and retarded (+) Green's functions, and we have neglected terms like ϕ^{AA}, ϕ^{RR} because they are inherently small (they have two poles on the same side). The ensuing calculation of ϕ_{ik}^{AR} consists of evaluating two classes of diagrams: the ladder diagrams and the maximally crossed diagrams. The latter represents the coherent backscattering effect that gives rise to localization.[9]

The ladder-diagram contributions to ϕ_{ik}^{AR}, denoted as $\phi_{ik}^{RA(0)}$, are shown in Fig. 1(a). For the $\perp$ component σ_{kk}, only the first term contributes because all other diagrams vanish after the summation of p_1 or p_2. By using the Einstein relation, $\sigma(E) = 2e^2\rho(E)D(E)$, where $\rho(E)$ is the density of states, we get

$$D_{\perp}^{(0)} = \frac{1}{2\pi\rho(E)} \frac{1}{N} \sum_{p} \frac{v_k^2(p)\Delta R_p}{\Delta \Sigma_p}. \tag{8a}$$

Here $\Delta Rp = R_p^+ - R_p^-$ and $\Delta \Sigma_p = \Sigma_p^+ - \Sigma_p^-$. For the $\|$ component of the diffusion constant, on the other hand, one can allow any number of scatterings in the z direction, since they preserve parallel momentum. Summation of the infinite series yields

$$D_{\|}^{(0)} = 3v_{\|}^2 / \pi W^2 \theta^2 \rho(E), \tag{8b}$$

where

$$v_{\|}^2 = \sum_p \Delta R_p \left[v_x^2(p) + v_y^2(p) \right] / \sum_p \Delta R_p. \tag{8c}$$

We note that as $\theta \to 0$, $D_{\|}^{(0)} \to \infty$, but $D_{\perp}^{(0)}$ is always finite due to the scattering in the z direction. The vertex correction $\delta\phi_{ik}^{RA(1)}$ due to one set of maximally crossed diagrams may be expressed as

$$\delta\phi_{ik}^{RA(1)} = \frac{1}{4\pi^2} \sum_{pp'} v_i(p) v_k(p') R_p^+ R_p^- R_{p'}^+ R_{p'}^- \, x$$

$$\sum_{p_1 p_2} U^{(0)}(p, p_1) U^{(M)}(p_1, p_2) U^{(0)}(p_2, p'). \tag{9}$$

Here $U^{(o)}$ represents the summation of ladder diagrams from the z scatterings as shown in Fig. 1(b), and $U^{(M)}$ consists of diagrams shown in Fig. 1(c). From $\delta\phi_{ik}^{RA(1)}$ one can easily write down the correction $\delta\phi_{ik}^{RA(n)}$ due to a series of n consecutive vertex corrections. By summing all the nth order contributions $\delta\phi_{kk}^{RA(n)}$ and denoting the result as $\delta\phi_{kk}^{RA}$, we get

$$\frac{D_{\perp}(E,\omega)}{D_{\perp}^{(0)}(E)} = 1 + \frac{\delta\phi_{kk}^{RA}}{\delta\phi_{kk}^{RA(0)}} \sim 1 - \frac{F_{\perp}(E)}{N} \sum_{K} \frac{\Delta\tau^{-2}(E)}{\left[\Delta\tau^{-1}(E) - i\omega + D_{\perp}^{(0)} K_{\perp}^2 \right]^2} \, x$$

$$\frac{D_{\perp}(E,\omega)}{-i\omega + D_{\perp}^{(0)} K_{\perp}^2 + D_{\|}^{(0)} K_{\|}^2}$$

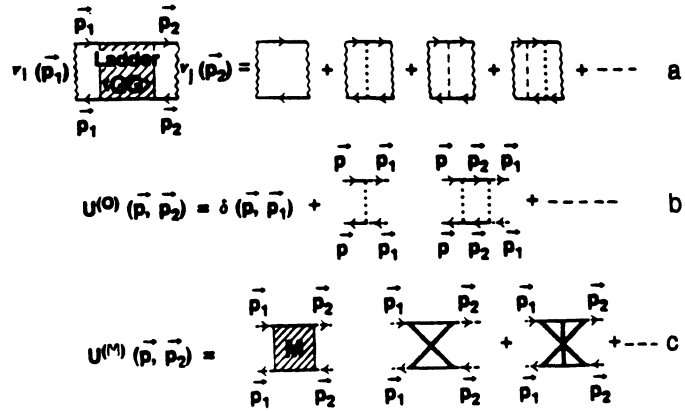

Fig. 1. (a) The ladder diagrams, consisting of two types of scattering. The dotted line denotes the z-direction scattering. Isotropic scattering is denoted by a dashed line. (b) The ladder diagrams that give rise to $U^{(0)}(p, p_1)$. (c) The maximally crossed diagrams that contribute to $U^{(M)}(p_1, p_2)$. The heavy lines represent the sum of isotropic and z-direction scatterings.

$$\frac{F_\perp(E)}{N_\perp}\left(1-\frac{\tau_\perp(E)}{\tau_\parallel(E)}\right)\sum_{K_\perp}\frac{D_\perp(E,\omega)}{\left[-i\omega/D_\perp^{(0)}(E)+K_\perp^2+\kappa_\perp^2\right]D_\perp^{(0)}(E)}, \tag{10a}$$

where

$$F_\perp(E)=\left[\pi\rho(E)D_\perp^{(0)}(E)\right]^{-1}, \Delta\tau=(1-\theta)^2/2\gamma(E)\theta^2, \kappa_\perp^2=\left(D_\perp^{(0)}\Delta\tau\right)^{-1},$$

$$\tau_\parallel=6/W^2\theta^2\pi\rho(E),$$

$$\tau_\perp=-i\sum_p\frac{1/\Delta\sum_p}{N}, \tag{10b}$$

and

$$\gamma(E)=-i\sum_p\frac{\Delta\sum_p}{2N}. \tag{10c}$$

It is straightforward to check that as $\theta\to 1$, $\Delta\sum_p=i\pi W\rho(E)/6$, $\tau_\parallel=\tau_\perp D_\perp^{(0)}=D_\parallel^{(0)}$, and we recover the isotropic result. For $\theta\to 0, \tau_\parallel\to\infty$, but

$\tau_\perp$ remains finite so that $\Delta\tau \to \infty$. That means the second term in Eq. (10a) vanishes, and we recover the result of a one-dimensional random system. Similarly, for the parallel component we get

$$\frac{D_\parallel(E,\omega)}{D_\parallel^{(0)}(E)} \simeq 1 - \frac{F_\parallel(E)}{N}\sum_K \frac{\Delta\tau^{-2}(E)}{\left[\Delta\tau^{-1}(E) - i\omega + D_\perp^{(0)}K_\perp^2\right]^2} \frac{D_\parallel(E.\omega)}{-i\omega + D_\perp^{(0)}K_\perp^2 + D_\parallel^{(0)}K_\perp^2} \tag{11}$$

where $F_\parallel(E) = 4\gamma(E)/\pi\rho(E)v_\parallel^2$, and $v_\parallel^2$ is defined by Eq. (8c). Again, in the $\theta \to 1$ limit we recover the isotropic result, whereas when $\theta \to 0, \tau_\parallel \to \infty$ so there is no localization effect in the parallel component as it should be. We propose to introduce self-consistency into Eqs. (10a) and (11) by writing $D_\perp(E,\omega)$ and $D_\parallel(E,\omega)$ for all the explicitly displayed $D_\perp^{(0)}$ and $D_\parallel^{(0)}$, respectively, but only the righthand sides.[5] The two equations are then coupled.

At mobility edge, both $D_\parallel(E,\omega = 0^+)$ and $D_\perp(E,\omega = 0^+)$ vanish. The equations to determine the mobility edge become

$$\frac{D_\perp(E)}{D_\perp^{(0)}} = 0 = 1 - F_\perp(E)r(E)\frac{1}{N}$$

$$\times \sum_K \frac{1}{r(E)K_\perp^2 + K_\parallel^2} - G(E)\,, \tag{12a}$$

$$\frac{D_\parallel(E)}{D_\parallel^{(0)}} = 0 = 1 - F_\parallel(E)\frac{1}{N}\sum_K \frac{1}{r(E)K_\perp^2 + K_\parallel^2}, \tag{12b}$$

where $r(E) = D_\perp(E)/D_\parallel(E)$ and $G(E)_d$ denotes the last term on the righthand side of Eq.(10a) after we set $D_\perp^{(0)} = D_\perp$ and $\omega = 0$. From the two equations, the ratio r(E) may be expressed explicitly as $r(E) = F_\parallel(E)[1 - G(E)]/F_\perp(E)$. This results in a single equation for the mobility edge:

$$1 = F_{\|}(E)F_{\perp}(E)\frac{1}{N}$$

$$\times \sum_{K} \frac{1}{F_{\perp}(E)K_{\|}^2 + F_{\|}(E)[1-G(E)]K_{\perp}^2} . \qquad (13)$$

Here the summation over K represents a double integral over $K_{\|}$ and $K_{\perp}$, each having an upper cutoff of $|K_{\|}| \le \chi_0 / \ell_{\|}(E)$ and $|K_{\perp}| \le \chi_0 / \ell_{\perp}(E)$, with $\ell_{\|} = 3\sqrt{2}D_{\|}^{(0)} / v_{\|}(E)$, $\ell_{\perp}(E) = 3D_{\perp}^{(0)} / v_k(E)$, and χ_0 chosen so that at $\theta = 1$, we recover the known critical value[11] of $W_c = 16.2$ at $E = 0$.

Based on Eq. (13), mobility-edge curves of $W_c(\theta)$ are calculated for the cases of E=0,4, and 6 and are shown in Fig. 2 in solid lines. The interesting feature about the curves is that for each E there is a critical value of $\theta = \theta_c$ (=0.18 for E=0, for example) below which all states are localized even for $W = 0^+$.

Above θ_c, the value of W_c is seen from Fig. 2 to have a peak that is above the 3D isotropic value. This is due to the net decrease of isotropic disorder, for a fixed W, as θ decreases from 1. As a result, W_c increases with decreasing θ until the effect of 1D scattering catches up. Another interesting effect is noted to exist for E ≈5-6, i.e., close to the band edge. Here, $W_c(\theta)$ is seen to form a loop so in a range of θ values there can be two values of W_c for a given θ. Our analysis reveals that the localization below the lower W_c is induced by the small density-of-states near the band edge, which favors localization. As W increases towards the lower W_c value for a fixed θ, the density-of-states near the band edge also increases (this can be seen in the coherent-potential-approximation calculation of the tight-binding model[12]), which, in turn, delocalizes the state for $W > W_c$ (lower).

In the localized regime, $\theta < \theta_c$, the equations for the localization lengths $\xi_{\perp}$ and $\xi_{\|}$ can be obtained from Eqs. (10) and (11) by first renormalizing the diffusion constants and then setting $\lim_{\omega \to 0}\left[-i\omega / D_{\perp,\|}(\omega, E)\right] = \xi_{\perp,\|}^{-2}(E)$. If we define the function r(E) as the square of the ratio of localization lengths, i.e., $r = \left(\xi_{\perp} / \xi_{\|}\right)^2$, the localization length equations become

$$1 = F_{\perp}(E)r(E)\frac{1}{N}\sum_{k}\frac{1}{r(E)\left[\xi_{\perp}^{-2}(E) + k_{\perp}^2\right] + k_{\|}^2} - F_{\perp}(E)\left[1 - \frac{\tau_{\perp}(E)}{\tau_{\|}(E)}\right]\frac{1}{N_{\perp}}$$

$$\times \sum_{k_{\perp}} \frac{1}{\xi_{\perp}^{-2}(E) + \kappa_{\perp}^2 + k_{\perp}^2}, \qquad (14)$$

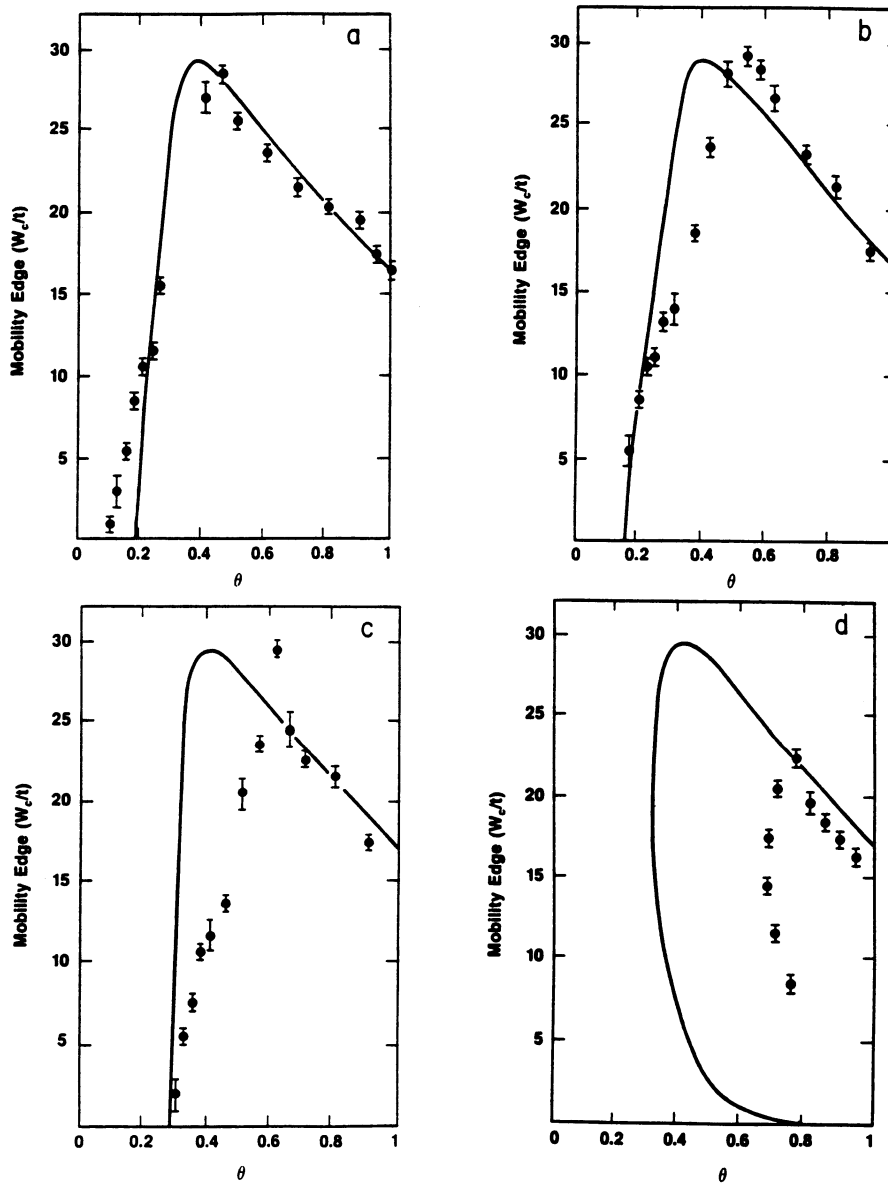

Fig. 2. Values of W_C plotted as a function of θ for (a) E=0, (b) E=2, (C) E=4, and (d) E=6. The solid lines denote the results calculated from diagrammatical analysis. Simulation results are denoted by solid circles together with their error bars.

and

$$1 = \frac{F_{\|}(E)}{N} \sum_{k} \frac{1}{r(E)\left[\xi_{\perp}^{-2}(E) + k_{\perp}^{2}\right] + k_{\|}^{2}} \,. \tag{15}$$

In general, Eqs. (14) and (15) must be solved numerically. However, at small randomness the asymptotic behavior of $\xi_{\perp}$ and $\xi_{\|}$ may be studied analytically. By writing $F_{\perp}$, $F_{\|}$, $\kappa_{\perp}$ and momentum cutoffs $k_{\perp}^{c}$ and $k_{\|}^{c}$ in Eqs. (14) and (15) to the first order in W^2, a simple analysis yields the following results,[5]

$$\xi_{\perp} \cong \frac{c(\theta)}{W^2} \,, \tag{16}$$

and

$$\xi_{\|} \cong g(\theta, W) \exp\left[\frac{d(\theta)}{W^4}\right] \,, \tag{17}$$

where $c(\theta)$ and $d(\theta)$ are independent of W, and the W dependence of the function $g(\theta,W)$ is in a power-law form. Equation (16) gives the same asymptotic behavior as the 1D result. However, Eq. (17) gives a behavior that is different from the standard 2D result[13] of $\xi_{2D} \cong \left(a_1 / W^2\right) \exp\left(a_2 / W^2\right)$.

Since $r = \left(\xi_{\perp} / \xi_{\|}\right)^2 \to 0$ as $W \to 0$, the localized regime below θ_c is essentially 1D in its character. If we fix W and let θ approach the mobility edge θ^* ($\theta^* \to \theta_c$ as $W \to 0$), our analysis shows that $c(\theta)$ diverges as $c(\theta) \propto \left(\theta - \theta^*\right)^{-1/2}$. In this limit, both $\xi_{\perp}$ and $\xi_{\|}$ diverge and r increases to order one. Thus, 3D character is recovered as the mobility edge is approached. These characteristics should be contrasted with those for the anisotropic hopping model, where an infinitesimal coupling between the 1D chains would yield the 3D behavior of delocalization below a W_c.

The reason behind the existence of θ_c in our anisotropic model is the existence of infinite-range correlation in the site energy along the layer plane, i.e., the term $(1-\theta)\gamma_k$ in Eq. (2). This term produces a unique ID scattering mechanism as can be seen in the last term of Eq. (6). Since this ID scattering does not have the coherent-backscattering effect for an electron moving along the layer direction, this breaks the symmetry between the transport behaviors in the transverse and the layering directions, as can be seen from the absence of ID coherent-backscattering term in Eq. (11), compared to Eq. (10a). It is this ID scattering mechanism which gives rise to all the novel characteristics of our anisotropic model discussed above.

Physically, the critical θ_c can be seen as a plausible consequence of competition between isotropic scattering, which would give rise to an isotropic mean-free path, and

the ID localization. As θ increases from 0 (the 1D limit), initially the isotropic mean-free path would be so much longer than the 1D localization length that the election would be 1D localized before it can be scattered out of the layering direction. As θ approaches θ_c, however, isotropic scattering becomes stronger and comparable to the 1D scattering, until finally it becomes dominant as θ crosses θ_c.

3b. Numerical Approach

Since the diagrammatical analysis described above does not represent a rigorous theory, we have numerically simulated the model described by Eqs. (1) and (2) to verify the validity of our analytical results.

We consider a 3D sample in a rod geometry of length N and cross section MxM, governed by the Hamiltonian defined in Eqs. (1) and (2). The layering direction is defined to be the lengthwise direction along the rod. Both ends of the rod are connected to perfect leads, i.e., W=0. For such a system, the transmission amplitude of an electron through the disordered rod can yield the localization length L_M of the rod.

If the periodic boundary condition is chosen in the transverse direction, then the propagating eigenstates in the ordered region are just plane waves labeled by a continuous momentum index K_z in the direction along the rod and two discrete transverse momentum indices K_x and $K_y = \pi n/(M+1)$ (n=0, $\pm$1,...,$\pm$M/2 if M is even; n=$\pm$1,$\pm$2,$\pm$(M+1)/2 if M is odd). The dispersion relation is then

$$E = 2(\cos K_z + \cos K_x + \cos K_y). \tag{18}$$

Consider each set (K_x,K_y) as a channel, denoted as I. There are a total of MxM channels in the rod. For a given energy E, the real solutions of K_z from Eq. (18) determine the number of channels open for wave propagation. The transmission matrix t_{IJ} between a channel I at one end of the rod and a channel J at the other end is related to Green's function $G_{IJ}(0,N+2)$ which can be calculated by using the recursive Green's function technique as described in the work of Lee and Fisher.[14] The result is

$$|t_{IJ}|^2 = v_I v_J |G_{IJ}(0,N+2)|^2, \tag{19}$$

where the channel velocity v_I in Eq. (19) is given by $\partial E/\partial K_z$ evaluated at $K_z(I)$. The localization length L_M of the rod is related to the transmission matrix by

$$L_M = \frac{-1}{2N} \ln \mathrm{Tr}\ t^+ t = \frac{-1}{2N} \sum_{IJ}^{L_0} |t_{IJ}|^2,$$

with L_0 denoting the numbers of propagating channels. The length N must be long enough so that L_M has converged to a constant value. In addition, the variance

$\Delta L_M(N)^2$ has to be small so that the value of L_M is accurate. This can be achieved either by averaging over many configurations or by considering a long rod. From the knowledge of L_M, the localization character of a state is determined by the behavior of L_M/M versus M as described by MacKinnon and co-workers,[15] i.e., L_M/M increasing with M indicates a delocalized state, whereas L_M/M decreasing with M indicates a localized state. The mobility edge curves so determined are shown in Fig. 2 for E=0, 2, 4 and 6. It is seen that for E=0 the agreement is remarkably good. Both the peak value of W_c as well as the sharp rise of W_c beyond $\theta_c \simeq 0.18$ are also in reasonable agreement with the numerically extrapolated value of $\theta_c \simeq 0.1$. However, quantitative agreement deteriorates as E increases towards the band edge, although the numerical results do indeed verify the main features of the theory, e.g., the re-entrant transitions for E near the band edge. We have also carried out simulations up to M=9 for θ slightly below θ_c and W small, i.e., θ=0.07, W=0.5 for E=0 and θ=0.1, W=1 for E=2, and verified that states are indeed still localized at these small values of W. Thus, our numerical simulations confirm the existence of a critical θ_c predicted by the diagrammatical theory.

4. THE FRACTAL-IMPURITY MODEL

In the fractal impurity model, we consider the case where the impurities form a connected critical percolation cluster, which has a known fractal dimension[16] $\bar{d} = 1.89$. Other random fractals, like diffusion-limited aggregates,[17] are also physically plausible systems. We would like to emphasize that our model differs from the long-range correlation model studied previously[3,4] where the site energy ε_α in Eq. (1) is correlated with a power-law decay, i.e., $\langle \varepsilon_\alpha \varepsilon_\beta \rangle \approx c / |R_\alpha - R_\beta|^\gamma$. In our case the value of c is not a constant and varies as a function of sample size. In fact, this situation is parallel to the case of a percolation system at the threshold p_c. If the isolated clusters are not removed, then the correlation function conditioned by connectivity has a power-law decay, yet the average density of the occupied sites is always p_c, independent of sample size. In our fractal model, since only the connected critical cluster is kept, the average density of the impurity decreases with the sample size according to $L^{\bar{d}-d}$, where d denotes the embedding space dimension. Thus, there exists no scale above which the system is macroscopically homogeneous. The fractal impurity model has been studied by using both numerical and analytical approaches. Since the system is not macroscopically homogeneous, the conventional diagrammatical method, which requires a uniform impurity density, does not apply. We have modified the diagrammatical method to study our fractal impurity model by calculating the conductance of a finite sample of size L, where the averaged density varies with L. However, since the connectivity of the fractally-correlated impurities cannot be

incorporated into our analytical theory, the results of the analytic calculations must be checked against numerical simulations. Below, we first present the numerical approach.

4a. Numerical Approach

The numerical method used here is similar in nature to that described in section 3b. A 2D fractal impurity sample of size LxL is generated by the following procedure. At $p=p_c=0.593$, site percolation clusters are generated numerically using the random number generator.[16] Only those configurations where percolation paths exist along both the horizontal and the vertical directions are kept. All the isolated clusters are removed, leaving only a single critical percolation cluster. We connect the sample by two perfect leads in the z-direction. The Hamiltonian of the disordered sample is governed by Eqs. (1) and (3), while, in the leads, we have the dispersion relation

$$E = 2(\cos k_x + \cos k_z). \tag{20}$$

By using the hardwall boundary condition, K_x has the values $K_x = \frac{\pi n}{L+2}$, n=1,2,..l.,L+1. Again, the real-number solution of k_z in Eq. (20) determines the number of propagating channels L_o. The dimensionless conductance is related to the transmission matrix t_{IJ} by[2]

$$g = \frac{G}{e^2/h} = \mathrm{Tr}\ t^{+}t = \sum_{I,J}^{L_o} |t_{IJ}|^2 . \tag{21}$$

Here $|t_{IJ}|^2$ is related to Green's function by Eq. (19), which can be evaluated by using the recursive Green's function method.[14] The results of numerical calculation at E=0.5 are shown in Fig. 3 (solid lines). The dashed lines are the results of diagrammatic evaluations to be described later. It is seen that for $W_o < W_o^c \approx 2.9 \pm 0.5$, <g> increases with L, indicating a delocalized behavior; whereas for $W_o > W_o^c$ <lng> decreases with L, indicating a localized behavior. For reference, the classical 2D conductance, i.e., pure diffusive behavior, is noted to be sample-size independent, and the ballistic transport behavior is generally characterized by linear variation of T with L, since in that case T is directly proportional to the number of channels. Therefore, the intermediate behavior of the delocalized regime, $0<W_o<W_o^c$, is indicative of superdiffusive transport that interpolates between diffusive and ballistic behaviors. We will discuss this regime in more detail later. For $W_o<W_o^c$, on the other hand, the

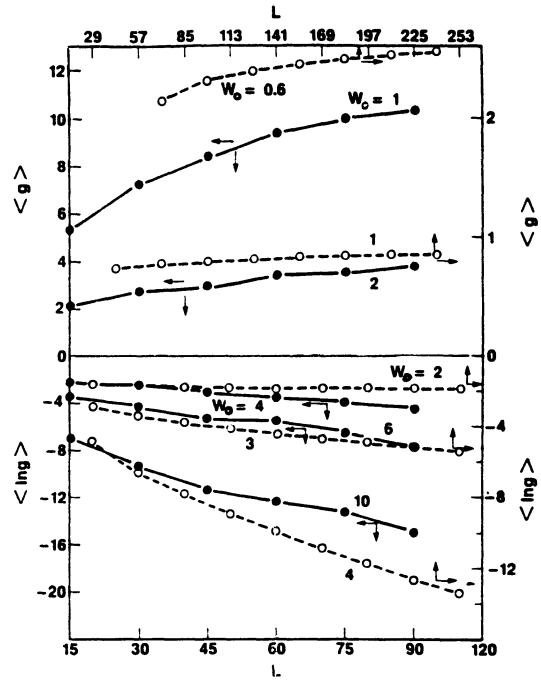

Fig. 3. Conductance variation as a function of sample size L for various values of W_0. The Fermi energy is 0.5. Solid lines denote the simulation results calculated by the recursive Green's function method, averaged over 3500 configurations for L=15 to 200 configurations for L=90. Dashed lines are calculated from solving the self-consistent diagrammatic theory. Classical 2D conductance (purely diffusive) would be a flat line (L independent). Ballistic transport is represented by a linear dependence on L. The vertical axis is linear for the delocalized regime and logarithmic for the localized regime.

variation of <lng> with L is nonlinear. This indicates a sub-exponential localization behavior.

As opposed to the homogeneous-impurities case, where in 2D all waves are localized, for impurities arranged with fractal symmetry a metal-insulator transition can occur in 2D through the variation of either the Fermi energy E or the scattering barrier height W_0, or both. In Fig. 4 we show the phase diagram calculated by the recursive Green's-function method as described above. For a fixed W_0=3.6, the drastic conductance changes as a function of E are illustrated in Fig. 5 as one crosses from the insulating regime to the conducting regime and then to the insulating regime again. The steepness of the conductance variation is noted to increase as the sample size increases. Thus for field-effect transistors it may be envisioned that based on the present metal-insulator transition phenomenon, one can have a gate-voltage-controlled

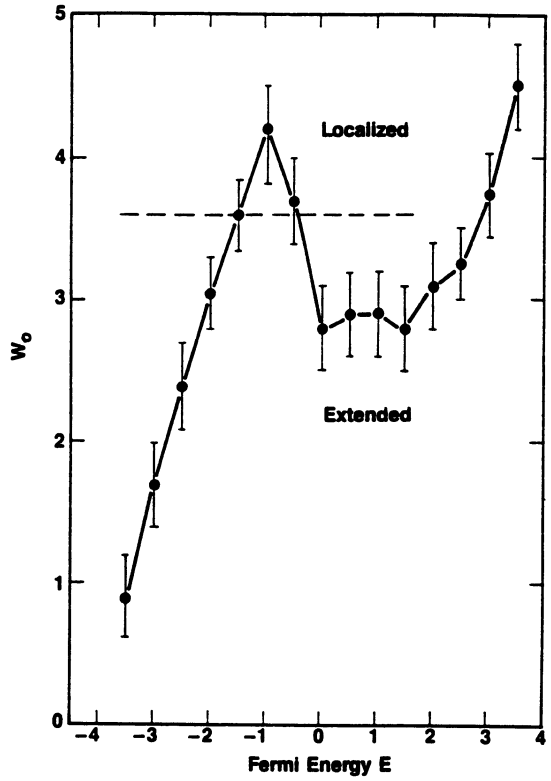

Fig. 4. Phase diagram as a function of W_0 and E calculated from recursive Green's function simulations. The bars indicate estimated error for each point. The transition in behavior is obtained by many runs at different W_0 and E, each averaged over 200-3000 configurations depending on the sample size. The dashed line indicates the cross section examined by Fig. 5.

switch (through the variation of Fermi energy) if the scattering impurities can be arranged in a fractal pattern.

In the extended regime, if we denote $g(L) \sim D(L) \propto L^s$, then the mean-square displacement $L^2 = D(L)\tau \propto L^s\tau$, or $L^2 \propto \tau^{2/(2-s)}$, where s varies between 0 and 1 depending on the values of W_0 and E. At E=0.5, the value of s can be extracted from Fig. 3, yielding $s \approx 0.43$ and 0.33 for $W_0 = 1$ and 2, respectively.

The superdiffusive transport and the transition between the localized and delocalized behaviors can also be studied in the space-time domain by directly solving the time-dependent Schrödinger's equation $i\partial\varphi / \partial\tau = H\varphi$, where the time τ is in units of $\hbar / t$ and H is given by Eq. (1). The diffusion constant D may often be evaluated as $D = d \langle\varphi|r^2|\varphi\rangle / d\tau$ as a function of τ. Besides offering a consistency check, the space-time simulation also offers the possibility of studying much larger sample sizes.

We have carried out time-domain simulations on 800x800 samples by using the unconditionally stable numerical scheme developed by de Raedt.[18] For comparison, we have also calculated the cases where the distribution of impurities is homogeneous.

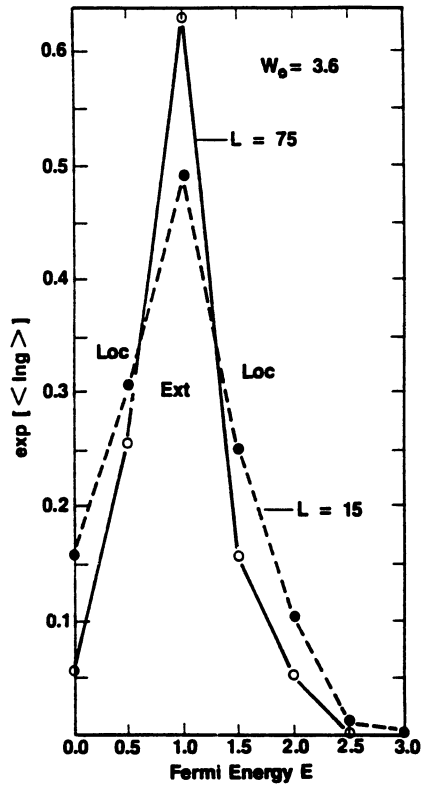

Fig. 5. Fermi-energy dependence of exp[<lng>] at W_0=3.6, for two sample sizes. The phenomenon of metal-insulator transition is clearly demonstrated by the sharp variations of the conductance as one crosses the mobility edges.

Figure 6 shows the comparison of the density variations of the two impurity distributions as a function of distance measured from the center of a 800x800 sample. For both fractal impurity sample (curve a) and homogeneous impurity sample (curve b) have the same overall density of p ≈0.34. A wave packet with <E>=0 is created at the center of the square, by using the projection operator method.[19] Figure 7 shows the calculated variation of $D=d<r^2>/d\tau$ as a function of time for three different values of W=1, 1.5, and 2. For the homogeneous cases, denoted by H, D is a slightly decreasing function of τ since the waves are localized, but the localization lengths are large due to the low density of scatterers. As a result the behavior is nearly diffusive, with D ≈const. For the fractal-impurities case, on the other hand, D is noted to be a monotonically increasing function of τ for $W_0<3$. The values of s deduced for W_0= 1 and 2 are 0.36 and 0.3, respectively. These results are consistent with the recursive Green's function calculations.

The value of s decreases monotonically to zero at W_0^c. Figure 8 shows the variations of D for W_0=2.5 and 3.5 on fractal impurity. The case of W_0=3.5 shows an insulating behavior with D ≈0. Thus, the value of W_0^c lies between 2.5 and 3.5. This is again consistent with the Green's function calculation which gives $W_0^c \approx 3$ for E ≈0.

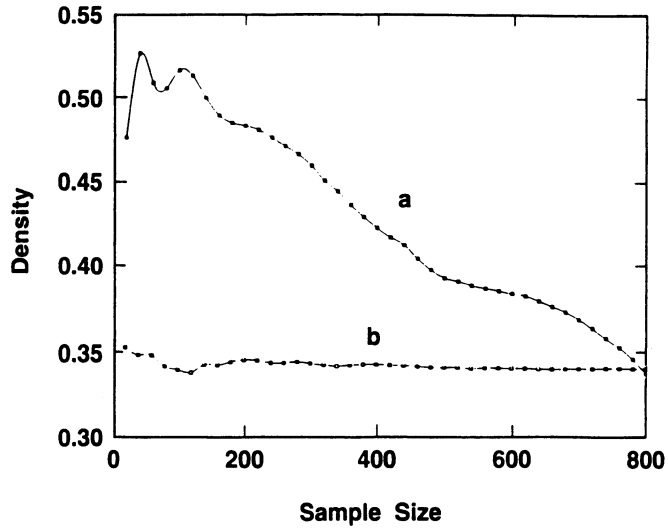

Fig. 6. Averaged impurity density measured as a function of sample size, up to 800x800; (a) critical percolation cluster, and (b) homogeneous distribution.

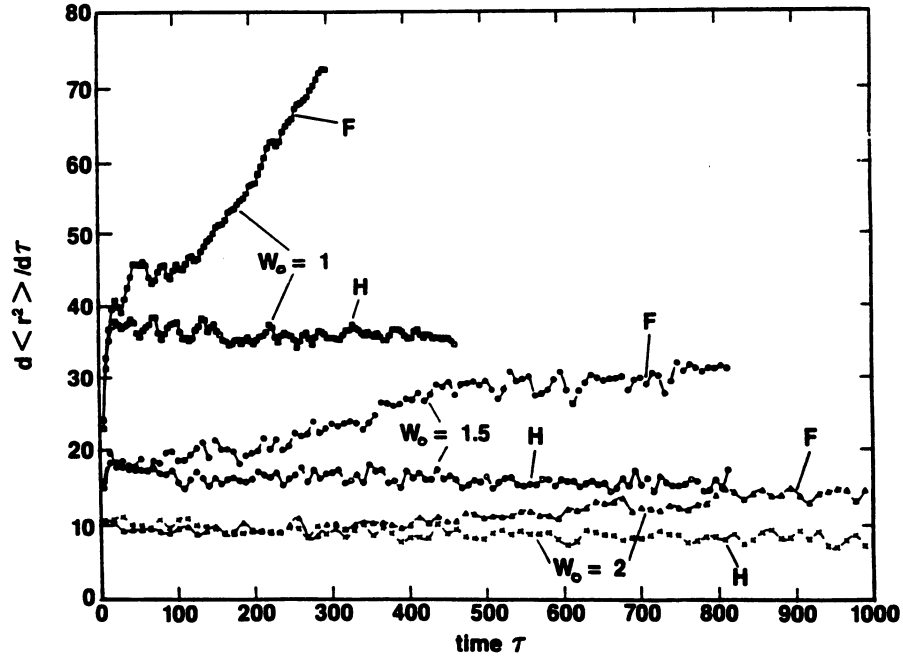

Fig. 7. Time dependence of $d<r^2>/d\tau$ for three values of W_0 evaluated from simulations on a single 800x800 configuration. Each pair of curves represents one case in which the scattering impurities are fractally correlated (denoted by F) and another case in which the impurities are homogeneously distributed with the same overall density (denoted by H).

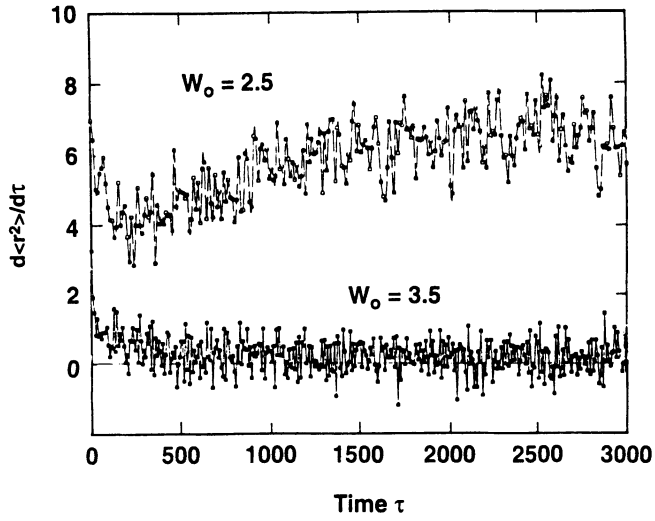

Fig. 8. Time dependence of $d<r^2>/d\tau$ for two values of W_0 close to the metal-insulator transition, evaluated from simulations on a single 800x800 configuration. Impurities are fractally correlated.

The physics of our model may be intuitively understood as resulting from the competition of two long-range effects: the coherent backscattering and the fractal correlation. For homogeneous 2D samples, the coherent backscattering effect diverges logarithmically as a function of L in the weak scattering limit. In the case of fractal scatterers, however, the density decays as a power law, and therefore one expects the delocalization tendency to always prevail. This is the source of the superdiffusive behavior. On the other hand, when the scattering becomes strong, i.e., W_0 large, the wave function can decay exponentially in areas where the local density of scatterers is high. Yet, due to the decreasing density of scatterers further out, there can always be leakage at the exponential-tail end of the wave function. This is evidenced by the sublinear decay of $<\ln g>$ for $W_0 > W_0^c$. An interesting question is whether such small leakage, when combined with the linear increase in the number of channels as L increases, can eventually result in the metallic behavior for $W_0 > W_0^c$ at extremely large L. To investigate this possibility, we have carried out diagrammatic calculations on a simplified model that takes into account only the power-law correlation of the scatterer density but not the connectivity that is inherent in the critical fractal percolation network. This is described in some detail in the next section.

4b. Analytic Approach

Since the average density of impurities is a function of sample size, the goal of the analytic theory is to calculate the conductance of a sample of finite size L and study its

size dependence. The Hamiltonian of a 2D infinite medium still has the form of Eq. (4),

$$H = H_0 + H_1 = \sum_p \varepsilon(p) a_p^+ a_p + \sum_{p,q} \nu(q) a_{p+q}^+ a_p , \tag{22a}$$

but with

$$\varepsilon(p) = 2(\cos p_x + \cos p_y), \tag{22b}$$

and

$$\nu(q) = \frac{1}{N} \sum_i \varepsilon_i e^{iq \cdot r_i}. \tag{22c}$$

For a fixed L, we require the impurity has the average density n(L) of the critical percolation cluster at size L. Thus, with Eq. (3), we have

$$\langle \varepsilon_i \rangle = n(L) W_O . \tag{23}$$

We also require the correlation between site energies obeys the form

$$\langle \varepsilon_i \varepsilon_j \rangle = n(L) W_o^2 C(R_{ij}) \tag{24a}$$

$$C(R_{ij}) = \begin{cases} 1, & i = j. \\ a / |R_{ij}|^{0.11}, & i \neq j; |x_{ij}|, |y_{ij}| \leq L/2 . \\ n(L), & \text{otherwise} \end{cases} \tag{24b}$$

The power 0.11 comes from the density correlation function of the critical percolation cluster,[16] i.e., $0.11 \cong d - \bar{d} = 2 - 91/48$. The value a = 0.5736 is obtained by fitting to the density variation of the critical percolation cluster n(L) numerically. It is easy to see that $C(R_{ij})$ satisfies the sum rule

$$\sum_{R_x = \frac{-L}{2}}^{\frac{L}{2}} \sum_{R_y = \frac{-L}{2}}^{\frac{L}{2}} C(R) = L^2 n(L) . \tag{25}$$

Although the impurity geometry so-constructed simulate that of the critical percolation cluster up to size L, yet the connectness property is neglected in Eq. (24). We will come to this point in later discussion.

Since we are interested in the conductance of a sample of size L, the coherent-back scattering effect beyond the scale L will not be included in the diagrammatic calculations. From Eq. (22a) the single-particle Green's function G can be expanded as

$$G = \frac{1}{z - H_0 - H_1} = G^o + G^o H_1 G^o + G^o H_1 G^o H_1 G^o + \ldots \quad (26)$$

with

$$G_p^o = \langle p | G^o | p \rangle = \left\langle p \left| \frac{1}{z - H_o} \right| p \right\rangle = \frac{1}{z - \varepsilon(p)}, \quad (27)$$

By using Eqs. (22)-(24) and (26) the self-energy $\Sigma_{\vec{p}}$ of the averaged Green's function,

$$R_p = \langle\langle p|G|p\rangle\rangle_c = \frac{1}{z - \varepsilon(p) - \Sigma_p}, \quad (28)$$

has the following expansion

$$\Sigma_p = \Sigma_p^{(1)} + \Sigma_p^{(2)} + \Sigma_p^{(3)} + \ldots \quad (29)$$

with

$$\Sigma_p^{(1)} = n(L) W_o \quad (30)$$

and

$$\Sigma_p^{(2)} = \frac{n^2(L) W_o}{N} \sum_q S(q)\, G_{p-q}^o, \quad (31)$$

where

$$S(q) = \sum_R \left[\frac{C(R)}{n(L)} - 1 \right] e^{iq \cdot R}. \quad (32)$$

Equations (24b) and (25) guarantee that $S(0)=0$. It is also easily seen that $S(q) = S(-q) = S(q+Q)$, with $Q = 2\pi(n\hat{i} + m\hat{j})$ for any integers n and m. Within the self-consistent Born appreciation, Σ_p is determined by

$$\Sigma_p(z) = n(L) W_o + \frac{n^2(L) W_o^2}{N} \sum_q S(q) \frac{1}{E - \varepsilon(p-q) - \Sigma_{p-q}(z)}. \quad (33)$$

To study the transport, we must solve the Bethe-Salpeter equation for the averaged two-particle Green's function.[9] In the case with impurity correlations, the formal solution of the Bethe-Salpeter equation has previously been obtained by Chu and Zhang in Ref. [4].

Let us define the renormalized energy $\bar{z}$ and self energy $\Delta_p(\bar{z})$ as

$$\bar{z} = z - n(L)W_o, \tag{34}$$

and

$$\Delta_p(\bar{z}) = \Sigma_p(z) - n(L)W_o. \tag{35}$$

Equation (33) can be rewritten as

$$\Delta_p(\bar{z}) = \frac{n^2(L)W_o^2}{N} \sum_q S(q) \frac{1}{\bar{E} - \varepsilon(p+q) - \Delta_{p-q}(z)} . \tag{36}$$

After solving Eq. (36) numerically, we obtain $R_{\tilde{p}}(z)$ which is required for the calculation of the diffusion constant. The density of states z is related to the imaginary part of the retarded Green's function by

$$\rho(\bar{E}) = \frac{-1}{\pi N} \sum_p \mathrm{Im}\, R_p^+(\bar{E}), \tag{37a}$$

where

$$R_p^+(\bar{E}) = R_p(\bar{z} = \bar{E} + i\eta). \tag{37b}$$

Since Eq. (36) has the same form as Eq. (3) of Ref. [4], the formulation derived in Ref. [4] is directly applicable here, except W^2 is to be replaced by $n^2(L)W_o^2$. From Eqs. (20) and (23) of Ref. [4], the bare and renormalized diffusion constants are

$$D_{BA}(\bar{E}) = \frac{2\pi\rho(\bar{E})v_{\bar{E}}^4}{\frac{8W_o^2 n^2(L)}{N^2} \sum_{p,p'} \mathrm{Im}\, R_p(\bar{E}) S(p-p') \mathrm{Im}\, R_{p'}(\bar{E}) (v_p - v_{p'}) \cdot v_p} \tag{38a}$$

where

$$v_p = \frac{\partial \varepsilon(p)}{\partial p} , \tag{38b}$$

and

$$v_{\bar{E}}^2 = - \frac{-1}{2\pi\rho(\bar{E})N} \sum_p v_p^2 \, \mathrm{Im}\, R_p^+(\bar{E}) \tag{38c}$$

and

$$D(\omega,\bar{E}) = D_{BA}(\bar{E})\left[1 - \frac{\beta(\bar{E})}{N}\sum_{q}{}' \frac{1}{q^2 - i\omega / D(\omega,\bar{E})}\right], \qquad (39a)$$

with

$$\beta(\bar{E}) = \frac{-8n^4(L)W_o^4}{\pi\rho(\bar{E})v\frac{4}{E}N^2}\sum_{p,p'} v_p^2 S(p-p')S(p+p')\left[\mathrm{Im}\,R_{p'}^{+}(\bar{E})\right]. \qquad (39b)$$

Defining the localization length ξ as $\lim_{\omega\to 0}\frac{-i\omega}{D(\omega,\bar{E})} = \xi^{-2}(\bar{E})$ from Eq.(39a), we obtain the following equation

$$1 = \frac{\beta(\bar{E})}{N}\sum_{q}{}' \frac{1}{q^2 + \xi_L^{-2}(\bar{E})}. \qquad (40)$$

The summation of q has an upper cutoff of q_u which is limited by the mean free path $\ell = 3D_{EA}(\bar{E})/v_{\bar{E}}$. We have chosen $q_u = 0.2/\ell$.

For a finite size sample, the diffusion constant $D_L(\bar{E})$ in the $\omega \to 0$ limit can be written, from Eq. (39a), as[13]

$$D_L(\bar{E}) = D_{BA}(\bar{E})\left[1 - \frac{\beta(\bar{E})}{N}\sum_{q}{}'' \frac{1}{q^2 + \xi_L^{-2}(\bar{E})}\right]. \qquad (41)$$

Besides the upper cutoff q_u, the summation q in Eq. (41) possesses also a lower cutoff q_L = 1/L which excludes the contribution of coherent backscattering effect from scales greater than L as mentioned earlier. By solving Eqs. (40) and (41), we find

$$D_L(\bar{E}) = \frac{1}{4\pi}D_{BA}(\bar{E})\beta(\bar{E})\ell n\left[1 + q_L^2\xi_L^2(\bar{E})\right], \qquad (42)$$

and

$$\xi_L(\bar{E}) = q_u^{-2}\left\{\exp\left[\frac{4\pi}{\beta(\bar{E})}\right] - 1\right\}. \qquad (43)$$

The dimensionless conductance $g_L(\bar{E})$ of can be obtained from the relation given by Wolfle and Vollhart,[13]

$$g_L(\bar{E}) = D_L(\bar{E})\rho(\bar{E})\left[1 + \frac{L}{\xi_L}\right]\exp[-L/\xi_L] \qquad (44)$$

It is worthwhile to point out that, in the limit $L/\xi_L >> 1$, , Eq. (44) gives the Einstein relation $g_L(\bar{E}) \cong D_L(\bar{E})\rho(\bar{E})$. While, in the other limit, $L/\xi_L >> 1$, the conductance has an exponential form $g_L(\bar{E}) \propto e^{-L/\xi_L}$. Also, as the sample size L varies, the Hamiltonian Eq. (24) also changes, so do the quantities D_L,ρ and ξ_L. Thus, in our model, an exponential form in Eq. (44) does not guarantee an exponential decay of g_L in the localized regime.

The results of $g_L(\bar{E})$ evaluated from Eq. (44) are plotted in dashed lines in Fig. 3 for E=0.5 and various values of W_0. It is seen that the behavior is qualitatively similar to that obtained by numerical simulation, thus providing further confirmation of the metal-insulator transition phenomenon. The phase diagram is plotted in Fig. 9, which also has similar behavior as Fig. 4, obtained from numerical simulation. At E=0.5, we have plotted $\ell n[D(L)]$ vs. $\ell n[L]$ for W_0=0.6 and 1.0. Two straight lines with slopes s=0.136 and 0.088 are seen, demonstrating the superdiffusive transport behavior in the extended regimes. In the localized regime, a subexponential decay is evident. Since $d(\ell n g_L)$ / dL is a decreasing function of L for W_0>2, one can ask if there is a value of L at which $d(\ln g_L)/dL$ changes sign. The accurate numerical solution of the self-consistent theory is possible up to L≈250, and $d(\ln g_L)/dL$ is found to be strictly negative in this regime for $W_0 \geq 2$. If we consider only the density effect by assuming $C(\vec{R})$ in Eq. (24) has the value one when $\vec{R} = 0$ and zero otherwise, the self-consistent equations may be solved analytically. It is found for W_0=2, $d(\ln g_L)/dL$ can change signs at $L=L_0 \cong 5 \times 10^4$. Moreover, L_0 increases exponentially as W_0 increases. That means if we consider only the effect of density decay, then for $L>L_0$ the small leaks of the exponential details of the quasilocalized states can combine to delocalize. However, the effect of connectivity, which is neglected in the diagrammatical calculation, is certain to push the crossover point to even higher values of L, if not to infinity. Therefore, until that point is resolved, the limiting $L \to 0$ behavior remains an open question. What may be concluded from the calculation is that, even if there is a finite crossover point L_0, that particular sample size is extremely large and increases exponentially with W_0.

5. CONCLUSIONS

We have introduced two different models with long-range impurity correlations: an anisotropic model which breaks the isotropic symmetry, and a fractal model which breaks the macroscopic homogeneity. Both models show novel localization characteristics not seen previously.

In the anisotropic model, an infinite-range correlation is introduced to the site energy in each layer. This correlation produces a 1D scattering mechanism and gives

rise to a non-zero critical anisotropy below which all states are localized and the system possesses 1D localization characters. Above this critical anistropy, three-dimensional localization behavior occurs. Our anisotropic model is different to models with anisotropic hopping,[6] where the problem can be mapped to the isotropic case by an anisotropic scale change and therefore described by the one-parameter scaling theory.[20] Here the existence of the transverse correlation in the randomness precludes the application of the real-space renormalization technique as generally formulated. This is also evident in the extra term in Eq. (10a) (due to the one-dimensional scattering that preserves the transverse momentum), which places the present model outside the realm of one-parameter scaling. Physically, our model corresponds to predominantly layered systems, such as the Earth's subsurface or random superlattices, with lateral inhomogeneities that may be either inherent to the system or deliberately introduced.

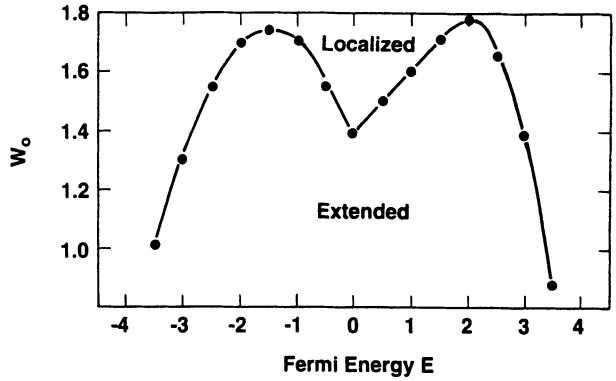

Fig. 9. Phase diagram as a function of W_0 and E, calculated from the analytic approach.

In the fractal model, the impurity is fractally correlated. We have studied the case of critical percolation clusters in two dimensions. Both numerical and analytic results show a metal-insulator transition in 2D. The transport behavior in the extended regime is shown to be superdiffusive. In the localized regime the conductance decays with sample size in a subexponential behavior. The question about the $L \to \infty$ limiting behavior is examined, with the conclusion that even if there is a crossover in behavior, it has to occur at transcendentally large sample sizes. An experimental verification of the present phenomenon would be important not only scientifically but may also demonstrate potential applications, e.g., in field-effect transistors.

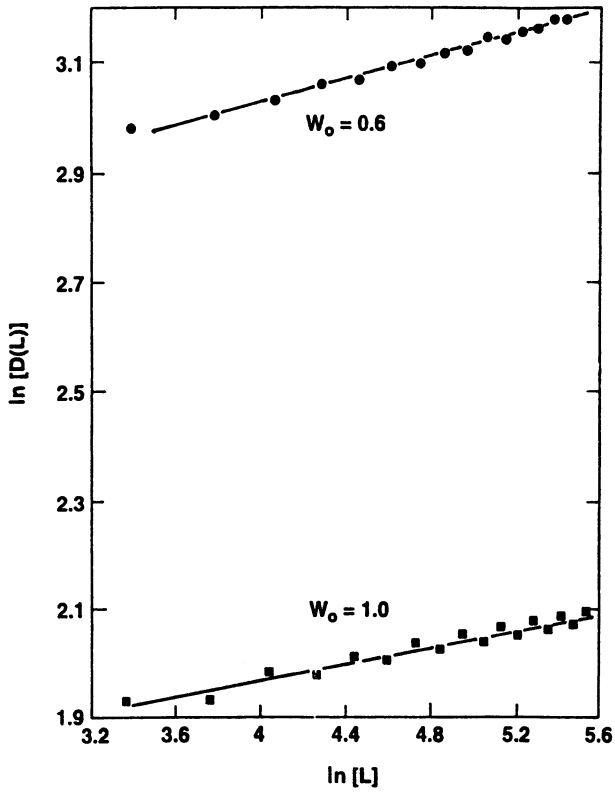

Fig. 10. $\ell n(D_L)$ vs $\ell n(L)$ at E=0.5 for W_O=0.6 and 1.0. The linear behavior demonstrates the superdiffusive behavior in the extended regime.

REFERENCES

1. P. W. Anderson, *Phys. Rev.* 109, 1492 (1958).
2. See for example, P. A. Lee and T. V. Ramakrishnan, *Rev. Mod. Phys.* 57, 287 (1985).
3. S. John and M. J. Stephen, *Phys. Rev.* B28, 6358 (1983).
4. Q. J. Chu and Z. Q. Zhang, *Phys. Rev.* B39, 7120 (1989).
5. W. Xue, P. Sheng, Q. J. Chu, and Z. Q. Zhang, *Phys. Rev. Lett.* 63, 2837 (1949); *Phys.Rev.* B42, 4613 (1990).
6. W. Apel and T. M. Rice, *J. Phys.* C16, L1151 (1983); Q. Li, C. M. Soukoulis, E. N. Economou, and G. S. Grest, *Phys. Rev.* B90 2825 (1989).
7. Y. E. Levy and B. Souillard, *Europhys. Lett.* 4, 233 (1987); A. B. Harris and A. Aharony, *Europhys. Lett.*4, 1355 (1987).
8. Z. Q. Zhang and P. Sheng, *Phys. Rev. Lett.* 67, 2541 (1991).
9. D. Vollhardt and P. Wolfle, *Phys. Rev. Lett.* 45, 842 (1980); *Phys. Rev.* B22, 4666 (1980).
10. R. Kubo, *J. Phys. Soc. Jpn.* 12, 570 (1957).
11. E. N. Economou, C. M. Soukoulis, and A. D. Zdetsis, *Phys. Rev.* B30, 1686 (1984).

12. See, for example, E. N. Economou, *Green's Function in Quantum Physics* (Springer-Verlag, New York, 1983), 2nd. Ed.
13. P. Wolfle and D. Vollhardt, in *Anderson Localization*, edited by Y. Nagaoka and H. Fukuyama (Springer-Verlag, Berlin, 1982).
14. P. A. Lee and D. Fisher, *Phys. Rev. Lett.* 47, 882 (1981).
15. R. Bulka, B. Kramer, and A. MacKinnon, *Z. Phys.* B60, 13 (1985).
16. See, for example, D. Stauffer, *Introduction to Percolation Theory* (Taylor & Francis, Philadelphia, 1985).
17. T. A. Witten and L. M. Sander, *Phys. Rev.* B27, 5606 (1983).
18. H. deRaedt, *Comput Phys*,. Rep. 7.I (1987).
19. D. Weaire and A. R. Williams, *J. Phys.* C10, 1239 (1977).
20. E. Abrahams, P. W. Anderson, D. C. Licciardello, and T. V. Ramakrishnan, *Phys. Rev. Lett.* 42, 673 (1979).

STATISTICAL INVERSION OF STRATIFIED MEDIA FROM ACOUSTIC PULSES SCATTERED AT TWO ANGLES OF INCIDENCE

Mark Asch,[1] Werner Kohler,[2] George Papanicolaou,[3]
Marie Postel,[4] and Benjamin White[5]

[1]Laboratoire d'Analyse Numerique
Batiment 425
Universite Paris XI
91405 Orsay, France

[2]Department of Mathematics
Virginia Polytechnic Institute and State University
Blacksburg, VA 24061, USA

[3]Courant Institute of Mathematical Sciences
New York University
251 Mercer Street
New York, NY 10012, USA

[4]Universite Pierre et Marie Curie
Laboratoire d'Analyse Numerique
4 Place Jussieu
75005 Paris, France

[5]Exxon Research and Engineering Co.
Route 22 East
Annandale, NJ 08801, USA

INTRODUCTION

We consider here a form of inverse scattering, that is, the remote sensing of a complex material by analyzing waves which have been reflected from it. A generic form of this problem is encountered in, e.g., exploration geophysics, where seismic waves which are generated at the surface penetrate the earth, scatter from inhomogeneities and, after possibly many multiple scatterings are reflected back to the surface where they are recorded and analyzed. In a simplified model consistent with the sedimentary process in many areas the earth is considered stratified, that is, the material properties are assumed to vary only with depth. In this case there are efficient algorithms[1,2] for recovering medium properties at any depth provided the scattering data have been recorded perfectly. In practice, however, these algorithms become unstable as they try to recover information from large depths.

Photonic Band Gaps and Localization, Edited by
C.M. Soukoulis, Plenum Press, New York, 1993

There is a theoretical reason why penetration to any depth should not be possible in practice. For stratified media so complex they may be considered random, the phenomenon of localization obtains: single frequency waves are attenuated exponentially with depth solely by the mechanism of random multiple scattering. The application of this concept to classical waves has received much attention recently,[3] and in particular estimates of the earth's localization length have been obtained.[4] However, the usual form of localization theory is not, strictly speaking, valid in this context since the medium is by no means a stationary random function of position. That is despite a stochastic microstructure there are significant large scale, i.e., background, trends in the material parameters.[4] In this paper we develop a stochastic inverse theory complementary to the usual deterministic methods, for recovering large scale trends at large depths in the presence of a stochastic microstructure.

The forward theory generalizes localization to include the two spatial scales, and further puts the theory into the time domain to analyze the reflection of pulses from such media. We assume that the pulse width is intermediate between the two spatial scales. Thus, while in the absence of a macroscale we include localization phenomena, in the absence of a microscale we recover geometrical acoustics. The present theory, which was developed in Refs. 4-13, unifies the two quite different wave propagation regimes. For a more comprehensive review, including inverse problems, see Ref. 5.

We consider here the backscattered signal when an acoustic plane wave pulse is incident on a medium as described above. This signal is not stationary in time. However, it is shown to be locally stationary. That is, if a time window of duration on the order of many pulse widths is extracted from the data record, it is a locally stationary Gaussian process whose statistics vary with the location of the window. We show how for each time window the power spectrum can be calculated by solution of an infinite system of hyperbolic equations. These "transport equations" do not depend on the details of the microstructure but only on some averaged second moments.

For the inverse problem we show how to use the forward theory to construct a maximum likelihood estimator for the medium properties. It is not, however, possible to recover all properties, but only a single function which includes information on the large scale background variations as well as information on how the microstructure statistics vary when viewed on the macroscale. Furthermore, one cannot recover how this function varies with depth, but only how it varies with travel time to a given depth, where wave travel time is measured relative to the macroscopic background. This situation is analogous to the deterministic theory, where for normal incidence only impedance can be recovered, and only as a function of travel time, not of true depth.[1,2] However, we show here that for constant density acoustics all macroscopic variables can be recovered, and recovered as functions of depth, by combining data from two distinct angles of incidence.

REFLECTION OF A PULSED PLANE WAVE FROM A RANDOM SLAB

We consider the acoustic equations for pressure p and velocity **u**

$$\begin{aligned} \rho\frac{\partial \mathbf{u}}{\partial t} + \nabla p &= 0 \\ \frac{1}{K}\frac{\partial p}{\partial t} + \nabla\cdot\mathbf{u} &= 0 \end{aligned} \tag{1}$$

where ρ is density and K is incompressibility. Let $\mathbf{x} = (x,y,z)^T$. We next represent a slab of stratified medium, a function of depth z only, occupying $-L < z < 0$, which has a slowly varying background and a stochastic microstructure. To do this let $\nu(z_1,z_2)$ be, for each fixed z_1, a mean zero stationary random process as a function of z_2. The statistics, however, may vary with z_1. If ε is a small parameter, $\nu(z,z/\varepsilon^2)$ then has a microstructure to background length scale of ε^2. We now let

$$\frac{1}{K(z)} = \begin{cases} \dfrac{1}{K_0} & \text{for } z > 0 \\ \dfrac{1}{K_1(z)}\,(1+\nu(z,z/\varepsilon^2)) & \text{for } -L < z < 0 \\ \dfrac{1}{K_2} & \text{for } z < -L \end{cases} \tag{2}$$

That is, $1/K_1$ is the spatially varying mean of 1/K in the random slab, which is sandwiched between two homogeneous half spaces. We take a piece-wise constant density

$$\rho = \begin{cases} \rho_0 & \text{for } z > 0 \\ \rho_1 & \text{for } -L < z < 0 \\ \rho_2 & \text{for } z < -L \end{cases} \tag{3}$$

Then the background speeds are

$$c_j = \sqrt{K_j/\rho_j} \quad \text{for } j = 0,1,2 \tag{4}$$

and we denote by c(z) the appropriate c_j for each of the regions in equations (2) and (3).

We next consider a pulsed plane wave incident from $z>0$ at incidence angle θ. Let f(t) be the pulse shape and let the incident field be

$$\mathbf{u}^{inc} = \frac{1}{\sqrt{\varepsilon}\rho_0 c_0} f\left(\frac{1}{\varepsilon}[t - \sin\theta\, x/c_0 + \cos\theta\, z/c_0]\right)\begin{pmatrix}\sin\theta\\ 0\\ -\cos\theta\end{pmatrix}$$
$$p^{inc} = \frac{1}{\sqrt{\varepsilon}} f\left(\frac{1}{\varepsilon}[t - \sin\theta\, x/c_0 + \cos\theta\, z/c_0]\right) \tag{5}$$

Note that the pulse width is of order ε, intermediate between the macroscale and microscale of the medium. The factor $\varepsilon^{-1/2}$ is inserted to preserve energy as ε is varied.

The horizontal slowness is

$$\kappa = \frac{\sin\theta}{c_0} \tag{6}$$

Setting

$$s = t - \kappa x \ , \tag{7}$$

we seek a solution of (1) of the form

$$\begin{aligned} \mathbf{u}(t,x) &= \bar{\mathbf{u}}(s,z) \\ p(t,x) &= \bar{p}(s,z) \end{aligned} \quad . \tag{8}$$

We introduce the scaled Fourier transforms

$$\begin{aligned} \hat{\mathbf{u}}(z,\omega) &= \int e^{i\omega s/\varepsilon}\, \bar{\mathbf{u}}(s,\omega)\, ds \qquad \hat{p}(z,\omega) = \int e^{i\omega s/\varepsilon}\, \bar{p}(s,\omega)\, ds \\ \hat{f}(\omega) &= \int e^{i\omega s}\, f(s)\, ds \end{aligned} \quad . \tag{9}$$

Insertion of (9) and (7) into (1) yields four scalar equations for $\hat{\mathbf{u}} = (\hat{u}_1, \hat{u}_2, \hat{u}_3)$ and $\hat{p}$. The first two equations yield that

$$\begin{aligned} \hat{u}_1 &= \frac{\kappa}{\rho}\, \hat{p} \\ \hat{u}_2 &= 0 \end{aligned} \quad . \tag{10}$$

Then using (10) we obtain the two coupled equations

$$\begin{aligned} \frac{\partial \hat{u}_3}{\partial z} &= \frac{i\omega}{\varepsilon}\left(\frac{1}{K} - \frac{\kappa^2}{\rho}\right)\hat{p} \\ \frac{\partial \hat{p}}{\partial z} &= \frac{i\omega}{\varepsilon}\, \rho\, \hat{u}_3 \end{aligned} \quad . \tag{11}$$

To study reflections caused by the incident field (5), we must decompose $\hat{u}_3$ and $\hat{p}$ into up and down-going waves. Let the (oblique) impedances be

$$\zeta_j = \rho_j c_j / \sqrt{1 - \kappa^2 c_j^{\,2}} \quad \text{for } j = 0,1,2 \tag{12}$$

and let ζ be the ζ_j for the appropriate region. Let the (oblique) background travel time be

$$\tau(z,\kappa) = \int_0^z \frac{\sqrt{1 - \kappa^2 c^2(z')}}{c(z')}\, dz' \quad . \tag{13}$$

Then we define the upgoing wave A and the downgoing wave B by the equations

$$\begin{aligned} \hat{p} &= \zeta^{1/2}\left[A\, e^{i\omega\tau/\varepsilon} - B\, e^{-i\omega\tau/\varepsilon}\right] \\ \hat{u}_3 &= \zeta^{-1/2}\left[A\, e^{i\omega\tau/\varepsilon} + B\, e^{-i\omega\tau/\varepsilon}\right] \end{aligned} \quad . \tag{14}$$

Equations for A and B are obtained by insertion of (14) into (11). However, since we shall only be interested in reflections, we write instead the equations obtained for the

reflection coefficient

$$\Gamma = A / B \quad . \tag{15}$$

For z in (-L,0) the equation becomes

$$\begin{aligned} \frac{\partial \Gamma}{\partial z} = & -\frac{i\omega}{\varepsilon} n \left\{ e^{-2i\omega\tau/\varepsilon} - 2\Gamma + e^{2i\omega\tau/\varepsilon} \Gamma^2 \right\} \\ & + \frac{1}{2\zeta} \frac{\partial \zeta}{\partial z} \left\{ e^{-2i\omega\tau/\varepsilon} - e^{2i\omega\tau/\varepsilon} \Gamma^2 \right\} \quad , \end{aligned} \tag{16}$$

where the two-scale stochastic process n is given by

$$n\left(z, z/\varepsilon^2, \kappa\right) = \frac{\nu\left(z, z/\varepsilon^2\right)}{2c_1(z)\sqrt{1-\kappa^2 c_1^2(z)}} \quad . \tag{17}$$

Boundary conditions for Γ are obtained by noting that p and **u** are continuous across interfaces and, hence, so is

$$\frac{\hat{p}}{\hat{u}_3} = \zeta \frac{\left(\Gamma - e^{-2i\omega\tau/\varepsilon}\right)}{\left(\Gamma + e^{-2i\omega\tau/\varepsilon}\right)} \quad . \tag{18}$$

The downgoing wave at $z=0^+$ is given by the Fourier transform of the incident field (5)

$$B\left(0^+, \omega\right) = B^{inc}\left(0^+, \omega\right) = -\zeta_0^{-1/2} \varepsilon^{1/2} \hat{f}(\omega) \quad . \tag{19}$$

We then obtain from continuity of (18) that

$$\Gamma\left(0^+, \omega\right) = \frac{\left(\Gamma\left(0^-, \omega\right) - \Gamma_I(0)\right)}{\left(1 - \Gamma_I(0)\,\Gamma\left(0^-, \omega\right)\right)} \quad , \tag{20}$$

where

$$\Gamma_I(0) = \frac{\zeta_1(0) - \zeta_0}{\zeta_1(0) + \zeta_0} \quad . \tag{21}$$

Similarly, there is no upgoing wave below z= -L and, hence, A and Γ are zero there. Thus,

$$\Gamma\left(-L^+, \omega\right) = \Gamma_I(-L)\, e^{-2i\omega\tau(-L)/\varepsilon} \tag{22}$$

$$\Gamma_I(-L) = \frac{\zeta_1(-L) - \zeta_2}{\zeta_1(-L) + \zeta_2} \quad . \tag{23}$$

Here $\Gamma_I(0), \Gamma_I(-L)$ are the interface reflection coefficients.

To summarize, we solve for the reflection coefficient Γ in (15) by starting with the initial condition (22) at $z= -L^+$. We next solve the Riccati equation (16) to propagate Γ from $z = -L^+$ to $z=0^-$. Jump condition (20) now gives Γ at $z=0^+$, just above the random slab, on the

side of the incident wave. To compute the reflected pressure at, say, x=0, z=0 we subtract the incident field there. Thus, using (14), (15), (19) we obtain

$$\hat{p}_{refl} = \zeta^{1/2} A e^{i\omega\tau/\varepsilon}\Big|_{z=0^+} = -\varepsilon^{1/2}\,\hat{f}(\omega)\,\Gamma(0^+,\omega) \quad . \tag{24}$$

The reflected wave at x=z=0 is then given for all time t by inversion of the Fourier transfom (9)

$$p_{refl}(t,0) = -\frac{1}{2\pi\sqrt{\varepsilon}} \int e^{-i\omega t/\varepsilon}\,\hat{f}(\omega)\,\Gamma(0^+,\omega)\,d\omega \quad . \tag{25}$$

STATISTICS OF THE REFLECTED PRESSURE

We next show how to compute the autocorrelation of the reflected pressure, asymptotically for small ε. In particular, consider

$$I(t,\bar{t}) = \lim_{\varepsilon\downarrow 0} \; E\left[p_{refl}(t+\varepsilon\bar{t}/2,0)\,p_{refl}(t-\varepsilon\bar{t}/2,0)\right] \quad . \tag{26}$$

By multiplying two expressions of the form (25) and taking expected values, we obtain (with * denoting complex conjugate)

$$\begin{aligned} I(t,\bar{t}) = \lim_{\varepsilon\downarrow 0} \; & \frac{1}{(2\pi)^2\varepsilon} \int d\omega_1 \int d\omega_2\, \hat{f}(\omega_1)\,\hat{f}^*(\omega_2)\, e^{-i(\omega_1+\omega_2)\bar{t}/2} \\ & e^{it(\omega_2-\omega_1)/\varepsilon} \;\; E\left[\Gamma(0^+,\omega_1)\,\Gamma(0^+,\omega_2)^*\right] \quad . \end{aligned} \tag{27}$$

Let $\omega_1 = \omega - \varepsilon h/2$, $\omega_1 = \omega + \varepsilon h/2$. Then formally letting $\varepsilon \downarrow 0$ we obtain

$$I(t,\bar{t}) = \frac{1}{2\pi} \int d\omega\, e^{-i\omega\bar{t}}\, S(t,\omega) \quad , \tag{28}$$

where

$$S(t,\omega) = \left|\hat{f}(\omega)\right|^2 \;\; \Lambda(t,\omega) \tag{29}$$

$$\Lambda(t,\omega) = \lim_{\varepsilon\downarrow 0} \; \frac{1}{2\pi} \int dh\, e^{ith}\, E\left[\Gamma(0^+,\omega-\varepsilon h/2)\Gamma^*(0^+,\omega+\varepsilon h/2)\right] \quad . \tag{30}$$

Of course, expressions (28) and (29) depend on existence of the limit in (30). We will show below how to calculate this limit, but first note the interpretation of these equations. Since the time difference in (26) is $\varepsilon\bar{t}$ the proper time scale for significant autocorrelations is of order ε, i.e., on the order of the intermediate scale of a pulse width. Let us extract from the total data record a time window centered at macroscopic time t and of duration on the order of many pulse widths, measured by $\varepsilon\bar{t}$. Then for fixed t, equation (28) gives the autocorrelation function of a stationary process within the extracted window. It is the Fourier transform of a power spectrum S(t,ω), where ω is dual to $\bar{t}$. Thus, our time windows are a collection of locally stationary processes with power spectra that vary with the location of the window center, macroscopic time t.

For N,M nonnegative integers let

$$\Gamma^{N,M}(z,\omega,h) \equiv \Gamma^{N}(z,\omega-\varepsilon h/2)\left(\Gamma^{*}(z,\omega+\varepsilon h/2)\right)^{M} \quad . \tag{31}$$

To calculate Λ in (30) we will get equations for the expected values of

$$\tilde{\Gamma}^{N,M}(z,\omega,t+(N+M)\tau(z)) = \frac{1}{2\pi}\int e^{ith}\,\Gamma^{N,M}(z,\omega,h)\,dh \quad . \tag{32}$$

Then from (31), (32) and (16) we obtain

$$\begin{aligned}\frac{\partial\tilde{\Gamma}^{N,M}}{\partial z}+(N+M)\frac{\partial\tau}{\partial z}\frac{\partial\tilde{\Gamma}^{N,M}}{\partial t} = {} & \frac{i\omega}{\varepsilon}N\,n\left[2\tilde{\Gamma}^{N,M}-e^{-i\omega\tau/\varepsilon}\,\tilde{\Gamma}^{N-1,M}-e^{2i\omega\tau/\varepsilon}\,\Gamma^{N+1,M}\right] \\ & -\frac{i\omega}{\varepsilon}M\,n\left[2\tilde{\Gamma}^{N,M}-e^{2i\omega\tau/\varepsilon}\,\tilde{\Gamma}^{N,M-1}-e^{-2i\omega\tau/\varepsilon}\,\Gamma^{N,M+1}\right] \\ & +\cdots\end{aligned} \tag{33}$$

where ... are rapidly-varying terms which average to zero. The system (33) is of the form

$$\frac{\partial\tilde{\Gamma}}{\partial z}+U_0\tilde{\Gamma} = \frac{1}{\varepsilon}U\left(z,\tau(z)/\varepsilon,z/\varepsilon^2\right)\tilde{\Gamma}+\cdots \tag{34}$$

where U_0 is a deterministic operator and U is an infinite matrix that has mean zero, varies periodically on the $\tau(z)/\varepsilon$ scale, and is random on the z/ε^2 scale. For small ε, $E\left[\tilde{\Gamma}\right]$ can be calculated by a limit theorem (see Ref. 5, Appendix B). It satisfies an equation of the form

$$\frac{\partial}{\partial z}E\left[\tilde{\Gamma}\right]+U_0\,E\left[\tilde{\Gamma}\right] = \overline{UU}\,E\left[\tilde{\Gamma}\right] \ , \tag{35}$$

where

$$\overline{UU} = \lim_{T\uparrow\infty}\frac{1}{T}\int_0^T d\tau\int_0^\infty dz'\,E\left[U(z,\tau,z')\,U(z,\tau,0)\right] \tag{36}$$

Letting

$$W^{N,M} = e^{-2i(M-N)\omega\tau(-L)/\varepsilon}\,E\left[\tilde{\Gamma}^{N,M}\right] \ , \tag{37}$$

we find that $W^{N,M}$ satisfies the transport equations

$$\begin{aligned}&\frac{\partial W^{N,M}}{\partial z}+\frac{\sqrt{1-\kappa^2c_1^{\,2}}}{c_1}(N+M)\frac{\partial W^{N,M}}{\partial t} = \\ &\frac{2\omega^2\alpha(z)NM}{c_1^{\,2}\left(1-\kappa^2c_1^{\,2}\right)}\left\{W^{N+1,M+1}-2W^{N,M}+W^{N-1,M-1}\right\}-\frac{6\omega^2\alpha(z)(N-M)^2}{c_1^{\,2}\left(1-\kappa^2c_1^{\,2}\right)}W^{N,M} \\ &W^{N,M}\big|_{z=-L} = \Gamma_I^{\,N+M}(-L)\,\delta(t) \ ,\end{aligned} \tag{38}$$

where

$$\alpha(z) = \frac{1}{4}\int_0^{\infty} E\left[\nu(z,z')\nu(z,0)\right] dz' \quad . \tag{39}$$

In particular, we look at the "matched medium," i.e., the case where $\zeta_1(0) = \zeta_0$ so that the homogeneous half space in z>0 is impedance matched to the background effective properties of the random slab. Then $\Gamma_I(0) = 0$ so that $\Gamma(0^+,\omega) = \Gamma(0^-,\omega)$. We also let $W^N = W^{N,N}$ to obtain

$$\begin{aligned} &\frac{\partial W^N}{\partial z} + 2\frac{\sqrt{1-\kappa^2 c_1^{\,2}}}{c_1} N \frac{\partial W^N}{\partial t} = \frac{2N^2\omega^2\alpha}{c_1^{\,2}\left(1-\kappa^2 c_1^{\,2}\right)}\left\{W^{N+1} - 2W^N + W^{N-1}\right\} \\ &W^N\big|_{z=-L} = \left(\Gamma_I(-L)\right)^{2N}\delta(t) \quad . \end{aligned} \tag{40}$$

From equations (29) - (32) the power spectrum is obtained from

$$\Lambda(t,\omega) = W^1(0,t,\omega) \quad . \tag{41}$$

For the inversion we will use an adjoint form to (40), (41). Let V^N satisfy

$$\begin{aligned} &\frac{\partial V^N}{\partial z} - 2N\frac{\sqrt{1-\kappa^2 c_1^{\,2}}}{c_1}\frac{\partial V^N}{\partial t} = \frac{-2\omega^2\alpha}{c_1^{\,2}\left(1-\kappa^2 c_1^{\,2}\right)}\left\{(N+1)^2 V^{N+1} - 2N^2 V^N + (N-1)^2 V^{N-1}\right\} \\ &V^N\big|_{z=0} = \delta_{N,1}\,\delta(t) \quad . \end{aligned} \tag{42}$$

Then

$$\Lambda(t,\omega) = V^0(-L,\omega,t) \quad . \tag{43}$$

For a uniform background, with c_1, α constant these equations can be solved in closed form, yielding

$$\Lambda(t,\omega) = \frac{\omega^2\tilde{\alpha}}{\left(1+\omega^2\tilde{\alpha}\,t\right)^2} \quad , \tag{44}$$

where

$$\tilde{\alpha} = \frac{\alpha}{c_1\left(1-\kappa^2 c_1^{\,2}\right)^{3/2}} \quad . \tag{45}$$

In particular, consider normal incidence $\kappa = 0$. Then Λ can be expressed in terms of the localization length

$$\ell(\omega) = \frac{c_1^{\,2}}{\alpha\omega^2} \tag{46}$$

as

$$\Lambda(t,\omega) = \frac{c_1\,\ell(\omega)}{\left[\ell(\omega) + c_1 t\right]^2} \quad . \tag{47}$$

Thus, when each time segment of the data is Fourier analyzed, its frequency dependence is determined entirely by that of the localization length.

In addition to including localization, its effects in the time domain, and the generalization of these phenomena to media which do not have a constant background, the transport equations also contain geometrical acoustics for the macroscale. Thus, if we take $\alpha = 0$ in (40), the N=1 term which determines Λ via (41) is obtained by propagation of a delta function with the appropriate reflection coefficient factor along the N=1 characteristic of this equation. But this amounts to propagation along a geometrical acoustics ray reflected from the basement interface at z = -L back to the surface at z = 0. For further interpretation along these lines, see Ref. 5.

THE INVERSE PROBLEM

Some simplification of the transport equations may be achieved by making the travel time transformation (13) in (42), replacing z by $\tau = \tau(z,\kappa)$. Let $\tilde{z}(\tau,\kappa)$ be the inverse of this transformation. Then (42) becomes

$$\begin{aligned} &\frac{\partial V^N}{\partial \tau} - 2N\frac{\partial V^N}{\partial t} = -2\omega^2 \tilde{\alpha}(\tau,\kappa)\left\{(N+1)^2 V^{N+1} - 2N^2 V^N + (N-1)^2 V^{N-1}\right\} \\ &V^N\big|_{\tau=0} = \delta_{N,1}\,\delta(t) \end{aligned} \tag{48}$$

where

$$\tilde{\alpha}(\tau,\kappa) = \frac{\alpha(\tilde{z}(\tau,\kappa))}{c_1(\tilde{z}(\tau,\kappa))\left(1-\kappa^2 c_1^2(\tilde{z}(\tau,\kappa))\right)^{3/2}} \ . \tag{49}$$

The characteristics of equation (48) are now the straight lines $t = t_0 - 2N\tau$. Furthermore , for the infinite slab problem, letting $L \to \infty$ in (43) would correspond to letting $\tau \to -\infty$ in the solution of (48). However, by considering propagation of the solution along characteristics, we see that V^N cannot change for $\tau < -t/2$. Thus

$$\Lambda(t,\omega) = V^0(\tau = -t/2,\omega,t) \ . \tag{50}$$

To picture the solution of (48), note that the delta function propagated along the N=1 characteristic is scattered into step functions by the righthand side of the equation. The step functions are then likewise propagated along characteristics, scattered, propagated and then scattered again into successively smoother functions. Details of this expansion are given in Ref. 7. Once this analytically calculable singular part of the solution is subtracted, the remaining equation is solvable by a stable numerical scheme.[8]

We can now consider the statistical inverse problem, that of determining the smoothly varying background of the medium by analyzing reflection data. First note from (48) that only the function $\tilde{\alpha}(\tau,\kappa)$ drives this equation. Thus, for a single incidence angle κ only the function $\tilde{\alpha}$ can be recovered and only as a function of the travel time τ, not as a function of true depth z. We will first show how to accomplish this, and then show how data from two distinct angles of incidence can be used to recover both c_1 and α as functions of true depth z.

We will recover $\tilde{\alpha}$ by a layer-peeling algorithm. Thus, consider a grid in time, $\tau_j = j\Delta, \quad j = 0,1,2,\cdots$, and approximate $\tilde{\alpha}(\tau,\kappa)$ as piece-wise linear between τ_j and τ_{j+1} . Let $\tilde{\alpha}_j = \tilde{\alpha}(\tau_j,\kappa)$ and assume that $\tilde{\alpha}_0, \tilde{\alpha}_1, \cdots, \tilde{\alpha}_{j-1}$ have been determined. We are to recover

the next layer $\tilde{\alpha}_j$ from knowledge of the previous layers $\tilde{\alpha}_0,\tilde{\alpha}_1,\cdots,\tilde{\alpha}_{j-1}$ and the power spectral estimates from the next time window $\hat{S}(t_j,\omega_k)$, $k=1,2,\cdots,N_f$ at frequencies ω_k, and time corresponding to the next layer at $t_j = -2\tau_j$. These power spectra are estimated by, say, Fourier transform of sampled reflection data.

Now suppose that $\tilde{\alpha}_j$ were known but $\hat{S}(t_j,\omega_k)$, $k=1,2,\cdots,N_f$ were not. From the theory of spectral estimation for a Gaussian process[14] we know that the probability density of $\hat{S}$ is exponential with mean

$$E\left[\hat{S}(t_j,\omega_k)\right] = \Lambda(t_j,\omega_k)\ \left|\hat{f}(\omega_k)\right|^2 \ . \tag{51}$$

Λ can be obtained by solution of (48), (50), and we emphasize its dependence on $\tilde{\alpha}_0,\tilde{\alpha}_1,\cdots,\tilde{\alpha}_{j-1}$ by writing $\Lambda = \Lambda(t_j,\omega_k;\tilde{\alpha}(\bullet))$. Then putting

$$S(t_j,\omega_k;\tilde{\alpha}(\bullet)) = \Lambda(t_j,\omega_k;\tilde{\alpha}(\bullet))\left|\hat{f}(\omega_k)\right|^2 \ , \tag{52}$$

we obtain the probability density of the spectral estimates in the form

$$P\left\{\hat{S}(t_j,\omega_k),\, k=1,2,\cdots,N_f;\tilde{\alpha}(\bullet)\right\} = \prod_{l=1}^{N_f} \frac{e^{-(\hat{S}(t_j,\omega_k)/S(t_j,\omega_k;\tilde{\alpha}(\bullet)))}}{S(t_j,\omega_k;\tilde{\alpha}(\bullet))} \ . \tag{53}$$

If now $\tilde{\alpha}_0,\tilde{\alpha}_1,\cdots,\tilde{\alpha}_{j-1}$ as well as $\hat{S}(t_j,\omega_k)$, $k=1,2,\cdots,N_f$ are known, the expression (53) is a function of the single variable $\tilde{\alpha}_j$. It is the likelihood function for estimation of this parameter and the value of α that maximizes it is the maximum likelihood estimator. This one-dimensional maximization can be accomplished numerically using a subroutine for solving the transport equations as described above. More details are given in Refs. 5,7,8. Further refinements are: allowing for an additive white noise error component in the spectral estimates (merely replace S by $S+\sigma^2$ in (53)),[8] and a Bayesian estimator that makes use of the fact that $\tilde{\alpha}(\tau,\kappa)$ is smooth.[13]

Suppose that data from two distinct angles, corresponding to κ_1,κ_2, have been inverted to yield $\tilde{\alpha}(\tau,\kappa_1),\tilde{\alpha}(\tau,\kappa_2)$. We will show how to combine these two functions to yield $\alpha(z)$, $c_1(z)$. Let

$$\tilde{\beta}(\tau,\kappa_j) = \int_0^{\tau}\left[\tilde{\alpha}(\tau',\kappa_j)\right]^{1/3} d\tau', \quad j=1,2 \ . \tag{54}$$

Substitution of (49), (13) into (54) yields

$$\tilde{\beta}(\tau,\kappa) = \int_0^{\tilde{z}(\tau,\kappa)}\left(\alpha(z)/c_1^4(z)\right)^{1/3} dz \equiv \beta(\tilde{z}(\tau,\kappa)) \ . \tag{55}$$

Thus $\tilde{\beta}(\tau_1,\kappa_1) = \tilde{\beta}(\tau_2,\kappa_2)$ if and only if $\tilde{z}(\tau_1,\kappa_1) = \tilde{z}(\tau_2,\kappa_2)$. That is, matching $\tilde{\beta}$ for the two angles synchronizes the depths from which the two signals emanate. Let $g(\tau,\kappa_1,\kappa_2)$ be the "time warp" that accomplishes this synchronization. That is, define g so that

$$\tilde{\beta}(\tau,\kappa_1) = \tilde{\beta}(g(\tau,\kappa_1,\kappa_2),\kappa_2) \ . \tag{56}$$

Then

$$\tilde{z}(\tau,\kappa_1)=\tilde{z}\big(g(\tau,\kappa_1,\kappa_2),\kappa_2\big) \quad . \tag{57}$$

Differentiation of (56) and use of (54) yields

$$g_\tau(\tau,\kappa_1,\kappa_2)=\left[\frac{\tilde{\alpha}(\tau,\kappa_1)}{\tilde{\alpha}\big(g(\tau,\kappa_1,\kappa_2),\kappa_2\big)}\right]^{1/3} \quad . \tag{58}$$

Differentiation of (13) and (57) yields

$$\tilde{z}_\tau(\tau,\kappa_1)=\sqrt{\frac{1-g_\tau{}^2(\tau,\kappa_1,\kappa_2)}{\kappa_2{}^2-\kappa_1{}^2}} \quad , \tag{59}$$

which can be inverted to give

$$c_1\big(\tilde{z}(\tau,\kappa)\big)=\frac{\tilde{z}_\tau(\tau,\kappa)}{\sqrt{1+\kappa^2\tilde{z}_\tau{}^2(\tau,\kappa)}} \quad . \tag{60}$$

The algorithm is then as follows: first $\tilde{\beta}(\tau,\kappa_1),\tilde{\beta}(\tau,\kappa_2)$ are computed from (54). Then the time warp g is computed from (56), and its derivative from (58). Now $\tilde{z}(\tau,\kappa_1)$ can be computed from integration of (59), while the propagation speed c_1 at each depth $\tilde{z}$ is computed from (60). Finally, $\alpha(z)$ is determined from (49) and knowledge of $\tilde{\alpha}$ and c_1.

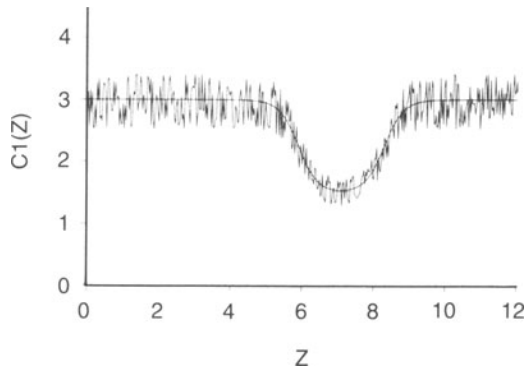

Figure 1. Noisy velocity profile.

An example of this inversion method is illustrated in Figures 1-3, which are reprinted from Ref. 5*. In Figure 1 a simulated sound speed profile is depicted. The background speed $c_1(z)$ varies from an inital 3 km/sec to 1.5 km/sec at the trough of a low velocity region, and then returns to 3 km/sec. Superimposed on this background are 4500 small layers each of width 2.7 m and within which the speed varies randomly and independently from microlayer to microlayer. Fluctuations of 1/K are 30% of the mean, and we have taken the value ε=.03

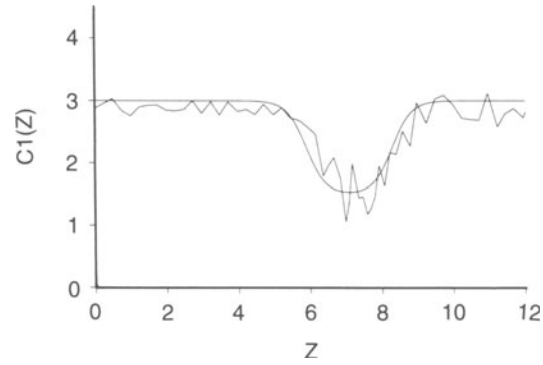

Figure 2. Inversion results when α is known, for plane waves incident at three different angles.

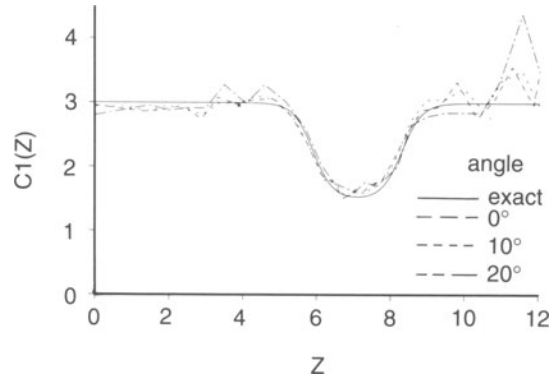

Figure 3. Inversion results with unknown α, from plane waves incident at the two angles $\theta = 0^{o}, 20^{o}$.

We generated 90 independent simulations of the medium and computed for each the reflected pressure when a plane wave pulse is incident at angle θ for three incidence angles $\theta = 0°$ (normal incidence), $10°$, $20°$. The calculations were done by a computer code which is described in Ref. 5. Power spectra were estimated at times t_j with $t_{j+1}-t_j = .326$ and for 30 frequencies with $\omega_k = 1$ and $\omega_{k+1}-\omega_k = .36$.

First $\tilde{\alpha}$ was computed by the layer-peeling algorithm by maximizing successively products of 90 likelihood functions of the form (53). Taking α as a known constant then enabled us to construct $c_1(z)$ from the data for each of the incidence angles. The three results are shown in Figure 2.

Of course in practice α is not known but must be estimated from the data along with $c_1(z)$. We accomplished this by the theory described above, using the two incidence angles $\theta = 0°$ and $\theta = 20°$. The results are in Fig. 3.

REFERENCES

1. J.F. Claerbout. "Fundamentals of Geophysical Data Processing: With Applications to Petroleum Prospecting," McGraw-Hill, New York (1976).
2. K. Aki and P.G. Richards. "Quantitative Seismology Theory and Methods, Vol. II," W.H. Freeman, San Francisco (1980).
3. P. Sheng, ed. "Scattering and Localization of Classical Waves in Random Media," World Scientific, Singapore (1990).
4. B. White, P. Sheng, and B. Nair, Localization and backscattering spectrum of seismic waves in stratified lithology, *Geophysics* 55:1158 (1990).
5. M. Asch, W. Kohler, G. Papanicolaou, M. Postel, and B. White, Frequency content of randomly scattered signals, *SIAM Rev.* 33:519 (1991).
6. R. Burridge, G. Papanicolaou, P. Sheng, and B. White, Probing a random medium with a pulse, *SIAM J. App. Math.* 49:582 (1989).
7. M. Asch, G. Papanicolaou, M. Postel, P. Sheng, and B. White, Frequency content of randomly scattered signals. Part I, *Wave Motion* 12:429 (1990).
8. G. Papanicolaou, M. Postel, P. Sheng, and B. White, Frequency content of randomly scattered signals. Part II: Inversion, *Wave Motion* 12:527 (1990).
9. W. Kohler, G. Papanicolaou, and B. White, Reflection of waves generated by a point source over a randomly layered medium, *Wave Motion* 13:53 (1991).
10. P. Sheng, Z.-Q. Zhang, B. White, and G. Papanicolaou, Multiple scattering noise in one dimension: universality through localization length scales, *Phys. Rev. Lett.* 57:1000 (1986).
11. B. White, P. Sheng, Z.-Q. Zhang and G. Papanicolaou, Wave localization characteristics in the time domain, *Phys. Rev. Lett.* 59:1918 (1987).
12. P. Sheng, B. White, Z.-Q. Zhang, and G. Papanicolaou, Wave localization and multiple scattering in randomly-layered media, *in* "Scattering and Localization of Classical Waves in Random Media", P. Sheng, ed., World Scientific, Singapore (1990).
13. B. White, P. Sheng, M. Postel, and G. Papanicolaou, Probing through cloudiness: Theory of statistical inversion for multiply scattered data, *Phys. Rev. Lett*. 63:2228 (1989).
14. D. Brillinger. "Time Series, Data Analysis and Theory", Holden-Day, San Francisco (1981).

WAVE PROPAGATION AND RANDOM MEDIA BEYOND EFFECTIVE MEDIUM THEORIES: THE THEORY OF AGGREGATES

Thierry Robin and Bernard Souillard

X-RS, Parc-Club
28, rue Jean Rostand
F - 91893 Orsay Cedex, France
Also at:
Centre de Physique Théorique
Ecole Polytechnique,
F - 91128 Palaiseau Cedex, France

INTRODUCTION

We present several physical situations connected with wave propagation in random media where the classical approaches, namely the Effective Medium Theories (EMT), cannot provide the correct answers and we set out the new approach we have developed to go *beyond* EMT.

We will consider the electromagnetic properties of fractal aggregates and composites made with conducting inclusions in a dielectric matrix. The inclusions can be made with metal, carbon, conducting polymer or other conducting or semiconducting material.

Such composites have many applications: radar stealth, infrared controlled emissivity, the PTC (Positive Temperature Coefficient) effect, electromagnetic shielding, radomes, ...

During the last two decades, the electromagnetic (optical, infrared, microwaves,...) properties of composites have been the subject of an intense interest. This is due in part to the need for an understanding of the properties of various technological materials, but the basic physics of the electromagnetic response leads to interesting questions about the theoretical description of physical phenomena in disordered materials. As a matter of fact, despite much work, a complete theoretical approach for this very difficult problem was still lacking.

Photonic Band Gaps and Localization, Edited by
C.M. Soukoulis, Plenum Press, New York, 1993

The existing theories work only for a small range of concentrations and/or for a small range of frequencies of incident radiation and a rather large proportion of experimental results is not clearly understood.

In contrast to other theories, our approach takes fully into account the microscopic structure of the composite. Since fractal aggregates often occurs in such heterogeneous systems, we had to calculate their electromagnetic properties which turned out to be an interesting problem by itself. In this case, we calculate their polarization and/or their cross-sections. We use these results to calculate the electromagnetic properties of 2D and 3D composites.

Part I is devoted to the definition of the problem. In Part II, we review briefly the traditional approaches for the modelization of the electromagnetic properties of composite systems and in particular the Effective Medium Theories. The spirit of our theory is presented in Part III. We present briefly the theory we have developed to calculate the optical properties of granular metallic films. Our theory is now more general and has been extended to many other cases, but the model for metallic conductors in 2D is, however, still interesting because it is more intuitive than the developments and it gives the essential ideas to go beyond the effective medium theories. Our new model for the electromagnetic properties of fractal aggregate and composites is presented in Part IV.

Close to the percolation threshold, we find two main regimes. The first one can be identified with the theory of percolation at small frequencies. We predicted the second one for the first time. It leads to a different frequency dependence of the electromagnetic properties.

We compared our theory with experimental results. It gives satisfactory answers including the cases where classical theories are wrong but which are essential for the applications.

I - DEFINITION OF THE PROBLEM

We study a composite made of spherical (or quasi-spherical) conducting grains placed in a dielectric matrix.

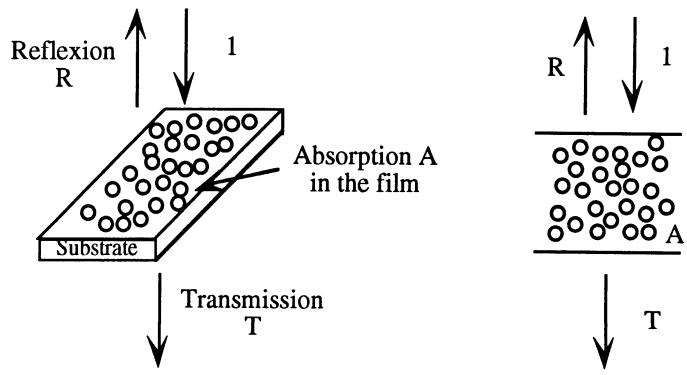

Figure 1. The two-dimensionnal and the three-dimensionnal cases

The problem that we want to solve is to calculate the Reflexion, Transmission and Absorption coefficients of a layer of composite. It can be (see figure 1) :

- a discontinuous planar film made with grains randomly disposed on a substrate: we will call it the two-dimensionnal situation,
- a layer of composite made of conducting spherical inclusions randomly dispersed in a dielectric matrix with thickness e : this is the three-dimensionnal situation.

When it has a real physical meaning (to be discussed later), we will also define an effective dielectric permittivity ε_e of the mixing. ε_i is the permittivity of the **insulating** matrix and ε_m the one of the **metallic** (or more generally conducting) inclusions. We denote by p the volumic concentration of the inclusions and a their radius.

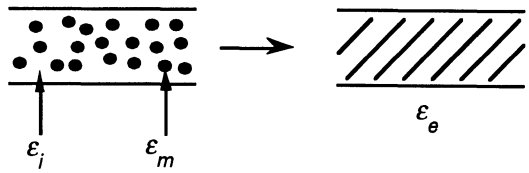

Figure 2. The effective medium equivalent to the composite

II - BACKGROUND

In this part, we briefly review the different theories which are frequently used to describe the electrical and electromagnetic properties of composites. The first section deals with the Effective Medium Theories (EMT) and, in the second section, we briefly remind the theory of percolation.

1 - Effective Medium Theories

Composite systems are traditionally studied through *Effective Medium Theories* (for a review, see e.g., Ref.1 and Ref.2) and improvements of them. These theories are supposed to be valid when the particles are much smaller than the wavelength, and to predict the effective dielectric constant of an equivalent homogeneous medium.

We will not detail the different EMT, since it has been done by many authors. The EMT which are frequently used to calculate the properties of composites are the following:

- The Looyenga-Landau-Lifschitz theory[3,4] (small contrast)
- The Clausius-Mosotti and Maxwell Garnett theory[5] (small concentration)
- The Bruggeman Theory[6] (self consistent theory which predicts the existence of a percolation threshold)

We have quoted these three theories because they represent some limits (small concentration / small contrast) or because they are simple and contain a real physical meaning. But, there exist many other "mixing laws" which are derived by making similar approximations (Böttcher, Krazewsky, ...). For a review of these theories, one can refer, for example, to Ref.1 and Ref.2.

The EMT have been shown to work quite well for low concentrations or for low contrast. But it has been increasingly recognized[7-10] that they could not describe correctly the electromagnetic properties of dielectric-conductor composites at intermediate concentrations, for example, near the insulator-conductor threshold.

Some attempts have been made in order to fix the effective medium theories.[11-14] Either they introduce arbitrary parameters and loose their predictive character, or they are still in poor agreement with the experimental results.

In the case of dielectric-conductor composites, according to us, the main reason for their failure at higher concentrations, and in particular in the vicinity of the insulator-conductor threshold, relies on the fact that a proportion of the inclusions can be close enough to form aggregates where the current can flow or where there is a strong electromagnetic interaction via induced polarization between the inclusions (see figure 3).

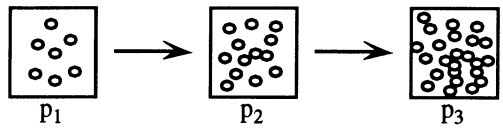

Figure 3. Schematic representation of a composite for increasing concentration

2 - Percolation theory: a reminder

The concept of percolation was invented and analyzed by Broadbent and Hammersley in 1957.[15,16]

Percolation is a theory which is able to describe the geometrical properties of various classes of composite systems. Let p be the volume concentration of inclusions in the matrix. Let p_c the percolation threshold above which an infinite cluster of inclusions appears.

If the percolation probability P_∞ is defined as the volume fraction occupied by inclusions belonging to the infinite cluster, we have:

$$P_\infty = 0 \text{ at } p \leq p_c$$
$$P_\infty \neq 0 \text{ at } p > p_c$$
$$(P_\infty = 1 \text{ for } p = 1)$$

The scaling theory of percolation[17,18] shows that near the concentration threshold p_c, there exists a typical largest cluster size s of spatial extension ξ. We have the following relations:

$$\xi = B\, a\, (p_c - p)^{-\nu} \quad \text{for } p < p_c$$

and:

$$\xi = B'\, a\, (p - p_c)^{-\nu} \quad \text{for } p > p_c$$

where a is the size of the inclusions and B and B' are numerical constants of order unity.

In addition, we have for the percolation probability:

$$\begin{cases} P_\infty = 0 & \text{for } p \le p_c \\ P_\infty = A\,(p - p_c)^\beta & \text{for } p \ge p_c \\ & p \text{ close to } p_c \end{cases}$$

The two latter relations imply, for example, that the infinite cluster (and also the finite clusters) is fractal up to a certain scale. In a box of size ξ, the mass of the infinite cluster is:

$$M_\infty(\xi) \propto P_\infty \,.\, \xi^d$$

where d is the dimensionality of space, and then:

$$M_\infty(\xi) \propto (p - p_c)^\beta \; \xi^d \propto \xi^{d - \beta/\nu}$$

In addition, for all scales $L < \xi$:[17]

$$M_\infty(L) \propto L^{d - \beta/\nu}$$

which is exactly the relation defining a fractal with fractal dimension: $d_f = d - \beta/\nu$

Actually, for the purpose of the present paper, we note that aggregates with a noticeable size do exist with a strong occurrence probability even at concentrations well below the percolation threshold.

The electrical conductivity near p_c has been shown to exhibit a new power law dependence on $p - p_c$ with a characteristic critical exponent t :

$$\begin{aligned} \sigma_e &= 0 && \text{for } p \le p_c \\ \sigma_c &= \sigma_m\,(p - p_c)^t && \text{for } p \ge p_c \end{aligned}$$

Table 1. Values of the percolation exponents at d = 2 and d = 3

d	β	ν	t	s	$\frac{s}{s+t}$
2	0.14	1.3	1.3	1.3	0.5
3	0.41	0.9	2.0	0.74	0.27

3 - Deutscher et al. models

In a first approach, Yagil and Deutscher[19] have tried to step out of the EMT. They consider the case of an electromagnetic wave incident on a granular metallic film and explain that in an optical measurement with wavelength λ, one probes whether, on the scale λ, the sample is essentially connected (metallic) or disconnected (dielectric). Then, in the limit of large values of λ, the sample is either uniformly connected ($p > p_c$) and then T has the same value as for a metallic film: $T \approx 0$, or it is uniformly disconnected ($p < p_c$) and $T \approx 1$. By a renormalization procedure up to scale λ, they derive near p_c the following form for the transmittance T:

$$T = T_c + \left(\frac{\lambda}{2\pi a}\right)^{1/\nu} (p_c - p)$$

At the threshold their theory predicts the transmittance is constant as a function of the wavelength. This phenomenological theory provides a challenging approach to the problem but cannot provide a detailed comparison with experiments, since, for example, it does not predict any value such as T_c.

Moreover, it is essentially a one-parameter approach and we will show that any relevant theory is a two-parameter one. Actually, as we will see, we predict a different behavior, in particular the reflectance (and also the transmittance) is not exactly constant at p_c in our theory. Also, we will obtain two regimes as a function of concentration near the threshold, a linear dependence followed by a stronger one.

Recently, a scaling based model was suggested for the optical properties of semicontinuous 2D metal films.[20] The outlines of this approach are the following:

- The effective dielectric constant has no physical meaning close to p_c. Moreover, one must average the reflectance and transmittance on different areas, where the film has different contributions.

- The local optical response is deduced from the local complex ac conductivity on the relevant length scale. This quantity is described by a bimodal distribution function, taking into account the ac conductivity of the metallic grains and the intercluster capacitance.

- The relevant length scale is much shorter than the optical wavelength and is given by the anomalous diffusion relation[21] $L(\omega) \sim L_0 (1/k)^{2+\theta}$ where k is the wavenumber, $\theta \approx 0.8$ for 2D and L_0 is a coefficient of the order of unity.

- The total ac conductivity of a square of linear size $L<\xi$ is calculated numerically.

III - THEORY OF AGGREGATES: THE SPIRIT OF OUR APPROACH

1 - Introduction

In the following, we will study an electromagnetic radiation with pulsation ω and wavelength in vacuum λ_0 (it can be infrared, microwave,...) perpendicularly incident on a disordered composite. The latter is made of metallic grains of size $a << \lambda_0$ randomly dispersed in a dielectric matrix. The filling factor is denoted by p.

The idea of the theory is to calculate a physical quantity (like the absorption A , for example) for an aggregate (C) depending on its size and frequency and taking into account interactions with other aggregates: $A(C,\omega)$.

Then, we sum all the contributions of the aggregates of various shapes and sizes to obtain the macroscopical quantity: $A(\omega) = \Sigma_{(C)} A(C,\omega)\, n(C)$ where $n(C)$ is the probability of the cluster (C). The statistic of occurrence of the clusters can be given by the theory of percolation or by any other theory of aggregation in a composite.

2 - Two-dimensionnal films

Our theory of aggregates was first developed in 1988 for the case of metallic discontinuous films in 2D. Our theory is now more general and has been extended to many other cases, but it appears to us that the first version of the theory for metallic conductors in 2D is, however, interesting because it may be more intuitive than the developments and it gives the essential ideas to go beyond the effective medium theories.

So we present now briefly our approach for the case of granular films developed elsewhere.[22,23] We consider, as an example, the case of disordered metallic films in the infrared wavelengths.

Experiments have been performed by Yagil and Deutscher[24] and by Gadenne and Lafait[8,25] on disordered metallic film with Au grains of 40 to 500 Å. Disagreement with effective medium theories is very clear, e.g., in reference,[8] where at the percolation threshold, reflectance can be found experimentally to be approximately 30 %, whereas effective medium theories cannot yield better than 15 % when used with relevant values of the physical parameters.

Following the general approach indicated in the previous section, we have developed a microscopic theory for the reflection by a disordered metallic film. This theory takes fully into account the geometrical structure of the clusters of metallic grains as given by the percolation theory, as well as other ingredients. This produces an essentially no free parameter theory, for the dependence of the reflectance as a function of the wavelength λ and of the concentration p . It gives results in good qualitative as well as quantitative agreement with the experimental results as can be seen on the above mentioned example for which we recover a 30 % reflectance up to a few percent, in contrast with effective medium theories. These results have been announced in a first paper.[22] The theory for the reflexion properties in the infrared has been first developed[23,26] and the paper[27] deals with the absorption properties in the infrared. We summarize here the results of our 2D theory.

We discriminated[22] four regions of concentrations corresponding to four different situations (see Figure 2):

- The "**dielectric region**" (A): it is defined by $\xi < \lambda/2\pi$ and $p < p_c$. All the clusters except very exceptional ones are smaller than the wavelength. Thus $R \approx 0$. It is the "dielectric" situation. It can be calculated by the effective medium theories.
- The "**threshold region**" (B): it corresponds to $\lambda/2\pi < \xi$. There is a significant number of finite (or infinite) clusters with extension larger than $\lambda/2\pi$ so there is already a significant reflection due to these finite but large clusters. We used the geometrical description of the clusters[23] as it appears from the scaling theory of percolation in order to calculate the expression for the reflectance R. The details of the calculation can be found elsewhere.[26] We obtained for the reflectance R_m due to the metal in this range of concentration:

$$R_m = \eta\, p_c\, \rho(e,\lambda) \left(\frac{\lambda}{2\pi a}\right)^{-\beta'/\nu} \left(1 + \mu\,(p - p_c) \left(\frac{\lambda}{2\pi a}\right)^{1/\nu}\right)$$

where μ and η are two numerical constants of order unity

In particular, for $p = p_c$, we have:

$$R_m(p=p_c) = \eta\, p_c\, \rho(e,\lambda) \left(\frac{\lambda}{2\pi a}\right)^{-\beta'/\nu}$$

with $\beta'/\nu \approx \beta_b/\nu \approx 0.4$ in two dimensions.

If we rewrite the expression for the reflectance in the following form:

$$R_m = \kappa\, \lambda^{-\beta'/\nu} \left(1 + \kappa'\,(p - p_c)\, \lambda^{1/\nu}\right)$$

we see the difference between our result and the one of Yagil and Deutscher[19] is the presence of the factor $\lambda^{-\beta'/\nu}$ which implies that, for $p = p_c$ and $\lambda \to \infty$, R_m tends to 0 instead of being constant.

For gold in the near infrared, the reflection coefficient $\rho(e,\lambda)$ slowly increases with λ and then saturates. In contrast, $(\lambda/2\pi a)^{-\beta'/\nu}$ decreases when λ increases. So, $R_m(p=p_c)$ is almost independent of the wavelength in a range of wavelength depending on the materials, but is predicted to finally decay to zero for larger λ.

The reflectance R of the film including the effects of the metal and of the substrate has the following expression:[26]

$$R = \rho_s + \eta\, p_c\, (\rho(e,\lambda) - \rho_s) \left(\frac{\lambda}{2\pi a}\right)^{-\beta'/\nu} \left(1 + \mu\,(p - p_c) \left(\frac{\lambda}{2\pi a}\right)^{1/\nu}\right)$$

where ρ_s is the reflection coefficient on a strip of substrate.

- The "**net region**" (C): it is defined by $\xi < \lambda/2\pi$ but $\xi > \lambda/10$ and $p > p_c$. The mean radius of the holes in the infinite cluster is smaller than $\lambda/2\pi$. The partial reflectance of these holes of size smaller than $\lambda/2\pi$ will increase the reflectance rapidly.
- The "**metallic region**" (D): it is defined by $\xi < \lambda/10$ and $p > p_c$. The holes are much smaller than $\lambda/2\pi$, so the reflectance $R \approx \rho(e,\lambda)$ is about the same as the reflectance of the full metallic film.

The schematic behavior of the reflectance versus concentration is represented in figure 4.

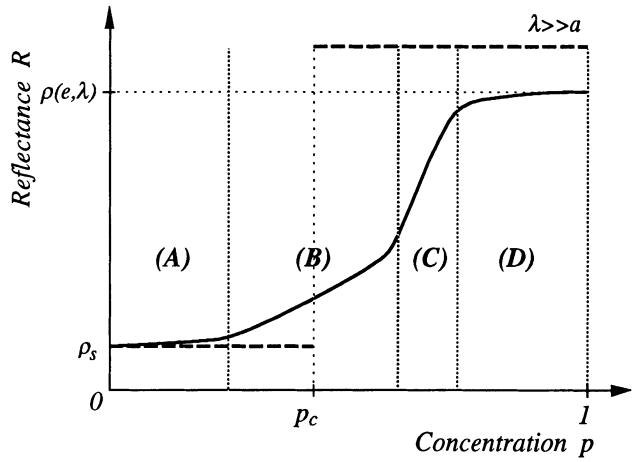

Figure 4. The schematic behavior of the reflectance versus the filling factor as predicted by the theory of aggregates in the 2D case

III - THE THEORY OF AGGREGATES: THE GENERAL NEW APPROACH

1 - Introduction

In the previous section, we presented the theory of aggregates for discontinuous metallic films in the infrared which is applicable for good metals, i.e., when the absorption is small and for 2D systems (thin films). We present here the theory that we have developed since to treat the general case and, in particular, to take into account metallic or non-metallic conductors and three-dimensional systems.

Other approaches have been proposed, based on scaling assumptions.[20,28] Our present approach turns out to be more predictive: we write an equation for the current on an aggregate taking into account its environment; the solution of the equation gives the polarization and/or cross-section of one single aggregate. Then, the properties of the composite are obtained by an appropriate summing of the properties of the aggregates. The distribution of form and size of the aggregates can be given by an aggregation theory. For the purpose of the present letter, we will restrict to the case of the usual theory of percolation.

In contrast to all the previous approaches, we find two main regimes in frequency for the dielectric permittivity. The first one can be identified as the theory of percolation at small frequencies. But, we predict a new regime at high frequency which is related to the propagation in the aggregate and leads to a different frequency dependence for the electromagnetic properties of the composite.

When one wants to calculate the electromagnetic response of composites including aggregates, there are various cases of "electrical microstructure." The first main case is when every two grains are separated, they are never close enough to allow the flow of the current. In this case, there exists generally a narrow layer of insulator between the two inclusions. The electromagnetic properties of this kind of composite are generally the same as the properties of insulators. The dielectric permittivity is then quasi independent of frequency and is only weakly dependent of the aggregation in the composite. The second case is when the two grains are in electric contact (the current can flow from one to the other). In this case, we cannot neglect the effects of aggregation. For the present paper, we restrict to the second case, i.e., we neglect the capacitive part of the interaction between grains in contact and only take into account the resistive part (for grains which are not in contact, we take into account, of course, the capacitive interaction since it is the only one). The general case will be discussed in the full paper.[29]

2 - Electromagnetic properties of one single aggregate

Let us denote by d the dimensionality of space and d_f the fractal dimension of the aggregates.

In Ref.30, the following expressions for the derivative of the capacitance, resistance, and inductance of an aggregate between plane 0 and x are derived:

$$C(x) = \frac{C_0}{a}\left(\frac{\Re}{a}\right)^{d_f-1}\left(\frac{x}{a}\right)^{c}$$

$$R(x) = \frac{R_0}{a}\left(\frac{\Re}{a}\right)^{1-d_f}\left(\frac{x}{a}\right)^{r}$$

$$L(x) = \frac{L_0}{a}\left(\frac{\Re}{a}\right)^{1-d_f}\left(\frac{x}{a}\right)^{l}$$

where $\Re$ is the radius of the aggregate and C_0 , R_0 , L_0 are, respectively, the capacitance, the resistance, and the inductance of a grain of size a.

For percolation clusters, the exponents of the scaling laws in x are: $c = s/\nu+d-d_f-2$, $r = t/\nu+d_f-d$ and $l = t'/\nu+d_f-d$ where t' is the analog of t for inductance properties (t'>t). Note that, even for percolation clusters, the expression for C(x) is actually more complicated and involves several scaling laws corresponding to different contributions.[29]

These coefficients appear in a new equation that we wrote[30] for the current $j(x)$ in an aggregate for an incident electrical field E_0 with frequency ω:

$$\frac{d^2j}{dx^2} = \frac{C'(x)}{C(x)}\frac{dj}{dx} + i\omega\, C(x)\,(R(x) + i\,L(x)\,\omega)\,j(x) + i\omega\, C(x)\,E_0$$

We call it the generalized antenna equation.

We have shown[30] there exists a length δ above which the current in an aggregate is not correlated to the current at the origin. We call δ the current correlation length. Its frequency dependence depends on the relative value of the resistance and inductance. More precisely, we find two opposite regimes:[30]

The regime (I) ($R >> L\omega$): $$\frac{\delta}{a} \sim (\omega\, R_0 C_0)^{-\frac{1}{r+c+2}}$$

The regime (II) ($R << L\omega$): $$\frac{\delta}{a} \sim \left(\omega\, L_0^{1/2} C_0^{1/2}\right)^{-\frac{2}{l+c+2}}$$

In the case of percolation clusters, the regime (I) can be identified to the usual case calculated by the "frequency dependent" theory of percolation. Since the latter theory calculates the properties of composites by an approximation of equivalent electrical networks, it is natural this regime takes place at small frequencies.

On the contrary, we predicted the regime (II)[30] for the first time. Since it takes into account magnetic effects as well as electrical ones, it is clear that it is related to the propagation of the current wave in the aggregate. We deduced that an aggregate with $\Re >> \delta$ can be seen as a set of blocks of size δ.

Let us introduce another important length in the problem, the wavelength λ. Since we always have $\delta \leq \lambda$, there are three principal cases for the properties of one aggregate:

• $\Re < \delta$: we are in the quasistatic case. The real part of the polarization of the aggregate is the same as the one at zero frequency and the imaginary part is small:[29,30]

$$\frac{P'}{E_0} = \alpha'\,\Re^3\, C(\Re) = \alpha'\,\frac{C_0}{a}\left(\frac{\Re}{a}\right)^{d_f + c + 2} a^3$$

$$\frac{P''}{E_0} = \alpha''\,\omega\,\Re^5\, R(\Re)\, C(\Re)^2 = \alpha''\,\omega\,\frac{R_0\, C_0^2}{a}\left(\frac{\Re}{a}\right)^{d_f + r + 2c + 4} a^3$$

in the first and the second regimes and where α' and α'' are two numerical constants of order unity.

• $\Re > \delta$ but $\Re << \lambda$: the current propagates in the aggregate but since $\Re << \lambda$, we are able to calculate the polarization of the aggregate.

- Regime (I) ($R >> L\omega$):

$$\frac{P(\Re,\omega)}{E_0} = \alpha_I \frac{C_0}{a}\left(\frac{\Re}{a}\right)^{d_f} a^3 \, (C_0 R_0 \omega)^{-y_I}$$

where:
$$y_I = \frac{c+2}{r+c+2}$$

for percolation clusters, we have:

$$y_I = \frac{\frac{s}{\nu} + d - d_f}{\frac{s}{\nu} + \frac{t}{\nu}} = \frac{s + \nu(d - d_f)}{s+t} = \frac{s+\beta}{s+t}$$

- Regime (II) ($R << L\omega$):

$$\frac{P(\Re,\omega)}{E_0} = \alpha_{II} \frac{C_0}{a}\left(\frac{\Re}{a}\right)^{d_f} a^3 \, (C_0^{1/2} L_0^{1/2} \omega)^{-y_{II}}$$

where:
$$y_{II} = 2\,\frac{c+2}{l+c+2}$$

for percolation clusters, we have:

$$y_{II} = 2\,\frac{\frac{s}{\nu} + d - d_f}{\frac{s}{\nu} + \frac{t'}{\nu}} = 2\,\frac{s + \nu(d - d_f)}{s+t'} = 2\,\frac{s+\beta}{s+t'}$$

α_I and α_{II} are two complex constants with a modulus of order unity.

It is interesting to note that the exponent y in regime (I) is not the same as the exponent predicted by the theory of percolation for the frequency dependence of the permittivity which is s/(s+t). In fact, we are calculating the response of one single aggregate. We will see in the next section that, after summing over all the aggregates with their correct statistical weight, we will recover in this regime (I) the exponent s/(s+t).

• $\Re > \lambda \geq \delta$: since the size of the aggregate is larger than the wavelength in the surrounding medium, we cannot calculate the polarization of the aggregate. Nevertheless, we can calculate the cross-sections. In fact, the aggregate can be seen as a set of blocks of size λ and we can evaluate the scattering and absorption cross-sections of an aggregate through:

$$\sigma(\Re,\omega) = (\Re/\lambda)^{d_f}\, \sigma(\lambda)$$

where the cross-sections of a block of size λ are evaluated through quasistatic formulae.[29]

3 - Electromagnetic properties of a composite

Let us denote by ξ the correlation length of the medium (i.e., the typical size of the aggregates and these of the heterogeneities) and by δ_p the penetration depth of the wave in the composite. The electromagnetic properties of the composite are to be described differently according to the following three main cases:[31]

- $\xi < \lambda$ (with $\xi > \delta$ or $\xi < \delta$), the homogeneities are smaller than the wavelength and we can define and calculate an equivalent dielectric permittivity for the composite.

- $\delta < \lambda < \xi$ (but $\delta_p > \delta$), the homogeneities are larger than the wavelength and we cannot define an equivalent dielectric permittivity for the composite. But like in Ref.26, we can compute directly the macroscopic hemispherical reflexion, hemispherical transmission and absorption of the composite.

- $\delta < \lambda < \xi$ (but $\delta_p < \delta$), we cannot define an equivalent dielectric permittivity and moreover the surface penetration (2D) effects must be taken into account.

The dielectric permittivity of a composite

We detail now the first case and we present the results for the dielectric permittivity of the composite. The other cases are detailed elsewhere.[29]

The calculation[29,31] assumes the statistical and geometrical description of the aggregates as given by the scaling theory of percolation. But the theory is more general and can treat other laws of aggregation.

Let $\Re_S$ denote the radius of a cluster containing S sites. We have:

$$\Re_S = k\, S^{1/df} \quad \text{where} \quad k \sim 1$$

The average polarization in the composite is obtained by summing over the aggregates and gives the equivalent dielectric permittivity:[31]

$$\varepsilon_{eq} \sim \langle P \rangle = \sum_S n_S\, P(\Re_S)$$

In Ref.31, we show there are three regions of concentrations corresponding to three different situations (see Figure 2).

- The "**dielectric region**" (A): it is defined by $\xi < \delta$ and $p < p_c$. All the clusters but very exceptional ones are smaller than δ. It is the "dielectric" situation. We obtain the following formula for the dielectric permittivity of the composite:

$$\varepsilon_{eq} = q_0\, C_0/a\, (\alpha' |p - p_c|^{-s} + i\, \alpha'' \omega |p - p_c|^{-(t+2s)})$$

• The "**threshold region**" (B): it corresponds to $\delta < \xi$. There is a significant number of finite (or infinite) clusters with extension larger than δ so that the electromagnetic response due to these finite but large clusters is dominant. We obtain the expression for the average polarization in the vicinity of the percolation threshold (η~1):

$$<P>_2 \approx \eta p_c C_0/a \, (\delta/a)^{s/\nu}$$

which gives:

- Regime (I) ($R >> L\omega$):

$$\varepsilon_{eq} \sim (R_0 C_0 \omega)^{-s/(s+t)}$$

- Regime (II) ($R << L\omega$):

$$\varepsilon_{eq} \sim (L_0^{1/2} C_0^{1/2} \omega)^{-2s/(s+t')}$$

The first regime can be identified with the theory of percolation at small frequencies and we find the same exponent ($s/(s+t) \approx 0.27$). But, the second regime (high frequency) is a new one which takes into account the propagation in the aggregate and which leads to a different frequency exponent for the permittivity of the composite: $2s/(s+t') \approx 0.5$.

• The "**metallic region**" (C): it is defined by $\xi < \delta$ and $p > p_c$. The behavior of the composite is about the same as the one of a classical conductor. In fact, the larger contribution is due to the infinite cluster and we have:[31]

$$\varepsilon_{eq} \sim i \sigma_0 |p - p_c|^t / \omega$$

We predict the dependence of the permittivity with concentration and frequency. The behavior for one class of systems is described in figure 5.

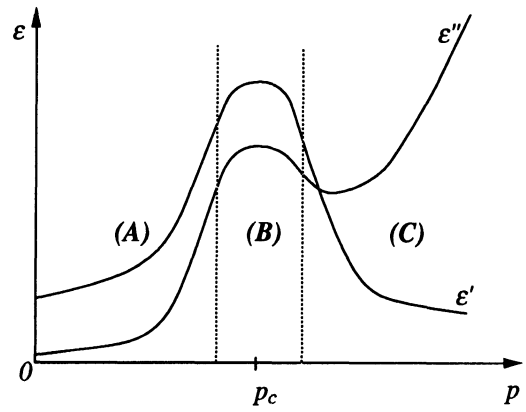

Figure 5. One of the schematic behavior of the dielectric permittivity versus concentration as predicted by the theory of aggregates

4 - Brief Comparison with the Experimental Results - Conclusion

Our theory has been compared with experiments in several cases in the first regime. The agreement is good for all concentrations including the vicinity of the percolation threshold whereas they strongly disagree with effective medium predictions.[29] The appearance of the second regime may have been observed, e.g., in Ref.32 where a high frequency dependence follows a smaller one. A quantitative comparison with our theory is difficult there because of the small number of experimental points.

In addition, our theory allows us to explain the results of Ref.9 where a high diffusive reflection appears in the vicinity of the percolation threshold (regime $\lambda<\xi$).[29]

We have presented a new theory which predicts quantitatively the electromagnetic properties of fractal aggregates and of dielectric-conductor composites. The main results are the following:

- The electromagnetic properties of fractal aggregates do not depend only on the transport properties but also on its fractal dimension. Let us note that our model for a single aggregate has been compared with a numerical algorithm based on completely different ideas. The results are in very good agreement.[33]

- We recover the results of the previous theories as limit cases.

- We predict the existence of a new regime for the polarization of aggregates and for the dielectric permittivity of composites. This regime takes place at high frequencies ($L\omega>>R$) and leads to the introduction of a new value for the frequency dependence exponent of the permittivity ($= 2s/(s+t')$).

- Our model is in good agreement with experimental results.

- Our theory put into evidence and explain anomalous behaviors of the permittivity (systems with hopping conduction between grains[34]) or of the reflexion/transmission properties (tridimensionnal composites in the diffusive regime and in the vicinity of the percolation threshold[29]).

Acknowledgments

We are glad to thank Guy LAVAL for very useful discussions during the development of this work.

This work has been supported in part by DRET under contract N° 89.317.

References

1. R. Landauer, in "Electrical Transport and Optical Properties of Inhomogeneous Media", AIP conference proceedings, 2 (1978).
2. J.L. Greffe and C. Grosse, in *Heterogeneous Materials,* PIER vol. 6, A. Priou editor, p. 41, Elsevier (1992).
3. H. Looyenga, Physica 31, 401 (1965).
4. L. Landau, E. Lifchitz in "Electrodynamique des milieux continus", Mir Moscou (1969).
5. J.C. Maxwell Garnett, Philos. Trans. R. Soc. London 203, 385 (1904).
   J.C. Maxwell Garnett, Philos. Trans. R. Soc. London 205, 237 (1906).
6. D.A.G. Bruggeman, Ann. Phys. (Leipz.) 24, 636 (1935).
7. S. Berthier, J. Lafait, C. Sella and T.K. Vien : Thin Solid Films 125, 171 (1985).
8. P. Gadenne, A. Beghdadi, J. Lafait, Optics Comm. 65, 17 (1988).
9. D. Ordiera, F. Carmona, J. Physique 44, 683 (1983).
10. D.S. McLachlan, A. Priou, E. Issac, I. Chénerie, F. Henry, J. Electromag. Wave and Appli. (September 1992).
11. R.W. Cohen, G.D. Cody, M.D. Coutts, B. Abeles, Phys. Rev. B 8, 3689 (1973).
12. C.G. Granqvist, Z. Physik B 30, 29 (1978).
13. Ping Sheng, Phys. Rev. Lett. 45, 60 (1980).
14. G.A. Niklasson, C.G. Granqvist, Phys. Rev. Lett. 56, 256 (1986).
15. S.R. Broadbent and J.M. Hammersley, Proc. Cambridge Philos. Soc. 53 (1957) 629.
16. J.M. Hammersley, in: Percolation Structures and Processes, G. Deutscher, R. Zallen and J. Adler, eds., Annals of the Israel Physical Society, vol. 5 (1983) pp. 47-57.
17. D. Stauffer, Phys. Rep. 54, 1 (1979).
18. D. Stauffer, *Introduction to Percolation Theory,* Taylor and Francis, London (1985).
19. Y. Yagil and G. Deutscher, Appl. Phys. Lett. 52, 373 (1988).
20. Y. Yagil, M. Yosefin, D. J. Bergman, G. Deutscher and P. Gadenne, Phys. Rev. B 43, 11342 (1991).
21. Y. Gefen, A. Aharony and S. Alexander, Phys. Rev. Lett. 50 (1983) 77.
22. Th. Robin and B. Souillard, Proceedings of the Second International Conference on Electrical Transport and Optical Properties of Inhomogeneous Media : Physica A 157, 285 (1989).
23. Th. Robin and B. Souillard, Europhys. Lett., 8 (8), 753 (1989).
24. Y. Yagil, G. Deutscher, Thin Solid Films 152, 465 (1987).
25. M. Gadenne, Thesis, Paris (1987).
26. Th. Robin and B. Souillard, a Microscopic Theory of the Reflection Properties of Metal-insulator Composite Films, Physica A to appear.
27. Th. Robin and B. Souillard, Optics Comm. 71 , 15 (1989).
28. J.P. Clerc, G. Giraud, J.M. Laugier, J.M. Luck, Adv. Phys. 39, 191 (1990).
29. Th. Robin and B. Souillard, Electromagnetic Properties of Fractal Aggregates and Composites : a Microscopic Theory, to be submitted to Physica A.
30. Th. Robin and B. Souillard, Electromagnetic Properties of Fractal Aggregates, Europhys. Lett. to appear.
31. Th. Robin and B. Souillard, A New Theory of the Electromagnetic Properties of Dielectric-Conductor Composites, submitted to Phys. Rev. Lett.
32. T. A. Ezquerra, F. Kremer and G. Wegner, *Heterogeneous Materials,* PIER vol. 6, A. Priou editor, p. 273, Elsevier (1992).

33. Th. Robin and B. Souillard, Electromagnetic Properties of Fractal Aggregates and Composites Systems : Comparison between a Theoretical Model and a Numerical Computation, submitted to J. Electromag. Wave and Appli.
34. Th. Robin and B. Souillard, Concentration Dependent Exponent for AC Hopping Conductivity and Permittivity, submitted to Europhys. Lett.

SCATTERING AND LOCALIZATION OF CLASSICAL WAVES ALONG A WAVE GUIDE WITH DISORDER AND DISSIPATION

M. Schreiber[1] and K. Maschke[2]

[1]Institut für Physikalische Chemie, Johannes-Gutenberg-Universität
Jakob-Welder-Weg 11, D-6500 Mainz, F.R.Germany

[2]Institut de Physique Appliquée, Ecole Polytechnique Fédérale
PHB-Ecublens, CH-1015 Lausanne, Switzerland

INTRODUCTION

The problem of localization of classical waves has recently attracted considerable attention.[1,2] Classical waves have, of course, been the subject of extensive research already in the last century, as emphasized by Landauer in his historical sketch.[3] A variety of interesting phenomena is associated with classical waves like seismic waves, tidal waves, acoustic as well as optical waves. A major topic is the transport of energy or information by these waves. The current interest in classical waves is stimulated by the development of microelectronics with its very small structures, in particular very thin wires (as connections between the components of integrated circuits) which may (or may not, depending on the situation) be considered as wave guides for the electrons. Similarly, optical wave guides like optical fibers for telephone connections are of technological interest. The interesting analogies between microelectronics and optics have been comprehensively discussed in a recent book.[4] There are, of course, important differences between quantum mechanical waves describing electrons and classical waves like optical or acoustic waves, as discussed by Landauer,[3] e.g., the conservation of electrons on the one hand or non-linear optics on the other hand. Nevertheless, it is promising to apply approaches, which have been successful in one area, to the other field.[2]

In the present contribution we apply a method which has been originally introduced for the description of the coherent motion of electrons along a one-dimensional system.[5] Later, dissipative effects have been incorporated into this model.[6] These dissipative effects arise, e. g., from inelastic scattering events of the electronic

Photonic Band Gaps and Localization, Edited by
C.M. Soukoulis, Plenum Press, New York, 1993

waves with local modes at impurities or with phonons, thus providing the coupling of the electronic system with a heat bath. In this way, irreversible processes can be imagined, which lead to a complete loss of the phase memory. As a consequence, the scattered waves are incoherent with the incident waves. A similar effect can be imagined in optics, considering the absorption and subsequent emission of photons.

Much more important in the optical case as well as for other classical waves, however, is the influence of disorder. Depending on the group velocity, already small disorder in one-dimensional (1D) systems can crucially restrict the band width which is available for information transport.[7] This effect can be understood as a localization of the classical waves due to disorder in analogy to the well-known localization of electronic states in disordered materials. It is the purpose of the present paper to study classical waves in a 1D system and to analyze the localization of these waves due to disorder.

By suitably utilizing the above-mentioned model, we can also incorporate leakage or absorption into our investigation. This allows us to treat another essential problem of large technological relevance, namely the loss of intensity of the waves travelling along the wave guide. For example, in the optical case, absorption processes as well as scattering events at the surface of the wave guide would provide appropriate leaks. For tidal waves in channels, the influence of not ideally reflecting banks could be taken into account in this way. Seismic waves would suffer similar dissipative effects by being scattered at soft strata. All these effects are treated in the same (parametrized) way in the present approach, therefore we shall use the terms dissipation, leakage or absorption interchangeably in the subsequent discussion.

In the following chapters, we shall first introduce the investigated model and construct the overall scattering matrix. Then, we discuss the case of purely elastic scattering, distinguishing regimes of localization and transmission. Finally, the influence of dissipation or absorption and the effect of disorder are analyzed.

MODEL OF THE SINGLE SCATTERER

We consider a series of N scatterers as displayed in Fig. 1. Waves travel along the chain between the ends 1 and 2. For each scatterer, incoming and outgoing waves in channels 1 and 2 are related by means of the elastic scattering matrix

$$\sigma = \begin{bmatrix} r & t \\ t & r \end{bmatrix} \tag{1}$$

with transmission coefficient t and reflection coefficient r. Characterizing the elastic scatterer by means of the transmission probability δ yields $t = \sqrt{\delta}$ and, as the scattering matrix must be unitary, $r = i\sqrt{1-\delta}$.

Formally, we add two more channels to the single scatterer and define the total scattering matrix of the single scatterer, which then is a 4×4 matrix:

$$\mathbf{S}^1 = \mathbf{s}^1 = \begin{bmatrix} \sqrt{1-\varepsilon}\,\sigma & \sqrt{\varepsilon}\;\mathbf{1} \\ \sqrt{\varepsilon}\;\mathbf{1} & -\sqrt{1-\varepsilon}\,\sigma^* \end{bmatrix} = \left[S^1_{ij} \right] \qquad i, j = 1, 2, 3, 4 \; . \qquad (2)$$

Here, the unitary matrix $\mathbf{1}$ supplies the coupling of the chain with the additional channels, controlled by the scattering strength ε. The matrix $-\sigma^*$ must be included to insure[8] the necessary unitarity of the matrix $\mathbf{S}^1$. The effect of this choice of the scattering matrix can be easily visualized in the special case of $\delta = 1$, i.e., no elastic scattering: An incoming wave in channel 1 is scattered into channel 3 with probability ε. With the same probability, a wave from channel 2 leaves the scatterer through channel 4. Accordingly, the direct transmission is reduced and occurs with probability $|s_{12}|^2 = (1-\varepsilon)\,\delta$. In this way, we have defined the leaks in our wave guide as discussed in the introduction.

For completeness, we note that in the original model[6] current conservation laws are invoked for the additional channels at each scatterer, so that leakage is prohibited. As a consequence, waves scattered into channels 3 and 4 reenter the system via these channels, but their phase is then not related to the original phase. Thus, it becomes clear how the scattering matrix (2) leads to a loss of phase memory and therefore describes inelastic scattering. The above choice of the matrix (2) for the

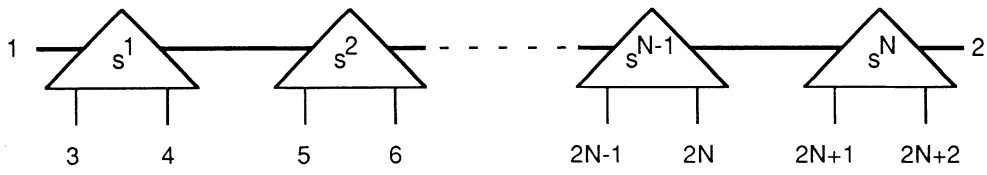

Figure 1. Series of N general scatterers described by $\mathbf{s}^1, \ldots, \mathbf{s}^N$. The labels count the channels as described in the text.

connection of the chain to the additional channels is a particular one, which produces maximal incoherence. Other possible choices have been discussed elsewhere.[9] In this connection, it has also been shown that it is sufficient to use 4 channels for each scatterer in order to cover the entire range of elastic and inelastic scattering strengths.[9] In the present context of classical waves, however, there is no need to require current conservation, in contrast we utilize channels 3 and 4 to allow explicitly for leakage.

CONSTRUCTION OF THE SCATTERING MATRIX OF THE ENTIRE CHAIN

The total scattering matrix of a chain of N scatterers at positions x_n $(n=1,...,N)$ can easily be constructed in an iterative way[10] as illustrated in Fig. 2. We assume that the scattering matrix $\mathbf{S}^{N-1}$ of N-1 scatterers has been found. Then the Nth scatterer described by $\mathbf{s}^N$ is appended. The scattering amplitudes of $\mathbf{s}^N$ are given by Eq. (2), relabelling the rows and columns of the matrix $\mathbf{s}^1$ as $i,j = 1, 2, 2N+1$, $2N+2$ in agreement with Fig. 2. It is straightforward to determine the matrix elements of the total scattering matrix by taking all possible paths into account. We obtain, for example, for the transmission from channel 1 into channel 2 (compare Fig. 2):

$$S^N_{21} = s^N_{21}\,\varphi\,S^{N-1}_{21} + s^N_{21}\,\varphi\,S^{N-1}_{22}\,\varphi\,s^N_{11}\,\varphi\,S^{N-1}_{21} + s^N_{21}\,\varphi\,S^{N-1}_{22}\,\varphi\,s^N_{11}\,\varphi\,S^{N-1}_{22}\,\varphi\,s^N_{11}\,\varphi\,S^{N-1}_{21} + \ldots \qquad (3)$$

Here, $\varphi = exp(iqa_N)$ reflects the phase that the outgoing wave out of channel 2 of $\mathbf{S}^{N-1}$ acquires before entering channel 1 of $\mathbf{s}^N$. The wave vector q reflects the energy of the incoming plane wave $exp(iq(x-x_0))$ under consideration, but we do not specify a particular dispersion relation. The distance between neighboring scatterers a_N is

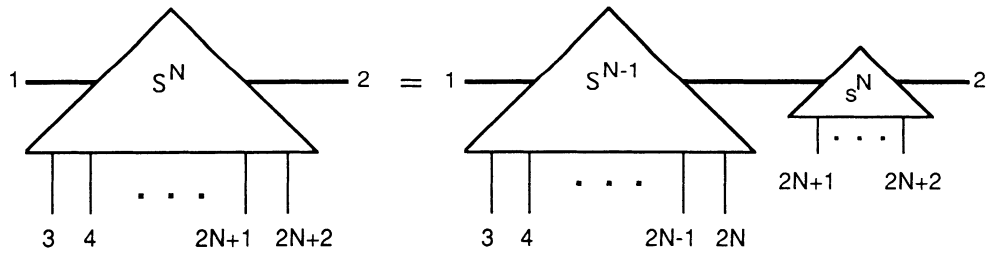

Figure 2. Adding the last scatterer $\mathbf{s}^N$ to an effective scatterer $\mathbf{S}^{N-1}$ which comprises the preceding series of N-1 scatterers allows a recursive construction of the series in Fig. 1.

constant in the ordered chain $a_N \equiv a$. In order to introduce disorder into our model, we choose the nearest-neighbor distance randomly from a uniform distribution of width W around this average distance a. All subsequent results for the disordered case have been obtained for the parameter value $W=a$.

As can be seen from Eq. (3), the multiple reflections between the two scatterers lead to a geometric series in $z = \varphi\,S^{N-1}_{22}\,\varphi\,s^N_{11}$ which can be easily summed. We obtain:

$$S^N_{iI} = s^N_{i1} \frac{\varphi}{1-z} S^{N-1}_{2I}, \qquad S^N_{Ii} = S^N_{iI} \tag{4a}$$

$$S^N_{IJ} = S^{N-1}_{IJ} + S^{N-1}_{I2} \varphi s^N_{11} \frac{\varphi}{1-z} S^{N-1}_{2J} \tag{4b}$$

$$S^N_{ij} = s^N_{ij} + s^N_{i1} \frac{\varphi}{1-z} S^{N-1}_{22} \varphi s^N_{1j} \tag{4c}$$

for $I,J = 1,3,4,\ldots,2N$ and $i,j = 2,2N+1,2N+2$. This recursion allows us to investigate relatively long chains with several hundreds of scatterers with reasonable numerical expense. A significant advantage of the iteration (4) is the exact sum of the geometric series of the multiple reflections. Moreover, if one is interested only in certain transmission probabilities, then it is sufficient to determine only a few of the matrix elements in Eq. (4). In particular, for the calculation of the overall transmission probability through the series of scatterers it is not necessary to treat the entire matrix $\mathbf{S}^N$. Therefore, the present algorithm is superior to our previous treatment of the chain by transforming the scattering matrix into transfer matrices.[8]

RESULTS AND DISCUSSION

Transmission probability through an ordered chain without dissipation

In the following we analyze the transmission probability across the whole sample, $T(\varepsilon,N,W) = |S^N_{21}|^2$ in its dependence on the wave vector q of the incoming waves, the dissipation parameter ε and the number of scatterers N. We have chosen a fixed value for the elastic scattering strength $\delta = 0.7$, because we know[10-12] for an intermediate elastic scattering the effects discussed below are most clearly seen. For small elastic scattering, the multiple reflections become negligible so the interplay between constructive interference and disorder is lost. For very large elastic scattering, the waves cannot travel in the sample so the importance of disorder is reduced. In this situation, the waves cannot penetrate into the system, or, if they are excited within the system, they are effectively confined between two scatterers, and in the extreme case, the waves are reflected back and forth until leakage is complete.

In Fig. 3 the dependence of the transmission probability on the number of scatterers N is displayed for different values of the wave vector q in the case of no leakage ($\varepsilon = 0$). For small wave vectors, incoming waves can only penetrate into the sample for a finite distance due to destructive interference of the multiply backscattered waves. For larger values of q, the multiple reflections lead to construc-

tive interference producing the strong oscillations of the transmission probability in Fig. 3, which do not decrease for longer chains. This is the fully transparent regime, in contrast to the opaque regime with the "confined states" for small wave vectors.

The transmission window can be seen even more clearly in Fig. 4, where the transmission probability is displayed in dependence on the wave vector. For the case without dissipation ($\varepsilon=0$), a band of high transmission can be observed with oscillations due to interference effects. There are even N-1 values of the wave vector, for which the transmission is perfect ($T=1$). On the sides of the transmission window, there are regions of vanishing transmission corresponding to the regime of the waves

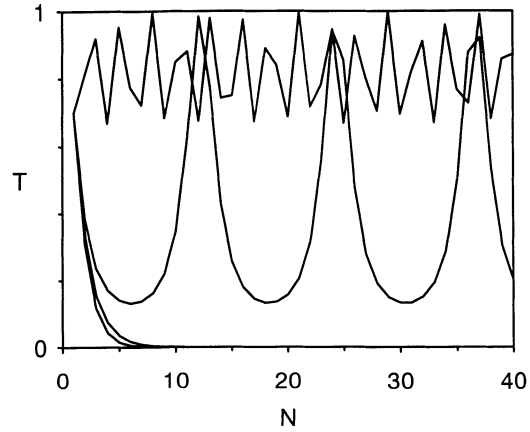

Figure 3. Transmission probability $T(0,N,0)$ through an ordered series of N -scatterers without dissipation ($\varepsilon=0$) with transmission probability $\delta=0.7$ for each scatterer. The wave vector of the incoming wave is $q=0.1$, 0.15, 0.2, and 0.4 π/a (from bottom to top).

with finite penetration depths in Fig. 3. We note this confinement cannot be interpreted as a localization effect as can be seen from an analogy with quantum mechanics: The transparent and the opaque regime correspond to bands and band gaps for electronic states in a perfect crystal structure. Accordingly, the width of the transmission window strongly depends on the scattering parameter δ as mentioned above. The width increases with increasing elastic transmission probability.

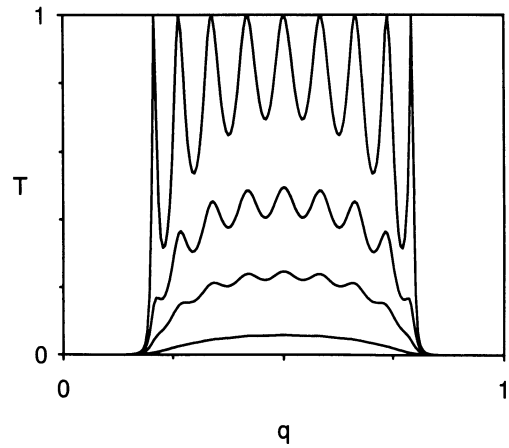

Figure 4. Transmission probability $T(\varepsilon,10,0)$ for an ordered series of 10 scatterers for dissipation parameters $\varepsilon=0$, 0.05, 0.1, and 0.2 (from top to bottom). The elastic transmission probability for each scatterer is $\delta=0.7$.

The influence of dissipation

On the other hand, the scattering strength ε does not influence the width of the transmission window. This can also be seen in Fig. 4, where the transmission probability is displayed for finite values of ε, too. Due to dissipation, the oscillations of the transmission probability are rapidly damped and the overall transmission decreases strongly. This decrease depends, of course, on the number of scatterers N and can be characterized by an exponential decay length ζ which we define by

$$T(\varepsilon,N,0) = T(0,N,0)\, e^{-N/\zeta} \quad . \tag{5}$$

On this length scale the incoming wave loses intensity due to the leakage. The convergence of the dissipation-induced decay length ζ is demonstrated in Fig. 5. In the transmission window the oscillations that were prominent in Fig. 3 are quickly damped already for weak leakage (cp. Fig. 5a). In the opaque regime, a large dissipation-induced decay length reflects a comparatively weak reduction of $T(\varepsilon,N,0)$ with respect to $T(0,N,0)$ because the latter already decays fast with the number of scatterers (cp. Fig. 5b). The dependence of the dissipation-induced decay length on the parameter ε is comprehended in Fig. 6. Here, the strongly growing influence of the leaks with increasing parameter ε is obvious: The decay length is drastically reduced in the transmission window as well as in the opaque regime.

The effect of disorder

The disorder-induced localization can be investigated in an analogous way as the influence effect of dissipation. We assume that the disorder gives rise to an exponential decay of the transmission probability, too, which is characterized by the respective decay length ξ defined by

$$T(\varepsilon,N,W) = T(\varepsilon,N,0)\ e^{-N/\xi}. \tag{6}$$

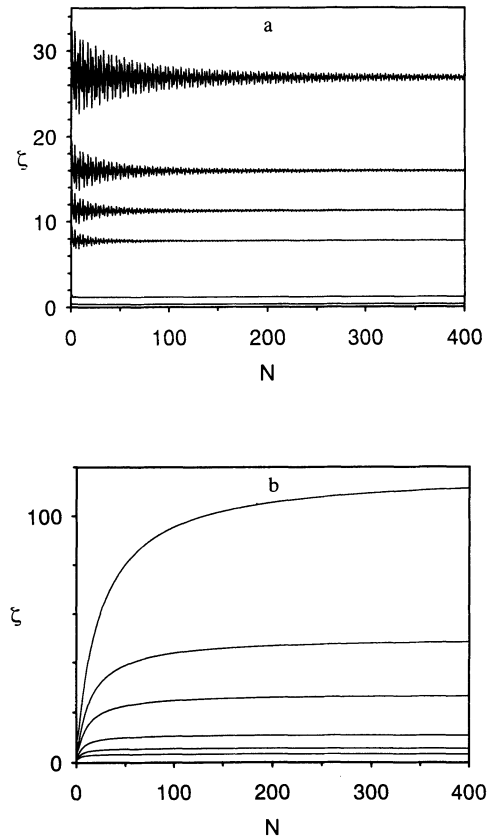

Figure 5. Dissipation-induced decay length ζ (in units of the distance a between adjacent scatterers) of the transmission probability $T(\varepsilon,N,0)$ through an ordered series of N scatterers. The elastic transmission probability for each scatterer is $\delta=0.7$, the wave vector q of the incoming wave and the dissipation parameter ε are a) $q=0.4\ \pi/a$, $\varepsilon=0.03$, 0.05, 0.07, 0.1, 0.5, and 0.9 (from top to bottom), and b) $q=0.1\ \pi/a$, $\varepsilon=0.1$, 0.15, 0.2, 0.3, 0.4, and 0.5 (from top to bottom).

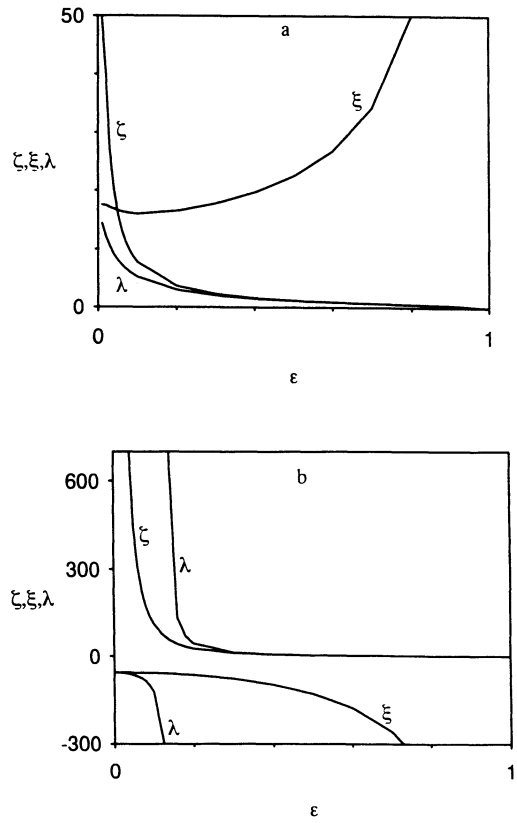

Figure 6. Asymptotic values (for $N \to \infty$) of the dissipation-induced decay length ζ, the disorder-induced decay length ξ, and the total localization length λ (in units of the average distance a between adjacent scatterers) of the transmission probability through a series of N scatterers for different values of the dissipation parameter ε. The elastic transmission probability for each scatterer is $\delta = 0.7$, the wave vector of the incoming wave is a) $q = 0.4\ \pi/a$, b) $q = 0.1\ \pi/a$.

The convergence of the defined length is displayed in Fig. 7. There are strong fluctuations due to the disorder, which decrease approximately with $\sqrt{N}$. It can be seen they are small enough for a series of several hundred scatterers so the decay length can indeed be defined in the asymptotic limit. The respective results are also compiled in Fig. 6 in dependence on the dissipation parameter ε. The small influence of the disorder for large leaks as reflected in the long decay lengths can be understood from the fact that in this regime the transmission probability is rather small already because of the leakage.

In the opaque regime, the definition (6) formally leads to negative values of the disorder-induced decay length, as displayed in Figs. 6b and 7b. This behavior

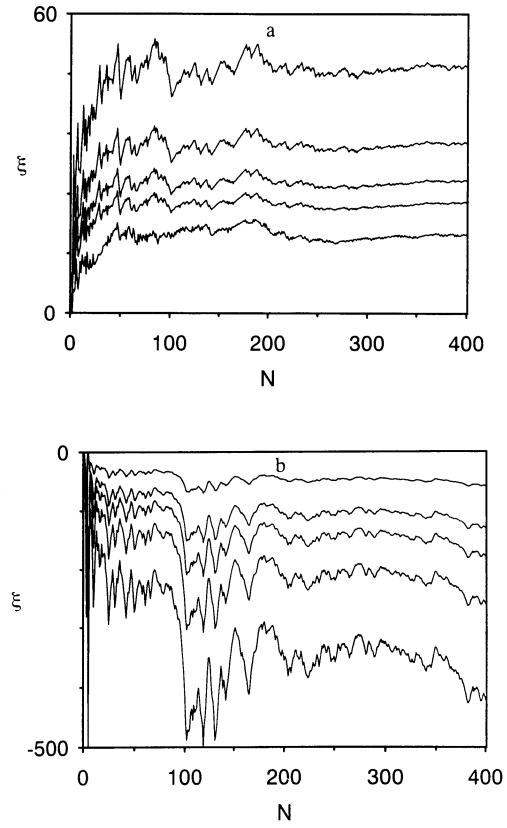

Figure 7. Disorder-induced decay length ξ (in units of the average distance a between adjacent scatteres) of the transmission probability $T(\varepsilon,N,a)$ through a series of N scatterers for different values of the dissipation parameter, $\varepsilon=0.1$, 0.5, 0.6, 0.7, and 0.8 (from bottom to top in a) and vice versa in b)). The elastic transmission probability for each scatterer is $\delta=0.7$, the wave vector of the incoming wave is a) $q=0.4\ \pi/a$, b) $q=0.1\ \pi/a$.

corresponds to an increase of the transmission probability, because the (in the opaque case destructive) coherence effects are reduced by the disorder.

For an ordered series of scatterers the behavior of the transmission probability is the same for wave vectors q and $\pi/a - q$, irrespective of the dissipation parameter. This can be seen in Fig. 4. Correspondingly, Fig. 5b (for $q = 0.1\,\pi/a$) is the same as the respective plot for the wave vector $q = 0.9\,\pi/a$. This is no longer true if disorder is introduced into the system, because the longer waves average more disorder effects than the shorter waves. Accordingly, for the wave vector $q = 0.9\,\pi/a$

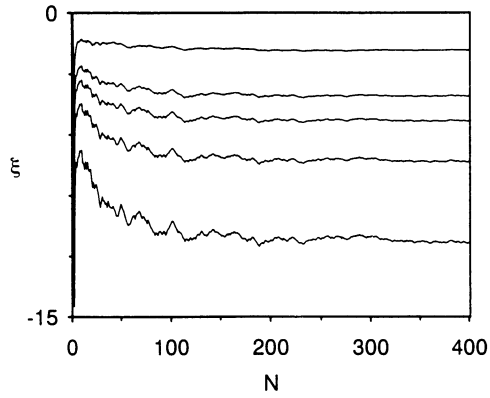

Figure 8. Disorder-induced decay length ξ as in Fig. 7b, but for q=0.9 π/a.

the influence of the disorder is stronger, as reflected in the shorter decay lengths shown in Figs. 8 and 9 in comparison with Figs. 7b and 6b, respectively.

The combined effect of disorder and dissipation is displayed in Figs. 6 and 9 where we also plot the overall localization length λ, defined by

$$T(\varepsilon,N,W) = T(0,N,0)\; e^{-N/\lambda} \tag{7}$$

which, together with Eqs. (5) and (6), yields

$$\lambda^{-1} = \zeta^{-1} + \xi^{-1}. \tag{8}$$

From Figs. 6 and 9 it becomes clear that the localization length depends on the intricate interplay between dissipation and disorder effects. In the transmission window, disorder plays an important role only for small values of the dissipation parameter ε. In the opaque regime, the influence of the disorder appears to be more prominent, in particular for the shorter waves. It must be taken into account, however, that for the considered wave vectors $q = 0.1\,\pi/a$ and $q = 0.9\,\pi/a$ the penetration depth is of the order of the distance between adjacent scatterers, as can be seen from Fig. 3. Therefore, the comparatively long decay lengths in Figs. 6b and 9 are not very significant. The situation would be different for wave vectors in the opaque regime, but close to the transmission window, e.g., $q = 0.18\,\pi/a$ or $q = 0.82\,\pi/a$. Then, however, the fluctuations due to the disorder are much stronger and, in particular, include changes between positive and negative values of the disorder-induced decay length. As a consequence, convergence is more difficult to obtain, and longer systems must be investigated. Preliminary results show that qualitatively the behavior of the asymptotic values of the decay lengths in Figs. 6 and 9 is retained. A comprehensive analysis of the localization length λ and its dependence on ε, δ, q and W will be given in a forthcoming paper.[11]

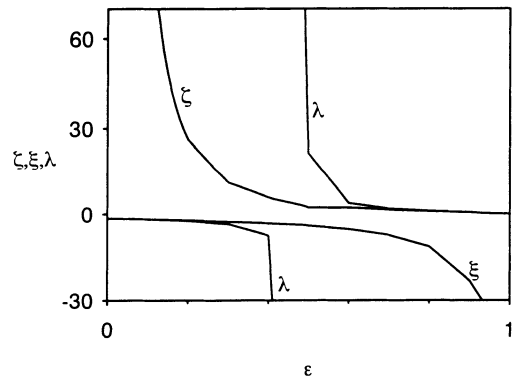

Figure 9. Decay lengths ζ, ξ, and λ as in Fig. 6, but for q=0.9 π/a.

CONCLUSIONS

We have presented an algorithm for the calculation of the transmission probability of classical waves through a series of scatterers which allow for elastic scattering as well as dissipative effects like leakage or absorption. It was shown that the transmission is impeded by three effects: For small elastic transmission probability the waves can penetrate only a small distance due to destructive interference.

Large leaks reduce the transmission quickly so that an effective localization results. Finally, disorder also leads to strong localization, because the constructive interference of multiply backscattered waves is lost. In contrast, in the opaque regime the penetration depth due to elastic scattering is enhanced, because the destructive interference by multiple backscattering is likewise decreased. As demonstrated by the behavior of the various decay lengths, we have, altogether, a rich variety of competing effects, which certainly deserve further study.

REFERENCES

1. For an overview, see E. N. Economou and C. M. Soukoulis, in: Scattering and Localization of Classical Waves in Random Media, ed. P. Sheng, World Scientific, Singapore (1989).
2. E. N. Economou, Physica A 167, 215 (1990) and references therein.
3. R. Landauer, in: Analogies in Optics and Microelectronics, eds. W. van Haeringen and D. Lenstra, Kluwer, Dordrecht (1990), p. 243.
4. W. van Haeringen and D. Lenstra (eds.), Analogies in Optics and Microelectronics, Kluwer, Dordrecht (1990).
5. R. Landauer, IBM Jl. Res. Dev. 1, 223 (1957); Phil. Mag. 21, 863 (1970); Phys. Lett. 85A, 91 (1981).
6. M. Büttiker, Phys. Rev. B 33, 3020 (1986); Phys. Rev. Lett. 57, 1761 (1986); Phys. Rev. B 40, 3409 (1989).
7. J. B. Pendry and P. D. Kirkman, J. Phys. C 17, 6711 (1984).
8. K. Maschke and M. Schreiber, Phys. Rev. B 44, 3385 (1991).
9. G. Burmeister, K. Maschke, and M. Schreiber, Phys. Rev. B, to be published.
10. M. Schreiber and K. Maschke, Phil. Mag. B 65, 639 (1992).
11. K. Maschke and M. Schreiber, to be published.
12. M. Schreiber and K. Maschke, Z. Phys. B 85, 123 (1991).

SECOND HARMONIC GENERATION IN PERIODICALLY MODULATED MEDIA

Marek Grabowski

Department of Physics
University of Colorado
Colorado Springs, CO 80933

INTRODUCTION

Many interesting phenomena associated with the propagation of electromagnetic waves in spatially periodic nonlinear media have recently been studied. Beginning with Delyon *et al.*[1], followed by Mills and Trullinger[2], as well as Grabowski and Hawrylak[3], these investigations led to fairly complete understanding of the regular (periodic), localized (solitons), and chaotic behavior of monochromatic waves in one-dimensional geometries. However, the full picture of spatio-temporal nonlinear phenomena is still missing.

As a first attempt toward understanding the propagation of pulsed classical waves, co-propagating fundamental and second harmonic fields are studied in the long wavelength limit. For inversion symmetric systems, such as optical glasses, the energy transfer between the two fields is due to third order susceptibility and must be mediated by the dc-electric field of the appropriate periodicity. This spatially periodic dc-field can be either internally self-generated, or externally imposed.

Indeed, such a self-generated periodic dc-field has been invoked as a possible explanation of a anomalous second harmonic generation observed in glass optical fibers (for a review see Chapter 10 of Agrawal[4]). Here, the dc-field is assumed to be externally imposed by periodic poling, thus allowing much more control over the resulting phenomena.

The nonlinear dynamics of the energy transfer process between the fundamental and second harmonic field in the presence of the periodic, phase matched dc-field is investigated in the context of the Hamiltonian formalism, under the Slowly Varying Envelope Approximation. In contrast to previously employed methods, the explicitly included self and cross phase modulation nonlinear terms lead to the growth of the second harmonic signal limited by the strength of the dc-field. However, for the seed second harmonic field exceeding a critical value, the up-conversion efficiency can be significantly enhanced. The new switching phenomenon is predicted in both up and down conversion

Photonic Band Gaps and Localization, Edited by
C.M. Soukoulis, Plenum Press, New York, 1993

regimes and its potential applications to the opto-electronic computing elements are suggested.

PROPAGATION EQUATIONS

The one-dimensional propagation of electromagnetic waves in an optical medium is described by the macroscopic wave equation for the electric field E, and the polarization of the medium P:

$$\left(\frac{\partial^2}{\partial z^2} - \frac{1}{c^2}\frac{\partial^2}{\partial t^2}\right)E(z,t) = \frac{4\pi}{c^2}\frac{\partial^2}{\partial t^2}P(z,t) \quad . \tag{1}$$

This field-induced polarization can be related to the electric field via the nonlinear susceptibility tensor, which in the degenerate case and for systems with inversion symmetry reduces to the first and third order terms[5] at a frequency ω:

$$P(z,\omega) = \frac{n_\omega^2 - 1}{4\pi}E(z,\omega) + \chi^{(3)}(\omega)E^3(z,\omega) \quad . \tag{2}$$

Here, the electric field is a superposition of a fundamental mode at a frequency ω, a second harmonic field at a frequency 2ω, and a static dc-field:

$$E(z,t) = E_\omega(z)e^{-i\omega t} + E_{2\omega}(z)e^{-i2\omega t} + \tfrac{1}{2}E_{dc}(z) + c.c. \tag{3}$$

Upon substitution of Eq. 3 into Eq. 2, the coupled propagation equations for fundamental and second harmonic field amplitudes follow from Eq. 1:

$$\begin{aligned}
&\partial_x^2 E_\omega + \left(n_\omega^2 + E_{dc}^2 + |E_\omega|^2 + 2|E_{2\omega}|^2\right)E_\omega + 2E_{dc}E_{2\omega}E_\omega^* = 0 \\
&\partial_x^2 E_{2\omega} + 4\left(n_{2\omega}^2 + E_{dc}^2 + |E_{2\omega}|^2 + 2|E_\omega|^2\right)E_{2\omega} + 4E_{dc}E_\omega^2 = 0 \quad ,
\end{aligned} \tag{4}$$

where $x = \omega z/c$, the factor $(12\pi\chi^{(3)})^{1/2}$ has been absorbed into the field amplitudes and the dispersion of $\chi^{(3)}$ has been ignored.

It is also convenient to consider Eq. 4 as arising from a Lagrangian for complex coupled fields with the spatial coordinate playing the role of time:

$$\begin{aligned}
L &= |\partial_x E_\omega|^2 + \tfrac{1}{4}|\partial_x E_{2\omega}|^2 - V \\
V &= \left(n_\omega^2 + E_{dc}^2\right)|E_\omega|^2 + \left(n_{2\omega}^2 + E_{dc}^2\right)|E_{2\omega}|^2 + \\
&\quad + \tfrac{1}{2}\left(|E_\omega|^4 + |E_{2\omega}|^4\right) + 2|E_\omega|^2|E_{2\omega}|^2 + E_{dc}\left(E_{2\omega}E_\omega^{*2} + E_{2\omega}^* E_\omega^2\right) \quad .
\end{aligned} \tag{5}$$

The first two terms in the effective potential V describe the linear propagation of independent fields in a medium with the dc-field modulated refractive index, the third and fourth terms are identified as the self and cross phase modulation terms, respectively, while the last term is responsible for the energy transfer between the fundamental and second harmonic fields.

Since the Lagrangian of Eq. 5 is globally gauge invariant, it is simple to identify the corresponding conserved current:

$$J = -\tfrac{i}{2}\left\{2\left(E_\omega^*\partial_x E_\omega - E_\omega\partial_x E_\omega^*\right) + \left(E_{2\omega}^*\partial_x E_{2\omega} - E_{2\omega}\partial_x E_{2\omega}^*\right)\right\} . \tag{6}$$

Clearly, $\partial_x J = 0$, reflecting the constancy of the energy flow in the direction of wave propagation. Consequently, the four degrees of freedom problem defined by Eq. 4 reduces to a three degrees of freedom Hamiltonian flow.[3] However, assuming that the spatial variation of the *dc*-field is on the scale much larger than the wavelength of the fundamental wave, one can significantly reduce the dimensionality of the propagation equations, Eq. 4. The so-called *Slowly Varying Envelope Approximation* (SVE) is described in the next section.

THE SVE APPROXIMATION

The fields are assumed to be of the form:

$$E_\omega(x) = E_1(x)e^{in_1 x}; \quad E_{2\omega}(x) = E_2(x)e^{i2n_2 x}; \quad E_{dc}(x) = E\cos 2nx; \tag{7}$$

with $n_2 > n_1 >> n$, and slowly varying amplitudes E_1, E_2, $E = const$ in the following sense:

$$\left|\partial_x E_1\right|^2 << n_1^2\left|E_1\right|^2; \quad \left|\partial_x E_2\right|^2 << n_2^2\left|E_2\right|^2; \tag{8}$$

Hence, under the SVE approximation, the Lagrangian of Eq. 5 takes the form:

$$\begin{aligned} L_{SVE} &= \mathrm{Im}\left(2n_1 E_1^*\partial_x E_1 + n_2 E_2^*\partial_x E_2\right) - V_{SVE} \\ V_{SVE} &= \left(\left|E_1\right|^2 + \left|E_2\right|^2\right)E^2 + \tfrac{1}{2}\left(\left|E_1\right|^4 + \left|E_2\right|^4\right) + 2\left|E_1\right|^2\left|E_2\right|^2 + \mathrm{Re}\left(E_2 E_1^{*2} e^{i2\Delta nx}\right)E \end{aligned} , \tag{9}$$

where $\Delta n = n_2 - n_1 - n$ and all variations faster than this scale have been neglected.

Further simplification of the Lagrangian of Eq. 9 can be accomplished by writing the complex fields in polar representation as,

$$E_j(x) = A_j(x)e^{ij\phi_j(x)} \qquad j = 1,2 \tag{10}$$

and observing that the conserved current of Eq. 6 becomes (under the SVE approximation) the total intensity of co-propagating fields:

$$W = n_1\left|E_1\right|^2 + n_2\left|E_2\right|^2 . \tag{11}$$

The above current conservation reduces the problem to just one degree of freedom. Indeed, for the variables rescaled as,

$$P = n_2\frac{A_2^2}{W}; \quad \psi = 2\left(\phi_2 - \phi_1\right); \quad \varepsilon = n_2\frac{E^2}{W}; \quad y = \frac{W}{n_1 n_2}x , \tag{12}$$

the Lagrangian, Eq. 9, takes the form:

$$L(P,\psi) = P\partial_y\psi - V(P,\psi)$$

$$V(P,\psi) = (1-P)\left[P + (\varepsilon P)^{1/2}\cos(\psi + 2\Delta n x)\right] - \left(\frac{n_2 - n_1}{n_1 n_2}\right)\left[n_1\varepsilon + n_2 - \tfrac{1}{2}(n_2 - n_1)P\right]P \,. \tag{13}$$

Furthermore, regarding the intensity of the second harmonic field, P, as the canonical "momentum" and the relative phase, ψ, as the conjugated "coordinate" one can treat the system described by Eq. 13 as Hamiltonian, with the "energy" function given by $V(P, \psi)$. This approach is particularly convenient when the next simplification is introduced.

To emphasize the major effects caused by the self and cross phase modulation terms, perfect phase matching (Δn =0) is assumed and terms proportional to $(n_2 - n_1)<<1$ are neglected. The resulting effective Hamiltonian,

$$h(P,\psi) = (1-P)\left[P + (\varepsilon P)^{1/2}\cos\psi\right] \tag{14}$$

represents the conserved "energy" of this reduced system. Consequently, for initial conditions given as $P(0) = p_0 < 1$, $\psi(0) = \psi_0 < \pi/2$, the dynamic of the system is restricted to the $h > 0$ manifold and the corresponding equations of motion are:

$$\partial_y P = (\varepsilon P)^{1/2}(1-P)\sin\psi$$

$$\partial_y\psi = \tfrac{1}{2}\left(\frac{\varepsilon}{P}\right)^{1/2}(1-3P)\cos\psi + (1-2P) \quad . \tag{15}$$

These equations can be decoupled using constancy of h, Eq. 14, and subsequently integrated in terms of elliptic functions. However, these explicit formulas are not particularly illuminating and shall not be presented here. Instead, graphical discussion of the results is given in the next section.

DISCUSSION OF SOLUTIONS

The phase space representation of the solutions to the equations of motion, Fig. 1, allows them to be classified into two categories. For the initial (seed) intensity of the second harmonic field below the critical intensity (curves outside the separatrix of Fig. 1), the solutions are periodic with $P(y)$ oscillating between P_0 and P_{max}, with maximum reached for the phase difference of π, and $\psi(y)$ increasing monotonically (rotation-like solutions). For P_0 approaching P_c the period of spatial oscillations tends to infinity (soliton-like kink solutions represented by the separatrix in Fig. 1). Finally, for $P_0 > P_c$, the solutions are again periodic, but libration-like with the phase difference $\psi(y)$ oscillating between zero and a maximum value less than π. These two types of the solutions are compared in Fig. 2.

The two solutions shown in Fig. 2 are chosen to illustrate the dramatic increase in the up conversion efficiency upon crossing of the critical seed intensity. For the fixed strength of the external electric field, $\varepsilon = 0.08$, the curves represent the intensity of the generated second harmonic intensity as a function of the propagation length. The lower curve is for $P_0 = 0.073$, while the upper one is for $P_0 = 0.098$ ($P_c = 0.085$). Thus, increasing the initial second harmonic intensity by just 2.5% of the fundamental mode leads to a jump in the gain in up conversion efficiency from zero to 85% (when measured at $y = 4\pi$). This behavior will be referred to as *switching*.

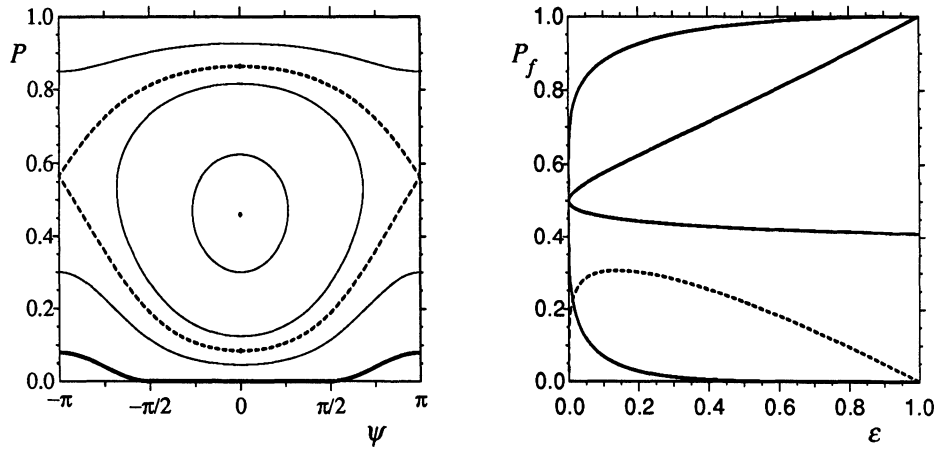

Figure 1. Phase space of the solution to the equations of motion for $\varepsilon = 0.08$ (left panel), with zero energy solutions (thick lines) and sample solutions inside and outside the separatrix (broken line). The variation of the special points with ε in the right panel, where the solid lines (from bottom to top) stand for the critical intensity, the elliptic and hyperbolic fixed points, and the maximum intensity. The broken line indicates the maximum switching gain.

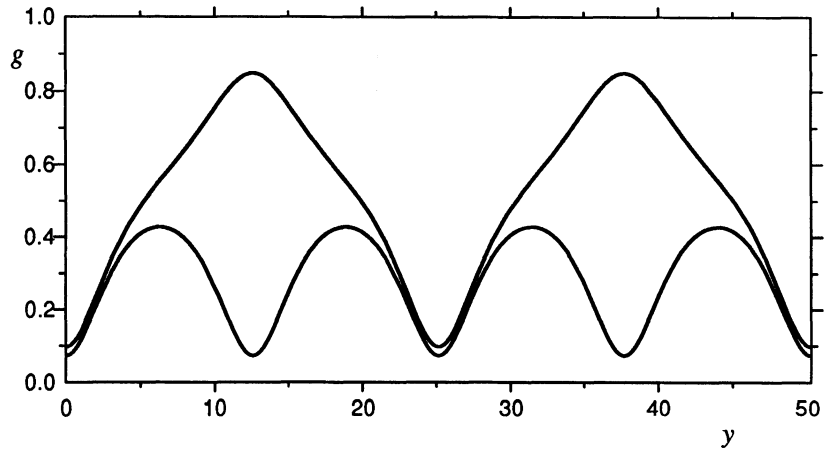

Figure 2. The intensity of the second harmonic signal as a function of the propagation length for two initial intensities straddling the critical seed intensity: $P_0 > P_c$ for the top curve, and $P_0 < P_c$ for the bottom one. The external electric field strength is again $\varepsilon = 0.08$.

The initial conditions for the solutions illustrated in Fig. 2 where chosen to enhance the switching effect -- the period of the libration-like solution is double of that for rotation-like solution. In practice, one would observe the generated second harmonic intensity at a fixed propagation length $y = L$ (at finite length of the fiber or waveguide). For a fixed external electric field strength ε, the measured output intensity would depend only on the input seed intensity P_0 in the oscillatory fashion (see Fig. 3). As P_0 increases from zero, the gain in up conversion, $g = P(L) - P_0$, varies between zero and the maximum gain (dashed line in Fig. 3) until P_0 reaches the critical value P_c where the switching effect takes place. For $P_0 > P_c$, the gain g decreases to zero, and changes sign (down conversion) only after a wide plateau. The down conversion gain exhibits switching when P_0 crosses the upper branch of the separatrix in Fig. 1 and it is again followed by oscillations. Similar behavior of the gain in up conversion efficiency is predicted[6] for fixed P_0 and varying ε.

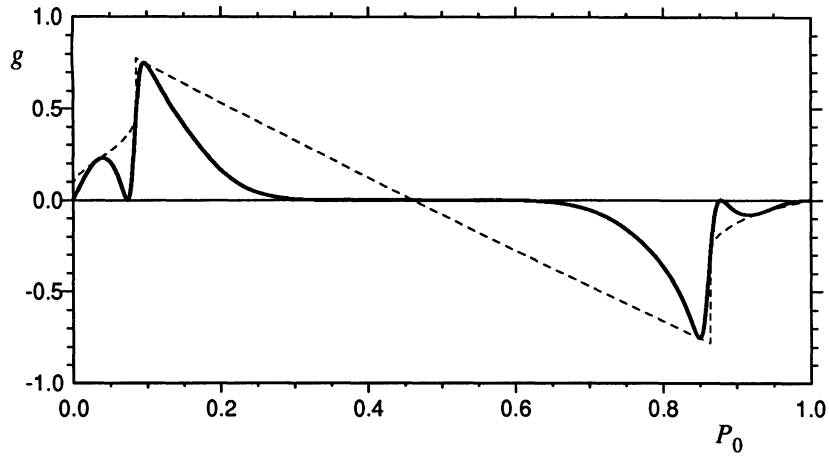

Figure 3. The fundamental to second harmonic conversion gain $g = P(4\pi) - P_0$ as a function of the seed intensity (solid line). The dashed curve indicates the maximum gain for a given input. Note both up and down conversion regimes and an intervening plateau ($\varepsilon = 0.08$).

In conclusion, several novel phenomena are predicted when two co-propagating electromagnetic waves interact and exchange energy via nonlinear cross and self phase modulation mediated by externally imposed, periodic electric field. Perhaps the most striking is the above discussed switching phenomenon with its wide ranging applications to integrated opto-electronic switching devices. Further studies of related phenomena of regular and chaotic multifrequency waves propagation are currently under way.

ACKNOWLEDGMENT

This work was performed while the author participated in the AFOSR Summer Research Program at the F.J. Seiler Research Laboratory and continued under the AFOSR Research Initiation grant.

REFERENCES

1. François Delyon, Yves-Emmanuel Lévy, and Bernard Souillard, *Phys. Rev. Lett.* **57**, 2010 (1986).
2. D.L. Mills and S.E. Trullinger, *Phys. Rev. B* **36**, 947 (1987).
3. Marek Grabowski and Pawel Hawrylak, *Phys. Rev. B* **41**, 5783 (1990).
4. Govind P. Agrawal, *"Nonlinear Fiber Optics"*, Academic Press (1989).
5. Y.R. Shen. *"Principles of Nonlinear Optics"*, Wiley, New York (1984).
6. Marek Grabowski, *Bichromatic wave propagation in periodically poled optical media*, submitted for publication.

A TRANSPORT EQUATION FOR RANDOM ELECTROMAGNETIC WAVE PROPAGATION

A. Tip

FOM Instituut voor Atoom- en Molecuulfysica
Kruislaan 407, 1098 SJ Amsterdam, the Netherlands

I. INTRODUCTION

An important question in the study of random wave propagation is the possible occurrence of (Anderson) localisation which leads to a vanishing diffusion coefficient. A complication occuring in random electron scattering is due to the Coulomb repulsion between the electrons, giving rise to difficulties in the interpretation of the results of actual measurements. The situation is more favourable with random light scattering (as long as Maxwell's equations are applicable) and indeed much research is taking place in this field, both theoretical and experimental[1,2,3]. The study of diffusion is an important tool to learn more about localisation and it is common practice in theoretical work to try to evaluate an adopted expression for the diffusion coefficient D. Ordinary linear response theory is not applicable in the present situation (there is no thermodynamical equilibrium state, containing an external driving force **F** in which we can linearise) but instead we can start from one of the oldest notions of diffusion, where we consider the mean square displacement $\langle\overline{\mathbf{x}^2(t)}\rangle$. If the latter grows linearly with t for large times, then, apart from a numerical factor, the proportionality constant is identified as the diffusion coefficient D. Another way of describing diffusion phenomena in a random medium is by means of a transport equation. Although not unrelated to the above approach it has somewhat more flexibility. Such an equation is readily derived for the Schrödinger case but seems not to have been developed for the electromagnetic situation. The subject of the present work is to fill this lacuna. A notable exception, however, is the wellknown paper by Watson[4]. His method and aims, however, are quite different from ours. There are a number of reasons why the formulation of a transport equation for the Maxwell case is more complicated . One is that the Maxwell equations, being a set of coupled equations for two three-dimensional vector-fields, give rise to a more

Photonic Band Gaps and Localization, Edited by
C.M. Soukoulis, Plenum Press, New York, 1993

complicated bookkeeping. What in fact happens are two things. The first is the continuous interchange of energy between the electric and magnetic field modes already present for free fields (even in the propagation of scalar waves in one dimension, described as a set of coupled first order equations in the time variable, this phenomenon occurs, leading to a two component state). Secondly the vector nature of the electromagnetic field, i.e. its spin, increases the bookkeeping further. Another snag, of a more troublesome nature, is the presence of longitudinal field modes which do not propagate and should be decoupled from the propagating transverse modes. A final point that needs attention is the nature of the initial state. In the Schrödinger case the former is usually taken to be deterministic but here we have to be more careful since the permeabilities relating the various fields are precisely the random quantities of the model. Thus a deterministic **D**-field at the initial time gives rise to an initial random **E**-field etc.

The model we consider consists of Maxwell's equations

$$\partial_t \mathbf{D} = \partial_x \times \mathbf{H}, \quad \partial_x \cdot \mathbf{D} = 0, \quad \partial_t \mathbf{B} = -\partial_x \times \mathbf{E}, \quad \partial_x \cdot \mathbf{B} = 0, \quad \mathbf{D} = \varepsilon \mathbf{E}, \quad \mathbf{H} = \mu^{-1} \mathbf{B}, \tag{1-1}$$

for a non-conducting medium with random electric and magnetic permeabilities $\varepsilon_\omega(\mathbf{x})$ and $\mu_\omega(\mathbf{x})$. Here is ω an element of an underlying probability measure space $(\Omega, \mathfrak{F}, P(d\omega))$ and we assume $\varepsilon_\omega(\mathbf{x})$ and $\mu_\omega(\mathbf{x})$ to be stationary under translations and rotations. Indicating averages (integrals over $P(d\omega)$) by a bar, we thus have $\varepsilon = \overline{\varepsilon_\omega(\mathbf{x})}$ and $\mu = \overline{\mu_\omega(\mathbf{x})}$ $\mathbf{x}$-independent and $\overline{\varepsilon_\omega(\mathbf{x})\mu_\omega(\mathbf{y})}$ only depending on $|\mathbf{x}-\mathbf{y}|$ etc.

A situation often encountered in experimental set-ups is the one where light propagates through a uniform background medium (for which we normalize $\varepsilon = \mu = 1$) containing immersed particles, usually assumed to be identical and stationary in the medium and with ε and μ deviating from unity. Statistics enters the formalism through the distribution law for the positions of the particles. Explicitly we now deal with the situation where

$$\begin{aligned} \varepsilon_\omega(\mathbf{x}) &= 1 + \Phi_\omega(\mathbf{x}) = 1 + \sum_j \phi(\mathbf{x}-\mathbf{x}_j) = 1 + \int \nu_\omega(d\mathbf{v})\phi(\mathbf{x}-\mathbf{v}) \\ \mu_\omega(\mathbf{x}) &= 1 + \Psi_\omega(\mathbf{x}) = 1 + \sum_j \psi(\mathbf{x}-\mathbf{x}_j) = 1 + \int \nu_\omega(d\mathbf{v})\psi(\mathbf{x}-\mathbf{v}). \end{aligned} \tag{1-2}$$

ϕ and ψ (which have the spatial extend of a particle as their support) measure the deviation from unity of ε and μ of an individual particle and the $\mathbf{x}_j$'s are their positions distributed according to a given probability law, i.e. each $\omega \in \Omega$ corresponds with $\mathbf{X} = (\mathbf{x}_1, \mathbf{x}_2, \mathbf{x}_3, \ldots)$. On the right hand sides we have written the sums in terms of the random point measure $\nu_\omega(d\mathbf{v})$. In fact the underlying statistics can conveniently be given in terms of such a random measure[5,6]. In particular no intermediate step involving a thermodynamic limit is needed. Among the various possibilities for the probability law the Poisson process has the advantage that explicit expressions for certain averages can be obtained, in particular asymptotically for low particle densities. On the other hand the Poisson model has the disadvantage that it does not describe correctly the high density case since it allows different particles to occupy overlapping volumes in space. In fact a nice alternative would be to use the probability law associated with the coordinate distribution for a hard sphere gas in thermodynamic equilibrium. The electromagnetic energy density

$$e_\omega(\mathbf{x},t) = 1/2\{\, \mathbf{E}_\omega(\mathbf{x},t)\cdot\mathbf{D}_\omega(\mathbf{x},t) + \mathbf{B}_\omega(\mathbf{x},t)\cdot\mathbf{H}_\omega(\mathbf{x},t)\} \tag{1-3}$$

satisfies the continuity equation $\partial_t e_\omega + \partial_x \cdot \mathbf{S}_\omega = 0$, where $\mathbf{S}_\omega = \mathbf{E}_\omega \times \mathbf{H}_\omega$ is the Poynting vector. Denoting $e = \overline{e_\omega}$ and $\mathbf{S} = \overline{\mathbf{S}_\omega}$ we then have $\partial_t e + \partial_x \cdot \mathbf{S} = 0$ and diffusive behaviour refers to the situation where, as $t \to \infty$, $\mathbf{S}(\mathbf{x},t) \sim D\, \partial_x e(\mathbf{x},t)$, D being the diffusion coefficient. A transport equation is then needed to actually calculate D for a given initial situation. Alternatively, the diffusion coefficient can be defined in terms of the long time behaviour of $\langle \mathbf{x}^2(t) \rangle$, the average of $\mathbf{x}^2$ over $e(\mathbf{x},t)$.

II. DETERMINISTIC TIME EVOLUTION

The time evolution problem (1-1) for the deterministic case has recently been discussed by Dorren and the author[7] in terms of a Hilbert space setting, based on energy conservation, for a large class of permeabilities $\varepsilon(\mathbf{x})$ and $\mu(\mathbf{x})$ (we refer to this reference for details concerning the remarks that follow). There a unitary time evolution (ε is the Levi-Civita tensor density, $\varepsilon_{123}=1$ and ε is antisymmetric in all indices, $\mathbf{p}=-i\partial_x$)

$$\mathbf{F}(t)=\exp[-i\mathbf{K}t]\cdot\mathbf{F}(0),\quad \mathbf{K}=\mathbf{A}\,\mathbf{K}_0\,\mathbf{A},\quad \mathbf{A}=\begin{pmatrix}\varepsilon^{-1/2} & 0\\ 0 & \mu^{-1/2}\end{pmatrix},\quad \mathbf{K}_0=\begin{pmatrix}0 & \varepsilon\cdot\mathbf{p}\\ -\varepsilon\cdot\mathbf{p} & 0\end{pmatrix}, \tag{2-1}$$

on the Hilbert space $\mathcal{H}=L^2(\mathbb{R}^3, d\mathbf{x}, \mathbb{C}^6)$ was found for

$$\mathbf{F}=\mathbf{A}\begin{pmatrix}\mathbf{D}\\ \mathbf{B}\end{pmatrix}=\mathbf{A}^{-1}\begin{pmatrix}\mathbf{E}\\ \mathbf{H}\end{pmatrix}. \tag{2-2}$$

We note that $\mathbf{K}$ possesses the eigenvalue zero. The associated eigenspace is the subspace of longitudinal fields that do not propagate in time. The complementary subspace is spanned by the transverse fields which *do* propagate in time. They are characterized by the conditions $\partial_x \cdot \mathbf{D}=0$, $\partial_x \cdot \mathbf{B}=0$. Refering back to eq.(1-3) we see that $e(\mathbf{x}, t)$ can be expressed in terms of the density operator (in quantum mechanics its trace is the total probability and hence equals one whereas here it is the total energy which is conserved but can have any nonnegative value)

$$\rho = \mathbf{F}\mathbf{x}\mathbf{F} \leftrightarrow \rho(\mathbf{x},\mathbf{y})=\begin{pmatrix}\mathbf{E}(\mathbf{x})\mathbf{D}(\mathbf{y}) & \mathbf{E}(\mathbf{x})\mathbf{B}(\mathbf{y})\\ \mathbf{H}(\mathbf{x})\mathbf{D}(\mathbf{y}) & \mathbf{H}(\mathbf{x})\mathbf{B}(\mathbf{y})\end{pmatrix}, \tag{2-3}$$

associated with $\mathbf{F}$, through $e(\mathbf{x})=1/2\ \mathrm{tr}^{(6x6)}\langle \mathbf{x}|\,\rho\,|\mathbf{x}\rangle$, where the trace is over the 6x6 matrix in (2-3). It is important to realize that only the diagonal terms in (2-3) enter into $e(\mathbf{x})$. Thus we can change the definition of ρ as long as the proper diagonal terms are retained. The price to be paid is that ρ is no longer a density operator in general. In the sequel it will turn out that such a change will be necessary in order to arrive at a useful transport equation.

III. RANDOM TIME EVOLUTION

We now turn to the random case. It is convenient to work in the space $\mathcal{K}=L^2(\Omega,P(d\omega),\mathcal{H})$, the Hilbert space of square integrable functions over $P(d\omega)$ which take their values in $\mathcal{H}$. Explicitly, for $\mathbf{f},\mathbf{g}\in\mathcal{K}$,

$$(\mathbf{f},\mathbf{g})_{\mathcal{K}}=\int_\Omega P(d\omega)\mathbf{f}_\omega(\mathbf{x})\cdot\overline{\mathbf{g}_\omega(\mathbf{x})}=\int_\Omega P(d\omega)(\mathbf{f}_\omega,\mathbf{g}_\omega)_{\mathcal{H}}. \tag{3-1}$$

Actually $\mathcal{H}$ is a subspace of $\mathcal{K}$, the associated projector $\mathbb{E}$ being integration over $P(d\omega)$; $\mathbb{E}\mathbf{f}:=\int_\Omega P(d\omega)\mathbf{f}_\omega$. For the time evolution we now have

$$\mathbf{F}_\omega(t)=\exp[-i\mathbf{K}_\omega t]\cdot\mathbf{F}_\omega(0),\quad \mathbf{K}_\omega=\mathbf{A}_\omega\,\mathbf{K}_0\,\mathbf{A}_\omega,\quad \mathbf{A}_\omega=\begin{pmatrix}(\varepsilon_\omega)^{-1/2} & 0\\ 0 & (\mu_\omega)^{-1/2}\end{pmatrix}, \tag{3-2}$$

or, now using the symbol $\mathbf{K}$ for the operator defined in $\mathfrak{K}$ by this expression, etc.

$$\mathbf{F}(t)=\exp[-i\mathbf{K}t]\cdot\mathbf{F}(0),\qquad \mathbf{F}(t)_\omega=\exp[-i\mathbf{K}_\omega t]\cdot\mathbf{F}_\omega(0). \tag{3-3}$$

Note that we leave the possibility open that $\mathbf{F}(0)$ is random.

We shall derive a transport equation by means of the projection operator method. Thus let ρ be a density operator or, more general, an element of the traceclass $\mathfrak{B}_1(\mathfrak{K})$ over $\mathfrak{K}$ and suppose that $\mathbf{L}$ generates a time evolution on $\mathfrak{B}_1(\mathfrak{K})$; $\rho(t)=$ $\exp[-i\mathbf{L}t]\rho$. Then, if $\mathbf{P}$ is a projector on $\mathfrak{B}_1(\mathfrak{K})$, $\mathbf{Q}=1-\mathbf{P}$,

$$\partial_t\mathbf{P}\rho(t)=-i\mathbf{P}\mathbf{L}\mathbf{P}\rho(t)-\int_0^t\mathbf{P}\mathbf{L}\mathbf{Q}\exp[-i\mathbf{Q}\mathbf{L}\mathbf{Q}s]\mathbf{Q}\mathbf{L}\mathbf{P}\rho(t-s)\,-i\mathbf{P}\mathbf{L}\mathbf{Q}\exp[-i\mathbf{Q}\mathbf{L}\mathbf{Q}t]\,\mathbf{Q}\rho. \tag{3-4}$$

The usual strategy is now to find a projector such that the last term on the right is a rapidly decaying function of time or actually vanishing. Then, at least asymptotically for large t, a closed equation for $\mathbf{P}\rho(t)$ is obtained. In addition, although not strictly necessary, the kernel $\exp[-i\mathbf{Q}\mathbf{L}\mathbf{Q}s]$ in the second term should preferably also decay rapidly. Finally, for (3-4) to be useful, $\mathbf{P}$ must be such that the quantities we are interested in can be expressed in terms of $\mathbf{P}\rho(t)$. In our case the latter are $\mathbf{e}(t)$ and $\mathbf{S}(t)$, introduced in section 1. An obvious choice would be to take the random version of (2-3) for ρ_ω and define $\mathbf{L}$ by $\exp[-i\mathbf{L}t]\rho)_\omega=\exp[-i\mathbf{K}_\omega t]\,\rho_\omega\exp[+i\mathbf{K}_\omega t]$. $\mathbf{P}$ could then be defined as averaging over ω. This, however, does not work. Even if we could take ρ to be deterministic, so that $\mathbf{Q}\rho$ vanishes, we run into the problem that $\mathbf{P}$ and the projector upon the transverse subspace of $\mathfrak{K}$ do not commute (the latter contains $\mathbf{A}_\omega$), leading to nondecaying contributions in $\exp[-i\mathbf{Q}\mathbf{L}\mathbf{Q}s]$. Fortunately there is a way out of this problem since a little consideration shows that deterministic initial $\mathbf{D}$ and $\mathbf{B}$-fields can be produced experimentally. Secondly the projector $\mathbf{P}_0^{tr}$ upon the transverse component of $\mathbf{I}=\binom{\mathbf{D}}{\mathbf{B}}=\mathbf{A}^{-1}\cdot\mathbf{F}$ does not depend on ω. Thus we may hope to be able to define a projector that suits our needs. We start with

$$\rho_\omega(t):=\mathbf{V}\mathbf{I}_\omega(t)\mathrm{x}\mathbf{I}_\omega(t)\mathbf{V}=\exp[-i\mathbf{V}\mathbf{K}_0\,\mathbf{A}_\omega^2\mathbf{V}^{-1}t]\rho_\omega(0)\exp[-i\mathbf{V}^{-1}\mathbf{A}_\omega^2\mathbf{K}_0\mathbf{V}t], \tag{3-5}$$

where $\mathbf{V}$ is a constant, invertible, diagonal 6x6-matrix. We observe that if $\rho_\omega(0)$ is a self-adjoint traceclass operator then so is $\rho_\omega(t)$ and if $\rho_\omega(0)\in\mathfrak{K}_0^{tr}=\mathbf{P}_0^{tr}\mathfrak{K}$, then so is $\rho_\omega(t)$, i.e. transversality is conserved. Next let $\{\mathbf{M}_\omega|\omega\in\Omega\}$ be a family of operators with invertible average and define $\mathbf{P}$ by (the symmetrisation is not strictly needed but has the advantage of preserving selfadjointness)

$$\mathbf{P}(\mathbf{T}_\omega):=\int_\Omega P(d\omega)1/2\{\bar{\mathbf{M}}^{-1}\mathbf{M}_\omega\mathbf{T}_\omega+\mathbf{T}_\omega\mathbf{M}_\omega\bar{\mathbf{M}}^{-1}\}. \tag{3-6}$$

Now $\mathbf{P}^2=\mathbf{P}$ and $\mathbf{P}\mathbf{T}=\mathbf{T}$ for deterministic $\mathbf{T}$. Taking $\mathbf{V}$ and $\mathbf{M}_\omega$ diagonal of the type (the nonzero entries are scalars times 3x3 unit matrices)

$$\mathbf{V}=\begin{pmatrix}v^{(1)} & 0\\ 0 & v^{(2)}\end{pmatrix}\qquad \mathbf{M}_\omega=\begin{pmatrix}m_\omega^{(1)} & 0\\ 0 & m_\omega^{(2)}\end{pmatrix} \tag{3-7}$$

and requiring $\mathbf{e}(\mathbf{x})=1/2\ \mathrm{tr}^{(6x6)}\langle\mathbf{x}|\,\mathbf{P}\rho\,|\mathbf{x}\rangle$ we find

$$\mathbf{M}_\omega = \mathbf{A}_\omega^2, \qquad \mathbf{V}=(\bar{\mathbf{A}}^2/2)^{1/2} \ . \tag{3-8}$$

We now have achieved our goal; the last term in (3-4) vanishes and transversality is conserved. In the general case PLP has a complicated structure. It simplifies considerably, however, if mw(x)∫1. Then, with c = (ew(x)-1)-1/2 being the average velocity of light,

$$\mathbf{PLPT} = (c/2)[\mathbf{K}_0, \mathbf{PT}]_- + (2c)^{-1}\{ \mathbf{A}^2 \mathbf{K}_0 \overline{\mathbf{A}_\omega^2(\mathbf{PT})\, \mathbf{A}_\omega^2}(\mathbf{A}^2)^{-1} - (\mathbf{A}^2)^{-1} \overline{\mathbf{A}_\omega^2(\mathbf{PT})\, \mathbf{A}_\omega^2}\ \mathbf{K}_0 \mathbf{A}^2 \}, \tag{3-9}$$

where $\mathbf{A}^2 = \begin{pmatrix} c^2 & 0 \\ 0 & 1 \end{pmatrix}$. With ρ instead of Pρ, the averaging being understood, and denoting $\mathbf{PLP}\rho = \hat{\mathbf{L}}\rho$ we have (the last term on the right denotes the middle one on the right in (3-4)).

$$\partial_t \rho(t) = -i\hat{\mathbf{L}}\rho(t) - \int_0^t ds \mathbf{J}(s)\rho(t-s) \ , \tag{3-10}$$

IV. POISSON STATISTICS

We now specialise to Poisson statistics, in which case the random measure $\nu_\omega(d\mathbf{v})$ is defined by the requirements[5] that $\nu_\omega(B_1)$, $\nu_\omega(B_2)$, $\nu_\omega(B_3)$,... are independent random variables for mutually disjoint Borel sets B_1, B_2, B_3,... in $\mathbb{R}^3$ and

$$\mathbb{E}\ \exp[-\langle f, \nu_\omega\rangle] = \exp[-n\int d\mathbf{v}\ \{1- \exp[-f(\mathbf{v})]\}], \qquad \langle f, \nu_\omega\rangle = \int \nu_\omega(d\mathbf{v}) f(\mathbf{v}). \tag{4-1}$$

Thus, using $[1+a]^{-1} = \int_0^\infty dt\ \exp[-t(1+a)]$ we obtain for instance

$$\mathbb{E}\ \varepsilon_\omega(\mathbf{x})^{-1} = \int_0^\infty dt\ \exp[-n\int d\mathbf{v}\ \{1- \exp[-t\phi(\mathbf{v})]\}] = 1 - n\int d\mathbf{v}\ \phi(\mathbf{v})/(1+\phi(\mathbf{v})) + \mathcal{O}(n^2), \tag{4-2}$$

$$\mathbb{E}\ \varepsilon_\omega(\mathbf{x})^{-1}\mu_\omega(\mathbf{y})^{-1} = 1 - n\int d\mathbf{v}\ \{1-[1+\phi(\mathbf{v}-\mathbf{x}+\mathbf{y})]^{-1}[1+\psi(\mathbf{v})]^{-1}\} + \mathcal{O}(n^2). \tag{4-3}$$

In general, if $F(\mathbf{p}, \mathbf{x}, \varepsilon_\omega(\mathbf{x}), \mu_\omega(\mathbf{x}))$ is a function of the operators **p** and **x** directly as well as a function of the operator **x** through the permeabilities, we have, recalling that $\phi(\mathbf{x}-\mathbf{v}) = \exp[-i\mathbf{v}\cdot\mathbf{p}]\phi(\mathbf{x})\exp[+i\mathbf{v}\cdot\mathbf{p}]$,

$$\mathbb{E}\ F(\mathbf{p}, \mathbf{x}, \varepsilon_\omega(\mathbf{x}), \mu_\omega(\mathbf{x})) = F(\mathbf{p}, \mathbf{x}, 1, 1) - n\int d\mathbf{v}\ \{F(\mathbf{p}, \mathbf{x}, 1, 1) - F(\mathbf{p}, \mathbf{x}, [1+\phi(\mathbf{x}-\mathbf{v})]^{-1}, [1+\psi(\mathbf{x}-\mathbf{v}))]^{-1}\} + \mathcal{O}(n^2). \tag{4-4}$$

Higher powers in n can be calculated in the same fashion but become quite cumbersome.

V. DISCUSSION AND OUTLOOK

In the previous sections an essentially rigorous transport equation has been obtained for random electromagnetic wave propagation. In contrast to the wave equation approach, usually adopted, polarisation effects are included. Secondly, systems containing an infinite number of scatterers are treated directly, no thermodynamic limit has to be taken. It allows calculations pertaining to random electromagnetic systems in full generality. In particular it can be used to study the effects of polarisation on the recently found slowing down of the speed of light in random systems[2]. In this instance it is sufficient to work to first order in the density, where the asymptotic expressions of section IV apply. This leads to the usual single

scatterer T-matrix in the collision operator, except that now it is a 6x6 array of operators. The latter can be simplified, however, and contact can be made with the corresponding transition operators on the wave equation level. At this stage the collision operator still features a time delay (the integral over ds in 3-10) and retention of the latter to first order beyond the Boltzmann (on shell T-matrix) contribution is essential to produce the decrease of the speed of light reported in ref. 2. In the analogous Schrödinger case such an effect does not occur unless the scatterers have internal degrees of freedom. It will be clear from section 4 that things become quite complicated in the next order in the density and beyond (as in other cases logarithmic density dependence shows up) and different approximation schemes have to be applied (summation of "most crossed" diagrams etc.).

ACKNOWLEDGEMENTS

This work is part of the research programme of the Stichting voor Fundamenteel Onderzoek der Materie (Foundation for Fundamental Research on Matter) and was made possible by financial support from the Nederlandse Organisatie voor Wetenschappelijk Onderzoek (Netherlands Organisation for Scientific Research).

REFERENCES

1. Scattering and Localization of Waves in Random Media, Ping Sheng ed. (World Scientific, Singapore, 1990).
2. M. P. van Albada, B. A. van Tiggelen, A. Lagendijk and A. Tip, Speed of Propagation of Classical Waves in Strongly Scattering Media. Phys. Rev. Lett. **66**, 3132 (1991).
3. Analogies in Optics and Micro Electronics, W. van Haeringen and D. Lenstra eds. (Kluwer, Dordrecht, 1990).
4. K. M. Watson, Multiple Scattering of Electromagnetic Waves in an Underdense Plasma. J. Math. Phys. **10**, 688 (1969).
5. W. Kirsch, Random Schrödinger operators, a Course, in "Schrödinger operators", H. Holden, A. Jensen eds., Springer Lecture Notes in Physics **345** (1989).
6. R. Carmona and J. Lacroix, Spectral Theory of Random Schrödinger Operators (Birkhäuser, Boston,1990).
7. H. J. S. Dorren and A. Tip, Maxwell's Equations for Nonsmooth Media; Fractal-shaped and Pointlike Objects. J. Math. Phys. **32**, 3060 (1991).

SYMMETRIZED TRANSVERSE VECTOR FIELDS

Revik Allakhverdyan

P. N. Lebedev Physical Institute
Russian Academy of Sciences
Leninsky prosp. 53, Moscow 117924 Russia

Periodic structures in two and three dimensions, such as perfect single crystals, superlattices, liquid crystals, biopolymers, microwave antenna systems, have a variety of applications in microelectronics, quantum electronics, high temperature superconductivity, molecular biophysics, holography, communication techniques information, and in numerous other areas, which rouses great interest in the study of general rules governing the propagation, scattering and emission of electromagnetic waves in these structures.

The main feature of these structures is that for the radiation wavelengths $l \leq 2a$ where a is the spatial structure periodicity, the plane vector waves get interrelated due to the Bragg scattering on periodic inhomogeneities. Two- and three-dimensional ordering of atoms and molecules leads to the possibility of existence in solids of one or more systems of atomic planes that satisfy the Bragg Law and at the same time allow two- or multi-wave diffraction of radiation. The field states corresponding to one-, two- and multi-wave solutions to the vector Maxwell equations for various photon energies in crystalline matter provide a full set of field states, *i. e.*, of resonant structural modes possessing a band-like frequency spectrum. These states of the radiation field arise due to scattering on dielectric constant inhomogeneities and are similar to the Bloch band electron states scattered by the periodic electromagnetic field of the crystal. The theory of Brillouin zones and the theory of electron states are the basis for understanding the numerous electric and magnetic phenomena in crystals. Similarly, the band theory of radiation states (Bloch photons) in crystals is a basis for the X-ray and γ-ray optics of solids and of its applications.

At present, at least four areas of modern applied physics can be pointed out which give a special interest to the creation of the band photon theory:

1. X-ray structure of crystals and macromolecules;

2. the problem of developing the γ laser and γ amplifier using the Mössbauer effect in solids;

3. infrared injection lasers (as well as amplifiers) with two-dimensional distributed feedback (DFB); the suppression of spontaneous emission in the given spectral ranges;

Photonic Band Gaps and Localization, Edited by
C.M. Soukoulis, Plenum Press, New York, 1993

4. the three-dimensional volume holography; the image identifying of symmetrical objects; information encoding; multiconnected optical elements for modern architecture optical computers.

Recently, in view of possible applications of the band structure of electromagnetic field (EMF) in dielectric superlattices to the purposes of creating new types of semiconductor lasers and other quantum electronic devices in the optical range, the Bloch photon theory has received a thorough study both in the scalar wave approximation [1–4] and within the approach that takes into account vector properties of EMF [5,6] The main results have been obtained numerically, using supercomputers of the Cray type, which necessitated considerable expenses and was fraught with a lack of a clear interpretation of the results. On the other hand, when constructing a mathematical theory of the radiation-lattice interaction and providing the physical interpretation of the final results, one ignores the main characteristic feature of periodic structures, *i. e.*, the spatial as well as pint symmetry of the lattice. To pattern the EMF eigenstates in lattices, a "full" set of quantum numbers corresponding to the symmetry of the system must be introduced into the general systematic description of the radiation itself. This is possible for both the free radiation and the radiation undergoing the potential Thomson scattering on atomic electron density inhomogeneities as well as the resonance scattering on the nuclei in crystals. It is shown in the present contribution that the band photon theory in periodical structures can be constructed analytically, without involving the numerical methods, via the application of group theory to the radiation vector field.

By analogy with the model of "free Bloch electrons" in crystals,[7] we will build a model of "free Bloch photons"in the approximation of an "empty" lattice, which will allow us to describe the general form together with the nature of degeneration of the models, and also set a basis for the correct description of the interaction of radiation with atoms and nuclei of the crystal in the approximation of "almost free photons" [8]

When describing a transverse vector field, one usually exploits either the symmetrized fields given by the electric- and magnetic- type multipoles which form the basis of irreducible representations (IR) of the full rotation group $O(3)$, or the symmetrized fields given by the full set of the Fourier modes of vector plane waves. To incorporate the spatial symmetry into the description of electromagnetic field via plane waves, it is necessary (much as in the case of elastic waves) to introduce a basis of IRs of the wave vector spatial group $G_{\mathbf{k}}$. The wave vector $\mathbf{k}$ of any plane wave can be written as $\mathbf{k} = \mathbf{k}_0 + \mathbf{b}$, where $\mathbf{k}_0$ is the reduced wave vector and $\mathbf{b}$ is the reciprocal lattice vector. All of the points of the reduced Brillouin zone are patterned according to the irreducible stars of the wave vector. Vector waves in different directions can be grouped together according to their belonging to one of the rays of the wave vector star. Every point of the Brillouin zone possesses a point symmetry described by one of the wave vector point groups. A wave vector $\mathbf{k}$ whose length exceeds the size of the Brillouin zone, can always be reduced to one of the interior points of the Brillouin zone.

The wave vector group $G_{\mathbf{k}}$, being a subgroup of the full spatial group G, consists of those symmetry operators $g = \{Q_l|\mathbf{v}_l + \mathbf{R}_s\}$ $(l = 1, \ldots, m)$ that either do not transform the vector $\mathbf{k}$ at all or map into an equivalent vector. That is, for any $g \in G$,

$$g\mathbf{k} = \mathbf{k} \quad \text{or} \quad g\mathbf{k} = \mathbf{k} + \mathbf{b}.$$

In the above, Q_l denotes the l^{th} rotation operator, $\mathbf{v}_l$ is the associated nontrivial translation, and $\mathbf{R}_s$ is a trivial translation. Denote by $M^{\alpha ls}$ the matrix representa-

tion of g in the α^{th} IR, and also denote by $\chi^{\alpha ls}$ the character of this matrix. Then $M^{\alpha ls} = e^{-\imath \mathbf{k}\mathbf{R}_s} M^{\alpha l}$, $\chi^{\alpha ls} = e^{-\imath \mathbf{k}\mathbf{R}_s}\chi^{\alpha l}$, where $M^{\alpha l}$ is the matrix representation of the element $\{Q_l|\mathbf{v}_l\}$ and $\chi^{\alpha l}$ is the character of $M^{\alpha l}$.

Now, consider the reducible representation of the wave vector group for the wave vector $\mathbf{k}$, with the element $\{Q_l|\mathbf{v}_l + \mathbf{R}_s\}$ represented by the matrix $M^{\alpha l} = e^{-\imath \mathbf{k}\mathbf{R}_s} M^l$ where M^l is the matrix representation of $\{Q_l|\mathbf{v}_l\}$, and assume that the character of IR $\chi^{ls} = e^{-\imath \mathbf{k}\mathbf{R}_s}\chi^l$.

The number which shows how many times the α^{th} IR is contained in the reducible representation, is given by,

$$c_\alpha = \frac{1}{mN}\sum_{l,s}\left(\chi^{\alpha ls}\right)^* \chi^{ls} = \frac{1}{m}\sum_{l}\left(\chi^{\alpha l}\right)^* \chi^{l} \quad , \tag{1}$$

where m equals the number of symmetry operators of the wave vector point group $F_{\mathbf{k}_0}$. This point group is isomorphic to the factor of $G_{\mathbf{k}}$ over the translation subgroup. The group $F_{\mathbf{k}_0}$ is determined by the vector $\mathbf{k}_o$ and is a subgroup of the group F of directions characterizing the crystal class.

To determine the character of the reducible representation furnished by all the vector plane waves, we assume there is a fictitious molecule in the reciprocal space with identical atoms attached to the ends of the wave vectors. As to the characters of the possible symmetry elements E, C_φ, S_φ, $\mathcal{I}$ or σ of the point group $F_{\mathbf{k}_0}$, the following can be deduced in the case of a transverse field. The symmetry elements given by the inversion $\mathcal{I}$ and the mirror rotation S_φ have zero characters, since none of the fictitious atoms sits in the 'fixed point' of the point group. The symmetry element σ given by the reflection in a plane also has a zero character, as can be seen by choosing the coordinates of the 'atoms' corresponding to the two polarization vectors of a plane wave, orthogonal to the wave vector, with one of the atoms lying in the symmetry plane while the polarization vector orthogonal to the plane. Indeed, in the coordinate system in which the OZ axis runs along the wave vector $\mathbf{k}$ and OX and OY are directed along the polarization vectors $\mathbf{e}_x$ and $\mathbf{e}_y$,respectively, and with the symmetry plane coinciding with the XZ (or YZ) plane, the action of the symmetry element on the polarization vectors results in that one of changes sign while the other remains unchanged. Non-vanishing in the reducible representation furnished by $2N$ transverse plane vector waves are the character of the identity element, $\chi^E_\perp = 2N$, and that of the rotation, $\chi^{C_\varphi}_\perp = 2N\cos\varphi$. Here N is the number of wave vectors that lie on the symmetry element.

As an example of photon bands, consider the classification of transverse plane vector waves with a reduced wave vector $\mathbf{k}^z_\Delta$ along the OZ axis in the Brillouin zone of a face-centered cubic lattice described by the spatial group O^7_h for the diamond type crystals (such as germanium, silicon, and others) in the "empty" lattice approximation. Consider the Bloch photon energy bands $\omega^2_p = c^2\left(\mathbf{k}^z_\Delta + \mathbf{b}_p\right)^2$, which correspond to the points of the reduced wave vector $\mathbf{k}_\Delta = \mathbf{k}^z_\Delta = \frac{2\pi}{a}(0,0,\xi)$ and to the reciprocal lattice vectors $\mathbf{b}_p = \frac{2\pi}{a}(p_1,p_2,p_3) \equiv \mathbf{b}_{p_1p_2p_3}$ whose indices $\{p_1p_2p_3\}$ belong to the set: 204, 024, $\bar{2}0\bar{4}$ and $0\bar{2}\bar{4}$. The vectors $\mathbf{k} = \mathbf{k}^z_\Delta + \mathbf{b}_p$ determine the frequency band $\Omega^2\left(\mathbf{k}^z_\Delta, \mathbf{b}_p\right) = \frac{\omega^2_p}{c^2}\frac{a^2}{(2\pi)^2} = 4+(\xi-4)^2$, which contains the characteristic X-ray radiation frequency of the K_α-line of copper Cu, with $\lambda_\alpha = 1.54$Å . The number of vector plane waves associated to the same reduced wave vector $\mathbf{k}^z_\Delta$ is equal to eight. In the general form, these waves are given by solutions of the wave equations $\Delta\mathbf{A} = \omega^2_p\mathbf{A}$ of the form $\mathbf{e}_{\mathbf{k}_i}e^{\imath\mathbf{k}_i\mathbf{r}}$ with the wave vectors

$$\mathbf{k}_1 = \mathbf{k}^z_\Delta + \mathbf{b}_1 = \mathbf{k}^z_\Delta + \mathbf{b}_{20\bar{4}} \equiv (2,0,\xi-4)$$
$$\mathbf{k}_2 = \mathbf{k}^z_\Delta + \mathbf{b}_2 = \mathbf{k}^z_\Delta + \mathbf{b}_{02\bar{4}} \equiv (0,2,\xi-4)$$
$$\mathbf{k}_3 = \mathbf{k}^z_\Delta + \mathbf{b}_3 = \mathbf{k}^z_\Delta + \mathbf{b}_{\bar{2}0\bar{4}} \equiv (\bar{2},0,\xi-4)$$
$$\mathbf{k}_4 = \mathbf{k}^z_\Delta + \mathbf{b}_4 = \mathbf{k}^z_\Delta + \mathbf{b}_{0\bar{2}\bar{4}} \equiv (0,\bar{2},\xi-4)$$
$$\mathbf{k}_2 = \mathbf{k}_1 + \overline{(2\bar{2}0)}; \qquad \mathbf{k}_3 = \mathbf{k}_1 + \overline{(\bar{4}00)}; \qquad \mathbf{k}_4 = \mathbf{k}_1 + \overline{(\bar{2}\bar{2}0)}\ .$$

This energy band connects the point Γ of the Brillouin zone with energy $\Omega^2(\Gamma) = 20$ with a point X on the edge of the frustrum of a tetrahedron with energy $\Omega^2(X) = 13$. The group $G_{\mathbf{k}}$ corresponding to the point $\mathbf{k}^z_\Delta$ contains the eight rotation operators $\hat{Q}_l$: $\hat{Q}_1(E)$, $\hat{Q}_4(C_{2z})$, $\hat{Q}_{23}(\sigma_{xy})$, $\hat{Q}_{24}(\sigma_{\bar{x}y})$, $\hat{Q}'_2 = \mathcal{I}Q_2(\sigma_x)$, $\hat{Q}'_3 = \mathcal{I}Q_3(\sigma_3)$, $\hat{Q}'_{17} = \mathcal{I}Q_{17}(\sigma_{yz})$, $\hat{Q}'_{18} = \mathcal{I}Q_{18}(C^3_{4z})$. The characters of the reducible representation χ^l for the operators $\hat{Q}_l$ and $\hat{Q}'_l$ are equal to, $\chi^1 = 0$, $\chi^i = 0$ (for $i = 4, 23, 24, 2', 3', 17', 18'$). With the IR characters of these operators borrowed from the tables,[7] it is not difficult to evaluate the multiplicities of the C_{4v} IRs in the reducible representation:

$$c_{\Delta_1} = 1; \qquad c_{\Delta'_1} = 1; \qquad c_{\Delta_2} = 1; \qquad c_{\Delta'_2} = 1; \qquad c_{\Delta_5} = 2\ .$$

Thus

$$\Gamma_\perp = \Delta_1 + \Delta'_1 + \Delta_2 + \Delta'_2 + 2\Delta_5. \tag{2}$$

Adding up the dimensions of these IRs, we find the number of the plane waves involved is $1+1+1+1+2\cdot 2 = 8$, as expected. As the initial polarization vectors of the plane waves, we choose the following orthonormalized vectors:

$$\mathbf{k}_1 = (2,0,\xi-4); \quad \mathbf{e}^{\mathrm{I}}_1 = \frac{1}{\sqrt{4+(\xi-4)^2}}[(\xi-4)\mathbf{e}_x - 2\mathbf{e}_z]; \quad \mathbf{e}^{\mathrm{II}}_1 = \mathbf{e}_y,$$
$$\mathbf{k}_2 = (0,2,\xi-4); \quad \mathbf{e}^{\mathrm{I}}_2 = \frac{1}{\sqrt{4+(\xi-4)^2}}[(\xi-4)\mathbf{e}_y - 2\mathbf{e}_z]; \quad \mathbf{e}^{\mathrm{II}}_2 = -\mathbf{e}_x,$$
$$\mathbf{k}_3 = (\bar{2},0,\xi-4); \quad \mathbf{e}^{\mathrm{I}}_3 = \frac{1}{\sqrt{4+(\xi-4)^2}}[-(\xi-4)\mathbf{e}_x - 2\mathbf{e}_z]; \quad \mathbf{e}^{\mathrm{II}}_3 = -\mathbf{e}_y,$$
$$\mathbf{k}_4 = (0,\bar{2},\xi-4); \quad \mathbf{e}^{\mathrm{I}}_4 = \frac{1}{\sqrt{4+(\xi-4)^2}}[-(\xi-4)\mathbf{e}_y - 2\mathbf{e}_z]; \quad \mathbf{e}^{\mathrm{II}}_4 = \mathbf{e}_x.$$

Applying to the vector plane waves $\mathbf{e}^{\mathrm{I}}_1 e^{i\mathbf{k}_1\mathbf{r}}$ and $\mathbf{e}^{\mathrm{II}}_2 e^{i\mathbf{k}_2\mathbf{r}}$ the method of projection operators, it is not difficult to get the correct zeroth approximation function, given by the symmetrized transverse vector fields corresponding to the IRs Δ_1, Δ'_1, Δ_2, Δ'_2, and Δ_5. They are solutions to the free Maxwell equations in the "empty" lattice approximation. These symmetrized fields are determined by the "full "sets of indices, originating from the crystal symmetry

$$\mathbf{A}^{(\mu)}_{\omega_p,\mathbf{k}^z_\Delta,\alpha,j}(\mathbf{r},t),$$

where the index ω_p determiners the $\mathbf{b}_p$ vector and plays the role similar to that of the principle atomic quantum number, $\mathbf{k}^z_\Delta$ is the translational index which at the same time determines the wave vector point group, μ accounts for inequivalent IRs of the same type, and α and j label the IR itself and a line of it.

Given below are the expressions obtained using the projection operators, for the orthonormalized symmetrized combinations of vector plane waves (SCVPW) that transform under the IR of the symmetry group of the system:

$$\mathbf{A}^{(\mu)}_{\omega_p,\mathbf{k}^z_\Delta,\alpha,j}(\mathbf{r},t) = e^{i\frac{2\pi}{a}\xi z}\mathbf{U}_{\omega_p,\alpha,j}(\mathbf{r})e^{-i\omega_p t}$$

where the functions $\mathbf{U}_{\omega_p,\alpha,j}(\mathbf{r})$ are given by,

for one-dimensional IRs

$$\begin{aligned}
\mathbf{U}_{\omega_p,\Delta_1}(\mathbf{r}) &= \frac{1}{2}\left\{-\left(e^{-i\mathbf{b}_{\bar{2}04}\mathbf{r}} - e^{-i\mathbf{b}_{024}\mathbf{r}}\right)\mathbf{e}_x + \left(e^{-i\mathbf{b}_{\bar{2}04}\mathbf{r}} - e^{-i\mathbf{b}_{0\bar{2}4}\mathbf{r}}\right)\mathbf{e}_y\right\} \\
\mathbf{U}_{\omega_p,\Delta_1'}(\mathbf{r}) &= \frac{1}{2}\frac{1}{\sqrt{4+(\xi-4)^2}}\left\{(\xi-4)\left(e^{-i\mathbf{b}_{\bar{2}04}\mathbf{r}} - e^{-i\mathbf{b}_{204}\mathbf{r}}\right)\mathbf{e}_x\right. \\
&\quad -(\xi-4)\left(e^{-i\mathbf{b}_{0\bar{2}4}\mathbf{r}} - e^{-i\mathbf{b}_{024}\mathbf{r}}\right)\mathbf{e}_y \\
&\quad \left.+2\left(e^{-i\mathbf{b}_{\bar{2}04}\mathbf{r}} - e^{-i\mathbf{b}_{204}\mathbf{r}} + e^{-i\mathbf{b}_{0\bar{2}4}\mathbf{r}} - e^{-i\mathbf{b}_{024}\mathbf{r}}\right)\mathbf{e}_z\right\} \\
\mathbf{U}_{\omega_p,\Delta_2}(\mathbf{r}) &= \frac{1}{2}\left\{-\left(e^{-i\mathbf{b}_{0\bar{2}4}\mathbf{r}} - e^{-i\mathbf{b}_{0\bar{2}4}\mathbf{r}}\right)\mathbf{e}_x + \left(e^{-i\mathbf{b}_{\bar{2}04}\mathbf{r}} - e^{-i\mathbf{b}_{204}\mathbf{r}}\right)\mathbf{e}_y\right\} \\
\mathbf{U}_{\omega_p,\Delta_2'}(\mathbf{r}) &= \frac{1}{2}\frac{1}{\sqrt{4+(\xi-4)^2}}\left\{(\xi-4)\left(e^{-i\mathbf{b}_{\bar{2}04}\mathbf{r}} - e^{-i\mathbf{b}_{0\bar{2}4}\mathbf{r}}\right)\mathbf{e}_x\right. \\
&\quad +(\xi-4)\left(e^{-i\mathbf{b}_{024}\mathbf{r}} - e^{-i\mathbf{b}_{204}\mathbf{r}}\right)\mathbf{e}_y \\
&\quad \left.+2\left(e^{-i\mathbf{b}_{\bar{2}04}\mathbf{r}} + e^{-i\mathbf{b}_{0\bar{2}4}\mathbf{r}} + e^{-i\mathbf{b}_{204}\mathbf{r}} + e^{-i\mathbf{b}_{024}\mathbf{r}}\right)\mathbf{e}_z\right\}
\end{aligned}$$

for two-dimensional IRs:

$$\left\{\begin{aligned}
\mathbf{U}^{(1)}_{\omega_p,\Delta_5,1}(\mathbf{r}) &= \frac{1}{\sqrt{2}}\frac{\xi-4}{\sqrt{4+(\xi-4)^2}}\left(e^{-i\mathbf{b}_{\bar{2}04}\mathbf{r}} + e^{-i\mathbf{b}_{204}\mathbf{r}}\right)\mathbf{e}_x \\
&\quad +\frac{\sqrt{2}}{\sqrt{4+(\xi-4)^2}}\left(e^{-i\mathbf{b}_{\bar{2}04}\mathbf{r}} - e^{-i\mathbf{b}_{204}\mathbf{r}}\right)\mathbf{e}_z \\
\mathbf{U}^{(1)}_{\omega_p,\Delta_5,2}(\mathbf{r}) &= \frac{1}{\sqrt{2}}\left(e^{-i\mathbf{b}_{0\bar{2}4}\mathbf{r}} + e^{-i\mathbf{b}_{024}\mathbf{r}}\right)\mathbf{e}_x
\end{aligned}\right.$$

$$\left\{\begin{aligned}
\mathbf{U}^{(2)}_{\omega_p,\Delta_5,1}(\mathbf{r}) &= \frac{1}{\sqrt{2}}\frac{\xi-4}{\sqrt{4+(\xi-4)^2}}\left(e^{-i\mathbf{b}_{0\bar{2}4}\mathbf{r}} + e^{-i\mathbf{b}_{024}\mathbf{r}}\right)\mathbf{e}_y \\
&\quad +\frac{\sqrt{2}}{\sqrt{4+(\xi-4)^2}}\left(e^{-i\mathbf{b}_{0\bar{2}4}\mathbf{r}} - e^{-i\mathbf{b}_{024}\mathbf{r}}\right)\mathbf{e}_z \\
\mathbf{U}^{(2)}_{\omega_p,\Delta_5,2}(\mathbf{r}) &= \frac{1}{\sqrt{2}}\left(e^{-i\mathbf{b}_{\bar{2}04}\mathbf{r}} + e^{-i\mathbf{b}_{204}\mathbf{r}}\right)\mathbf{e}_y
\end{aligned}\right.$$

These expressions are determined by the crystalline symmetry only. Such symmetrized vector waves can be found for any point of the Brillouin zone in the **k**-space for any spatial symmetry group of an arbitrary crystal.

The SCVPW characterizes the field structure within the unit cell regardless of the chemical composition and the number of atoms in the cell base. SCVPW reproduces the oscillatory 'normal' modes of the X-radiation field in the unit cell of an infinite crystal and illustrates the relative positions of atoms and nuclei in the unit cell with respect to the three-dimensional field structure.

Taking into account the interaction of the SCVPW with the electrons and the nuclei in crystals, does not change the linear approximation expressions for the field structures of normal modes. Therefore, for all the real periodical structures (*e.g.,* crystals, superlattices, *etc.*) with a given space symmetry group, they are of quite a general nature and, in particular, are independent of the chemical composition of the medium, and so can be tabulated in *International Tables for X-Ray Crystallography*.

The introduction of the new objects of study in classical optics, the SCVPW, entails the need to reconsider some of the notions of statistical optics which are related to the space coherence theory, noises, statistics of photons, and so forth.

Previously, the photon, *i. e.*, the EMF quantum, was related to the squared field amplitude of a single plane wave; now, a quantum should be related to the squared field amplitude of the multiwave configuration as a whole. Thus, the very nature of the free field quantization changes drastically, and new objects of study in the quantum optics arise, the SCVPW.

Cross-sections of the standard quantum electrodynamics processes, such as the spontaneous emission, photoeffect, internal conversion, the Auger effect, and so on, should be reconsidered for the case of the SCVRW radiation interacting with atoms and nuclei in anisotropic and periodical structures such as the molecules of crystals.

A more detailed account of the concept of symmetrized fields, of both the transverse and longitudinal types, will be given in a Lebedev Institute preprint and in a paper submitted for publication to Physical Review Letters.

REFERENCES

1. E. Yablonovitch, Inhibited spontaneous emission in solid-state physics and Electronics, *Phys. Rev. Lett.* 58:2059 (1987).

2. E.N. Economou and A. Zdetsis, Classical wave propagation in periodic structures, *Phys. Rev. B*40:1334 (1989).

3. S. Satpathy, Ze Zhang, and M.P. Salehpour, Theory of photon bands in three-dimensional periodic dielectric structures, *Phys. Rev. Lett.* 64:1239 (1990; 65:2478 (E) (1990).

4. K.M. Leung and Y.F. Liu, Photon band structures: the plane wave method, *Phys. Rev. B*41:10188 (1990).

5. K.M. Leung and Y.F. Liu, Full vector wave calculation of photonic band structures in face-centered-cubic dielectric media, *Phys. Rev. Lett.* 65:2646 (1990).

6. K.M. Ho, C.T.Chan, and C.M. Soukoulis,Existence of a photonic gap in periodic dielectric structures, *Phys. Rev. Lett.* 65:3152 (1990).

7. D.J. Morgan, Group theory and electronic states in perfect crystals, *in*: "Solid State Theory", P.T.Landsberg, ed., London (1969).

8. H. Jones. "The Theory of Brillouin Zones and Electronic States in Crystals", North Holland, Amsterdam (1962).

1-D DISORDERED SYSTEM WITH ABSORPTION AS A MODEL OF REAL MEDIA OF PROPAGATION

Valentin Freilikher

Department of Physics
Bar-Ilan University
Ramat-Gan 52900
Israel

INTRODUCTION

One-dimensional disordered systems are considered at present as abstract mathematical models which are used in the theory of wave propagation as limiting cases for testing approximations only. The possibility of computer simulations of all feasible 1-d propagation processes was the reason for the decrease in interest, during the last few years, in the analytical studies of such systems.

I demonstrate in this paper that there are some practical problems which may be reduced, under some assumptions, to a one-dimensional Schrödinger-type equation with effective complex-valued random potential. All these problems, being of the different physical nature, nevertheless, have one trait in common: non-one-dimensionality of scattering processes may be taken into account by means of effective absorption term in 1-d wave equation. The examples under consideration demonstrate cogently that in spite of seeming completeness of the theory of systems with 1-d disorder, there are many questions requiring special analytical and numerical investigations.

UHF RADIO WAVES PROPAGATION IN THE ATMOSPHERE

Consider the electric field $\boldsymbol{E}$ of the wave generated by a vertical dipole situated in the atmosphere over the earth surface. Its radial component $\boldsymbol{E}$ may be represented in the form

$$E_r(R) = \frac{\exp(ikx)}{x} W(R) , \qquad (1)$$

where x is the coordinate along the earth surface, and W(R) is so-called attenuation function, obeying the parabolic equation

Photonic Band Gaps and Localization, Edited by
C.M. Soukoulis, Plenum Press, New York, 1993

$$2ik\frac{\partial W}{\partial x} + \Delta_\perp W + k^2[\varepsilon_M(x,y,z)-1]W = 0 \qquad (2)$$

$$\text{where} \quad \Delta_\perp = \frac{\partial^2}{\partial y^2} + \frac{\partial^2}{\partial z^2} \quad , \quad \varepsilon_M = \varepsilon(x,y,z;t) + \frac{2z}{a}$$

and a is the equivalent radius of the earth. Since dielectric constant ε depends parametrically on time t, W describes the instantaneous value of attenuation function W. In practice, however, all really measured quantities are averaged over a certain time interval. Let us average Eq. (2) over a finite time T (denoting the average values as $< \ldots >_T$) and make use of the "locally frozen" stationary turbulence hypothesis. This hypothesis implies that variations of the random field $\varepsilon(R,t)$ with time result solely from the motion of the turbulent flow at a velocity v which can be a random value, too. Introducing $\delta_{\varepsilon T} = \varepsilon_M(R) - <\varepsilon_M(R)>_T$ and transforming Eq. (2) to the integral form we obtain[1]

$$<W(x,y,z)>_T = W(o,y,z)<e^{i\frac{k}{2}\int_o^x dx'\delta\varepsilon_T(x',y,z)}>_T -$$

$$-\frac{1}{2ik}<\int_o^x dx' e^{i\frac{k}{2}\int_{x'}^x dx''\delta\varepsilon_T(x'',y,z)} \times \qquad (3)$$

$$\times [\Delta_\perp + k^2(<\varepsilon_M(x,y,z)>_T - 1)]W(x,y,z)>_T \quad .$$

Instead of averaging the functionals depending on $\delta\varepsilon_T$ over time T, one can perform averaging over the ensemble of ε as $\delta\varepsilon_T$ do not contain greater scale times than T. On the other hand, $<\varepsilon_M(x,y,z)>_T$ may be considered invariant over times $t \leq T$. Assuming statistical independence of v and $\delta\varepsilon_T$ fluctuations, we can perform averaging over $\delta\varepsilon_T$, which gives for $W_T \equiv <W(R)>_T$

$$2ik\frac{\partial W_T}{\partial x} + \Delta_\perp W_T + [k^2(<\varepsilon_M(\vec{R})>_T - 1) + 2ik\gamma_T]W_T = 0 \qquad (4)$$

provided that the wave propagation can be regarded as a Markovian process, i.e., the conditions are met

$$L_\perp \ll kL_z^2 \quad , \quad \sigma_\varepsilon^2 k^2 L_\perp^2 \ll 1 \qquad (5)$$

(here $L_\perp = \sqrt{L_x^2 + L_y^2}$ and L_z are, respectively, the horizontal and the vertical scale sizes of the inhomogeneities and σ_ε^2 is the r.m.s. magnitude of fluctuations in ε). The attenuation rate γ_T averaged over the fluctuations is given by the relation

$$\gamma_T = \frac{\pi k^2}{4}\int dH_y \int dH_z \Phi_\varepsilon(O,H_y,H_z) \quad ,$$

$$\underline{with} \quad |H_y| > H_y^o \quad , \quad |H_z| > H_z^o \quad , \tag{6}$$

$$\underline{and} \quad H_y^o = (V_\perp T)^{-1} \quad \underline{and} \quad H_z^o = \left[\int_o^T d\tau (T-\tau) B_{v_z}(\tau)\right]^{-1/2} \quad ;$$

$V_\perp$ is the mean horizontal transfer velocity of the inhomogeneities and $B_v(\tau)$ is the correlation function of pulsations of the vertical velocity. As can be seen from Eq. (6), the major contribution to the damping rate γ_T of the coherent field component is given by the components of the inhomogeneity spectrum with $H_{y,z} > H^o_{y,z}$. The function $<\varepsilon_M(R)>_T$ involved in Eq. (4) is a much slower function of x and y than $\varepsilon_M(x,y,z)$, at least for sufficiently long averaging time. The effect of "fast" small-scale fluctuations is included now in the effective attenuation γ_T.

If the time of averaging T is large enough[1], the x and y dependencies of $<\varepsilon_M>_T$ can be totally neglected, i.e., $<\varepsilon_M(x,y,z)>_T$ in Eq. (4) can be replaced by $\varepsilon_T(z)$. Then the Fourier transform $W_T(\kappa;x,z)$ of the attenuation function W_T with respect to coordinate y,

$$\tilde{W}_T(\kappa;x,z) = \int W_T(x,y,z) e^{ik_y} dy \quad , \tag{7}$$

obeys the equation

$$2ik\frac{\partial \tilde{W}_T}{\partial x} + \frac{\partial^2 \tilde{W}_T}{\partial z^2} + [k^2(\varepsilon_T(z)-1) - \kappa^2 + 2ik\gamma_T]\tilde{W}_T = 0 \quad , \tag{8}$$

which coincides with non-stationary one-dimensional Schrödinger equation, where time is replaced by longitudinal coordinate x and potential energy is proportional to

$$-[k^2(\varepsilon_T(z)-1) - \kappa^2 + 2ik\gamma_T] \quad . \tag{9}$$

The imaginary part $2ik\gamma_T$ of the effective potential describes nondissipative attenuation arising due to scatterings on three-dimensional small-scale fluctuations.

SURFACE WAVES ON A RANDOM SURFACE

Another example of an application of 1-d Schrödinger equation concerns a random surface scattering problem. Consider the Green function $G(R,R_o)$ of this problem, which satisfies the equation

$$\Delta G(\vec{R},\vec{R}_o) + k_o^2 G(\vec{R},\vec{R}_o) = 2\pi\delta(\vec{R},\vec{R}_o)$$
$$\vec{R} = (x,z) \quad , \tag{10}$$

and the random impedance boundary conditions

$$\{\frac{\partial G}{\partial z} + [\eta_o - \eta(x)]G\}_{z=0} = 0 \tag{11}$$

Here k_o is the vacuum wavenumber and $\eta(x)$ is a small perturbation of the regular surface impedance η_o. Such a boundary condition arises also in the problem of scattering from a slightly rough surface. In that case, $\eta(x)$ is proportional to the random deviations of the interface from the plane z=0.[2]

Using the Green theorem, closed integral equation for

$$G(x,x_o) \equiv G(\vec{R},\vec{R}_o)|_{z=z_o=0} \quad .$$

may be obtained, which in Fourier representation takes the form

$$G(P,P_o) = G_o(P)[\delta(P-P_o) + \int dP' \eta(P-P') G(P',P_o)] \tag{12}$$

Here

$$F(P) \equiv \frac{1}{2\pi}\int F(x) e^{-iPx} dx$$

$\delta(P-P_o)$ is the Dirac delta-function, and G_o is the Green function of unperturbed ($\eta(x)=0$) problem, which is equal to

$$G_o(P) = \frac{1}{i\sqrt{K_o^2 - P^2} + \eta_o} \quad . \tag{13}$$

If $\eta_o>0$, $G_o(P)$ has two poles at real $P = \pm P_s = \pm\sqrt{K_o^2+\eta_o^2}$ (discrete spectrum) which corresponds to surface waves (SW) with wave numbers $\pm P_s$, propagating without attenuation in opposite directions along the unperturbed surface z=0. Note that continuous spectrum $-K_o \le P \le K_o$ describes volume waves (VW), which, being reflected from the surface, propagate in the halfspace Z>0 at angles $\theta = \pm$ arccos P/K_o.

Fluctuations $\eta(x)$ of the surface impedance effect drastically surface waves propagation. There exist two kinds of scattering processes of SW when $\eta(x) \neq 0$: SW⇔SW forward and back multiple scatterings, and SW⇒VW transformations which may be considered as single if $\eta(x)$ is small enough. The reflections are of a resonance nature in this case, which means that the cross section of $P_1 \Rightarrow P_2$ scattering is proportional to the squared modulus of the amplitude of the spatial harmonics in the spectrum of the fluctuations $\eta(x)$ with the period $\Lambda = 2\pi/q$, $q = |P_1 - P_2|$. This is clear that the main contribution to the SW⇔SW scatterings are given by the spectral components with $q \sim \pm 2P_s$ (back) and $q \sim 0$ (forward), as well as SW⇒VW transitions are provided by resonant modes with wave numbers q of order $P_s \pm K_o$.

This consideration enables us[3] to select only resonant harmonics $\eta(P)$ which is similar to so-called resonant approximation in the theory of 1-d disordered systems.[4,5,6] Generalizing this approximation, we introduce, instead of $\eta(P)$, four functions $\eta_{ss}(P)$, $\eta_{sv}(P)$, $\eta_{vs}(P)$, and $\eta_{vv}(P)$, which are peaked near different argument values and govern different scattering processes. For instance, $\eta_{ss}(P)$ is concentrated near $P = \pm 2P_S$ and $P = 0$, and provides SW⇔SW transitions between surface waves only; $\eta_{vs}(P)$ in non zero only for P in the vicinity $(P_s - K_o)$ and $P_s + K_o$ and provides SW⇒VW scatterings of surface wave into volume modes.

The same representation must be done for the Green function. We introduce the matrix

$$\hat{G}(P,P') = \begin{pmatrix} G_{ss}(P,P') & G_{sv}(P,P') \\ G_{vs}(P,P') & G_{vv}(P,P') \end{pmatrix} , \qquad (14)$$

where indices indicate to what regions of wavenumbers arguments belong (first index indicates the location of the first argument, second corresponds to the second one).

The equation for G may be written in the form

$$\hat{G}(P,P') = \hat{G}_o(P)\delta(P-P') + \int dp'' \hat{\eta}(P-P'')\hat{G}(P'',P') , \qquad (15)$$

where

$$\hat{\eta} = \begin{pmatrix} h_{ss} & h_{sv} \\ h_{vs} & h_{vv} \end{pmatrix} , \qquad (16)$$

G_o is diagonal matrix, in this representation (see Eq. (13)), and G_{oss} is approximately equal to

$$G_{oss} \approx \frac{\eta_o}{P_s(P_s - |P|)} \quad . \tag{17}$$

We shall use later on the symbolic form of Eq. (15):

$$\hat{G} = \hat{G}_o + \hat{G}_o \hat{\eta} \hat{G} \quad . \tag{18}$$

It is easy to show that matrix G obeys also the equation

$$\hat{G} = \hat{G}^d + \hat{G}^d \hat{\eta}^{nd} \hat{G} \quad , \tag{19}$$

where G^d is the solution of the equation

$$\hat{G}^d = \hat{G}_o + \hat{G}_o \eta^d \hat{G}^d \quad , \tag{20}$$

η^d and η^{nd} are the diagonal and nondiagonal parts of $\eta = \eta^d + \eta^{nd}$.

If we take "SS" and "VS" matrix elements of Eq. (19), and then eliminate G_{VS} we find the equation for G_{SS} as follows

$$G_{ss} = G_s^d + G_s^d V G_{ss} \tag{21}$$

where

$$V = \eta_{SV} G_V^d \eta_{VS} \tag{22}$$

is the renormalized effective potential for SW part of the Green function. It is important to stress that G_v^d is a smooth function, because all singularities are included in G_s^d and G_{SS} Green functions only. This enables us to replace G_v^d to G_{ov} in Eq. (22) and to write

$$\begin{aligned} V(P,P') \approx \eta_{SV} G_{OV} \eta_{VS} \equiv \int dP_1 \eta_{SV}(P-P_1) G_{OV}(P_1) \eta_{VS}(P_1-P') \approx \\ \approx \delta(P-P') \int dP_1 G_{OV} W(P-P_1) \equiv \delta(P-P') \sum_V (P) \end{aligned} \tag{23}$$

where W(P) is determined from the equality $\langle \eta_{SV}(P) \eta_{SV}(P') \rangle = \delta(P+P')W(P)$. Taking into account Eqs. (20), (21), (22) and (23) we have finally:

$$G_{SS} = g + g\eta_{SS}G_{SS} \quad , \tag{24}$$

$$g = \frac{c}{(P_s - |P| + i\Delta_V)} \quad ; \quad c = \frac{\eta_o}{P_s} \quad . \tag{25}$$

Here $\Delta_V = -cJm\Sigma_V$, which is proportional to the imaginary part of the mass operator calculated in the Born approximation. We omitted the real part of Σ_V in Eq. (25) which gives in this case the small correction to P_S.

The integral equation, which corresponds to the coordinate representation of Eq. (24), may be written in the differential form:

$$\frac{1}{2P_S}\left(\frac{d^2}{dx^2} + P_s^2\right)G_{SS}(x,x') + (\eta_{SS}(x) + i\Delta_V)G_{SS} = \delta(x-x') \quad . \tag{26}$$

In this way we find that the problem of derivation of SW Green function is reduced to one-dimensional problem with scattering potential η_{SS} and effective attenuation Δ_V which is of a nondissipative nature, but is connected with transitions from surface waves to outgoing volume ones.

WHAT DO WE KNOW ABOUT WAVE PROPAGATION IN A LOSSY ONE-DIMENSIONAL MEDIUM?

It is well known that nonelastic scatterings destroy strong localization of electrons, but so far it is not clear enough, what is the effect of absorption on localization of classical waves. Since the behavior of the modulus of the reflection coefficient for a 1-d slab of absorbing random medium was studied many years ago[7,8], there are no satisfactory analytical results on the transmission coefficient, which is the quantity of interest for many applications. Our numerical calculations show[8,9] that the dependence of localization length on absorption and on parameters of scatterers is very complicated, and moreover, the transmittivity may be, under some ratio of parameters, a non-monotonic function of attenuation rate.

REFERENCES

1. A. Kukushkin, V. Feilikher, I. Fuks, The effect of a random atmospheric stratification on the UHF coherent component beyond the horizon, Sov. Radiophys., 26:1064 (1983).
2. F. Bass, I. Fuks. "Wave Scattering from statistically rough surface", Pergamon Press (1979).
3. V. Freilikher, I. Yurkevitch, Propagation and localization of surface waves on random surfaces, Phys. Let. A (in press).
4. A. Abrikosov, L. Ryzhkin, Conductivity of quasi-one-dimensional metal systems, Adv. Phys., 27:147 (1978).

5. E. Kaner, L. Chebotarev, The spatial dispersion of conductivity in one-dimensional disordered metals, Phys. Rep., 150:179 (1987).
6. V. Freilikher, Yu. Tarasov, Localization of the field of a point source in a randomly layered medium, IEEE Trans. on AP, 39:197 (1991).
7. W. Kohler, G. Papanicolaou, Power reflection from a lossy one-dimensional random medium, SIAM I. Appl. Math., 30:263 (1976).
8. V. V. Klyatskin. "The imbedding Method in the theory of wave propagation", "Nanka", Moscow, 1986.
9. Freilikher et. al., Effect of absorption on strong localization of classical waves in 1-d disordered system, Phys. Let. A (in press).

TRANSIENT WAVE PROPAGATION IN PERIODICALLY LAYERED MEDIA

Doğan Turhan and Ibrahim A. Alshaikh

Middle East Technical University
Department of Engineering Sciences
Ankara 06531, Turkey

INTRODUCTION

In this paper, transient wave propagation in periodically layered composites consisting of alternating isotropic and homogeneous high-strength reinforcing and low-strength matrix layers is investigated. First, some results from our recently published work[1,2] will be given. In our recent work,[1,2] the propagation of dilatational waves is investigated. The layers of the composite medium can be plane, circular cylindrical or spherical. Furthermore, the layers can be linearly thermoelastic or linearly viscoelastic. The viscoelastic material of the bodies is modelled as a standard linear solid. A common formulation is used for the three types of layered media. The bodies are subjected to uniform time-dependent dynamic inputs at their inner surfaces and the outer surfaces are either fixed or free. The composite bodies are initially at rest.

In the second part of this study, propagation of transient out-of-plane shear waves in layered media consisting of alternating reinforcing and matrix layers is investigated. The layers of the composite medium can be plane or circular cylindrical. Moreover, the layers are isotropic, homogeneous and linearly elastic or linearly viscoelastic. The viscoelastic material is modelled as a standard linear solid. A common formulation is used by introducing a tracing constant p which takes the values 0 and 1 for the plane and cylindrical layered composites, respectively.

The composite bodies are subjected to uniform time-dependent dynamic inputs at their inner surfaces. The dynamic input may be shear traction or particle velocity in the axial direction for the cylindrical problem and in the out-of-plane direction for the plane problem. The outer surfaces are either fixed or free of surface tractions and the bodies are assumed to be initially at rest. The method of characteristics is employed in obtaining the solutions.

The numerical results are obtained when the dynamic input applied at the inner surface is a step shear traction with an initial ramp and the outer surface is free of surface tractions. Curves are plotted denoting the variations of the shear stress with time at different locations. These curves reveal the effects of reflections and refractions at the boundaries and the interfaces of the layers, the effects of geometry and the effects of viscosity.

PROPAGATION OF DILATATIONAL WAVES

The plane, cylindrical and spherical layered composites are referred, respectively, to cartesian, cylindrical and spherical coordinate systems in which x denotes the distances perpendicular to the layering in the plane composite and the radial distance in the other two problems, see Fig. 1. In the thermoelastic problems, the generalized dynamical theory of

Photonic Band Gaps and Localization, Edited by
C.M. Soukoulis, Plenum Press, New York, 1993

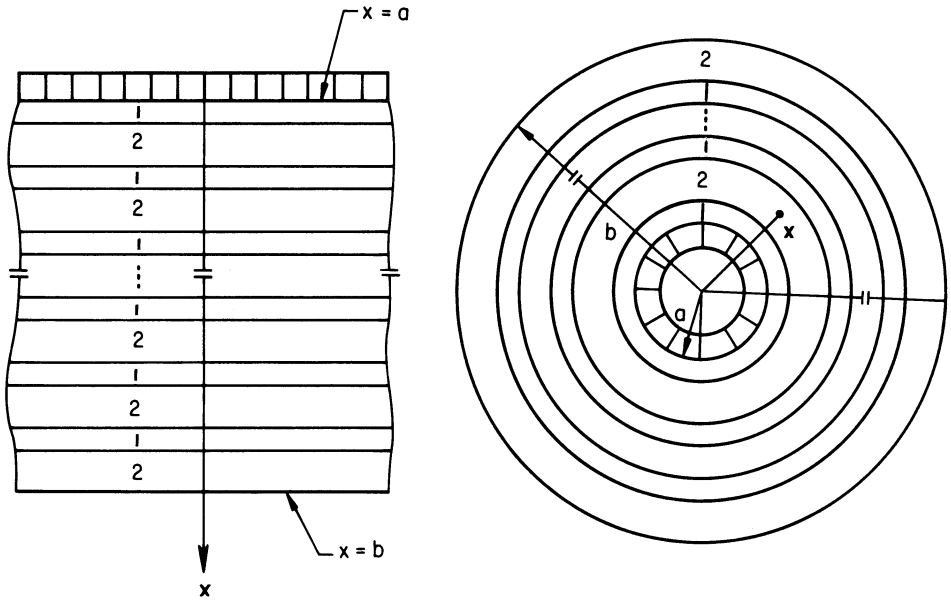

Figure 1. The layered media.

coupled thermoelasticity with thermal relaxation proposed by Lord and Shulman[3] is employed. An exhaustive review of the literature on generalized thermoelasticity theories is given by Chandrasekharaiah.[4]

The numerical results are obtained when the dynamic input applied at the inner surface is a step pressure with an initial ramp and the outer surface is free of surface tractions. For the thermoelastic problems, in addititon, the temperature deviation is kept zero on the inner and outer surfaces. Quiescent initial conditions are assumed. In Fig. 2 taken from our work[1] with the permission of Academic Press, the variation of the non-dimensional normal stress σ_1 / P_0 with dimensionless time $\bar{t}$ at the location $\bar{x} = 1.6$ is shown for the three types of layered media. We note that σ_1 is the normal stress in the direction normal to the layering for the plane laminated composite and in the radial direction for the other two problems. The curves resemble a sinusoidal pattern with decreasing amplitudes. The highest stress levels occur in the plane problem which is followed by the cylindrical and spherical problems. The effects of thermal dispersion on the wave profiles are apparent in the curves as well.

Figure 3, taken from our recent work[2] with the permission of Elsevier Applied Science, displays the variation of the normal stress σ_1 / P_0 with time $\bar{t}$ at the location $\bar{x} = 1.123$ for the plane, cylindrical, and spherical viscoelastic layered composites. The curves reveal the effects of reflections and refractions from the interfaces and the inner and outer boundaries of the layered media. The effects of geometry are also apparent in the curves. The highest levels of the normal stress σ_1/P_0 occur in the plane problem which is followed by the cylindrical and spherical problems. Attenuation in the wave profiles caused by the viscous effects can be investigated by comparing the viscoelastic curves with the corresponding elastic curves. These together with detailed analyses of the above two problems can be found in the above cited references.[1, 2]

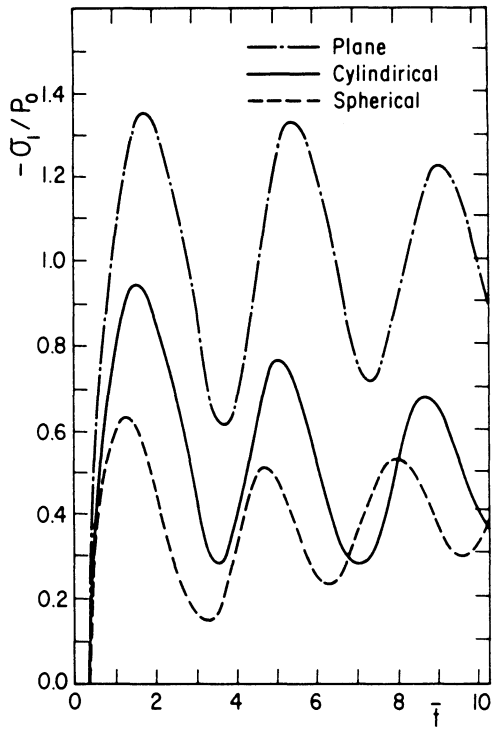

Figure 2. Variation of σ_1 / P_0 with $\bar{t}$ at $\bar{x} = 1.6$ (after Turhan, et al.[1]).

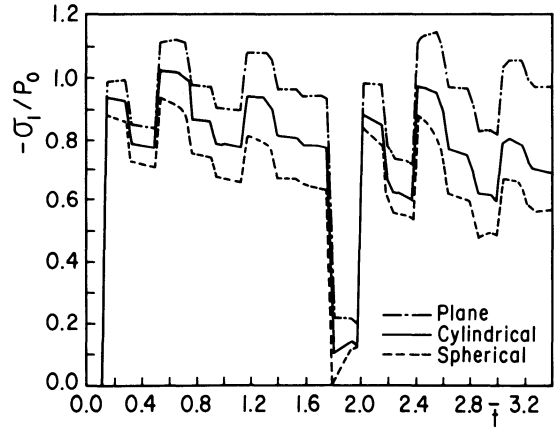

Figure 3. Variation of σ_1 / P_0 with $\bar{t}$ at $\bar{x} = 1.123$ for composite material one (after Turhan, et al.[2]).

PROPAGATION OF SHEAR WAVES

The plane and cylindrical layered viscoelastic composites in which propagation of transient shear waves is investigated are also referred to cartesian and cylindrical coordinate systems given in Fig. 1. The symmetry conditions of the problem imply that all the field variables depend on the distance x and time t, only. Moreover, the only nonvanishing displacement component is u, that is the displacement component in the axial direction for the cylindrical layered medium and in the out-of-plane direction for the plane problem. Then, the stress equation of motion in unified form for a typical layer, which can be a reinforcing or matrix layer, can be written as

$$\frac{\partial \tau}{\partial x} + \frac{p\tau}{x} = \rho \frac{\partial v}{\partial t} , \tag{1}$$

where τ is the axial shear stress for the cylindrical problem and the out-of-plane shear stress for the plane problem, $v = \partial u/\partial t$ is the particle velocity and ρ is the mass density. Furthermore, p is the tracing constant taking the values 0 and 1 for the plane and cylindrical problems, respectively.

The constitutive equation for the standard linear solid in differential equation form can be written as follows[5]

$$a_0 \tau + a_1 \frac{\partial \tau}{\partial t} = b_0 \epsilon + b_1 \frac{\partial \epsilon}{\partial t} , \tag{2}$$

where a_0, a_1, b_0 and b_1 are specified material constants and

$$\epsilon = \frac{1}{2} \left(\frac{\partial u}{\partial x} \right) \tag{3}$$

is the axial shear strain for the cylindrical problem and the out-of-plane shear strain for the plane problem.

The formulation of the problems is completed by stating the boundary, initial and interface conditions. Depending on whether the dynamic input is a shear traction or particle velocity, we might have two types of boundary conditions at the inner surface x = a. They can be expressed as

$$\tau (a, t) = - f (t) H (t) \quad \text{or} \quad v (a, t) = v^* (t) H (t) , \tag{4}$$

where f (t) and v*(t) are some prescribed functions of time and H(t) is the Heaviside step function. The outer surfaces x = b of the composite bodies are either free or fixed:

$$\tau (b,t) = 0 \quad \text{or} \quad v (b,t) = 0 . \tag{5}$$

The bodies are assumed to be initialy at rest and hence all the field variables are zero at t = 0. The layers of the composite bodies are assumed to be perfectly bonded to each other. This implies that the shear stress and the particle velocity are continuous across the interfaces of the layers.

The formulation of the problems is thus complete. The governing field equations, Eqs. (1-3), are now applied to each layer and the solutions are required to satisfy the continuity conditions at the interfaces, the boundary conditions at the inner and outer surfaces and quiescent initial conditions. In the analysis, the method of characteristics is employed. In the method of characteristics,[6] the system of governing partial differential equations is transformed into a system of ordinary differential equations, each is valid along a different family of characteristic lines. These equations, called the canonical equations, are more suitable for numerical analysis because the use of the canonical form makes it possible to obtain the solution by a step-by-step integration procedure. The details of the method of characteristics can be found in Courant and Hilbert.[6]

The numerical computations are carried out and the results are displayed in terms of non-dimensional quantities. The computer program has been written for layered composites consisting of n pairs of layers. The numerical results have been obtained for composite bodies consisting of three pairs of layers. The alternating layers of the composite bodies are denoted as layers 1 and layers 2. All the quantities pertaining to layers 1 are denoted by superscripts or subscripts 1 whereas all the quantities pertaining to layers 2 are specified by superscripts or subscripts 2. In the numerical examples, the innermost layer of the composite bodies is taken as layer 1, whereas the outermost layer is taken as layer 2. The dimensionless quantities relevant to the presentation here are defined as

$$\bar{x} = \frac{x}{a};\ \bar{t} = \frac{t c_1}{a};\ \bar{\rho}_i = \frac{\rho_i}{\rho_1};\ \bar{a} = 1;\ \bar{b} = \frac{b}{a}$$

$$\bar{h}_i = \frac{h_i}{a};\ (\bar{G}_{10}^{(i)}, \bar{G}_{1F}^{(i)}) = \frac{1}{\rho_1 c_1^2}\ (G_{10}^{(i)}, G_{1F}^{(i)})\ , \tag{6}$$

where i= 1, 2 denote quantities pertaining to layers 1 and 2, respectively. In Eqs. (6), the non-dimensional quantities are shown by putting bars over them and

$$G_{10}^{(i)} = \frac{b_1^{(i)}}{a_1^{(i)}};\quad G_{1F}^{(i)} = \frac{b_0^{(i)}}{a_0^{(i)}};\ \bar{\tau}_1^{(i)} = \frac{a_1^{(i)}}{a_0^{(i)}} \qquad (i = 1, 2)\ . \tag{7}$$

Furthermore, in Eqs. (6), $2h_i$ denotes the thicknesses of the layers.

In the numerical examples, two types of composite materials are considered. The numerical values assumed for the non-dimensional material properties of these two composites are as follows:

a) Composite material one

$$\bar{\rho}_1 = 1.0\ ;\ \bar{G}_{10}^{(1)} = 2.0\ ;\ \bar{\tau}_1^{(1)} = 3.0\ ;\ \bar{G}_{1F}^{(1)} = 0.8$$

$$\bar{\rho}_2 = 0.83\ ;\ \bar{G}_{10}^{(2)} = 1.33\ ;\ \bar{\tau}_1^{(2)} = 1.5\ ;\ \bar{G}_{1F}^{(2)} = 0.266 \tag{8}$$

b) Composite material two

$$\bar{\rho}_1 = 1.0\ ;\ \bar{G}_{10}^{(1)} = 2.0\ ;\ \bar{\tau}_1^{(1)} = 1.5\ ;\ \bar{G}_{1F}^{(1)} = 0.4$$

$$\bar{\rho}_2 = 0.83\ ;\ \bar{G}_{10}^{(2)} = 1.33\ ;\ \bar{\tau}_1^{(2)} = 0.75\ ;\ \bar{G}_{1F}^{(2)} = 0.133\ . \tag{9}$$

The network of characteristic lines used in the numerical analysis is defined by

$$\Delta\bar{t} = \Delta\bar{t}_1 = \Delta\bar{t}_2 = 0.0222\ . \tag{10}$$

The thicknesses of the layers and the inner and outer surfaces are taken as

$$2\bar{h}_1 = 0.111\ ;\ 2\bar{h}_2 = 0.222\ ;\ \bar{a} = 1\ ;\ \bar{b} = 2.0\ . \tag{11}$$

In the numerical examples, the dynamical input is assumed to be a uniform shear traction acting on the inner surface $\bar{x} = \bar{a} = 1$ and the outer boundary $\bar{x} = \bar{b} = 2$ is considered

to be free of surface tractions. In the method of characteristics, we are free to choose any time dependency for the shear traction. We here choose a step time variation with an initial ramp, see Fig. 4. The applied shear traction is zero at $\bar{t} = 0$, linearly rises to a constant value $\bar{f}_0$ during a rise time of $2\Delta\bar{t} = 0.0444$, after which it remains constant. The initial ramp in the step variation eliminates the complicated circumstances of having first-order discontinuities in the disturbed region; furthermore, it is physically more realistic as a boundary condition than a step variation without a ramp.

The numerical results are displayed in Figs. 4-5. In Fig. 4, the variation of the dimensionless shear stress τ/f_0 with $\bar{t}$ and $\bar{x} = 1.21$ is shown for the laminated composite with plane layers. The curves are given for the elastic case, i.e., when the viscous effects are

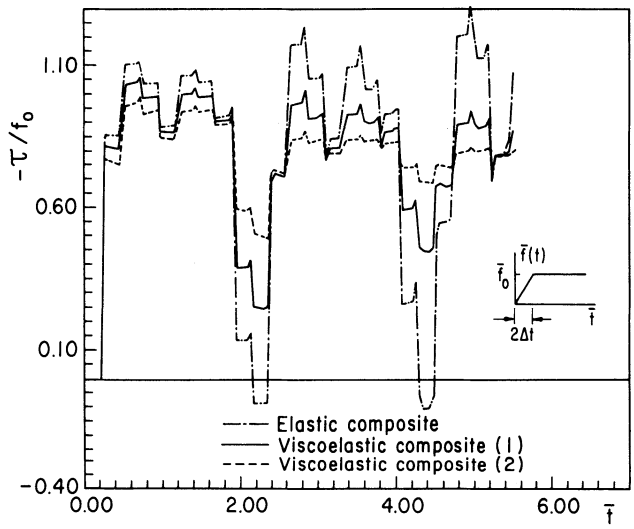

Figure 4. Variation of τ/f_0 wilh $\bar{t}$ at $\bar{x} = 1.21$ for a plane layered composite.

neglected, and for the cases of viscoelastic composite materials 1 and 2. These in the sequel are described as elastic and viscoelastic solutions 1 and 2, respectively. The curves in Fig. 4 denote clearly the dispersion caused by the viscous effects in the wave profiles. We note that composite material 2 is more viscous than 1 and this is revealed in the curves by a larger discrepany with the elastic solution. Furthermore, the discrepancies between the elastic and viscoelastic solutions tend to increase as time passes. The sudden changes in the stress levels in the curves correspond to the arrivals of reflected and refracted waves from the boundaries and interfaces of the laminated composite at the position considered. The maximum values of the shear stress τ/f_0 are smaller in the viscoelastic solutions than the elastic solution and they get even smaller as time increases. In the viscoelastic composites, being more pronounced in composite two, the differences between the maximum and minimum stress levels tends to decrease as time passes. In Fig. 5, the variation of τ/f_0 with time at the location $\bar{x} = 1.21$ is displayed for the cylindrical layered composite. The curves

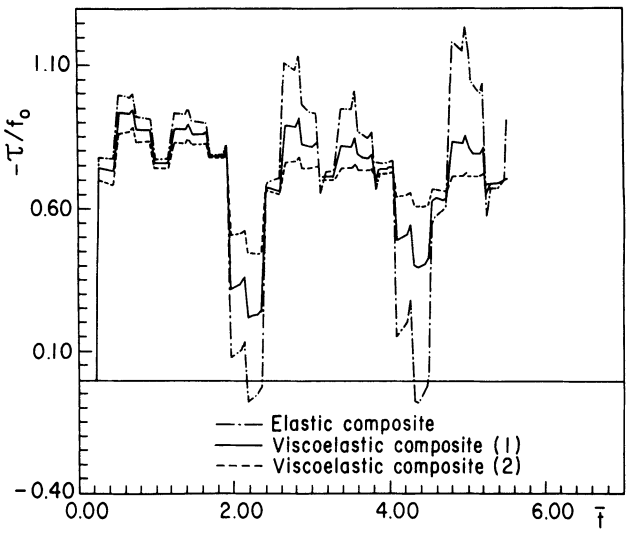

Figure 5 . Variation of τ/f_0 with $\bar{t}$ at $\bar{x} = 1.21$ for a cylindrical layered composite.

exhibit similar trends as those of plane layered composites. In addition, these curves reveal the geometric effects as well. The maximum stress levels are smaller in this case than the maximum stress levels in the plane problem.

REFERENCES

1. D.Turhan, Z. Celep and E. K. Zain-Edden, Transient wave propagation in layered media conducting heat, *J.of Sound and Vib.*, 144: 247 (1991).
2. D.Turhan and Y. Calayır, "Transient dynamic response of viscoelastic layered composites, *in: Structural Dynamics: Recent Advances*, M.Petyt, H.F. Wolfe, and C.Mei, eds., Elsevier Applied Sciences, London (1991).
3. H.W. Lord and Y. Shulman, A generalized dynamical theory of thermoelasticity, *J. Mech. Phys. Solids*. 15:299 (1967).
4. D.S. Chandrasekharaiah, Thermoelasticity with second sound: a review, *Appl. Mech. Review*. 39: 355 (1986).
5. Y. C. Fung, *Foundations of Solid Mechanics*, Prentice-Hall, Englewood Cliff (1965).
6. R. Courant and D. Hilbert, *Methods of Mathematical Physics Vol. II*, Interscience, New York (1966).

A METHOD FOR ANALYZING WAVES IN LAYERED STRUCTURES WITH PERIODIC DISCONTINUITIES LIKE STRIPS OR SLOTS

Eugene J. Danicki

Polish Academy of Sciences, IFTR
21 Świętokrzyska Str., 00-049 Warsaw, Poland

INTRODUCTION

Several papers have been published recently on EM scattering and waveguiding by periodic strips.[1] There is also interest in investigation of analogous problems for elastic waves in elastic body with slots.[2]

A new method is proposed for analyzing electromagnetic or elastic waves in periodic systems of thin and perfectly conducting in-plane strips, or slots. Scattering, waveguiding, and radiation of waves in the system in arbitrary anisotropic media can be easily analyzed with help from the method, which is particularly effective in a case of low order Bragg scattering of waves.

In a case of EM waves, sample analysis is presented concerning scattering by a system of strips (arbitrary polarization and angle of incidence), leaky wave antenna, and certain inhomogeneous problem of EM radiation by a supplied single strip in periodic systems. In the case of elastic waves, Bragg scattering of elastic guided wave by the in-plane system of periodic slots in the body is analyzed. A generalization of the method for analyzing nonperiodic systems is sketched.

The proposed method was first presented by Chu[3] and afterwards applied in the theory of interdigital transducers (IDT) of surface acoustic wave (SAW) concerning the eigenvalue problem,[4] and 3-dimensional eigenvalue and nonhomogeneous problems.[5] It was generalized to elastic,[6] and EM waves,[7,8] quite recently. The method is based on known Fourier expansion of periodic function vanishing in one domain of the period, and having square-root singularities at the edges of the other domain. In fact, it exploits known analytical solutions to certain electrostatic problems concerning periodic systems of perfectly conducting strips.

Briefly, the solution to electric charge distribution, and to electric tangential field in the plane of strips are correspondingly ($\theta = 2\pi x/\Lambda$, Λ - strip period, $\Delta = \pi w/\Lambda$, w

Photonic Band Gaps and Localization, Edited by
C.M. Soukoulis, Plenum Press, New York, 1993

is strip width, P - Legendre function[4,9])

$$\frac{\sqrt{2}\exp(j\theta/2)}{(\cos\theta-\cos\Delta)^{1/2}}=\sum_{n=-\infty}^{\infty}D_n e^{-jn\theta},\quad D_n=P_n(\cos\Delta)$$
$$-\frac{\theta}{|\theta|}\frac{\sqrt{2}\exp(j\theta/2)}{(\cos\Delta-\cos\theta)^{1/2}}=\sum_{n=-\infty}^{\infty}E_n e^{-jn\theta},\quad E_n=j\frac{n}{|n|}P_n(\cos\Delta) \qquad (*)$$

where the validity of the left-hand sides is constrained to domains where they have real values.

Most important are Fourier expansions given in the right hand sides of Eqs.(*). As known, the Green's function making charge distribution dependent on tangential electric field on the plane is in spectral domain (k real)

$$D(k)=-j\epsilon S_k E(k),\quad S_k=k/|k| \qquad (**)$$

Indeed, in Eqs.(*), field components D_n and E_n expressed in spectral domain are subjected to this dependence (for $k=nK$, $K=2\pi/\Lambda$, $\epsilon=1$).

The method presented in this paper exploits heavily this particular property, that the dependence between two certain spectral functions like $D(k)$ and $E(k)$, (the dependence given by Green's function, for instance) has the asymptotic form (**) for $|k|$ large. This helps in modelling field in spectral domain.

In what follows, we will use the following identities[4,9] resulting from (*)

$$\sum_{n=-\infty}^{\infty}\alpha_m P_{n-m}(\cos\Delta)e^{-jn\theta}=\begin{cases}\sqrt{2}\dfrac{\alpha_m\exp(-jm\theta)}{\sqrt{\cos\theta-\cos\Delta}}e^{j\theta/2}, & |\theta|<\Delta\\ 0, & \Delta<|\theta|<\pi\end{cases}$$
$$\sum_{n=-\infty}^{\infty}\beta_m S_{n-m}P_{n-m}(\cos\Delta)e^{-jn\theta}=\begin{cases}0, & \dots\\ -jS_\theta\sqrt{2}\dfrac{\beta_m\exp(-jm\theta)}{\sqrt{\cos\Delta-\cos\theta}}e^{j\theta/2}, & \dots\end{cases} \qquad (I)$$

where $S_\nu=1$ for $\nu\geq 0$, and -1 otherwise, α_m and β_m are arbitrary constants.

The above pair of functions allows to model any periodic function, vanishing in one domain of the period, and having square-root singularities at the edges of the other domain, provided that the function is smooth enough in order to be represented by finite Fourier series $\exp(-jm\theta)$. There is also[9] ($X=\cos\Delta$)

$$P_{-\nu}(-X)=\frac{\sin\pi\nu}{\pi}\sum_{n=-\infty}^{\infty}\frac{S_n P_n(X)}{\nu+n},\quad P_{-\nu}(X)=\frac{\sin\pi\nu}{\pi}\sum_{n=-\infty}^{\infty}\frac{(-1)^n P_n(X)}{\nu+n} \qquad (II)$$

Summarizing, three features make the functions (I) well-suited for modelling EM field in the considered structures of periodic strips:

- they are periodic functions as required by Floquet's theorem,
- the functions vanish in certain adjacent domains, as required for some EM field components by the boundary conditions on, or between strips,
- they exhibit square-root singularity at the bounds of the above-mentioned domains, similar singularities occur in the EM field at the strip edges.

In the paper, summation over n always takes place in infinite limits, like in Eqs.(I), for convenience the infinite summation limits will be dropped.

The paper is organized as follows. In the next Section, three sample electromagnetic problems will be analyzed with the help of the method, presenting its usefulness in scattering, waveguiding and certain inhomogeneous problems. The following Section is devoted to mechanical problems. In Conclusions, a generalization of the method is sketched.

Formulation of the Scattering Problem

Let's consider the system shown in Fig.1a), where periodic strips of width w and period $\Lambda = 2\pi/K$ are arranged on $y = 0$ plane in vacuum. Harmonic electromagnetic field of angular frequency ω (the term $\exp j\omega t$ will be dropped throughout the paper) can be expressed by Hertz electric and magnetic potentials,[10] $\vec{a}_y\Phi$ and $\vec{a}_y\Psi$ (with exception of a very particular case of TEM wave propagating in the y -direction), $\vec{a}_y$ is unitary vector along y-axis

$$\begin{aligned} \vec{E} &= -j\omega\mu_o\nabla\times\vec{a}_y\Psi + \nabla\nabla\cdot\vec{a}_y\Phi + k_o^2\vec{a}_y\Phi \\ \vec{H} &= \nabla\nabla\cdot\vec{a}_y\Psi + k_o^2\Psi + j\omega\times\vec{a}_y\Phi \end{aligned} \quad , \quad \nabla^2\begin{pmatrix}\Phi\\ \Psi\end{pmatrix} + k_o^2\begin{pmatrix}\Phi\\ \Psi\end{pmatrix} = 0 \tag{1}$$

where ϵ_o, μ_o and $k_o = \omega\sqrt{\epsilon_o\mu_o}$ are standard denotations.

The EM field in the system of periodic strips can be represented by a series of harmonic waves. For example, x-components of electric field in the upper halfspace (index +), and the lower halfspace (index −) are

$$\left.\begin{aligned} E_x^{+,-} &= \sum_n E_{xn}^{+,-}\exp(-jr_nx - js_n^{+,-}y - jkz),\ \ r_n = r + nK \\ s_n^+ &= s_n = (k_o^2 - r_n^2 - k^2)^{1/2}, \text{ for real } s_n \\ s_n^+ &= s_n = -j(k_o^2 - r_n^2 - k^2)^{1/2}, \ (\mathrm{Im}\{s_n\} < 0) \end{aligned}\right\},\ \ s_n^- = -s_n\,, \tag{2}$$

where $0 < r < K$ (that always can be assumed), and the chosen values for $s_n^{\pm}$ satisfy the radiation condition at $y \to \pm\infty$.

Applying (1) we obtain (indices '+' and '−' have been dropped)

$$\begin{aligned} E_{xn} &= \omega\mu_o k\Psi_n - r_n s_n\Phi_n & H_{xn} &= -r_n s_n\Psi_n - \omega\epsilon_o k\Phi_n \\ E_{yn} &= (r_n^2 + k^2)\Phi_n & H_{yn} &= (r_n^2 + k^2)\Psi_n \\ E_{zn} &= -\omega\mu_o r_n\Psi_n - ks_n\Phi_n & H_{zn} &= -ks_n\Psi_n + \omega\epsilon_o r_n\Phi_n \end{aligned} \quad . \tag{3}$$

The incident wave incoming from infinity in the upper halfspace is represented by Hertz potentials having corresponding amplitudes Φ^I and Ψ^I (δ_{nI} is Kroenecker delta)

$$\delta_{nI}\begin{pmatrix}\Phi^I\\ \Psi^I\end{pmatrix}\exp(-jr_nx + js_ny - jkz)\,. \tag{4}$$

It results from boundary conditions at $y = 0$ that

$$\begin{aligned} E_x^+ &= E_x^- & E_z^+ &= E_z^- & \Psi_n^- &= \Psi_n + \delta_{nI}\Psi^I \\ E_{xn}^+ &= E_{xn}^- & E_{zn}^+ &= E_{zn}^- & \Phi_n^- &= -\Phi_n + \delta_{nI}\Phi^I\,, \end{aligned} \tag{5}$$

where Φ_n and Ψ_n are scattered field amplitudes in the upper halfspace, and

$$\begin{aligned} E_x^+ &= 0, & E_z^+ &= 0, & &\text{on strips} \\ H_x^+ - H_x^- &= [H_x] = 0, & H_z^+ - H_z^- &= [H_z] = 0, & &\text{between strips.} \end{aligned} \tag{6}$$

In the method proposed in this paper, we apply the above boundary conditions somewhat changed, namely instead of Eqs.(6) taken for z-components of the EM field, we apply two *equivalent conditions* that the field x-derivative, $\partial_x E_z$, or $\partial_x(H_z^+ - H_z^-)$

vanishes on, or between strips, correspondingly, and *additionally*, that $E_z = 0$ at $x = 0, \pm\Lambda, \ldots$, and $H_z^+ - H_z^- = 0$ at $x = \pm\Lambda/2, \pm\Lambda/2 \pm \Lambda, \ldots$. Explicitly,

$$\begin{aligned} \sum_n E_{xn}^+ e^{-jn\vartheta} &= \begin{cases} = 0; \text{ for } |\vartheta| < \Delta \\ \neq 0; \text{ for } \Delta < |\vartheta| < \pi \end{cases} \\ \frac{z_o}{2} \sum_n (H_{xn}^+ - H_{xn}^-) e^{-jn\vartheta} &= \begin{cases} \neq 0; \text{ for } |\vartheta| < \Delta \\ = 0; \text{ for } \Delta < |\vartheta| < \pi \end{cases} \end{aligned} \tag{7}$$

where $z_o = \sqrt{\mu_o/\epsilon_o}$, $\vartheta = Kx$, $\Delta = Kw/2$, the term $\exp(-jrx - jkz)$ has been dropped, and

$$\begin{aligned} \frac{j}{k_o} \partial_x E_z = \frac{j}{k_o} \sum_n -jr_n E_{zn}^+ e^{-jn\vartheta} &= \begin{cases} = 0; \text{ for } |\vartheta| < \Delta \\ \neq 0; \text{ for } \Delta < |\vartheta| < \pi \end{cases} \\ \frac{jz_o}{2k_o} \partial_x [H_z] = \frac{jz_o}{2k_o} \sum_n -jr_n (H_{zn}^+ - H_{zn}^-) e^{-jn\vartheta} &= \begin{cases} \neq 0; \ |\vartheta| < \Delta \\ = 0; \ \Delta < |\vartheta| < \pi \end{cases} \end{aligned} \tag{8}$$

while the above-mentioned *additional conditions* are

$$E_z(x = 0) = \sum_n E_{zn}^+ = 0, \ \frac{z_o}{2}[H_z(x = \frac{\Lambda}{2})] = \frac{z_o}{2} \sum_n (-1)^n (H_{zn}^+ - H_{zn}^-) = 0 . \tag{9}$$

A Method of Solution

Let's compare (8) and (I). We see that Eqs.(8) will be satisfied if we put for every n separately ($\hat{=}$ marks the represented functions)

$$\begin{aligned} \frac{j}{k_o} \partial_x E_z &\hat{=} -r_n^2 (\Psi_n + \delta_{nI} \Psi^I) - \frac{k}{k_o} r_n s_n (\Phi_n - \delta_{nI} \Phi^I) = \sum_m \alpha_m S_{n-m} P_{n-m} \\ \frac{jz_o}{2k_o} \partial_x [H_z] &\hat{=} -\frac{k}{k_o} z_o r_n s_n \Psi_n + r_n^2 \Phi_n = \sum_m \beta_m P_{n-m}, \quad P_\nu = P_\nu(\cos\Delta) \end{aligned} \tag{10}$$

where α_m and β_m are arbitrary constants unknown yet, temporarily we admit summation over m in some large, but finite limits. Equations (10) can be easily solved for Φ_n and Ψ_n which subtituted into (3) yield for E_{xn} and $(z_o/2)[H_{xn}]$

$$\begin{aligned} \frac{-\frac{k}{k_o}\alpha_m S_{n-m} P_{n-m} - \frac{s_n}{r_n}\beta_m P_{n-m} + (z_o \frac{k}{k_o} s_n^2 \Psi^I + r_n s_n \Phi^I)\delta_{nI}}{1 - k^2/k_o^2} &= \alpha'_m S_{n-m} P_{n-m} \\ \frac{\frac{s_n}{r_n}\alpha_m S_{n-m} P_{n-m} - \frac{k}{k_o}\beta_m P_{n-m} + (z_o r_n s_n \Psi^I - \frac{k}{k_o} s_n^2 \Phi^I)\delta_{nI}}{1 - k^2/k_o^2} &= \beta'_m P_{n-m} \end{aligned} \tag{11}$$

correspondingly (the symbol $\sum_m$ has been dropped), where another expansion involving unknown α'_m and β'_m is applied in order to satisfy conditions (7).

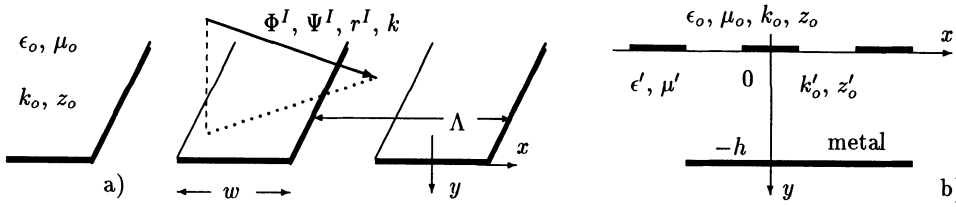

Figure 1. a) Periodic system of strips in vacuum. **b)** Periodic strips on dielectric layer.

Further discussion allows us to eliminate constants α'_m and β'_m from the solution. Let's consider large values of $|n|$, say $n < N^-$ or $n > N^+$, where both $-N^-$ and N^+ are so large that we can apply approximations $r_n \approx nK$ and $s_n \approx -j|nK|$. If additionally we assume $N^- \leq I \leq N^+$ and allow m

$$N^- \leq M^- \leq m \leq M^+ \leq N^+ + 1, \quad (0 < r < K \text{ assumed}) \tag{12}$$

we will easily note that Eqs.(11) are satisfied automatically for all n outside the limited domain $[N^-, N^+]$, if only

$$\alpha'_m = \frac{-\frac{k}{k_o}\alpha_m + j\beta_m}{1 - k^2/k_o^2}, \quad \beta'_m = \frac{-\frac{k}{k_o}\beta_m - j\alpha_m}{1 - k^2/k_o^2} \tag{13}$$

Equations (11) must be satisfied for all n, however. Applying (13), we thus obtain the following equations, which must be satisfied for each $n \in [N^-, N^+]$

$$\begin{aligned} \sum_m \beta_m \left(j\frac{s_n}{r_n} - S_{n-m}\right) P_{n-m}(\cos\Delta) &= \left(z_o \frac{k}{k_o} s_n^2 \Psi^I + r_n s_n \Phi^I\right) \delta_{nI} \\ \sum_m \alpha_m \left(j\frac{s_n}{r_n} S_{n-m} - 1\right) P_{n-m}(\cos\Delta) &= \left(z_o r_n s_n \Psi^I - \frac{k}{k_o} s_n^2 \Phi^I\right) \delta_{nI} \end{aligned} \tag{14}$$

where summation over m is assumed in limits (12).

There are double $M^+ - M^- + 1$ unknowns, and double $N^+ - N^- + 1$ equations (14) *plus* two *additional* equations resulting from (9), thus we have double $N^+ - N^- + 2$ equations altogether. Keeping in mind (12), the limits *must be*

$$M^- = N^-, \quad M^+ = N^+ + 1 \tag{15}$$

in order to obtain the closed system of equations for α_m, β_m.

Equations (9) give (the sums over n are explicitly evaluated with the help of (II))

$$\begin{aligned} \frac{1}{k_o} E_z(0) &= \sum_{m,n} \alpha_m \frac{S_{n-m} P_{n-m}}{r + nK} = \frac{\pi/K}{\sin \pi \frac{r}{K}} \sum_m (-1)^m \alpha_m P_{-m-r/K}(-\cos\Delta) = 0 \\ \frac{z_o}{2k_o}[H_z(\frac{\Lambda}{2})] &= \frac{\pi/K}{\sin \pi \frac{r}{K}} \sum_{m,n} \beta_m \frac{(-1)^n P_{n-m}}{r + nK} = \sum_m \alpha_m P_{-m-r/K}(\cos\Delta) = 0 \end{aligned} \tag{16}$$

Solving Eqs.(14) and (16) for unknowns α_m and β_m ($M^- \leq m \leq M^+$), as dependent on known Φ^I and Ψ^I, we can evaluate Hertz potentials and EM fields in both halfspaces by the parameters characterizing incident wave. This concludes the solution of the problem (some numerical examples are given in,[8] an analog to Brewster angle seemingly exists).

For example, we can evaluate the amplitude of total current flowing along strips in the z-direction (apply Eqs.(7) to extend the integration limits)

$$J = \int_{-w/2}^{w/2} \sum_n [H_{xn}^+ - H_{xn}^-] dx = -\frac{z_o}{2} \int_{-\Lambda/2}^{\Lambda/2} \sum_{m,n} \frac{j\alpha_m + \frac{k}{k_o}\beta_m}{1 - k^2/k_o^2} P_{n-m} e^{-j(r+nK)x} dx \tag{17}$$

which is dependent on r. Applying (II) one obtains

$$J(r) = -\frac{2\Lambda}{z_o} \sum_{m=M^-}^{M^+} \frac{j\alpha_m + \frac{k}{k_o}\beta_m}{1 - k^2/k_o^2} P_{-m-r/K}(\cos\Delta). \tag{18}$$

Sample Eigenvalue Problem

The considered dielectric slab, Fig.1b) has its upper surface covered by periodic strips and its bottom surface metallized. The EM field in a vacuum above the slab is governed by Eqs.(1)-(3). Similar relations for the dielectric layer can be obtained by substitutions $\epsilon_o \to \epsilon'$, $\mu_o \to \mu'$, $k_o \to k'$, $z_o \to z'$ and $s_n \to s'_n$.

The EM field in the slab includes both solutions, s'_n and $-s'_n$, for example,

$$\Phi^- = \sum_n [\Phi_n \exp(-js'_n y) + \Phi'_n \exp(js'_n y)] \tag{19}$$

and similarly for Ψ^-, E^-, H^-. The boundary conditions at $y = -h$

$$E_\nu^- \triangleq E_{\nu n} e^{js'_n h} + E'_{\nu n} e^{-js'_n h} = 0, \ \nu = x \text{ or } z \tag{20}$$

allow us to evaluate Φ' and Ψ' by Φ and Ψ.

Proceeding in the way shown in the Section above, we arrive at

$$\begin{gathered}
E_{xn} = k_o k z_o \Psi_n - r_n s_n \Phi_n = \alpha'_m S_{n-m} P_{n-m}(\cos\Delta) \\
\tfrac{z_o}{2}[H^+_{xn} - H^-_{xn}] = -r_n S_n A_n z_o \Psi_n - k k_o B_n \Phi_n = \beta'_m P_{n-m}(\cos\Delta) \\
A_n = \tfrac{1}{2}\left(1 - \frac{s'_n}{s_n}\frac{\mu_o}{\mu'}\frac{1+\exp(js_n 2h)}{1-\exp(js_n 2h)}\right), \ B_n = \tfrac{1}{2}\left(1 - \frac{s_n}{s'_n}\frac{\epsilon'}{\epsilon_o}\frac{1+\exp(js_n 2h)}{1-\exp(js_n 2h)}\right) \\
\frac{r_n}{k_o} E_{zn} = -r_n^2 z_o \Psi_n - \frac{k}{k_o} r_n s_n \Phi_n = \alpha_m S_{n-m} P_{n-m}(\cos\Delta) \\
\frac{z_o}{2}\frac{r_n}{k_o}[H^+_{zn} - H^-_{zn}] = -\frac{k}{k_o} r_n S_n A_n z_o \Psi_n + k k_o B_n \Phi_n = \beta_m P_{n-m}(\cos\Delta)
\end{gathered} \tag{21}$$

while relations (16) remain in the previous form.

The pair of unknowns α'_m and β'_m is eliminated from the above solution for EM field in the same manner as previously described. Taking into account that

$$\exp(js'_n 2h) \to \infty, \ A_n \to A', \ B_n \to B', \text{ if } n \to \infty \ (n < N^- \text{ or } n > N^+), \tag{22}$$

we obtain relations analogous to (14), which must be fulfilled for every $n \in [N^-, N^+]$

$$\begin{gathered}
\textstyle\sum_{m=M^-}^{M^+} \Big\{ \alpha_m \left[\frac{A_n + E_n(B_n - A_n)}{A_n + C D_n (B_n - A_n)} - \frac{A'}{A' + C(B' - A')}\right] \frac{k}{k_o} S_{n-m} - \\
j\beta_m \left[\frac{j s_n / r_n}{A_n + C D_n (B_n - A_n)} - \frac{S_{n-m}}{A' + C(B' - A')}\right] \Big\} P_{n-m}(\cos\Delta) = 0 \\
\textstyle\sum_{m=M^-}^{M^+} \Big\{ j\alpha_m \left[\frac{j s_n / (r_n) A_n B_n}{A_n + C D_n (B_n - A_n)} S_{n-m} - \frac{A' B'}{A' + C(B' - A')}\right] + \\
\beta_m \left[\frac{A_n + E_n(B_n - A_n)}{A_n + C D_n (B_n - A_n)} - \frac{A'}{A' + C(B' - A')}\right] \frac{k}{k_o} \Big\} P_{n-m}(\cos\Delta) = 0 \\
C = 1/(1 - k^2/k_o^2), \ D_n = r_n^2/(r_n^2 + k^2), \ E_n = k_o^2/(r_n^2 + k^2).
\end{gathered} \tag{23}$$

The eigenvalue problem is then closed in the system of homogeneous equations (23) plus (16), depending on r, k (ω given). The dispersive relation is

$$\mathrm{Det}(r, k; \omega) = 0 \tag{24}$$

where Det is the determinant of the above-mentioned system of equations.

The relation (24) describes wave-number of EM modes propagating in arbitrary direction. Following the assumption $0 < r < K$, this curve is represented in a single Brillouin zone. Complex solutions for r can occur for two reasons[4,5,11]

- Bragg reflection of waves from strips that can take place at $r \approx K/2$,
- radiation of waves into a vacuum above the strips, if some s_n, for example, s_{-1} is a wave vector component of propagating mode in a vacuum. This is the generalized case of so-called leaky wave antenna[12] ($k \neq 0$).

Summarizing this Section let's note, that in case of multilayered structure, we can use the presented method of analysis, applying representation of fields on the border between the layers like that in (4). This allows us to express fields scattered by one system of strips having period Λ, in the form of Floquet expansion suitable for another periodic system with different period Λ' and even orientation (in which case we should rotate the system of coordinates). There is always a finite number of field harmonics which must be accounted for in the expansion because, due to imaginary-valued s_n, higher harmonics vanish fast and do not contribute to the field in the neighbouring layer.

Certain Nonhomogeneous Problem

Let's consider a case of strips shown in Fig.1a) for $k = 0$, $E_x = 0$ for simplification, that results in $[H_z] = 0$, $\Phi = 0$, thus also $\beta_m = 0$ in expansion (10).

Imagine that strips are transversely scratched, and in each scratch there is a uniform electric field E_z applied, that excites current along the strip. The scratching is infinitely dense and the electric source is perfectly conducting.

In equations (16), E_z is evaluated in the strip center as dependent on spectral variable r (in this Section $E_z \neq 0$, however). Its inverse Fourier transform (see Appendix) gives us the value dependent on strip number q

$$E_z(q\Lambda) = E_q = -j\frac{k_o}{K}\int_0^K \frac{\pi/K}{\sin \pi r/K} \sum_{m=M^-}^{M^+} (-1)^m \alpha_m P_{-m-r/K}(-\cos\Delta) e^{-jrq\Lambda} dr \qquad (25)$$

where α_m, which are subjected to Eqs.(14) (but not to (16)), are dependent on α_0 that is allowed to be a function of r.

Let's denote the solution of Eqs.(14) by $\bar{\alpha}_m$. In order to satisfy (25) we must apply

$$\alpha_0(r) = j\frac{\sin \pi r/K}{\pi k_o/K} \frac{E_q e^{jrq\Lambda}}{(-1)^m \bar{\alpha}_m P_{-m-r/K}(-\cos\Delta)} \qquad (26)$$

which substituted into (18), and after applying inverse Fourier transform yields

$$J_p = \frac{4}{z_o k_o} E_q \int_0^K \frac{\bar{\alpha}_m P_{-m-r/K}(\cos\Delta)\sin \pi r/K}{(-1)^m \bar{\alpha}_m P_{-m-r/K}(-\cos\Delta)} e^{jr(q-p)\Lambda} \sin \pi \frac{r}{K} dr/K\,. \qquad (27)$$

This is the total current flowing in the p-th strip and excited by a given E_q, constant along q-th strip ($k = 0$). Allowing E_q dependent on z, we must account for β_m and the spectral variable k in the considerations.

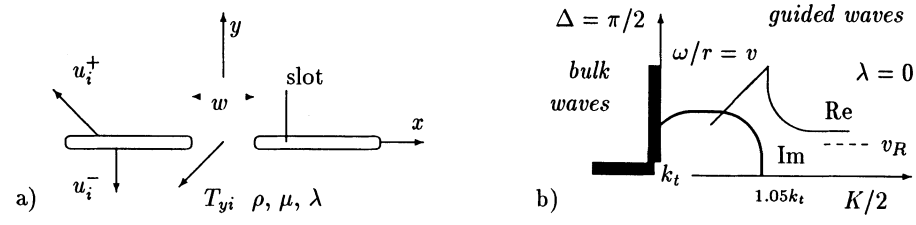

Figure 2. **a)** Periodic slots in elasic body. **b)** Dispersive curve in Bragg reflection area.

ELASTIC WAVES - PLANAR PERIODIC SLOTS

In this Section we consider the eigenvalue problem for waves propagating along a planar system of periodic slots in an elastic body. It can be considered, that two elastic halfspaces are bonded each to the other, where the bonding is perfect between slots, and there is a traction-free area in slots (Fig.2a). Thus

$$\begin{gathered}\mathbf{T} = \mathbf{T}^+ = \mathbf{T}^-,\ \mathbf{T} = 0, \quad \text{on slots} \\ \mathbf{v} = \partial_x[\mathbf{u}] = \partial_x[\mathbf{u}^+ - \mathbf{u}^-] = 0, \quad \text{between slots} \\ [\mathbf{u}] = 0, \quad \text{in the middle between slots, } x = 0\end{gathered} \tag{28}$$

where $\mathbf{T} = [T_{yx}, T_{yy}, T_{yz}]$ are stress components, and $\mathbf{u} = [u_x, u_y, u_z]$ are particle displacements. In what follows, we will consider the case[7] $T_{yz} = 0$, $u_z = 0$ and, in correspondence to the previous Section, we apply $k = 0$ for simplicity.

Let's apply traction $\mathbf{T}\exp(j\omega t - jkx)$ to the surface of the upper halfspace. The amplitude of the particle displacement vector is (apply $\mathrm{Im}\{s^\nu\} < 0$)

$$\begin{gathered}\mathbf{u}^+ = \mathbf{g}(k)\mathbf{T} \\ s^\nu = (k_\nu^2 - k^2)^{1/2},\ \nu = t, l \qquad \mathbf{g} = \begin{bmatrix} \frac{k_t^2 s^t}{\mu w} & jk\frac{k_t^2 - 2r^2 + 2s^t s_l}{\mu w} \\ -jk\frac{k_t^2 - 2r^2 + 2s^t s_l}{\mu w} & \frac{k_t^2 s^l}{\mu w} \end{bmatrix} \\ k_t = \omega\sqrt{\tfrac{\rho}{\mu}},\ k_l = \omega\sqrt{\tfrac{\rho}{\lambda+2\mu}}\end{gathered} \tag{29}$$

$$w = (k_t^2 - 2k^2)^2 + 4k^2 s^t s^l \qquad w(k \to \pm\infty) = (k_t^2 - k_l^2)(k_t^2 - 2k^2)$$

where ρ, μ, λ are mass density and Lamé constants of the body. For lower halfspace the relations are analogous, but we must apply substitution $s^\nu \to -s^\nu$ in order to satisfy the radiation condition, the substitution resulting in $\mathbf{g}(k) \to \mathbf{g}'(k)$. Note, that $w(k_R) = 0$ is the Rayleigh-wave solution. Below, $k \to r + nK$.

In accordance with the method and in order to satisfy boundary conditions (28) we apply a representation for n-th harmonic components of $\mathbf{T}$ and $\mathbf{v}= \partial_x[\mathbf{u}]$

$$\mathbf{T}_n = \mathbf{a}_m P_{n-m}(\cos\Delta), \quad \mathbf{v}_n = \mathbf{b}_m S_{n-m} P_{n-m}(\cos\Delta) \tag{30}$$

($\mathbf{a}$, $\mathbf{b}$ - vectors). On the strength of (29), the relation between them is

$$\begin{gathered}\mathbf{v}_n = \mathbf{G}(r + nK)\mathbf{T}_n \\ \mathbf{G}(k) = j2\frac{k_t^2}{\mu}\begin{bmatrix} \frac{ks^t}{w} & 0 \\ 0 & \frac{ks^l}{w} \end{bmatrix}, \quad \mathbf{G}(|k| \to \infty) = S_k\mathbf{G}_\infty = \frac{k_t^2/\mu}{k_t^2 - k_l^2}S_k\mathbf{I}.\end{gathered} \tag{31}$$

Note that the asymptotic relation between $\mathbf{v}_n$ and $\mathbf{T}_n$ is as required by the method, resulting from similar singularities of the corresponding functions at the slot edges.

The consistency condition (for $|n|$ large) requires that

$$\mathbf{b}_m = \mathbf{G}_\infty \mathbf{a}_m \tag{32}$$

so that we arrive at the following equations which should be satisfied for all n

$$\sum_m [\mathbf{G} - S_{n-m}\mathbf{G}_\infty]\,\mathbf{a}_m P_{n-m}(\cos\Delta) = 0, \quad \text{that is,} \quad \begin{bmatrix} \cdot & & & & & & & \\ \cdot & \cdot & & & & & & \\ \cdot & \cdot & \cdot & \cdot & \cdot & \cdot & \cdot & \\ \cdot & \cdot & \cdot & \cdot & \cdot & \cdot & \cdot & \\ \cdot & \cdot & \cdot & \cdot & \cdot & \cdot & \cdot & \\ & & & & & & & \cdot \end{bmatrix} [\mathbf{a}_m] = 0 \tag{33}$$

The limits for m are given in (15), they can also be deduced from the general form of the matrix (33) (its dimension depends on how fast $\mathbf{G}$ becomes $\mathbf{G}_\infty$).

Equations (33), together with the following one resulting from (28)

$$\sum_m (-1)^m \mathbf{a}_m P_{-m-r/K}(-\cos\Delta) = 0 \tag{34}$$

are a closed system of equations, the resulting dispersive relation is like (24).

Two examples below show how easy the method is in the case of relatively dense slots (strips in EM case), where (N^-, N^+) is narrow.

Example - dense system of slots. Consider $T_{yy} = 0$, $[u_y] = 0$ on $y = 0$, and $K \gg k_t$ resulting in $N^- = N^+ = 0$. That is, in equations (33) we have $m = 0, 1$ and $n = 0$ only. Following the above assumption we have $\mathbf{a}_m = [\alpha_m, 0]$, thus (33) yields

$$(2\frac{rs^t}{w} + \frac{1}{k_t^2 - k_l^2})\alpha_0 + (2\frac{rs^t}{w} - \frac{1}{k_t^2 - k_l^2})\alpha_1 = 0 \tag{35}$$

where s^ν and w are evaluated from (29) at $k = r$. Dispersive relation (24) is

$$s^t = \frac{w}{2r(k_t^2 - k_l^2)} \frac{P_{-r/K} - P_{r/K}}{P_{-r/K} + P_{r/K}}, \quad \text{that is } \approx 0. \tag{36}$$

Because $w(r) > 0$ for $r \in (k_t, k_R$, the solution for r exists, and $k_t < r < k_R$. It is not surprising. For a slot system denser and denser, we arrive at the free surface $y = 0$, where the Rayleigh wave solution exists.

In a complementary case $[u_x] = 0$, we arrive at (36) but with replacement $s^t \to s^l$, in which case the real solution to r does not exists (w is complex when s^l is small).

Example - wave-guiding and Bragg reflection by strips. This example concerns the case $K \approx r \approx 2k_t$ and $[u_y] = 0$, $T_{yy} = 0$ on $y = 0$. It is evident we must apply at least $N^- = -1$ and $N^+ = 0$. Denotations are $s'_0 = \sqrt{r^2 - k_t^2}$, $s'_{-1} = \sqrt{(r-K)^2 - k_t^2}$, and analogously $w'_n = \frac{1}{2}w(r + nK)/(k_t^2 - k_l^2)$. Equations (33) yield for $n = -1, 0$ correspondingly (denotation for α_m as in previous example, and $R = r - K$)

$$\begin{aligned} \alpha_{-1}\left(\frac{Rs'_{-1}}{w'_{-1}} + 1\right) + \alpha_0\left(\frac{Rs'_{-1}}{w'_{-1}} - 1\right) + \alpha_1\left(\frac{Rs'_{-1}}{w'_{-1}} - 1\right)\cos\Delta = 0 \\ \alpha_{-1}\left(\frac{rs'_0}{w'_0} + 1\right)\cos\Delta + \alpha_0\left(\frac{rs'_0}{w'_0} + 1\right) + \alpha_1\left(\frac{rs'_0}{w'_0} - 1\right) = 0 \end{aligned} \tag{37}$$

A numerical solution to the dispersive relation resulting from the above equations and (34), is shown in Fig.2.b) for the case $\lambda = 0$ and $\cos\Delta = 0$. There is a complex solution if $K/2$ is a little above k_t, and a real solution for larger K. Both shows guided waves propagating along the system of slots, where the wave-field vanishes deep into the body. Complex wave number r (a stopband) results from Bragg reflections phenomena taking place in the periodic system of strips.

This phenomenon is expected to have some application in SAW devices.[13,14] Consider two piezoelectric substrates bonded by metal strips which serve as electrodes of IDT exciting the guided wave in the system. In stopband we have a 'resonator', a compact structure that need not be packed in a metal case. The device like RAC, in which guided wave propagate slant to strips and where 2-dimensional Bragg reflection is exploited, can also be constructed and analyzed in a similar way.

CONCLUSIONS

We have shown the usefulness of the method[3–5] in analysis of certain wave problems for isotropic media. In a similar way we can treat the anisotropic cases, dealing with E and H fields directly instead with Hertz potentials. Corresponding boundary conditions must be, following the method, stated for fields or their derivatives exhibiting the same singularity at the strip edges, like $[H_x]$ and $\partial_x E_z$ above. Relations will be much more complicated in this case.

It is also interesting, that relations (I) have more general form, concerning functions which behave as $(\cos\Delta - \cos\theta)^{\mu}$, $\mu > -1$. However they are much more complicated and there is open question, if a similar method to that presented in this paper can work with them efficiently.[6]

As mentioned in the Introduction, we exploited certain solutions (*) to electrostatic problems (**) for periodic strips. One may arrive at the conclusion, that having other and much more complicated planar system of strips, an analogous method can be applied provided that the corresponding electrostatic solution is known. The solution should include some degree of freedom in order to satisfy separate boundary conditions, one for every strip in the group. Indeed, such a solution is known[11] in the case of periodic systems of groups of 'periodic strips'.

However, further generalization is possible. Consider the finite plane system of p strips having edges at $x_q, q = 1, \ldots, 2p$. The solution of the electrostatic problem having the required degrees of freedom in arbitrary b_q (usually, they are evaluated from known strip potentials), is[15]

$$E = \mathrm{Re}\{F(x)\},\ D = \mathrm{Im}\{F(x)\},\ F = \Big(\sum_{q=1}^{p} b_q x^{q-1}\Big)\left(\prod_{q=1}^{2p}(x - x_q)\right)^{-1/2} \qquad (***)$$

In the case of sparse periodic systems of the above groups of strips (Λ large), we can apply the above-expressed functions to model real fields in the system. The following key step in the purpose to obtain relation analogous to (*), is the application of FFT, yielding harmonic expansions with coefficients E_n and $D_n = S_n E_n$, just analogous to P_n and $S_n P_n$ in (*). The calculations should be performed with a long series, as required by the method in Eq.(12).

Acknowledgments

The author wish to express his deep gratitude to Professor C.M. Soukoulis and Dr. R.A. Shivvers for their editorial comments with regard to the paper style and grammar.

Work supported by National Scientific Committee under Grant 3 1212 9101. The main thesis of this paper has been presented at seminars in Rensselaer Polytechnic Institute in Troy, Dec. 10, 1990, and in Trondheim University, Jan. 13, 1992. Discussions with Prof. Harry F. Tiersten and Prof. Kjell Bløtekjær are acknowledged.

Appendix

Let a certain function depending on $r \in (0,\ K)$ have the form (see (I) for instance)

$$F(r) = \alpha_m(r) P_{n-m}(\cos\Delta)$$

which can be rewritten as a function spanned over a whole axis $r' \in (-\infty, \infty)$

$$F(r') = \{\alpha_m(K(r' - n)) P_{n-m}, \text{ for } n \le r' < n + 1\}\ .$$

Assuming that F is a Fourier transform and r' is spectral variable, its inverse Fourier transform evaluated for $x = p\Lambda$ is

$$f(x) = \int_{-\infty}^{\infty} F(r')e^{-j2\pi r'x/\Lambda}dr' = \frac{1}{K}\int_0^K \sum_{n=-\infty}^{\infty} \alpha_m(r)P_{n-m}e^{-jrp\Lambda}dr\,.$$

REFERENCES

1. K. Uchida, T. Noda, T. Matsunaga, Spectral domain analysis of electromagnetic wave scattering by an infinite metallic grating in case of oblique incidence and arbitrary polarization, *IEEE Trans.*, **AP-36**, pp. 415–422 (1988)
2. J.D. Achenbach, Z.I. Li, Propagation of horizontally polarized transverse waves in a solid with a periodic distribution of cracks, *Wave Motion*, **8**, pp. 371–379 (1986)
3. Chiao-Min Chu, Propagation of waves in helical wave guides, *J. Appl. Phys.*, **29**, pp. 88–99 (1958)
4. K. Bløtekjær, K.A. Ingebrigtsen, H. Skeie, A method for analyzing waves in structures consisting of metal strips on dispersive media, *IEEE Trans.*, **ED-20**, pp. 1133–1138 (1978); Acoustic surface waves in piezoelectric material with periodic Mmtal strips on the substrate, *ibid.*, pp. 1139–1146
5. E. Danicki, Theory of periodic interdigital transducers (IDT) of surface acoustic waves (SAW), *J. Tech. Phys.*, **19**, 1, pp. 89-102 (1978); Theory of surface acoustic wave slant propagation in periodic electrode system, *ibid.*, pp.69–77
6. E. Danicki, New approach in the theory of multistrip waveguides, *Arch. of Acoust.*, **15**, 1-2, pp. 45–48 (1990)
7. E. Danicki, Analysis of surface acoustic wave in a layered structure with periodic delamination, in O. Leroy, M.A. Breazeale, *Physical Acoustics, Fundamentals and Applications*, Plenum Press, NY, 1991, pp.281–285
8. B. Langli, Electromagnetic waves in periodic structures, master-degree thesis, University of Trondheim, NTH, 1992
9. A. Erdélyi, W. Magnus, F. Oberhettinger, F. G. Tricomi, *Higher Transcendental Functions*, McGraw-Hill, NY 1953, v.1
10. R.E. Collin, *Field Theory of Guided Waves*, McGraw-Hill, 1960
11. E. Danicki, D. Gafka, Propagation, generation, and detection of SAW in a multiperiodic system of metal strips on a piezoelectric substrate, *JASA*, **89**, pp. 27–38 (1991)
12. M. Ghomi, H. Baudrand, C. Cavalli, New approach for computing radiation pattern of dielectric leaky-wave antenna, *Electr. Lett.*, **25**, 5, pp. 345-346 (1989)
13. E. Danicki, Perturbation theory of surface acoustic wave reflection from a periodic structure with arbitrary angle of incidence, *Arch. Mech.*, **36**, 5-6, pp. 623–638 (1984)
14. E. Danicki, SAW Scattering by perfectly conducting elliptic disk on anisotropic piezoelectric halfspace, *1990 IEEE Ultras. Symp.Proc.*, pp. 109–112
15. R.C. Peach, A General approach to the electrostatic problem of the SAW interdigital transducer, *IEEE Trans.*, **SU-28**, 2, pp. 96–105 (1981)

SYNCHRONOUS FORWARD TO BACKWARD SURFACE ACOUSTIC WAVE COUPLING IN REVERSING MULTISTRIP COUPLER

Eugene J. Danicki

Polish Academy of Sciences, IFTR
21 Świętokrzyska Str., 00-049 Warsaw, Poland

INTRODUCTION

Surface acoustic wave (SAW) propagating on a surface of piezoelectric substrates is accompanied with a wave of electric potential on the surface. SAW can be excited by metal strips on the surface of a piezoelectric body when they are supplied with electric potential. Multistrip coupler is the directional coupler of two adjacent SAW channels where the coupling is provided by periodic metal strips covering both channels.

A new reversing multistrip coupler (rmsc) is proposed and analyzed, where the strips are interlaced between the channels. This results in coupling of forward propagating potential wave in one channel to the backward propagating wave in the other channel in certain frequency bands. The device can find many applications in SAW technology, allowing construction of SAW pass-band and dispersive filters.

An interesting mathematical problem arises in modelling the above system of interlaced strips. A 'continuous' eigenvalue problem with mixed electric, and mechanical boundary conditions must be solved to characterize SAW propagation in periodic systems of thin metal strips. Another 'discrete' eigenvalue problem is encountered in rmsc, resulting from the equality of certain strip currents and potentials in both acoustic channels.

Let's consider surface acoustic wave propagating in a piezoelectric halfspace $y \geq 0$. We observe a wave of particle displacement $\vec{\mathbf{u}} \exp(j\omega t - jk_v x)$ on the substrate surface, and a wave of electric potential $\varphi \exp(j\omega t - jkx)$ accompanying SAW due to the substrate piezoelectricity, ω and k_v are angular frequency and wave-number. If the substrate surface is metallized, the SAW wave number takes another value, k_o where $k_o > k_v$, and instead of surface electric potential which is zero, there is surface electric charge density $\Delta D_\perp$ equal to electric flux discontinuity on both sides of metallization. The relative velocity change $\Delta v/v = (k_v - k_o)/k_o$ is an important parameter characterizing piezoelectric substrates (another parameter[1] is the 'effective surface permitivity' ε_e).

Photonic Band Gaps and Localization, Edited by
C.M. Soukoulis, Plenum Press, New York, 1993

In the case of part surface metallization in the form of a periodic metal strip deposited on the substrate surface, the corresponding wave-numbers of SAW propagating perpendicularly to strips are r_v and r_o for free, and short-circuited strips, $k_v < r_v < r_o < k_o$. Let the system of strips span over two adjacent acoustic channels, and let the SAW beam propagate only in the upper channel (Fig.1.a). The electric potential induced on the strips by SAW is distributed over the lower channel as well. This is the travelling-wave potential which excites SAW in the lower channel. This is synchronous excitation because SAWs in both channels have the same velocity. The system of strips is then a directional coupler of two acoustic channels, the microstrip coupler[2] (msc).

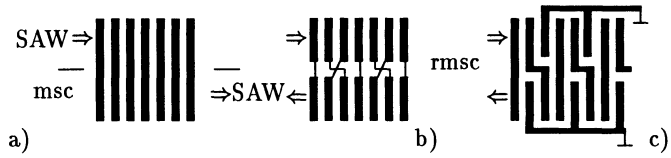

Figure 1. a) Multistrip coupler (msc). **b)** Reversing msc in basic configuration and **c)** practical structure

Let's consider periodic strips with three strips per wave-length of SAW. Thus, the following strip potentials are phase-shifted by $0°$, $-120°$, $-240°$, corresponding to $\exp(j\omega t - jrn\Lambda)$, $\Lambda = \frac{1}{3}\omega/r$ and $n = 0, 1, 2$. Let the system of strips has every second and third strip interlaced between the channels (Fig.2.b). In the lower channel, the following strips potentials have phases $0°$, $-240°$, $-120°$, equivalent to $0°$, $120°$, $240°$ respectively. This is a potential wave in synchronism with SAW propagating in the opposite direction as compared to SAW in the upper channel. The system shown in Fig.1b) is reversing directional coupler,[3-5] 'rmsc'.

It is somewhat difficult to make a planar system of strips with strips crossing one over the other. Among several possible solutions in this paper, we consider the system where every third strip is grounded (Fig.1.c). Such strip structures can easily be made with the help of microelectronic technology.

In the next Section, some general theoretical results necessary for description of msc and rmsc are presented. We apply a perfect strip model, that is, we neglect strip elasticity[6] and mass, and also assume perfect strip conductivity. This allows us to apply directly the developed method[7,8] for analyzing waves in periodic strips. The following Sections present the theory of rmsc. In Conclusions, we discuss possible applications of rmsc in SAW devices like SAW filters, resonators, and dispersive delay lines for signal processing.

SAW IN PERIODIC SYSTEM OF STRIPS

Simplified Description Of Piezoelectric Halfspace

Let's apply a traction $T_{yj}\exp(j\omega t - jkx)$ to the surface $y = 0$ of piezoelectric halfspace. If $k > k_s$ where k_s is cut-off wave number of bulk waves, the response of the

substrate will be described by a hermitian Green's matrix

$$u_i = -z_i z_j^* \frac{T_{yj}}{k-k_v} + z_i \frac{\kappa}{k-k_v}\frac{\Delta D_\perp}{\sqrt{\varepsilon_e}}, \quad \varphi = z_j^* \frac{\kappa}{k-k_v}\frac{T_{yj}}{\sqrt{\varepsilon_e}} + \frac{k-k_o}{k-k_v}\frac{\Delta D_\perp}{k\varepsilon_e} \tag{1}$$

where $\kappa^2 = (k_o - k_v)/k_o = \Delta v/v$, and $z_i = z_i(k)$, $z_i(-k) = z_i^*(k)$.

Wave numbers k_v and k_o are the eigenvalues of boundary problems for free and metallized piezoelectric halfspace, $[T_{yj}, \Delta D_\perp]^T = \mathbf{G}(\omega; k)[u_i, \varphi]^T = 0$ and $[T_{yj}, \varphi]^T = \mathbf{G}'(\omega, k)[u_i, \Delta D_\perp]^T = 0$, correspondingly. In narrow bounds $r \approx k_v, k_o$, both $\mathbf{G}$ and $\mathbf{G}'$ resulting from equations of motion of a piezoelectric body can be approximated by the linear functions of k; this was exploited to obtain Eqs.(1) (otherwise, we should apply a more general approximation[9]).

Constraining k to the area close to (k_v, k_o), which is usually very narrow as compared to $k_v - k_s$, z_i can be applied as a constant

$$z_i = -\frac{\kappa}{\sqrt{\varepsilon_e}}\frac{U_i^{(v)}}{\Phi^{(v)}} = k_v \kappa \sqrt{\varepsilon_e}\frac{U_i^{(o)}}{D_\perp^{(o)}}, \quad \varepsilon_e = -\frac{U_i^{(v)}}{k_v \Phi^{(v)}}\frac{D_\perp^{(o)}}{U_i^{(o)}}, \quad \kappa^2 \approx -\frac{v}{4}\Phi^{(v)*} D_\perp^{(o)} \tag{2}$$

where capital letters denote normalized wave-field amplitudes of SAW propagating on free (index v), or metallized (index o), substrate surface $y = 0$.

As mentioned earlier, we apply approximation of perfect weightless conducting strips, that is $T_{yj} = 0$. Eqs.(1) can be transformed into

$$\left.\begin{aligned} A = \frac{u_i}{z_i} \approx \frac{\sqrt{\varepsilon_e}}{\kappa}\left(-\varphi + \frac{1}{k\varepsilon_e}\Delta D_\perp\right) \\ \varepsilon_e(k-k_v)k\varphi - (k-k_o)\Delta D_\perp = 0 \end{aligned}\right\} \quad \text{for } \mathrm{Re}\{k\} > 0$$
$$\text{apply: } k \to -k \text{ and } z_i \leftrightarrow z_i^* \qquad \text{for } \mathrm{Re}\{k\} < 0 \tag{3}$$

It should be stressed that bulk waves, which can be generated in the body by the surface traction if $k < k_s$, are not included in the above description, thus neglected.

To complete characterization of SAW by its wave number k and wave-field amplitudes φ and A, let's introduce SAW's amplitude a, by definition involved in the relation for SAW Poynting vector magnitude $\Pi = \frac{1}{2}|a|^2$. It can be obtained from Eqs.(1) that

$$a = A\sqrt{\omega/2} \tag{4}$$

with accuracy, little dependent on electric boundary conditions, as far as the SAW wave number is close to (k_v, k_o).

Eigenvalue Boundary Problem

The considered boundary problem concerns wave-propagation in periodic systems, thus applying Floquet's theorem, the solution is searched in the form (term $\exp j\omega t$ dropped)

$$E_\parallel(x) = \sum_{n=-\infty}^{\infty} E_n e^{-j(r+nK)x}, \quad \Delta D_\perp(x) = \sum_{n=-\infty}^{\infty} D_n e^{-j(r+nK)x} \tag{5}$$

where r is assumed in the first Brillouin zone $(0 < r < K)$ and $E_\parallel(x) = -\partial_x \varphi(x)$.

Complex amplitudes D_n and E_n are dependent on each other on the strength of Eqs.(3), where we apply $k = r + nK$

$$D_n = -j\varepsilon_e S_{n+r/K}\frac{r+nK-k_v}{r+nK-k_o}E_n$$
$$E_n = j(r+nK)\varphi_n, \quad S_\nu = \begin{cases} 1 & \text{for } \nu \geq 0 \\ -1 & \text{for } \nu < 0 \end{cases}. \tag{6}$$

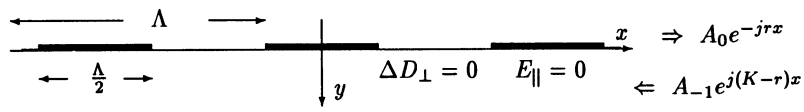

Figure 2. Periodic system of strips on piezoelectric halfspace

It is assumed below, that $K > k_o$. In fact, rmsc works at $K \approx 3k_o \gg k_s$, allowing several simplifications in the following considerations, primarily $(r + nK - k_v)/(r + nK - k_o) \approx 1$ for all n except $n = 0$ or $n = -1$, and r in the assumed domain.

Electric field is shielded under perfectly conducting strips, and the electric charge can be different from zero only on strips (Fig.2), that is

$$\begin{aligned} E_\parallel(x) &= 0, \text{ on strips, } l\Lambda - w < x < l\Lambda + w \\ \Delta D_\perp(x) &= 0, \text{ between strips, } (l-1)\Lambda + w < x < l\Lambda - w \end{aligned} \tag{7}$$

are mixed electric boundary conditions at $y = 0$ plane.

The l-th strip potential and current

$$V_l = V(r)e^{-jrl\Lambda}, \quad I_l = I(r)e^{-jrl\Lambda} \tag{8}$$

depend on r. Below, we consider the two most important cases
- short-circuited (grounded) strips, where strip potentials are zero

$$V(r) = \sum_{n=-\infty}^{\infty} \varphi_n = -j \sum_{n=-\infty}^{\infty} \frac{1}{r + nK} E_n = 0 \tag{9}$$

- free (open) strips, where the electric current flowing to a strip is zero

$$I(r) = j\omega \int_{-w}^{w} \Delta D_\perp(x)\, dx = j2\omega \sin r\frac{\Lambda}{2} \sum_{n=-\infty}^{\infty} \frac{(-1)^n}{r + nK} D_n = 0 \tag{10}$$

A Method Of Solution

Following the method,[7] we apply the representation for the given n-th harmonic components E_n and D_n in the form of finite series including certain new unknowns α_m

$$E_n = \sum_{m=M}^{N+1} \alpha_m S_{n-m} P_{n-m}(\Delta), \quad D_n = -j\varepsilon_e \sum_{m=M}^{N+1} \alpha_m P_{n-m}(\Delta), \tag{11}$$

where S_ν is as defined above in Eqs.(6) and $P_\nu(\Delta) = P_\nu$ - Legendre function (Appendix), $\Delta = \cos Kw = 0$ in the case considered in this paper, limits $M \leq 0$ and $N \geq 0$ are certain integers.

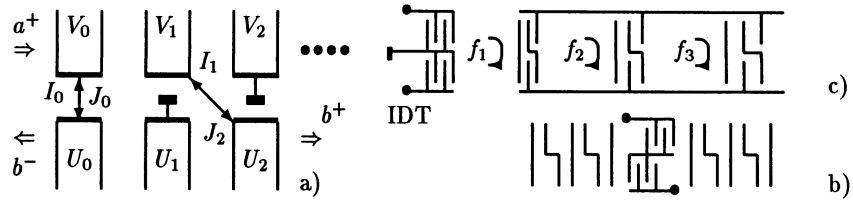

Fig. 3. a) One section of rmsc. **b)** SAW resonator and **c)** dispersive delay line with rmsc.

The representations (11), satisfying the electric boundary conditions (7) (see Appendix), will satisfy also Eqs.(6) if

$$\sum_m \alpha_m \left(1 - S_{n-m} S_{n+r/K} \frac{r + nK - k_v}{r + nK - k_o}\right) P_{n-m} = 0 . \tag{12}$$

In the considered case $K \gg k_o$, the number of unknowns α_m is not large. Indeed, let's note that the solution (11) satisfies Eq.(12) for every $n < M$ and $n > N$ automatically. Assuming $M = -1$ and $N = 0$, we get Eqs.(6) satisfied by the solution in the above two domains of n, independently on α_m, $m \in [-1, 1]$, provided that $K > k_o$ and $0 < r < K$.

Solving Eqs.(12) and applying Eqs.(3) ($A(x) = \sum A_n e^{-j(r+nK)x}$), we obtain

$$\begin{aligned} \alpha_1 &= \alpha_0 \frac{\kappa^2}{2} \frac{r}{r-k}, \quad A_0 = -j\alpha_0 \frac{\kappa\sqrt{\varepsilon_e}}{r-k} \\ \alpha_{-1} &= \alpha_0 \frac{\kappa^2}{2} \frac{K-r}{K-r-k}, \quad A_{-1} = -j\alpha_0 \frac{\kappa\sqrt{\varepsilon_e}}{K-r-k}, \end{aligned} \tag{13}$$

where $k = (k_v + k_o)/2 = \omega/k$, α_o is arbitrary constant.

Propagation of SAW in a Periodic System of Strips

The last condition to be satisfied is either Eq.(9) or (10) which can be rewritten in the form (evaluation of the the series over n, see Appendix)

$$\begin{aligned} V(r) &= \alpha_0 \frac{\pi}{jK \sin \pi r/K} V_r, \qquad I(r) = \alpha_0 \omega \varepsilon_e \Lambda I_r \\ V_r &= \sum_m \frac{\alpha_m}{\alpha_0} (-1)^m P_{-m-r/K}, \quad I_r = \sum_m \frac{\alpha_m}{\alpha_0} P_{-m-r/K} . \end{aligned} \tag{14}$$

Corresponding dispersion relations are

$V_r = 0$, $r = r_o$, for short-circuited strips,

$I_r = 0$, $r = r_v$, for open strips

which explicitly are (apply '$-$' for r_o and '$+$' for r_v)

$$(r-k)(K-r-k) \mp \kappa^2 K p (K/2 - k) = 0, \quad p = \frac{\sin \pi r/K}{\pi (P_{-r/K})^2} \approx \frac{r}{K}\left(1 - \frac{r}{K}\right) \tag{15}$$

Well outside the Bragg stopband ($K/2 \neq k$; in case of rmsc $K \approx 3k$), we have

$$r_o \approx k \left(1 + \frac{1}{2}\frac{\Delta v}{v}\left(1 - \frac{k}{K}\right)\right), \quad r_v \approx k \left(1 - \frac{1}{2}\frac{\Delta v}{v}\left(1 - \frac{k}{K}\right)\right) \tag{16}$$

Finally, the symmetry in Eqs.(14) allows to write

$$I(r) = j2\omega\varepsilon_e V(r) \frac{(r - r_v)(K - r - r_v)}{(r - r_o)(K - r - r_o)} \sin \pi r/K \tag{17}$$

and

$$\begin{aligned} A_0 &= V(r) \frac{\kappa\sqrt{\varepsilon_e}}{\pi P_{-r/K}} \frac{K - r - k}{(r - r_o)(K - r - r_o)} K \sin \pi r/K \\ A_{-1} &= V(r) \frac{\kappa\sqrt{\varepsilon_e}}{\pi P_{-r/K}} \frac{r - k}{(r - r_o)(K - r - r_o)} K \sin \pi r/K \end{aligned} \tag{18}$$

where, following Eqs.(3)

$$A_0(r) e^{-jrx} \quad \text{and} \quad A_{-1}(r) e^{-j(r-K)x} \tag{19}$$

are forward and backward propagating SAWs, depicted in Fig.2.

THEORY OF RMSC

Modelling of Electric Field in the System

It is seen in Fig.1.c) that the considered system is periodic with period 3Λ. Hence, the Floquet theorem requires the following representation for strip potentials and currents

$$\sum_{n=0}^{2} V(s+nK')e^{-j(s+nK')x}, \quad \sum_{n=0}^{2} I(s+nK')e^{-j(s+nK')x}, \quad x = l\Lambda \tag{20}$$

where, in order to adopt the results of the previous Section, we must apply

$$0 < r = s + nK' < K, \quad K' = \frac{K}{3} \tag{21}$$

In what follows, we consider rmsc working in a narrow frequency band where coupling between forward wave in the upper acoustic channel and backward wave in the lower channel is strongest. This takes place at

$$s = K' + \delta, \quad |\delta| \ll K', \quad r_v \approx K' \approx r_o \approx k = \omega/v \tag{22}$$

so that in Eqs.(21), we must apply either $n = 0, 1, 2$ for $\delta < 0$, or $n = -1, 0, 1$ when $\delta > 0$, and similarly in Eqs.(20).

On the strength of the previous Section and the above assumption

$$\begin{gathered} I(s+nK') = y_n V^n, \quad V^n = V(s+nK') \\ y_0 = Y\frac{d_v+\delta}{d_o+\delta}, \quad y_1 = Y\frac{d_v-\delta}{d_o-\delta} \\ Y = j\omega\varepsilon_e\sqrt{3}, \quad d_v = K' - r_v, \quad d_o = K' - r_o \end{gathered} \tag{23}$$

and $y_2 \approx 0$ (or $y_{-1} \approx 0$ in case $\delta > 0$), see Eq.(17).

Discrete Eigen-Problem

It is seen from Eqs.(20) that we can consider only three strips numbered $l = 0, 1, 2$ (Fig.3a), and having potentials V_l, U_l and currents flowing to them I_l and J_l, in upper and lower channels correspondingly. Kirchhoff's laws yield

$$\begin{gathered} V_0 = V^0 + V^1 + V^2 = U_0 = U^0 + U^1 + U^2 \\ V_1 = zV^0 + \alpha zV^1 + \alpha^2 zV^2 = U_2 = z^2U^0 + \alpha^2 z^2 U^1 + \alpha^4 z^2 U^2 \\ V_2 = z^2V^0 + \alpha zV^1 + \alpha^2 zV^2 = 0 \\ U_1 = zU^0 + \alpha zU^1 + \alpha^2 zU^2 = 0, \; I_0 + J_0 = y_0V^0 + y_1V^1 + y_0U^0 + y_1U^1 = 0 \\ I_1 + J_2 = zy_0V^0 + \alpha zy_1V^1 + z^2y_0U^0 + \alpha^2 z^2 y_1U^1 = 0 \\ \alpha = \exp(-jK'\Lambda) = \exp(-j2\pi/3), \; 1-\alpha = -j\sqrt{3}\alpha, \; 1+\alpha = -\alpha^2, \; \alpha^3 = 1 \\ z = \exp(-js\Lambda) = \alpha z', \quad z' = \exp(-j\delta\Lambda) \approx 1 \end{gathered} \tag{24}$$

resulting in the following homogeneous set of linear equations

$$\begin{bmatrix} (d_o+\delta) & -\alpha(d_o-\delta) & \alpha(d_o+\delta) & -(d_o-\delta) \\ (d_o+\delta) & -(d_o-\delta) & z'(d_o+\delta) & -z'(d_o-\delta) \\ (d_v+\delta) & (d_v-\delta) & (d_v+\delta) & (d_v-\delta) \\ (d_v+\delta) & \alpha(d_v-\delta) & \alpha z'(d_v+\delta) & z'(d_o-\delta) \end{bmatrix} \begin{bmatrix} V^0/(d_o+\delta) \\ V^1/(d_o-\delta) \\ U^0/(d_o+\delta) \\ U^1/(d_o-\delta) \end{bmatrix} = 0 \tag{25}$$

The determinant of the above system of equations should be equal to zero

$$\left\{\sqrt{3}[(d_o+\delta)(d_v-\delta)-(d_v+\delta)(d_o-\delta)]\cos\delta\frac{\Lambda}{2}-\right.$$
$$\left.[(d_o+\delta)(d_v-\delta)+(d_v+\delta)(d_o-\delta)]\sin\delta\frac{\Lambda}{2}\right\}^2+12(d_o^2-\delta^2)(d_v^2-\delta^2)=0 \tag{26}$$

which most important solutions (δ small as assumed before) are

$$\delta_1^2=d_od_v,\quad\text{and}\quad\delta_2^2\approx d_od_v(1-\frac{2}{\sqrt{3}}\Lambda(d_v-d_o)) \tag{27}$$

One may see there are stopbands in both SAW modes, having wave numbers $s_1=K'+\delta_1$ and $s_2=K'+\delta_2$. This happens if δ_n is complex, that is if $d_od_v=(K'-r_o)(K'-r_v)<0$. From Eqs.(16), we obtain the relative stopband width is $\frac{2}{3}\Delta v/v$, thus maximum imaginary value of δ_n is $\frac{1}{3}k\Delta v/v$ when $k\approx K'=K/3$.

The corresponding eigenvalue-eigenvector pairs of the system (25) are

$$\left\{\delta,[V^0,V^1,U^0,U^1]^T\right\}=\left\{\delta_1,\,[1,1,1,1]^T\right\},\,\left\{\delta_2,\,[\beta,\beta^*,\beta^*,\beta]^T\right\},\;\beta=1+j\frac{4}{\sqrt{3}} \tag{28}$$

SAW Wave-Field in the System

The above-discussed potential waves $V^n\exp(-j(s+nK')x)$ in the upper channel and $U^n\exp(-j(s+nK')x)$ in the lower one are accompanied with corresponding particle-displacement waves at the substrate surface. They are

$$A_0^c(r+nK')e^{-j(s+nK')x},\quad A_{-1}^c(s+nK')e^{-j(s+nK'-K)x} \tag{29}$$

where amplitudes A_n^c, $n=0,-1$ can be evaluated from Eqs.(18), c denote the channel.

Most important wave-components are these which wave numbers fall in the vicinity of SAW wave numbers, r_o or $-r_o$, because they are closely related to SAW amplitudes, Eq.(3). Following the applied assumptions $K'\approx k\approx r_o$ one obtains that the important wave-component are A_0 related to V^0, U^0 and A_{-1} related to V^1, U^1. For convienence, their corresponding amplitudes are expressed below by means of SAW amplitudes, a and b in the upper and the lower channels

$$a_0=\frac{\kappa\sqrt{3\omega\varepsilon_e/2}}{\pi P_{-1/3}}\frac{V^0}{K'-r_o+\delta},\quad a_{-1}=\frac{\kappa\sqrt{3\omega\varepsilon_e/2}}{\pi P_{-1/3}}\frac{V^1}{K'-r_o-\delta}$$
$$b_0=\frac{\kappa\sqrt{3\omega\varepsilon_e/2}}{\pi P_{-1/3}}\frac{U^0}{K'-r_o+\delta},\quad b_{-1}=\frac{\kappa\sqrt{3\omega\varepsilon_e/2}}{\pi P_{-1/3}}\frac{U^1}{K'-r_o-\delta} \tag{30}$$

where δ_1 or δ_2 should be substituted in place of δ; thus, amplitudes a and b should be provided by yet another index $n=1,2$.

Note, that V^0, V^1, U^0, U^1 are eigenvectors dependent on δ_n, as given by Eqs.(28). Let the amplitude of SAW mode corresponding to eigenvalue δ_1 is a and that corresponding to δ_2 is b. Hence, the SAW wave-fields in the system in upper and lower channels are correspondingly

$$a(1+\gamma_1e^{j2K'x})e^{-j(K'+\delta_1)x}+b(\beta+\beta^*\gamma_2e^{j2K'x})e^{-j(K'+\delta_2)x},$$
$$a(1+\gamma_1e^{j2K'x})e^{-j(K'+\delta_1)x}+b(\beta^*+\beta\gamma_2e^{j2K'x})e^{-j(K'+\delta_2)x},$$
$$\gamma_n=\frac{K'-r_o+\delta_n}{K'-r_o-\delta_n},\;n=1,2,\;\delta_2\approx\delta_1=-\sqrt{(K'-r_o)(K'-r_v)} \tag{31}$$

Let's finally note, that we can apply either $+\delta_n$ or $-\delta_n$ in the above relations (happily, β does not depend on sign of δ_n), or both of them, in case of finite structure. The corresponding waves are modes propagating right (if $\mathrm{Im}\{\delta_n\} < 0$), and left (if $\mathrm{Im}\{\delta_n\} > 0$), each modes composed of forward, and backward-propagating components, the relation between their amplitudes involves γ_n.

PROPERTY OF HALF-INFINITE RMSC

In case of half-infinite system of strips, we must choose only these solutions for δ_n which fulfill radiation condition at infinity ($x \to \infty$). For example in stopband, the corresponding δ_n must have a negative imaginary value. Assuming the proper values are chosen for δ_n, Eqs.(31) completely describes SAW wave-field in the system.

Let's assume there is incident SAW in the upper channel only (Fig.3a)

$$a^+ e^{-jkx}. \tag{32}$$

We need boundary conditions at the border between rmsc and the free area ($x = 0$). The only simple possibility to get this condition is to compare SAW wave-fields on both sides of the border which have similar wave numbers. This stays for equality of both particle displacements, and stress on both side of $x = 0$ (note that stress is expressed by spatial derivatives of particle-displacement field, and this is, in fact, the reason that we must put equality for wave components with similar wave numbers, including sign, separately). Hence, we obtain at $x = 0$

$$\left.\begin{array}{l} a + \beta b = a^+ \\ a + \beta^* b = 0 \end{array}\right\}, \quad \left\{\begin{array}{l} a^- = a\gamma_1 + b\gamma_2\beta^* \\ b^- = a\gamma_1 + b\gamma_2\beta \\ b^+ = a\gamma_1 + b\gamma_2\beta^* \end{array}\right. \tag{33}$$

where a^- and $b^\pm$ are searched SAW amplitudes, Fig.3a.

We obtain following solution, describing property of half-infinite rmsc working in stopband, or close to stopband (δ_n small assumed)

$$\begin{array}{ll} a^- = \beta^* \dfrac{\gamma_1 - \gamma_2}{\beta^* - \beta} a^+ \approx 0 & \omega_o = vK'(1 - \frac{1}{3}\Delta v/v),\ \omega_v = vK'(1 + \frac{1}{3}\Delta v/v) \\ b^- = \dfrac{\beta^*\gamma_1 - \beta\gamma_2}{\beta^* - \beta} a^+ \approx \gamma a^+ & b^+ \approx 0,\quad \gamma \approx \dfrac{1 - \sqrt{(\omega - \omega_v)/(\omega - \omega_o)}}{1 + \sqrt{(\omega - \omega_v)/(\omega - \omega_o)}} \end{array} \tag{34}$$

where $\gamma = \gamma_1 \approx \gamma_2$, $|\gamma| = 1$ in stopband and $\gamma \to 0$ for frequencies outside the stopband (ω_o, ω_v).

Let's summarize the features of the discussed rmsc
- its scattering property is perfect in narrow stopband,
- there is no back reflection in the same channel ($a^- \approx 0$),
- there is no transmission in forward direction in the other channel ($b^+ \approx 0$),

as far as we consider rmsc in frame of the above developed simple theory.

CONCLUSIONS

The structure of rmsc can be applied in several SAW devices. First of all it can serve like a "mirrors" and simultaneous track-changer of SAW in SAW resonators (Fig.3b), making their performance better for at least three reasons

- reduction of bulk-wave spurious signals (bulk waves excited by IDT in one channel is not detected by IDT in the other channel),
- the "mirror" good reflection performance is limited to narrow frequency band what reduces the spurious passband of the resonator,
- the reflection of SAW by rmsc is of 'regeneration' nature so that SAW diffraction effects are seriously limited.

Other advantage is simple one-step technology.

Fig.3c) shows dispersive delay line, similar to the so-called RAC SAW device, but with technologically difficult surface grooved reflective array replaced by rmsc. In this rmsc the strip period changes along the structure so that different frequencies are 'track-changed' in different places. This makes SAW path between IDTs dependent on frequency - that is, dispersive delay line.

Acknowledgment

The author wish to express his deep gratitude to Professor C.M. Soukoulis and Dr. R.A. Shivvers of Ames Laboratory for their editorial comments with regard to the paper style and grammar.

This work was supported in part by National Committee for Scientific Research under Grant 3 1212 9101.

Appendix

The identity can be found[10] for periodic function with period 2π (it is assumed that $0 < \theta < \pi$ and $\mathrm{Re}\{\mu\} < 1/2$)

$$\Gamma(\frac{1}{2}-\mu)\sum_{n=0}^{\infty} P_n^{\mu}(\cos\theta)\cos(n+\frac{1}{2})v = \begin{cases} \dfrac{(\pi/2)^{1/2}\sin^{\mu}\theta}{(\cos v-\cos\theta)^{\mu+1/2}}, & 0 \le v < \theta \\ 0, & \theta < v < \pi \end{cases}$$

where P is Legendre function ($P_{\nu}^{0} = P_{\nu}$),

$$P_{-\nu-1}^{\mu}(x) = P_{\nu}^{\mu}(x),\ P_n(-x) = (-1)^n P_n(x),\ n \ge 0,\ P_{\nu}(0) \approx 1-\nu,\ 0 < \nu < 1\,.$$

The first equation can be rewritten as follows for $-\pi < \theta < \pi$, $0 < \Delta < \pi$

$$\sum_{n=-\infty}^{\infty} \alpha_m P_{n-m}(\cos\Delta)e^{-jn\theta} = \begin{cases} \sqrt{2}\dfrac{\alpha_m \exp(-jm\theta)}{\sqrt{\cos\theta-\cos\Delta}}e^{j\theta/2}, & |\theta| < \Delta \\ 0, & \Delta < |\theta| < \pi \end{cases}$$

$$\sum_{n=-\infty}^{\infty} \beta_m S_{n-m} P_{n-m}(\cos\Delta)e^{-jn\theta} = \begin{cases} 0, & |\theta| < \Delta \\ -jS_{\theta}\sqrt{2}\dfrac{\beta_m \exp(-jm\theta)}{\sqrt{\cos\Delta-\cos\theta}}e^{j\theta/2}, & \Delta < |\theta| < \pi \end{cases}$$

where $S_{\nu} = 1$ for $\nu \ge 0$, and -1 otherwise, α_m and β_m are arbitrary constants.

As can be easily noticed, the above pair of functions allows modeling of any periodic function, vanishing in one domain of the period, and having square-root singularities at the edges of the other domain, provided that the function is smooth enough in order to be represented by finite Fourier series $\exp(-jm\theta)$.

Useful identities resulting from Dougall's expansion[7,10] are

$$P_{-\nu}(-\cos\Delta) = \frac{\sin\pi\nu}{\pi}\sum_{n=-\infty}^{\infty}\frac{S_n P_n(\cos\Delta)}{\nu+n}$$

$$P_{-\nu}(\cos\Delta) = \frac{\sin\pi\nu}{pi}\sum_{n=-\infty}^{\infty}\frac{(-1)^n P_n(\cos\Delta)}{\nu+n}$$

$$P_\nu(\Delta)P_{-\nu}(-\Delta) + P_\nu(-\Delta)P_{-\nu}(\Delta) = 2\frac{\sin\pi\nu}{\pi\nu}$$

REFERENCES

1. K.A. Ingebrigtsen, Surface waves in piezoelectrics, *J. Appl. Phys.*, **40**, pp. 2681–2686 (1969)
2. F.G. Marshall, E.G.S. Paige, Novel acoustic-surface-wave directional coupler with diverse applications, *Electr. Lett.*, **7**, pp. 460–464 (1971)
3. E. Danicki, Reversing multistrip coupler, patent pending, P-290108, Apr. 30, 1991
4. A.L. Chamorro, Low loss SAW filter design using reflector multistrip coupler, *IEEE Ultras. Symp. Abstracts*, PO-6, Dec., 1991
5. H. Engan, private communication, Jan., 1992
6. E. Danicki, Generation, and Bragg reflection of SAW in nearly periodic system of elastic metal strips on piezoelectric halfspace, subm. for publ. in *JASA*, 1992
7. K. Bløtekjær, K.A. Ingebrigtsen, H. Skeie, A method for analyzing waves in structures consisting of metal strips on dispersive media, *IEEE Trans*, **ED-20**, pp. 1133–1138 (1973); Acoustic surface waves in piezoelectric materials with periodic metal strips on the surface, *ibid.*, pp. 1139–1146
8. E. Danicki, Theory of periodic interdigital transducer of surface acoustic waves, *J. Techn. Phys.*, **19**, pp. 89–102 (1978)
9. E. Danicki, Propagation of transverse surface acoustic waves in rotated Y-cut quartz substrates under heavy periodic metal electrodes, *IEEE Trans*, **SU-30**, pp. 303–312 (1983)
10. A. Erdélyi, W. Magnus, F. Oberhettinger, F.G. Tricomi, *Higher Transcendental Functions*, McGraw-Hill, NY 1953, v.1

BAND TAILS IN A DISORDERED SYSTEM

M. C. W. van Rossum[1], Th. M. Nieuwenhuizen[1],
E. Hofstetter[2] and M. Schreiber[2]

[1]Van der Waals-Zeeman Laboratorium, Universiteit van Amsterdam
Valckenierstraat 65, 1018 XE Amsterdam, The Netherlands
[2]Institut für Physikalische Chemie, Johannes-Gutenberg-Universität
Jakob-Welder-Weg 11, 6500 Mainz, F.R. Germany

INTRODUCTION

In crystalline solids electronic excitations have a band structure. Energy intervals, in which excitations occur, are separated by band gaps, where the density of electronic states vanishes. At the band edge the density-of-states (DOS) has power law singularities, so-called van Hove singularities.

When a small amount of disorder is introduced into the medium, states occur inside the band gaps of the unperturbed system. This results in a shift of the band edge and a smearing of the singularity of the DOS at the new band edge. As a result, the band edges will have a small tail. Experiments are often fitted to an exponential decay, often termed as the Urbach tail [1]. Theoretical results are available for binary disorder (Lifshitz tail [2]), for Gaussian disorder in continuous and discrete space (Halperin-Lax tail [3–4]) and the Lloyd model [5]. It is the purpose of the present work to provide a precise theory for the DOS.

The problem has been studied extensively, see for instance references [6–8]. Most of the previous approaches use either techniques like the CPA method and its extensions, or use field theoretical methods. Both methods have drawbacks. The first is not suited to calculate the tails in the DOS if the random values of the potential are bounded. In the second method, to our knowledge, the correct prefactors have not been calculated for a lattice model. It is the purpose of the present work to provide a theory using a field theoretical approach for the tail in the DOS without adjustable parameters. We show that renormalization improves our results. Furthermore, we present a new type of effective medium theory to calculate the DOS inside the band. We have also performed extensive numerical simulations, which extend previous results [9–10] to more and larger systems. In this way the statistical fluctuations, even in the far tail, are small and a comparison with the theoretical predictions over a large energy range can be made.

Photonic Band Gaps and Localization, Edited by
C.M. Soukoulis, Plenum Press, New York, 1993

THEORY

We consider the Anderson model on a simple square lattice. Hopping is described by a lattice Laplacian. In addition, there is a random potential V. At each lattice site r, its value V_r is drawn at random from a distribution $\nu(V)$. The Hamiltonian is thus given by

$$H = -\Delta + V \,. \tag{1}$$

We are interested in the density-of-states

$$\rho(E) = \lim_{N\to\infty} \frac{1}{N} \sum_{i=1}^{N} \delta(E - E_i) \,, \tag{2}$$

where N is the number of lattice points and where the E_i are the eigenvalues of the Schrödinger equation $H\psi_i = E_i\psi_i$

Apart from describing amorphous materials, the model can also be used to describe electrons interacting with phonons in a pure crystal. The disorder is caused by displacement of atoms, hence this model is valid on short time-scales when the phonons are frozen. The disorder will have a Gaussian distribution. Urbach originally stated his experimental rule for the absorption intensity of such a system (the absorption intensity is closely related to the DOS, see reference [9]). The density-of-states follows from Green's function as

$$\rho(E) = \frac{1}{\pi N} \sum_{r} \mathrm{Im}\, \overline{G_{r,r}(E + i0)} \,. \tag{3}$$

The bar indicates averaging over all disorder configurations. Green's function is written as a path integral

$$G_{r,r'}(E) = \int D\overline{\Psi} D\Psi \exp[\sum_{r} -\overline{\Psi}_r(-\Delta - E + V_r)\Psi_r]\ \phi^*_r \phi_{r'} \,. \tag{4}$$

This expression involves the two-component field $\Psi_r = (\phi_r, \chi_r)$, where ϕ_r is a boson field and where χ_r is a Grassman field [11]. This allows Green's function to be averaged over the impurity potentials, yielding

$$\overline{G_{r,r'}(E)} = \int D\overline{\Psi} D\Psi \exp(-A) \phi^*_r \phi_{r'} \,, \tag{5}$$

with an 'action'

$$A = \sum_{r} [-\overline{\Psi}_r(\Delta\Psi)_r - E\overline{\Psi}_r\Psi_r + U(\overline{\Psi}_r\Psi_r)] \,. \tag{6}$$

The effective potential U depends on the distribution of the disordered potential $\nu(V)$,

$$U(x) = -\ln \int dV \nu(V) e^{-Vx} \,. \tag{7}$$

For Gaussian disorder with $\langle V_r \rangle = 0$ and $\langle V_r^2 \rangle = \sigma^2$, the result $U(x) = -\sigma^2 x^2/2$ leads to a ϕ^4-field theory.

Equation (5) is exact, and now approximations must be made to calculate it. The dominant contribution to the tail in the DOS can be obtained from a saddle point solution (also called classical solution or instanton). Fixing the instanton in the boson direction, one inserts $\Psi_r = (f_r, 0)$. The action is stationary when f satisfies the 'classical' equation of motion

$$-\Delta f - Ef + U'(f^2) f = 0 \,. \tag{8}$$

The prefactor of the DOS is determined by the fluctuations around the instanton. At first we approximate the fluctuations with the quadratic terms. Integrating the fluctuations and taking care of the zero mode of the fluctuation matrices, one finally obtains for the tail of the density-of-states:

$$\rho(E) = \left(\frac{\det' M_T}{-\det M_L} \frac{\sum_r f_r^2}{\pi} \right)^{1/2} \exp(-A_c) \,. \tag{9}$$

This expression involves the determinants of the longitudinal and transversal fluctuation matrices

$$M_L = -\Delta - E + U'(f^2) + 2f^2 U''(f^2) \,, \qquad M_T = -\Delta - E + U'(f^2) \,. \tag{10}$$

The matrix M_T has one zero eigenvalue, which has been excluded from the evaluation of the determinant, as indicated by the prime. M_L has one negative eigenvalue.

RENORMALIZATION

The above result can be improved by performing a selfconsistent one-loop renormalization or Hartree approximation [12]. In the continuum renormalization is needed in two or more dimensions to obtain a finite DOS [13]. Although on the lattice the result without renormalization is finite, renormalization leads to an improvement in the prediction for the DOS. In the case of Gaussian disorder, one has a ϕ^4-field theory. Here the renormalization leads to a renormalized energy

$$E_R = E + \sigma^2 g(E_R) \,. \tag{11}$$

With g being the return Green's function, $g(E) = (\frac{1}{-\Delta - E})_{0,0}$. We use the renormalized energy to refine the prediction of the density-of-states [12]. Comparison with numerical data shows us that renormalization significantly improves the theoretical prediction for the tail.

A NEW EFFECTIVE MEDIUM THEORY

We also present a new type of coherent potential approximation for the DOS inside the band. It is based on the same Hartree approximation to the self-energy in our field theoretical description. As stated above, the tail of the DOS is dominated by the instanton solution of (6). Inside the band, the trivial solution ($f = 0$) becomes the most important one and we obtain the self consistent equation for g:

$$g = \left(\frac{1}{-\Delta - E - \sigma^2 g} \right)_{0,0} \,. \tag{12}$$

Since g is a complex quantity now, the DOS can be extracted immediately using

$$\rho(E) = \frac{1}{\pi} \mathrm{Im}\, g(E + i0) \,. \tag{13}$$

The transition between the renormalized instanton and this regime occurs at the band edge of the new effective medium theory. This band edge is given by

$$\frac{dE}{dE_R} = 0 \,. \tag{14}$$

RESULTS

The above theory has been applied to a particle on a square lattice in the presence of a Gaussian white-noise potential. The potential V has average zero and is delta-correlated with variance $\sigma^2 = \frac{4}{3}$. We have solved numerically the non-linear equation of motion (8). The determinants were also determined numerically. The results are presented in Figure 1. In the absence of disorder, the unperturbed band edge lies at $E = 0$. In the presence of disorder there is a tail which extends to $E = -\infty$. The dotted curve in Figure 1 represents the predictions from the bare instanton calculation and already gives a good description of the data for energies deep in the tail. The solid curves represent the predictions from the renormalized theory and further improve the theoretical prediction. This improvement can be seen by comparing the bare instanton theory and the renormalized instanton curves with the result of our numerical experiment.

The numerical data for the density-of-states have been obtained on a square 100x100 lattice with periodic boundary conditions. The matrix (1) was diagonalized by means of the Lanczos algorithm. The resulting eigenstates yield a strongly fluctuating density-of-states, corresponding to the actual configuration of the disordered potential. To improve the statistics, an average over 70 samples in the Hartree band edge regime and up to 2100 samples in the far tail was taken.

Figure 1 clearly shows a reasonable agreement between the numerical simulation and the bare instanton approach. After renormalization, the agreement is very good. It should be noted that the absolute values of the DOS are plotted, as all prefactors are explicitly taken into account in our theory. It can also be seen that Urbach's rule, which would correspond to a straight line in Figure 1, works quite well.

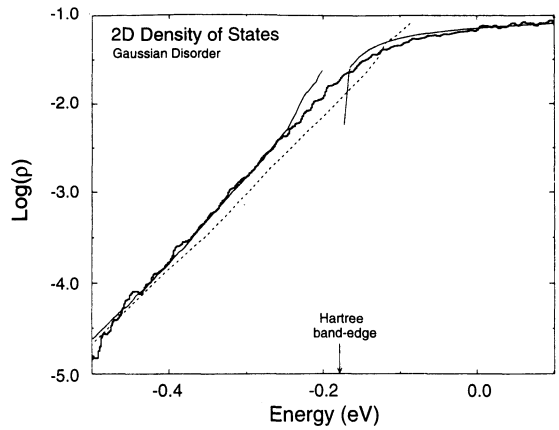

Figure 1. Density-of-states for a tight-binding model on a square lattice in the presence of a random potential with Gaussian statistics. Histogram: data from the numerical simulation. Dashed curve: bare instanton theory. Full curves: instanton after Hartree summation (left part), CPA-like Hartree summation (right part).

CONCLUSION

We have presented a precise method to calculate the tail of the density-of-states of a disordered system. It includes all numerical prefactors and there are no adjustable parameters. It can be used in the continuum and on the lattice, in all dimensions. Various disorder distributions are also possible, for instance binary [14] or uniform disorder. The results of our method match the numerical data very well, especially if renormalization is used. We also presented a new effective medium theory to calculate the density-of-states inside the band. This method also agrees with numerical simulation.

It may be possible to use the same technique for calculating transport properties like the ac-conductivity of disordered systems. The calculation would be more elaborate as two-instanton solutions are needed [15].

References

[1] F. Urbach. Phys. Rev. **92** (1953) 1324.

[2] I.M. Lifshitz. Adv. Phys. **13** (1964) 483.

[3] B. I. Halperin. Phys. Rev. A **139** (1965) 104.

[4] B.I. Halperin and M. Lax. Phys. Rev **148** (1966) 722.

[5] P. Lloyd. J. Phys. C **2** (1969) 1717.

[6] S. John, M.Y. Chou, M. H. Cohen, and C. M. Soukoulis. Phys. Rev. B **37** (1988) 6963.

[7] M. H. Cohen, M. Y. Chou, E. N. Economou, S. John, and C. M. Soukoulis. IBM J. Res. Dev. **32** (1988) 82.

[8] E. N. Economou, C. M. Soukoulis, M. H. Cohen, and A. D. Zdetsis. Phys. Rev. B **31** (1985) 6172.

[9] M. Schreiber and Y. Toyozawa. J. Phys. Soc. Jpn. **51** (1982) 1528, 1537, 1544 1551.

[10] M. Schreiber and Y. Toyozawa. J. Phys. Soc. Jpn. **52** (1983) 318.

[11] Th. M. Nieuwenhuizen and G. Forgacs. Europhys. Lett. **15** (1991) 837.

[12] Th. M. Nieuwenhuizen. Physica A **167** (1990) 43.

[13] E. Brezin and G. Parisi. J. Phys. C **13** (1980) 307.

[14] Th. M. Nieuwenhuizen. Phys. Rev. Lett. **62** (1989) 357.

[15] R. Hayn and W. John. Nucl. Phys. B **348** (1991) 766.

WORKSHOP ON LOCALIZATION AND PROPAGATION OF CLASSICAL WAVES IN RANDOM AND PERIODIC MEDIA
held on May 26-30, 1992
in Aghia Pelaghia, Heraklion, Crete

AUTHOR INDEX

INDEX